QST-M-2

QST Takasaki Annual Report 2015

Takasaki Advanced Radiation Research Institute

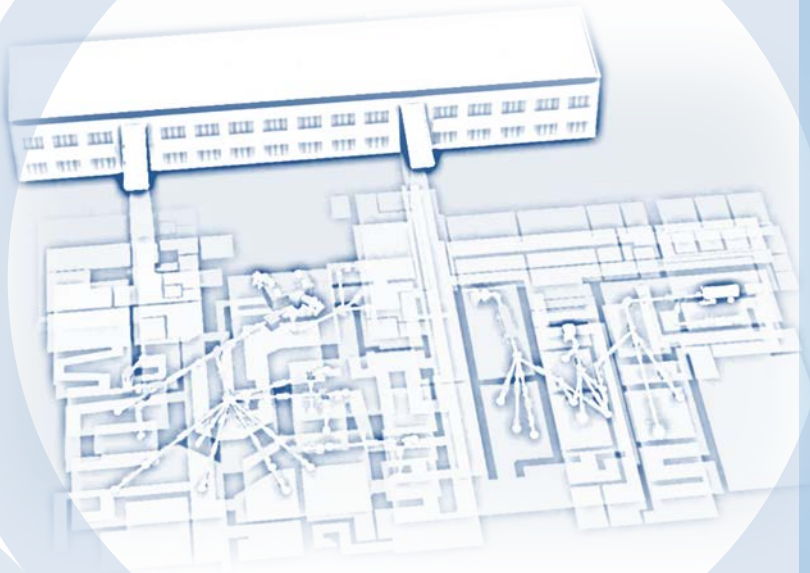

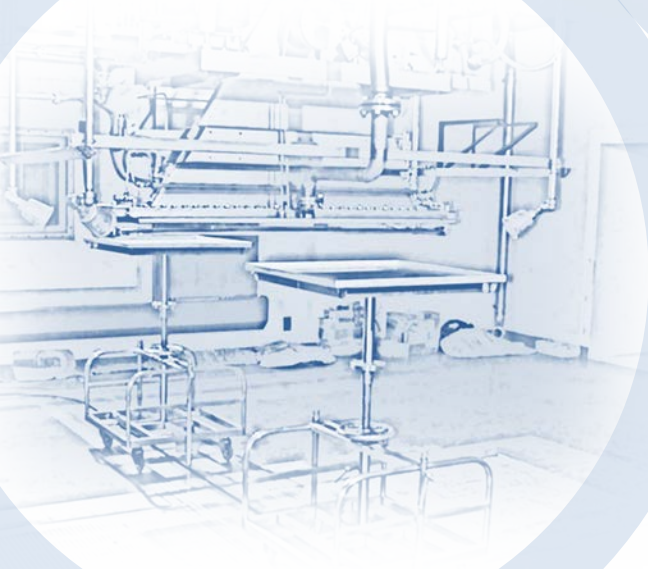

National Institutes for Quantum and

Radiological Science and Technology

Preface

Hisayoshi Itoh

Director General
Takasaki Advanced Radiation Research Institute
Quantum Beam Science Research Directorate
National Institutes for Quantum and Radiological Science and Technology

National Institutes for Quantum and Radiological Science and Technology (QST) was established in April of 2016 by integrating the National Institute of Radiological Sciences (NIRS) and some institutes promoting quantum beam science research and nuclear fusion research in the Japan Atomic Energy Agency (JAEA). The QST has three R&D directorates, *i.e.*, Quantum Beam Science Research Directorate (QuBS), Radiological Science Research and Development Directorate, and Fusion Energy Research and Development Directorate. In the QuBS, in which two research institutes of Takasaki Advanced Radiation Research Institute (TARRI) and Kansai Photon Science Institute (KPSI) are involved, we are intensively performing fundamental and applied research in a wide range of fields like materials science, life science, and quantum beam technology, using advanced beam facilities. Every institute has two research sites, *i.e.*, Takasaki and Tokai sites of TARRI, and Kizu and Harima sites of KPSI. Typical beam facilities we used are Takasaki Ion Accelerators for Advanced Radiation Application (TIARA) at the Takasaki site, Japan Proton Accelerator Research Complex (J-PARC) at the Tokai site, Kansai Advanced Relativistic Engineering Laser System (J-KAREN) at Kizu site, and highly sophisticated beamlines of Super Photon Ring-8 GeV (SPring-8) at Harima site.

In the TARRI, we have 15 Research Projects making quantum beam science R&Ds with TIARA, 2 MeV electron accelerator, ^{60}Co gamma-ray irradiation facilities, etc., for contributing to the progress of science and technology as well as the promotion of industry. We are also performing R&D of advanced ion beam technology at the Beam Engineering Section of the Department of Advanced Radiation Technology. In addition, our beam facilities are open to industry, academia, and governmental research institutes, and the beam time is allocated for users based on the evaluation of their R&D programs.

This Annual Report covers the research activities at the TARRI primarily for the fiscal year 2015 (FY 2015). This report consists of two parts, Part I and Part II. In Part I, the recent activities of all Research Projects of TARRI are described. Every Research Project has been steadily promoting its R&D, and several excellent topics were obtained as followings. In the field of materials science, single photon source (SPS) can be introduced in SiC *pn* diodes, which were fabricated by hot-implantation of P or Al ions at 800 ºC into *p*- or *n*-type epitaxial layer substrates,

respectively, and subsequent annealing up to 1,800 ºC. Observation of bright electro-luminescence revealed SPS fabrication with high thermal stability. In the field of life science, identification of a new gene that controls anthocyanin accumulation in plant seed coats has been succeeded. By detailed analyses of the mutant, the *FFT* promoter activity was detected in the seed-coat layers that accumulate anthocyanins. The results suggest that the FFT protein acts at vacuolar membrane and is essential for anthocyanin accumulation in vacuoles of the plant seed coat cells. In the field of advanced quantum-beam technology, an adsorbent for extraction chromatography was analyzed by particle induced X-ray emission combined with computer tomography (PIXE-CT). Cross sectional distributions of residual Nd can be non-destructively analyzed with spatial resolution of several μm.

Part II describes the recent R&D results obtained by using quantum beam facilities of the TARRI. This part is composed of 154 research papers in the fields of materials science, life science, and advanced quantum beam technology, and 8 status reports on operation/ maintenance of the quantum beam facilities. Typical topics are described below.

In the field of materials science, the intensive studies have been conducted for radiation effects in electronic components used in space. R&D of radiation effects focusing on radiation damages and tolerance has been continued for developing semiconductor devices such as SiC Schottky barrier diodes and high electron mobility transistors, GaAs and GaN based solar cells, and quantum-well-based hall sensors in connection with their application to artificial satellites and space crafts. The radiation induced structural changes, which relate to radiation damages and tolerance, in metallic materials such as steels and Ni alloys, have been intensively investigated as R&D of nuclear fission technology. Similar R&D has been also conducted for nuclear fusion materials like hydrogen isotope-W and SiC fibers, and for J-PARC components such as charge stripper foils and rotation target. Concerning nano/micro fabrication using quantum beams, new functional devices like SPS have been successfully obtained by ion or electron irradiation to wide bandgap semiconductors like SiC. The new architectures of inorganic and organic materials in the scale ranges from nano- to micro-meters have also been fabricated; *i.e.*, Cu nano-corns and near-perfect optical absorbers were developed using ion track etching technique, fuel cell catalysts and membranes were fabricated by metal implantation and ion beam-induced grafting, and hydrogel nanowires were created by proton-beam-writing (PBW). In addition, gamma-ray and electron beam induced graft-polymerization techniques have widely been studied for functional polymer fabrics and membranes; the formers were applied to fibrous catalyst for bio-diesel fuels and antivirus materials, and the latters were applied to proton-exchange membranes to concentrate HI in the IS process, gas separation membranes, and anion exchange membranes for platinum free fuel cells. Ion implantation into carbon ceramic and silica glass materials is also utilized to develop

new catalysts with high oxygen reduction activity for fuel cells and magnetic/optical materials. Regarding R&D for decommission of Fukushima power plants, practically available results were obtained for evaluation of radiolytic hydrogen generation and radiation resistance for inorganic absorbents in Advanced Liquid Processing System (ALPS) wastes. The radiation resistance of semiconductor devices used for decommission was also evaluated. The new analytical method using PIXE was adopted for low level radioactive wastes.

In the field of life science, radiation-induced bystander effects between human normal and cancer cells were examined. The cells for irradiation were inoculated in a co-culture insert and irradiated with ^{60}Co gamma-rays. Thereafter, irradiated and non-irradiated cells were co-cultured for 24 hours, and the extent of bystander effects were examined with colony formation assay without reseeding non-irradiated bystander cells. The result indicates that the bystander cell-killing effect was not induced between different type cells in these experimental conditions. On the other hand, the ion microbeam analysis with particle-induced X-ray/gamma-ray emission (micro-PIXE/PIGE) system for elemental mapping of bio-medical samples was widely applied to investigation of the effects of wakosil (silica gel as a model of PM2.5) and nicotine in lung microvascular endothelial cells, analysis of intracellular boron distribution of cultured cells, analysis of multiple myeloma cell line, fluoride varnish remaining after physical stress for tooth, protamine-hyaluronic acid particles as a drug delivery system utilizing radiotherapy, and so on. Radionuclides produced by charged particles or accelerator neutrons have great potential for medical applications. As a new approach for Positron Emission Tomography (PET) imaging of cancer with ^{64}Cu ions, the specific cellular uptake of ^{64}Cu ions was evaluated using several kinds of cancer, such as human glioblastoma, human colon adenocarcinoma, and human cholangiocarcinoma. Higher radioisotope production rates of ^{67}Cu and ^{90}Y were achieved by the Be(d,n) reaction and 50 MeV deuterons increased by 10 MeV from 40 MeV. Radiotracer imaging technologies elucidated the effects of glutathione on cadmium translocation in Oilseed rape plants, and patterns of root secretions of organic substances in soybean seeds, using a positron-emitting tracer imaging system (PETIS) and radioisotopes of ^{107}Cd and $^{11}CO_2$. In medical imaging, noninvasive beam monitoring method by measuring secondary electron bremsstrahlung (SEB) is being developed to control dosages in particle beam therapies. In particular, a development of Cherenkov light imaging technique featured the latest breakthroughs in spatial resolution of the radiotracer imaging for life science studies. The ion beam breeding technology has been continuously applied to generate valuable plants and microorganisms. Remarkably, under the international cooperation of the Forum for Nuclear Cooperation in Asia (FNCA), the project “Mutation Breeding of Rice for Sustainable Agriculture” has been conducted and some attractive rice mutant candidates were reported from several countries such as Bangladesh, Vietnam and Malaysia.

As for the advanced quantum beam technology, neutron energy spectra of keV region in the high energy quasi-monoenergetic neutron field at TIARA were obtained for the first time using single pulse beams. A roll-to-roll irradiation system was developed for continuous irradiation of long polymer membranes with a horizontally-elongated (ribbon-shaped) heavy ion beam formed by octupole magnetic field. Fundamental and applicational researches of cluster ion beam systematically proceeded on modification of semiconductor surface or magnetic property of FeRh films, development of nano-organic materials, emission of secondary ions from organic or inorganic materials, as well as experimental and theoretical investigation of interaction between cluster ions and matters. Analyses of various materials were performed using PIXE/PIGE and ion beam-induced luminescence (IBIL) with an ion microbeam, Rutherford backscattering spectrometry (RBS) and elastic recoil detection (ERD) with a usual ion beams, and electron spin resonance (ESR): the micro-PIXE-CT was applied to measurement of 3D distribution of cesium in clay particles. Evaluation of epitaxial quality was examined by means of RBS-channeling method. ESR was used to estimate sediment provenance in Toki Gravel Formation. Developments of practical technology were also in progress with regard to active magnetic field stabilization by PID (proportional-integral-derivative) control of the magnet coil current based on the measured magnetic field strength for more stable microbeam utilization and phosphor screen monitor for real-time tuning of the large-area 2D fluence distribution at the cyclotron, and a negative-C_{60} ion source for higher intensity at the tandem accelerator.

Concerning the status of quantum beam facilities, four accelerators in TIARA, the AVF cyclotron, the 3 MV tandem accelerator, the 3 MV single ended accelerator and the 400 kV ion implanter, were operated steadily and safely as well as ^{60}Co gamma-ray irradiation facilities in FY2015, whereas the electron accelerator had machine troubles due to its aged deterioration. Since a lot of time was needed for repairing troubles in the electron accelerator, its operation time in FY2015 decreased to 80% of that in the normal operation case. Total operation times of the cyclotron, the tandem accelerator, the single-ended accelerator and the ion implanter were 78,164, 44,648, 51,175 and 39,627 hours, respectively, which were counted from their first operation, *i.e.*, 1991 for the cyclotron and the tandem, and 1993 for the single-ended and the ion implanter. The total number of experiments made by various users using the AVF cyclotron was 11,354 from the first beam extraction in 1991 to March 2016, as a result of continuous efforts such as regular maintenance and troubleshooting.

Finally, we extend gratitude to both our domestic and foreign colleagues for their cooperation, support, and encouragement for our quantum beam science R&Ds as well as technological advance in the facilities of TARRI.

Facilities

Charged particle beams and RI facilities

Takasaki Ion Accelerators for Advanced Radiation Application (TIARA) consisting of four ion accelerators, an electron accelerator, and gamma irradiation facilities are available to researchers in QST and other organizations for R&D activities on new functional and environmentally friendly materials, biotechnology, radiation effects of materials, and quantum beam analysis. We are developing microbeams, single ion hits and uniform wide-area irradiation technique at the cyclotron. In addition, technical developments of three dimensional in-air PIXE analysis and production/acceleration of cluster ion beam such as C_{60} fullerene at the electrostatic accelerators are in progress.

Takasaki Ion Accelerators for Advanced Radiation Application: TIARA

TIARA buildings

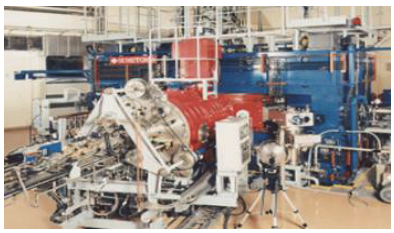

Cyclotron

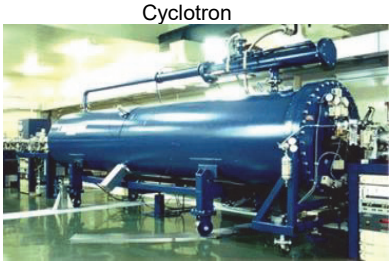

Tandem accelerator

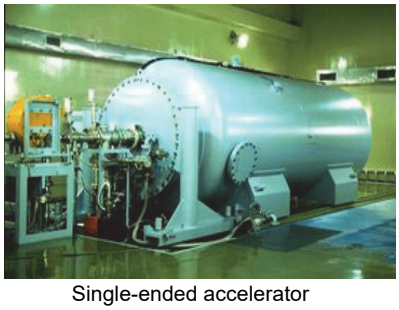

Single-ended accelerator

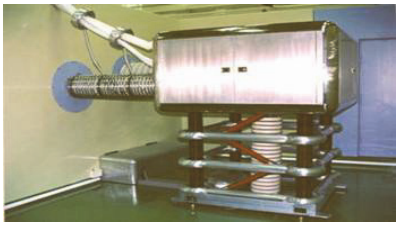

Ion implanter

Typical available ions

Accelerator	Ion	Energy (MeV)
AVF Cyclotron (K=110MeV)	H	10～ 90
	He	20～107
	C	75～320
	Ne	75～350
	Ar	150～520
	Fe	200～400
	Kr	210～520
	Xe	324～560
	Os	490
Tandem Accelerator (3 MV)	H	0.8～ 6.0
	C	0.8～18.0
	Ni	0.8～18.0
	Au	0.8～18.0
	C_{60}	0.8～6.0
Single-ended Accelerator (3 MV)	H	0.4～ 3.0
	D	0.4～ 3.0
	He	0.4～ 3.0
	e^-	0.4～ 3.0
Ion Implanter (400 kV)	H	0.02～0.38
	Ar	0.02～0.38
	Bi	0.02～0.37
	C_{60}	0.02～0.36

Energy-element range covered by the four accelerators

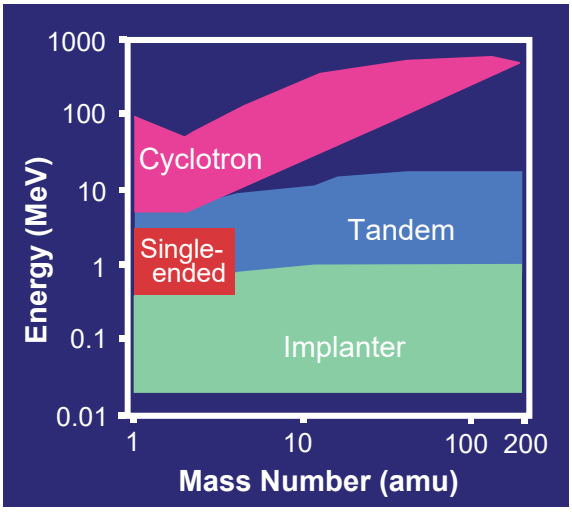

Cobalt-60 gamma-ray and electron beam irradiation facilities

Gamma-ray irradiation facility building

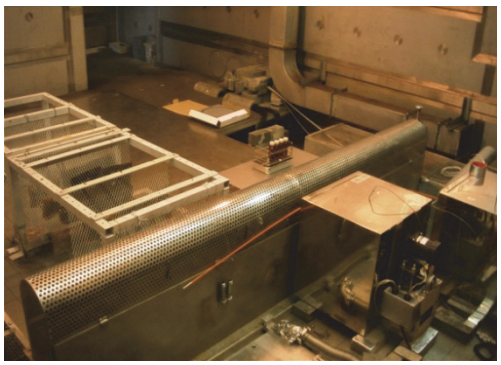

Gamma-ray irradiation room

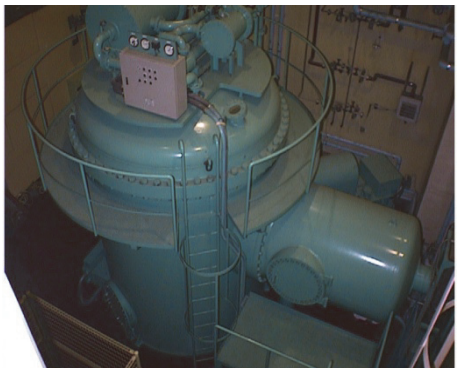

Electron accelerator
(0.5～2.0 MeV 0.1～30 mA)

Electron irradiation room with conveyor system

Specification

Apr.2016

Name of facility	Cobalt-60 activity(PBq)	Number of rooms	Purpose
Co No.1 bld.	10.4	3	Radiation-resistance test Radiation effects on polymers
Co No.2 bld.	10.8	3	R & D on functional organic materials, dosimetry
Food Irrad.	3.7	2	Radiation effects on biological substance and semiconductors

Dose-rate range

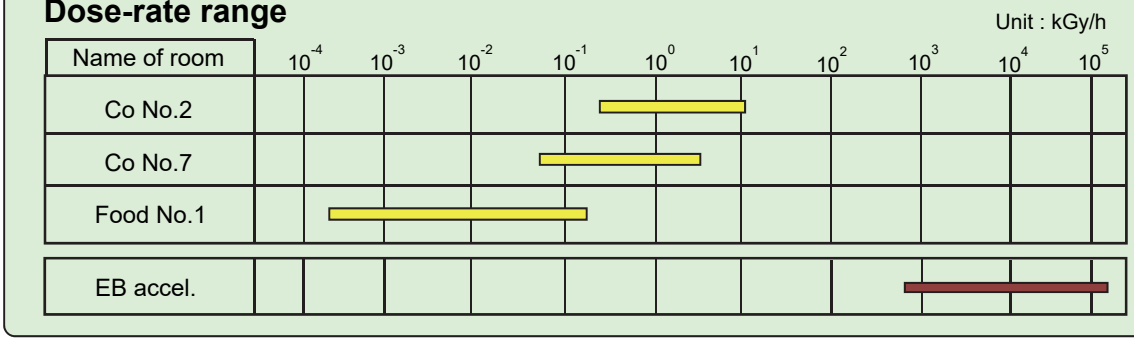

Contents

Part I

Part II

Part I

Part I

1. Materials Science

P1-1 Functional Polymer Research Project

Leader : Yasunari Maekawa

Project “Functional Polymer Research” has been developing the functional polymer materials for high performance fuel cells and hydrogen collection systems by using quantum beams such as electron beams, γ-rays and ion beams. We have synthesized the proton- and anion-conducting electrolyte membranes (PEM and AEM) and the hydrogen permselective membranes. We report herein two recent developments: poly(ether ether keton) (PEEK)-based PEMs and poly(ethylene-co-tetrafluoroethylene) (ETFE)-based AEMs for hydrogen- and alkaline hydrated hydrazine-fuel cells applied in automobiles. {1-21~22 in Part II}

PEEK-based PEMs for high conducting under various humidified conditions [1]

Recent main concerns for PEMs are higher proton conductivity at low relative humidity (RH) and superior mechanical properties under humid conditions because these properties affect the power generation efficiency and the durability under extreme operating conditions in fuel cell systems.

In order to break through the trade-off relationship between the conductivity and mechanical properties, we had selected PEEK as a base film that possesses the highest mechanical and thermal properties among super engineering plastics. PEEK-based PEMs were prepared via a three-step process [2]. The prepared PEEK-PEMs with ion exchange capacities (IECs) > 3.08 mmol/g exhibited similar conductivity (9 mS/cm) under 30% RH and showed 1.4 times higher tensile strength (14 MPa) under 100% RH at 80 °C, compared with those of Nafion212. The membrane/ electrolyte assembly (MEA) fabricated by using the PEEK-PEM with IEC = 2.45 mmol/g showed a maximum power densities (*Emax*) of 860 and 826 mW/cm^2 at 2140 and 2180 mA/cm^2 under 100% and 30% RH, respectively, as shown in Fig. 1. The PEEK-PEM showed low RH dependence of *Emax*; as a result, at 30% RH, the PEEK-PEM exhibited 2.5 times higher *Emax* than that of Nafion212. Based on X-ray scattering analyses, the crystallinity of ca. 28-32% were maintained in the PEEK- PEMs even after the graft-polymerization. Therefore, it was found that the higher conductivity and tensile strengths compared with Nafion resulted from the unique structure in the PEEK-PEM.

Development of the 4-vinylimidazolium/St-co-grafted AEMs {1-22}

In the previous study, we reported the properties of AEMs prepared by radiation-induced grafting of *N*-vinylimidazole into ETFE films, and followed by *N*-alkylation with methyl iodide. The prepared AEMs (NVIm-AEM) degraded via rapid β-elimination at the initial period and slow hydrolytic ring opening reaction of the imidazolium unit at the later period [3].

To prevent the β-elimination and the ring opening reaction we newly synthesized the ETFE-based AEM with the graft chains consisting of 2-metyl-N-methyl-4-vinylimidazole (2Me-NMe-4Vim) and styrene (St). The prepared 2Me-NMe-4Vim/St-AEM with 1.74 mmol/g of IEC exhibited the conductivity of 157 mS/cm and the water uptake of 86%. Figure 2 shows the alkaline stability of AEMs in 1M KOH aqueous solution at 80 ºC. The conductivity of NVIm-AEM decreased with increasing immersion time and reached almost 0 mS/cm after 100 h, while 2Me-NMe-4Vim/St-AEM showed the conductivity of 104 mS/cm after 86 h. Thus, the decrease in the conductivity at the initial period was effectively suppressed by the shift of vinyl substituent from 1- to 4-positon of the imidazolium ring and by the copolymerization with hydrophobic styrene. On the other hand, the ring opening reaction inducing the decreases in the conductivity at the later period was avoided by the methyl-protection at 2-position of the imidazolium ring. Accordingly, the 2Me-NMe-4Vim/St-AEM processed excellent initial and long term alkaline stabilities.

References

[1] T. Hamada *et al.*, J. Mater. Chem., **3**, 20983 (2015).
[2] S. Hasegawa *et al.*, Polymer, **52**, 98 (2011).
[3] K. Yoshimura *et al.*, Electrochem. Soc., **161**, F889 (2014).

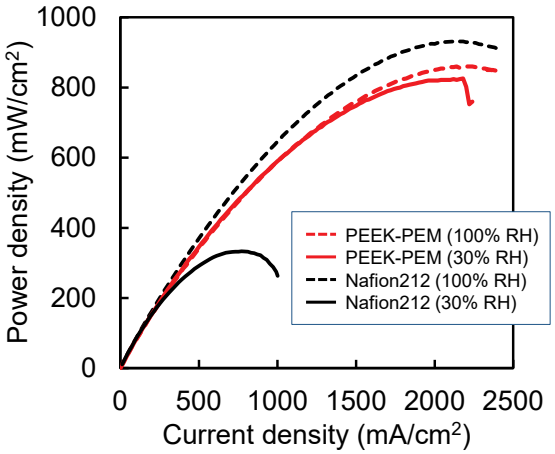

Fig. 1. Fuel cell performance of MEAs fabricated with PEEK-PEM and Nafion212 under various RHs at 80 °C.

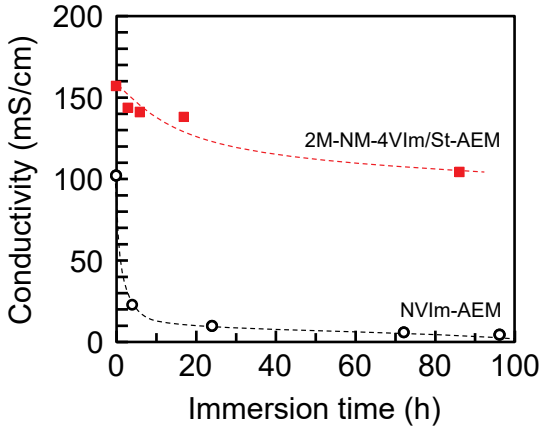

Fig. 2. Alkaline stabilities of NVIm- and 2M-NM-4Vim/St- AEMs.

P1-2 Advanced Catalyst Research Project

Leader : Tetsuya Yamaki

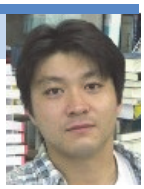

We have been developing catalytic materials for next-generation energy devices such as secondary batteries and fuel cells by effective use of ion beams, electron beams and γ-rays. The advantage of our overarching research strategy is that these quantum beams can lead to high-energy defect creation, active-site formation via non-equilibrium chemical reactions, and micro-to-nano fabrication, which have a great potential to facilitate the development of novel functional materials through innovative interdisciplinary methodologies. This report deals with applications of the charged-particle beams to nanomaterials science for oxygen reduction reactions (ORR) in rechargeable metal-air batteries and polymer electrolyte fuel cells (PEFCs). {1-13~19, 1-23~25, 1-28~30, 3-12 in Part II}

Preparation of non- and low-platinum electrocatalysts by irradiation with keV-ion and electron beams {1-14, 1-25, 1-30, 1-28~29}

Non- or low-platinum (Pt) ORR electrocatalysts are needed to lower the device cost. Quite recently, we have reported ion-implanted phosphorus- or boron-doped silicon nanoparticles (NPs) and heterostructured silicon carbide nanotubes [1, 2], confirming high controllability of impurity doping and defect formation. Therefore, our advanced methods using low-energy keV ions as well as electron beams were pursued for preparation of carbon-based non-Pt catalysts and highly-active Pt NPs.

Nitrogen-doped (N-doped) carbon materials are expected as Pt alternatives, and however there have been so far no established methods to introduce N atoms into graphene structures. Thus, N doping in carbon-based catalysts has been attempted by electron beam irradiation in ammonia or pulsed laser deposition in N_2. Implantation of 100 keV N^+ was also considered in order to clarify the ORR mechanism and involved active sites.

Additionally, we found that the Pt NPs supported on a glassy carbon (GC) substrate pre-irradiated with 380 keV Ar^+ exhibited strong electronic interactions with carbon atoms at the interface (Fig. 1) [3]. These unique interactions originating from the ion-beam-induced lattice defects could affect the ORR activity of the Pt NPs by tuning their electronic structures. X-ray absorption fine structure (XAFS) measurements in combination with theoretical calculations are now in progress to examine the local interfacial structures.

This work was partly performed under the RIKEN-NIMS -JAEA-QST Cooperative Research Program on Quantum Beam Science and Technology.

New nano-sized materials prepared by swift-heavy-ion technology and their high applicability {1-13~14, 1-24}

An MeV-GeV heavy-ion beam gives one-dimensional polymer nanostructures through its high energy deposition within a limited cylindrical area along the path, *i.e.*, an ion track. Crosslinking reactions occur in the ion track, yielding a nanowire by subsequent development to remove the non-crosslinked parts, while degradation reactions occur to afford a straight nanopore after preferential dissolution of the ion track. We prepared a variety of new nanomaterials for PEFC applications [4], ion-conductive membranes and catalytic systems, using these characteristic nanostructures.

We fabricated polymer/metal-NP hybrid nanowires with extremely high specific surface area for electrocatalysts [5]. Polyvinylpyrrolidone (PVP), known as capping agent of metal NPs, was chosen as a base material. The PVP films containing hexachloroplatinic acid (H_2PtCl_6) were bombarded with 490 MeV ^{192}Os. Interestingly, each of the ion tracks underwent not only the PVP crosslinking but also the reduction of Pt ions. The radius of the nanowires and the number density of Pt NPs were controlled by the H_2PtCl_6 concentration (Fig. 2).

Stacked 25-μm thick polyethylene terephthalate (PET) films were irradiated with 250 MeV ^{40}Ar. The lowermost film, inside which the bombarding ions were found to stop, was etched chemically to prepare an ion-track membrane with non-penetrating conical pores. A combination of plasma sputter deposition and electroplating provided Pt nanocones with a base diameter of 330 nm and a height of 2.5 μm.

References

[1] T. Nakamura *et al.*, Phys. Rev. B, **91**, 165424 (2015).
[2] T. Taguchi *et al.*, Carbon, **95**, 279 (2015).
[3] T. Kimata *et al.*, Surf. Coat. Tech., in press.
[4] N. Nuryanthi *et al.*, Trans. Mater. Res. Soc. Jpn., **40**, 359 (2015).
[5] S. Tsukuda *et al.*, Radiat. Phys. Chem., **118**, 16 (2016).

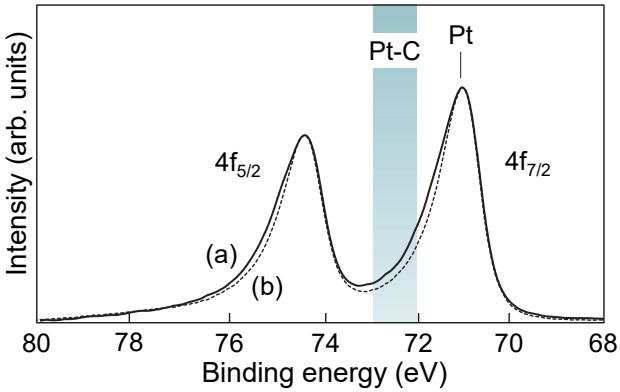

Fig. 1. Pt 4f X-ray photoelectron spectra of (a) the Pt NPs on the GC substrate pre-irradiated with 380 keV Ar^+ at a fluence of 1.0×10^{16} ions/cm^2 (solid line) and (b) the standard Pt foil (dashed line).

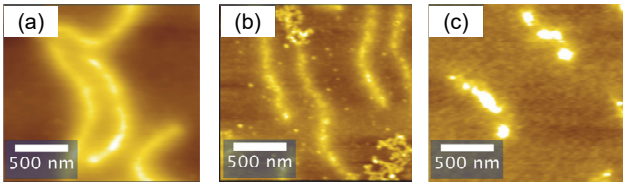

Fig. 2. Atomic force microscopy images of (a) PVP and (b–c) PVP/Pt-NPs nanowires. The PVP/H_2PtCl_6 precursor films were prepared from the solution containing (b) 0.125 or (c) 0.375 wt% $H_2PtCl_6\cdot6H_2O$.

P1-3 Positron Nano-Science Research Project

Leader : Atsuo Kawasuso

Spintronics is promising to go beyond traditional electronics. The aim of our research is to reveal detailed characteristics of spintronics materials using spin-polarized positron beam. We are currently investigating the band structure of half-metals, vacancy-induced ferromagnetism in semiconductors, current-induced spin polarization (CISP) at metal surfaces and so on. We are also developing the further new technique such as spin-polarized positronium time-of-flight method to obtain spin-polarized density of states associated with metal surfaces.

Vacancy-induced ferromagnetism of ZnO

Various metal-oxides and metal-carbides show ferromagnetism depending on crystal growth condition, heat treatment and particle bombardment even though those are not ferromagnets originally. Defects are thought to be one reason for such ferromagnetism. That is, both anion and cation vacancies, interstitials and some strains can be the sources of ferromagnetism. Previous positron annihilation studies combined with magnetization measurement suggest that cation vacancies give rise to ferromagnetism in ZnO and SnO_2 [1]. However, simple comparison of ordinary positron annihilation spectroscopy and magnetization measurement provides an indirect evidence that vacancies are the source for ferromagnetism. In light of this, detection of magnetic moments at vacancies using spin-polarized positron annihilation spectroscopy will be a direct evidence of vacancy-induced ferromagnetism. In this study, we apply this method to ion-irradiated ZnO.

Samples used in this study are hydro-thermally grown ZnO(0001) single crystals. To improve crystallinity, these are subjected to heat treatment at 1,200 °C in air. Subsequently, these are irradiated with 100 keV oxygen ions up to a dose of 5×10^{16} ions/cm^2 at room temperature. Magnetization measurements are carried out using a superconducting quantum interference device (SQUID) apparatus. The Doppler broadening of annihilation radiation (DBAR) measurements are performed at room temperature in magnetic fields (±1 Tesla). The obtained experimental data are compared with the first principles calculation.

Figure 1 shows, magnetization curves obtained before and after oxygen-irradiation, and after post-irradiation annealing. For the unirradiated state, no magnetism is found. After oxygen irradiation, a clear ferromagnetic behaviour appears. Furthermore, the ferromagnetism disappears by annealing below 1,200 °C. The above results manifest that ferromagnetism is induced by oxygen irradiation and it disappears with the recovery of irradiation-induced damage by heat treatment.

Figure 2 shows the differential Doppler broadening of annihilation radiation spectra obtained for unirradiated and oxygen-irradiated ZnO single crystals in positive and negative magnetic fields. For the unirradiated state, no apparent difference is found upon field reversal. After oxygen irradiation, a clear difference appears upon field reversal. After oxygen irradiation, most positrons are found to be trapped by vacancy defects. The solid line drawn in Fig. 2 is theoretical DBAR curve for electrically neutral zinc vacancies. Three unpaired electrons involved in a neutral zinc vacancy cause the filed reversal effect. Agreement between experiment and theory is good suggesting that zinc vacancies are responsible for the ferromagnetism. To our knowledge, this is the first direct evidence that vacancy-induced ferromagnetism in ZnO [2].

References

[1] A. Sarkar *et al.,* RSC Adv. **5** 1148-52 (2015).
[2] M. Maekawa *et al*., to be published.

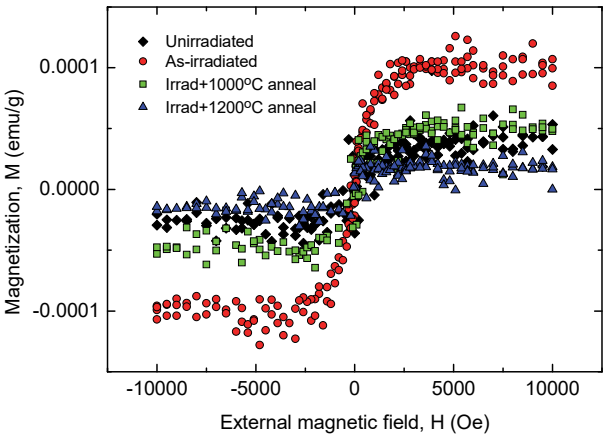

Fig. 1. Magnetization curves for ZnO obtained before and after 100 keV oxygen irradiation and after the post irradiation annealing at 1,000 and 1,200 °C.

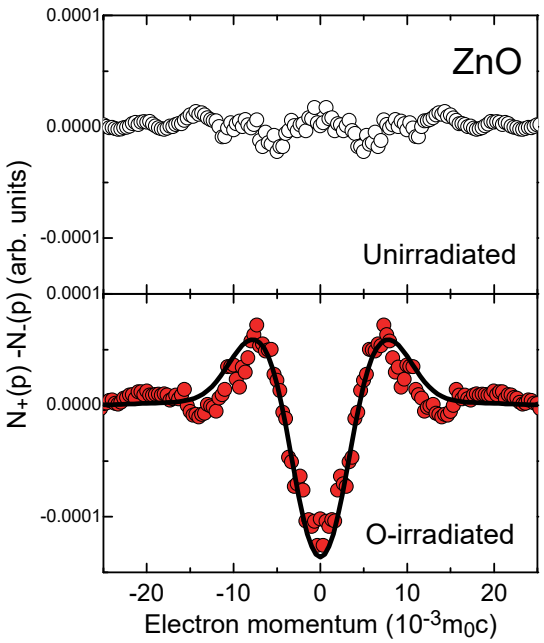

Fig. 2 Differential DBAR spectra between positive and negative magnetic fields obtained for unirradiated and oxygen-irradiated ZnO at room temperature. Solid line is the theoretical DBAR curve for electrically neutral zinc vacancies.

P1-4 Semiconductor Analysis and Radiation Effects Research Project

Leader: Takeshi Ohshima

Technologies based on quantum effects, *i.e.* quantum computation, quantum information and quantum sensing, are expected for our life to be more comfortable, safer and more secure. In order to realize those technologies, single photon sources (SPSs) operating with robust and steady are indispensable. We study defect engineering using ion and electron beams for the creation of SPSs in wide bandgap semiconductors such as diamond and silicon carbide (SiC). Besides, when semiconductor devices are irradiated with radiations such as ion, electrons and gamma-rays, degradation and malfunctions occur in devices. We also study radiation response of semiconductor devices to reveal the radiation degradation/malfunction mechanisms and in addition, establish radiation resistant technologies for development of long lifetime and highly reliable semiconductor devices that can be used in high radiation environments such as space, nuclear and accelerator facilities. {1-01~1-06, 1-09, 1-11, 1-26 in Part II}

Bright SPSs with high thermal stability found in SiC diodes

SiC is regarded as a promising candidate to host SPSs for quantum spintronics, quantum photonics and quantum sensing applications. For example, the silicon vacancy (V_{Si}), divacancy ($V_{Si}V_C$), and carbon antisite carbon vacancy ($C_{Si}V_C$) defects are known to act as SPSs, and their luminescence properties can be controlled at room temperature (RT) [1-4]. In addition, we found a new SPS in SiC *pn* diodes [5]. The *pn* diodes were fabricated on either *n* or *p*-type epitaxial layer hexagonal (4H) SiC substrates. Phosphorus and aluminium ion implantation at 800 °C followed by subsequent annealing at temperatures up to 1,800 °C was carried out to form *n* and *p* type regions, respectively. Figure 1 shows an electro-luminescence (EL) mapping image obtained from the edge of an electrode for a SiC *pn* diode by a confocal fluorescence microscope (CFM). During the CFM measurement, the forward bias above 3.1 V was applied to the diode. A bright EL spot is observed in the figure. The EL spot was confirmed to be a SPS by auto-correlation function measurements at RT. Thus, the EL spot exhibited anti-bunching characteristics. Since annealing at 1,800 °C was carried out to the diode during fabrication process, it can be concluded that the SPS obtained in this study has very high thermal stability.

Gamma-ray radiation response of SiC metal-oxide-semiconductor field effect transistors (MOSFETs) in high dose region

Recently, demand on electronic devices used in harsh radiation environments, such as nuclear and accelerator facilities, increases. For example, electronic devices with extremely high radiation resistance (MGy order) are required for decommissioning of Tokyo electric power Fukushima Daiichi nuclear power station. SiC is regarded as a promising candidate material for high radiation resistant electronics as well as power devices with outstanding excellent characteristics. In this study, radiation response of vertical structure power 4H SiC MOSFETs was investigated [6]. The MOSFETs were irradiated with gamma-rays up to 5.8 MGy(SiO_2) at a dose rate of 3.6 kGy(SiO_2)/h in N_2 atmosphere either at RT or 150 °C. Figure 2 shows the change in threshold voltage (V_T) for the MOSFETs due to irradiation. The values of V_T were estimated from the value at the intersection between the gate voltage (V_G)-axis and the line extrapolated from the curve of the square root of drain current vs. V_G in the saturation region. The shift of V_T due to irradiation was suppressed by irradiation at elevated temperature (150 °C). No significant change or slight recovery in V_T for the MOSFETs irradiated at 150 °C was observed above 1 MGy although the value of V_T for MOSFETs irradiated at RT decreases with increasing dose. This suggests that the degradation of SiC MOSFETs can be suppressed by irradiation at elevated temperature.

References

[1] S. Castelletto *et al.*, Nature Materials, **13**, 151 (2014).
[2] D. J. Christle *et al.*, Nature Materials, **14**, 160 (2015).
[3] M. Widmann et al., Nature Materials, **14**, 164 (2015).
[4] F. Fuchs *et al.*, Nature Comm., **6**, 7578 (2015).
[5] A. Lohrmann *et al.*, Nature Comm., **6**, 7783 (2015).
[6] T. Ohshima *et al.*, Jpn. J. Appl. Phys., **55,** 01AD01 (2016).

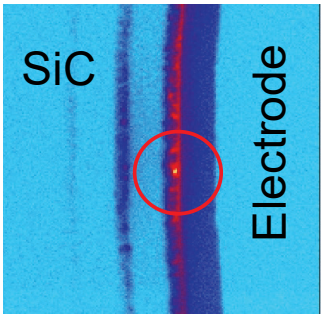

Fig. 1. EL mapping image (100 μm x 100 μm) obtained from the edge of an electrode for a SiC *pn* diode at RT by a CFM. An EL spot is observed in the center of the red circle.

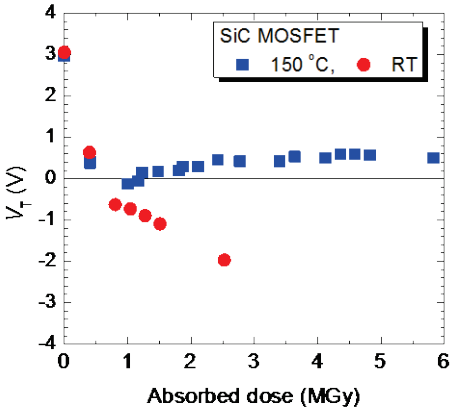

Fig. 2. Change in V_T for SiC MOSFETs due to irradiation. Squares and circles indicate the results obtained for MOSFETs irradiated at 150 °C and RT, respectively.

P1-5 Biocompatible Materials Research Project

Leader : Mitsumasa Taguchi

The research objective of Project "Biocompatible Materials Research" is to investigate the functional materials in the medical field using natural polymers based on the radiation-induced crosslinking and polymerization techniques. The obtained materials are not only environment-friendly but also can be utilized for the advanced cancer therapy and bio-devices. {1-69~70 in Part II}

Effect of heavy ion irradiation on optical property of radiation-crosslinked polymer gel dosimeter

In recent years, the radiation therapy techniques have progressed remarkably. In the advanced therapy such as heavy ion radiotherapy, dose can be effectively delivered to a cancer tissue while preserving a surrounding normal tissue. So an evaluation of dose distribution becomes more important for the heavy ion radiotherapy. It is necessary to investigate the sensitivity of dosimeters depending on LET (linear energy transfer) and dose rate of incident ions for utilization to the radiation therapy.

The polymer gel dosimeters that consist of 2-hydroxyethyl methacrylate, polyethylene glycol dimethacrylate, and tetrakis(hydroxymethyl)phosphonium chloride with radiation-crosslinked hydroxypropyl cellulose gel matrix were prepared by the immersion method [1]. The dosimeters were irradiated with 150 MeV/u He ions, 290 MeV/u C ions, and 500 MeV/u Fe ions at HIMAC facility. The LET values of He, C, and Fe ions were 2.2, 13, and 182 eV/nm, respectively, as a result of calculation by using SRIM code. The dosimeters were optically analyzed by using a UV-Vis spectrophotometer before and after the irradiation. Absorbance of the irradiated dosimeters increased with an increase in the dose up to 10 Gy as shown in Fig. 1. The absorbance at the dose of 5 Gy decreased with increasing dose rate in all used heavy ions. The dosimeter exhibited the lowest dose response of the absorbance for Fe ion irradiation. It was found that the sensitivity of the dosimeter decreased with increasing dose rate as well as LET values of the incident heavy ions.

Crosslinking of polysaccharides in room temperature ionic liquids by ionizing radiation {1-70}

Natural polysaccharides are recognized to be the most promising materials because of outstanding properties such as high biocompatibility and biodegradability, and procurability from animals and plants on the Earth. Most polysaccharides are, however, radiation degradation type polymers and have poor solubility in water and organic solvents as well as low chemical reactivity. These limitations could be circumvented by use of specific solvents such as RTILs (room temperature ionic liquids). Carboxylate-based RTILs, in particular, have high proton-accepting ability and can cleave the hydrogen bonds between polysaccharide main chains to form solution in the concentration range of 0.1-20 wt.%.

Hydrogels of polysaccharides were obtained in RTILs by ionizing radiation under humid condition and their crosslinking structure was investigated by the scavenging method, X-ray photoelectron spectroscopy (XPS) and fluorescent analysis [2]. Radiation chemical yields of hydroxyl radicals from dissolved water molecule inducing the crosslinking of cellulose were estimated by the scavenging method with phenol, and increased with water content in 1-ethyl-3-methylimidazolium acetate (EMI-acetate). Expected elements of carbon and oxygen were detected in neat cellulose by XPS, while additional nitrogen was detected in the radiation-crosslinked cellulose gel produced in EMI-acetate. Cellulose gel was also produced in fluorescent RTILs, 1,3-dibutylimidazolium acetate (DBI-acetate). Light emission of DBI-acetate in the cellulose gel was observed and 20-nm red shifted at a maximum wavelength of 415 nm when excited at 323 nm. These results indicate that RTILs is incorporated in the cellulose gel. Chitin gel was first obtained in 1-butyl-3-methyimidazolium chloride by γ-ray irradiations, and its gel fraction increased with the dose and reached 86% at 60 kGy as shown in Fig. 2.

References

[1] A. Hiroki *et al.*, Nucl. Instrum. Meth. Phys. Res. B, **365**, 583 (2015).
[2] A. Kimura *et al.*, Radiat. Phys. Chem., **124**, 130 (2016).

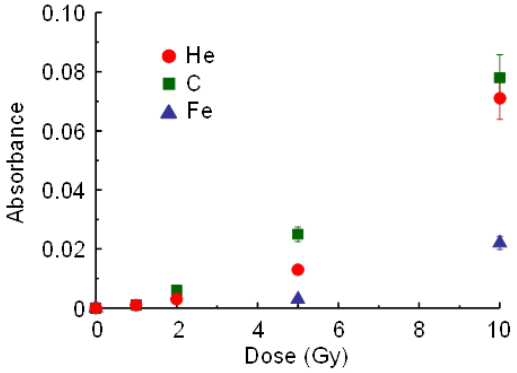

Fig. 1. Dose response of the absorbance of the polymer gel dosimeter irradiated with He, C, and Fe ions at 660 nm. Dose rates of He, C, and Fe ions were 2.6, 2.1, and 3.3 Gy/min, respectively.

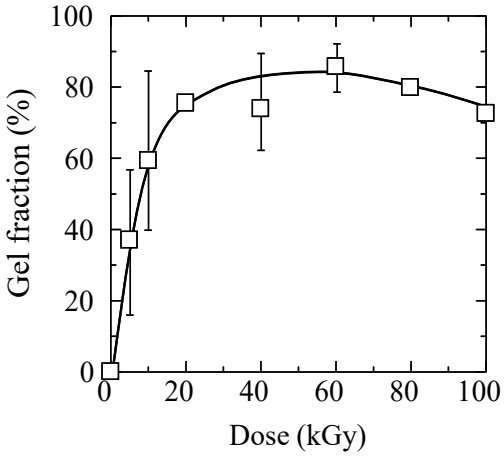

Fig. 2. Gel fraction of 10 wt.% chitin in 1-butyl-3-methyl-imidazolium chloride with water content of 17 wt.% at 298 K as function of absorbed dose.

P1-6 Environmental Polymer Research Project

Leader : Noriaki Seko

The research objective of Environmental Polymer Research Project is to develop functional materials for especially environmental preservation by radiation induced graft polymerization techniques such as electron beams and γ-rays. Fibrous metal adsorbents obtained by this technique can be used for the recovery of rare metals because their adsorption performances are superior to commercial granular resins. {1-71~76 in Part II}

Modification of porous PTFE filters with highly hydrophilic properties by radiation grafting techniques {1-76}

The porous polytetrafluoroethylene (PTFE) filters can be used in a harsh condition such as high temperature and strong chemical environment due to their excellently thermal and chemical stability. To develop a high-performance filter which can be used in an aqueous separation, we tried to modify the porous PTFE filter with highly hydrophilic properties by radiation grafting techniques. For this purpose, three hydrophilic vinyl monomers, styrene sulfonic acid sodium (SSS), acrylic acid (AA), N-vinylpyrrolidone (NVP), along with a crosslinker, ethylene glycol dimethacrylate (1G), were used for the grafting on the porous PTFE filters. The co-grafting of AA and SSS in aqueous solution using the pre-irradiation grafting methods showed a low grafting yield of 13.3% as well as a low water uptake of 15.8%. Such a low grafting yield cannot give the filter adequate hydrophilic properties. On the contrary, by addition of a small amount of 1G, the grafting yield increased to 38.6% under the same grafting conditions. The latter modified filters showed a high water uptake of 24.9%. Furthermore, as shown in Fig. 1, the water contact angle of the PTFE filter largely decreased from 135º to 62º, indicating that the surface of PTFE filter after grafting were hydrophilic. On the contrary, the high grafting yield (> 100%) was obtained by simultaneous grafting of the above-mentioned monomers using the γ-ray and UV as the irradiation sources. These results were very useful for the designing and preparation of the hydrophilic filters in the future works.

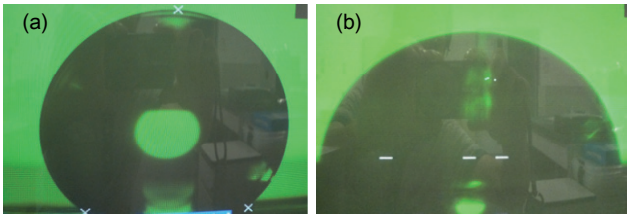

Fig. 1. Contact angle of the PTFE filter before (a) and after (b) hydrophilic monomer grafting.

A new eco-modification method for introducing of functional groups {1-72}

A large amount of arsenic waste solution, which was dissolved in neutral aqueous media, was generated from the manufacturing process of gallium arsenide component in semiconductor industry. As for arsenic removal, an adsorbent was developed by radiation grafting and its subsequent chemical modification with *N*-methyl-D-glucamine (NMDG) as a functional group. Furthermore, the grafting and the modification were carried out using water based solvent instead of organic solvent in view of an environmental emission and a working environment. The solvents were comprised of water and surfactant (Tw20), and the adsorption performances compared with a conventional method synthesized in 1,4-dioxane (Diox) of organic solvent. An optimal degree of grafting (D.g.) was around 200% because the grafted adsorbent with highly D.g. was sustained physical damages. From the pH dependency studies, the developed grafted adsorbent gave high removal ratio in a neutral media area for both arsenic species. Breakthrough capacities in the column mode tests for arsenic(III) and arsenic(V) were 0.3 and 18 mg/g at pH 6.5, respectively. To know the effect of pH on arsenic adsorption, Tw20-adsorbent and Diox-adsorbent were evaluated in 1 ppm solution for 2 h in the pH range from 2 to 11. The results of both arsenic(III) and arsenic(V) adsorption were shown in Fig. 2. Though neither adsorbent adsorbed for arsenic(III) in the acidic range less than pH 3, they showed high affinity in the neutral pH range from pH 5 to 10. The best adsorption performance for arsenic(III) was appeared at pH 10. Comparing Tw20-adsorbent and Diox-adsorbent about the adsorption performance, Tw20-adsorbent adsorbed 1.6-1.8 times as much as Diox-adsorbent in the neutral range [1]. As for arsenic(V) adsorption, both Tw20-adsorbent and Diox-adsorbent had similar tendency at pH range from 4 to 9. As a result, the amount of adsorptions for arsenic(III) and arsenic(V) at pH 6.5 were 3.2 times and 2.1 times higher than our previous fibrous adsorbent [2].

References

[1] H. Amada *et al.*, J. Ion Exchange, **25**(4), 109 (2014).
[2] H. Hoshina *et al.*, Int. J. Org. Chem., **2**, 173 (2012).

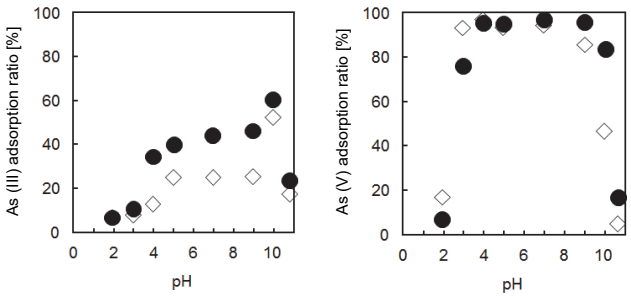

Fig. 2. pH dependencies of As(III) and As(V) removal. (●) Tw20-adsorbent; (◇) Diox-adsorbent.

P1-7 Element Separation and Analysis Research Project

Leader: Hironori Ohba

Quantum beams are versatile sources for materials processing. Our project explores basic process of the laser-matter interaction to separate elements from radioactive waste, and performs synthesis of novel nanomaterials by ion or electron irradiation. For element separation, we study coherent quantum control of molecules or atoms by taking advantage of coherence or monochromaticity of laser light. For materials synthesis, newly structured multi-walled carbon nanotubes inside silicon carbide nanotubes have been found. The recent results of our project are introduced as follows.

Quantum control of physical and chemical processes

Quantum control has many applications such as chemical reactions, element separation, molecular alignment, and quantum computation. Here we outline our recent study on quantum control of ozone isomerization from the open isomer to the cyclic counterpart. In many theoretical studies cyclic ozone was predicted to be at a local minimum of potential surface, but it has never been detected in the gas phase to date probably because the energy of cyclic isomer is considerably higher than the dissociation limit to the oxygen molecule and atom. We have been working on optimal-control-theory (OCT) calculations aiming at obtaining optimal electric fields that can realize the ozone open-cyclic isomerization at high efficiency. Using a one-dimensional three-state model shown in Fig. 1(a), we carried out OCT calculations and obtained the final yield of 0.950. Figures 1(b) and 1(c) show the optimized electric field and its spectrum, respectively. In the first half of the optimal field (Fig. 1(b)) the field oscillation is quite high, corresponding to the electronic transition between the ground and first excited states (V_{11} and V_{22}). In the last half the oscillation is much lower, corresponding to vibrational transitions on V_{22}. The spectrum (Fig. 1(c)) shows that there are two distinct frequency regions; frequencies around 0.15 a.u. correspond to the electronic transition and lower frequencies correspond to the vibrational transitions. We thus theoretically obtained an optimal electric field that enables the ozone open-cyclic isomerization at a nearly perfect efficiency. The present example strongly suggests that quantum control can serve as potentially a powerful tool to efficiently realize a desired control with a new technique way beyond conventional approaches [1].

Synthesis of heterostructured SiC nanotubes and new-structured multi-walled carbon nanotubes inside SiC nanotubes by ion irradiation {1-30 in Part II}

Amorphous SiC nanotubes were successfully synthesized for the first time by the irradiation of polycrystalline SiC nanotubes with 340 keV Si^+ ions. A polycrystalline/ amorphous heterostructured SiC nanotube, in which polycrystalline SiC and amorphous SiC coexist in the same nanotube, was also synthesized by ion irradiation with a mask in front of the polycrystalline SiC nanotube. According to evaluation by electron energy loss spectroscopy, the plasmon energies of the SiC nanotube change rapidly at the interface between the polycrystalline and amorphous regions. The volume swelling induced by amorphization, as evaluated from the differences in plasmon energies, is approximately 5.0%. This result reveals that more relaxed amorphous SiC nanotubes with higher densities can be produced. Figure 2 shows the typical TEM image and selected area electron diffraction (SAED) patterns of the irradiated C-SiC coaxial nanotube. The graphitic shells in the carbon layer of C-SiC nanotubes are found to gradually bend to align with the radial directions of the nanotubes by ion irradiation. Since graphite (002) spots in the SAED pattern are clearly observed even after ion irradiation, the carbon layer in the C-SiC nanotube maintains crystallinity (Fig. 2 (b)). From these results, a new multi-walled carbon nanotube with graphitic shells completely parallel to the radial direction of the nanotube is also produced inside the amorphous SiC tubular layer, in the case of large-calibre C-SiC nanotubes [2].

References

[1] Y. Kurosaki *et al.*, Chem. Phys. **469**, 115 (2016).
[2] T. Taguchi *et al.*, Carbon, **95**, 279 (2015).

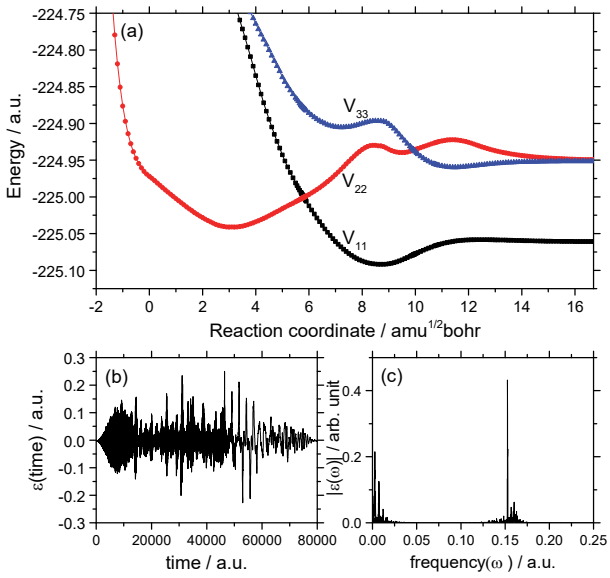

Fig. 1. (a) One-dimensional three-state potential model. Reaction coordinate has the dimension (mass)1/2 x length; (b) optimized field; (c) its spectrum.

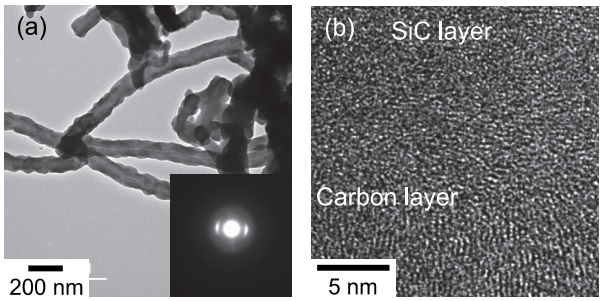

Fig. 2. (a) Low-magnification TEM image and SAED patterns, and (b) high-resolution TEM image of new structured multi-walled carbon nanotube inside SiC nanotube.

Part I

2. Life Science

P2-1 Ion Beam Mutagenesis Research Project

Leader : Yutaka Oono

The long-term objectives of our project is to develop applications of quantum beam technology in a wide range of applied biological fields including sustainable agriculture and environmental conservation through creating valuable genetic resources of plants and microorganisms. For this purpose, we have been trying to establish efficient ion-beam mutagenesis techniques as well as to generate new plants and microbes by ion-beam under collaboration with academic or industrial research organizations. {2-20~22, 2-27~29 in Part II}. Detailed analyses of obtained mutants in model organisms such as yeast, *Arabidopsis*, and rice shed light on a mechanism of mutagenesis and enable to identify a novel gene linked to an important biological function {2-19, 2-25~26, 2-31}. Understanding of molecular biological basis of radio resistance in wide range of radio resistant organisms is another major interest in our project {2-30}.

Identification of a new gene that controls anthocyanin accumulation in plant seed coats

Anthocyanins, polyphenol compounds of plant pigments, contribute to determine colors of flowers, fruits, leaves, and seeds. They are also known to have a strong anti-oxidant activity and expected to promote human health as functional ingredients in foods. Although the anthocyanin biosynthetic pathway is well elucidated, little is known about a mechanism how anthocyanins are accumulated into a special organelle, vacuole, in a plant cell. With ion beams, we used a special line of *Arabidopsis thaliana* that produces red anthocyanin pigment in immature seed coat, mutagenized it as a parent line, and screened for mutants with pale colored immature seeds in which the amount of anthocyanin accumulation is decreased (Fig. 1).

Detailed analyses of the mutant discovered that the MATE-type transporter gene *FFT* is disrupted in the mutant genome. Introduction of the *FFT* gene into the mutant restored normal color in the immature seed coat, suggesting that the loss of *FFT* gene caused the pale color mutant phenotype. The *FFT* promoter activity was detected in the seed-coat layers that accumulate anthocyanins. The FFT protein fused to Green Florescent Protein (GFP) mainly localized in the vacuolar membrane (Fig. 2). These results suggest that the FFT protein acts at vacuolar membrane and is essential for anthocyanin accumulation in vacuoles of the plant seed coat cells [1].

Determination of the draft genome sequence of the radioresistant bacterium *Deinococcus grandis*

Although radiations are harmful to living organisms, a group of bacteria, *Deinococcus*, shows extraordinary resistance to radiations. The resistance of *Deinococcus* species is attributed to highly proficient DNA repair capacity. As part of efforts to elucidate mechanism of radioresistance of this bacterial species, we have determined the draft genome sequence of *Deinococcus grandis*, which was isolated from freshwater fish in Japan [2]. The sequence suggested that the whole genome of *D. grandis* is approximately 4.1 Mbp in size and consists of 5 circular DNA molecules (Table 1) although sequence gaps remain in the circular No. 3. A total of 4,043 protein-coding sequences (CDSs) were annotated in the draft genome sequence. The presence of a DNA damage response regulator (encoded by a *pprI* homolog) and radiation/desiccation response (RDR) regulons such as *recA*, *ddrA*, *ddrO*, *pprA*, and *gyrA* homologs in the annotated genome suggests that *D. grandis* has a similar RDR system to *D. radiodurans*, the best-characterized extreme radioresistant bacteria. Further genome comparative analyses of *Deinococcus* species are expected to reveal common principles for extraordinary resistance of this bacterial species against radiation.

References

[1] S. Kitamura *et al.*, Plant Mol. Biol., **90**, 7 (2016).
[2] K. Satoh *et al.*, Genome Announc. **4**, e01631-15 (2016).

Fig. 1. Phenotype of immature seeds of parent (top) and mutant (bottom) lines. The mutant showing pale color seeds with reduced anthocyanin content in the seed coats was isolated from the ion-beam mutagenized population of the parent line whose seeds appear red.

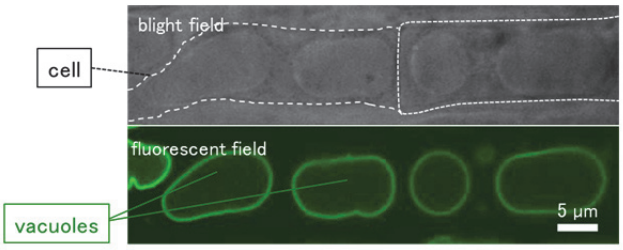

Fig. 2. Subcellular localization of the FFT protein. Microscopic images in blight (top) and florescent (bottom) field of epidermal cells of the root meristem. Florescent signal of the GFP fused with the FFT protein mainly localized in the vacuolar membrane. Dashed lines indicate cell walls.

Table 1 Summary of *D. grandis* genome.

Circular DNA No.	1	2	3	4	5	Total
Size (kbp)	3,250	389	354	91	8	4,092
Gap size (kbp)	0	0	> 29	0	0	> 29
GC content (%)	70.2	71.6	60.8	68.7	64.9	69.5
No. of CDSs	3,172	336	287	139	9	4,043
No. of tRNA genes	49	0	1	1	0	51
No. of 5S rRNA genes	3	0	1	0	0	4
No. of 16S rRNA genes	3	0	1	0	0	4
No. of 23S rRNA genes	3	0	1	0	0	4

P2-2 Microbeam Radiation Biology Research Project

Leader : Tomoo Funayama

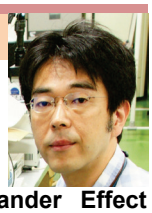

Target irradiation of biological samples using heavy-ion microbeam is a useful means for exploring high and unique biological effectiveness of heavy-ion radiation. Therefore, we have developed the heavy-ion microbeam systems in QST-Takasaki, and utilized for analyzing biological effects of the heavy-ions [1-2]. In our project, we are developing and improving a microbeam system and irradiation methods for various biological targets with heavy-ion microbeam {2-01 in Part II}, and, using the established methods, we are carrying out researches from three points of view: 1) molecular analysis of radiation induced bystander effect {2-03, 2-08~11}; 2) basic research of heavy-ion hit effect on mammalian cells for medical and agricultural application {2-02, 2-04~07, 2-13~14, 2-43}; 3) effect of local irradiation on individuals {2-12, 2-15~16}. Our final goal is to utilize microbeam irradiation in a wide range of biological research.

Development of Live-Cell Imaging System for Long-Term Analysis of Bystander Cell Populations Irradiated with Heavy-Ion Microbeams {2-01}

Using the heavy-ion microbeam system of TIARA, we have been carrying out a lot of analyses of bystander effect for assessing the effect of heavy-ion radiation on biological system [3-8]. However, the responses of bystander effect are not uniformly induced in the cells of the bystander cell population. To clarify the whole picture of the bystander response, we need to analyze all cells individually in the bystander population over the long term after the microbeam irradiation. Thus, we developed a live-cell imaging system to carry out a long-term automatic observation of bystander cell populations irradiated with heavy-ion microbeam.

In the development, we introduced three components to the offline cell-observation system, which is a part of the cell targeting system of collimating heavy-ion microbeam. For avoiding the exposure effect of the excitation light and obtaining clear image from weak fluorescent light during long-term observation, a high-sensitivity CMOS camera (ORCA-Flash4.0, Hamamatsu-Photonics) was introduced. An automatic focus-control unit (IX81-ZDC2, Olympus) was also add in the PC-controllable inverted microscope (IX81, Olympus) to avoid focus drift during long-term observation. To keep irradiated cell samples with suitable culture condition on the observation microscope stage, a stage-top cell incubator (Tokai-hit Corp.) was brought in to keep irradiated cell samples with suitable culture condition.

A software for carrying out long-time live-imaging was developed from a software framework, which enable to build multiple software for multiple experimental purpose from single source code set of the cell targeting software of the microbeam system. Function modules for compensating drifted-focus by automatic focus unit, and capturing images automatically during long-term observation was developed, then integrated to the framework to establish a control software for more-than-week long-term bystander analysis.

Analysis of Gamma-ray Induced Bystander Effect between Human Lung Normal and Cancer Cells {2-03}

To clarify the possibility whether the radiation induced bystander effect will increase risk for radiotherapy patients, we carried out experiments to assess an extent of bystander cell killing between normal human lung fibroblasts WI38, and non-small cell lung cancer cell lines, H1299, with different *TP53*-gene status (wild, mutated and null).

To evaluate bystander effect between normal and cancer cells, we separate two populations physically with microporous membrane, which is able to diffuse media containing inter-cellular irradiation signals via small pore in the membrane. A detail scheme of the experiment was showed in Fig. 1 of {100} in part II. The cells inoculated into the culture insert was irradiated with a 0.5 or 5.0 Gy of ^{60}Co gamma ray of TARRI, then non-contact co-culture between irradiated and unirradiated cells were carried out for 24 h. Thereafter, the insert with irradiated cells were removed and the bystander effect in the unirradiated cells were evaluated with clonogenic survival assay.

Differently from the conventionally reported result, even the survival rate of bystander normal cells co-cultured with irradiated normal cells showed no significant differences compared to the rate of control cells. In addition, when the combination of irradiated cells and unirradiated cells was reversed, no significant difference was found regardless of the *TP53*-gene status.

These results indicate that the bystander cell-killing effect was not induced between different type cells in these experimental conditions. In a similar experiment using co-culture systems, it was reported that cancer (chondrosarcoma) cells could release bystander stimulations but could not develop bystander responses by observing the amount of micronucleus formation. Therefore, even though further researches will probably be necessary to carry out, it might be said from our current result that, for radiotherapy patients, it is not necessary to consider risks by gamma-ray-induced bystander effects.

References

[1] T. Funayama *et al.*, J. Radiat. Res., **49**, 71 (2008).
[2] T. Funayama *et al.*, IEEE Trans. Plasma. Sci., **36**, 1432 (2008).
[3] N. Autsavapromporn *et al.*, Int. J. Radiat. Biol., **91**, 62 (2015).
[4] M. Tomita *et al.*, Life Sci. Space Res., **6**, 36 (2015).
[5] Y. Matsumoto *et al.*, Radiat. Prot. Dosim., **166**, 152 (2015).
[6] Y. Yokota *et al.*, Int. J. Radiat. Biol., **91**, 383 (2015).
[7] N. Autsavapromporn *et al.*, Radiat. Res., **180**, 367 (2013).
[8] Y. Mutou-Yoshihara *et al.*, Int. J. Radiat. Biol., **88**, 258 (2012).

P2-3 Medical Radioisotope Application Research Project

Leader : Noriko S. Ishioka

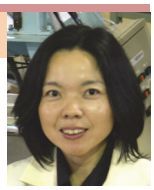

The research objective of our project is to develop the radiopharmaceuticals labeled with useful radioisotopes for cancer diagnosis and therapy. Our group focuses on research of the radioisotope drug delivery system (RI-DDS) using bioactive compounds such as antibodies and peptides in order to make the most of the ability of radioisotopes. We also search for novel molecular targets that enable effective diagnosis or therapy with radiopharmaceuticals.

Synthesis and *in vitro* evaluation of F(*p*-^{131}I)KCCYSL for targeting HER2

Radioiodinated peptides are promising for applications in nuclear medicine such as diagnosis and therapy. Among radioiodines, ^{131}I ($t_{1/2}$ = 8.0 days) is a useful radionuclide in both clinical imaging and therapeutic applications. KCCYSL (Lys^1-Cys^2-Cys^3-Tyr^4-Ser^5-Leu^6) peptide has potential as a molecular probe targeting tumor cells overexpressing the human epidermal growth factor receptor type 2 (HER2). ^{131}I-labeled KCCYSL peptide is therefore promising as a radiopharmaceutical of HER2 overexpressing tumors. In this study, we report synthesis and *in vitro* evaluation of novel ^{131}I-labeled KCCYSL peptides [1].

We designed two ^{131}I-labeled KCCYSL peptides, F(*p*-^{131}I)KCCYSL **(1)** and F(*p*-^{131}I)GSGKCCYSL **(2)**, which were introduced F(*p*-^{131}I) into the *N*-terminal of the peptides. Precursor peptides, Boc-F(*p*-$SnBu_3$)K(Boc) C(Trt)C(Trt)Y(^{t}Bu)S(^{t}Bu)L-OH and Boc-F(*p*-$SnBu_3$)GS(^{t}Bu) G-K(Boc)C(Trt)C(Trt)Y(^{t}Bu)S(^{t}Bu)L-OH, were synthesized by the Fmoc solid phase peptide synthesis. Then, precursor peptides were radioiodinated via electrophilic destannylation in the presence of *N*-chlorosuccinimide, and they were deprotected to obtain **(1)** and **(2)** in radiochemical yield 15% and 17%, respectively.

In order to evaluate the ^{131}I-labeled KCCYSL peptides as clinical imaging and therapeutic agents, cellular binding assay and studies on stability in human serum were carried out. The binding assay showed high affinity for tumor cells. However, the KCCYSL peptides had low stability in serum due to the hydrolysis by peptidases. We are considering that improvement of the stability of F(*p*-^{131}I)KCCYSL by the chemical modification (D-amino acid substitution and α-methylation) of amino acids to avoid degradation by peptidases.

Medical radioisotope production with accelerator neutrons by deuterons {2-38 in Part II}

We have proposed a new system for the generation of medical radioisotopes such as ^{99}Mo ($T_{1/2}$ = 66 h), ^{90}Y ($T_{1/2}$ = 64 h), ^{67}Cu ($T_{1/2}$ = 61.8 h), and ^{64}Cu ($T_{1/2}$ = 12.7 h) with accelerator neutrons by deuterons [2].

^{67}Cu is an attractive radionuclide for cancer therapy, because of emissions of medium energy beta particle (a mean energy of 141 keV) and gamma rays (91, 93, 185 keV) suitable for imaging, and its appropriate half-life. However, the use of ^{67}Cu in clinical research has been limited due to the difficulty in obtaining a sufficient amount of ^{67}Cu. We have investigated the production of ^{67}Cu by the ^{68}Zn(*n,x*)^{67}Cu reaction (*x = n'p, d*) using accelerator neutrons from ^{nat}C(*d,n*) or ^{nat}Be(*d,n*) reaction. The highly purified ^{67}Cu was obtained from a considerable amount (33 g) of ZnO sample by two columns (chelate resin and anion exchange resin) separation method [3].

The irradiated sample was dissolved in concentrated HCl, and the pH value was adjusted to be about 3.5-4.0 with 10 M NaOH solution. The solution was fed into a chelate resin column and an anion exchange resin column to separate ^{67}Cu from the ZnO sample. The 2 M HCl eluent containing ^{67}Cu was evaporated and dissolved with 0.1 M ammonium acetate (pH = 5.5). Finally, the solution was purified with a 0.22 μm filtration system. The radionuclidic purity of ^{67}Cu in the separated sample was more than 99% as shown in Fig. 1.

By using the obtained ^{67}Cu solution, the labelling of DOTA and TETA which are useful bifunctional ligands for the labelling monoclonal antibodies was succeeded in more than 97% yield. In addition, we successfully developed a recycling process of the used ^{68}ZnO sample by precipitating ^{68}Zn(OH)$_2$ from the separated Zn fraction. It was confirmed that the recycled sample did not include the extra impurities inhibiting the labelling reaction of DOTA or TETA.

The present results demonstrate that the medical radioisotope ^{67}Cu can be produced with a minimum level of impurity radionuclides by using accelerator neutrons, and high quality no-carrier added ^{67}Cu can be obtained by the chemical separation method in this production system.

References

[1] I. Sasaki *et al.*, Peptide Science 2015, 243 (2016).
[2] Y. Nagai *et al.*, J. Phys. Soc. Jpn., **82**, 064201-1 (2013).
[3] M. Kawabata *et al.*, J. Radioanal. Nucl. Chem., **303**, 1205 (2015).

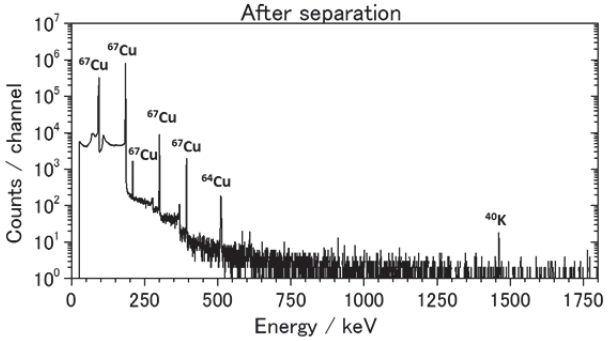

Fig. 1. Gamma-ray spectrum of the ^{67}Cu solution after the chemical separation, measured for 10,000 s.

P2-4 Radiotracer Imaging Research Project

Leader: Naoki Kawachi

The aim of our radiotracer imaging research project is to precisely measure, visualize, and characterize the biological processes of organs. Our project will establish systematized techniques for live-imaging using radiotracers, nuclear imaging apparatus, and kinetic analytical methods for understanding the transport function related to agriculture and medicine within living systems. {2-32,2-34~35 in Part II}

Imaging of radiocesium uptake dynamics in a plant body using a developed gamma camera

Vast agricultural and forest areas in Japan were contaminated with radiocesium (^{134}Cs and ^{137}Cs) because of the Fukushima Daiichi nuclear disaster in March 2011. Many agricultural studies focused on topics such as fertilizer management and plant breeding have been undertaken for reducing radiocesium uptake in crops or enhancing uptake and transportation via phytoremediation. These studies examine the control of radiocesium dynamics in plant bodies from the viewpoint of plant physiology. Previously, we established a radiotracer imaging method by using the positron-emitting tracer imaging system (PETIS) and ^{107}Cd to quantitatively assess the transport of cadmium, a major soil pollutant found worldwide, in plants. We successfully elucidated the dynamics of transport of cadmium in rice.

In this study, we developed a new gamma camera [1] specifically for plant nutritional research and successfully performed live imaging of the uptake and partitioning of ^{137}Cs in plants. The gamma camera was specially designed for high-energy gamma photons from ^{137}Cs (662 keV). To obtain reliable images, a pinhole collimator made of tungsten heavy alloy was used to reduce penetration and scattering of gamma photons (Fig. 1). A single-crystal scintillator, Ce-doped $Gd_3Al_2Ga_3O_{12}$, with high sensitivity, no natural radioactivity, and no hygroscopicity, was used. The array block of the scintillator was coupled to a high-quantum efficiency position sensitive photomultiplier tube to obtain accurate images. The completed gamma camera had a sensitivity of 0.83 count s^{-1} MBq^{-1} for ^{137}Cs with an energy window from 600 keV to 730 keV and a spatial resolution of 23.5 mm.

We used this gamma camera to study Cs kinetics in soybean plants that were hydroponically grown and fed with 2.0 MBq of ^{137}Cs for 6 days to visualize and investigate the transport dynamics in aerial plant parts. Figure 2 shows the imaging result in which ^{137}Cs gradually appeared in the shoot several hours after feeding, and then accumulated preferentially and intensively in growing pods and seeds; very little accumulation was observed in mature leaves. These patterns of ^{137}Cs movement suggest that radiocesium is mainly transported directly to the growing organs in the aerial part, particularly developing pods and seeds, without accumulating in the mature soybean leaves in the reproductive growth stage. We speculated that xylem-to-phloem transfer of radiocesium may occur in the stem before radiocesium reaches the mature leaves through the transpiration stream in the xylem.

Our results suggest that this method using a gamma camera may serve as a practical analyzing tool for breeding crops and improving cultivation techniques resulting in low accumulation of radiocesium in the consumable parts of plants. We have high expectations that this technology will be widely adopted in the future and provide new insights to researchers who investigate radioactive contamination [2].

References

[1] S. Yamamoto, H. Watabe, N. Kawachi *et al.,* Nucl. Instrum. Meth. Phys. Res. A., **743**, 124 (2014).

[2] N. Kawachi *et al.,* J. Environ. Radioact., **151**, 461 (2016).

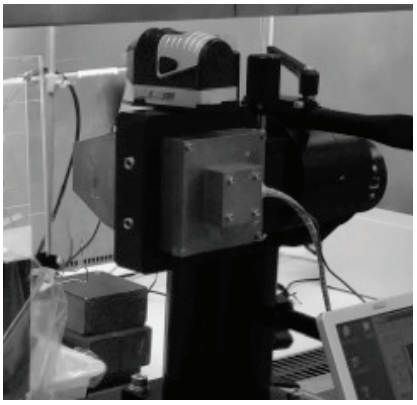

Fig. 1. Photograph of the developed gamma camera.

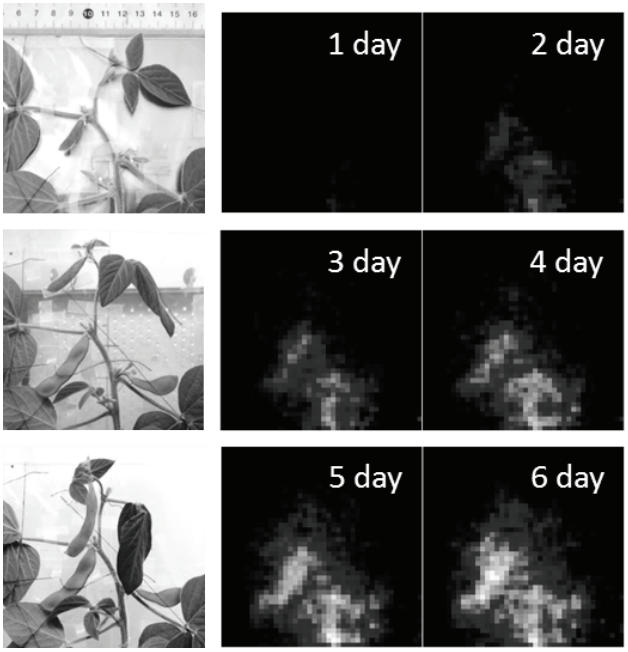

Fig. 2. Photographs of the soybean and serial images of ^{137}Cs dynamics in the field of view of the gamma camera after feeding ^{137}Cs into the hydroponic culture.

P2-5 Radiation and Biomolecular Science Research Project

Leader : Akinari Yokoya

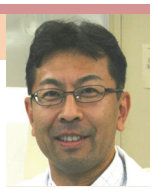

The research objective of our project is to elucidate radiation effects of living systems from molecular to cellular level. Advanced light sources, such as highly monochromatic soft X-rays to induce innershell ionization/excitation of a specific atom in DNA, X-ray microbeam to target a single cell or organelle, or circular polarized lights in the energy region below vacuum ultraviolet to measure circular dichroism (CD), have been used. Theoretical approaches are also applied for modeling molecular and cellular responses to irradiation using computer simulation techniques. Monte Carlo simulation and molecular dynamics calculation have revealed the correlation between radiation track structure and spatial distribution of DNA or cellular damage, and physical or chemical reaction of biomolecules. An approach of system biology has also been applied to reveal the correlation between a single cell response and multicellular system. It is one of unique characters of our group that both experimental and theoretical researchers cooperate closely to promote their projects. This allows us to understand the complex radiobiological phenomena, particularly "low-dose" radiation effects on living system.

Here we report our recent progresses in a novel experimental approach using circular dichroism, and also theoretical research to contribute the issue of low dose risk, particularly in nuclear disasters.

Structural change of histone proteins (H2A and H2B) induced in human cells exposed to X-rays

From an experimental approach, we have studied the protein structures and functions involved in radiobiological responses in nuclei in cells exposed to ionizing radiation. Ultraviolet circular dichroism (CD) spectroscopy is very sensitive to structural change of proteins, and has several notable advantages over X-ray crystallography or nuclear magnetic resonance (NMR). Particularly, revealing the secondary structural changes by post-transcriptional modifications of key enzymes will strongly contribute to elucidation of regulation mechanism of protein-networks responsible for cellular responses to stresses such as ionizing radiation. We have performed a typical application of CD to protein structural study, particularly the secondary structural change of histones in responding to ionizing irradiation in living cells.

A Histone Purification Kit (Active Motif, Inc., CA, USA) was used to extract H2A, H2B, and their variants from X-irradiated (40 Gy) and unirradiated human cancer (HeLa) cells. The kit is designed to extract H2A-H2B from core histones in chromatins with maintaining post-translational modification of H2A-H2B. Sodium dodecyl sulfate polyacrylamide gel electrophoresis (SDS-PAGE) analysis was done to confirm the purity of histone protein samples using NuPAGE 12% Bis-Tris gels in MES running buffer (Life Technologies Corporation, CA, USA). The CD spectra of these histone samples were measured using a CD spectrometer J-725 (JASCO Corporation, Tokyo, Japan).

Two negative CD peaks at approximately 208 and 222 nm were observed in the unirradiated sample (Fig. 1). Those peaks at these wavelengths are characteristic CD peaks of α-helix structure assigned to $\pi \rightarrow \pi^*$ and $n \rightarrow \pi^*$ transitions of peptide bonds, respectively. The spectra were analyzed using the SELCON3 software and reference data set “IBasis 4” [1], applied at a wavelength of 200 to 240 nm to obtain the contents of secondary structures (Table 1). Compared to unirradiated cells, a relative increase in α-helix structure and decrease in other secondary structures was observed in X-irradiated cells [2, 3]. The spectral change was significantly different from that induced by direct X-ray exposure to a purified histone protein solution. These structural alterations persisted for at least 24 hours in the cell, which is substantially longer than the DNA repair time, about 2 hours, generally known to be required for rejoining of DNA double strand breaks.

In collaboration with groups of Dr. M.-A. Hervé du Penhoat and Dr. C. Houée-Lévin in France, we have extended the CD spectroscopy into a higher energy (vacuum ultraviolet) region at the "Dichroism, Imaging & Spectrometry for Chemistry and biOlogy" beamline (DISCO) in a third generation French synchrotron facility (SOLEIL), Orsay, France, to measure much precisely the structural alterations in respect of thermodynamic parameters, such as enthalpy and entropy.

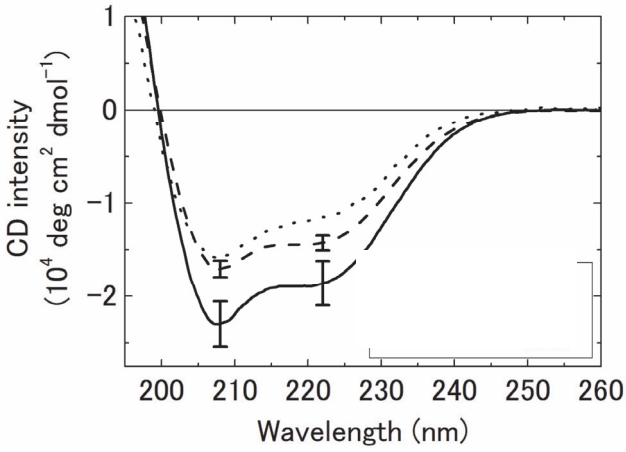

Fig. 1. CD spectra of histones H2A and H2B. Solid line: histones extracted from X-irradiated cells, dashed line: histones extracted from unirradiated cells, and dotted line: histones directly exposed to X-rays. For easy to see, error bars are only shown at 208 and 222 nm.

Table 1. Contents (%) of secondary structures analyzed.

Sample	α-Helix	β-Strand	Turn	Un-ordered
Un-irradiated cells	45.9	10.4	17.0	27.7
Irradiated cells	62.6	4.5	13.5	22.1
X-irradiated H2A and H2B	38.4	14.7	18.4	29.5

Evaluation of DNA damage induced by internal and external exposure by ^{137}Cs

Mechanistic studies of low dose risk, as well as epidemiological approaches, have long been addressed as a critical issue of nuclear disasters. Computer simulation is one of powerful approach because low dose experiments are sometimes difficult to detect significant biological effects overcoming background noise signal.

We performed a simulation of radiation-induced DNA damage to understand the biological effects of external and internal exposure by ^{137}Cs [4]. The biological effects of internal and external exposure by ^{137}Cs nuclei have received considerable public attention after the Fukushima Daiichi nuclear disaster. Internal exposure by ^{137}Cs is mainly caused by electrons emitted after γ-decay. The ^{137}Cs nucleus decays by ejecting γ-rays with maximum energies of 512 keV (94.6%) and 1.174 MeV (5.4%), and the daughter nuclei ^{137}Ba decay by emitting γ-rays (89.7%) and by internal conversion (10.3%). The internal conversion emits internal conversion electrons and low-energy (10.9 eV to 35.6 keV) Auger electrons. The γ-rays, which are mainly responsible for external exposure, have an energy of 662 keV. The biological effects of the 512-keV electrons and 662-keV photons are generally thought to be similar at the same absorbed dose. However, low-energy electrons as Auger electrons can induce dense energy deposition. A dense energy deposition around the DNA molecule has the potential to induce a complex type of DNA damage that can lead to serious biological consequences. ^{137}Cs nuclei are regarded as being homogeneously distributed in cells, and the Auger process is not the main process. However, the contribution of electrons to internal exposure is often discussed in relation to the intake of ^{137}Cs. Therefore, we examined the DNA damage induced by directly emitted electrons (γ-rays, internal conversion electrons, and Auger electrons) from ^{137}Cs. The simulations focused on the relationship between the initial electron energy spectrum and the DNA damage spectrum in a simplified system.

Monte Carlo track simulations were used to calculate microscopic energy deposition patterns in liquid water. The simulations were performed using two simple, microscale target systems. The radiation sources were placed on the inside in one system and on the outside in the second system. To simulate the energy deposition by electrons directly emitted from ^{137}Cs placed inside of the system, multiple ejections of electrons after internal conversion were considered. In the target systems, the induction of DNA damage was modelled and simulated for both direct energy deposition and the water radical reaction on DNA. The yield and spatial distribution of simple and complex DNA damage including strand breaks and base lesions were calculated for irradiation by electrons and γ-rays from ^{137}Cs.

The calculated yields of single- (SSB) and double-strand break (DSB) by external exposure of ^{137}Cs showed a reasonable agreement with several previously reported experimental values. Figure 2 shows the calculated complex DNA damage yields by internal and external exposure of ^{137}Cs. The DSB-type damage was classified into DSB and complex DSB (CDSB). Damage including base lesions was classified into damage sites including one base lesion and one strand break (BD&SB), those including two base lesions (BD&BD), and those including more than three lesions (CL10). The contribution of complex damage to total damage is similar in both exposure conditions, and the significant difference in the damage spectrum was not observed (Fig. 2).

Auger electrons are produced by approximately 10% of the ^{137}Cs nuclei. Although the ejection probability of electrons with energies lower than approximately 100 eV is not small (>0.3 per ^{137}Cs nucleus), the total energy deposited by the Auger electrons is only 0.23% of the total energy deposited in the system. Also, ^{137}Cs nuclei do not selectively bind to DNA and distribute randomly in the irradiated volume. Therefore, it can be concluded that the localization of energy deposition is too small to induce complex DNA damage.

This work supports the general perception that internal and external exposures are similar. However, the present study focused on only local (within a few tens of DNA base pairs) effects on DNA damage. Further examination of the damage to a larger area of cellular DNA using an improved simulation model could increase the accuracy of the evaluation of DNA damage.

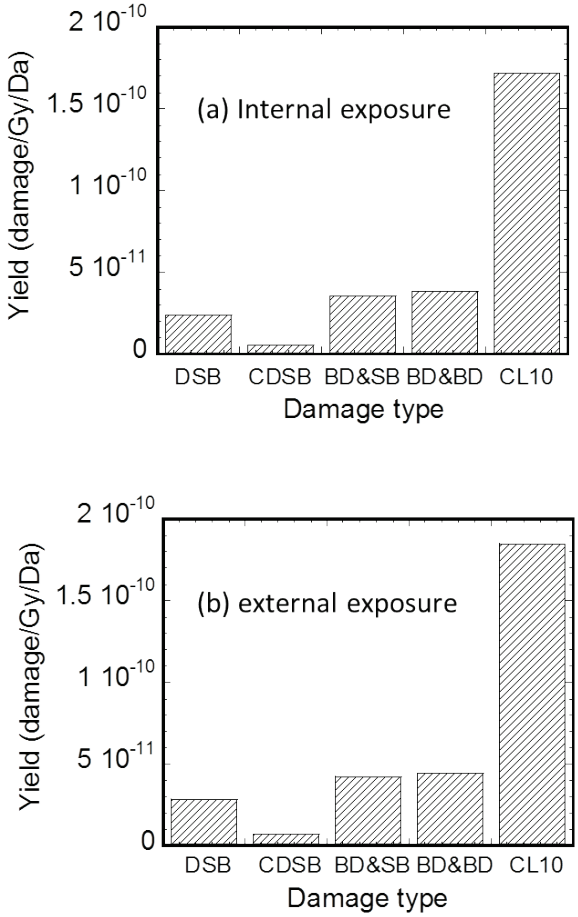

Fig. 2. Spectra of complex DNA damage for pseudo internal and external exposure conditions by ^{137}Cs. The damage types are classified as DSB, complex DSB (CDSB), damage site with one base lesion and one strand break (BD&SB), damage site with two base lesions (BD&BD), and damage site with more than three lesions (CL10).

References

[1] N. Sreerama *et al.*, Protein Sci., **8**, 370 (1999).
[2] Y. Izumi *et al.*, Radiat. Res., **184**, 554 (2015).
[3] Y. Izumi *et al.*, Radiat. Biol. Res. Comm., **51**, 91 (2016) (in Japanese).
[4] R. Watanabe *et al.*, Int. J. Radiat. Biol., **24**, 1 (2016).

P2-6 Biomolecular Function Research Project

Leader : Motoyasu Adachi

Protein molecules play fundamental roles in biological system and exhibit unique functions on molecular recognitions, chemical reactions and energy transfer. Our research project has been focused on developments of the techniques for protein functional analysis using neutron, X-ray diffractions and ultra-short pulse laser. Here, we introduce our basic research concept and activities regarding to two protein functional analyses to obtain useful knowledge for molecular engineering and application as follows.

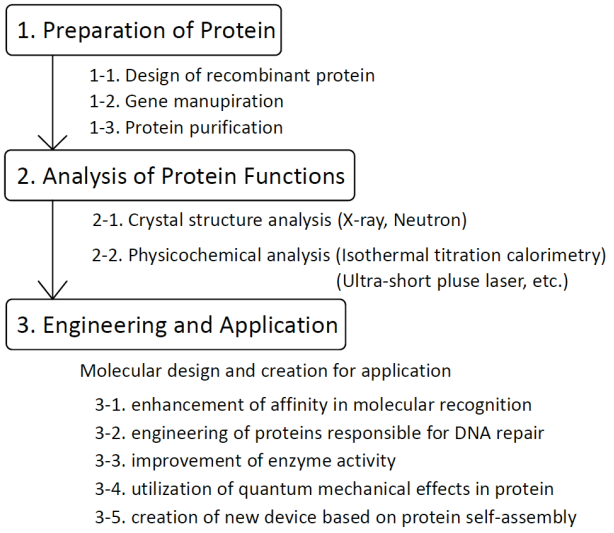

Fig. 1. Research concept of our project.

The catalytic mechanism of decarboxylative hydroxylation of salicylate hydroxylase revealed by crystal structure analysis at 2.5 Å resolution

FAD(Flavin Adenine Dinucleotide) is a key cofactor that functions as an energy carrier in cells and exhibits quantum mechanical effects in proteins (Fig. 1; 3-3, 3-4). We solved the X-ray crystal structure of recombinant salicylate hydroxylase from *Pseudomonas putida* S-1 complexed with cofactor FAD and substrate salicylate to a resolution of 2.5 Å (Fig. 2a) [1]. When compared with other known hydroxylases, structural conservation with p- or m-hydroxybenzoate hydroxylase is very good throughout the topology, despite a low amino sequence identity of 20-40%. Salicylate hydroxylase is composed of three distinct domains and includes FAD accessible to solvent. In this report, we have reported analyses for the tertiary structure of the enzyme, the unique reaction of salicylate, *i.e.* decarboxylative hydroxylation, and the structural roles of amino acids surrounding the substrate. Now, preparation of large crystals is in progress for neutron crystallography to reveal the catalytic mechanism including structural information of hydrogen atoms.

Nucleoside Diphosphate Kinase from Psychrophilic *Pseudoalteromonas* sp. AS-131 Isolated from Antarctic Ocean

NDK (Nucleoside diphosphate kinase) is a house-keeping enzyme catalyzing a transfer of γ-phosphate group of nucleoside triphosphate to nucleoside diphosphate. While most of NDKs were known to form hexameric or tetrameric subunit assembly, we have shown that halophilic NDKs form native and active dimer, which is a basic unit of other hexameric (trimer of this dimer unit) or tetrameric (dimer of this dimer unit). We consider that the study for quaternary structure and molecular functions of NDKs is important for engineering in self-assembely of protein (Fig. 1; 3-5).

Here, we report characterizations and engineering of new target molecule of NDK isolated from psychrophilic *Pseudoalteromonas* sp. AS-131 (ASNDK) [2]. Previously, it was demonstrated that the 134th–136th region play a key role in formation of quaternary structure of NDK. Figure 2b shows a model of putative ASNDK structure on assumption that it had formed tetrameric structure. This model suggests a possibility that ASNDK is a dimer not tetramer due to the bulky Glu136 residue. Actually, wild-type and D135A/E136T mutant ASNDK were expressed in *Escherichia coli* and purified to homogeneity. Cross-linking experiment showed that wild-type and the mutant ASNDK form dimer and tetramer structures, respectively, indicating success in engineering self-assembly. This result and further characterizations will aid to molecular design for engineering on self-assembly of proteins.

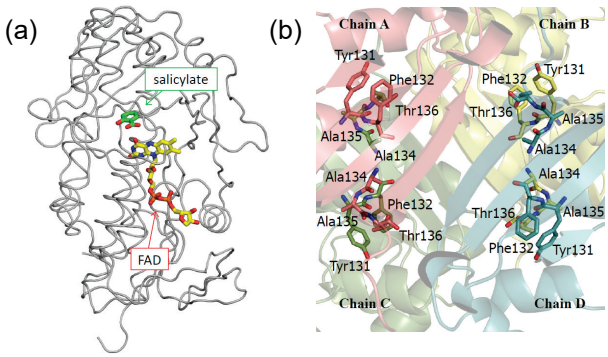

Fig. 2. Structure models of Salicylate hydroxylase (a) and wild-type ASNDK (b). (a) The enzyme and bound ligand molecules of salicylate and FAD are shown by wired and stick models, respectively. (b) Putative tetrameric model was constructed on the basis of the X-ray crystal structure of HaNDK (PDB ID: 3VGU). Key residues in the interaction sites between protomer are shown by stick model.

References

[1] T. Umemura *et al.*, Biochem. Biophys. Res. Commun. **469**, 158 (2016).
[2] Y. Yonezawa, Protein J., **34**, 275 (2015).

P2-7 Biomolecular Structure and Dynamics Research Project

Leader : Taro Tamada

The relationship between protein structure and dynamics is important for ultimate understanding of protein functions. This project aims to contribute to a wide range of biological and life sciences by performing research and development of molecular imaging method using neutrons, along with other quantum beams like X-rays and computer simulations. In this report, we describe our latest activities for protein structure and dynamics.

Elucidation of the reaction mechanism of anti-cancer drug at the atomic level [1]

The fully human monoclonal antibody KMTR2 clusters tumor necrosis factor-related apoptosis-inducing ligand (TRAIL) receptor 2 (TRAIL-R2) on tumor cell surfaces, and acts as a strong direct agonist for TRAIL-R2, which is capable of inducing apoptotic cell death without cross-linking. Therefore, specifically targeting the apoptotic pathway through TRAIL-R2 using direct agonistic antibodies, including KMTR2, may provide a novel therapeutic strategy for malignant tumors.

To investigate the mechanism of direct agonistic activity induced by KMTR2, the crystal structure of the extracellular region of TRAIL-R2 and a Fab fragment derived from KMTR2 (KMTR2-Fab) was determined to 2.1 Å resolution. Two KMTR2-Fabs assembled with the complementarity-determining region 2 of the light chain via two-fold crystallographic symmetry, suggesting that the KMTR2-Fab assembly tended to enhance TRAIL-R2 oligomerization (Fig. 1(a)). We designed a mutant, Asn53 to Arg, in the light chain of KMTR2 to prevent dimerization at this site (Fig. 1(b)). Several biochemical experiments showed that a single mutation at Asn53 to Arg located at the two-fold interface in the KMTR2 abolished the higher oligomerization of TRAIL-R2 and resulted in a loss of its apoptotic activity, although it retained its antigen-binding activity. These results indicate that the strong agonistic activity, such as apoptotic signaling and tumor regression, induced by KMTR2 is attributed to TRAIL-R2 superoligomerization induced by the interdimerization of KMTR2.

Detection of unusual behaviour of human α-synuclein [2]

Alpha-synuclein (αSyn) is a protein consisting of 140 amino acid residues and is abundant in the presynaptic nerve terminals in the brain. Although its precise function is unknown, the filamentous aggregates (amyloid fibrils) of αSyn have been shown to be involved in the pathogenesis of Parkinson's disease, which is a progressive neurodegenerative disorder.

To understand the pathogenesis mechanism of this disease, the mechanism of the amyloid fibril formation of αSyn must be elucidated. Purified αSyn from bacterial expression is monomeric but intrinsically disordered in solution and forms amyloid fibrils under various conditions. As a first step toward elucidating the mechanism of the fibril formation of αSyn, we investigated dynamical behaviour of the purified αSyn in the monomeric state and the fibril state using quasielastic neutron scattering (QENS). The QENS measurements on the solution samples of purified αSyn in the monomeric and fibril states in D_2O were performed using the near-backscattering spectrometer, BL02 (DNA), at the MLF/J-PARC. Figures 2(a) and (b) show examples of the QENS spectra obtained. Analysis of the spectra showed that diffusive global motions are observed in the monomeric state but largely suppressed in the fibril state (Fig. 2(c)). On the other hand, the amplitudes of the side chain motions were found to be larger in the fibril state than in the monomeric state (Fig. 2(d)). This implies that significant solvent space exists within the fibrils, presumably due to a conformational distribution of αSyn within the fibrils. The larger amplitude of the side chain motion in the fibril state than in the monomeric state implies that the fibril state is entropically favorable.

References

[1] T. Tamada *et al.*, Sci. Rep., **5**, 17936 (2015).
[2] S. Fujiwara *et al.*, Plos One, **11**, e0151447 (2016).

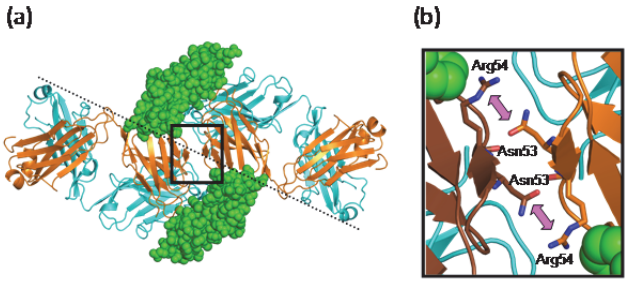

Fig. 1. Dimeric structure of a TRAIL-R2/KMTR2-Fab complex rendered by crystallographic two-fold symmetry. The TRAIL-R2 molecule and the heavy and light chains of KMTR2 are colored green, cyan and orange, respectively. (a) Overall structure. Dashed line and square indicates the two-fold axis and the interface between two KMTR2-Fab molecules, respectively. (b) Close-up view of the interface.

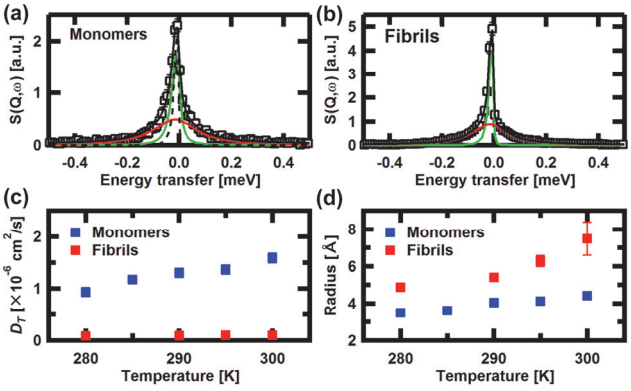

Fig. 2. The QENS spectra of αSyn at Q = 1.225 Å^{-1} and at 280 K in (a) the monomeric state and (b) the fibril state. (c) The temperature dependence of the translational diffusion coefficients of the entire αSyn molecules. (d) The temperature dependence of the amplitudes of the local side chain motions.

Part I

3. Advanced Quantum-Beam Technology

P3-1 Laser Compton Scattering γ-ray Research Project

Leader : Ryoichi Hajima

The research objective of LCS γ-ray Research Project is developing the technologies of high-brilliance γ-ray generation and exploring its scientific and industrial applications such as nuclear physics, nuclear astrophysics and non-destructive measurement of nuclear material. The γ-ray source is based on laser Compton scattering (LCS), which enables one to generate energy-tunable mono-energetic γ-rays. In the research project, we are developing critical components for electron accelerators to achieve small-emittance and high-average current beams, γ-ray optics and a Monte Carlo simulation code.

Diffraction of γ-rays with energies of 1.17 and 1.33 MeV by a flat Si crystal [1]

Generation of high-energy photons via collision of relativistic electrons and laser photons is called laser Compton scattering (LCS). Over the last three decades LCS γ-ray facilities have provided intense energy-tunable mono-energetic γ-ray beams for various scientific and industrial applications.

Recent progress of electron accelerator and laser technologies will open a door to the next-generation LCS γ-ray sources. An electron beam of small emittance and high-average current contributes to improving spectral brightness and flux of LCS photons. In the research project, we are developing γ-ray optics for the next-generation LCS γ-ray sources.

It is known that γ-rays can be diffracted by a crystal according to Bragg's law as well as X-rays. A small divergence of LCS γ-ray works favorably to select γ-rays in a narrow energy region by using crystal monochromators. By combining the next-generation LCS γ-ray sources with new crystal monochromators optimized for such γ-ray beams, we can explore fundamental science and various applications with these γ-ray beams.

As the first step of γ-ray monochromator development, we measure diffraction of γ-rays by a flat Si crystal using a high flux ^{60}Co source with an intensity of 2.3 TBq. The diffraction intensities of the γ-rays with energies of 1.17 and 1.33 MeV were measured as a function of the rotation angle of the crystal. Three peaks corresponding to the Si(440) and Si(220) diffractions for 1.17 MeV and the Si(440) diffraction for 1.33 MeV were measured. The heights and shapes of these three peaks are well reproduced by taking into account Bragg's law and the experimental geometry.

Figure 1 is a schematic view of the measurement setup and Fig. 2 shows observed diffraction intensity for 1.33 MeV γ-rays with calculated results.

As a result of the measurements, we can conclude that high flux ^{60}Co source is useful for developing diffractive optical devices suitable for high-brightness γ-ray beams from the next-generation LCS sources.

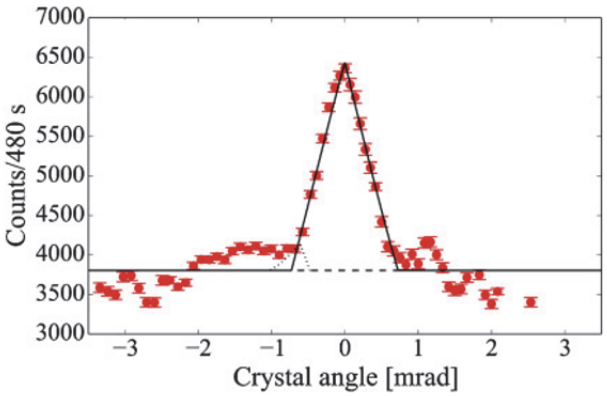

Fig. 2. Observed diffraction intensity for 1.33 MeV γ-rays. The solid line and the dotted line are the calculated results for the Si(440) and (220) diffractions, respectively. The circles are the measured data.

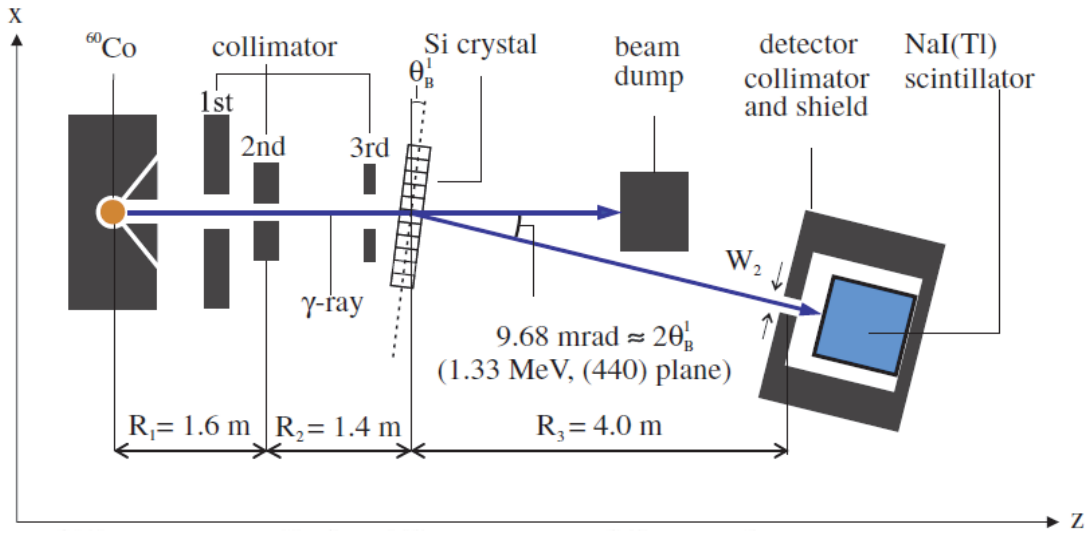

Fig. 1. Schematic view of the measurement setup for γ-ray diffraction by a Si crystal.

Narrow-band GeV photons generated from an X-ray free-electron laser oscillator [2]

We proposed a scheme to generate narrow-band GeV photons, γ-rays, via Compton scattering of hard X-ray photons in an X-ray free-electron laser oscillator (XFELO). Figure 3 is a schematic view of this γ-ray source, XFELO-γ. The XFEL oscillator consists of two normal-incidence sapphire crystals and compound refractive lenses. Compton scattered γ-rays are generated by collision of an electron bunch and an X-ray pulse built up in the oscillator. Figure 4 shows calculated γ-ray spectra for a 7-GeV XFELO-γ. XFELO-γ can generate γ-rays of a narrow-band spectrum with a sharp peak, ~0.1% (FWHM), due to large momentum transfer from electrons to photons. The γ -ray beam has a spectral density of ~10^2 ph/(MeV s) with a typical set of parameters based on a 7-GeV electron beam operated at 3-MHz repetition. The energy of γ-ray is tunable by varying the electron beam energy as far as XFELO is lasing. A circularly polarized γ-ray beam can be generated in XFELO-γ with a spin-polarized electron beam.

The XFELO-γ will open a new opportunity for studying the charmed quark (c-quark) production dynamics from the proton and the neutron which mainly consist of u- and d-quarks. In the past, the production of ϕ, Λ and Σ particles including strangeness quarks has been studied at the Jefferson Laboratory and at the SPring-8. In the future, new types of experiments with an XFELO-γ will be realized to produce, *i.e.*, the J/Ψ meson and charmed baryons from the u- and d-quark medium.

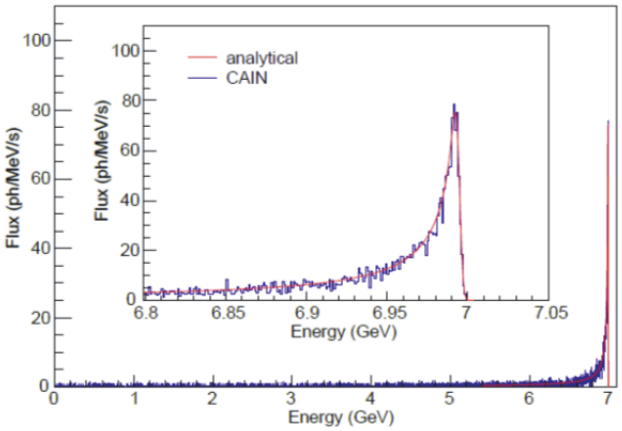

Fig. 4. Gamma-ray spectra of a 7-GeV XFELO-γ calculated by analytical formula with electron energy spread (red) and a Monte Carlo simulation (blue).

References

[1] S. Matsuba *et al.*, Jpn. J. Appl. Phys., **54**, 052203 (2016).
[2] R. Hajima *et al.*, Phys. Rev. Accel. Beams, **19**, 020702 (2016)

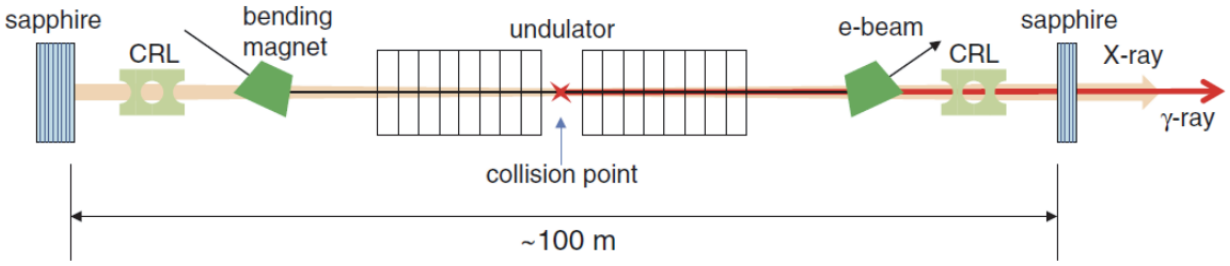

Fig. 3. Schematic view of a γ-ray source based on X-ray FEL oscillator. The oscillator consists of two normal-incidence sapphire crystals and compound refractive lenses (CRL).

P3-2 Beam Engineering Section

Section Manager : Yasuyuki Ishii

The research objectives in our section are many kinds of development of accelerator related techniques which include ion beam irradiation techniques and ion beam analyses. Each member has been engaging in individual researches more than one. In the recent and remarkable studies, the single-pulse ion beam accelerated by AVF Cyclotron was successfully formed using a chopping system and the 3-dimensional element distribution in a small sample was measured using the PIXE-CT analysis. {1-33~35, 1-56, 2-39~44, 3-01, 3-03, 3-06~08, 3-10, 3-12, 3-15~17, 3-20~24, 3-30, 3-33~35 in Part II}

Enhancement of beam pulse controllability for a single-pulse formation system of a cyclotron

The improvement of a single-pulse formation technique with pulse intervals over 1 μs for the JAEA cyclotron was carried out by the upgrade of the chopping system as well as improving the controllability of the beam phase width restriction, the acceleration phase optimization, and the cyclotron magnetic field stabilization. Moreover, a technique to increase the intensity of the single-pulse beam was also performed using a subharmonic beam buncher.

A combination of the acceleration phase control and the phase slits use enabled us to effectively reduce the number of plus beams which reached to and was extracted from the extraction area in the cyclotron (multi-turn extraction). As shown in Fig. 1, a single-pulse beam of high-energy H^+ was successfully formed by the further reduction of the multi-turn extraction on the basis of adding a beam chopping system in an incident beam line. The ratio of the unwanted beam pulses (sub-pulses) to the main pulse was quite low, less than 1×10^{-4}, within 3 μs shown in Fig. 1. In addition, a 65 MeV single-pulse H^+ beam was also formed [1].{3-06}

Particle induced X-ray emission-computed tomography analysis of an adsorbent for extraction chromatography

The PIXE-computed tomography (PIXE-CT) with scanning transmission ion microscopy (STIM-CT) and maximum likelihood expectation maximumzation (ML-EM) iterative image reconstruction method was developed and applied to analyze trace elements in a small sample. The trace elements of a porous silica adsorbent having the residual neodymium (Nd) were nondestructively measured using PIXE-CT.

The cross-sectional distributions of Nd obtained by PIXE-CT are shown in Fig. 2. The image was reconstructed by a modified ML-EM method from the projection map of X-ray counts with 9 degrees resolution. In the modified ML-EM method, each projection map of X-ray counts was corrected for the production cross-section and adsorption coefficient of X-rays using the STIM-CT data, without which the contour would be falsely enhanced. Nd existed both in the central region and the outer surface. Especially, the central region had a higher Nd concentration. The recovery rate of the elements could be improved by investigating the structure of the adsorbent based on visualizing the elements using PIEX-CT [2].{1-56}

References

[1] S. Kurashima *et al.*, Rev. Sci. Instrum. **86**, 073311 (2015).

[2] T. Satoh *et al.*, Nucl. Instrum. Meth. Phys. Res. B, **371**, 419-23 (2016).

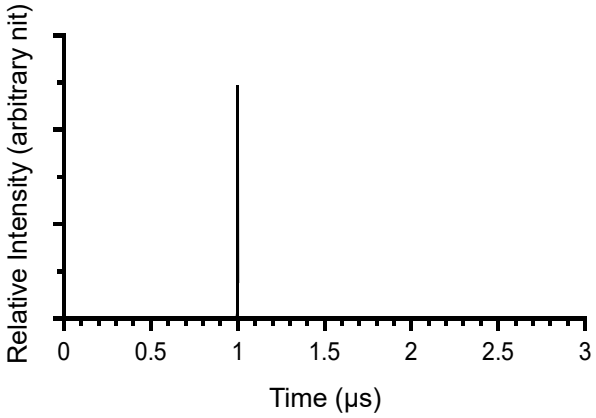

Fig. 1. Beam pulse trains of the 50 MeV $^4He^{2+}$ beam measured by plastic scintillators using the P- and S-choppers.

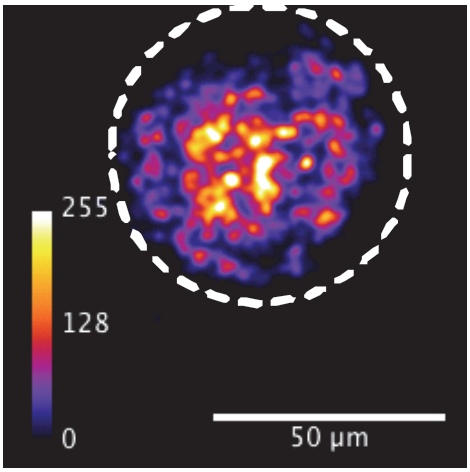

Fig. 2. Cross-sectional distributions of Nd in the adsorbent, obtained by PIXE-CT and modified ML-EM image reconstruction from projection images with 9 resolution. The calibration bar indicates the relative concentration in each tomogram.

Part II

Part II

1. Materials Science

1-23 Anisotropic Swelling of Hydrogel Nanowires Fabricated by Single Particle Nanofabrication Technique (SPNT)・・・・・・・・・・・・・・・・・・・・・・・・・・・・・・・・ 51
M. Sugimoto, S. Tsukuda, T. Yamaki and S. Seki

1-24 Nitrogen Doping in Carbon-Based Cathode Catalysts Using Electron Beam Process・・・・・・・・・・・・・・・・・・・

1-01 Epitaxial Layer Thickness Dependence of Charge Collection in SiC Schottky Barrier Diodes

T. Makino [a], S. Onoda [a], N. Hoshino [b], H. Tsuchida [b] and T. Ohshima [a]

[a] Department of Advanced Functional Materials Research, TARRI, QST,
[b] Material Science Research Laboratory, Central Research Institute of Electric Power Industry

One of the catastrophic failures in semiconductor devices induced by the incidence of ions is known as Single Event Burnout (SEB). The issue of SEB arises in power devices for not only space but also terrestrial applications led by neutrons created by cosmic rays even on the ground. Silicon Carbide (SiC) is a promising wide-band-gap semiconductor for electronic devices. Silicon carbide can endure an electric field about eight times greater than silicon or GaAs before exhibiting avalanche breakdown. High breakdown electric fields allow for very high-voltage, high-power devices. Permanent malfunctions can be induced in power devices by SEBs, and the probability of SEBs increases with increasing electric field in the device[1]. However, SEB in SiC devices is not yet fully understood. To understand the mechanisms of SEB, we investigated epitaxial layer thickness dependence of charge collection in SiC Schottky Barrier Diodes (SBDs).

The samples used in this study were SiC-SBDs fabricated on either a 25 μm or 69 μm thick n-type 4H-SiC epitaxial layer grown on an n-type 4H-SiC substrate by Chemical Vapor Deposition (CVD)[2]. The donor concentration in the 25 and 69 μm epitaxial layers were 4.7×10^{14} and 9.1×10^{14} /cm^3, respectively. Schottky contacts with 1×1 mm^2 (80 nm thick) were formed on the epitaxial layers using the deposition of Ni.

The anode of the samples was grounded and the cathode biased +100 V, +200 V, and +400 V by a high-voltage supply via a charge-sensitive pre-amplifier (ORTEC 142C). Collected charge signals from the pre-amplifier were shaped as voltage-pulses having pulse-heights proportional to the collected charges. The pulse-height distributions analyzed by Pulse-Height Analyzer (PHA) basically correspond to the collected charge distribution. The absolute value of the collected charge in SBDs was calibrated using Si-Solid State Detector. The heavy ion irradiation was performed at the Takasaki Ion Accelerators for Advanced Radiation Application (TIARA) Takasaki, Japan[3]. The SBDs were irradiated with a broad beam of 322 MeV Krypton (Kr) at an irradiation angle of 0 degrees in a vacuum chamber. The projected ion range in the SiC epi-layer was estimated to be 27 μm by a simulation code SRIM[4]. The depletion region thickness of SBDs with the 25 and the 69 μm epi-layers at 400 V are estimated to be 25 and 22 μm from their capacitance-voltage characteristics respectively. Note that the 25 μm epi-layer is fully-depleted. Thus, the electric field in the depletion region of SBDs with the 25 and 69 μm epi-layers at 400 V are 0.16 and 0.18 MV/cm, respectively. In addition, the values of charge induced in the depletion region of SBDs with the 25 μm and 69 μm epi-layers are calculated to be 6.4 pC at 400 V, respectively.

Figure 1 is the histograms of ion-induced charge collection from SBDs. Counts of ion-induced charge collection events are plotted as a function of measured collected charge value. An ion-induced peak for SBDs was observed at each bias. In the case of 100 V and 200 V, the peak values are smaller than 6.6 pC, which corresponds to the charge value theoretically induced in 4H-SiC by fully-stopped 322 MeV of a Kr ion (dashed line in Figure). On the other hand, the peak for both SBDs shifts to higher values than 6.6 pC at a bias voltage of 400 V. Thus, this indicates that more anomalous charge than the theoretical value is collected from SBDs at a bias of 400 V. Here, the peak values of the collected charges at 400 V are 9.6 and 7.7 pC, respectively, as shown in the figures. As a result, the gain of ion-induced charge on the depletion region of SBDs with the 25 μm and 69 μm epi-layers is estimated to be 1.5 and 1.3 by comparing with theoretically maximum charge collection, respectively. The value of charge anomalously collected from SBD with 25 μm epi-layer is larger than that from SBD with 69 μm epi-layer in spite that the electric field in the former one is lower than the later one. From these results, we can assume that the relation between the ion ranges in a SiC SBD and the epi-layer thickness of the SiC SBDs is a key to clarify the mechanism of anomalous charge collection. This is useful information for simulation study of charge collection in future work.

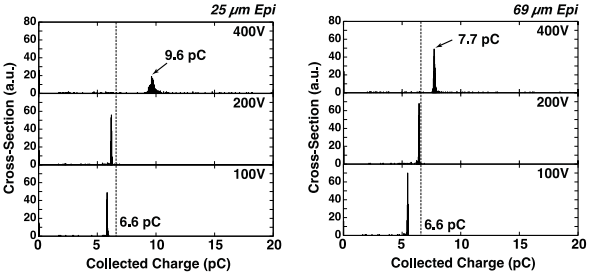

Fig. 1 Collected charge spectra from SBDs with 25 μm thick and 69 μm thick epitaxial layers.

References

1) T. Makino *et al.*, IEEE Trans. Nucl. Sci., **60,** 2647 (2013).
2) M. Ito *et al.*, Appl. Phys. Express., 015001-1 (2008).
3) Home page of TIARA, http://www.taka.qst.go.jp/tiara/tiara/index_j.php.
4) J. F. Ziegler, Program SRIM/TRIM, Available:http://www.srim.org.

1 -02

Experimental Study on Radiation Effects on Magnetic Tunnel Junctions 4

D. Kobayashi [a)], K. Hirose [a)]
S. Ikeda [b)], H. Sato [b)], E. C. I. Enobio [b)], T. Endoh [b)], H. Ohno [b)],
T. Makino [c)], S. Onoda [c)] and T. Ohshima [c)]

[a)] Institute of Space and Astronautical Science, JAXA,
[b)] Center for Spintronics Integrated Systems, Tohoku University,
[c)] Department of Advanced Functional Materials Research, TARRI, QST

Si-based electron devices such as central processing units or CPUs play vital roles in today's information technology. Miniaturization of their structures has progressed for more than 50 years to increase their operating speeds, and thereby leading to undesired increases in their power consumption and susceptibility to radiation. To overcome these hurdles, spintronics, an electron device technology reinforced by magnetization- or spin-dependent phenomena, is promising.

Magnetic tunnel junctions (MTJs) are the key structure of the technology. They usually consist of a stack of layers that include a tunnel insulator film sandwiched by two ferromagnetic layers. Each MTJ works as a two terminal resistive device, interestingly offering two stable resistance states, low or high (R_P or R_{AP}), which are respectively dependent on the relative directions of the magnetizations programmed in those ferromagnetic films, *i.e.*, parallel (P) or anti-parallel (AP). Digital signal processing in the spintronics, in general, relies on this bi-stable feature.

It has been said that MTJs are immune to radiation, which is so far supported in the literature. Compared to tested devices in those previous works, on the other hand, recent, advanced MTJs are way smaller and dependent on a new switching mechanism that stems from spin transfer torque (STT). Their radiation sensitivity is not yet completely understood. To address this concern, we have been carrying out an experimental study in the TIARA facility since 2011. Our previous reports[1-4)] demonstrate no radiation-induced switching in tested MTJs, which are characterized by its diameter D of 70 nm, during 15-MeV Si^{4+}, 15-MeV Fe^{5+}, and 400-MeV Fe^{15+} irradiation. This annual report delivers a review of our recent results[5)], which come from MTJs further downsized to D of 40 nm.

The samples are fabricated in Tohoku University [6)] through the same process recipe as that in our previous works. Each MTJ pillar is fabricated between two metal layers, electrodes for measurement, so as to connect them like a "via" metal. It should be noted that the samples conform to perpendicular anisotropy, which stems from a careful design of CoFeB ferromagnetic and MgO insulator; hence the samples are denoted as p-MTJ hereinafter.

In a vacuum chamber at the end of the HE2 port, the p-MTJs received 400-MeV Fe^{15+} ions from the K=110 AVF cyclotron. During the irradiation, a small voltage bias of 0.1 V was fed to each sample so as to monitor its resistance evolution as a function of time.

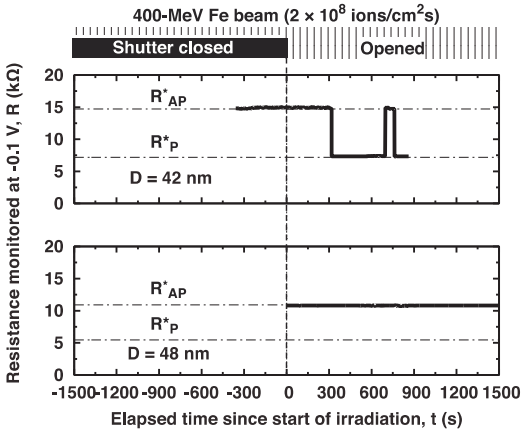

Fig. 1 Measured resistance evolutions of p-MTJs exposed to 400-MeV Fe^{15+} bombardments. Here the asterisk signs indicate the biased states, which are slightly different from the unbiased AP and P configurations.

Figure 1 shows experimental results, in the top of which abrupt resistive switching between AP and P states is observed during the irradiation. The result reveals for the first time, to our knowledge, that MTJs can react with heavy ions. As seen in Fig. 1(bottom), on the other hand, another sample that has a larger diameter than the flipped one exhibits no switching. This fact indicates that D is a characteristic parameter to describe the phenomenon, from which we have developed a possible reaction model so as to discuss the potential risk, data loss frequency, of the p-MTJ exposed to the space radiation environment. It is expected to be negligibly small for practical use, more specifically, as small as that of a commercial radiation-hardened memory [7)].

References

1) D. Kobayashi *et al.*, JAEA Takasaki Annu. Rep. 2011, JAEA-Review 2012-046, 15 (2013).
2) D. Kobayashi *et al.*, JAEA Takasaki Annu. Rep. 2012, JAEA-Review 2013-059, 14 (2014).
3) D. Kobayashi *et al.*, JAEA Takasaki Annu. Rep. 2014, JAEA-Review 2015-022, 10 (2016).
4) D. Kobayashi *et al.*, IEEE Trans. Nucl. Sci., **62,** 1710 (2014).
5) D. Kobayashi *et al.*, IEEE Nucl. Space Radiat. Eff. Conf. (NSREC) 2016 late-news paper.
6) S. Ikeda *et al.*, Nature Materials **9** (2010) 721.
7) K. Hirose *et al.*, IEEE Trans. Nucl. Sci., **49,** 2965 (2002).

1-03 Frequency Dependence of Single Event Transient (SET) Error Rate for Silicon on Insulator (SOI) Devices

K. Sakamoto [a)], A. Maru [a)], H. Shindou [a)], S. Kuboyama [a)], K. Suzuki [a)], A. Takeyama [b)] and T. Ohshima [b)]

[a)] Japan Aerospace Exploration Agency, JAXA,
[b)] Department of Advanced Functional Materials Research, TARRI, QST

As space missions have been upgraded more and more, the requirement to data processing performance of Micro Processing Unit (MPU) for space becomes a critical issue. The solution of this issue is to develop semiconductor devices (transistors) which has excellent operating speed and low power consumption. Generally, performance of transistors can be improved by downsizing which is called scaling theory. However, it is difficult to apply smaller size transistors to the space-crafts. In such a small size transistors, radiation effects called Single Event Effect (SEE) tend to be easy to occur. As transistors based on Silicon on Insulator (SOI) structure have smaller active region than bulk silicon one, SEE tolerance is excellent compared with bulk silicon [1)]. Especially, Single Event Latch-up (SEL) never occurs in this device.

Heavy ion irradiation test was performed on MPU with 256 kbits SRAM-cells which was fabricated by using 0.15 μm FD-SOI process with radiation hardness by design (RHBD) technique. One-bit SRAM cell have 12- transistors because a pair of transistors is used for the purpose of enhancement of radiation tolerant. However, it remains the radiation sensitivity at "Read-Out" time (Fig. 1). As shown in Fig. 1, soon after the transfer gate opened, the signal levels of both bit-line pairs are considerably near value. Therefore, bit-error caused by SET is easy to occur in this duration. In this study, MPU operation frequency dependence of SET for SRAM cells was evaluated. Heavy ion irradiation testing was performed with constant flux of 1E+4 particles/cm^2/sec and total fluence of 5E+7 particles/cm^2.

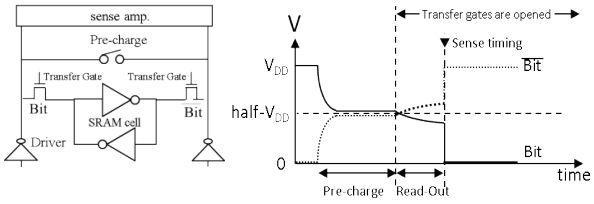

Fig. 1 Read-operation sequence of SRAM-cell which is implemented in the MPU.

Table 1 Heavy-ions used in this experiment.

Ion	Energy (MeV)	LET@surface (MeV/(mg/cm^2))	Range (μm)
Ne	75	6.5	38.9
Ar	150	15.8	36.0
Kr	322	40.3	37.3
Xe	1345	24.7	183

Retention data in the SRAMs were continually read and compared with expected data during irradiation test. If the compared results are wrong, it is identified to be a bit error occurred. Heavy ions listed in Table 1 were obtained from the heavy-ion accelerator at the Japan Atomic Energy Agency (JAEA) in Takasaki. A part of this work was performed under the Shared Use Program of JAEA Facilities.

Relationship of SET error rate versus operation frequencies is shown in Fig. 2. MPU was operated with 500 kHz, 5 MHz, and 50 MHz operation frequency, respectively. No bit-error was observed by Ne ion irradiation with LET of 6.5 MeV/(mg/cm^2). On the other hand, a few bit-error was observed when heavy ions with LET ≧ 15.8 MeV/(mg/cm^2) were irradiated. Note that the SEU tolerance of this device is confirmed up to LET of 40 MeV/(mg/cm^2) at the previous static test. "Static test" means that the SRAM-cell is in standby state with data holding while heavy ion irradiation. This result suggested that the bit-error by SET may occur, although SRAM cells were applied RHBD technique. It seems that there is week correlation between frequency and SET error rate in Fig. 2. However, the increase in cross section is not simply proportional to operation frequency. It means that SET tolerance of these SOI SRAM-cells is not explained the total amount of "Read-Out" time (Fig. 1) in an irradiation test. There may be cause of SET error that is not related operation frequency dependence. Due to clarify frequency dependent presence as the next step, additional experiment of extended operation frequency is needed.

Reference

1) P. E. Dodd *et al.*, IEEE Trans. Nucl. Sci., **48**, 1893-903 (2001).

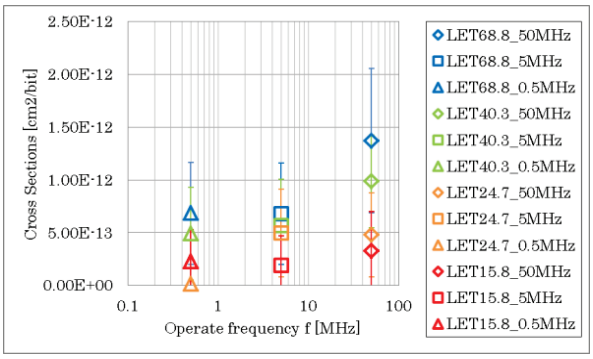

Fig. 2 Operate frequency dependence of SET based SEU error.

1-04

Study on Radiation Resistance of Inverted Metamorphic Triple-junction Solar Cells

Y. Shibata [a)], T. Nakamura [a)], T. Sumita [a)], M. Imaizumi [a)], S-I. Sato [b)] and T. Ohshima [b)]

[a)] Research and Development Directorate, JAXA,
[b)] Department of Advanced Functional Materials Research, TARRI, QST

InGaP/GaAs/InGaAs inverted metamorphic (IMM) triple-junction (3J) solar cells are expected to be applied to space because of their high conversion efficiency, high radiation resistance, light-weight and flexibility [1)]. Radiation resistance is one of the important properties for space solar cells. We should well understand radiation response of electrical output characteristics, such as degradation curves and relative damage coefficients (RDCs), in order to improve radiation tolerance of solar cells and also accurately predict degradation of performance in orbit.

In this study, we prepared two types (Type-A and Type-B) of IMM 3J solar cells with the size of 2 cm×2 cm to compare the radiation resistance. Type-A is designed with an emphasis on radiation resistance for geostationary orbit applications. Type-B is designed with higher initial convertion efficiency for low earth orbit or short-term mission applications. No cover-glass or film was applied to the front surface of the cells so that there is no shielding effect. The cells were irradiated with protons with following energies; 50 keV, 200 keV, 3 MeV and 10 MeV. Then remaining factors of short-circuit current (Isc), open-circuit voltage (Voc), maximum power (Pmax) and fill factor (FF) were calcurated from I-V characteristics under air mass zero (AM0) illumination before and after the irradiation. Finally, we calcurate RDCs by the ratio of the fluence at certain specified degradation levels (e.g. 80% of Pmax) between 10 MeV and each energies. According to SRIM simulation, 50 keV and 200 keV protons intensively make damage to the InGaP top-cell and the GaAs middle-cell, respectively. Three MeV and 10 MeV protons make damage to all the sub-cells uniformly.

Figure 1 shows degradation curves of Isc, Voc, Pmax and FF for the IMM 3J cells irradiated with 10 MeV protons. The remaining factor of Isc for Type-A is superior to that of Type-B. It is due to a result of the current margin design of the sub-cells. While Type-A and Type-B have almost equal degradation tendency in Voc, the remaining factor of Pmax for Type-A is inferior to that of Type-B. It is caused by the FF degradation. Therefore, it should be clarified that difference of the FF degradation tendency between Type-A and Type-B. Figure 2 illustrates RDCs for the IMM 3J cells proton energy. Radiation resistance of the IMM 3J cells compares with that of conventional InGaP/GaAs/Ge 3J cells. Therefore, the IMM 3J solar cells can be said to have sufficient radiation resistance for space applications.

Reference

1) T. Takamoto *et al.*, IEEE 40th Photovolt. Specialist Conf. (PVSC) (2014).

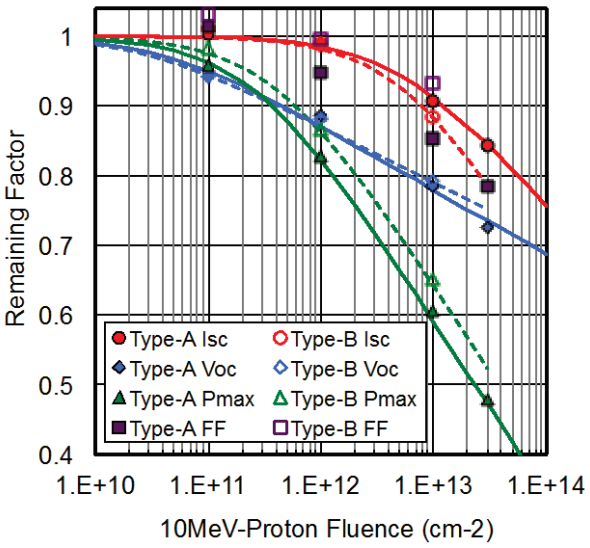

Fig. 1 Degradation curves of Isc, Voc, Pmax and FF for the IMM 3J cells irradiated with 10 MeV protons.

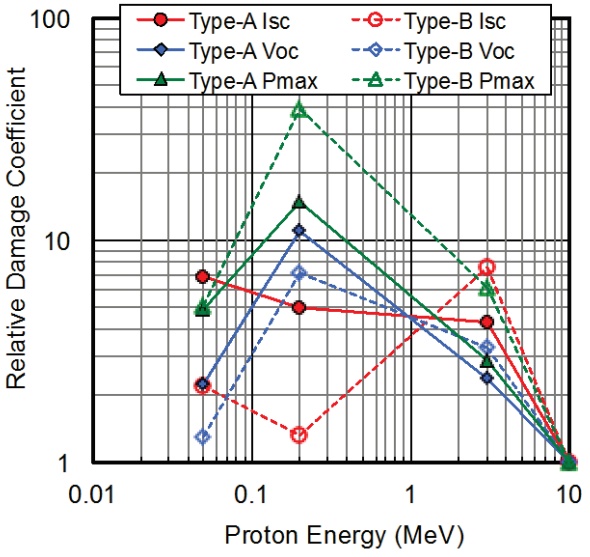

Fig. 2 Relative damage coefficients for the IMM 3J cells on proton energy.

1 -05

Irradiation Effects of Ni ions on AlGaN/GaN High Electron Mobility Transistors

S. Onoda [a)], T. Ohshima [a)], H. Sasaki [b)], Y. Nabeshima [b)], T. Hisaka [b)], K. Kadoiwa [b)], H. Koyama [b)], Y. Kamo [b)] and Y. Yamamoto [b)]

[a)] Department of Advanced Functional Materials Research, TARRI, QST,
[b)] High Frequency & Optical Device Works, Mitsubishi Electric Corporation

AlGaN/GaN High Electron Mobility Transistor (HEMTs) is one of the most promising candidates for a high-frequency and high-power electronics. The benefit of AlGaN/GaN HEMTs is that compact, lightweight, and energy-efficient devices operating at high temperature can be developed. Moreover, AlGaN/GaN HEMTs are known to be resistant to radiation damage owing to its high displacement energy. To use AlGaN/GaN HEMTs in a space radiation environment, it is necessary to understand the response to variety of radiations. The previous study investigated the change in electrical properties of AlGaN/GaN HEMT [1,2]. In this study, for more detailed investigation of the displacement damage, we have applied various methods of observation such as Photo-Emission Microscopy (PEM), Optical Beam Induced Resistance Change (OBIRCH) and Photo-Luminescence (PL) spectroscopy [3].

The device under test was the conventional AlGaN/GaN HEMTs fabricated at Mitsubishi Electric Corporation. Nickel ions were irradiated using the focused microbeam system at National Institutes for Quantum and Radiological Science and Technology (QST), Takasaki Ion Accelerators for Advanced Radiation Applications (TIARA) facility. PEM and OBIRCH were measured using Hamamatsu Photonics PHEMOS-1000 with biases of V_{gd}=-70 and -10V, respectively.

Figure 1 shows the PEM, OBIRCH and PL images before and after the 18 MeV-Ni ion irradiation at 7×10^{12} ions/cm^2. For the un-irradiated samples, the relatively uniform emission is observed for all measurements. After Ni ion microbeam irradiation, each image shows decrease of intensities at the center of gate electrode. The dotted squares in Fig. 1 show the irradiation area. The decrease in PEM intensity indicates a decrease in drain current or electric field at the irradiated area. The OBIRCH image indicates a resistance change caused by laser beam irradiation. Therefore, the decrease in the intensity is caused by a decrease in leakage current. The PL image also shows a decrease in intensity at the irradiated area. This indicates a degradation of crystal quality.

On the other hand to these optical measurements, the electrical characteristics are evaluated. As a result, no significant increase in leakage current is observed at the gate Schottky electrode. However, the drain current and transfer conductance decrease with increase of irradiation fluence. These decreases are caused by the reduction in two-dimensional electron gas (2DEG) and carrier mobility by the created crystal defects by the ion irradiation. The threshold voltage does not show any change even if the 2DEG decreases, because there are both damaged and undamaged regions in one transistor finger. The maximum drain current is stable until 1×10^{11} ions/cm^2.

We investigated displacement damage effects by heavy ion irradiation on AlGaN/GaN HEMT. We found no increases in the electric field concentration and leakage current through ions irradiation by means of PEM, OBIRCH, PL and electrical characteristics. This indicates a high reliability of displacement damage for heavy ions. Degrading the device requires irradiation more than 1×10^{11} ions/cm^2 for Ni ions. Above results indicate that AlGaN/GaN HEMT has a potential to be extremely tolerant for the radiation environment of space.

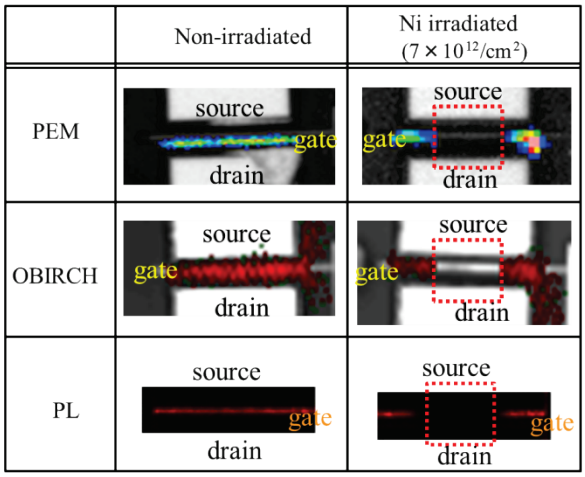

Fig. 1 Photo Emission Microscope (PEM), Optical Beam Induced Current Change (OBIRCH) and Photo Luminescence (PL) images before and after 18 MeV-Ni ions irradiation at 7×10^{12} ions/cm^2.

Acknowledgment

The authors are grateful to Kazuki Nakano and Kazuyuki Sudo of Mitsubishi Electric Corporation for PEM, OBIRCH and PL measurement.

References

1) S. Onoda *et al.*, IEEE Trans. Nucl. Sci., **60**, 4446 (2013).
2) Lv. Ling *et al.*, Microelectron. Reliab., **51**, 2168 (2011).
3) H. Sasaki *et al.*, Proc. 31st Annu. JEDEC ROCS Workshop, 59 (2016).

1-06

Minority Carrier Traps in GaAs Devices with Embedded InAs Quantum Dot Layers

S-I. Sato and T. Ohshima

Department of Advanced Functional Materials Research, TARRI, QST

I. Introduction

Since solar cells in spacecraft gradually degrade during a mission due to space radiations such as trapped electrons and protons, the radiation degradation behavior should be known and the development of a prediction method of radiation degradation is required. The mainstream of space photovoltaics are III-V triple-junction (TJ) solar cells and improvement of their efficiency and radiation tolerance by embedding quantum dots (QDs) have been recently considered. It is possible to increase the current generated in solar cells by introducing QDs because of the increase in absorption of longer wavelength light via an intermediate band within the bandgap of the host material. In order to apply this technology to space solar cells, radiation effects on GaAs devices embedded with QDs should be clarified. However, there are few reports on the direct measurement of electronic defect states (e.g. deep level traps) of QDs, which may play a direct role in the reduction of minority carrier lifetime through increased non-radiative recombination.

In this study, minority carrier traps (hole traps) in GaAs pn-junction diodes embedded with InAs QD layers are investigated using Deep Level Transient Spectroscopy (DLTS) and the origin of observed traps is discussed.

II. Experimental

The samples were GaAs p^+n diode with and without embedded 10 layer InAs QDs, which are represented as 10xQD sample and baseline sample, respectively. In the 10xQD sample, GaP strain compensating layers were introduced so as to allow multiple layers of high quality QDs to be grown. The baseline sample was the same as the QD sample except that the QD region was not grown. The samples were irradiated with 3 MeV protons at two different fluences: 1×10^{11} cm^{-2} and 7×10^{11} cm^{-2} at room temperature. The measurement of DLTS was performed in order to characterize minority carrier traps in the QD structure.

III. Results

Figure 1 shows variation of DLTS spectra of the 10xQD samples due to 3 MeV proton irradiation. A large negative peak appears at around 80 K, which is represented as Trap A in the figure. The peak height of Trap A didn't change by irradiation. On the other hand, no peak was observed at around 80 K in the baseline samples regardless of irradiation. These results indicate that an unique minority carrier trap appeared in the QD structure before irradiation and was never enhanced by irradiation.

Activation energy ($E_T - E_V$) and capture cross section (σ_n) of Trap A was obtained by analyzing DLTS spectra. The result is given in Table 1. It has been reported that a similar minority carrier (hole) trap as Trap A was found in GaP pn-junction devices [1, 2] and potentially related to Ga-vacancies (V_{Ga}) [3]. It can be concluded that Trap A probably originates from V_{Ga} in the GaP strain balancing layers. The creation of V_{Ga} in GaAs are unlikely because V_{Ga} and Ga_i pairs recombine immediately even at low temperature [4]. From its DLTS signal peak height, the density of Trap A is estimated to be substantially large and might cause a significant reduction to minority carrier lifetime in the devices. Therefore, incorporation of Trap A during the growth of GaP layers should be reduced in order to improve the device quality.

References

1) M. Matyáš Jr., Phys. Status Solidi (a), **97**, 297 (1986).
2) A. V. Skazochkin *et al.*, Semicond. Sci. Tech., **11**, 495 (1996).
3) W. Schairer, J. Electron. Mater., **8**, 139 (1979).
4) D. Pons and J. C. Bourgoin, J. Phys. C: Solid State Phys., **18**, 3839 (1985).

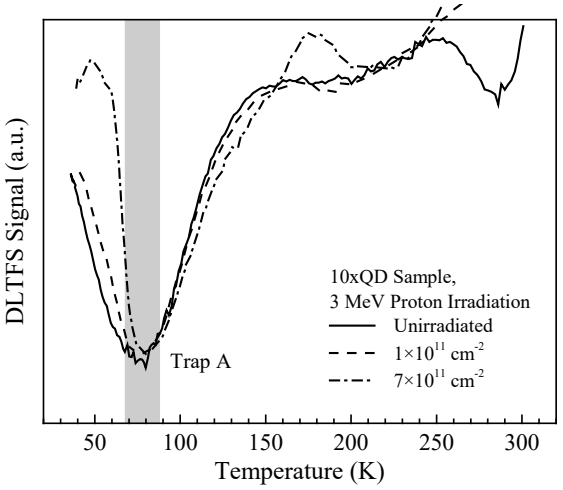

Fig. 1 Variation of DLTS spectra of the 10xQD samples due to 3 MeV proton irradiation. The irradiation fluences are shown in the figure and the peak location (Trap A) is represented as shaded zone.

Table 1 Activation energy and capture cross section of the minority carrier trap observed in Fig. 1.

Sample	Trap	$E_T - E_V$ (eV)	σ_n (cm^{-2})
10x QD	A	0.093	3×10^{-19}

1-07 Study of the Thermal Recovery for Si:C S/D n-MOSFETs

K. Takakura [a)], I. Tsunoda [a)], M. Yoneoka [a)] and M. Sugiyama [b)]

[a)] Department of Information, Communication and Electronic Engineering, National Institute of Technology, Kumamoto College,
[b)] Department of Electrical Engineering, Faculty of Science and Technology, Tokyo University of Science

The scaling of CMOS technologies leads to an intrinsic hardening against certain radiation effects, like displacement damage effect, so that the implementation of commercial-of-the-shelf ULSI components and circuits for harsh environments is becoming more popular. There is currently a strong interest in the development of deep submicron CMOS on substrates with high-channel-mobility materials and therefore methods for creating strained channels like germanium or strained silicon are being explored. One solution for these problems received special attention, i.e., using strained Source and Drain (S/D). This technique improves the carrier mobility by introducing strain in the Si channel by using a hetero junction technology, for example, carbon (C) addition to the S/D of the MOSFETs. We have investigated the 2-MeV electron irradiation effects and the relation between strained Si and the electron mobility in Si:C S/D n-type MOSFETs [1)]. In this study, the recovery behavior of 2-MeV electron irradiated strained Si channel n-MOSFETs by thermal annealing is studied.

The devices were fabricated at imec. The tensile strain in the channel was achieved by the 1%-C doping in the S/D by selective epitaxial growth using Reduced Pressure Chemical Vapor Deposition. The channel length, channel width and gate oxide film thickness are 0.25 μm, 10 μm and 1.5 nm, respectively. The samples were subjected to 2-MeV electrons at room temperature using the electron accelerator of Japan Atomic Energy Agency (JAEA). Electron fluence is 5×10^{17} e/cm^2. Thermal annealing in inert (N_2) gas ambient was performed to the devices at the temperature ranges up to 573 K for 15 min.

The recovery of channel mobility was observed by the annealing, as shown in Fig. 1. When one assumes that the recovery process is a first-order reaction [2)], the annealing rate ($1/\tau$) is given by eq. (1)

$$f_I = \exp\left(-\frac{t}{\tau}\right) = \frac{1/\mu_{AA}-1/\mu_B}{1/\mu_A-1/\mu_B}, \qquad (1)$$

where, f_I is the unannealed fraction, τ is the annealing time. The μ_{AA} and μ_A denote the mobility after and before annealing, respectively, and μ_B is the mobility before irradiation. The relationship between the annealing rate and the activation energy of recovery process is defined as

$$\frac{1}{\tau} = \nu_0 \exp\left(-\frac{E_a}{kT}\right), \qquad (2)$$

where k is the Boltzmann constant and ν_0 and T the frequency factor and annealing temperature, respectively.

Figure 2 shows the Arrhenius plot of $1/\tau$ versus annealing temperature of the undoped and C doped devices. Activation energies estimated from the Arrhenius plots are 0.10 eV and 0.11 eV for undoped and C doped devices, respectively. The nature of the responsible defects is not established at the moment. It is noted that the observation of the same activation energy for both devices allows to conclude C doping into S/D does not affect the creation of defects in the channel region.

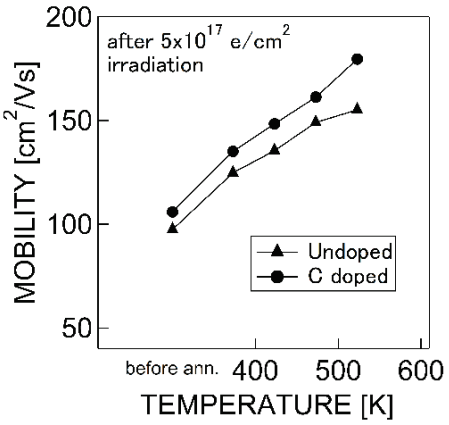

Fig. 1 Annealing temperature dependence of the electron mobility of undoped and C doped S/D n-MOSFETs after the 5×10^{17} e/cm^2 electron irradiation.

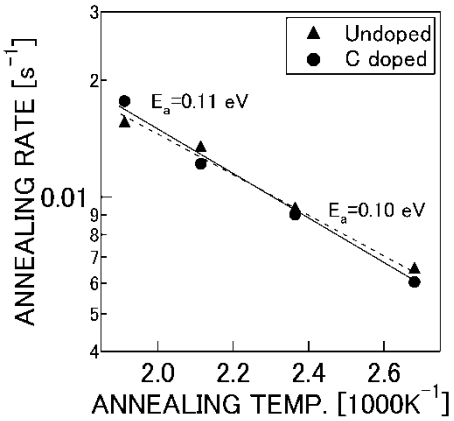

Fig. 2 The annealing rates of the mobility for undoped and C doped S/D n-MOSFETs after the thermal annealing.

References

1) M. Hori *et al.*, Mater. Sci. Forum., **778-80**, 1197-200 (2014).
2) A. O. Evwaraye and E. Sun, J. Appl. Phys., **47**, 3776-80 (1976).

1-08

Soft Error Tolerance of Redundant Flip-Flop by Heavy-Ion Beam Tests in 65 nm Bulk and FDSOI Processes

J. Furuta, E. Sonezaki, M. Hifumi and K. Kobayashi

Graduate School of Science & Technology, Kyoto Institute of Technology

We evaluated tolerance for soft errors of low power redundant FFs by combining redundant FFs and low power techniques by heavy ions. FFs were fabricated in 65 nm bulk and Fully-Depleted Silicon On Insulator (FDSOI) processes.

近年の集積回路の微細化に伴い、放射線起因の一過性のエラーであるソフトエラーが信頼性の問題として注目されている。特に宇宙空間では高エネルギーかつ高 LET（Linear Energy Transfer: 線エネルギー付与）を持つ重イオンが存在するため、多重化回路（同一の回路を複数実装して出力の多数決を行う回路）に代表される回路の対策ではソフトエラーを完全に防ぐことできない。特に近年では複数の回路が放射線によって同時に反転する多ビットエラーが増加しており、三重化回路の放射線耐性は低下し続けている [1]。放射線対策として Fully-Depleted Silicon On Insulator（FDSOI）プロセスがある。FDSOI プロセスでは基板とトランジスタの間に Buried OXide（BOX）層と呼ばれる埋め込み酸化膜を持つため、放射線によって生じた電荷の影響を低減でき、ソフトエラーの発生を抑制できる。製造コストは高くなるものの、回路性能と信頼性を両立可能である。本研究では 65 nm のバルクプロセスと FDSOI プロセスを用いて記憶素子の一種であるフリップフロップ（Flip-Flop: FF）と、放射線対策を施した多重化 FF を設計し、それらのソフトエラー率の評価を行った。ソフトエラー率の測定には高崎量子応用研究所の AVF サイクロトロンを用いた照射実験を利用した。Ar イオンと Kr イオンを設計した LSI に照射する加速試験を行い、各フリップフロップのソフトエラー率の評価を行った。設計した LSI とそのフロアプランを Fig. 1 に示す。本稿では通常の FF である TGFF と低電力向けの ACFF [2]、多重化回路として BCDMR（Bistable Cross-coupled Dual Modular Redundancy）FF [3]と ACFF ベースである BCDMR ACFF に限定してそのソフトエラー評価結果を報告する。バルクプロセスにおける測定結果を Fig. 2 に、FDSOI プロセスの結果を Fig. 3 に示す。

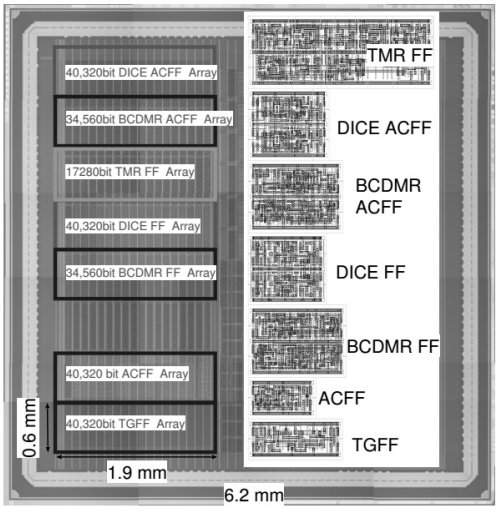

Fig. 1 Fabricated test chip and floorplan.

バルクプロセスでは二重化回路である BCDMR でもソフトエラーが生じている。BCDMR は 2 重化回路の一種であるため、消費電力や面積は 2 倍以上増加している。しかしそのソフトエラー耐性の向上は ACFF や TGFF の 10-30 倍程度であり、FDSOI の TGFF や ACFF の方が高耐性である。ACFF と TGFF を比較すると、ACFF の方が 3-10 倍耐性が高い。一方で FDSOI プロセスの BCDMR ではエラーが発生しなかった。基板とトランジスタが BOX 層によって分離されており、多ビットエラーが発生しにくいため、FDSOI ではソフトエラーが生じないと推測される。以上より、宇宙空間では FDSOI プロセスと多重化回路を組み合わせることで十分なソフトエラー耐性を実現できることを確認した。

References

1) S. Jagannathan *et al.*, Int. Reliability Phys. Symp., SE.5.1-5.5 (2011).
2) K. T. Chen *et al.*, Int. Solid State Conf., 338-40 (2011).
3) J. Fururta *et al.*, VLSI Circuit Symp., 123-24 (2010).

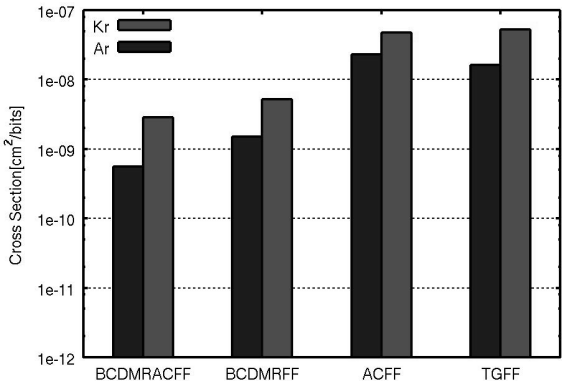

Fig. 2 Cross sections of BCDMR and non-redundant FFs in the bulk process.

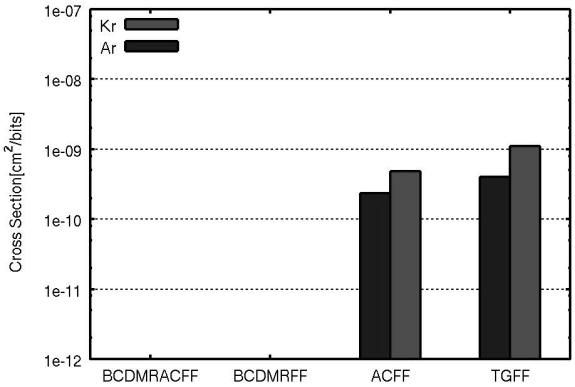

Fig. 3 Cross sections of BCDMR and non-redundant FFs in FDSOI process.

1 -09

Proton Irradiation Effects on InAsSb Quantum-Well-Based Hall Sensors

H. Okada [a,b], A. Aberrahmane [a,b], I. Shibasaki [b], A. Sandhu [a,b], A. Wakahara [b], S-I. Sato [c] and T. Ohshima [c]

[a] Electronics-Inspired Interdisciplinary Research Institute, Toyohashi University of Technology, [b] Department of Electrical and Electronic Information Engineering, Toyohashi University of Technology, [c] Department of Advanced Functional Materials Research, TARRI, QST

Proton irradiation effects on AlInSb/InAsSb/AlInSb quantum-well-based hall sensor is studied. Decrease of the magnetic sensitivity was seen at a proton fluence of 10^{13} protons/cm^2. By increasing proton fluence, although the further degradation of the sensitivity was confirmed, the decrease remained in single digit after the proton fluence of 10^{16} cm^{-2}. These results suggest that InAsSb quantum-well based hall sensor is suitable for irradiation environment.

高感度な半導体ホールセンサはモータの回転制御などに応用されており、精密小型モータやハードディスク、DVD ドライブなどにも搭載されている。InSb 系材料は、室温において数万 cm^2/Vs の高い電子移動度を示し、高速、高感度なホールセンサ材料として用いられている。このように重要な構成要素として広く用いられている InSb 系ホールセンサであるが、これまでにその放射線耐性や照射効果の検討はあまりなされていなかった。我々は過去に InAsSb ヘテロ構造型のホールセンサが 10^{16} protons/cm^{2}の高い陽子線照射後も感度劣化が少ないことを報告してきた [1]。本報告では、InSb 系ホールセンサの陽子線照射効果について詳細なデータを得るとともに、ドーピング濃度が異なるホールセンサ試料についても検討を行った。

Figure 1(a)に検討に用いた試料の層構造を示す。$Al_{0.1}In_{0.9}Sb$ を障壁層、$InAs_{0.1}Sb_{0.9}$を量子井戸層とするヘテロ構造であり、今回は、井戸層である InAsSb にドナーとして Sn を5×10^{16}, 7×10^{16}, 10^{17} cm^{-3}ドーピングした。フォトリソグラフィーによりメサエッチングを行った後にオーミック電極を形成し、ホールセンサとした。TIARA における 380 keV の陽子線照射では試料のパッケージングなど封入は行わず、試料に直接照射を行った。評価は電流源と電圧計、磁気コイルを用いた四端子法により室温で行った。

Figure 1(b) にホールセンサの感度(S_I)を陽子線照射量に対してプロットしたものを示す。ホールセンサの感度はホール起電力 V_H、定電流 I、印加外部磁場 $B_\perp$ により $S_I = V_H/(IB_\perp)$のように書ける。ホール起電力はホールセンサのシートキャリア密度と逆比例の関係があり、未照射試料(ref.)の感度の違いはドーピング濃度の差によると考えられる。いずれの試料でも高い陽子線照射量で感度の低下が観測されたが、感度低下は 10^{14} cm^{-2}以上の照射後であり、10^{16} cm^{2}の照射後でも、初期感度からの感度の減少は1桁以内であることがわかる [2]。

Figure 1(b) の挿入図にホールセンサのシートキャリア濃度の陽子線照射量依存性を示す。照射量増加に伴ってシートキャリア密度の増大が観測された。即ち、照射による感度低下はキャリア濃度の増大によるものと考えられる。Brudnyĭらによる種々の半導体への照射によるキャリア密度変化をモデル化した報告 [3] によると、アニオンとして Sb を含む化合物半導体では、照射欠陥によるホール濃度増大が示唆され、InAs では電子濃度増加が示唆されている。今回の実験で用いているような三元混晶での振る舞いは未知であるが、定性的には競合関係からドナー性の欠陥によるチャネル中の電子濃度増大が観測されたと考えられる。また、AlInSb/InAsSb ヘテロ界面では、一方のバンドギャップが他方のバンドギャップに内包される type-I 型の接続ではなく、片方の半導体の価電子帯上端と伝導帯下端が同じエネルギー方向にずれる type-II 型の接続が予測され、界面での電子と正孔の蓄積を前提とした解析が必要であり、照射効果の解明にはより詳細な検討が必要である。

References

1) A. Abderrahmane *et al.*, IEEE Trans. Magn., **48**, (11), 4421 (2012).
2) A. Abderrahmane *et al.*, IEEE Electron. Device Lett., **35**, 1305 (2014).
3) V. N. Brudnyĭ *et al.*, Semiconductors, **41**, 1011 (2007).

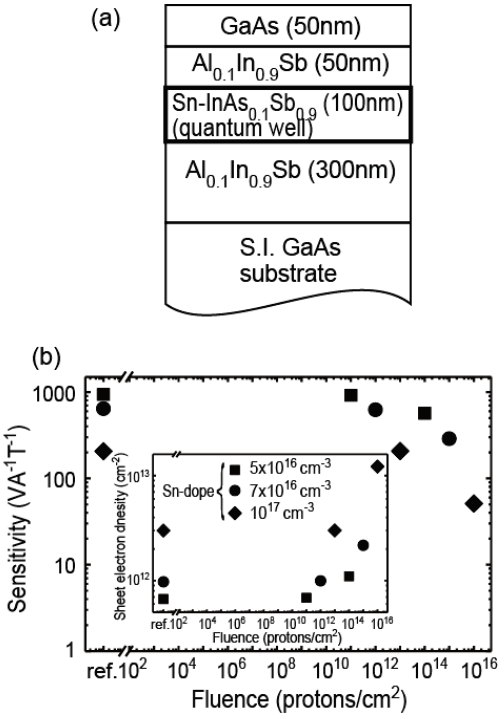

Fig. 1 (a) AlInSb/InAsSb/AlInSb heterostructure for magnetic Hall sensor used in this study, and (b) dependence of sensitivity on proton irradiation fluence. The inset shows sheet carrier density dependence on the fluence.

1 -10

Research of the Radiation Tolerance in Space Environment of General Electronic Devices

T. Maeda [a)], K. Tomita [a)], Y. Kakehashi [a)], K. Akashi [a)],
T. Ohshima [b)], S. Onoda [b)] and T. Makino [b)]

[a)] Advanced Engineering Services Co., Ltd. (AES),
[b)] Department of Advanced Functional Materials Research, TARRI, QST

In small satellite development, general electronic commercial off-the-shelf (COTS) devices are needed to use due to some severe restrictions of resource for installed components. For this reason, it is important to keep reliability for using COTS devices in small satellite development. Therefore, in order to ensure reliability for small satellite, our company has evaluated COTS devices mainly for tolerance of single event at Takasaki Advanced Radiation Research Institute (TARRI) from fiscal year 2008.

近年、小型人工衛星の開発が盛んになり、衛星搭載機器の低コスト化、小型化、及び高機能化が要求されている。これらの要求を満たすため、民生電子部品の使用が望まれている。しかしながら、一般的に民生電子部品は宇宙環境下での使用を考慮して設計されておらず、耐放射線性は不明である。そこで民生電子部品の宇宙環境における動作状況、劣化状況を放射線試験により確認し、宇宙への適合性を把握する。

放射線の電子部品への影響は、大きくトータルドーズ効果（TID: Total Ionization Dose）とシングルイベント効果（SEE: Single Event Effect）に分けられる。TID はβ線、γ線、陽子線により発生する電子部品の性能劣化である。また、SEE は重粒子の入射により引き起こされる機能障害である。本研究において、民生電子部品の使用を想定している小型人工衛星は運用期間が1年と短いため、TID による影響は少ないと考える。一方、SEE は1度の発生で電子部品そのものや周辺回路を破壊する可能性がある。そこで本研究は、様々な民生電子部品の SEE 試験を行い、宇宙環境における耐放射線性の評価を行うことを目的としている。

本研究は、高崎量子応用研究所の AVF サイクロトロン No.12 散乱ビーム照射試験装置（第4重イオン室）にてカクテルビーム（N, Ne, Ar, Kr の4線種）を使用し、実施した。SEE 発生頻度は、試験により得られた反転断面積、LET（Linear Energy Transfer）閾値と CREME96［Cosmic Ray Effects on Micro-Electronics（1996 Revision）］を用いて計算した軌道上放射線分布より算出した。

本研究で民生電子部品の使用を想定している小型人工衛星の軌道条件は、高度 700 km、軌道傾斜角 98 度、衛星構体は 2 mm 厚アルミニウム、運用期間1年である。算出した SEE 発生頻度と想定運用期間を比較し、民生電子部品の耐放射線性を評価した。表 1 に昨年度実施した試料、評価項目、試験結果、及び使用を想定している軌道条件を用いて試験結果から算出した SEE 及び異常動作発生頻度を示す。

Table 1 より、メモリ（SRAM）の SEU（Single Event Upset）、DA コンバータの SEL（Single Event Latch-up）、SEU 及び PLL シンセサイザの SEU の発生頻度は想定している1年という運用期間に対して大きく、十分な耐放射線性を有さないことが確認できた。実際に用いる際は、発生頻度を考慮した設計とする必要がある。イメージセンサの画像異常についても、全ての線種で SEU の発生が見られたため、設計時にはこれを考慮する必要がある。イメージセンサの SEL、異常動作、メモリ、PLL シンセサイザの SEL、及び DA コンバータの異常動作の発生頻度は、想定している 1 年という運用期間に対して小さく、十分な耐放射線性を有することが確認できた。

最後に試料である民生電子部品は、宇宙環境での使用を想定して製造されたものではないため、本試験の結果が部品自身の性能・機能の優劣を示すものではないということを付記しておく。

Table 1　Single event probability.

Specimen	Evaluation Item	LET Threshold (MeV/mg/cm^2)	Cross-sectional area (cm^2)	Singlle Event Probability (event/year)
Image sensor (With cover glass)	SEL	34	9.10E-07	1.13E-09
Image sensor (Without cover glass)	SEL	14	1.54E-06	8.08E-06
	Control software Error	3	3.33E-06	8.10E-04
SRAM	SEL	14	9.84E-07	6.53E-06
	SEU	0.001	1.98E-08 *	1.57E-06 **
DA converter	SEL	5.9	1.52E-04	7.08E-03
	SEU	0.014	8.19E-04	3.78E-01
	Other Errors	14	7.59E-08	4.12E-05
PLL synthesizer	SEL	14	1.91E-06	1.04E-05
	SEU	0.001	1.44E-05	1.31E-02

* cm^2/bit,　** event/bit/year.

1-11 Fabrication of Quantum Registers and Array of Quantum Sensors in Diamond by Nano-Hole Ion Implantation

J. Isoya [a)], T. Umeda [b)], S. Onoda [c)] and T. Ohshima [c)]

[a)] Research Center for Knowledge Communities, University of Tsukuba,
[b)] Faculty of Pure and Applied Science, University of Tsukuba,
[c)] Department of Advanced Functional Materials Research, TARRI, QST

Quantum registers and atom-sized, high-sensitivity magnetic sensors are emerging solid-state quantum devices which operate under ambient conditions by utilizing a NV (nitrogen-vacancy) center in diamond. The nitrogen molecular ions were implanted via shadow mask with array of nano-holes (diameter: 10 nm ~ 30 nm) on the diamond. The nano-holes in shadow mask made by PMMA (thickness: ~200 nm) were fabricated by EB (electron-beam) lithography technique. We used high purity ^{12}C-enriched (99.998%) CVD layers grown on type-Ib substrates.

Quantum registers in which several qubits are coherently coupled have potential applications in quantum computing and quantum communication. With the extraordinary properties such as optical initialization, optical readout, ability of spin-manipulation by microwave pulse and long coherence time, single electron spin of single NV center is outstanding as solid-state spin qubit at room temperature. Here, coherently-coupled multiple NV centers with an average distance of ~12 nm were fabricated by implantation of $^{15}N_2^+$ (20 keV) ions through nano-hole (diameter ~10 nm) and subsequent annealing (1,000 °C, 2 h). The number of NV centers formed at each implantation spot obeys a Poisson distribution. It has been found that the average number could be controlled to be 1~24 by varying the implantation dose.

Thus, our fabrication method provides potentially scalable, quantum register. The key factor of scalability is the ratio between the coherence time and the 2 qubit CNOT gate operation time. While fast gate operation is expected from strong dipole-dipole interaction arising from short distance (~12 nm) estimated from SRIM simulation, the observed short coherence time (~30 μs) is ascribed to the proximity (~15 nm) to the surface and the presence of unwanted paramagnetic species originating from excess implants. To improve the coherence time, overgrowing of additional ^{12}C layer on the top surface and co-implanting $^{12}C^+$ ions to increase the yield is being carried out.

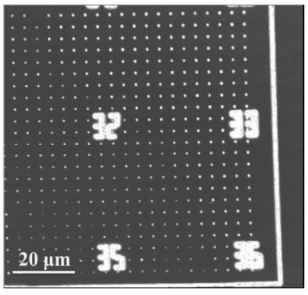

Fig. 1 Confocal microscopy image (xy-scan) of array of spots consisting of several NV^- centers fabricated by nano-hole implantation of N_2^+ (20 keV).

At the maximum, 4-qubits can be individually addressable since different N-V directions give different EPR frequencies. Creation of four single NV centers with four different N-V directions in a spot has been confirmed from the ODMR spectrum as shown in Fig. 2.

NV centers formed at near-surface are promising sensor of detecting external spins such as nuclear spins of molecules placed on the surface of diamond. Pulse sequence such as XY8-N of repeating π pulses provides high resolution by prolonging coherence time by averaging out the noises and high selectivity of particular nuclear spins by matching the pulse separation with the NMR frequency. For this application a regular array of shallow, single NV center with address markers are useful. In the resist mask, letter-shaped holes were made together with arrays of nano-holes. After implantation and annealing, address markers composed of NV centers are easily noticeable (Fig. 1). By using a lower dose of N^+ (5 keV) ions with larger nano-holes (diameter 30 nm), we have fabricated regular arrays of single NV center (the average number ~1.0 of Poisson distribution).

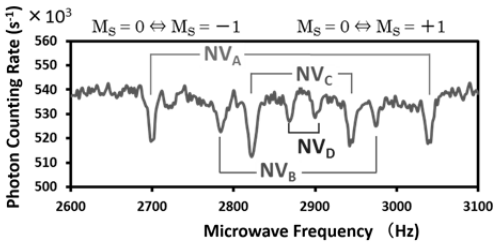

Fig. 2 ODMR spectrum of a spot consisting of four NV centers of four different N-V directions.

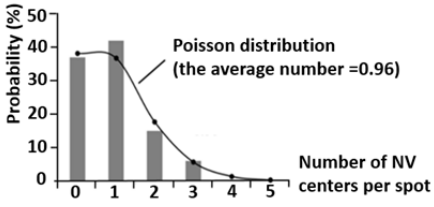

Fig. 3 Distribution of the number of NV centers per spot fabricated by nano-hole implantation of N^+ (5keV).

Acknowledgements

The present work is a collaboration with Dr. T. Teraji (NIMS), Prof. T. Tanii (Waseda University) and Prof. F. Jelezko (University of Ulm).

1-12 Investigation of Deep Levels in Diamond by Transient Charge Spectroscopy with Heavy Ion Microbeam

T. Kamiya [a)], Y. Ando [a),b)], Y. Kambayashi [a),b)], W. Kada [b)], S. Onoda [a)], T. Makino [a)], S. Sato [b)], H. Umezawa [c)], Y. Mokuno [c)], S. Shikata [d)], O. Hanaizumi [b)] and T. Ohshima [a)]

[a)] Department of Advanced Radiation Technology, TARRI, QST,
[b)] Faculty of Science and Technology, Gunma University,
[c)] Department of Energy and Environment, AIST,
[d)] School of Science and Technology, Kwansei Gakuin University

Single-crystalline (SC) diamond is regarded as an ideal candidate for the next-generation radiation detector, which has not only excellent electrical, mechanical properties but also high radiation tolerance[1-2]. Although diamond crystal growth techniques have been advanced in recent years, it is still necessary to investigate the deep levels which are affective to the electrical properties of the detector. However, conventional deep level transient spectroscopy (DLTS) cannot be well applied for characterization of the defects in high-resistive wafers which are often used for radiation detectors.

In this study, we investigate electrically-active deep levels in unintentionally doped single-crystalline diamond using heavy ion charge transient spectroscopy, HIQTS, using the heavy ion microbeam system at JAEA-TARRI[3]. A free-standing unintentionally doped (UID) (001) SC diamond substrate with dimension of 3 mm × 3 mm and thickness of 100 μm was fabricated by lift-off process using ion implantation [4] and employed for the evaluation. Heavy ion microbeams of oxygens with 10.5 MeV and carbons with 9 MeV with an equivalent scanning area of 400 × 400 μm were employed for HIQTS. A low count rate of approximately 20 cps in average was used for the measurement to prevent the crystal from the permanent damage of heavy ion bombardment. The ion-induced charges generated in diamond detector were measured using a charge sensitive preamplifier (CSP; ORTEC, 142A).

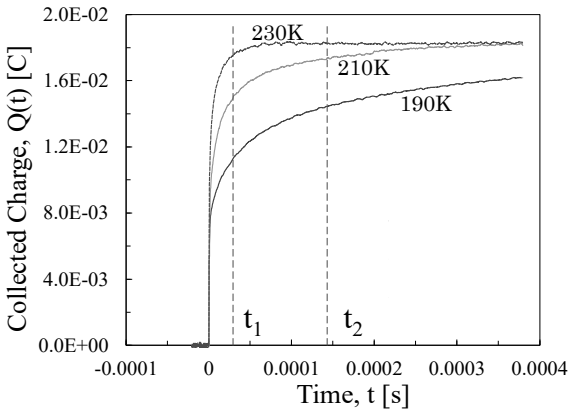

Fig. 1 Temperature dependence of HIQTS charge signals induced by 10.5 MeV oxygen microprobe.

The shapes of output signals were recorded using a digital storage oscilloscope (DSO; Agilent, DSO2024A). These signals were handled by use of the in-house software based on NI LabVIEW. Examples of obtained CSP output at different temperature were obtained as shown in Fig. 1.

HIQTS spectrum were collected in temperature ranges from 180 K to 280 K, as shown in Fig. 2. A peak was observed in each spectrum with different time span of t_1 and t_2. From the Arrhenius plot of the peak, the activation energy of this deep level was estimated as 0.35 eV which had similar to the activation energy of boron. Similar activation energy was obtained at HIQTS measurement with different excitation probe of oxygen. The existence of boron was examined by SIMS analysis, therefore these experimental result of HIQTS seem to suggest that these deep levels of boron may affect to the charge collection of the detector.

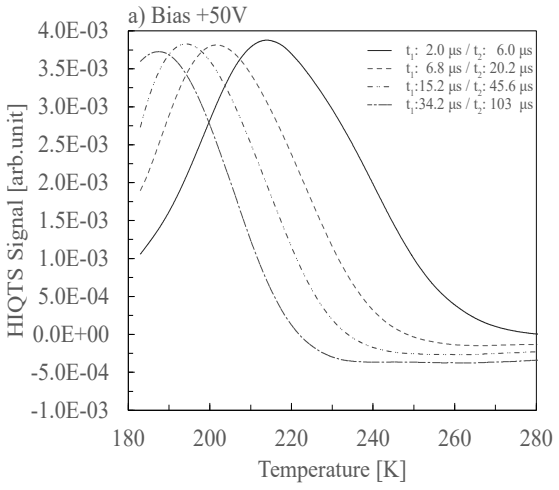

Fig. 2 Example of HIQTS spectra of the UID CVD diamond detector induced by 9 MeV carbon microprobe.

References

1) J. Isberg *et al.*, Science, **297**, 1670 (2002).
2) H. Pernegger *et al.*, Nucl. Instrum. Meth. Phys. Res. A, **535**, 108 (2004).
3) W. Kada, Y. Kambayashi, N. Iwamoto, S. Onoda, T. Makino, M. Koka, T. Kamiya, *et al.*, Nucl. Instrum. Meth. Phys. Res. B, **348**, 240 (2015).
4) Y. Mokuno *et al.*, Diam. Relat. Mater., **17**, 415 (2008).

1-13 Preparation of Copper Nanocones in Ion-Track Membranes of Polyimides

H. Koshikawa, S. Yamamoto, M. Sugimoto, S. Sawada and T. Yamaki

Department of Advanced Functional Materials Research, TARRI, QST

Chemical etching of polymer films irradiated with heavy ions of several hundred MeV leads to the formation of ion-track membranes with nanometer-to-micrometer pores in different shapes[1,2]. The ion-track membranes have been used as templates for generating nanostructures of metals and semiconductors. Particularly, penetrating conical pores were prepared by selectively etching the ion tracks from one side to obtain metal nanocones[3]. Due to their high surface area, nanocone arrays were expected as catalysts for applications to next-generation electrochemical devices[4]. In this preliminary study, therefore, we tried a new method of preparing copper nanocones involving the formation of *non-penetrating* conical pores of ion-track membranes, vapor-deposition and electroplating.

Five, 12 or 25-μm thick polyimide (PI) films stacked on an Al plate were irradiated with 330 MeV ^{40}Ar ions at a fluence of 3.0×10^{7} or 3.0×10^{8} ions/cm^2. The lowermost film, inside which the bombarding ions were found to stop, was etched in a sodium hypochlorite solution at 60 °C for 0.5-1.5 h, leading to the formation of *non-penetrating* conical pores. A very thin Au layer was vapor-deposited on the pore side of these ion-track membranes; then, it was used as a cathode for electroplating copper into the pores. The electroplating was conducted in a 1.0 M copper sulfate aqueous solution of pH 1 at a voltage of 0.2-1.0 V. The obtained samples were observed with scanning electron microscopy (SEM).

Figure 1 shows the representative SEM images of the ion-track membrane just for checking to be sure of the shape of the etched pores. In (a), we can see the circular pores on the surface and their diameter decreasing at larger depths. Figure 1 (b) enables us to confirm a perfectly conical shape from the cross-sectional view of the membrane.

Figure 2 indicated that dissolution of the PI templates finally left the copper nanocone ca. 510 nm in base diameter and 1.2 μm in height. An aspect ratio, defined as a ratio of the height to base diameter, was calculated to be 2.4, which is reasonably close to that of the nanopores used as a template.

In conclusion, the ion-track membranes with *non-penetrating* conical pores were easily obtained by adjusting the sample thickness in accordance with the projective range of the bombarding ion. The nanocones with an aspect ratio of 2.4 were prepared within this template by combination of vapor-deposition and electroplating methods. An investigation for the higher aspect ratio is now in progress by optimizing template materials and the experimental conditions.

References

1) T. Yamaki *et al.*, Nucl. Instrum. Meth. Phys. Res. B, **314**, 77-81 (2013).
2) N. Nuryanthi *et al.*, Nucl. Instrum. Meth. Phys. Res. B, **314**, 95-98 (2013).
3) H. Koshikawa *et al.*, J. Membr. Sci., **327**, 182-87 (2009).
4) J. N. Tiwari *et al.*, J. Power Sources, **182**, 510-14 (2008).

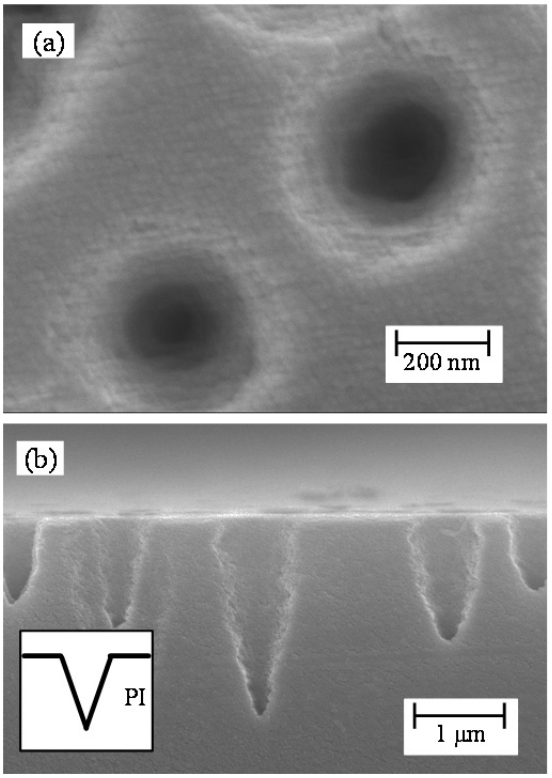

Fig. 1 Representative SEM images of (a) the surface and (b) cross-section of the PI ion-track membranes.

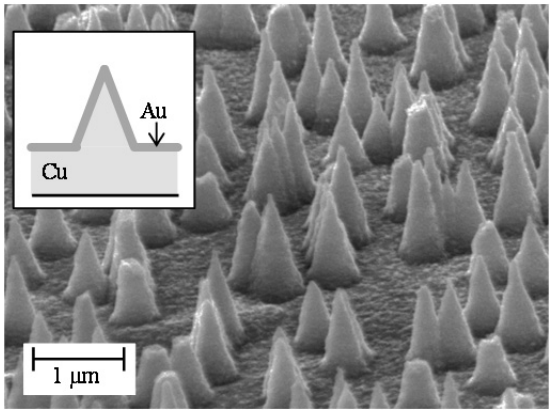

Fig. 2 SEM image of copper nanocones.

1 - 14

Catalytic Activity of Pt Nanoparticles on a Glassy Carbon Substrate Pre-Irradiated with Ar Ions

K. Kakitani [a)], T. Kimata [a)], T. Yamaki [b)], S. Yamamoto [b)], D. Matsumura [c)], I. Shimoyama [c)], A. Iwase [d)], T. Kobayashi [e)] and T. Terai [a)]

[a)] Department of Nuclear Engineering & Management, The University of Tokyo,
[b)] Department of Advanced Functional Materials Research, TARRI, QST,
[c)] Materials Sciences Research Center, JAEA,
[d)] Department of Materials Science, Osaka Prefecture University,
[e)] Neutron Beam Technology Team, RIKEN

Platinum (Pt) nanoparticles are usually employed as cathode catalysts for the oxygen reduction reaction (ORR) in proton exchange membrane fuel cells (PEFCs). In order to widely commercialize PEFCs, Pt nanoparticles with the high ORR activity have been actively pursued worldwide. Quite recently, Pt nanoparticles supported on the glassy carbon (GC) substrate pre-irradiated with Ar ions were found to exhibit strong electronic interactions with carbon atoms at the interface [1, 2)]. These unique interactions induced by the ion irradiation could affect the ORR activity of the Pt nanoparticles by tuning their electronic structures. The objective of this report is to investigate the effect of the Ar-ion irradiation on the ORR activity of the supported Pt nanoparticles.

A GC substrate was irradiated with 380 keV Ar ions at a fluence of 1.0×10^{16} ions/cm^2 in an IA chamber at the TIARA ion implanter and then heated at 400 °C in a N_2 atmosphere for 1 h. Platinum nanoparticles were deposited by RF magnetron sputtering on the pre-irradiated and non-irradiated GC substrates. Figure 1 shows a transmission electron microscope (TEM) image of Pt nanoparticles deposited directly on a TEM grid under the same conditions. Pt nanoparticles observed as black circles had an average diameter of about 5 nm. Cyclic voltammetry and rotating disk voltammetry were performed to determine the ORR activity of the prepared samples. Those electrochemical measurements were carried out in a cell containing 0.1 M H_2SO_4 aqueous electrolyte at 25 °C.

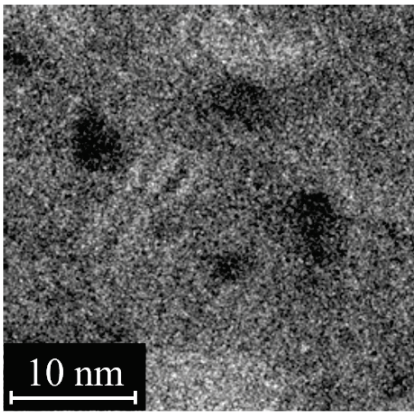

Fig. 1 TEM image of the Pt nanoparticles deposited on a grid mesh.

Figure 2 shows Tafel plots, which represent a specific ORR activity standardized by the electrochemical surface area. The specific activity was higher for the pre-irradiated sample than for the non-irradiated one at the same voltage. Strikingly, only by using the pre-irradiated GC support, the specific activity at 0.85 V versus RHE was increased by 2.5 times [3)].

In conclusion, the surface modification of the GC substrate by Ar-ion irradiation enhanced the ORR activity of the supported Pt nanoparticles through the strengthened interfacial interactions. An X-ray absorption fine structure (XAFS) measurement [4)] is now in progress to investigate the local structures at the nanoparticle-substrate interface.

Acknowledgements

This work was partly performed under the NIMS-RIKEN-JAEA-QST Cooperative Research Program on Quantum Beam Science and Technology.

References

1) T. Kimata *et al.*, JAEA Takasaki Annu. Rep. 2014, JAEA-Review 2015-022, 41 (2016).
2) T. Kimata *et al.*, Surf. Coat. Tech., in press (2016).
3) K. Kakitani *et al.*, Abst. ECSJ 2016 83rd Spring Meet., 1K31 (2016).
4) T. Kimata *et al.*, Abst. 29th Annu. Meet., JSR 7Aa007 (2016).

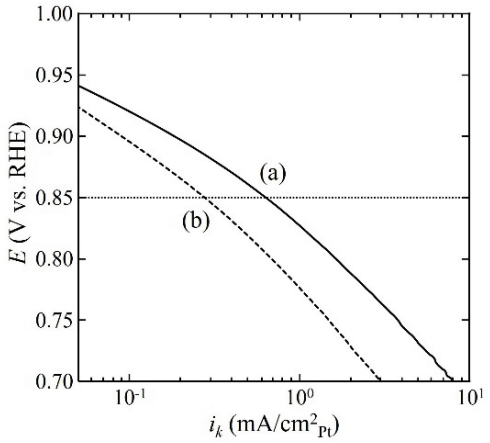

Fig. 2 Tafel plots for ORR. The Pt nanoparticles on the (a) pre-irradiated and (b) pristine GC substrates.

1-15

Ion-Track Grafting of Vinylbenzyl Chloride into Poly(ethylene-*co*-tetrafluoroethylene) Films: Comparison between Different Ions

N. Nuryanthi [a,c], T. Yamaki [a], S. Saiki [a], A. Kitamura [b], H. Koshikawa [a], K. Yoshimura [a], S. Sawada [a] and T. Terai [c]

[a] Department of Advanced Functional Materials Research, TARRI, QST,
[b] Fuels and Material Engineering Division, NSEC, JAEA,
[c] Department of Nuclear Engineering and Management, The University of Tokyo

We have recently used the ion-track grafting technique to prepare anion exchange membranes (AEMs) for fuel cell applications. In this technique, the reaction occurs only inside latent tracks of swift heavy ions in a base polymer. Thus, the resulting AEMs will have a heterogeneously-distributed structure (grafted and ungrafted area), which can improve their performances. We studied here the effect of different-ion irradiation in term of grafting reactivity and radical behavior. The radical behavior was analyzed by electron spin resonance (ESR) measurements.

A 25-μm-thick poly(ethylene-*co*-tetrafluoroethylene) (ETFE) film was irradiated in a vacuum chamber of the LD beamline with 560 MeV ^{129}Xe and 330 MeV ^{40}Ar at different fluences between 2.0×10^{8} and 6.0×10^{9} ions/cm^2. The irradiated films were then stored in air at −80 °C until just before the grafting. The grafting polymerization was initiated by immersing the irradiated ETFE film in 20 vol% vinyl benzyl chloride (VBC) mixed with water. The degree of grafting (DG) was calculated by

$$\mathrm{DG} = \frac{(W_g - W_0)}{W_0} \times 100\ (\%) \quad (1)$$

where W_0 and W_g are the weights of the film before and after the grafting, respectively. The ESR spectra were measured at room temperature using a microwave power of 1 mW, modulation width of 0.2 mT, time constant of 1 s and sweep time of 1 min.

All the irradiated ETFE films exhibited an almost-symmetrical singlet spectrum (not shown), which implies the formation of the same type of radicals by the different ions. Figures 1 (a) and (b) plot the ESR spectral intensity (filled circle) and the DG (open circle) as a function of absorption dose for the ^{129}Xe and ^{40}Ar ions, respectively. The fluence was converted to the dose by the following equation: LET (MeV/μm)×fluence (ions/cm^2)×A, where A denotes a conversion factor involving the density of ETFE and physical constant (9.4×10^{-10}). In these figures, both of the ESR signal intensity and DG were higher for the Ar-irradiated film than for the Xe-irradiated one within the same range of dose. The SRIM calculation indicates that the Xe ion has six times as high LET as the Ar, and thus the Xe ion would produce higher concentration of radicals just after the bombardment. Such high density of radical formation is likely to increase the probability of radical recombination, thereby decreasing the total radical concentration in the film and finally lowering the DG.

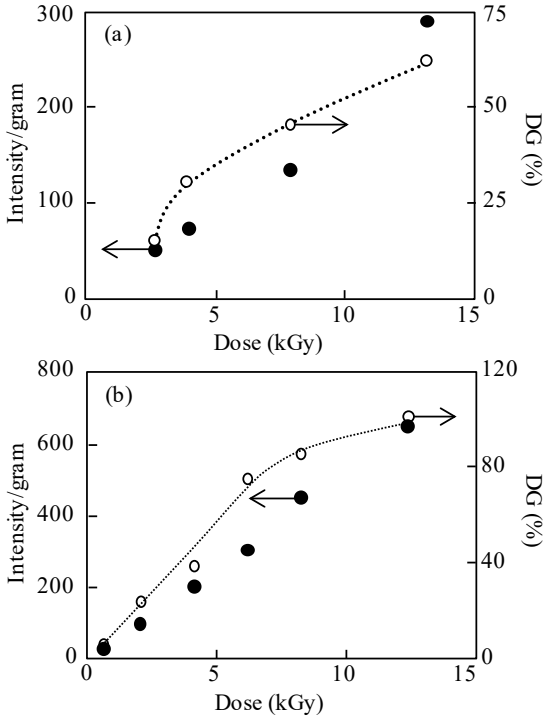

Fig. 1 The ESR spectral intensity (filled circle) and DG of VBC into the ETFE film (open circle) as a function of dose for (a) 560 MeV ^{129}Xe and (b) 330 MeV ^{40}Ar.

Interestingly, we can also observe a different increasing trend between the ESR signal intensity and DG. In other words, the ESR signal increased approximately linearly with the dose, but in contrast an increase rate of the DG was becoming lower at higher doses. This seems surprising for most researchers because the DG would normally be governed by the density of free radicals. At present, we can rationalize it by considering the temperature dependence of the radical-recombination probability. A linear increase in the ESR signal observed at room temperature suggests a limited impact on the recombination in this range of radical density. On the other hand, at 60 °C for the grafting reaction, the probability of the radical recombination would be enhanced especially in a high-dose range, thereby reducing an increase rate of the DG.

Reference

1) B. S. Rao *et al.*, Radiat. Eff. Def. Solids, **161**, 31-39 (2006).

1-16 Improvement of HI Concentration Performance Using Crosslinked Radiation-Grafted Membranes

N. Tanaka [a], S. Sawada [b], T. Yamaki [b], S. Kubo [a] and T. Terai [c]

[a] Hydrogen Application Research and Development Division, NHARC, JAEA,
[b] Department of Advanced Functional Materials Research, TARRI, QST,
[c] Department of Nuclear Engineering and Management, The University of Tokyo

Thermochemical water-splitting Iodine-Sulfur (IS) process[1] is known to be a promising method for hydrogen production. In the IS process, a new cation-exchange membrane prepared by the radiation-induced graft polymerization has been applied to the electro-electrodialysis (EED) in order to enrich hydrogen iodide (HI) in an HI-I_2-H_2O mixture (HIx solution)[2, 3]. The membrane performance should be improved for the efficient HI concentration. The performance can be represented by indexes such as proton transport number (t_+) and water permeation factor (β). Our previous study[2] suggested that the permeation of anionic species and water must be inhibited to increase the t_+ and to lower the β values. In the present study, we attempted to achieve this requirement by introduction of crosslinking structures inside the cation-exchange membrane using divinylbenzene (DVB). The t_+ and β indexes were also evaluated experimentally for the styrene (St)/DVB-grafted and sulfonated poly(ethylene-*co*-tetrafluoroethylene) (ETFE-St) membranes.

The membranes were prepared by pre-irradiation of the ETFE film with γ-rays, the graft polymerization of St with 5 vol% DVB or without DVB, and the sulfonation of the grafted materials. The resulting crosslinked and non-crosslinked membranes are referred to as ETFE-St/DVB and ETFE-St, and their ion exchange capacity (IEC) ranged 1.1-1.6 and 1.3-2.1 mmol/g, respectively. The t_+ and β values were measured using a filter-press type EED cell[2], to which a direct current of 200 mA/cm^2 was supplied for 4 h at 313 K. The feeding HIx solution contained 10 mol/kg of HI and 10 mol/kg of I_2.

Figure 1 shows the variation of t_+ as a function of IEC. The t_+ value of ETFE-St/DVB decreased with an increase in IEC; interestingly, however, it was higher than that of ETFE-St. This means that the crosslinking could improve proton selectivity.

Figure 2 shows the variation of β as a function of IEC. The β value of ETFE-St/DVB appeared to increase with an increase in IEC. However, it was lower than that of ETFE-St in the similar IEC range. This means that the crosslinking could prevent water from permeating through the membrane.

The introduction of DVB makes a network structure in the membrane by forming bonds between the grafted chains, thereby narrowing a flow channel in the less swollen membranes. In this manner, it is predicted that water and I^- permeations could be restricted in the ETFE-St/DVB during the HI concentration. The restriction of I^- permeation means that H^+ selectivity is apparently improved, in other words, t_+ value is enhanced. Naturally, the restricted water permeation can decrease the β value as well.

In conclusion, we could confirm the positive effect of crosslinked membranes for the improvement of concentration performance. An investigation for further improvement in the membrane performance is now in progress by optimizing the amount of crosslinks.

References

1) S. Kubo *et al.*, Nucl. Eng. Des., **233**, 355-62 (2004).
2) N. Tanaka *et al.*, J. Membr. Sci., **411-12**, 99-108 (2012).
3) T. Yamaki *et al.*, Polymer, **45**, 6569-73 (2004).
4) N. Tanaka *et al.*, J. Membr. Sci., **456**, 31-41 (2014).

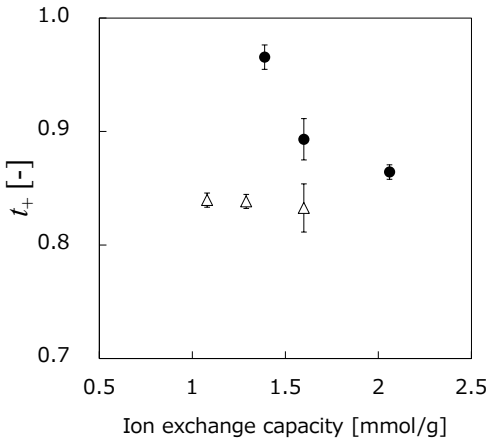

Fig. 1 Ion exchange capacity dependence of transport number, t_+ (△: ETFE-St,●: ETFE-St/DVB).

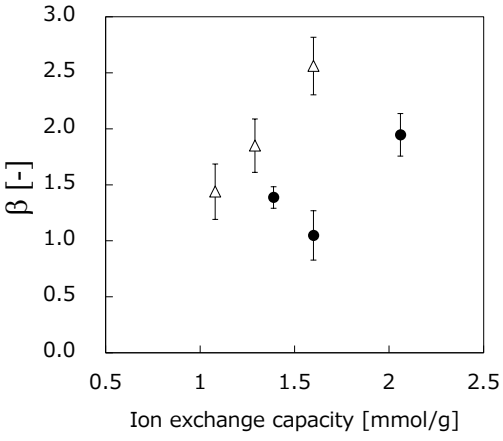

Fig. 2 Ion exchange capacity dependence of water permeation factor, β (△: ETFE-St,●: ETFE-St/DVB).

1-17 Development of Radiation-Grafted Cation-Exchange Membranes for Redox-Type Reactors in the IS Process

M. Nomura [a)], T. Kodaira [a)], T. Kimura [a)], A. Ikeda [a)], Y. Naka [a)], Y. Nishijima [a)], S. Imabayashi [a)], S. Sawada [b)], T. Yamaki [b)], N. Tanaka [c)] and S. Kubo [c)]

[a)] Department of Applied Chemistry, Shibaura Institute of Technology,
[b)] Department of Advanced Functional Materials Research, TARRI, QST,
[c)] Hydrogen Application Research and Development Division, NHARC, JAEA

The thermochemical water-splitting IS process using I_2 and SO_2 as catalysts has been developed for large-scale hydrogen production. In this process, separation techniques are crucial toward an ideal thermal efficiency over 40% [1]. One of key reactions, called the Bunsen reaction ($I_2+SO_2+H_2O \rightarrow 2HI+H_2SO_4$), has been operated with excess amounts of I_2 to separate HI and H_2SO_4. In order to reduce circulating I_2 volume, a redox-type reactor with a cation exchange membrane was proposed [2]. Effects of reaction temperatures and solution concentrations on the cell voltage were investigated by using Nafion as a cation exchange membrane. However, no one has attempted the cell operation especially under low-I_2 conditions using a new membrane. We investigated membrane properties such as a proton transport number (t_+) and electroosmotic coefficient (β) of the ion exchange membranes prepared by a radiation-graft polymerization method [3,4].

A poly(ethylene-*co*-tetrafluoroethylene) substrate was irradiated with γ-rays in ^{60}Co irradiation facilities in an Ar atmosphere, followed by graft polymerization and sulfonation. The irradiation period was 1 h at a dose rate of 15 kGy h^{-1}. The irradiated film was immersed in a styrene solution in toluene at 60 °C for different times. The grafted film was sulfonated in a chlorosulfonic acid solution at 50 °C. An anolyte and catholyte of the redox-type reactor divided by the cation exchange membrane contained H_2SO_4 (3 mol $kg_{\text{-}H2O}^{-1}$) saturated with SO_2 gas and HI_x (HI=2.5 mol $kg_{\text{-}H2O}^{-1}$, I_2=1.5 mol $kg_{\text{-}H2O}^{-1}$), respectively. A current density was kept at 200 mA cm^{-2}. Concentrations of the solutions were evaluated by titration with a 0.1 mol $kg_{\text{-}H2O}^{-1}$ NaOH aqueous solution for H^+ and with a 0.1 mol $kg_{\text{-}H2O}^{-1}$ $Na_2S_2O_3$ aqueous solution for I_2. The values of t_+ and β were calculated from the concentration profile of HI.

Figure 1 shows the concentrations in the catholyte and anolyte plotted as a function of the operation time. The cathode reaction is $I_2+2H^++2e^- \rightarrow 2HI$ while the anode reaction is $SO_2+2H_2O \rightarrow H_2SO_4+2H^++2e^-$. In other words, HI and H_2SO_4 are the products in the catholyte and anolyte solutions of the redox-type reactor. Their concentrations proportionally increased with increasing operation time, suggesting that the reactions on both the electrodes occurred ideally without any side reactions. On the other hand, concentrations of I_2 and SO_2 decreased proportionally. The membrane and the electrodes were stable in the HI and H_2SO_4 solutions during the 3-h operation. The membrane turned slightly brown in color, but its ion exchange capacity was unchanged. The color change might be due to I_2 adsorption in the catholyte. Regression analysis in Fig. 1 enabled us to estimate both of the t_+ and β values to be 1. Thus, the cation exchange membrane developed by the radiation-graft polymerization method was promising for the Bunsen reaction in the redox-type reactor. The final I_2/SO_2 ratio was 1.7, which is less than half of what was previously discussed without redox type reactors ($I_2/SO_2=4$)[1]. This is the first report to operate the Bunsen reaction at $I_2/SO_2 < 2$.

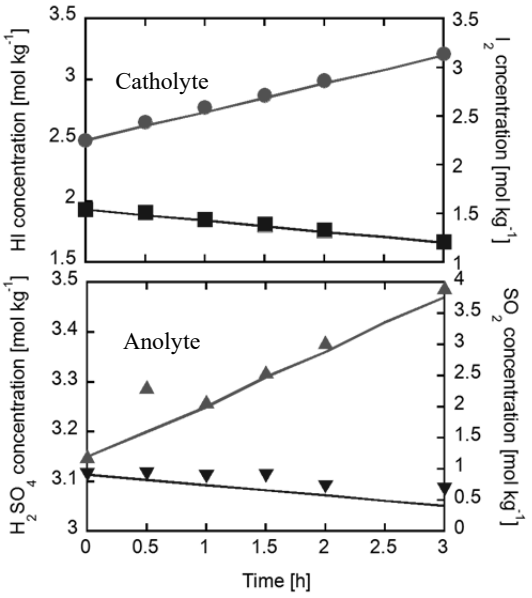

Fig. 1 Concentration profiles in the anolyte and catholyte for the Bunsen reaction in the redox-type reactor (●:HI, ■:I_2, ▲:H_2SO_4, ▼:SO_2, ──:calculated line).

Acknowledgement

This work was partially supported by Council for Science, Technology and Innovation (CSTI), Cross-ministerial Strategic Innovation Promotion Program (SIP), "energy carrier" (Funding agency: JST).

References

1) S. Kasahara *et al.*, J. Chem. Eng. Jpn., **36**, 887-99 (2003).
2) M. Nomura *et al.*, AIChE J., **50**, 1991-98 (2004).
3) T. Yamaki, J. Power Sources, **195**, 5848-55 (2010).
4) T. Kodaira *et al.*, JAEA Takasaki Annu. Rep. 2014, JAEA-Review 2015-022, 51 (2016).

1-18 Reproduction of Heavy-Ion Irradiation Effect on Organic Polymers Using Radiation Transport Simulation Code

T. Ogawa [a], T. Yamaki [b] and T. Sato [a]

[a] Environment and Radiation Sciences Division, NSEC, JAEA,
[b] Department of Advanced Functional Materials Research, TARRI, QST

General-purpose radiation transport simulation code PHITS [1], developed for prediction of radiation transport in accelerators and reactors, is used not only for radiation protection and shielding design but also for space radiation sciences, radiology and radiation biology recently. For example, energy deposition simulation in a submicron scale followed by analysis of radiochemical damage to chromosomes has been performed for the application of PHITS to radiation biology[2]. We attempted reproduction of radiation effects on organic polymer materials by applying PHITS because chemical effects in a submicron scale are the key for radiation effects on materials.

So far, radiation effects on materials were explained merely based on the absorbed dose. Additional effect was considered only when the absorbed dose is not enough to explain the experimental results. Therefore, as one of such examples, the following experimental data were analyzed. In the experiment, elongation at break (EB) of Poly-Ether Sulfone (PES) irradiated under various conditions was measured (Fig. 1) [3]. Simulation was performed to reproduce the experimental data using the microscopic energy deposition model (T-SED) in PHITS. As indicated by the experimental data in Fig. 2, protons and helium ions are more efficient for EB reduction than carbon ions at the same absorbed dose. Here it is assumed that deposition of 100 eV (corresponding to scission of 20 monomers) in a spherical cell volume with 50 nm diameter (2×10^6 monomers) induces loss of mechanical strength against elongation. Under this assumption, degradation of EB, the number of cells which received 100 eV of energy deposition was calculated and plotted in Fig. 3 for the three particle species from 0 to 2.5 MGy. Our calculation showed that energy larger than 100 eV is deposited in 1.6×10^{14}, 1.7×10^{14}, and 7.0×10^{13} cells (i.e., cells which lost mechanical strength) par one proton, helium ion, and carbon ion, respectively. Therefore at 0.1 MGy, where a saturation effect is negligible and the irradiation effect is proportional to the number of broken cells, EB was decreased by 20% in case of proton and helium whereas less for carbon (Fig. 3). Moreover, the trend of particle species dependence agrees with the experiment. Reduction of EB with an increase in the absorbed dose and its saturation trend was well reproduced.

References

1) T. Sato *et al.*, J. Nucl. Sci. Tech., **50:9**, 913-23 (2013).
2) T. Sato *et al.*, Int. J. Radiat. Biol., **88**, 143-50 (2012).
3) High intensity proton accelerator development center, JAERI-Data/Code 2003-015 (2003).

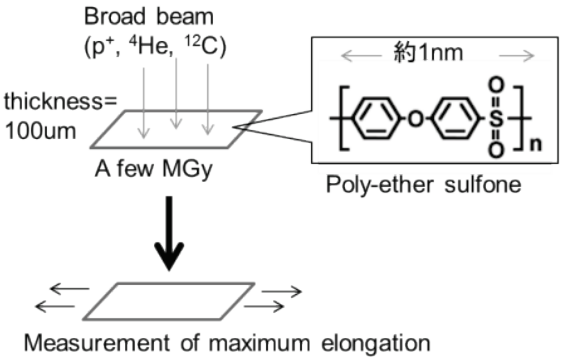

Fig. 1 Schematic view of the experiment performed in ref. 3).

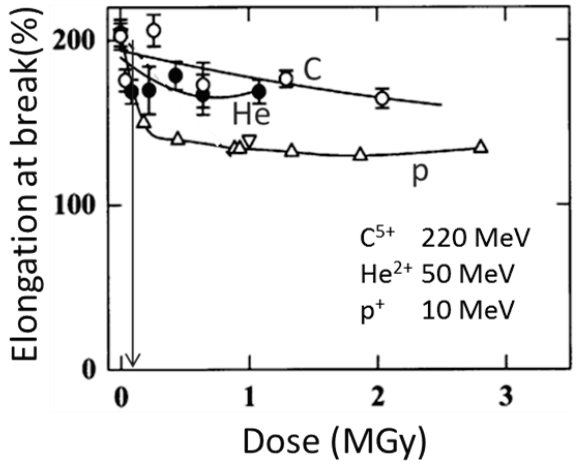

Fig. 2 Experimental result from ref. 3). Vertical arrow indicates a dose of 0.1 MGy.

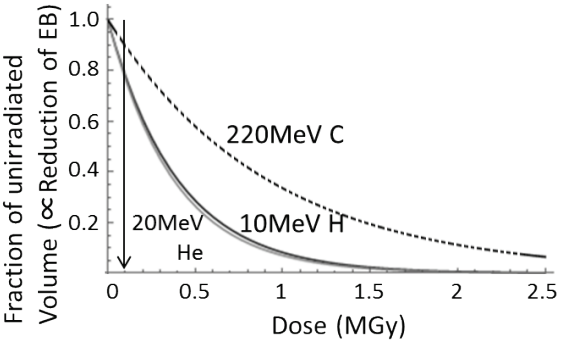

Fig. 3 EB simulated by PHITS combined with the assumption described in the text. A vertical arrow indicates a dose of 0.1 MGy.

1 -19

Design and Fabrication of Near-Perfect Optical Absorbers Using Etched Ion Tracks

K. Amemiya [a)], H. Koshikawa [b)], T. Yamaki [b)], Y. Maekawa [b)], H. Shitomi [a)], T. Numata [a)], K. Kinoshita [a)], M. Tanabe [a)] and D. Fukuda [a)]

[a)] National Metrology Institute of Japan, AIST,
[b)] Department of Advanced Functional Materials Research, TARRI, QST

The novel broadband near-perfect black absorber having micro-structured surface using etched ion tracks has been developed. CR-39 plastic plates were irradiated with swift heavy ion beams from AVF cyclotron of TIARA; the samples were then etched in NaOH solution to produce etch pits filled on its surface, followed by Diamond-Like Carbon (DLC) black layer coating. The prototype exhibited low reflectance of < 1% in UV – VIS, < 2% in NIR respectively. Furthermore, the prototype of the novel black absorber also exhibited good mechanical durability.

極低反射率を持つ黒色素材は太陽熱エネルギー吸収体、熱型絶対放射計用の光吸収体、高放射率黒体、迷光防止用黒色材、高視認性標識の背景色など、幅広い用途がある。平板型で、可視域～近赤外域にわたり吸収率99.9%以上を誇る黒体には、配向カーボンナノチューブ（VACNT）[1,2]やニッケル-リン（NiP）ブラック[3,4]がある。前者は低面密度に配向した CNT フォレストにより、実効屈折率を1に近づけることで表面反射を抑えているのに対し、後者では入射光が表面のマイクロピット構造中で多重反射するうちに吸収が促進され、正味の反射率が抑えられている。ただし、これらはいずれも機械的強度に乏しく、取扱いの困難さが広い普及を妨げていた。

筆者らは、理論計算を通じて、NiP ブラックの反射率が表面マイクロピット構造の急峻さ（アスペクト比）及び光吸収層の厚みに強く依存することを明らかにしてきた[4]。本研究ではこの知見に基づき、機械的にロバストな基板上に、表面マイクロピット構造を狙った通りに形成することで、新規な極低反射光吸収体の開発を目指している。マイクロピット構造形成にはイオンビーム照射によるトラックエッチング法[5]を用いると、対象とする光の波長域に合わせてピット構造のサイズやアスペクト比を容易に最適化できる利点がある。

2014 年度までに、時間領域差分法（FDTD 法）計算により、0.1%級の極低反射率を達成できる条件[ピット構造アスペクト比>3、ピット開口径～入射光波長と同等以上、黒色材層はアモルファスカーボン（DLC）]が得られていた[6]。この条件を満たす構造を形成するため、CR-39 樹脂基板に TIARA AVF サイクロトロンからの $^{14}O^{7+}$ ビーム 335 MeV や $^{20}Ne^{7+}$ ビーム 260 MeV, $^{40}Ar^{14+}$ ビーム 520 MeV を照射し、エッチング・黒色コートすることで、光吸収体を試作した。

作製した光吸収体試作品の断面図を Fig. 1 に示す。各試料の分光反射率を分光光度計（PerkinElmer LAMBDA 900）により計測したところ、紫外～可視域ではいずれも $R < 1\%$、近赤外域でも高ピットアスペクト比の試料では $R < 2\%$ の低反射率を示す結果が得られた（Fig. 2）。DLC 平坦面の表面反射率は約 16%なので、大幅に反射率が低減したことになる。また、本試作品の機械的強度を調べるため、エアスプレーによるブロー、及びスコッチテープの貼付・引き剥し試験も行ったが、試験後の分光反射率は試験前と 0.1%程度以内で一致していることがわかり、従来の極低反射素材（NiP ブラック、VACNT ブラック）にない耐性が確認できた。

本試作品は、理論予測上は近赤外域でも $R < 1\%$ の反射率が得られる試算であったが、CR-39 基板が近赤外域において光吸収性に乏しいことを考慮に入れると妥当な実測値といえる。試作品の光透過率も別途調べたところ、特に近赤外域では 10%程度の値が得られたことから、今後、正味の光吸収率を 100%に近づけるには、不透明な基板上にマイクロピット構造を形成する工夫が必要になると考えている。

本研究は東京大学大学院工学系研究科原子力専攻の原子力機構施設利用総合共同研究制度、日本原子力研究開発機構（現・量子科学技術研究開発機構）の施設供用制度により実施された。ここに感謝の意を表す。

References

1) Z.P. Yang *et al.*, Nano Lett., **8**, 446-51 (2008).
2) K. Mizuno *et al.*, Proc. Natl. Acad. Sci. U.S.A. **106**, 6044-47 (2009).
3) S. Kodama *et al.*, IEEE Trans. Instrum. Meas., **39**, 230-32 (1990).
4) K. Amemiya *et al.*, Appl. Opt., **51**, 6917-25 (2012).
5) S. Kodaira *et al.*, Radiat. Meas., **46**, 1782-85 (2011).
6) K. Amemiya *et al.*, Nucl. Instrum. Meth. Phys. Res. B, **356-57**, 154-59 (2015).

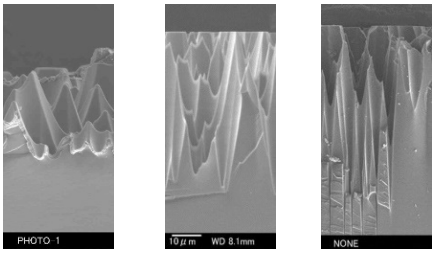

Fig. 1 SEM images of the cross section of the micro-structured optical absorber. Pit aspect ratios were ~3 (left), ~6 (center), ~15 (right), respectively.

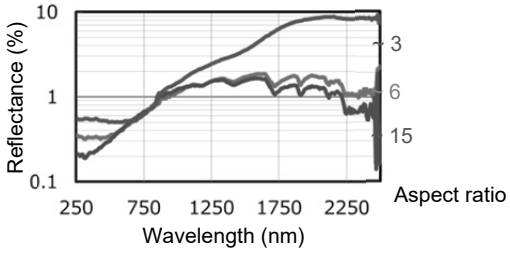

Fig. 2 Spectral reflectance of the micro-structured optical absorbers.

1 - 20

Atomistic Transformation Processes Due to the Correlation of Implanted N-Ions with Ti Thin Films

Y. Kasukabe [a),b)], H. Shimoda [b)], S. Yamamoto [c)] and M. Yoshikawa [c)]

[a)] Global Learning Center, Tohoku University, [b)] Department of Metallurgy, Tohoku University, [c)] Department of Advanced Functional Materials Research, TARRI, QST

Non-stoichiometric titanium nitrides, TiN_y, have covalent properties as well as metallic and ionic properties, which make them fascinating for both fundamental research and technological applications. Recently, it has been revealed that the interesting physical properties are related to the crystallographic (preferred oriented) and electronic structures[1)]. However, atomistic growth processes of TiN_y films due to ion implantation, especially correlations between implanted ions and deposited Ti films in the early N-implantation stage, have not been sufficiently studied. In order to clarify atomistic transformation processes of Ti films, in-situ observations by using transmission electron microscope (TEM) and electron energy loss spectroscope (EELS) have been carried out, along with the characterization of the electronic structure by molecular orbital calculations.

The as-deposited Ti films on thermally cleaned NaCl substrates consisted of both TiH_x and hcp-Ti with some preferred orientations at RT. The N_2^+ ions with 62 keV were implanted into hcp-Ti and TiH_x with preferred orientations in the 400 kV analytic high resolution TEM combined with ion accelerators at JAEA-Takasaki[2)].

In-situ TEM observations have revealed that the (110)-oriented TiN_y is formed by nitriding the (110)-oriented TiH_x in the band-like TEM contrast region of the as-deposited Ti film, whereas the (001)-oriented TiN_y is mainly formed by the transformation of the $(03\cdot5)$-oriented hcp-Ti to (001)-oriented fcc-Ti. In-situ EELS observations have elucidated that the release of H atoms in TiH_x proceeds preferentially in the early N-implantation stage, and that in the subsequent N-implantation stage the electron density in the hybridized band by N 2p and Ti 3d-Ti 4p states increases gradually with increasing N-concentration, which means that the number of N atoms bonding to Ti atoms increases gradually. The changes in lattice constants of crystallites in Ti films with the dose of N are measured and the variation of the c/a ratio of the hcp-Ti with the N/Ti ratio in this experiment is given in Fig. 1. It is well known that the lattice parameter ratio, c/a, of the ideal hcp structure is 1.633, and that the c/a of all metals with an hcp structure is not just equal to the ideal ratio[3)]. For instance, the c/a of hcp-Mg, 1.624, is the closest to the ideal ratio in all hcp structure metals. The dotted line marked by an arrow in Fig. 1 represents 1.633, the c/a of the ideal hcp lattice. From Fig. 1, it can be seen that the c/a ratio increases with increasing the N/Ti ratio, and is up to 1.628 for N/Ti = 0.81, which is closer to the ideal ratio than that of hcp-Mg. This means that the hcp-Ti lattice during N-implantation come close to the ideal close packing of hard spheres. In other words, the chemical bonds between Ti atoms weaken during N-implantation, which makes the hcp-fcc transformation easy.

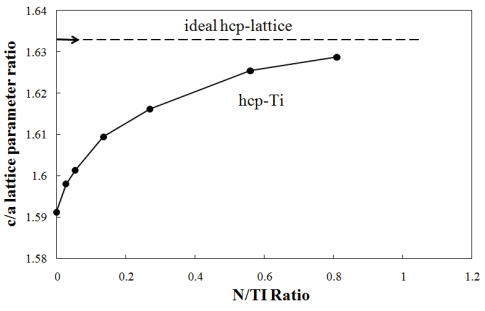

Fig. 1 The variation in c/a, lattice parameter ratio of hcp-Ti with respect to the N/Ti ratio.

In order to elucidate the atomistic nitriding processes of the epitaxial trans- formation of Ti thin films due to N-implantation in detail, DV- MO calculations have been performed for the Ti_{19} cluster and $Ti_{19}N$ cluster models shown in Fig. 2. The Ti_{19} cluster model, which does not include a nitrogen atom indicated by a gray circle G in Fig. 2, corre- sponds to a part of the hcp-Ti structure. The site indicated by G in Fig. 2 is the central position (O-site) of the octahedron with larger space as formed by A-F atoms in the Ti_{19} cluster, and has lower electron density (~1/5,000 of electron density of site A). Thus, O-sites have smaller repulsion for electrons of N atoms, and admit the invasion of N atoms easier. Therefore, the nitrogen atom, indicated by G, occupies the center (O-site) of the octahedron as formed by A-F atoms, which leads to the formation of a $Ti_{19}N$ cluster, as shown in Fig. 2 and the growth (evolution) of nucleus of the hcp-fcc transformation.

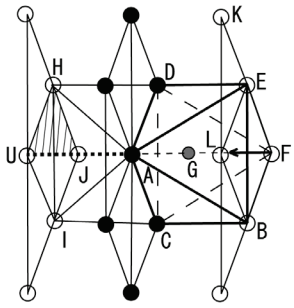

Fig. 2 Schematic illustrations of Ti_{19} and $Ti_{19}N$ cluster models. Solid circles and open circles represent Ti atoms and a gray circle represents a N atom, respectively.

References

1) S. Hao *et al.*, Phys. Rev. B **74**, 035424-1 (2006).
2) H. Abe *et al.*, JAERI-Res., **96-047**, 1 (1996).
3) M. H. Yoo, Metall. Trans. A, **12**, 409 (1981).

1-21 Development of Hydrogen Permselective Membranes by Radiation-induced Graft Polymerization into Porous PVDF Films

S. Hasegawa, S. Azami, S. Sawada and Y. Maekawa

Department of Advanced Functional Materials Research, TARRI, JAEA

An establishment of non-electric power hydrogen collection system is required to prevent an explosion of the nuclear power plants. For developing the non-electric power hydrogen collection system, a combination of hydrogen permselective membranes with hydrogen storage materials has been proposed. The hydrogen permselective membranes play an important role for a separation of hydrogen from air consisting of water and oxygen model. In this work, the hydrogen permselective membranes based on porous polyvinylden fluoride (PVDF) films were prepared by using radiation-induced graft polymerization technique[1]. To control the permeability, the porosity and the interaction between grafted polymer chains and gas molecules were adjusted.

Graft polymerization was carried out with commercially available porous PVDF film (MERCK MILLIPORE GVWP09050, pore size 0.22 μm, 110 μm thickness) γ-irradiated with 30 or 160 kGy. The irradiated PVDF films were immersed into 10-50 wt% aqueous solutions of acrylic acid (AAc) with 0.5 wt% Mohr's salt at 50 °C or 100% styrene (St) at 60 °C (Fig. 1).

Grafting degrees (*GDs*) of AAc and St in the porous PVDF film are plotted as a function of reaction time in Fig. 2. The *GDs* of AAc-grafed PVDF reached 38%, 54%, and 63% for 10, 30, and 50 wt% monomer solutions at 7 hours, respectively. The *GDs* of St, which was controlled by absorbed doses and reaction time, were in the range from 41% (30 kGy, 3 hours) to 144% (160 kGy, 14 hours).

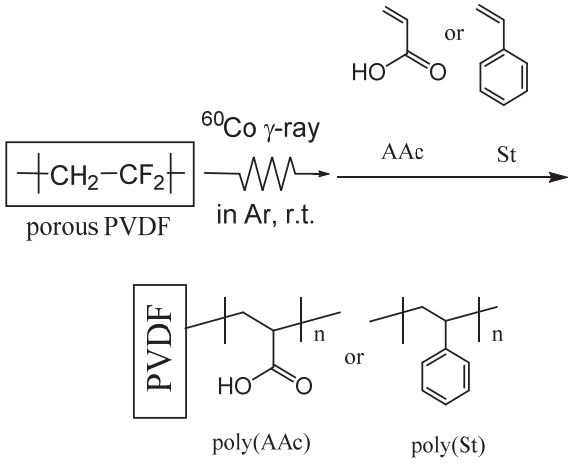

Fig. 1 Synthetic scheme of gas selectivity film by radiation-induced graft polymerizations.

The porosities of porous membranes (c.a. 63%) scarcely changed by the grafting. In order to control the porosity, the grafted membranes were hot-pressed at 159 °C, 1 MPa for 10 min. The porosities of AAc- and St-grafted membranes were reduced from 63% to 39% and 44%, respectively. Gas permeability of the grafted membranes was controlled in the range of 10^{-9} to 10^{-8} mol/(m^2 s Pa), and the hydrogen permeability was higher than those of water vapor and nitrogen (oxygen model). The AAc- and St-grafted membranes exhibited 3.5 and 7.1 of permeation ratios (H_2/H_2O), respectively.

In conclusion, the graft polymerization technique was useful for the development of hydrogen permeselective membrane based on the porous films.

Reference

1) S. Hasegawa *et al.*, Polymer, **54**, 2895-900 (2013).

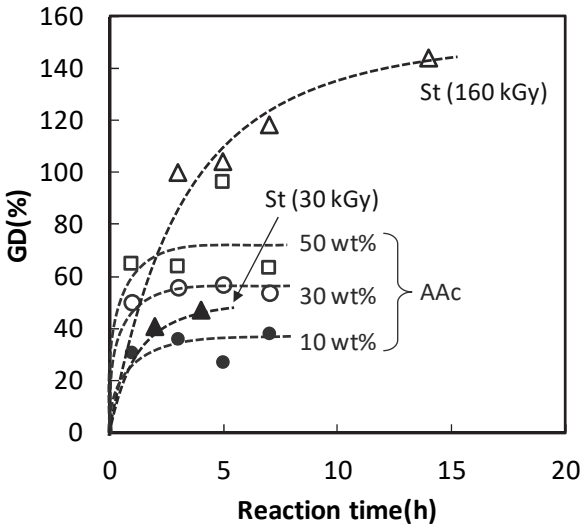

Fig. 2 Plots of *GD*s as a function of grafting time.

Table 1 Permeability and permeation ratio with AAc or St grafted porous PVDF membranes after hot press treatment.

Graft Chains	GD (%)	Porosity (%)	Permeability ×10^{-8} mol/sec·m^2·Pa			H_2/H_2O	H_2/N_2
			H_2	H_2O	N_2		
-	0	28	26	52	14	0.5	1.9
AAc	76	39	9.4	2.7	3.2	3.5	2.9
St	63	44	0.26	0.036	0.12	7.1	2.1

1-22 Synthesis, Characterization, and Alkaline Stabilities of Radiation Grafted 4-Vinylimidazolium-Based Anion Conducting Polymer Electrolyte Membranes

K. Yoshimura [a)], S. Watanabe [b)], A. Hiroki [a)], H. Shishitani [c)], S. Yamaguchi [c)], H. Tanaka [c)] and Y. Maekawa [a)]

[a)] Department of Advanced Functional Materials Research, TARRI, QST,
[b)] Saitama Institute of Technology, [c)] Daihatsu Motor Co., Ltd.

There has been a growing interest in noble metal-free alkaline fuel cells (AFC). Anion conducting polymer electrolyte membranes (AEMs) are one of the key materials for AFC and are required highly alkaline durability because of high temperature and highly basic condition in the fuel cells. In recent years, we have developed *N*-vinylimidazolium-based AEMs by radiation-induced grafting[1]. The prepared poly(*N*-vinylimidazolium)-grafted AEMs (**NVIm-AEM**) degraded via rapid *β*-elimination at the initial stage and slow hydrolytic ring opening reaction of the imidazolium unit at the later stage[2]. In this work, we synthesized the AEM based on the graft chains of 2-methyl-*N*-methyl-4-vinylimidazole (2Me-NMe-4VIm) with styrene (St) to prevent the *β*-elimination and ring opening reaction.

The 2Me-NMe-4VIm monomer was newly synthesized from 4-vinylimidazole with *N*- and 2-methylation reactions. Poly(ethylene-co-tetrafluoroethylene) (ETFE) films were irradiated with a dose of 80 kGy from a ^{60}Co *γ*-ray source at room temperature in argon atmosphere. The pre-irradiated ETFE films were grafted in the argon-purged monomer solution consisting of 2Me-NMe-4VIm or a mixture of 2Me-NMe-4VIm and St in 1,4-dioxane (33 wt%) at 60 °C to obtain the films with grafting degrees of 33% and 54%, respectively. The grafted films were then *N*-methylated and ion exchanged quantitatively to obtain the hydroxide from of **2Me-NMe-4VIm-AEM** and **2Me-NMe-4VIm/St-AEM** with a molar ratio of 75/25 of 2Me-NMe-4VIm/St with IECs of 1.38 and 1.74 mmol/g (Scheme 1).

The **2Me-NMe-4VIm-AEM** and **2Me-NMe-4VIm/St (75/25)-AEM** showed conductivities of 175 and 157 mS/cm with water uptakes of 53 and 86%. Compared with **NVIm-AEM**, these AEMs show significantly higher conductivities with lower water uptakes, which are desirable properties for fuel cell applications. The alkaline stability of AEMs was evaluated by the change in conductivity of AEMs in 1 M KOH at 80 °C. As shown in Fig. 1, the conductivity of **NVIm-AEM** (*N*-vinyl type AEM) decreased to 0 mS/cm after 100 h, while **2Me-NMe-4VIm-AEM** showed the conductivity of 23 mS/cm after 100 h. The conductivity of the **2Me-NMe-4VIm-AEM** indicates that the initial conductivity drop resulting from *β*-elimination was effectively suppressed by the shift of vinyl substituent from 1- to 4-positon of the imidazolium ring. Also, the decreases of conductivity at the later period, arising from ring opening degradation become much slower, owing to the methyl substitution effect at 2-position of the imidazolium ring. Furthermore, the **2Me-NMe-4VIm/St-AEM**, which has copolymerized hydrophobic styrene units, possesses excellent initial and long term alkaline stabilities.

In conclusion, for vinylimidazolium-containing graft-type AEMs, the control of vinyl position, the methyl-protection at 2-positon, and copolymerization with styrene should be promising strategy to improve the alkaline stability, which is the essential property for AFCs.

Scheme 1 AEM synthesis of 2-methyl-*N*-methyl-4-vinyl-imidazolium graft AEMs.

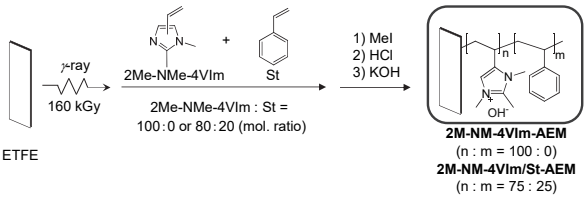

Acknowledgement

This work was supported by the Advanced Low Carbon Technology Research and Development Program (ALCA) from the Japan Science and Technology Agency (JST).

References

1) K. Yoshimura *et al.*, J. Electrochem. Soc., **161**(9), F889 (2014).
2) Y. Ye *et al.*, Macromolecules, **44**, 8494 (2011).

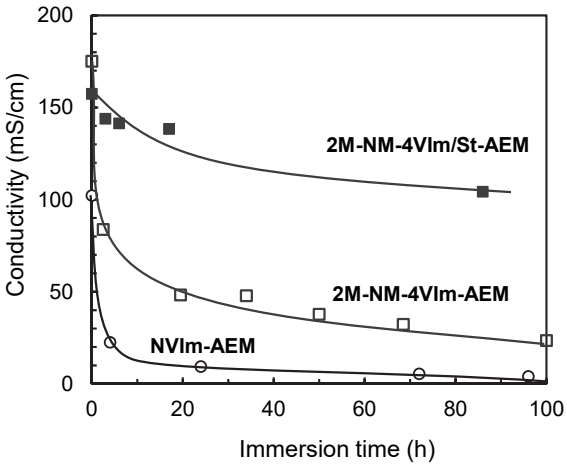

Fig. 1 Alkaline stabilities of *N*-vinyl and 2-methyl-*N*-methyl-4-vinyl AEMs.

1-23 Anisotropic Swelling of Hydrogel Nanowires Fabricated by Single Particle Nanofabrication Technique (SPNT)

M. Sugimoto [a], S. Tsukuda [b], T. Yamaki [a] and S. Seki [c]

[a] Advanced Functional Materials Research Division, TARRI, QST,
[b] Institute of Multidisciplinary Research for Advanced Materials, Tohoku University,
[c] Department of Molecular Engineering, Kyoto University

The poly(vinylpyrrolidone) (PVP) and N,N'-methylenebis(acrylamide) (MBA) hybrid nanowires were fabricated by a single particle nanofabrication technique (SPNT), which enables us to fabricate various types of polymeric nanowires using a single ion event. The crosslinking reaction of polymer chains occurs within the ion tracks along the paths; in principle, the length and radius of the nanowires were controlled by changing a film thickness and the amount of crosslinkers. We demonstrated here that the PVP/MBA nanowires exhibited anisotropic swelling along the length and radius in aqueous environments.

PVP was dissolved in isopropanol (IPA) at 2, 5, and 10 wt%. MBA was added to the solution as crosslinking agent at 15, 20, and 30 wt% against dissolved PVP, controlling the degree of crosslinking in the track. These solutions were spin-coated on Si substrates. The resulting thin films were exposed to a beam of 490 MeV ^{192}Os. After development procedures, nanowires were observed by AFM for investigating their morphological and swelling properties in air and water.

Figure 1 shows AFM micrographs of the nanowires prepared by 490 MeV ^{192}Os irradiation of the PVP/MBA films at different ratios. The PVP film without any crosslinkers gave no observable nanowires (Fig. 1 (d)), and the nanowires were still too fragile to become extended when the crosslinker concentration was low (Fig. 1 (a)). These suggests that some quantity of MBA would be necessary to have stiff, long nanowires on the substrate as seen in Figs. 1 (b) and (c).

In the SPNT, the length of nanowires can be controlled very easily because it usually corresponds to the film thickness. As shown in Fig. 2, however, the length of the PVP nanowires was longer than the film thickness. This result could be attributed to the swelling due to water during the development procedure. Once the nanowires swelled to become longer and thicker, their size could not be changed so much in a drying step because they stick to the substrate.

Additionally, the lengths of the PVP nanowires appeared to increase linearly, which implies homogeneous energy deposition in the depth direction of the film. A length/thickness ratio decreased with an increase in the amount of MBA. The higher crosslinker concentrations probably made it possible to restrict the swelling ratio because of high-density crosslinks in the nanowire.

References

1) S. Seki *et al.*, Adv. Mater., **13**, 1663-65 (2001).
2) S. Tsukuda *et al.*, Radiat. Phys. Chem., **84**, 39-41 (2013).

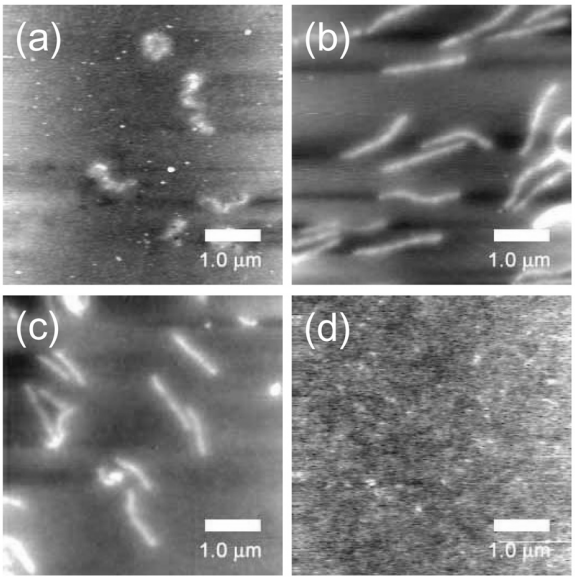

Fig. 1 AFM micrographs of the nanowires prepared by irradiation of PVP/MBA ((a)100/5, (b)100/15, (c)100/30, and (d)100/0) thin films with 490 MeV ^{192}Os at a fluence of 5.0×10^7 ions/cm^2.

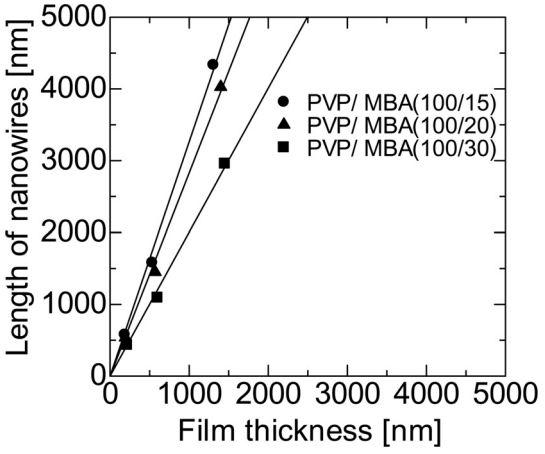

Fig. 2 Relationship between the film thickness and the length of the PVP nanowires.

1-24 Nitrogen Doping in Carbon-Based Cathode Catalysts Using Electron Beam Process

M. Sugimoto [a)], T. Ohta [b)], S. Yamamoto [a)], H. Koshikawa [a)], T. Yamaki [a)] and T. Hagiwara [b)]

[a)] Department of Advanced Functional Materials Research, TARRI, QST,
[b)] Faculty of Engineering, Saitama Institute of Technology

Nitrogen-doped (N-doped) carbon-based catalysts for oxygen reduction reactions (ORRs) are expected as platinum-alternative material[1]. It has been predicted that the ORR activity should be related to the chemical states of N atoms doped in graphite. However, no one has so far established a method for introducing the N-related active sites reproducibly and quantitatively because there is a difficulty in controlling the atomic concentration of N and the graphite structures independently. We prepared N-doped carbons by heating aromatic polymer precursors in an ammonia (NH_3) atmosphere under electron-beam (EB) irradiation and then examined the irradiation effect on the doping and ORR properties in terms of thermally non-equilibrated kinetics.

A precursor was phenolic resin (Gunei Chemical, PSK-2320) or its mixture with 5 wt% cobalt(II) chloride ($CoCl_2$). It was irradiated with 2 MeV EB at a dose of up to 6 MGy in 0.1 vol% NH_3 at 500 °C. The irradiated powder was then subjected to carbonization at 800 °C for 1 h in Ar. The synthesis conditions are summarized in Table 1. The resulting samples were analyzed by transmission electron microscopy (TEM) and X-ray photoelectron spectroscopy (XPS). The electrocatalytic activity was tested by linear sweep voltammetry with a rotating disk electrode (RDE). The catalyst powder acid-washed to remove the Co species was dispersed in a mixture with a Nafion solution and then coated on the surface of a glassy carbon electrode. The measurements were performed in a 0.1 M aqueous perchloric acid solution. The ORR activity was determined from voltammograms in a manner similar to that reported elsewhere[2,3], where the electrolyte was saturated with O_2 or N_2 gas.

Samples (b) and (d) comprised a graphite phase while samples (a) and (c) were amorphous. This result suggests an important role of $CoCl_2$ in the formation of crystalline structures. Figure 1 shows N 1s XPS spectra, enabling us to confirm the existence of N dopants. As a whole, the samples prepared by the EB irradiation exhibited a high N concentration; therefore, the EB-induced non-equilibrated process would activate the N-doping reactions. A doping level reached an atomic concentration of nitrogen about 0.5% when 5 wt% $CoCl_2$ was mixed in the precursor (sample (d)).

Figure 2 shows the ORR potential as an indicator of the activity. Strikingly, sample (d) exhibited a potential of 0.93 V versus a reversible hydrogen electrode (RHE), which is comparable to that of a Pt standard sample (1.05 V). In conclusion, we were able to present the possibility of developing the carbon-based ORR catalysts through thermally non-equilibrated reactions during the EB irradiation.

References

1) J. Ozaki *et al.*, Carbon, **44**, 1298-352 (2006).
2) K. Lee *et al.*, Electrochim. Acta, **49**, 3479-85 (2004).
3) J.-H. Kim *et al.*, Electrochim. Acta, **52**, 2492-97 (2007).

Table 1 Conditions of our sample preparation.

Sample	$CoCl_2$ (wt%)	Doping Method	Carbonization
(a)	0	500 °C in 0.1% NH_3 without EB	800 °C in N_2
(b)	5		
(c)	0	500 °C in 0.1% NH_3 with 2 MeV EB	
(d)	5		

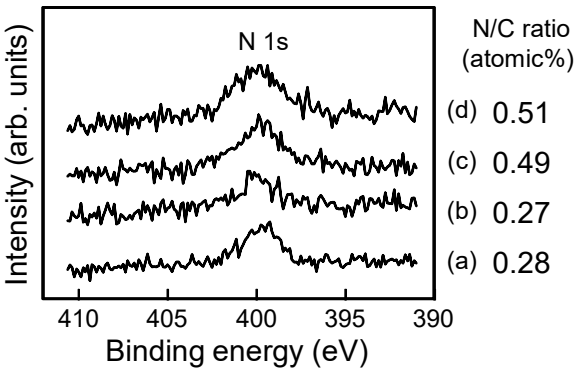

Fig. 1 N 1s XPS spectra of samples (a) to (d) and N/C ratios estimated by these data.

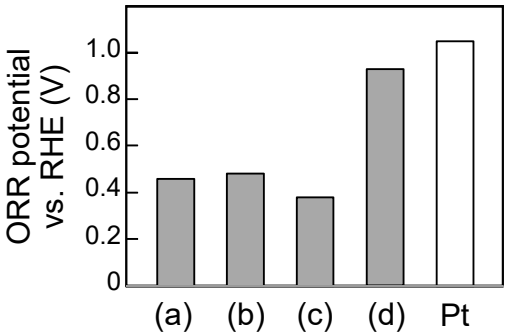

Fig. 2 ORR potential vs. RHE of samples (a) to (d) and the Pt standard sample.

1-25 Utilization of Ion Implantation for Synthesis of Nitrogen-doped Carbon Material with Catalytic Activity

A. Idesaki, M. Sugimoto, S. Yamamoto, M. Taguchi and T. Yamaki

Department of Advanced Functional Materials Research, TARRI, QST

Nitrogen-doped (N-doped) carbon materials which exhibit catalytic activity for an oxygen reduction reaction (ORR), $O_2+4H^++4e^-\rightarrow 2H_2O$, are expected to be applied for a catalyst alternative to a platinum-catalyst. As far, several synthesis processes have been proposed; a chemical vapor deposition method, a polymer precursor method, and so on[1]. Among them, the polymer precursor method is advantageous to other methods from the view point of formability, that is, polymers are easy to be formed into various shapes such as fiber, coating film, and so on. Furthermore, composition of material can be controlled by blending and/or alloying with other compounds. In the polymer precursor method, polymers mixed with metal-phthalocyanines (metal=Co, Fe, etc.) or metal- compounds ($CoCl_2$, $FeCl_2$, etc.) are pyrolyzed in an inert atmosphere to obtain N-doped carbon materials with the ORR activity[2,3]. In these reports, powder materials have been often used. In such cases, N atoms (catalytic active sites) are considered not to distribute uniformly in the powder bulk. This suggests that the obtained N-doped carbon materials cannot exhibit the best performance because the active sites inside the powder bulk cannot contribute to the ORR. Here, we propose ion implantation into polymer precursor with the aim for synthesis of a N-doped carbon material which possesses the ORR active sites with high number density at surface. In this work, N^+ ions were implanted into a polyimide film and possibility to synthesize an ORR active N-doped carbon material was examined.

A polyimide film (Kapton®, Du Pont-Toray Co., Ltd., thickness of 8 μm, $C_{22}N_2O_5H_{10}$) was irradiated by 100 keV N^+ ions at room temperature under vacuum using 400 keV ion implanter at TIARA. The number density of implanted N^+ ion was 4×10^{15} ions/cm^2. Since the number of carbon atoms included in 1 cm^2-area is calculated as approximately 4×10^{19} from the value of covalent radius[4], the number of implanted N^+ ion is estimated as 1/10,000 in number ratio of N/C. The penetration depth of N^+ ion into the polyimide film was calculated by SRIM code[5]; the depth of 300 nm was obtained for 100 keV.

The irradiated polyimide film was pyrolyzed at 800 °C in a nitrogen atmosphere. After the pyrolysis, the ORR activity was evaluated by a cyclic voltammetry (CV) method with a rotating disk electrode. The CV measurement was conducted in an oxygen-saturated 0.1 M $HClO_4$ electrolyte with 50 mV/sec scan rate and 1,500 rpm rotating velocity. Figure 1 shows the relationship between potential (vs. Ag/AgCl) and current density. The ORR is observed with rapid decreasing in the current density against the potential. Although the ORR activity was almost negligible in case of unirradiated polyimide film, the irradiated polyimide film exhibited the ORR activity with onset of potential at around 0.2 V (Ag/AgCl). This result indicates that ion implantation into polymer precursor is useful to synthesize the ORR active N-doped carbon material.

In this work, we demonstrated effectiveness of ion implantation to synthesize the ORR active N-doped carbon material. In future, production and change behavior of C-N chemical bonds in the polymer precursor by the implantation and subsequent heat treatment will be investigated in order to clarify the detailed irradiation effect of N^+ ions on the polymer precursor.

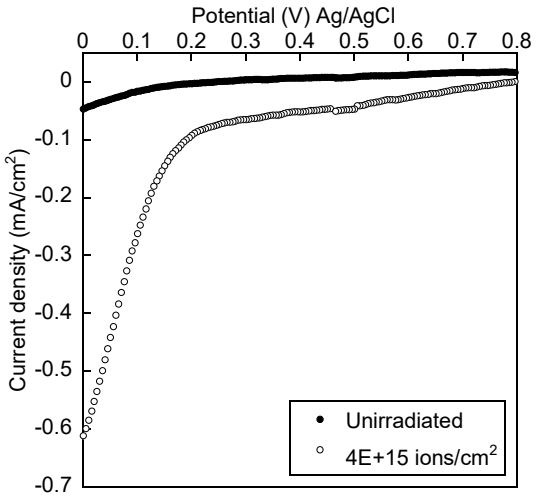

Fig. 1 ORR activity of obtained N-doped carbon material.

Acknowledgement

This work was partly supported by JSPS KAKENHI Grant Number 15K04736.

References

1) H. Wang *et al.*, ACS Catal., **2**, 781-94 (2012).
2) J. Ozaki *et al.*, Carbon, **44**, 1324-26 (2006).
3) C. H. Choi *et al.*, Appl. Catal. B: Environmental, **119-20**, 123-31 (2012).
4) M. Winter, "WebElements (www.webelemwnts.com)".
5) J. F. Ziegler, and J. P. Biersack, "SRIM - The Stopping and Range of Ions in Solids" (www.srim.org) (1985).

1-26 Formation Mechanism of Nanometer-sized Pores in Polymer-derived Silicon Carbide Film by Pyrolysis

A. Takeyama, A. Idesaki, M. Sugimoto, S. Yamamoto and M. Yoshikawa

Department of Advanced Functional Materials Research, TARRI, QST

Crystalline silicon carbide (SiC) is expected as a substrate for epitaxial growth of large-scale graphene via thermal decomposition[1]. In contrast, a few nano-meter-sized and hollow structured graphite exhibits high catalytic activity for the oxygen reduction reaction[2]. We expect a nano-porous polymer-derived SiC film to be used as the substrate for hollow structured graphite. In this report, we aim at clarifying the formation mechanism of nano-sized pores in polymer-derived SiC films.

Using 3, 5 and 10 mass% polycarbosilane (PCS) solutions, PCS films were dip-coated on silicon (Si) substrates for thickness and on porous alumina for gas permeation measurements. Coating conditions were determined to prevent cracks in the pyrolyzed PCS film. The film was irradiated with the electron beam up to 12 MGy, followed by annealing at 673 K to kill radicals formed in PCS. Subsequently, they were pyrolyzed at 773, 873, 973 and 1,073 K for 30 minutes in argon. The thickness of the film was measured using a step profiler. Gas permeance of films was measured for hydrogen (H_2) or nitrogen (N_2) at room temperature to suppress temperature activated diffusion of these gases.

The thickness of PCS films coated on Si substrates was plotted in Fig. 1 as a function of PCS concentration. The left hand axis shows the thickness normalized by that before pyrolysis. The right hand axis shows thickness before pyrolysis. At 773 K, the slight decrease of the normalized thickness was observed, although at 873 K, the normalized thickness significantly decreased. This large shrinkage at 873 K was attributed to conversion of PCS into SiC. We previously reported that evolution of decomposition gas due to the conversion swelled PCS[3]. However, when the amount of evolved gas was small, shrinkage rather than swelling predominantly took place. In the case of 3 mass%, the smallest thickness before pyrolysis gave rise to the insufficient amount of evolved gas and the largest shrinkage. At 973 and 1,073 K, normalized thickness increased proportional to that before pyrolysis. This also indicates evolved gas swelled these films.

In Fig. 2, room temperature permeances and selectivity of films pyrolyzed at 973 K are plotted. Gas permeances for 10 mass% is slightly larger than for 3 mass%. This indicates that the amount of pores increased with increasing the film thickness. The selectivity about 3.7 means Knudsen diffusion of gases and suggests the pore diameter was less than 7 nm, which is approximately 10% of the mean free path[4]. The no significant change of selectivity was observed with increasing the concentration (thickness). This suggests volume shrinkage of the film prevented agglomeration of pores as well as swelling. We note that in the case of PCS powder, most of pores disappeared at 973 K by volume shrinkage[3]. Since the PCS film stuck on the Si substrate, isotropic shrinkage due to conversion was disturbed and pores could remain in the film. In summary, nano-sized pores were introduced in the pyrolyzed PCS film due to evolution of decomposed gas. The thick film including the large amount of pores would be applicable to the substrate for the large-scale growth of hollow structured graphite.

References

1) D. Waldmann *et al.*, ACS Nano., **7**, 4441 (2013).
2) R. Kobayashi *et al.*, Chem. Lett., **38**, 396 (2009).
3) A. Takeyama *et al.*, J. Asia. Cer. Soc., **3**, 402 (2015).
4) R. T. Yang, "Gas Separation by Adsorption Processes", Imperial College Press, London (1997).

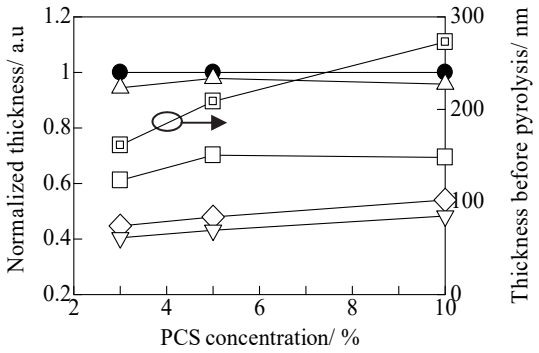

Fig. 1 Temperature and PCS concentration dependence of PCS film thickness. ●: before pyrolysis, △: 773 K, □: 873 K, ◇: 973 K, ▽: 1,073 K.

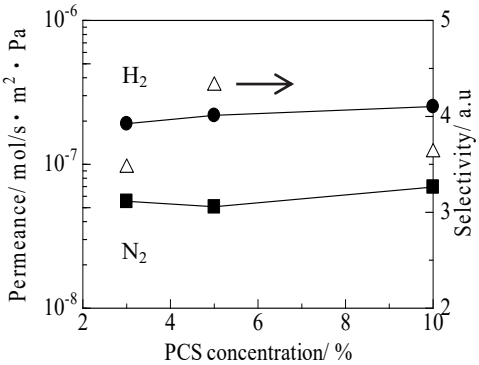

Fig. 2 Permeances and selectivity plotted as a function of PCS concentration. The pyrolysis temperature was 973 K.

1-27 Design of Functional Interfaces of Fuel Cell Materials

T. Mori [a)], K. Takahashi [a)], S. Chauhan [a)], A.Suzuki [a)], S.Yamamoto[b)], Y. Maekawa [b)], A. Hiroki [b)], K. Yoshimura [b)] and T. Kobayashi [c)]

[a)] Center for Green Research on Energy and Environmental Materials, NIMS, [b)] Department of Advanced Functional Materials Research, TARRI, QST, [c)] Center for Advanced Photonics, RIKEN

To design the high quality fuel cell materials, quantum beam (*i.e.* proton beam, electron beam and gamma ray) irradiation techniques were used. In the joint projects among QST, NIMS and RIKEN, four projects were conducted in this year. The outline of aforementioned joint projects is shown in Fig. 1.

First project is for development of extremely low concentration of Pt in cathode of polymer membrane fuel cells. In this challenge, we successfully activated the surface of small amount Pt loaded ceria nanowire by using proton beam irradiation technique.

Figure 2 shows Tafel plot derived from proton beam irradiation sample. In this experiment, 0.5 wt% Pt loaded ceria nanowire/C was used. As shown in Fig. 2, Tafel line derived from proton beam irradiated sample shifted into higher kinetic current region. Also, the slop of Tafel line became steep as compared to commercially available 20 wt% Pt/C. Those results indicate that the surface of low concentration Pt loaded ceria nanowire/C is conspicuously activated by proton beam irradiation. Also, it is confirmed that the electron beam irradiation method (i.e. second project) can provide us similar effect for surface activation of low concertation Pt loaded ceria nanowire, although relatively long irradiation time and high exposure dose are required.

Now, we are preparing joint paper on the basis of our experimental results. Before we submit it to the international journal, joint patents were already filed [1,2].

Third project is for design of three phase boundaries of membrane electrolyte assembly (MEA) by using gamma ray irradiation technique.

Nowadays, minimization of Pt content in cathode layer of MEA is key from the perspective of lowering of environmental burden in the R & D of polymer membrane fuel cells. So far, we observed that the inner resistance of fuel cell device with Pt loaded ceria nanowire/C in the cathode layer of MEA was successfully decreased by using gamma ray irradiation technique. Also, we observed high OCV (open circuit potential) from our MEA. It suggests that our challenge (*i.e.* design of three phase boundary in MEA by using gamma ray irradiation technique) is one of promising approach for development of high quality fuel cell devices.

On the basis of all experimental results in the third project, it is expected that high quality low concentration Pt cathode with high quality will be developed by design of interfaces of cathode layer of MEA in the near future.

The fourth joint project is for development of high quality solid oxide fuel cell (SOFC) devices which can show high performance at intermediate temperature region such as 700 °C. So far, the conventional SOFC devices which consist of yttrium oxide stabilized zirconia electrolyte can be used above 800 °C. In this case, the stainless steel interconnector which is useful for fabrication of budget stack cell of SOFC cannot be used at such high temperature. We expect that our challenge will provide us new breakthrough in R&D field of SOFC.

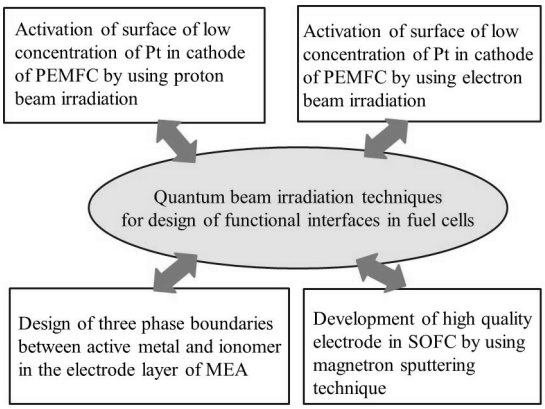

Fig. 1 Schematic diagram of outline of joint projects among QST, NIMS and RIKEN for design of functional interfaces in fuel cells by using quantum beam irradiation techniques.

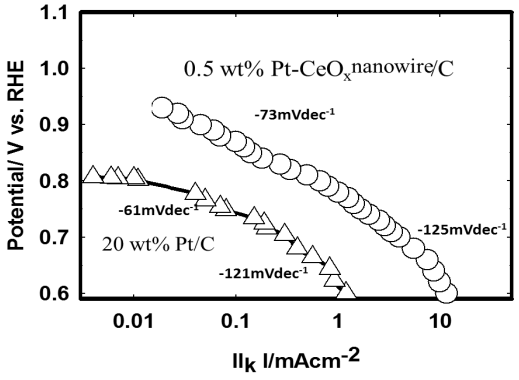

Fig. 2 Tafel lines derived from 0.5 wt% Pt loaded ceria nanowire/C which was irradiated by proton beam and commercially available 20 wt% Pt/C. Electrolyte: 0.5 M H_2SO_4 aqueous solution.

References

1) T. Mori *et al.*, Japanese patent filing number: 2015-009968.
2) T. Mori *et al.*, Japanese patent filing number: 2016-004627.

1-28 Oxygen Reduction Activity of Iron and Nitrogen Doped Carbon Films

S. Yamamoto, A. Shimada, T. Hakoda, M. Sugimoto, H. Koshikawa and T. Yamaki

Department of Advanced Functional Materials Research, TARRI, QST

Polymer electrode membrane fuel cells (PEMFCs) using precious metals (Pt, Ru, etc.) at the cathode catalysts have attracted much attention because of their higher energy densities, low operating temperatures and lack of pollutant emissions. However, a large portion of the cost of the PEMFCs is associated with the cathode catalysts such as Pt and Pt alloys for oxygen reduction reaction (ORR). To widely spread the use of the PEMFCs, development of low Pt loading catalysts and non-Pt catalysts for the PEMFCs cathode has been intensively required. One promising cathode catalyst is based on the transition metal (TM)-nitrogen (N)-carbon (C) composites (TM: Fe, Co, Ni, etc.) [1]. In the present study, we investigated the ORR activity of Fe and N doped carbon films on glassy carbon (GC) substrates prepared by pulsed laser deposition (PLD) in the different presence of N_2 gas. The ORR activity of the films was examined by electrochemical measurements. The composition and structural features of the films were characterized by X-ray photoelectron spectroscopy (XPS), X-ray diffraction (XRD), and Rutherford backscattering spectroscopy (RBS).

The films were prepared at 800 °C in the presence of 6.66–666.7 Pa N_2 gas by PLD using a Nd:YAG laser. After the deposition, the films were immersed in a 2 mol dm^{-3} HCl solution to dissolve metal Fe from the film. The ORR activity of the films was electrochemically determined using a rotating disk electrode system. The reference and counter electrodes were Ag/AgCl with a saturated KCl solution and a Pt wire, respectively. The electrolyte was a 0.5 mol dm^{-3} H_2SO_4 aqueous solution. The RBS analysis confirmed that depth distribution of doped Fe was homogeneous in the as-deposited Fe-N-C film and the doped Fe was almost removed from the film after HCl washing treatment. The XRD suggested that the Fe-N-C films have nano sized grains or amorphous structure.

The ORR potentials (E_{ORR}) to give the ORR activity are plotted with the N_2 gas pressure during the deposition as shown in Fig. 1. The ORR activity of Fe-N-C films increased with increasing the N_2 gas pressure. The Fe-N-C film prepared in the presence of 667 Pa N_2 showed high ORR activity; its E_{ORR} was 0.75 V (vs. NHE). However, this E_{ORR} of the Fe-N-C film is still insufficient compared to that of Pt film on GG substrate (E_{ORR}: 0.85 V) measured by our rotating disk electrode system.

Figure 2 shows the atomic concentration of nitrogen and iron relative to carbon for Fe-N-C films after the ORR measurements. The atomic concentration of N, Fe and C was determined from the XPS N1s, Fe2p3 and C1s spectra. The nitrogen content in the films increases with increasing the N_2 gas pressure during the deposition. In contrast, the iron content in the films has no clear dependence on the N_2 gas pressures. In addition, the XPS was used to investigate the relationship between the ORR activity and the nitrogen species such as pyridinic-N, pyrrolic-N, and graphitic-N. The results suggested that the ORR activity of Fe-N-C films relates to graphitic-N. Thus, controlling the concentration of doped nitrogen with graphitic-N in carbon enables further improvement in the ORR activity of Fe-N-C films.

Reference

1) C. W. B. Bezerra *et al.*, Electrochimica Acta, **53**, 4937-51 (2008).

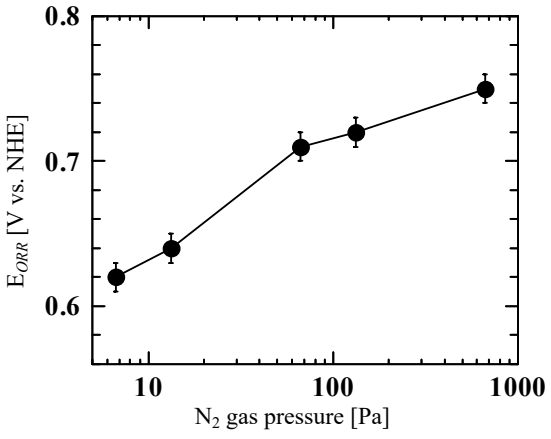

Fig. 1 The E_{ORR} for Fe-N-C films as function of N_2 gas pressure during the deposition.

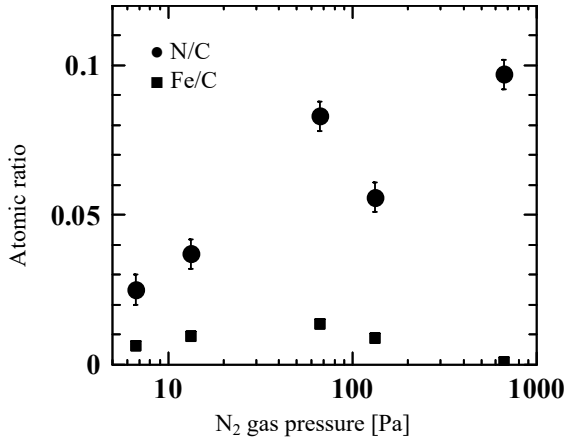

Fig. 2 The N/C and Fe/C atomic ratio of Fe-N-C films after the ORR measurements.

1 - 29

Photoluminescence Properties of Ion-implanted Phosphorous- and Boron-codoped Si Nanocrystals

T. Nakamura [a)], S. Adachi [a)], M. Fujii [b)], H. Sugimoto [b)], K. Miura [a)] and S. Yamamoto [c)]

[a)] Graduate School of Science and Technology, Gunma University, [b)] Graduate School of Engineering, Kobe University, [c)] Department of Advanced Functional Materials Research, TARRI, QST

Si nanocrystals (Si-nc) have been intensively investigated because of their interesting photoluminescence (PL) properties. Si-nc exhibit strong and visible emission at room temperature due to the enhancement of the radiative recombination rate and band-gap widening resulting from carrier confinement in the nanostructured region [1)]. The doping of impurities into Si-nc is a promising technique for the further optimization of their PL properties [2)]. However, although intensive theoretical calculations of optical properties of codoped Si-nc have been performed [3)], the size dependence of carrier doping on the electronic and optical properties of Si nc remains unresolved. In this study, we systematically investigated the dependence of the PL properties of phosphorous- and boron (PB) -codoped Si-nc on the nanocrystallite size and dopant concentration.

Si-nc embedded SiO_2 films were prepared using RF sputtering method [4)]. Three different types of Si-nc samples (S1, S2, and S3) were prepared. The average diameters of Si-nc formed in the S1, S2, and S3 samples to be 3.5, 4.4, and 5.2 nm, respectively. The PB-codoped Si-nc samples were prepared using ion implantation. P^+ or B^+ ions were implanted into the Si-nc films using an ion implanter (Takasaki Ion Accelerators for Advanced Radiation Application, the Japan Atomic Energy Agency). The implantation energies of the P^+ and B^+ ions were 250 and 100 keV, respectively, and the P^+ and B^+ ion doses were varied from 0.1 to 4.5×10^{16} cm^{-2}.

Figures 2(a)-2(c) show the PL spectra of pure (undoped) and PB-codoped Si NCs for different ion doses for samples S1, S2, and S3, respectively. The spectral shapes are strongly dependent on the ion dose and at higher ion doses, additional peaks appear at lower energies. To clarify these peak structures, each spectrum was fitted with three Gaussian peaks (A, B, and C) and obtained each peak energy. Figure 2 shows the peak shift Δ of emission bands A, B, and C with respect to the peak energies of the pure Si-nc samples as a function of the square root of the ion dose. As shown in the inset of Fig. 2, the peak shifts of bands B and C are almost independent of the PB dose. On the other hand, the shift of A depends on the PB dose. The peak shift of band A can be attributed to the band-to-band recombination involving the conduction and valence bands perturbed by the impurity doping [5)]. The degree of band gap reduction in bulk Si is known to follow the $n^{1/3}$ law [5)], where n is the dopant concentration. The solid lines represent the $n^{1/3}$ law. Because the experimental data agree with the law, the peak A is confirmed to be due to the band-to-band recombination at the reduced band gap. The most prominent feature of the dopant-concentration dependence is that its magnitude increases between S3 and S1. This indicates that the magnitude is dependent on the size of the Si-nc; i.e., the smaller the Si-nc sample, the larger shift.

Our present finding that the band gap reduction can be controlled by varying the Si-nc size and the dopant concentration advances the fundamental understanding of doping effects in an indirect band-gap semiconductor nanocrystal.

References

1) C. Delerue *et al.*, Phys. Rev. B, **11024-36**, 38 (1993).
2) M. Fujii *et al.*, Appl. Phys. Lett., **1158**, 85 (2008).
3) F. Iori *et al.*, Phys. Rev. B, **085302**, 76 (2009).
4) S. Takeoka et al., Phys. Rev. B, **16820-25**, 62 (2000).
5) J. Wagner, Phys. Rev. B, **1323-5**, 29 (2000).

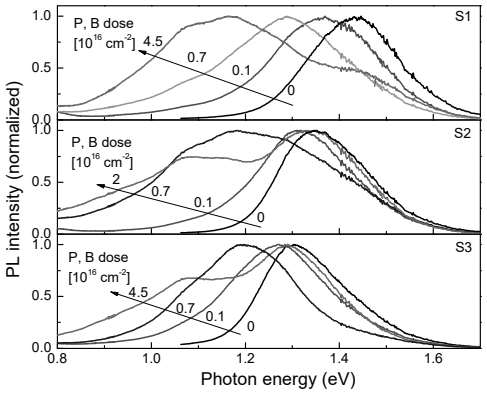

Fig. 1 PL spectra of PB-codoped Si-nc for various ion doses of 0.1-4.5×10^{16} cm^{-2}: Samples (a) S1; (b) S2; and (c) S3.

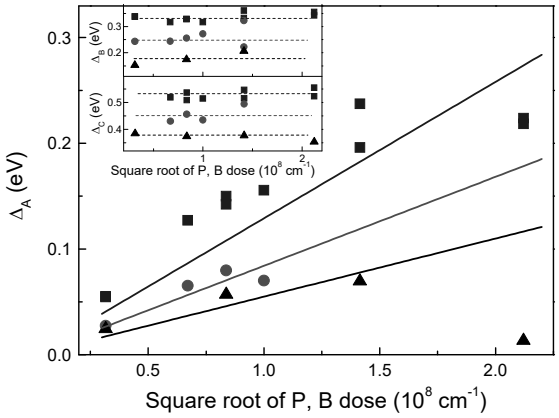

Fig. 2 Peak energy shift of band A with respect to that of the intrinsic Si-nc. The inset shows those of bands B and C. The solid lines in (b) show fit results for the $n^{1/3}$ law.

1 - 30

Synthesis of New-structured Multi-walled Carbon Nanotubes inside Silicon Carbide Nanotubes

T. Taguchi [a)], S. Yamamoto [b)] and H. Ohba [a)]

[a)] Tokai Quantum Beam Science Center, TARRI, QST,
[b)] Department of Advanced Functional Materials Research, TARRI, QST

Carbon nanomaterials such as fullerenes, carbon nanotubes, and graphene have attracted particular attention due to their fascinating geometries and physical properties. In particular, carbon nanotubes represent an interesting and important class of carbon based nanomaterials with wide-ranging applications. It is, therefore, required to synthesize the carbon nanotubes with new structure in order to develop and broaden the application of carbon nanotubes. Here we report the synthesis of new-structured multi-walled carbon nanotubes inside silicon carbide (SiC) nanotubes.

Multi-walled carbon nanotubes (GSI creos Corporation, Tokyo, Japan) were used as template materials. The C-SiC coaxial nanotubes were synthesized by heating multi-walled carbon nanotubes with Si powder at 1,200 ºC for 100 h in a vacuum [1,2)]. The C-SiC coaxial nanotubes were irradiated with 340 keV Si^+ ions from 400 kV ion implanter of TIARA at room temperature. The projected range of 340 keV Si^+ ions into the SiC target was calculated to be approximately 400 nm by Stopping and Range of Ions in Matter (SRIM) 2008 software [3)], which indicated that the irradiated Si^+ would completely penetrate the C-SiC coaxial nanotubes. The ion fluence was 2.4×10^{20} ions/m^2, and the corresponding irradiation damage (displacement per atom, dpa) was calculated by SRIM 2008[3)] to be 6.8 dpa.

Figure 1 shows the typical TEM image and selected area electron diffraction (SAED) patterns of the irradiated C-SiC coaxial nanotube. According to high-resolution (HR) TEM image, the amorphous structure is observed in the SiC layer of C-SiC coaxial nanotube. The crystal state of SiC layer in C-SiC coaxial nanotube transforms from polycrystalline to amorphous by ion irradiation at room temperature. However, the tubular shape of the C-SiC coaxial nanotube is retained even after ion irradiation.

The orientation of the graphitic shells in the C-SiC coaxial nanotubes before ion irradiation was almost parallel to the length directions of the nanotubes. However, HR-TEM observation indicates that the orientation of graphitic shells after ion irradiation changes such that they are completely parallel to the radial directions of the nanotubes. These results are consistent with that of the SAED pattern from the C-SiC coaxial nanotube, as depicted in the inset in Fig. 1(a). The graphite (002) spots in the SAED image are clearly observed even after ion irradiation up to 6.8 dpa, indicating the certain crystallinity of the carbon layer in the C-SiC coaxial nanotube. In this study, the C-SiC coaxial nanotubes are irradiated up to 6.8 dpa. However, the carbon layers in the C-SiC coaxial nanotubes are not transformed to a completely amorphous structure. The graphitic structure is still observed in HR-TEM images of the shells. The remaining graphitic portions of the shells have bent to align completely with the radial directions of the nanotubes, as shown in Fig. 1(b). The synthesis of multi-walled carbon nanotubes with graphitic shells completely oriented parallel to the radial direction of the nanotube has not been reported yet. Such a multi-walled carbon nanotubes with this new structure may be expected to find new applications.

References

1) T. Taguchi *et al.*, J. Am. Ceram. Soc., **88**, 459-61 (2005).
2) T. Taguchi *et al.*, Physica E, **28**, 431-38 (2005).
3) J. F. Ziegler *et al.*, Nucl. Instrum. Meth. Phys. Res. B, **268**, 1818-23 (2008).

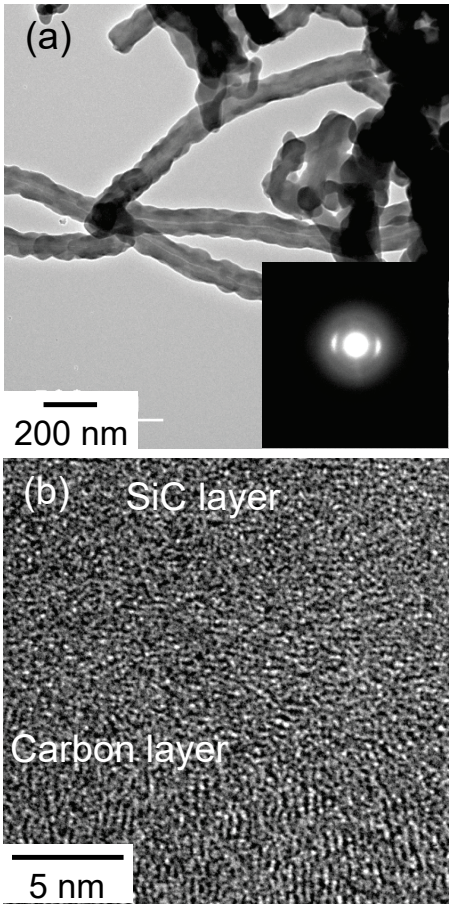

Fig. 1 (a) Low-magnification TEM image and SAED patterns, and (b) high-resolution TEM image of new structured multi-walled carbon nanotube inside SiC nanotube.

1-31

Improvement on Hydriding Characteristics for Hydrogen Storage La-Ni Based Alloy by Ion Beam

H. Abe [a)], S. Ohnuki [b)], Y. Matsumura [c)] and H. Uchida [c)]

[a)] Department of Advanced Functional Materials Research, TARRI, QST,
[b)] Course of Applied Science, Graduate School of Engineering, Tokai University,
[c)] Department of Energy Science and Engineering, School of Engineering, Tokai University

Hydrogen storage alloys are required to attain high responses of hydrogen absorption for application to the negative electrode of the nickel-metal hydride (Ni-MH) batteries. The surface modification is crucial to improve the reactivity of hydrogen with hydrogen storage alloys, and this facilitates the rate of dissociation of the H_2 molecules in the gas phase or the dissociation of the H_2O molecules in an electrochemical process is the first step of the overall reaction of hydrogen absorption for hydrogen storage alloys. In this study, improvement effects of ion beam irradiation on hydriding characteristics for La-Ni base AB_5 type alloys were studied.

The samples used in this study were $LaNi_{4.6}Al_{0.4}$ hydrogen storage alloy. These were ion-irradiated at an energy of 350 keV with a dose from 14×10^{18} to 1×10^{21} /m^2 at the room temperature using the 400 kV ion implanter at TIARA, JAEA. The rate of initial hydriding rate measurements was also performed for the irradiated samples and un-irradiated ones using an electrolytic cell with as $LaNi_{4.6}Al_{0.4}$ cathode apparatus. Details of the electro-chemical hydrogen absorption rate are reported elsewhere [1)].

Figure 1 shows hydrogen absorption curves of $LaNi_{4.6}Al_{0.4}$ irradiated by 350 keV He^+, K^+ and Bi^+. Figure 1-b) is a partial expansion of Fig. 1-a). The charge capacity at 120 minutes of He^+ (×: dose of 1×10^{21} /m^2), K^+ (▲: 1×10^{18} /m^2 and ▼: 1×10^{20} /m^2), Bi^+ (■: 2×10^{18} /m^2 and ●: 1×10^{20} /m^2) irradiated samples and un-irradiated (◆) were 8.88×10^3, 8.70×10^3, 1.10×10^4, 6.79×10^4, 1.31×10^5 and 6.45×10^3 As/m^2, respectively. The $LaNi_{4.6}Al_{0.4}$ irradiated by the Bi^+ at a dose of 1×10^{20} /m^2 (●) exhibited the highest rate of initial hydrogen absorption in all samples, and the hydrogen absorption rate became about 20 times higher than that of un-irradiated sample (◆). These vacancy type defects may act as hydrogen trapping sites, and increase hydrogen concentration near the surface region due to irradiation of Bi^+ into $LaNi_{4.6}Al_{0.4}$. Ion irradiation onto the surface of a metal effectively induces defects, such as vacancies, dislocations, micro-cracks or impurities near the surface. As for the dissociation of the hydrogen molecule, at the surface of the samples, the nucleation site of the hydride formation might be effective for the hydrogen atom in the $LaNi_{4.6}Al_{0.4}$ surface region because of the formation of vacancies with high concentration. All the irradiated samples showed a rate of initial hydrogen absorption that was higher than the un-irradiated one. However, He^+- and K^+-irradiated (1×10^{18} / m^2) samples showed almost similar curves. According to the result of the TRIM/SRIM simulation [2)], a peak of the vacancy defects concentration by the He+ and K+-irradiation is indicated in 800 and 100 nm depth from the sample surface neighborhood. Furthermore, the vacancy of the high concentration is different from two of ion species describe the above, and is produced around the surface neighborhood by the Bi^+ irradiation. The vacancy by the recoil is more predominant than by the ionic excitation in the heavier Bi^+. Thus, the vacancy defects of the high concentration by the heavy ion irradiation are very effective for the surface modification of hydrogen absorption materials. And this result, it was revealed that the defect introduced by ion irradiation contributes to improvement of the initial hydrogen reaction rate. The ion with defect distribution more widely than an ion with a peak is faster at the initial hydrogen reaction rate in depth direction.

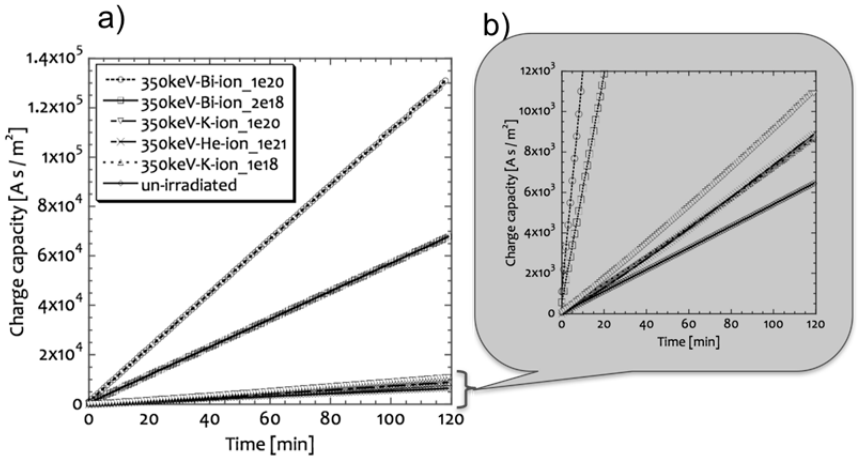

Fig. 1 a): Hydrogen absorption curves of the ion irraidiated/un-irradiated $LaNi_{4.6}Al_{0.4}$ alloy. b): expansion view of the vertical axis of Fig. 1-a).

References

1) H. H. Uchida *et al.*, J. Alloys Compd. **231**, 679 (1995).
2) P. Asoka-Kumar *et al.*, Appl. Phys. Lett. **57**, 163 (1990).

1 - 32

Vacancy-Induced Magnetism in ZnO Probed by Spin-Polarized Positron Beam

M. Maekawa, H. Abe, S. Sakai and A. Kawasuso

Department of Advanced Functional Materials Research, TARRI, QST

Zinc oxide (ZnO), which is a wide-bandgap semiconductor, is known to show d^0 ferromagnetism [1]. This ferro-magnetism could be induced by lattice defects. *Ab initio* studies predicted that cation (Zn) vacancies cause the ferromagnetism in ZnO [2]. However, experimental results suggest that cation or anion vacancies, oxygen interstitials, dislocations, lattice distortions, or grain boundaries cause the ferromagnetism. The cause of this chaotic situation is the lack of the measurement technique which can estimate the relation between macroscopic ferromagnetism and lattice defects. We expect that spin-polarized positron annihilation spectroscopy (SP-PAS) can solve this problem. Because positrons are sensitive to vacancies and electron spins, the SP-PAS technique may detect magnetic moments associated with vacancies. For this purpose, we have developed a longitudinally spin-polarized positron beam [3] and have applied for the study of vacancy-induced ferromagnetism in ZnO crystal.

Oxygen ion were implanted to the hydrothermally-grown ZnO single crystals with a dose of 5×10^{16} cm^{-2} at 100 keV. Vacancy defects were created in the range of 100 - 200 nm from the surface. After irradiation, the Doppler-broadening of annihilation radiation (DBAR) measurements were carried out in the magnetic field of ± 0.91 T.

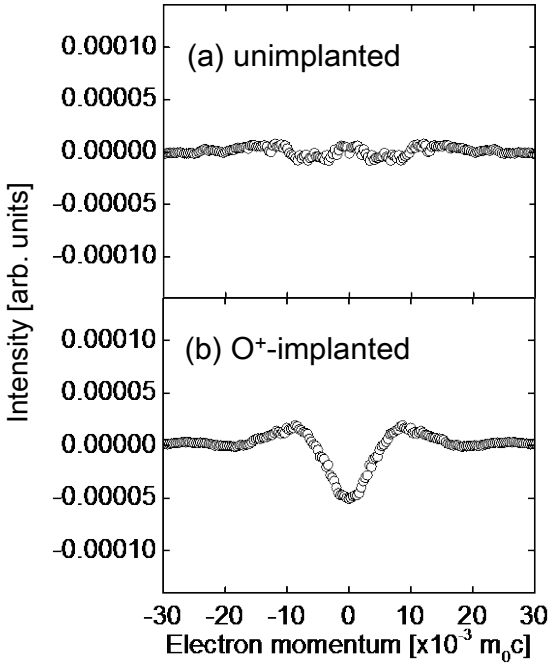

Fig. 1 Difference DBAR spectra between positive and negative magnetic fields obtained for (a) unimplanted and (b) O+-implanted ZnO samples.

Figure 1 shows the differential DBAR spectra between positive and negative magnetic fields. The DBAR spectra of the unimplanted ZnO sample show no differences upon field reversal, suggesting no spin polarization of electrons participating in positron annihilation. On the contrary, the oxygen-implanted ZnO spectra show a difference upon field reversal, providing information about the spin polarization of the electrons participating in positron annihilation. Previous work showed that positrons implanted in oxygen-implanted ZnO are fully trapped at Zn vacancies [4]. This result means that the magnetic moments at Zn vacancies and their ordering respond to external magnetic fields.

Figure 2 shows the differential DBAR intensity as a function of annealing temperature. Magnetization obtained from superconducting quantum interference device (SQUID) method are also shown. With increasing of annealing temperature, both DBAR intensity and magnetization decrease. It is inferred that the recovery of vacancy defects is accompanied with the elimination of the electron spin which positrons annihilate.

These results are the first result that found that electron spins at Zn vacancies is related to d^0 magnetism directly.

References

1) N. H. Hong *et al.*, J. Phys. Cond. Matter, **19**, 036219 (2007).
2) Q. Wang *et al.*, Phys. Rev. B, **77**, 205411 (2008).
3) M. Maekawa *et al.*, Jpn. J. Appl. Phys. Conf. Proc., **2**, 011305 (2014).
4) Z. Q. Chen, M. Maekawa, *et al.*, Appl. Phys. Lett., **87**, 091910 (2005).

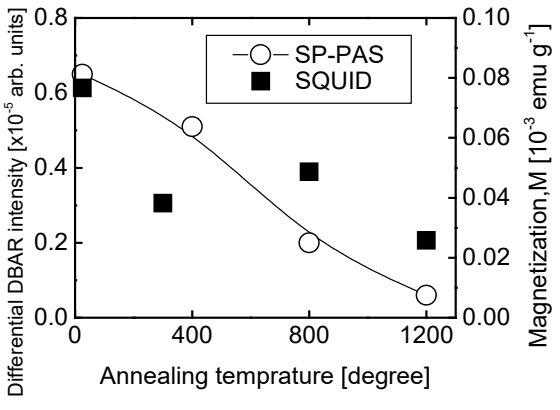

Fig. 2 The differential DBAR intensity and magnetization as a function of annealing temperature.

1 - 33

Lattice Structure Transformation and Change in Surface Hardness of Ni_3Ta Intermetallic Compounds Induced by Energetic Ion Beam Irradiation

H. Kojima [a)], Y. Kaneno [a)], S. Semboshi [b)], Y. Saitoh [c)] and A. Iwase [a)]

[a)] Department of Materials Science, Osaka Prefecture University,
[b)] Institute for Materials Research, Tohoku University,
[c)] Department of Advanced Radiation Technology, TARRI, QST

Energetic ion irradiation locally gives high density energy deposition into a target, and it can induce non-thermal equilibrium phases. In ordered alloys (intermetallic compounds), such as AB or A_3B, each of the A and B atoms occupies specific sub-lattice sites, and their atomic ordering is described by the long-range order parameter. For these alloys, an irradiation-induced rearrangement of A and B atoms can give rise to a change in long-range parameter. A great deal of experimental data has demonstrated that ordered alloys such as Ni_3Al, Zr_3Al, CuTi, $NiZr_2$ show the transition to a disordered structure or an amorphous state by ion or electron irradiations. Such lattice structure transformations were mainly investigated by using the transmission electron microscopy, but, changes in physical properties which are accompanied by the irradiation-induced lattice structure transformations have little been discussed so far. In our previous results, we showed the energetic ion irradiation induced lattice structure transformation and the change in Vickers hardness for Ni_3Al [1)], Ni_3V [2)] and dual-phase Ni_3Al-Ni_3V intermetallic compounds. In the present study, we have chosen Ni_3Ta intermetallic compound as targets for the irradiation study. The intermetallic compound Ni_3Ta, which shows limited ductility, has been considered as a reinforced phase in directionally solidified Ni based eutectic alloys. In this report, we will show the effect of energetic ion irradiation on the lattice structures and hardness for Ni_3Ta intermetallic compounds.

Ni_3Ta bulk ingot was thermally annealed at 1,273 K for 144 h. After the annealing, the ingot was cut into the sheets with the dimension of $15 \times 1 \times 0.1$ cm^3. They were irradiated at room temperature with 16 MeV Au^{5+} ions by using the 3 MV tandem accelerator of TIARA. The ion fluences were from 1×10^{12} to 5×10^{14} cm^{-2}. After the ion irradiation, we performed the grazing incidence x-ray diffraction (GIXD) measurements and the Vickers hardness measurements with a load of 10 gf.

Figure 1 shows the results of GIXD spectra for the unirradiated Ni_3Ta sample and those irradiated with Au ions. All the peaks for the unirradiated sample correspond to the ordered monoclinic lattice structure, which has been reported as a thermal equilibrium structure of Ni_3Ta at room temperature. For the Au ion irradiated Ni_3Ta, the ordered peaks tend to disappear with an increase in ion fluence. The peaks for the ordered structure nearly completely disappear after the irradiation with the fluence of 5×10^{14} $/cm^2$. Similarly to Ni_3Nb, this result suggests that Ni_3Ta transforms from the monoclinic ordered structure to the amorphous state by the ion irradiation at room temperature. Figure 2 shows the relative change in Vickers hardness for Ni_3V, Ni_3Nb and Ni_3Ta intermetallic compounds. The Vickers hardness for Ni_3V decreases with increasing ion fluence because the disordered structure is more deformable than the ordered structure. On the other hand, for Ni_3Nb and Ni_3Ta, the Vickers hardness increases with increasing ion fluence. This result can be explained as the conventional fact that the value of hardness for the amorphous state is larger than that for the crystal structure.

References

1) H. Yoshizaki *et al.*, Nucl. Instrum. Meth. Phys. Res. B, **354**, 287 (2015).
2) A. Hashimoto *et al.*, Nucl. Instrum. Meth. Phys. Res. B, **338**, 72 (2014).

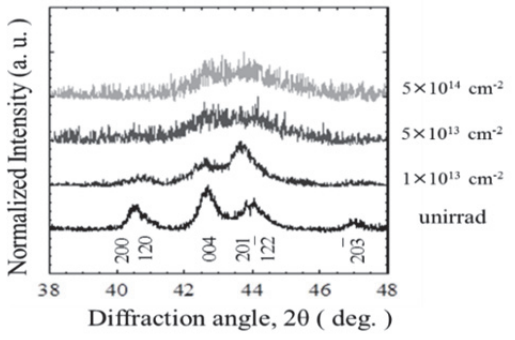

Fig. 1 GIXD spectra of unirradiated and irradiated Ni_3Ta intermetallic compound.

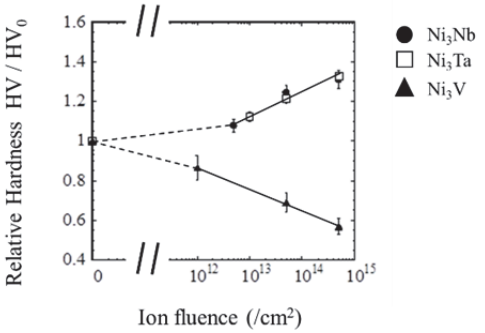

Fig. 2 Relative change in Vickers hardness as a function of ion fluence for Ni_3V, Ni_3Nb and Ni_3Ta intermetallic compounds.

1-34 Amorphization of NiTi Intermetallic Compounds Induced by Energetic Ion Bombardment

M. Ochi [a], H. Kojima [a], Y. Kaneno [a], F. Hori [a] S. Semboshi [b], Y. Saitoh [c] and A. Iwase [a]

[a] Department of Materials Science, Osaka Prefecture University,
[b] Institute for Materials Research, Tohoku University,
[c] Department of Advanced Radiation Technology, TARRI, QST

A lot of papers on the irradiation effects on the lattice structures of intermetallic compounds have already been published. Most of them, however, have reported experimental results for thin films by using transmission electron microscope (TEM) observations. Recently, we have reported the effect of energetic ion irradiation not only on lattice structures but also on mechanical properties of some bulk Ni-based intermetallic compounds[1,2]. In the present study, Ni-50.8%Ti alloy was used as target samples.

NiTi bulk ingot was thermally annealed at 973 K for 30 min. After the annealing, the ingot was cut into sheets with the dimension of $1 \times 1 \times 0.15$ cm^3. They were irradiated at room temperature with 16 MeV Au^{5+} ions by using the 3 MV tandem accelerator of TIARA. Some samples were irradiated with 200 MeV Xe ions at JAEA-Tokai. The ion fluences were from 1×10^{12} to 5×10^{14} cm^{-2}. After the ion irradiation, the effect of the irradiation on the lattice structure was estimated by using grazing incidence X-ray diffraction (GIXD). The change in Vickers hardness by the irradiation was also measured.

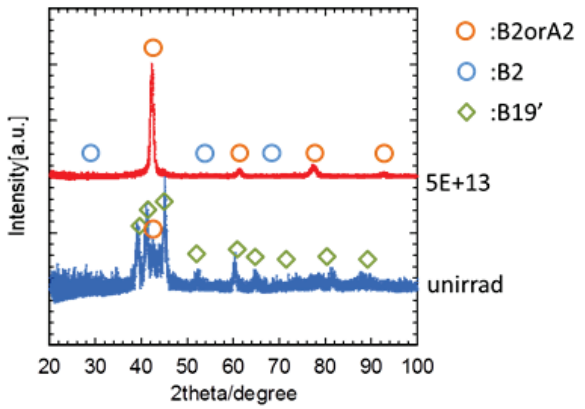

Fig. 1 GIXD profiles of NiTi bulk alloy before and after 200 MeV Xe ion irradiation.

As can be seen in Fig. 1, the GIXD result shows that, before the irradiation, NiTi samples have the monoclinic (B19') structure, and after the 200 MeV Xe ion irradiation with the fluence of 5×10^{13} /cm^2, the lattice structure changes from the monoclinic to the bcc-based structure (B2 or A2). On the other hand, Fig. 2 shows that after the 16 MeV Au ion irradiation, a broad XRD peak appears around 42.5 degree, which implies that the samples are amorphized by the Au ion irradiation. The difference in the lattice structure change between by 200 MeV Xe and by 16 MeV Au irradiations can be explained in terms of the amount of energy deposited into the samples through the process of elastic collisions between target atoms and energetic ions. For larger deposited energy, the samples can be amorphised more easily. The Vickers hardness measurement shows that the hardness of the samples increases with increasing the ion fluence.

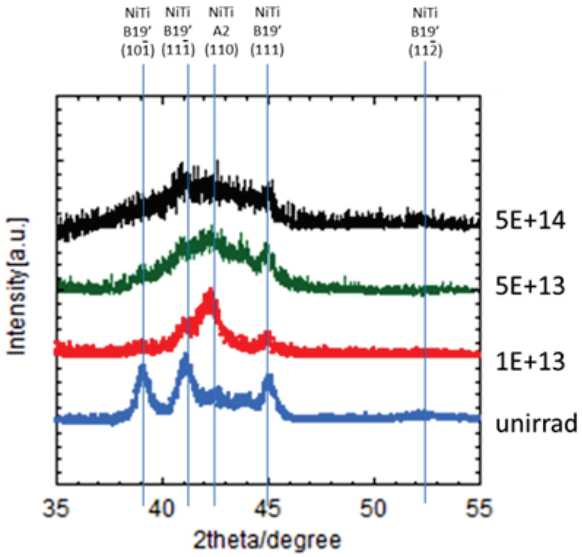

Fig. 2 GIXD profiles of NiTi bulk alloy before and after 16 MeV Au ion irradiation.

References

1) A. Hashimoto *et al.*, Jpn. J. Appl. Phys., **53**, 05FC08 (2014).
2) H. Yoshizaki *et al.*, Nucl. Instrum. Meth. Phys. Res. B, **354**, 287-91 (2015).

1 - 35

Clustering of Metal Atoms by High Energy Ion Implantation in Silica Glass and the Effects on Magnetic and Optical Properties

K. Fukuda [a)], Y. Fujimura [a)], Y. Yamamoto [a)], Y. Okamoto [b)], S. Semboshi [c)], Y. Saitoh [d)] and A. Iwase [a)]

[a)] Department of Materials Science, Osaka Prefecture University,
[b)] Quantum Beam Science Center, JAEA, [c)] Institute for Materials Research, Tohoku University,
[d)] Department of Advanced Radiation Technology, TARRI, QST

Nanocomposite glasses containing metal or semiconductor nanoparticles have become an object of interest among a lot of researchers because of their promising utilization [1)]. The presence of metal nanoparticles leads to physical property modifications of the glass matrix.

There are several well-known methods to prepare nanocomposite glasses. Ion implantation is one of the most suitable techniques for the incorporation of metal nanoparticle in the solid glass matrix. The advantages of ion implantation are the possibilities to choose a wide variety of elements to be implanted, to overcome the solubility limits and to control the implantation depth and distribution [1)].

In the present work, magnetic and optical properties of transparent oxides implanted with energetic Fe or Ag ions have been studied. Target samples were SiO_2 (silica glasses). They were implanted with 380 keV Fe ions or Ag ions at various fluences. The effects of the implantation on magnetic properties were studied by using SQUID magnetometer. The change in optical absorption was also studied. To investigate the chemical states of the implanted ions, the X-ray absorption near the edge structure (XANES) was used.

Figure 1 shows the magnetization-magnetic field (M-H) curves at room temperature obtained by the SQUID measurement for Fe-implanted SiO_2.

The figure shows that the magnetic state of implanted Fe changed from the (super) paramagnetic to the ferromagnetic state with increasing the amount of implanted Fe ions. This implies that during the implantation, small Fe clusters were produced and that the lattice structure of Fe clusters became the BCC structure. XANES observation confirms the change in the Fe state from isolated Fe atoms to metallic Fe clusters during the implantation.

Figure 2 shows the optical absorption spectra for Ag-implanted SiO_2. An absorption band around 410 nm, corresponding to the surface plasmon resonance of Ag nanoparticles, was confirmed. With increasing the amount of implanted Ag ions, the intensity of 410 nm peak increased and another peak appeared around 700 nm. This experimental result suggests that the shape of Ag clusters changed during the Ag implantation.

Reference

1) S. Vytykacova *et al.*, Nucl. Instrum. Meth. Phys. Res. B, **371**, 245-50 (2016).

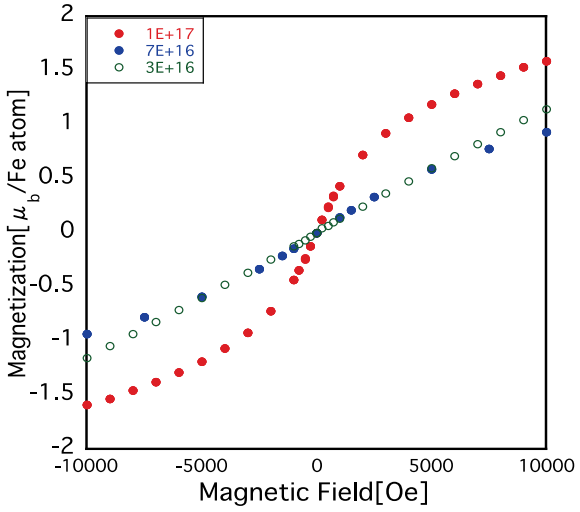

Fig. 1 Magnetization for Fe implanted SiO_2 matrix at 300 K as a function of magnetic field.

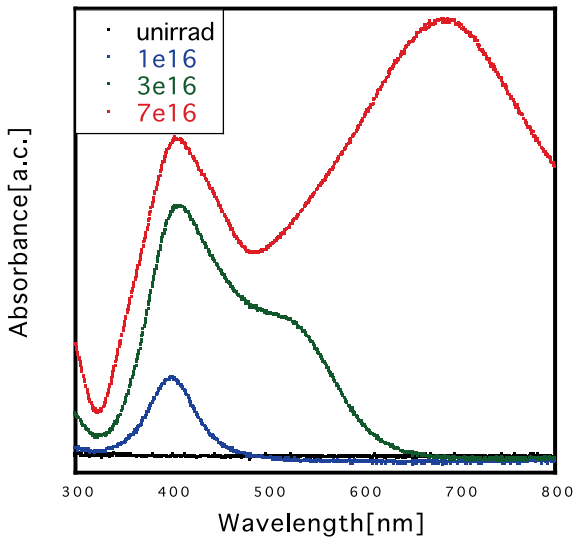

Fig. 2 Absorption spectra of SiO_2 implanted with Ag ions at various fluences.

1-36 Depth-Directional Magnetic Modification for Bulk FeRh by High Energetic Ion-Irradiation

R. Soma [a], A. Iwase [a], Y. Saitoh [b], R. Ishigami [c] and T. Matsui [d]

[a] Department of Materials Science, Osaka Prefecture University, [b] Department of Advanced Radiation Technology, TARRI, QST, [c] Research and Development, The Wakasawan Energy Research Center, [d] Research Organization for the 21st Century, Osaka Prefecture University

FeRh alloy with B2 (CsCl type) ordered structure is well known to exhibit a first order phase transition from anti-ferromagnetic (AF) to ferromagnetic (FM) near the room temperature. In our previous studies, we revealed that energetic ion beam irradiation induced FM state below room temperature where AF state was originally stable. Further irradiation of FeRh caused structural phase transition to high temperature phase that resulted in exhibiting paramagnetic (PM) nature. In addition, we revealed that the change in magnetizations was related directly to the density of energy deposited through elastic collisions between ions and the samples as can be seen in Fig. 1 [1].

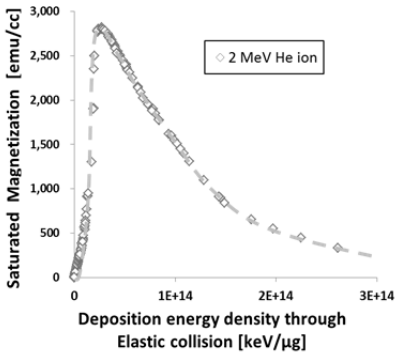

Fig. 1 Value of saturated magnetization at 5 K, as a function of energy density deposited through elastic collisions for irradiated (2 MeV He ions).

By considering a suitable condition of ion beam irradiation to modify magnetizations, it may become possible to produce magnetic layered structures such as FM-PM-FM-AF in bulk or thick film FeRh samples from the surface. In the present studies, we examined the possibility to control depth-directional magnetic modify-cation by high energetic ion-irradiation for FeRh.

Homogenized $Fe_{50}Rh_{50}$ bulk samples were irradiated with 2 MeV He ions in the range of fluence of 1.5×10^{14} ~1.5×10^{16} ions/cm^2 at room temperature. Then, magnetic properties were characterized by a SQUID magnetometer. The design of the depth-directional magnetization profile was performed by deposition energy profile simulations using a TRIM code.

The overall experimental results suggest that depth-directional magnetic modification can be realized by high energetic ion-irradiation for bulk FeRh. Figures 2 and 3 show the estimated magnetic depth profiles of the FeRh bulk samples irradiated with 2 MeV He ions of the ion fluence of 1.5×10^{14} ions/cm^2 and 1.5×10^{16} ions/cm^2, respectively. In accordance with the SQUID measurement for the corresponding sample, the sample had the almost same magnetization as that calculated from the estimated depth profile in Fig. 1.

Hence, we can reveal that the designed magnetic layered structure can be produced in FeRh bulk by using the technique mentioned above, which is quite attractive from the view point of magnetic device application of this material.

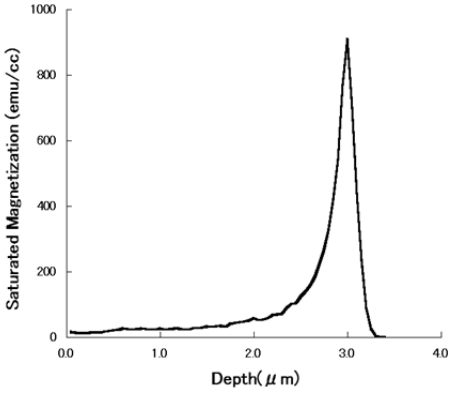

Fig. 2 Saturated magnetization at 5 K of the irradiated (1.5×10^{14} ions/cm^2) bulk FeRh as a function of depth.

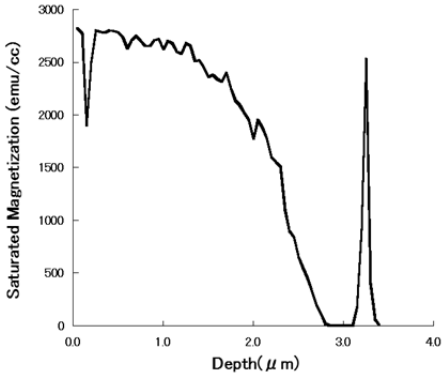

Fig. 3 Saturated magnetization at 5 K of the irradiated (1.5×10^{16} ions/cm^2) bulk FeRh as a function of depth.

Reference

1) N. Fujita *et al.*, J. Appl. Phys., **107**, 09E302 (2010).

1-37 Synergetic Effect of He, H and Displacement Damages on Irradiation Hardening and Microstructures of F82H

D. Hamaguchi , M. Ando and H. Tanigawa

Department of Fusion Reactor Materials Research, RFI, QST

Reduced activation ferritic/martensitic steels (RAFMs) such as F82H are the most promising candidates for the blanket structural materials in fusion reactor[1]. There have been an extensive works to reveal the neutron irradiation effects on RAFMs but there still remains a lot of uncertainty regarding the fusion neutron irradiation effects. One of difficulties to predict the development of damages under fusion neutron irradiations is a lack of irradiation facility that can reproduce an irradiation conditions such as a neutron spectrum regarding fusion reactor environment. Therefore, we need to collect information on particular events that are expected to be specific under fusion neutron irradiations by using existing irradiation facilities. Regarding fusion neutron irradiation on ferritic steels, one of main differences compared to fission neutron irradiation is a very high He and H transmutation gas production rate. To understand the effect of He and/or H gas on the development of irradiation damages, complex beam ion irradiation experiments are essential. Therefore in this study, multiple ion irradiation experiments were carried out using TIARA complex irradiation facility to examine the synergetic effect of He and H with displacement damage on irradiation hardening and microstructure evolutions of F82H.

The materials used in this study were reduced activation ferritic/martensitic steel F82H with couple of different versions: IEA, Mod3, BA07 and BA12. IEA is a standard version of F82H whereas Mod3, BA07 and BA12 are modified versions with slightly different compositions and the heat treatment conditions in order to achieve finer grain sizes for better toughness under neutron irradiation. The basic composition of IEA is Fe-8Cr-2W-0.2V-0.04Ta-0.1C whereas Mod3 and BA12 have a higher Ta content of 0.1% and 0.08%, respectively. For heat treatment, IEA was normalized at 1,040 °C for 0.63 h followed by a tempering at 750 °C for 1 h whereas other modified versions have normalizing temperature ranged from 1,080-1,020 °C and tempering temperature of 740 °C. The irradiations were carried out with 10.5 MeV Fe^{3+} ions with/without 1.05 MeV He^{+} and 0.38 MeV H^{+}. He and H ion implantations were performed using aluminum foil energy degraders in order to achieve the same depth as displacement by Fe ions. The irradiation was performed up to 20 dpa at the depth of 1.0 μm. Post-irradiation experiments (PIE) were performed at Rokkasho Fusion Institute. The irradiation hardening was measured using nano-indentation technique with ENT-1100a (Elionix INC) and some microstructures were observed with JEOL JEM-2100F transmission electron microscope (TEM) operating at 200 kV.

Figure 1 shows the micro-hardness data for F82H-IEA, Mod3, BA07 and BA12 irradiated at the temperature ranged form 300 °C to 500 °C at 20 dpa. In this year, the data were mainly collected form the irradiations at 300 °C and 350 °C. It has been revealed that for all the versions of F82H, the irradiation hardening peaks at around 350 °C and tends to decrease along with irradiation temperatures above 400 °C. On the other hand, the most pronounce effect of co-implantation with He and H are seen only at 300 °C.

In this study, void swelling behaviors were also examined. Figure 2 shows the cavity microstructure of F82H-BA07 irradiated at 470 °C with multiple ions. From the examination, it is revealed that the swelling of BA07 was very small compared to IEA. This can be due to a stable lath microstructure at higher temperatures compared to IEA, but further investigation is needed for the details.

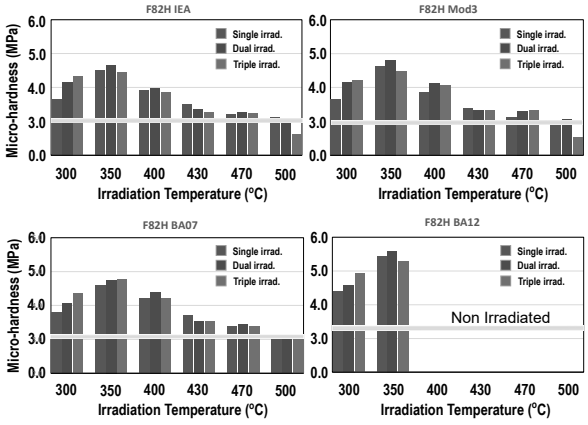

Fig. 1 Micro-hardness data for F82H irradiated up to 20 dpa with multiple ions.

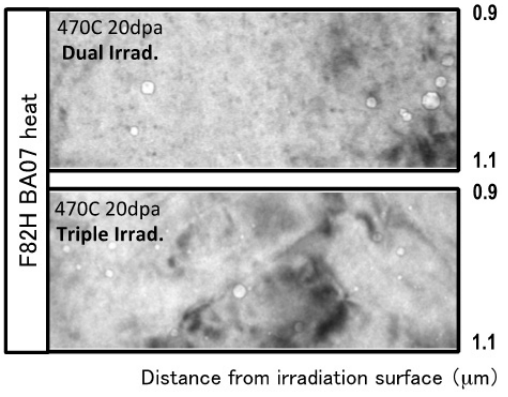

Fig. 2 Cavity microstructure of F82H-BA07 irradiated at 470 °C up to 20 dpa with multiple ions.

Reference

1) H. Tanigawa *et al.*, J. Nucl. Mater., **417**, 9-15 (2011).

1-38 Helium Effects on Hardening Behaviors of Ni Metal and Austenitic Stainless Steel Irradiated up to 200 dpa

N. Okubo and N. Ishikawa

Fuels and Materials Engineering Division, NSEC, JAEA

Effects of simultaneous irradiation of helium ions with displacement damage by accelerated self ions on hardening have been studied for Ni metal and SUS316L austenitic stainless steel to evaluate fundamental mechanical properties and the irradiation response in high irradiation fields as a spallation target and fusion systems.

In TEF-T facility (Transmutation experimental facility on Target for ADS), which will be constructed in J-PARC (Japan Proton Accelerator Research Complex) around 2019, SUS316L steel is a candidate material for the first stage target window because of the high reliability for neutron and proton irradiation. The MLF (Materials and Life Science Experimental Facility) in J-PARC has used SUS316L as a target window material from the first beam in 2008, in the mercury target system[1]. The second target material used at high proton beam power will be ferritic martensitic steel, like a T91.

Irradiation hardening behavior of ion irradiation and neutron irradiation was compared by using dual-beam for energy technology (DuET) facility of the University of Kyoto and HFIR (High Flux Isotope Reactor) in ORNL (Oak Ridge National Laboratory)[2]. Further irradiation damage effect over 100 dpa at 300 °C and He effect on the hardening behavior due to single and dual ion irradiation was studied by using TIARA (Takasaki Ion Accelerators for Advanced Radiation Application) triple ion beam chamber in QST. In this report, we address irradiation hardening behaviors of SUS316L steels in the case of simultaneous irradiation of helium at considerably high damage levels up to around 200 dpa. And Ni metal was also irradiated as the basic reference material.

Ion irradiations of 10 MeV-Fe^{3+} and 1.05 MeV-He^{+}, which depth distribution was extended by energy degrader made of 800 nm Al foil, was conducted for the SUS316L (solution annealed) and Ni metal at 300 °C. Each specimen size is 3 mm height, 6 mm width and 0.5-1.0 mm thickness. Achieved damage level was 200 and 172 dpa in single and dual irradiation, respectively. The irradiation rate was 1.2×10^{-3} dpa/s and Helium rate was about 100 appmHe/dpa. After the irradiation, the micro-hardness was measured by using nano-indentation.

Hardening behaviors of 316L and Ni, single and dual irradiations are shown in Fig. 1. In the case of Ni, radiation hardening induced by the dual ion beams is a little higher than that induced by single ion beam. On the other hands, in the case of 316L, almost no He effect was observed. These 4 types of irradiations showed the saturation of hardening around 50 dpa in these experiments and kept constant up to 200 dpa.

Previous study showed that ferritic martensitic steel, F82H had He effect on the radiation hardening as an extra hardening around 100 dpa[3]. In this experiment, however, SUS316L and Ni do not have the He effect remarkably. Both SUS316L and Ni have a FCC (Face Center Cubic) crystal structure. The F82H has a BCC (Body Center Cubic) crystal structure. This implies that the FCC crystal structure does not have susceptibility to He effect on radiation hardening, which is caused by the accumulation of interstitial loops. More detailed experiments will be necessary for estimation of He effect on radiation hardening, which depends on the crystal structure, or not.

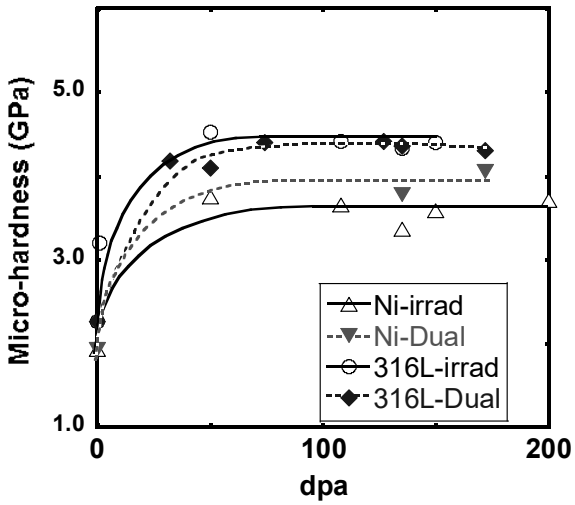

Fig. 1 Dpa dependence of irradiation hardening for single and dual irradiated each Ni and SUS316L.

References

1) M. Tomizawa, Nucl. Phys. B, **154**, 123-28 (2006).
2) M. Ando *et al.*, J. Nucl. Mater., **307-11**, 260 (2002).
3) N. Okubo *et al.*, JAEA Takasaski Annu. Rep. 2013, JAEA-Reviw 2014-050, 38 (2015).

1 -39

Simultaneous Irradiation Effect of He and H with Displacement Damage on Swelling Behavior of T91 Steel

N. Okubo and N. Ishikawa

Nuclear Science and Engineering Center, JAEA

In a future ADS (Accelerator Driven System) plant, the target window, which is an important boundary between a high energy accelerator for protons and a spallation target of Lead-Bismuth Eutectic (LBE), and fuel cladding materials will be heavily irradiated under severe conditions, where considerable displacement damages, and high concentration of He and H atom accumulations will occur simultaneously due to high energy proton and spallation neutron irradiations. Degradation of mechanical properties and volume change of the components after irradiation at relatively high temperature, ex. from 450 to 550 °C, should be suppressed within a range permissible for the ADS design. High fluence neutron irradiation experiments up to about 20 and 100 dpa, which are estimated as upper limits of window and cladding material irradiation damage, respectively, are practically difficult due to the long time irradiation and the irradiation cost. Especially, nuclear transmutation gas concentration in the present experimental reactor irradiation is not sufficient for estimating He and H impacts over ADS system irradiation conditions. Simultaneous multiple ion irradiation is a powerful technique for simulating ADS irradiation fields in order to select candidate materials prior to material irradiation experiments, so called a transmutation experimental facility (TEF-T), which will be constructed on the site of J-PARC. In this study, we address the swelling behavior of the T91 steel, which is one of the candidate materials for the target window and fuel clad, in the case of simultaneous irradiation of helium and/or hydrogen at relatively high temperature at 500 °C.

Ion irradiations at the TIARA facility in QST were performed with 10.5 MeV-Fe^{3+} (single irradiation), 10.5 MeV-Fe^{3+} with simultaneous 1.05 MeV-He^{+} ions (dual irradiation) and 10.5 MeV-Fe^{3+} with simultaneous 1.05 MeV-He^{+} and 0.38 MeV-H^{+} ions (Triple irradiation) up to 40 dpa for T91 steels at 500 °C. Depth distributions of He and H were broadened around 1 micron depth by using 800 nm thick aluminum energy degrader. Helium rate was about 15 appmHe/dpa. Hydrogen rate was about 110 appmH/dpa. Concentrations of He and H are 750 appmHe and 5,600 appmH, respectively, for irradiation of 40 dpa. After irradiations, the swelling behavior was estimated by using TEM (Transmission Electron Microscopy) observation of a specimen picked up from around 2 micron depth with an FIB (Focused Ion Beam) technique.

Figure 1 shows a cross sectional TEM images of single, dual and triple irradiations from surface to around 1.5 μm depth, where the region was multi ion irradiated. In the case of single irradiation, no cavities observed at 500 °C and 40 dpa around 1 μm depth (even at 100 dpa at displacement peak depth). In the cases of dual and triple irradiation, lots of cavities appeared as white dots shown by arrows and caused swelling around depth from 0.9 to 1.6 μm. The number density (ND) and average size of cavities irradiated by dual and triple ions and the swelling in T91 are shown in Fig. 2. In the case of dual irradiation, the maximum swelling was 3% for the depth of 1.2 μm and the average cavity size was about 5 nm. The supplemental hydrogen irradiation makes the cavities grow up and increases the swelling up to 6.5%, almost twice around 1.5 μm depth.

Hydrogen atoms encouraged the swelling considerably around 1.5 μm depth. Helium atoms are known to be effective against swelling through sink balance between voids & interstitials. Comparing with ND and cavity size in triple and dual irradiation, it is suggested that H enhanced vacancy transfer to larger cavities as a growth mechanism something like an Ostwald ripening.

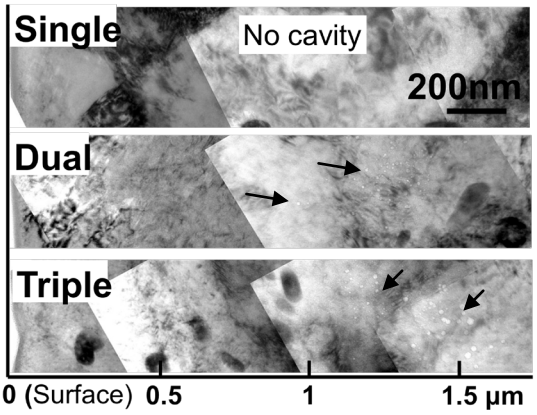

Fig. 1 Cross sectional TEM images of T91, single, dual and triple irradiations.

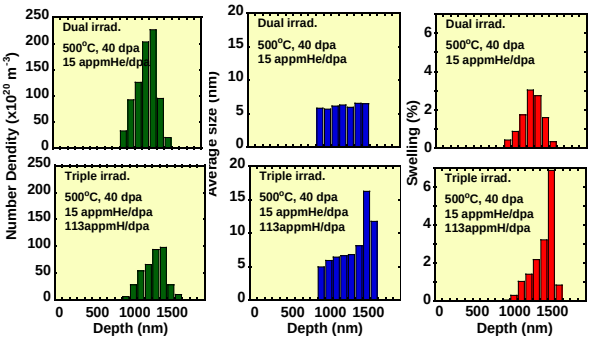

Fig. 2 Number density and average size of cavities irradiated by dual and triple ions and swelling in T91.

1 - 40

Morphology Change of CeO_2 Thin Film Induced by He Precipitation

H. Serizawa[a)], S. Yamamoto[b)] and K. Yasunaga[c)]

[a)]Fuels and Materials Engineering Division, NSEC, JAEA,
[b)]Department of Advanced Functional Materials Research, TARRI, QST,
[c)] Research & Development Department, WERC

Recent investigation performed by JAEA showed that a gas bubble bounded by facets is formed in UO_2 during a process of a precipitation of helium followed by injection with Hot Isostatic Pressing (HIP).

The interest phenomenon they found is that the shape of the negative crystal changes depending on the inner pressure of cavity, which implies that the shape of the cavity can be controlled by the condition of helium release from the cavity followed by the injection. The shape controllable negative crystal is named an image crystal. On the other hand, the study on the morphology of the facets on Wulff-shaped UO_2 cavity showed that the structure of (001) facet has complicated trench structure composed of {111} and {001}. Recently, we are studying the variation of morphology of FCC-type material by the precipitation of He using CeO_2 thin film. This paper addresses the detailed observation of the gas bubble formation in the thin film using STEM.

Pieces of CeO_2(100) thin film were heat treated at 1,273 K for 2 h. The films were irradiated with 130-keV He^+ ions using the 400-kV ion implanter of TIARA. The ion doped film was heat treated at 1,773 K for 2 h in air. Its surface morphology was analyzed by FIB-STEM. Figure 1 shows the surface morphology of the annealed film. It was found that many blisters were formed on the surface of the thin film. The idea of gas-driven blister growth on a metal surface was first proposed by Evans[1)]. Although he addressed his attention only to metals, Kuri *et al.* showed that a similar phenomenon was observed in the surface region of a ceramic (yttria-stabilized zirconia)[2)]. So, the blisters seen in Fig. 1 are considered to be formed by gas bubble accompanied by the precipitation of He beneath the surface. The lid of the blister is blown away since the sample is ceramics. The morphology of the sample cross-section observed by BF-STEM is shown in Fig. 2.

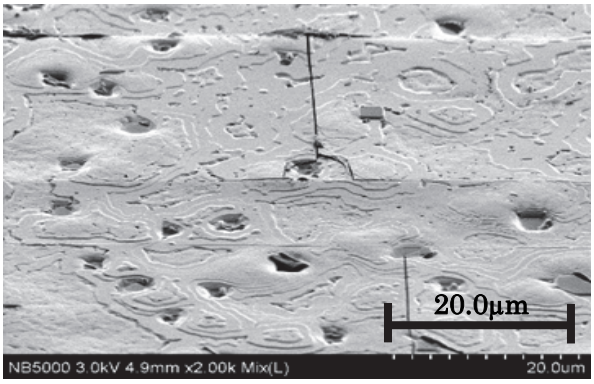

Fig. 1 Morphology of film surface observed by FIB-SEM.

Many gas bubbles are formed in the thin film. The size of the gas bubble falls within the range from 30 to 100 nm in diameter.

Figure 3 is a high-magnification STEM image of one of the gas bubble in Fig. 2. The shape of the gas bubble is truncated octahedron but clearly different from that of void, which mean that the existence of He in the gas bubble affects on its shape.

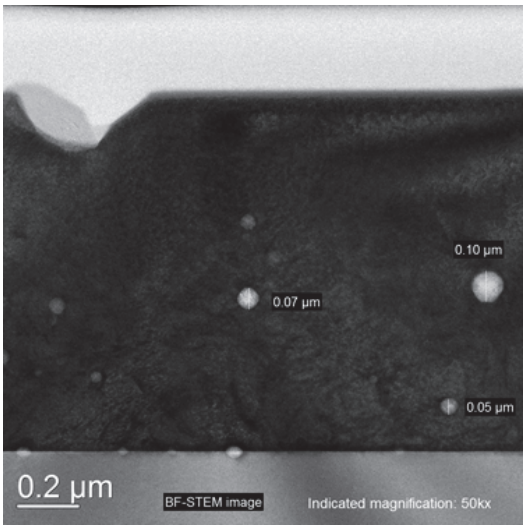

Fig. 2 BF-Cross sectional BF-STEM image of He doped film.

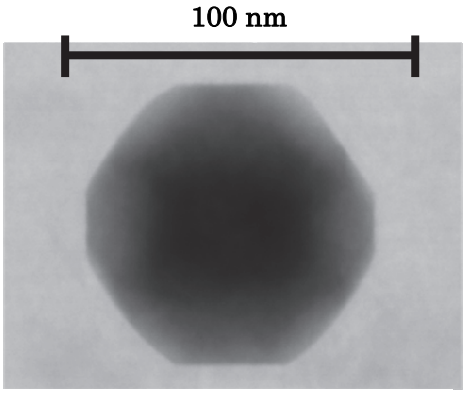

Fig. 3 STEM image of the gas bubble.

References

1) J. H. Evans, J. Nucl. Mater., **76/77**, 228-34 (1978).
2) G. Kuri, M. D. Beli and D. Gavillet, Nucl. Instrum. Meth. Phys. Res. B, **245**, 445-54 (2006).

1-41 Evaluation of Irradiation Resistance of ODS Ferritic Steel for Fast Reactor Application

T. Tanno, H. Oka, S. Ohtsuka, Y. Yano and T. Kaito

Fast Reactor Fuel Cycle Technology Development Department, AFRC, JAEA

Fuel cladding tube which has long life time, high temperature strength and good irradiation resistivity, is key technology for high performance fast reactors (FRs). They will be exposed heavy irradiation up to 250 dpa, and the temperature of them will reach to 700 °C during normal operation. Japan Atomic Energy Agency (JAEA) had been developed oxide dispersion strengthen (ODS) steels as the candidate materials, and tempered martensitic 9 and 11Cr-ODS steels are promising. Recently, the quality of them got better by improvement of manufacturing process.

The high temperature strength corresponding to the durability of the ODS steels is provided by fine and dense oxide particles. Hence, the stability of dispersed oxide particles under the irradiation has to be evaluated. In addition, 11Cr-ODS steel has been developed in order to enhance the corrosion resistivity, though higher Cr content could induce an irradiation embrittlement around 400 °C. However, the new high-quality JAEA 9 and 11Cr-ODS steels have been never irradiated in any reactor. Thus this study aims to evaluate the irradiation behavior of the new JAEA-ODS steels early, using ion beam irradiation. The target dose is over 250 dpa which is the peak dose at the end of the life of an advanced FR fuel.

The irradiation materials were the new JAEA 9 and 11Cr-ODS steels. Furnace slow cooling treatment from 1,050 °C (FC) or normalizing (1,050 °C) and tempering 800 °C heat treatments (NT) were conducted before the irradiation [1]. In order to induce large amount of irradiation damage in short time, 10.5-MeV Fe^{3+} ion beam irradiation tests have been carried out at 700 and 400 °C using tandem accelerator in TIARA. Fe self-ion beam irradiation could induce irradiation damage efficiently without undesirable effects of unrelated element atom penetrations. Some of specimens have been irradiated with 10.5-MeV Fe^{3+} and 1.1-MeV He^{+} dual ion beam from tandem and single-end accelerators at 470 °C to simulate the simultaneous effect of the irradiation dose and transmutation He in the ODS steel FR fuel cladding tube. The dual beam irradiation temperature was selected in order to maximize the he effects, such as the He bubble formation and swelling [2].

Multi-year repeated irradiations achieved 140 dpa at 700 °C, 230 dpa at 400 °C and 60 dpa with 0.3 appmHe/dpa at 470 °C; the dose is calculated at 1,300 nm depth [1]. Nano-indentation tests were carried out to evaluate hardness change by the irradiations. The hardness is a useful index indicating the oxide particle coarsening (softening), and extreme hardening due to spinodal decomposition or He bubble formation. The indentation test of the specimens irradiated over 100 dpa at 700 °C could not be carried out because the surface was oxidized [1]. The evaluation of them will be carried out by microstructural observation.

Figure 1 shows the hardness (H_{IT}) change due to Fe ion single beam at 400 °C. The hardness of irradiated ODS steels were increased at first, and decreased over 150 dpa. The hardening should be induced by fine and dense dislocation loops that are irradiation defect clusters. The hardness of FC materials saturated earlier than that of NT materials. In FC materials (deformed ferrite matrix), the amount of sinks of irradiation defects is smaller than NT materials (martensitic matrix). The difference seems to be the reason why the hardness of FC materials saturated earlier. At higher dose, the dislocation loops is coarsened and the number decreases. Consequently, the hardness would decrease over 150 dpa. In addition, the behavior of 9 and 11Cr-ODS steels were almost same, so that, the Cr enrichment from 9 to 11 wt% did not affect the irradiation hardening behavior.

The irradiation hardening at 470 °C with He was negligible or much smaller than that of ~50 dpa irradiated at 400 °C without He. Since higher temperature enhances the mobility of irradiation defects, they could reach to the sinks such as sub-grain boundaries easily. Therefore, the defect cluster formation would be suppressed. As a result, the He effect on irradiation hardening was not distinct.

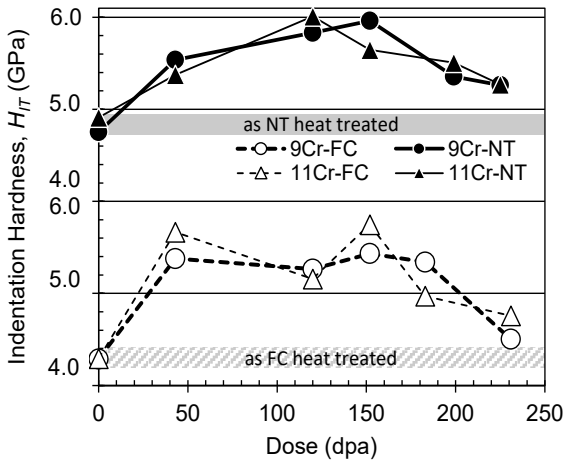

Fig. 1 Indentation hardness change due to Fe ion single beam irradiation.

Reference

1) T. Tanno *et al.*, JAEA Takasaki Annu. Rep. 2014, JAEA-Review 2015-022, 166 (2016).
2) H. Ogiwara *et al.*, J. Nucl. Mater., **307-311**, 299-303 (2002).

1-42 Void Swelling Resistance of High-Nickel Alloy during Irradiation

T. Inoue [a,b], S. Yamashita [a,c], I. Yamagata [b], S. Ohtsuka [a], T. Kaito [a] and I. Ioka [d]

[a] Advanced Fast Reactor Cycle System R&D Center, JAEA, [b] Fukushima Fuels and Materials Department, ORDC, JAEA, [c] Fuels and Material Engineering Division, NSEC, JAEA, [d] LWR Key Technology Development Division, NSEC, JAEA

1. Introduction

Precipitation-strengthened high-nickel alloys have been developed for fast reactor fuel cladding material because of their intrinsic good dimensional stability. Nimonic PE16 is known as the representative high-nickel alloy, and it is a material strengthened by an intermetallic compound such as ordered phase γ' [Ni_3 (Ti, Al)] formed in the matrix. The most important issue in development of high-nickel alloy is considered to be the improvement of mechanical properties at elevated temperature; the significant ductility is lost due to irradiation at high temperature. The cause of this problem was believed to be the re-distribution of ordered phase γ' and solute segregation to defect sink sites, such as grain boundary, dislocation and void surface, during irradiation[1]. In this study, several types of precipitation-strengthened high-nickel alloys were developed and then the phase stability (precipitate stability and swelling resistance) in these alloys during irradiation was evaluated by using TIARA facility.

2. Experimental

The materials used in this study were three types of high-nickel alloys and an austenitic stainless steel for the comparison; carbo-nitride phase strengthened high-nickel alloy (8NK_A), carbo-nitride phase strengthened and cold-worked high-nickel alloy (22NK-28, the same chemical composition as that of 8NK_A) and Ti-modified SUS316 stainless steel (PNC316) (see Table 1, 2).

Specimens were irradiated at the TIARA facility by 12.0 MeV Ni^{3+} ions with 1.05 MeV He^{+} ions and 0.38 MeV H^{+} ions. The irradiation was mainly performed to 100 and 250 dpa at 600 °C at the depth of 1.0 μm and the damage rate was about 1.0×10^{-3} dpa/s at this depth. The implantation rates for He and H were 1 appmHe/dpa and 15 appmH/dpa, respectively.

Table 1 Major chemical composition of 8NK_A, 22NK-28 and PNC316 (wt%).

	Ni	Cr	Mo	W	Nb	V	Ti
8NK_A	35	15	2.3	1.5	0.35	0.2	0.01
22NK-28	35	15	2.3	1.5	0.32	0.2	<0.01
PNC316	14	16	2.5	-	0.1 (Nb+Ta)	0.01	0.10

Table 2 Thermal and cold forming history of 8NK_A, 22NK-28 and PNC316.

8NK_A	SA(1,130 °C × 2 min)+23%CW+HT(720 °C × 10 h)
22NK-28	SA(1,130 °C × 2 min)+23%CW+HT(720 °C × 10 h)+10%CW
PNC316	SA(1,095 °C × 1 min)+20%CW

(SA: Solution Annealing, HT: Heat Treatment, CW: Cold Working)

Thin foils for transmission electron microscopy (TEM) were fabricated using a focused ion beam (FIB) instrument. TEM observations for void swelling of ion-irradiated high-nickel alloys were carried out with a JEM-4000FX operated at 400 kV.

3. Results and Discussion

Figure 1 shows irradiation fluence dependence of void swelling of 8NK_A, 22NK-28 and PNC316. And these alloy swelling peak temperature is around 600 °C [2-4]. This result indicates that cold-worked high-nickel alloy (22NK-28) keeps superior swelling resistant property to the other alloys in high fluence. It is considered that the effect of cold working improves its void swelling resistance and that dislocations induced by cold working would be effective sink sites for point defects in high fluence.

References

1) W. J. S. Yang *et al.*, J. Nucl. Mater., **132**, 249 (1985).
2) S. Yamashita *et al.*, JAEA Takasaki Annu. Rep. 2012, JAEA-Review 2013-059, 35 (2014).
3) T. Inoue *et al.*, JAEA Takasaki Annu. Rep. 2013, JAEA-Review 2014-050, 36 (2015).
4) T. Inoue *et al.*, JAEA Takasaki Annu. Rep. 2014, JAEA-Review 2015-022, 32 (2016).

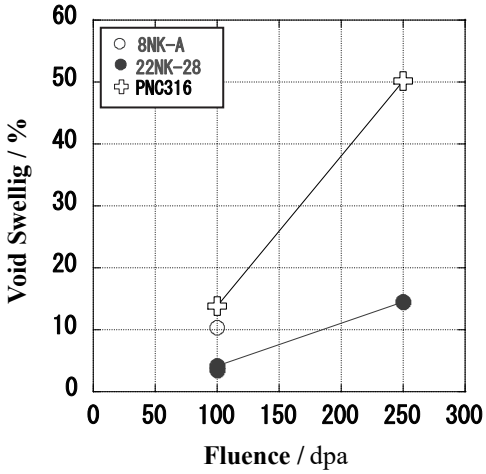

Fig. 1 Void swelling fluence dependence under high-nickel alloys in triple (Ni^{3+}+He^{+}+H^{+}) beam ion-irradiated at 600 °C.

1-43

Proton Irradiation Effect on Mössbauer Effect of the $Fe_{65}Ni_{35}$ Alloy

M. Matsushita [a)], H. Wada [a)], Y. Saito [b)] and S. Kitao [c)]

[a)] Department of Mechanical Engineering, Ehime University,
[b)] National Institutes for Quantum Radiological Science and Technology,
[c)] Kyoto University Research Reactor Institute

Curie temperature of the Fe-Ni Invar alloys increase due to irradiation with high energy electron and some kind particles. In this study, proton irradiation effects upon Mössbauer effect in the $Fe_{65}Ni_{35}$ alloy have been investigated. From the analysis results for Mössbauer spectra, in $Fe_{65}Ni_{35}$ irradiated by proton with 2 MeV, the magnetic component with hyperfine field at 10 T is more stable than that in non-irradiated $Fe_{65}Ni_{35}$. Further analysis for the hyperfine field distribution, we need the Mössbauer spectra measurements for more large and ^{57}Fe-rich $Fe_{65}Ni_{35}$ irradiated by high energy ion.

高エネルギー粒子線照射が磁性を改質する新たな手法として注目されている。$Fe_{65}Ni_{35}$ 近傍組成の合金(いわゆるインバー合金)の強磁性が、高エネルギー粒子線によって高温側に拡大することは、1970 年代より報告されており、磁性とイオン照射の相関についての研究としては長い歴史をもつ [1)]。これまでの研究によれば、上記現象は、高エネルギー粒子と構成元素の衝突によるはじき出しに伴う空孔形成と相関すると考えられる。一方、照射によって誘起された強磁性の特徴については、磁化測定など巨視的な測定による研究が多く、微視的な側面から研究された例はない。本研究ではイオン照射が $Fe_{65}Ni_{35}$ に与える微視的な変化を調査することを目的とし、イオン照射を行った $Fe_{65}Ni_{35}$ についてメスバウアー分光測定を実施した。

本研究では、厚さ 10 μm の $Fe_{65}Ni_{35}$ 箔を二枚重ね、2 MeV の proton を 1×10^{16} ions/mm^2 照射した(Fig. 1 参照)。照射領域は 5×5 mm である。TRIM を用いたシミュレーションによれば、Proton の飛程は 18 μm であり、前方側(front)サンプルを貫通し、後方側(rear)サンプル中に停止する。そのため、後方側サンプルに多くの collision event が集中する。

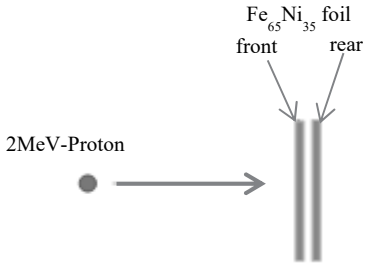

Fig. 1 Schematic diagram of proton irradiation.

照射後のサンプルのキュリー温度(T_C)を交流磁化率測定により測定したところ、前方側、後方側の両サンプルともに T_C が高温側へとシフトしている。特に多くの energy deposition が発生したと考えられる後方側サンプルで大きな T_C の上昇が確認された。本結果は Ref. 2), 3)とよく一致する。次に、上記サンプルならびに未照射の $Fe_{65}Ni_{35}$ 箔について、室温から 573 K にかけて透過法によるメスバウアー分光測定を実施した。Figure 2 に未照射の $Fe_{65}Ni_{35}$ 箔と照射済後方側サンプルのメスバウアースペクトルを示す。室温でのメスバウアースペクトルには差がみられない。しかし、523 K では未照射の $Fe_{65}Ni_{35}$ のメスバウアースペクトルは分裂していないのに対し、照射済後方側サンプルでは明確なスペクトルの分裂が確認できる。Figure 2 のスペクトルより内部磁場分布解析を行ったところ、室温での内部磁場分布には差がみられないが、昇温とともに 10 T 近傍にピークをもつ成分が、照射後、未照射の $Fe_{65}Ni_{35}$ ともに表れ始める。照射後サンプルのほうが、10 T 近傍にピークをもつ成分がより温度に対し安定であり、この磁気成分がマクロな強磁性領域の高温側への拡大に寄与したと考えられる。

本研究を通じ、新奇な現象を発見するに至ったが、詳細な分析をするには大きな表面積をもち ^{57}Fe を富化した照射済サンプルが必要である。今後、上記課題を解決可能なサンプルに対し照射を行いメスバウアー分光を再度実施する計画である。

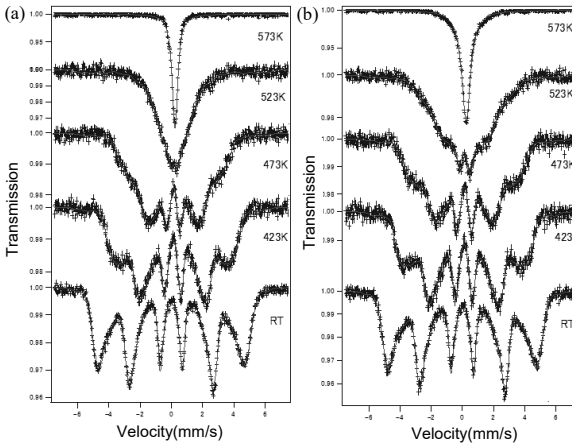

Fig. 2 Mössbauer spectra for non-irradiated $Fe_{65}Ni_{35}$ (a) and irradiated $Fe_{65}Ni_{35}$ (b).

本研究は、日本原子力研究開発機構施設供用制度を利用し、実施いたしました。

References

1) A. Chambered *et al.*, J. Magn. Magn. Mater., **10** (2/3) ,139-44 (1979).
2) Y. Chimi *et al.*, Nucl. Instrum. Meth. Phys. Res. **B**, **257**, 388-91 (2007).
3) M. Matsushita *et al.*, J. Magn. Magn. Mater., **394**, 491-95 (2015).

1-44 Effect of Damage Depth Profile on Hydrogen Isotopes Dynamics in Tungsten

Y. Oya, K. Yuyama, H. Fujita, S. Sakurada, Y. Uemura, C. Hu, T. Miyazawa and T. Chikada

Graduate School of Science and Technology, Shizuoka University

Thermal annealing effects on deuterium (D) retention for Fe^{2+} damaged tungsten were studied. It was found that total D retention in 0.1 dpa damaged W was clearly reduced as the annealing temperature was increased. In particular, retention of D trapped by voids was significantly reduced by annealing at 1,173 K. However, increasing defect density, the large reduction of D retention was not found. These results suggest the recovery behavior of defects would be controlled by defect concentration.

Introduction

タングステン(W)は将来の DT 核融合炉において、プラズマ対向機器への利用が検討されている。W には炉心プラズマから中性子等の高エネルギー粒子が入射し、種々の照射欠陥が形成されるため、燃料である水素同位体が W 中に滞留すると考えられ、燃料効率の観点から水素同位体滞留挙動の解明は重要である。高温環境下では欠陥が回復/集合するため、炉運転時の水素同位体滞留挙動を評価するには加熱アニーリング効果の理解が必要である。本研究では、種々の照射量で欠陥導入した W を 1,173 K にて加熱し、重水素滞留挙動を評価した。

Experimental

アライドマテリアル社製歪取加工済 W 試料(10 mm^{φ} × 0.5 mm^{t})に対して、不純物除去のために 1,173 K にて 30 分間の加熱処理を行った後、高崎量子応用研究所の 3 MV タンデム加速器(TIARA)を用いて、6 MeV の Fe^{2+}を室温にて 0.01-1.0 dpa まで照射した。その後、静岡大学にて、573-1,173 K にて 30 分間加熱した。これらの試料に対し、1.0 keV の D_2^+をフラックス 1.0×10^{18} D m^{-2} s^{-1} にて、フルエンスが 1.0×10^{22} D m^{-2} となるまで照射し、昇温脱離法(Thermal Desorption Spectroscopy; TDS)を用いて、重水素の滞留挙動を評価した。

Result & Discussion

Figure 1 に室温にて Fe^{2+}照射した W 試料を各温度にて加熱した後に重水素照射した際の重水素放出スペクトルを示す。重水素の放出は主に 400 K、600 K、800 K に見られた。Peak 1 は表面吸着された重水素及び転位ループに捕捉された重水素の放出、Peak 2 は原子空孔からの放出、Peak 3 はボイドからの放出であるとそれぞれ帰属した[1-3]。加熱温度が上昇するにつれて、Peak 3 における重水素滞留量は大きく減少することが分かった。これは加熱によりボイドが回復したためであると考えた。一方で、Peak 1 における重水素滞留量は、加熱温度が上昇してもほとんど変化しなかった。

次に、0.01 dpa から 1.0 dpa まで損傷量を変化させて Fe^{2+}を照射した後に 1,173 K で焼鈍した試料における重水素 TDS スペクトルを Fig. 2 に示す。損傷量が 0.3 dpa 以上では、Peak 3 における重水素の放出量に 0.1 dpa の場合のような大きな減少は見られなかった。これは損傷量が増加したことにより欠陥密度が上昇し、欠陥が集合しやすくなったためだと考えられる。また、損傷量が増加するにつれ、Peak 3 における重水素の脱離温度が高温側にシフトした。これは欠陥密度の上昇により、重水素が脱離際の捕捉/脱捕捉過程の寄与が大きくなったためであると考えられる。

これらの結果から、加熱することで欠陥の回復により重水素滞留量は減少するが、欠陥の回復挙動は欠陥の濃度によって大きく変化することがわかった。

References

1) Y. Oya *et al.*, J. Nucl. Mater., **461**, 336 (2015).
2) H. Eleveld, A. Van Veen, J. Nucl. Mater., **191**, 433 (1992).
3) T. Troev *et al.*, Nucl. Instrum. Meth. Phys. Res. B., **267**, 535 (2009).

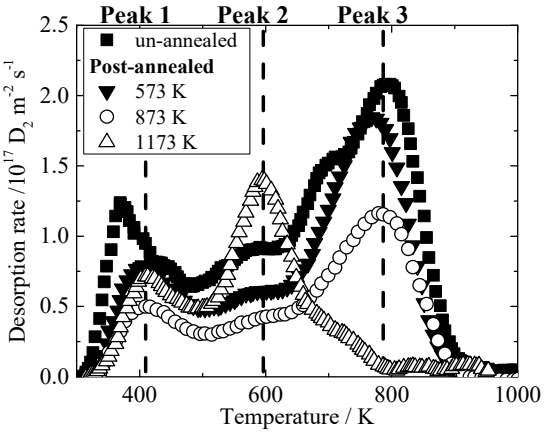

Fig. 1 D_2 TDS spectra for 0.1 dpa damaged W with post-annealing at various temperatures.

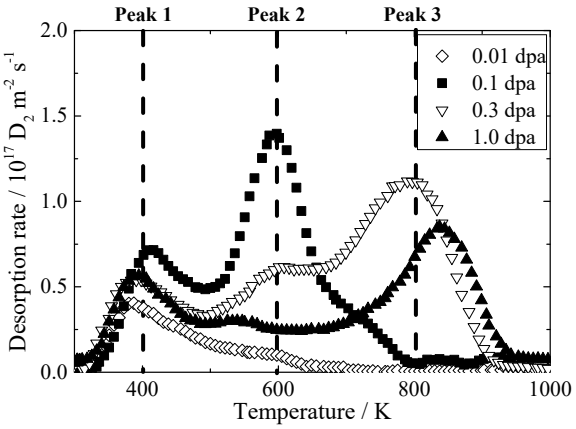

Fig. 2 TDS spectra for post-annealed W at 1,173 K in the damage levels of 0.01-1.0 dpa.

1-45 Effects of Ion Irradiation on Hardness and Microstructure of Pure Tungsten

K. Ozawa [a)], T.-H. Hwang [b)], M. Fukuda [b)], S. Nogami [b)], A. Hasegawa [b)] and H. Tanigawa [a)]

[a)] Department of Fusion Reactor Materials Research, RFI, JAEA, [b)] Tohoku University

Tungsten (W) is the primary candidate materials as a diverter or a plasma facing material (PFM) [1)] in fusion devices, primarily due to its high melting temperature, good thermal conductivity and low sputtering rate.

For diverter, recrystallization and radiation induced embrittlement, the effects of transmutated atoms of W itself are key issues. Process optimization are in progress and more radiation-tolerant W alloys are being made. However, information of its irradiation effects is quite required, because recent neutron irradiation results [2)] suggest that behavior of W after irradiation is complicated and that radiation induced defects depends on neutron/ion irradiation sources. At the first step, examining especially only the effect of displacement was desired.

Pure-W after removal of residual stress was chosen as materials. Ion irradiation was performed at TIARA facility of JAEA. Eighteen MeV W^{6+} ions were irradiated to induce displacement damages (single-ion irradiation). Irradiation condition is ~5 dpa, and 500 and 800 °C. Nano indentation hardness was evaluated using a nano indenter with a triangular pyramid Berkovich diamond tip. The direction of indentation was chosen to be parallel to the ion-beam axis. For a microstructural investigation, the irradiated samples were subjected to a thin foil processing using a focused ion beam device (FIB) and electrochemical-polishing. Microscopy was performed by a field emission transmission electron microscope (FE-TEM).

Irradiation hardening to ~3 GPa, which was also observed in neutron irradiation study [2)], was saturated for pure-W (Fig. 1) after 1dpa irradiation. The FE-TEM results where small dislocation loops and voids were detected (Fig. 2) suggest that these defects can be one major mechanism for the irradiation hardening.

To confirm these microstructural factors affect nano-indentation hardness, Orowan's equation (Eq. (1)), relationship between yield stress and Vickers hardness (Eq. (2)), relationship between Vickers hardness and nano-indentation hardness (Eq. (3)) were used for calculation;

$$\Delta\sigma_y = M\alpha\mu b\sqrt{Nd} \quad (1)$$

$$\Delta\sigma_y = 3.06\Delta H_v \quad (2)$$

$$H_v = (0.8/9.8)\times 10^3 \times H \quad (3)$$

where $\Delta\sigma_y$ = yield stress change, M = Taylor factor, μ = stiffness, b = Burger's vector, α = strength factor, N=number density, d=loop diameter, H_v=Vickers hardness, H=nano-indentation hardness, respectively.

As a result of calculation, 2.9 GPa of increase was calculated (vs. 2.7 GPa for experimental value) after 500 °C irradiation, and 3.0 GPa vs. 2.9 GPa after 800 °C irradiation. Experimental values were correspond to calculated values.

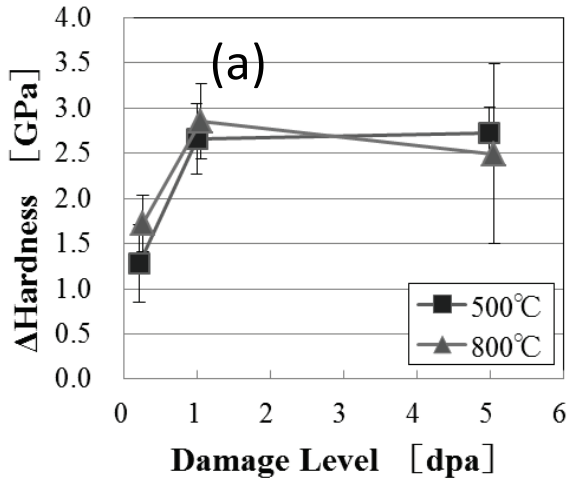

Fig. 1 Irradiation hardening of pure-W at 500 and 800 °C.

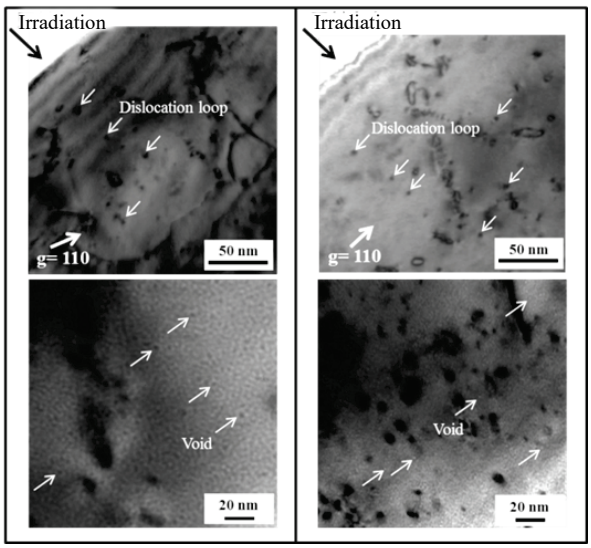

Fig. 2 TEM microstructure of pure-W irradiated to 1 dpa at 500 °C (*left*), and at 800 °C (*right*).

References

1) H. Bolt *et al.*, J. Nucl. Mater. **329-333**, 66 (2004).
2) M. Fukuda *et al.*, J. Nucl. Mater. **442**, S273 (2013).

1-46

Irradiation-Induced Microstructural Changes of Highly-Crystalline SiC Fibers

T. Nozawa, K. Ozawa and H. Tanigawa

Department of Fusion Reactor Materials Research, RFI, JAEA

A silicon carbide fiber-reinforced silicon carbide matrix (SiC/SiC) composite is a promising candidate material for an advanced fusion DEMO blanket because of the excellent thermo-mechanical, -physical, and -chemical properties and irradiation tolerance of SiC itself [1]. The irradiation stability of highly-crystalline and near-stoichiometric SiC fibers is therefore believed to be similar as that of high purity monolithic bulk SiC materials because of many similarities in microstructure. However, based on the recent irradiation experiment results, it was claimed that the irradiation behavior of the SiC fibers, especially Hi-Nicalon Type-S fiber, was quite different from the bulk SiC material. The severe shrinkage of the SiC fibers was expected by high-dose irradiation. According to the previous results irradiated to 100 dpa at 300 °C[2], carbon phases, which were located inside the SiC fiber as residual phases as well as at the fiber/matrix (F/M) interface, tended to be reduced or diminished. The FE-TEM results and EELS analysis eventually suggest that the shrinkage would be responsible for the transport of excess carbon atoms from intergranular phase into SiC grains, and resulting production of excess C_{Si} antisites. This resulted in interphase and fiber deterioration, eventually decreasing composite strength[3].

Interphase carbon and reinforcing SiC fibers are therefore key to ensure the strength of SiC/SiC composites. Despite its importance, the information of dimensional stability and "detailed" microstructure are still insufficient. In the series of our study, irradiation-induced microstructural and mechanical changes of SiC/SiC composites have been evaluated by both ion and neutron irradiation. In this year, irradiation induced microstructures of the other "nuclear-grade" SiC fiber, Tyranno-SA3, were examined.

The materials used in this study were plain-weave Hi-Nicalon Type-S (HNLS) and Tyranno-SA3 (TySA3) composites produced via the chemical vapor infiltration (CVI) process with the multi-layered F/M interface of the $(PyC^{20nm}/SiC^{100nm})^5$ sequence. Six MeV Si^{2+} single ion irradiation tests were conducted at TIARA facility in JAEA and supplementary at DuET in Kyoto University. Irradiation dose and temperature was ~100 dpa at 300 and 600 °C, respectively. After the ion irradiation, micro-structure was examined by FE-TEM.

Figure 1 shows the microstructure of the HNLS and TySA3 fibers after ion irradiation to 50 dpa at 600 °C at the TIARA facility. In the unirradiated HNLS fiber, residual carbon packets are located at grain triple junctions. According to the previous results irradiated to 100 dpa at 300 °C [2], these carbon phases tended to be reduced or diminished. The tendency was confirmed in the case of 600 °C irradiation; carbon packets corresponding to white contrasts in the TEM images and amorphous phase at around very small SiC grains (<~20 nm) were diminishing with irradiation dose. Other feature of the microstructure after irradiation was the change of grain size of silicon carbide; the size is coarsening after the irradiation.

The microstructure of the TySA3 before and after the irradiation was also shown in Fig. 1. In non-irradiated condition, unlikely to the HNLS fiber, TySA3 fiber consists of larger SiC grain with the size of ~200 nm. Additionally carbon phases were also existed. After the irradiation, the grain size seems to remain unchanged. Additionally interaction between SiC grains and carbon packets were not quite severe by irradiation compared with HNLS fiber case. The examination of the detail microstructure of SiC including carbon phases is underway. However, from a microstructural point of view, it looks like the TySA3 SiC fiber is more stable than HNLS fiber at the high dose irradiation condition over 50 dpa.

References

1) Y. Katoh *et al.*, J. Nucl. Mater., **448**, 448 (2014).
2) S. Kondo *et al.*, Acta Mater., **83**, 1 (2015).
3) Y. Katoh *et al.*, J. Nucl. Mater., **462**, 450 (2015).

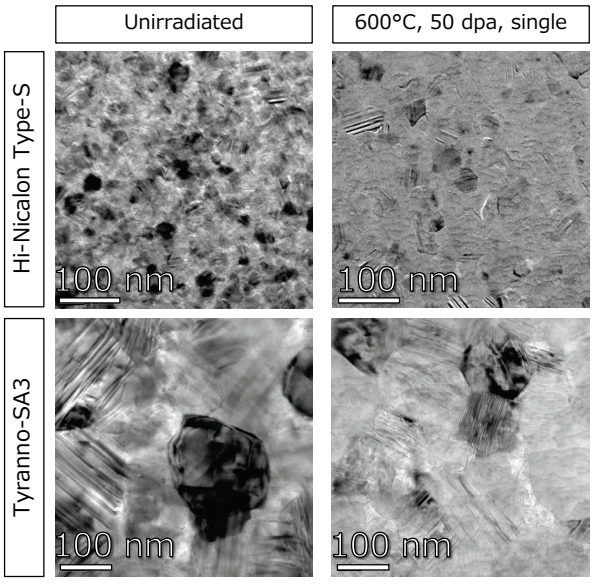

Fig. 1 Typical TEM microstructural images of the Hi-Nicalon Type-S and Tyranno-SA3 SiC fibers after ion irradiation.

1-47 Gamma Ray Irradiation Effect of Ceramics

M. Kinsho [a)], S. Takeda [a)], B. Mikashima [b)] and J. Sugawara [b)]

[a)] Accelerator Division, J-PARC, JAEA,
[b)] Ceramics Division, KROSAKI HARIMA CORPORATION

We are apprehensive that beam loss will increase in proportion to beam power in the 3 GeV synchrotron accelerator (RCS) of the J-PARC. Since loss beam activates the accelerator components, it is worry that this loss leads to failure to the equipment of the RCS. In particular, changes in mechanical strength and thermal expansion coefficient of ceramics materials being used as a structural material for accelerator is concerned. The purpose of this experiment is measurement of gamma ray irradiation effect for new ceramics materials which are developed at KUROSAKI HARIMA CORPORATION.

Gamma rays from Cobalt-60 (2.5 kGy/h of ^{60}Co-γ-ray) were irradiated in the ceramic samples up to about maximum 10 MGy, and the gamma-ray irradiation effects of the mechanical strength and the thermal expansion coefficient were measured. The samples used in this experiment are shown in the Table 1, and the specific method described below.

Table 1 Irradiation Samples.

		Material	Characteristics
Glass	1	Zerodur	-
	2	CLEARCER AM	-
	3	ULE	-
	4	Fused Quartz	High purity
Cordierite	5	NEXCERA	Color: Black
	6	NEXCERA	Color: Lavender
Nitride Ceramics	7	Sialon	Strength : High
	8	Sialon	Strength : Middle
	9	Sialon	Generic
	10	ALN	170 W/mK
Carbide Ceramics	11	Pressureless Sintered SiC	Al-B-C Auxiliary
	12	Pressureless Sintered SiC	B-C Auxiliary
	13	Pressureless Sintered B_4C	Al-C Auxiliary
Oxide Ceramics	14	99.5% Alumina	Generic Alumina
	15	99.7% Alumina	Generic Alumina
	16	Partially Stabilized Zirconia	3 mol% Y_2O_3
	17	Pressureless Sintered Yttria	-
Machinable Ceramics	18	Fluorophlogopite	Standard White
	19	Fluorophlogopite	Standard Beige Moderate price
	20	Fluorophlogopite	Low Thermal Expansion White

(1) Mechanical strength measurement

1) Sample

Samples were made by cutting out about 20 to 22 pieces of the same plate material. The irradiation test has been carried out in any of the ten, and the remaining samples were used for non-irradiation samples.

2) Mechanical strength measurement

Mechanical strength of samples was measured by the four-point bending method (JIS R1601).

(2) Coefficient of thermal expansion (CTE) measurement

1) Sample

Samples were made by processing the same plate as mechanical strength samples to the shape of φ5×13.

2) CTE measurement

The CTE was measured by a laser interference method (JIS R3251-1990) before and after gamma radiation.

Experimental Results

(1) Mechanical strength

In the irradiation of up to absorbed dose 10 MGy of Cobalt-60 gamma rays, the strength reduction in partially stabilized zirconia (MZR) was observed, but the strength decrease of the others which are cordierite, alumina, sialon, SiC, AlN, and Fluorophlogopite such as fine ceramics materials, was not observed. Also, it was not found that the strength of a glass material changed due to gamma ray. The relative strength ratio before and after gamma ray irradiation is shown in Fig. 1. The relative strength ratio of ULE, fused quartz, NEXCERA, S110, S120, SiC, alumina, and Fluorophlogopite slightly improved after gamma ray irradiation. Since the statistical variation in the average intensity by the sampling in n=10 of the Weibull strength distribution is estimated to be a few percent with a standard deviation (about 5% in the case of the Weibull modulus m=10), it is not necessarily significant for strength increase of a few percent in this experiment. However, the possibility of healing effect can not deny due to gamma ray irradiation with respect to the materials that were seen of more than 10%. It is considered that there is no practically mechanical strength change because the improvement of these mechanical strength relatively not large.

(2) Thermal expansion coefficient measurement

Thermal expansion coefficient (CTE) of NEXCERA which was measured at room temperature was not changed by gamma ray irradiation of 10 MGy.

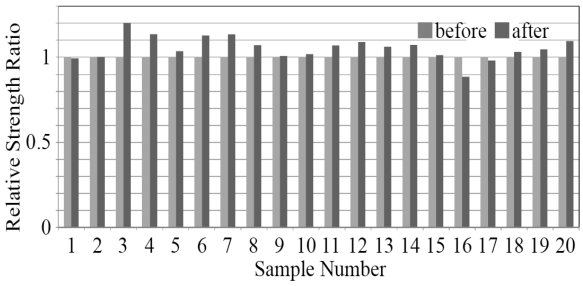

Fig. 1 The relative mechanical strength of samples before and after 10 MGy gamma ray irradiation.

1-48 Evaluation Trial for the Lifetime of Charge Stripper Foils in the 3-GeV RCS of J-PARC

Y. Yamazaki [a)], M. Yoshimoto [a)], P. K. Saha [a)], M. Kinsho [a)], T. Taguchi [b)], S. Yamamoto [c)] and I. Sugai [d)]

[a)] Accelerator Division, J-PARC, JAEA, [b)] Tokai Quantum Beam Science Center, TARRI, QST,
[c)] Department of Advanced Functional Materials Research, TARRI, QST,
[d)] High Energy Accelerator Research Organization, KEK

For the 3 GeV Rapid Cycling Synchrotron (RCS) in J-PARC, charge stripper foil is a key technology to keep high operating rate for multi-turn injection of high-power proton synchrotrons. For a charge stripper foil in the RCS, we applied a Hybrid type thick Boron-doped Carbon (HBC: Boron 25%) foil which is produced with the arc-discharge method. The required foil thickness is about 1.5 μm (333 μg/cm^2) corresponding to a conversion efficiency of 99.7% for 400 MeV injection from the linac. Actually it has enough toughness to stand high-intensity beam operation less than 500 kW. But after the beam operation these foils were occurred deformation and activation in order of mSv/h. It is very important for 1 MW beam operation to predict the lifetime of foils. We have investigated by the microscopic analyses such as TEM for damage of foils by the Argon ion irradiation in energy of 300 keV of TIARA. Now we cannot estimate the lifetime of the HBC foil for the 400 MeV beam operation from the results of offline foils study in TIARA. In order to evaluate the lifetime of HBC foils quantitatively, we started to obtain Raman spectra of foils irradiated by each ion such as H, He and Ar with a different energy such as 0.35, 2, and 3 MeV. Generally Raman spectra of amorphous carbon film were composed of so called D and G-band broad peaks. These peaks were shifted by ion beam irradiation damage. Then we will try to predict the lifetime of foils by estimating peaks' shifts of Raman spectra as an indicator corresponding to DPA (Displacement Per Atom) by simulation code PHITS.

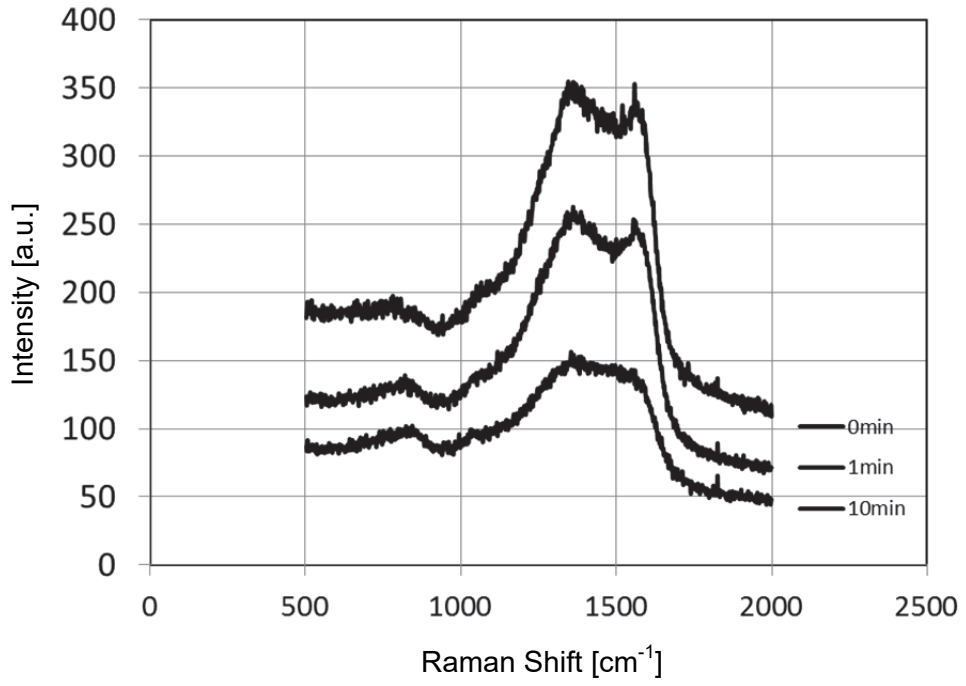

Fig. 1 One of the Raman spectra variation for HBC foil by Ar^+ irradiation period in energy 350 keV, in current 2 μA with the beam spot size 5 mm diameter, where the horizontal-axis represents the Raman shift in the wave number and the vertical-axis the intensity of the Raman spectrum. Around 1,600 cm^{-1} corresponds to the G-band peak, and 1,350 cm^{-1} to the D-band.

1 - 49

Radiation Resistance Test of Insulation for JT-60SA In-vessel Coils

D. Tsuru, H. Murakami, M. Takechi, A. Sukegawa and Y. Koide

Department of Tokamak System Technology, NFI, QST

JT-60SA is under construction as one of the Broader Approach activities [1]. It has three types of in-vessel coils, i.e., Error Field Correction Coil (EFCC), Fast Plasma position Control Coil (FPCC) and Resistive Wall Mode Coil (RWMC), as shown in Fig. 1. Glass fibre reinforced resin will be employed for the insulation material of these in-vessel coils. The insulation is required to withstand the irradiation through the lifetime, which is estimate at about 10 MGy. In addition, high heat resistance is required for RWMC insulation material because there will be no cooling for RWMC during 200 °C baking. The radiation resistance of resin strongly depends on the kind of resins in the range of a few MGy to tens of MGy [2], and the same resin as the actual coils should be used for the radiation resistance tests. In this study, radiation resistance tests were carried out for three candidate insulation materials, i.e., epoxy resin (by TESLA Eng. Ltd in UK) which is the candidate material for the EFCC, and two types of cyanate ester, BA-3000 and PT-60 (by Lonza), which are high heat resistive and are the candidate materials for the RWMC.

Dumbbell shaped tensile samples were produced using the three candidate materials under the same curing conditions as expected for the actual coils. The tensile samples were irradiated at the Gamma-ray irradiation facility in JAEA Takasaki Institute up to 15 MGy, which is higher than the irradiation of actual in-vessel coils, 10 MGy. There are five patterns of irradiation, i.e., non-irradiated, 2 MGy, 5 MGy, 10 MGy and 15 MGy. The number of samples is 45 in total; three candidate insulation materials, five irradiation patterns and three samples for each.

Tensile tests were carried out using a tensile test machine shown in Fig. 2. Figure 3 shows the samples after the irradiation and the tensile tests. The epoxy resin is cream coloured for non-irradiated and it becomes darker coloured by heavier irradiation. The two cyanate ester materials show no change of colour by irradiation. Figure 4 shows the tensile test results. No degradation of tensile strength due to irradiation is observed. Tensile strengths of all samples exceed 50% of that of non-irradiated samples. They also exceed the maximum stress expected in the actual EFCC, 30 MPa. It is concluded that all of the three candidate materials have sufficient radiation resistance performance as an insulation material for in-vessel coils of JT-60SA.

References

1) S. Ishida *et al.*, Nucl. Fusion, **51**, 094018 (2011).
2) J. Kusano *et al.*, JAERI-Data/Code, 2003-015 (2003).

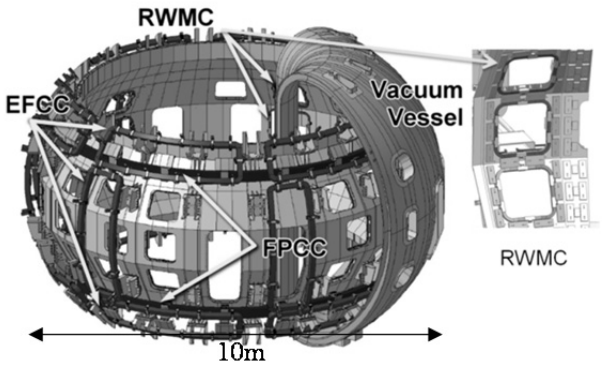

Fig. 1 In-vessel coils for JT-60SA.

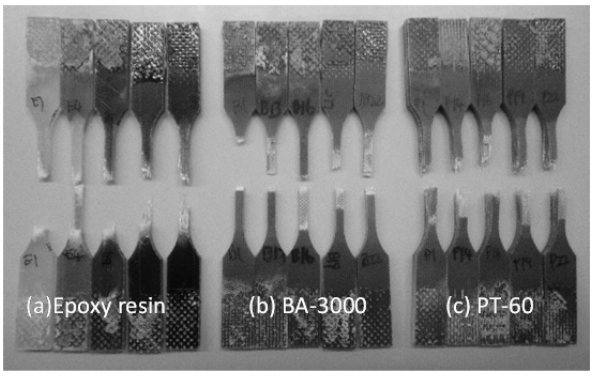

Fig. 3 Samples after tensile test.

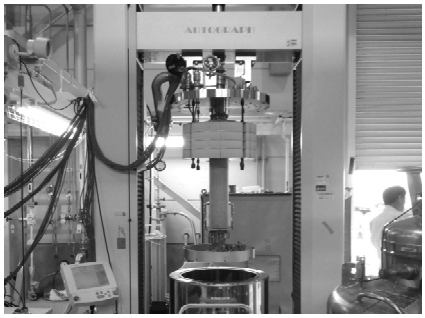

Fig. 2 Tensile test machine.

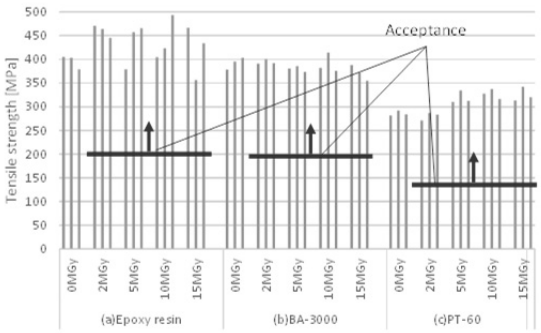

Fig. 4 Tensile test results.

1-50 Radiation Tolerance Test of the Rotation Target for the J-PARC Beam Scraper and the ILC Positron Source

T. Omori [a)], K. Hirano [b)], Y. Yuri [c)], R. Yamagata [c)], T. Takahashi [d)], M. Kuriki [d)], K. Nanmo [e)], T. Sugimura [e)], J. Urakawa [e)] and K. Yokoya [e)]

[a)] Institute of Particle and Nuclear Studies, High Energy Accelerator Research Organization, KEK,
[b)] J-PARC Center, JAEA, [c)] Department of Advanced Radiation Technology, TARRI, QST,
[d)] Graduate School of Advanced Sciences of Matter, Hiroshima University,
[e)] Accelerator Laboratory, High Energy Accelerator Research Organization, KEK

We made radiation test of an electric motor of a rotation target at Takasaki Advanced Radiation Research Institute. In the view point of the radiation, the electric motor is one of possible weak points of the rotation target. We prepared a commercially available small rotation target with an electric motor. The target is irradiated with 0.63 MGy in the Co-60 gamma-ray irradiation facilities. The dose of 0.63 MGy corresponds to about one ILC (International Linear Collider) year at the electric motor of the ILC positron production target. After the irradiation we tested the rotation of the target and no problem was found.

J-PARC リニアック加速器では RF チョッパ空洞とビームスクレーパ[1)]によって、パルスビームを作り出している。ビームスクレーパとして、真空中で回転するターゲットが検討されている。また、国際リニアコライダー（ILC）で提案されているコンベンショナル陽電子源[2,3)]では、真空中で回転する金属標的が検討されている。いずれの場合にも、回転ターゲットには、ビームラインの真空を保持するため、磁性流体シール等による真空回転導入器が必要である。これらは製品として販売され、広く利用されているが、これまで高放射線環境下における健全性は十分には確認されていない。そこで、本研究においては、耐放射線性能を明らかとすることを目的とする。

回転導入器で、磁性流体シール部、回転のためのモーター部などが放射線に対して脆弱な可能性がある。現設計案では、磁性流体シール及びモーター部は可能な限り放射線シールドで保護されるようになっている。この状態で磁性流体の1年間の吸収線量は約 1.5 MGy、モーター部分のそれは約 0.63 MGy であることが GEANT4 によるシミュレーションで示されている。

2014 年度は磁性流体に ILC の 3 年運転に相当する 4.5 MGy 照射をおこない、それを市販の回転シールに組み込んで実際に回転させて問題なく真空が保持されることを確認した（昨年度報告参照）。

2015 年度はターゲットの脆弱部と考えられるモーター部分の耐久性を見るために市販のターゲット全体に対して ILC の 1 年運転相当の照射を行った。モーターでは回転をモニターするホール素子、電磁石の巻線の絶縁などが脆弱部と考えられるが、今回のテストではターゲット全体に照射することで、予断を排して予想し得えなかった脆弱部（がもしあれば）を見つけることも狙った。Figure 1 に照射室内に置かれたターゲットを示す。

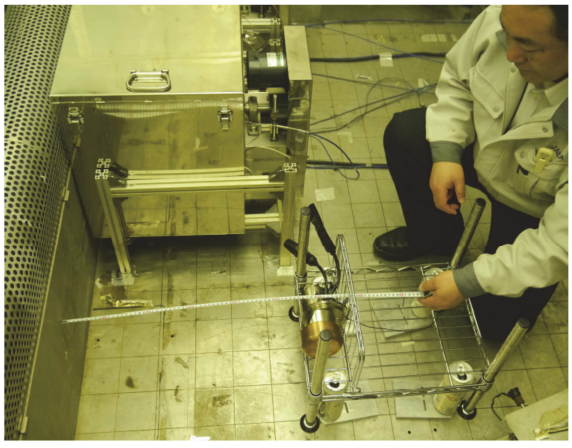

Fig. 1 The target in the irradiation chamber.

照射済みのターゲットは全体が変色していたが（Fig. 2）、これは照射中に発生していたオゾンによるものと思われる。その他外観に異常は見られなかった。ターゲットは真空槽に取り付け、通常の手順にしたがってターッゲト本体を水冷しながら真空槽を 200 °C でベーキングし、その後、真空を保ちつつ回転テストをおこなった。2014 年度の試験の結果から当然予想されたことだが真空には異常はなかった。またターゲットは何の異常も起こさず正常に回転した。つまり脆弱部と考えられたモーター部を含めて少なくとも 1 年間の ILC 運転に耐えることが示された。

Fig. 2 The target after the irradiation.

References

1) T. Sugimura *et al.*, Proc. **10th** Annu. Meet. Part. Accel. Soc. Jpn. 862 (2013/08).
2) T. Omori *et al.*, Nucl. Instrum. Meth. Phys. Res. A, **672**, 52-56 (2012).
3) Y. Seimiya *et al.*, PTEP, 103G01 (2015).

1-51 Survey of Consumer Electronic Parts in the 3D Scanner with Radiation Resistance

M. Nakamura [a)], T. Muramatsu [a)] and H. Abe [b)]

[a)] Applied Laser Technology Institute, JAEA,
[b)] Department of Advanced Functional Materials Research, TARRI, QST

Radiation resistance of electronic parts, is one big keyword in performing the nuclear reactor decommissioning. In the decommissioning, since it is necessary to put the device in the reactor. Because effects of radiation degrade electronic parts, optical parts, a resin, etc., it cannot ensure the normal operation of the equipment without countermeasures.

Currently, electronic parts remarkably excellent in radiation resistance in the space field are used. They are very expensive and cannot be obtained easily. In consumer electronic parts, aimed to see if they have high radiation resistance.

Current Laser Technology Institute owns a 3D scanner that pulse-Tech Co., Ltd. has been manufacturing. Internal electronic parts of this 3D scanner and their selection candidates such as the 20 types CMOS and D/A converter are prepared. Conducted a ^{60}Co-γ-ray irradiation at TARRI, gamma-ray irradiation was performed at an intensity of 8.49~8.86 kGy/h in silicon conversion until the accumulated dose in 10 levels (Table 1). The maximum accumulated dose was set to the 2 MGy [1)].

The electronic parts were tied with cotton thread after tacking with double-sided tape in a stainless steel wire mesh, Parallel placed with the source, and to allow uniform irradiation (Picture 1). Radiation was made as much as possible continuously until target accumulated dose.

A post-irradiation experiment is planned to check the effects of the irradiated electronic parts on the 3D scanner performance (Fig. 1). Carry out the verification of the performance degradation as a whole 3D scanner unit rather than the electronic parts alone.

This time of the test is carried out on the subject of electronic parts, for the optical parts and resin.

Reference

1) IRID, Request for Proposal (RFP) for Conceptual Study of Innovative Approach for Fuel Debris Retrieval and Feasibility Study of Essential Technology Part2-B (2013).

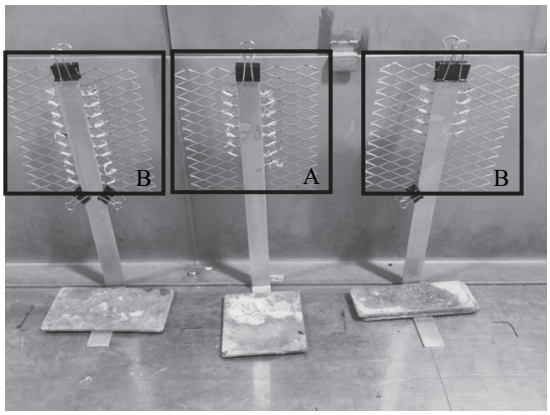

Picture 1 Electronic parts were fixed to be parallel to the radiation source. The area A of the target 8.86 kGy/h, the area B is a dose of 8.49 kGy/h has been irradiated.

Table 1 Ten levels of ^{60}Co-γ-ray irradiation conditions in silicon conversion set as a reference. If the accumulated dose exceeds 2 MGy, it was set to be maximum.

Accumulated dose (kGy)	Irradiation dose rate (kGy/h)
1.00	8.86
10.0	8.49
20.0	8.49
71.0	8.49
8.5	8.49
100	8.49
201	8.86
548	8.86
1,120	8.86
2,520	8.86

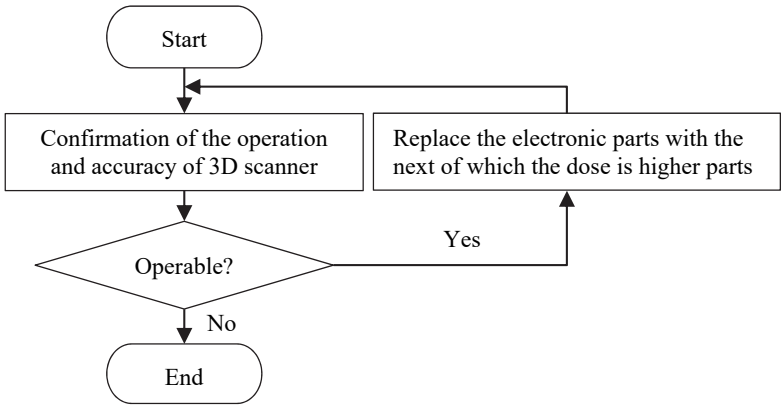

Fig. 1 Operation verification flow chart of the Post-irradiation experiment for electronic parts.

1-52 Degradation Behavior of Surface-mounted LED by Gamma Irradiation

T. Takeuchi, N. Otsuka, T. Uehara, H. Kumahara and K. Tsuchiya

Neutron Irradiation and Testing Reactor Center, ORDC, JAEA

In JMTR, wired-instrumented capsules had enabled users to perform in-situ measurements of the temperature, neutron flux and so on. However, not all the capsules can be instrumented because there is no enough space for wires of instrumentations. On the other hand, after the restart of JMTR, almost all of the instrumented capsules are already booked in irradiation schedule, which results in users not being able to obtain satisfying irradiation data.

Therefore, in order to make all of the capsules instrumented, a development of in-water remote sensing techniques which can realize instrumented capsules without wires was started from FY2012. According to the result of the comparison for in-water wireless transmission methods, acoustic wave radio and wave are disadvantageous due to low transmission rate and high attenuation coefficient in water, respectively. As a result, visible light was selected as the in-water transmission method. As the light emitting and the receiving devices of the system, light emitting diodes (LEDs) and photo diodes (PDs) were used, respectively. From FY2012 to FY2013, gamma irradiation effects on PDs and bullet-shaped LEDs were evaluated. The results suggested that the main cause of the decreases of the light sensitivity of the PDs and the total luminous flux of the LEDs were not the degradation of the semiconductor parts but the coloring of the resin parts by the irradiation [1].

In this study, gamma irradiation degradation of surface-mounted LEDs was investigated in the hope of low decrease of total luminous flux by irradiation since the surface-mounted LEDs have thinner resin part than the bullet-shaped LEDs.

The three types of LEDs were irradiated at the ^{60}Co gamma-ray irradiation facility [2]. The specifications of the LEDs and the irradiation conditions are shown in Table 1 and 2, respectively. The total luminous flux with their current rating and current-voltage property were measured before and after the irradiation.

The dose dependence of the total luminous flux of the LEDs is shown in Fig. 1. For comparison, the result of the bullet-shaped LED previously tested by our group is also plotted as circles with dashed line. As is case for the bullet-shaped LED, the total luminous fluxes of all the surface-mouted LEDs decreased with gamma absorbed dose. Then, the the resin lenses turned orange-yellow and their coloring became dark with the irradiation dose though the current-voltage characteristics almost unchanged. Therefore, the main cause of the degradation of the surface-mounted LEDs is probably the same as the bullet-shaped one. On the other hand, the decrease rates of the total lumious fluxes with gamma absorbed dose of the former was smaller than those of the latter.

These results indicate that the sufrace-mounted LEDs are more suitable candidates than the bullet-shaped one for the light emitting devices of the developing in-water transmission system.

Acknowledgement

The authors would like to thank to Mr. R. Yamagata at the irradiation facility in JAEA for supporting the experiments.

References

1) T. Takeuchi *et al.*, JAEA Takasaki Annu. Rep. 2013, JAEA-Review 2014-050, 33 (2015).
2) H. Saito *et al.*, JAEA-Tech. 2008-071 (2008).

Table 1 Specifications of the LEDs.

Item \ Type	Surface-mounted
Peak emission wavelength (nm)	635(Red), 522(Green), 465(Blue)
Lens material	Epoxy resin

Table 2 Gamma irradiation conditions.

Absorbed dose [kGy]	Absorbed dose rate [kGy/h]	Temperature [°C]
10, 20, 50, 100, 1,000	10	~ 20

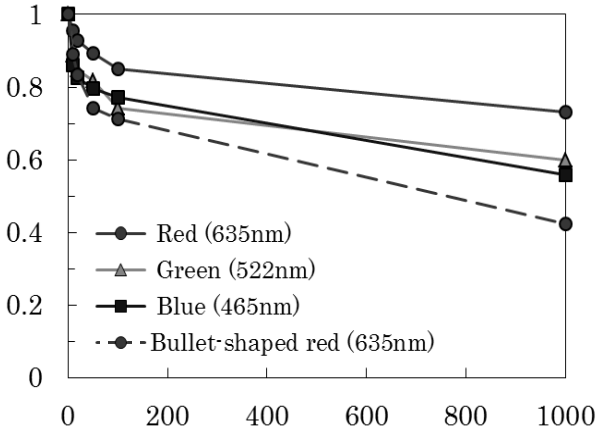

Fig. 1 The total luminous flux of the LEDs with dose.

1-53 Irradiation Test of Semiconductor Components on the Shelf for Nuclear Robots Based on Fukushima Accidents

S. Kawatsuma [a)], K. Nakai [a)], Y. Suzuki [a)] and T. Kase [b)]

[a)] Naraha Remote Technology Development Center, JAEA,
[b)] Collaborative Laboratories for Advanced Decommissioning Science, JAEA

Introduction

Radiation tolerance of semiconductor components on the shelf, utilized on the robots for emergency response or decommissioning in nuclear facilities, should be estimated.

Just after the Fukushima daiichi NPPs accidents occurred, a guideline, of estimation and management method of semiconductor components on the shelf, was tried to be made based on the old database developed in the course of Bilateral Servo Manipulator under the high radiation and high contamination environments[1-3]. The estimation was conservative, because the data in the database were old and mainly based on the test results of silicon semiconductors. GaAs Semiconductors are coming major recently, and expected to be higher radiation tolerance.

Irradiation Testing

Semiconductor components on the shelf to be irradiated for test were chosen from the key components utilized on Unmanned Ground Vehicles, Unmanned Underwater Vehicles and Unmanned Air Vehicles that JAEA had prepared as Remote Operation Tools for Nuclear Emergency.

Those were mini personal computers, box type personal computers, web cameras and servo drivers, which were key components for robot control and most sensitive components for radiation effects.

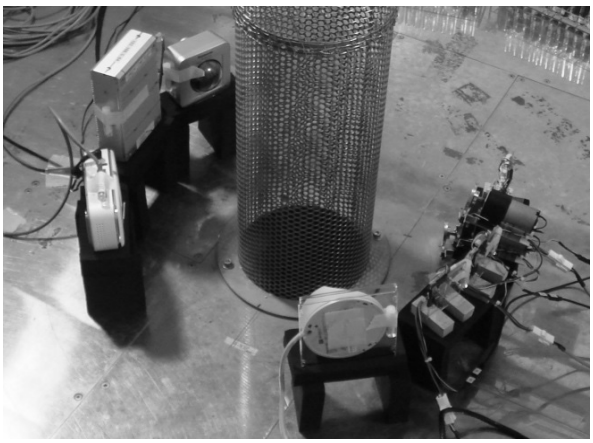

Fig. 1 Components in ^{60}Co irradiation facility.

The irradiation testing was done during March 23th and 25th at the ^{60}Co gamma ray irradiation facility of Takasaki Advanced Radiation Research Institute.

Test Results

Most of all components tested had survived up to 300 Gy or 400 Gy in total. See Table 1.

The tolerance of mini personal computer was over 400 Gy, but the box type computer was only 250 Gy. However, additional tests may be required to show radiation tolerance because of only the one test sample.

The one of C-MOS type web camera was around 400 Gy, and the servo drivers are around 300 Gy.

Table 1 Irradiation test results of components.

Components	Radiation Tolerance
mini-PC No.1	428 Gy
mini-PC No.2	458 Gy
mini-PC No.3	445 Gy
box-PC	254 Gy
web camera No.1*	405 Gy
web camera No.2*	412 Gy
servo driver No.1	350 Gy
servo driver No.2	381 Gy
servo driver No.3	330 Gy

* : Web cameras No.1 and 2 are different models.

Consideration

The robot with above-mentioned semi-component can survive more than 200 Gy. The robot could be more than 300 Gy, if the interface could be radiation hardened.

References

1) M. Fukushima, S. Kawatsuma, *et al.*, PNC TN8410, 93-192 (1993).
2) https://roboticstaskforce.files.wordpress.com/2011/05/20110427-rcpt-radiation.pdf.
3) S. Kawatsuma and H. Asama, Proc. Annu. Meet. Robot. Soc. Jpn. 2016 (2016) to be published.

1-54

Development of Radiation-Resistant Braided Aramid Fiber Bar

K. Izumi [a)], K. Oka [b)], R. Yamagata [c)] and M. Kamikawa [a)]

[a)] Kandenko Co., Ltd., [b)] Department of Quantum Beam Life Science, KPSI, QST,
[c)] Department of Advanced Radiation Technology, TARRI, QST

We have developed a radiation-resistant braided aramid fiber bar. The braided aramid fiber bar is suitable for long-life concrete structures. In this study, a radiation-resistant performance was added to a standard type of braised aramid fiber bar. In the future, a radiation safety management facility is required to be long-life building, and less production of radioactive waste is also preferable in the time of dissolution of the building.

原子炉施設など放射線管理施設の解体時には、鉄筋の一部は放射化しており放射物として保管が必要となる。今後、新たな放射線管理施設を建設する場合には、将来の解体時も考慮した材料選定が必要と考える。本報告では、鉄筋にかわる構造材料としてアラミド筋に着目し、アラミド筋の性能に、放射線で劣化しにくい性能（以下、耐放射線性）を加えた新しいアラミド筋について報告する。

アラミド筋（Fig. 1）は、アラミド繊維を編み込みエポキシ樹脂で熱硬化させた材料である。使用後は、加熱処理することで、減容化が可能である。

Fig. 1　Braided aramid fiber bar.

アラミド筋の性能は、電気的絶縁性があり、非腐食性であることから、電食の心配がなく、鉄筋のように錆ないことから、コンクリートがはがれる現象（爆裂現象）が起きにくい材料である。そのため、長寿命の建築物に適した構造材用である。アラミド筋の基本性能に耐放射線性を加えた性能をFig. 2 に示す。

Fig. 2　Performance of new braided aramid fiber bar.

耐放射線性試験（γ線照射）は、高崎量子応用研究所内の Co-60 照射施設にて実施した。試験体は、通常のアラミド筋に改良を加え、直径 9 mm のアラミド筋を製作し、未照射、3 MGy、5 MGy の各吸収線量まで照射した。

γ線照射後の試験体は、色が茶色に変色はしたが、それ以外の目視上の大きな変化はなかった。照射した試験体に対し、引張試験時の抜け防止対策のため、両端部に金属の装着部を装着し（Fig. 3）引張試験を行った。

Fig. 3　Sample of braided aramid bar after γ-ray irradiation test.

引張り試験の結果をFig. 4 に示す。5 MGy 照射後も規格の引っ張り荷重以上の強度があり、未照射の試験体と比べても引張り強度の大きな低下がみられないことから、本材料の耐放射線性が確認できた。

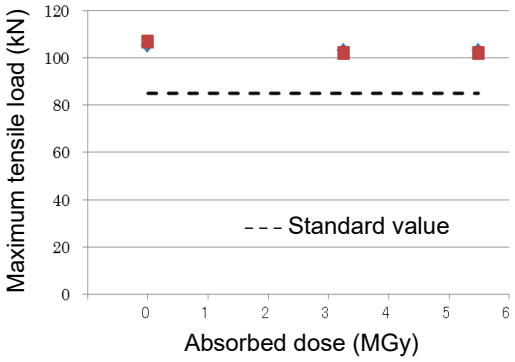

Fig. 4　The results of the tensile test after γ-ray irradiation.

本開発により、放射線管理施設の建設に有効な構造材料が開発できた。今後、実施される原子炉の解体工事の結果、保管しなければならない放射化物が増大し、放射化物保管庫の必要性が出てくる。放射化物保管庫は、一般的な建築物とくらべ長寿命である必要性があり、本材料を使用することで安心安全な放射化物の管理が行えると考えている。

今後は、既存の放射化物保管庫の補強を考慮して、耐放射線性を向上させたアラミド繊維を用いたシート補強工法の開発を目指す。アラミドシート補強は、コンクリート表面にシートを張り付け補強する工法である。

1-55 Element Distribution Measurement in Incineration Ash Using Micro-PIXE Analysis

T. Abe [a)], T. Shimazaki [a)], T. Nakayama [a)], O. Ohsone [a)], T. Osugi [a)], O. Nakazawa [a)], Y. Yuri [b)], N. Yamada [b)] and T. Satoh [b)]

[a)] Nuclear Backend Technology Center, NFCEL, JAEA,
[b)] Department of Advanced Radiation Technology, TARRI, QST

The treatment and disposal promotion of radioactive waste is the important activity in the Japanese nuclear industry. Recently, chemical hazardous substances contained in low level radioactive wastes have been concerned since they can cause environmental pollution after disposal. Incineration ash is one of the important wastes because the chemical hazardous substances are concentrated through an incineration process.

The incineration ash is planned to be solidified into drum with cement before disposal. To establish the solidification method of the ash, many studies have been conducted[1]. The understanding of the ash cementation mechanism, however, is not enough to clear the operating conditions of solidification treatment. In particular, the behavior of elements in the cementation process is not yet clear. The behavior of an element is predicted to affect many properties of a solidified product, for example, hardening time, solubility, and strength and so forth. The leachability of chemical hazardous substance is also conformed. We have thus focused on clarifying the behaviors of elements from the incineration ash to aqueous solution and from the cement hydrate to aqueous solutions.

To achieve the objective above, choice of the analysis method is limited. It is necessary to analyze high concentration resolution and spatial resolution for the incineration ash sample. The micro-particle induced X-ray emission (Micro-PIXE) analysis has enough resolution, as compared with scanning electron microscope / energy dispersive X-ray spectroscopy (SEM-EDX) and X-ray fluorescence (XRF) analysis. We therefore attempted to apply the Micro-PIXE analysis to the study of the behavior of the element in cement solidification process. As a first step, the element analysis of an ash particle was performed using the Micro-PIXE system of a 3-MeV proton beam in TIARA.

Incineration ash was prepared by burning cotton gloves. The ash was taken from the bottom of the incinerator. Several particles with different sizes were picked up from the ash. Then, those particles were embedded in one resin material. The surface of those particles was exposed for irradiation.

Figure 1 shows one of the composition analysis results. There are two particles with different sizes in the image. Comparing the particle ① and ②, it is clear that the peak of silicon (Si), sulfur (S), and potassium (K) are different from each other. Figure 2 shows mapping images of Si, S, and K. Si was mainly concentrated in the particle ①, on the other hand S and K existed mainly in the particle ②. It is found that the difference of the composition and the difference of distribution between ash particles several 100 μm size can be detected using the Micro-PIXE analysis.

Element analysis of an ash particle using the Micro-PIXE analysis was conducted. In conclusion, it was found that Micro-PIXE analysis was capable of analyzing and discriminating the ash composition. In addition, a difference of the sulfur content, which affects cement solidification strongly, could be analyzed.

It is shown that the Micro-PIXE analysis is a useful tool for cement research. We intend to develop a new type of cement with improved confinement of hazardous substances.

Reference

1) Y. Kawato *et al.*, JAEA-Tech., 2010-013 (2010).

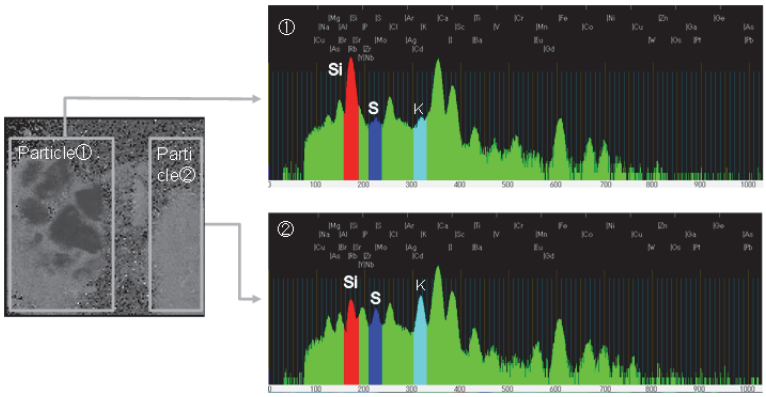

Fig. 1 Microscope images of particles and elemental analysis results. The left gray frame indicates particles ① and ②.

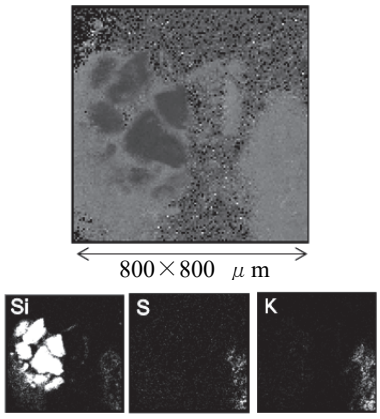

Fig. 2 Elements mapping image of Si, S, and K in the same area as Fig. 1.

1-56 Distribution of Zr Inside an Adsorbent for the Extraction Chromatography Technology

S. Watanabe [a)], Y. Sano [a)], R. Abe [b)],T.Arai [b)], M. Koka [c)] and T. Satoh [c)]

[a)] Fast Reactor Fuel Cycle Technology Development Department, AFRC, JAEA,
[b)] Shibaura Institute of Technology, [c)] Department of Advanced Radiation Technology, TARRI, QST

1. INTRODUCTION

Partitioning and transmutation of minor actinides (MA(III): Am and Cm) in high level liquid waste (HLLW) generated from reprocessing of spent nuclear fuel is one of the most important strategy for reduction in volume and radiotoxicity of the final vitrified waste. Japan Atomic Energy Agency has proposed the extraction chromatography technology as the most promising method for the MA(III) recovery since it generates less secondary waste and requires compact equipment than solvent extraction technology.

One of the promising flow-sheet employs CMPO adsorbent for MA(III) and lanthanide (Ln(III)) co-recovery from the HLLW [1)], and Mo and Zr are desirable to be decontaminated in advance with the operation due to their strong affinities to the CMPO.

In this study, feasibility of HDEHP adsorbent for selective Mo and Zr decontamination was evaluated through adsorption/elution performance and distribution of Mo and Zr inside the adsorbent.

2. EXPERIMENTAL

2.1 Adsorption/elution experiments

Batch-wise adsorption/elution experiments and column separation experiments with HDEHP adsorbent were carried out on simulated HLLW. Oxalic acid and hydrogen peroxide were utilized as eluents for Mo and Zr, respectively.

2.2 Micro-PIXE analysis

Treated adsorbents in the above batch-wise experiments were analyzed by micro-PIXE analysis to evaluate distribution of non-eluted elements inside the particle.

3. RESULTS AND DISCUSSION

3.1 Adsorption/elution experiments

Mo and Zr were selectively adsorbed by the HDEHP adsorbent from 4 M HNO_3 solution while trivalent Ln(III), divalent Sr(II) or monovalent Cs(I) were stayed in the solution. MA might also be remained in the HLLW since chemical behavior of MA(III) is quite similar to those of Ln(III). Therefore, the HDEHP adsorbent is promising for decontamination of Mo and Zr in advance with the MA(III) recovery column operation.

Elution performance of Mo and Zr from the adsorbent is important for repeated use of the adsorbent. Mo was successfully stripped by the adsorbent though Zr stayed in the particle even after contacting with the eluent.

3.2 Micro-PIXE analysis

X-ray spectra obtained for the adsorbents after the adsorption or the elution operations are shown in Fig. 1. Predominant peaks observed at 1.75, 2.00 and 2.30 keV were attributed to Si Kα, Zr Lα and Mo Lα characteristic X-ray, respectively. Intensity of the Mo Lα peak drastically decreased after the elution operation, while those of Si Kα and Zr Lα were not affected by the operation. This tendency reasonably agrees with the results obtained by the elution experiments.

The residual Zr inside the particle, which must form complex with HDEHP, was revealed to have crystal-like structure by X-ray diffraction measurements. In order to discharge the remaining Zr from the particle, further analysis on the crystal and selection of an appropriate wash solution are necessary. Three dimensional distribution of Zr inside the adsorbent is currently tried to be evaluated, and the information will contribute to determine operational conditions of the elution.

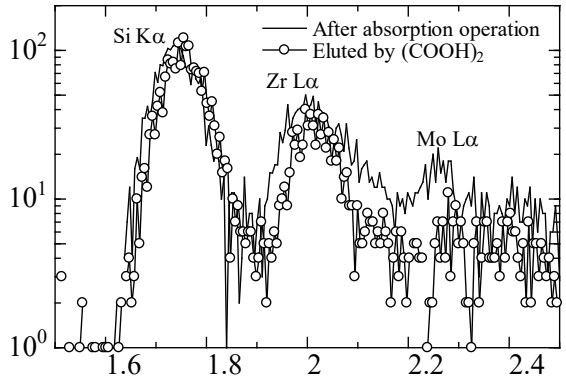

Fig. 1 X-ray spectra obtained by micro-PIXE analysis on adsorbents.

Reference

1) S. Watanabe *et al.*, Proc. GLOBAL 2011 [Chiba] (2011), AESJ, [Tokyo] (2011) (CD-ROM).

1-57 Alpha-ray Degradation of Adsorbents for MA Recovery

S. Watanabe, Y. Sano, H. Kofuji and M. Takeuchi

Fast Reactor Fuel Cycle Technology Development Department, AFRC, JAEA

1. INTRODUCTION

The extraction chromatography technology is one of the promising methods for the partitioning of minor actinide (MA: Am and Cm) from spent nuclear fuel[1], and Japan Atomic Energy Agency (JAEA) has been conducting research and development for the implementation. In order to progress the implementation, not only the performance of the column but also the safety of this system has to be guaranteed.

The adsorbent for extraction chromatography is prepared by impregnating an extractant into the support of porous silica particle coated with styrene-divinylbenzene copolymer (referred as SiO_2-P). Radioactive elements form complexes with the extractant during the operation, thus degradations of materials in the adsorbent by irradiation are unavoidable in the process.

Alpha-ray irradiation effect on adsorption/elution performances of the adsorbents has been investigated so far [2], however the detailed information about the degradation products has not been reported. In this study, alpha-ray degradation products of octyl(phenyl)-N, N-diisobutylcarbonoylmethylphosphine oxide (CMPO)/SiO_2- adsorbent were identified after He^{2+} ion beam irradiation.

2. EXPERIMENTAL

CMPO/SiO_2-P adsorbent was prepared according to an article[3]. The adsorbent was mixed with water, and then the slurry was put in a stainless steel container with 50 mm diameter and 0.5 mm thickness. The container was sealed with a Kapton film. The surface of the sample was uniformly irradiated with He^{2+} ions passing through the Kapton film. He^{2+} ions accelerated by 3 MV tandem accelerator of TIARA to be 9 MeV were reduced by the Kapton film and atmosphere to be 5.0 MeV when the beam reached at the surface of the sample. Thickness of the sample was larger than penetration range of the He^{2+} ion with 5.0 MeV, therefore we assumed that all incident energy of the ions was transferred to the sample. Irradiation dose was calculated from size and weight of the sample, fluence of the beam, incident energy of He^{2+} ions and the beam current.

The irradiated adsorbents were washed with 1,2-dichloroethane, then the degradation products remaining on the adsorbent were transferred to the organic phase. The chemical species extracted in the 1,2-dichloroethane were analyzed by GC/MS, NMR and FT-IR measurements. The ingredients in the 1,2-dichloroethane were derivatized by N,O-Bis(trimethylsilyl)trifluoroacetamide (BSTFA: $CF_3C[OSi(CH_3)_3]=NSi(CH_3)_3$), and then they were also analyzed by GC/MS to identify the degradation products which are hardly eluted from the column.

3. RESULTS AND DISCUSSION

Structures of CMPO and the degradation products identified in this study are shown in Table 1. Those degradation products must be produced by dissociation between N atom and C atom of the CMPO molecule. Since bond energy of C-N bond is smaller than those of C-C, C-O and C=O bonds for simple molecules[4], C-N bond of CMPO molecule might be also weak and easy to be dissociated.

Two oxygen atoms of the CMPO are the functional groups for the MA extraction, thus the degradation products are also possible to extract MA. In order to evaluate accumulation behavior of MA inside the packed bed, elution property of MA form the product should be investigated.

This study was focused only on the products generated by the alpha-ray irradiation, however those produced by gamma-ray irradiation are also necessary to be investigated.

Table 1 Structures of CMPO and the degradation products.

Name	Structure
CMPO	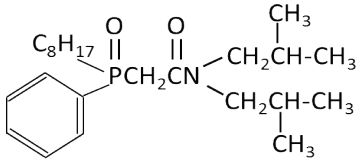
Degradation product No.1	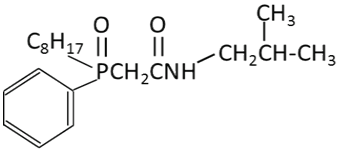
Degradation product No. 2	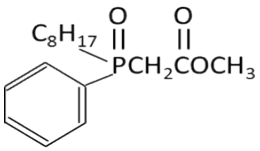

References

1) E. P. Horwitz *et al.*, Anal. Chim. Acta, **310**, 63-78 (1995).
2) S. Watanabe *et al.*, Proc. OECD/NEA 12th IEMPT, [Prague, Czech], 1-12 (2012).
3) Y. Z. Wei *et al.*, Nucl. Tech., **132,** 413-23 (2000).
4) B. deB. Darwent, Nat. Stand. Ref. Data Ser., Nat. Bur. Stand. (U.S.), **31**, 18 pp (1970).

1-58 Gamma-ray Degradation of HDEHP Adsorbent for MA Recovery

S. Watanabe, Y. Sano, H. Kofuji and M. Takeuchi

Fast Reactor Fuel Cycle Technology Development Department, AFRC, JAEA

1. INTRODUCTION

Minor actinides (MA(III): Am and Cm) involved in spent nuclear fuel are desirable to be separated from other fission products due to their strong radiotoxicity. The separated MA(III) are currently studied to be transmuted in the fast reactors or in the ADS. Separation of MA(III) from other fission products is one of the most challenging tasks since chemical behavior of MA(III) are quite similar to those of lanthanides (Ln(III)). Our group propose the extraction chromatography technology as the promising methods for the partitioning of MA(III), and we have been performing research and development for the implementation of the technology.

The technology utilizes a porous silica based adsorbent which is coated by styrene-divinylbenzene copolymer and an extractant is impregnated into the polymer. The adsorbent with bis-(2-ethylhexyl) hydrogen phosphate (HDEHP) extractant is one of the candidate for the MA(III) separation form Ln(III). The adsorbent is exposed to irradiation environment, and degradation of the adsorbent is suspect to influence on both performance of the adsorbent and safety of the system. Gamma-ray irradiation effect on adsorption/elution performances of the adsorbents has been investigated so far[1], however the detailed information about the degradation products has not been reported. In this study, degradation products of the HDEHP adsorbent generated by gamma-ray irradiation were analyzed to evaluate influence of the irradiation on the system.

2. EXPERIMENTAL

Gamma-ray irradiation experiments were carried out at the irradiation room No. 1 of Co-60 Gamma-ray Irradiation Facility. One g of the adsorbent and 10 mL of water were put in glass vial with 100 mL volume and sealed, and then they were irradiated with 3 kGy/h up to 2 MGy. The irradiated adsorbents were separated from the solution and washed with 1,2-dichloroethane. Organic species in the nitric acid solution were extracted by liquid-liquid extraction with 1,2-dichloroethane. Chemical species in the 1,2-dichloroethane were identified by GC-MS analysis.

The ingredients in the 1,2-dichloroethane were derivatized by N,O-Bis(trimethylsilyl) trifluoroacetamide (BSTFA: $CF_3C[OSi(CH_3)_3]=NSi(CH_3)_3$), and then they were also analyzed by GC-MS to identify the degradation products which are hardly eluted from the column.

3. RESULTS AND DISCUSSION

Structure of HDEHP and representative degradation products are shown in Table 2. HDEHP form dimers and 3 dimers contribute to extraction of MA(III) or Ln(III) as following equation,

$$M^{3+} + 3\overline{(H_2A_2)} \leftrightarrow \overline{\left(M(HA_2)_3\right)} + 3H^+, \qquad (1)$$

where HA, H_2A_2, HA_2 are HDEHP molecule, dimerized HDEHP molecule and deprotonated dimirized molecule, respectively.

Both 2-ethylhexanol and phosphoric acid do not form dimers like HDEHP or form complexes with MA(III) or Ln(III), thus they cannot extract MA(III) or Ln(III). Our previous study reported that adsorption capacity of HDEHP adsorbent for Ln(III) drastically decrease with increasing gamma-ray irradiation dose and that elution ratio from the HDEHP adsorbent was not influenced by the irradiation[2]. Those results reasonably explained by interaction of the degradation products with Ln(III). Adsorbed MA(III) are not accumulated inside the packed column but eluted by the irradiation consequently. Flash points and ignition points of those degradation products are one of the most important information for the safety assessment. In addition to that, chemical reactivity of those products with nitric acid solution has to be investigated to evaluate the total safety of the system.

Table 1 Structures of HDEHP and the degradation products.

Name	Structure
HDEHP	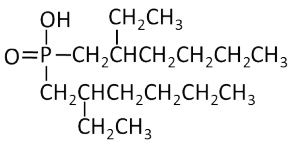
2-Ethylhexanol	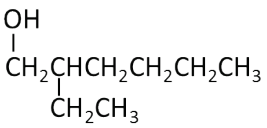
Phosphoric acid	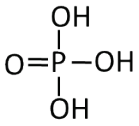

References

1) S. Watanabe *et al.*, Proc. OECD/NEA 12th IEMPT, [Prague, Czech] (2012).
2) Y. Koma, S. Watanabe, *et al.*, ATALANTE 2008, [Montpellier, France] (2008) [CD-ROM].

1-59

The Hydrogen Gas Generation by Electron-beam Irradiation from ALPS Adsorbents Solidified by Several Inorganic Materials

J. Sato [a,b], S. Suzuki [c], J. Kato [a,b], T. Sakakibara [a,b], Y. Meguro [a,b] and O. Nakazawa [a,b]

[a] Nuclear Backend Technology Center, NFCEL, JAEA, [b] International Research Institute for Nuclear Decommissioning, [c] Inspection Development Company Ltd.

Several kinds of adsorbents have been used in Advanced Liquid Processing System (ALPS) at Fukushima Daiichi Nuclear Power Station. Those adsorbents contain large amount of radionuclides including beta emitters generating the hydrogen gas. Two adsorbents, crystalline silicotitanate (CST) and Sb-adsorbent (SbA) made of cerium oxide, were studied for solidification using several inorganic materials such as Ordinary Portland Cement (OPC), Portland Blast-Furnace Slag Cement Type-B (BB) and Geopolymer (GP) as reported in Ref. 1. Hydrogen gas would be generated by radiolysis of the water in the waste form because of the some non-reacting water remaining in the solidified samples of OPC, BB and GP. In this study, the hydrogen gas generation from solidified samples was measured by irradiation with an electron beam from the 1st accelerator in substitution for the beta ray. Then we considered the influence of the compounds in wastes and kinds of radiation, an electron beam and a gamma ray, on hydrogen gas generation.

CST and SbA which are actually adsorbents in ALPS system were used for the solidification test. Each adsorbent was mixed and solidified with OPC, BB and GP in the 40 wt% filling ratio, and several different water-matrix ratios (Table 1) were examined. The OPC and BB samples were added 2% high-range water-reducing admixture to improve workability. In addition the reference sample without adsorbents was made with OPC (No. 7) or BB (No. 8). The fluid mixture was filled into a container (φ13 mm × 50 mm) and put into a glass ampoule (φ18 mm × 150 mm) after curing at room temperature for 28 days. Ampoules were irradiated with the vertical electron beam under the condition (2.0 MeV, 0.2 mA, 60 sec). The irradiation dose and its rate were determined by CTA films which were put into the vial container. Hydrogen gas concentration was determined by gas chromatography. The amount of water in the samples was determined by measuring weight change of the samples after heating at 110 °C for 24 h. A total dose was 13.7 ± 0.3 kGy.

The amount of hydrogen gas (nmol/g water • kGy) was shown in Table 2. The amount of hydrogen gas from CST samples (No. 1, 2 and 3) was less than the one from SbA samples (No. 4, 5 and 6). And the amount of hydrogen gas from reference samples (No. 7 and 8) was in between CST samples and SbA samples.

The hydrogen gas generation by an electron beam showed the similar trend to that by irradiation of a gamma ray. In conclusion, it was considered the hydrogen gas generation is not dependent on the kinds of radiation. However, the amount of hydrogen generated by electron beam irradiation was extremely low compared with that of gamma ray in all the samples. As the result, it was predicted that the evaluation of the absorbed dose for solidified samples by using a CTA film was failed. Thus, the total adsorbed dose might be overestimated in this study. It is necessary to consider the relationship between the decay of an electron beam associated with the depth of solidified samples and the total adsorbed dose. In the next step, we plan to evaluate the total absorbed dose of solidified samples and calculate the G-values of hydrogen gas generation by electron beam irradiation.

Table 1 Conditions of solidified samples.

Sample		Composition		
		Material	Waste (40 wt%)	Water/Matrix ratio
No. 1	OPC-CST	OPC	CST	1.0
No. 2	BB-CST	BB		1.0
No. 3	GP-CST	GP		1.2
No. 4	OPC-SbA	OPC	SbA	0.6
No. 5	BB-SbA	BB		0.6
No. 6	GP-SbA	GP		1.2
No. 7	Ref-OPC	OPC	-	0.7
No. 8	Ref-BB	BB	-	0.7

Table 2 Hydrogen generation by irradiation.

Sample		Amount of hydrogen gas (nmol/g water • kGy)	
		Electron beam	Gamma ray
No. 1	OPC-CST	14	1047
No. 2	BB-CST	36	933
No. 3	GP-CST	9	466
No. 4	OPC-SbA	62	2298
No. 5	BB-SbA	73	3316
No. 6	GP-SbA	81	2935
No. 7	Ref-OPC	46	1304
No. 8	Ref-BB	66	1956

Acknowledgements

This work includes a part of the result from the subsidy program "Project of Decommissioning and Contaminated Water Management (R&D for treatment and disposal of solid radioactive waste)" by METI.

Reference

1) J. Sato *et al.*, JAEA Takasaki Annu. Rep. 2014, JAEA-Review 2015-022, 14 (2016).

1-60

The Hydrogen Gas Generation by Gamma-ray Irradiation from ALPS Adsorbents Solidified by Several Inorganic Materials

J. Sato [a,b], S. Suzuki [c], J. Kato [a,b], T. Sakakibara [a,b], Y. Meguro [a,b] and O. Nakazawa [a,b]

[a] Nuclear Backend Technology Center, NFCEL, JAEA, [b] International Research Institute for Nuclear Decommissioning, [c] Inspection Development Company Ltd.

Radioactive wastes, two kinds of slurries and several kinds of adsorbents have been generated from Advanced Liquid Processing System (ALPS) in Fukushima Daiichi Nuclear Power Station. These wastes contain large amount of radioactive nuclides. We studied to solidify two kinds of unused ALPS adsorbents, crystalline silicotitanate (CST) and Sb-adsorbent (SbA) made with cerium oxide, using several inorganic solidification materials such as Ordinary Portland Cement (OPC), Portland Blast-Furnace Slag Cement Type-B (BB) and Geopolymer (GP). Because of the non-reacting water remained in the solidified samples of OPC, BB and GP, the hydrogen gas would be generated by radiolysis from the water in the waste form. In this study, we prepared solidified samples containing simulated adsorbents and measured the amount of hydrogen gas generated by gamma ray irradiation. Then we calculated the G-value of hydrogen gas generation and considered the influence of the compounds in wastes on G-value.

CST and SbA which are used in ALPS system actually were used for the solidification test. Each adsorbent was mixed with inorganic matrices in 40 wt% filling ratio and solidified, with different water-matrix ratio (Table 1). The OPC and BB samples were added 2% high-range water-reducing admixture to improve workability. In addition the reference sample without simulated adsorbents was prepared by using OPC (No. 7). The fluid mixture was filled into a container (φ13 mm × 50 mm) and put into a glass ampoule (φ18 mm × 150 mm) after curing at room temperature for 28 days.

The sample was irradiated by ^{60}Co γ-rays at 10 Gy/h for 300 h in the γ-ray irradiation facility. Hydrogen gas concentration in the glass ampoule was determined by gas chromatography. The G-value was calculated by the gas concentration, the sample weight and total absorbed dose. The amount of water in the samples was determined by measuring weight change of the samples after heating at 110 °C for 24 h.

The G-values of hydrogen gas were summarized in Table 2. The G-values of CST (No. 1, 2 and 3) were lower than the one of reference (No. 7). On the other hand, the G-value of SbA samples (No. 4, 5 and 6) was higher than the one of reference sample. In previous study[1], G-values of solidified samples including titanium were low as well as this study. As the result, titanium in solidified samples might influence the G-values of hydrogen gas generation.

In conclusion, the hydrogen gas generation is influenced by the kinds of wastes because the G-values did not depend on the ratio of free water. For example, CST in water suppresses the hydrogen gas generation by gamma-ray irradiation [2], while cerium oxide in water enhances the generation of hydrogen gas by irradiation[3]. It was surmised that those wastes may influence the radiolysis of free water in solidified samples by the same mechanism as above.

In the next step, it is necessary to investigate the influence of the wastes in the solidified samples on the hydrogen gas generation in more detail to realize the mechanism of hydrogen gas generation from the actual waste form.

Acknowledgements

This work includes a part of the results from the subsidy program "Project of Decommissioning and Contaminated Water Management (R&D for treatment and disposal of solid radioactive waste)" by METI.

References

1) J. Sato *et al.*, JAEA Takasaki Annu. Rep. 2014, JAEA-Review 2015-022, 15 (2016).
2) Jay A. LaVerne *et al.*, J. Phys. Chem. **B, 106**, 380-86 (2002).
3) N. E. Bibler *et al.*, WSCR-RP-98-01143 (1998).

Table 1 Conditions of solidified samples.

Sample		Composition		
		Material	Waste (40 wt%)	Water/Matrix ratio
No. 1	OPC-CST	OPC	CST	1.0
No. 2	BB-CST	BB		1.0
No. 3	GP-CST	GP		1.2
No. 4	OPC-SbA	OPC	SbA	0.6
No. 5	BB-SbA	BB		0.6
No. 6	GP-SbA	GP		1.2
No. 7	Reference	OPC	-	0.7

Table 2 Result of the irradiation test.

Sample	G-value(H_2) (/100 eV) (n=3)	Ratio of free water (g/g sample)
No. 1	0.15 ± 0.02	0.10
No. 2	0.13 ± 0.01	0.09
No. 3	0.09 ± 0.01	0.13
No. 4	0.23 ± 0.02	0.07
No. 5	0.29 ± 0.00	0.06
No. 6	0.40 ± 0.03	0.09
No. 7	0.20	0.11

1-61 Hydrogen Generation from Cement Solidified Sample Loading Carbonate by Gamma Irradiation

Y. Itoh, F. Satoh and J. Kojima

Tokai Reprocessing Technology Development Center, NFCEL, JAEA

Cement solidification of low-level radioactive liquid wastes (LLW) generated from Tokai reprocessing plant is planned in Low-level radioactive Waste Treatment Facility (LWTF). Here, the LLW are "carbonate effluent" with a comparatively low radioactivity and "slurry effluent" with relatively high radioactivity, which will be generated from radionuclide separation process and nitric acid ion decomposition process[1].

It is known that $G(H_2)$ value of cement solidified products containing radionuclides are varied by cement and effluent composition. Thus, we are studying hydrogen production from the cement solidified sample containing the carbonate effluent and the slurry effluent.

The carbonate effluent will be solidified with cement, which consists of Ordinary Portland Cement (OPC) and Blast Furnace Slag (BFS). In this study, we acquired $G(H_2)$ values of hydrogen gas due to mixture ratio of BFS and OPC in the cement. And also we investigated influence of carbonate loading ratio in the solidified sample on $G(H_2)$ value.

Irradiation samples were prepared by mixing simulated liquid waste (carbonate effluent including sodium nitrate) and cement shown in Table 1, then filled into a container (φ13 mm × 50 mmH) at 20 °C for 28 days. After curing, each sample was put into a vial container (50 mL) and was sealed with rubber septum. The samples were irradiated by Co-60 gamma-rays at about 2.5 kGy/h for 20 hours. After the gamma irradiation, the concentration of hydrogen gas generated in the vial was measured by gas chromatography.

Figure 1 shows $G(H_2)$ values of hydrogen gas by the mixture ratio of BFS and OPC. Here, irradiated samples were solidified without loading carbonate, and the water-cement ratio was 0.40 or 0.45. The $G(H_2)$ value increased with content of the OPC. As shown in Table 1, CaO content in the cement was increased with OPC content, so it was suggested that the $G(H_2)$ value in the Type-A cement was high by the influence of the CaO content.

Figure 2 shows relationship between carbonate loading ratio in the solidified sample and $G(H_2)$ value. The $G(H_2)$ value of the carbonate loading sample was about 0.05 (/100 eV) and it was 1/3-1/4 of the $G(H_2)$ value without carbonate. And also it was slightly decreased with increasing carbonate loading ratio. It was considered that the $G(H_2)$ value of the carbonate loading sample was decreased by the influence of the sodium nitrate in the carbonate effluent, because the nitric acid ion in solution reduce hydrogen production by gamma irradiation[2].

These $G(H_2)$ values obtained by this study will contribute to the evaluation of hydrogen production by storing the solidified products.

References

1) A. Sugaya *et al.*, WM2011 Conf., 11078 (2011).
2) N. Nakagiri, T. Miyata, J. Atom. Energy Soc. Jpn., **36**, 42 (1994).

Table 1 Oxide composition of cement [wt%].

Cement	BFS/OPC	CaO	SiO_2	Al_2O_3	Fe_2O_3	MgO	Other
BFS	100/0	44.4	32.9	13.9	0.36	4.91	3.53
Type-B	90/10	46.2	31.7	13.2	0.62	4.69	3.59
Type-A	70/30	49.9	29.5	11.6	1.16	4.00	3.84

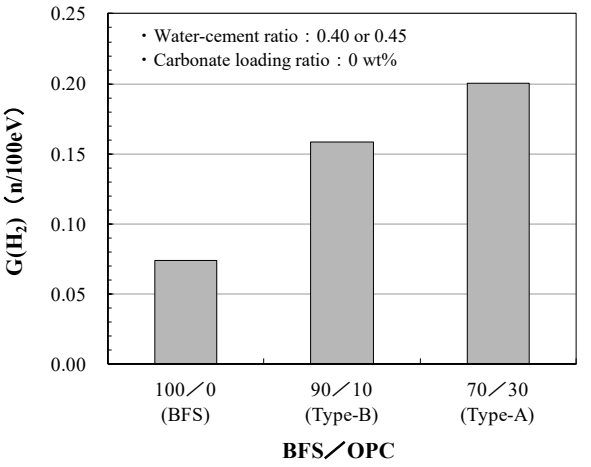

Fig. 1 G(H2) value of hydrogen gas due to mixture ratio of BFS and OPC in cement.

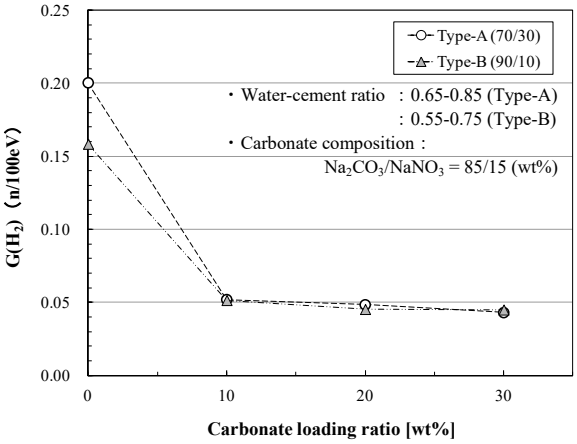

Fig. 2 Relationship between carbonate loading ratio in the solidified sample and G(H2) value.

1-62 Effect of Seawater on Corrosion of SUS316L in HAW under γ-ray Irradiation

H. Ambai [a)], Y. Nishizuka [b)], Y. Sano [a)], N. Uchida [b)] and S. Iijima [b)]

[a)] Department of Fukushima Technology Development, NFCEL, JAEA,
[b)] Tokai Reprocessing Technology Development Center, NFCEL, JAEA

The spent fuel stored in the storage pools at the Fukushima Daiichi Nuclear Power Plant of Tokyo Electric Power Company Holdings, Inc. (TEPCO) is exposed with the environment containing seawater components, owing to the injection of seawater into the storage pools. Therefore, during reprocessing, it is expected that the spent fuel will be contaminated with seawater components, and the influence of seawater on reprocessing needs to be investigated.

It was reported that seawater components are not extracted during the separation process of U and Pu [1)]. Thus, seawater components move to the devices treating high active liquid waste (HAW). Therefore, we investigated the corrosion behaviour of the HAW storage tanks.

Immersion tests were performed with SUS316L used in the fabrication of tanks. Total immersion time was 960 hours. The corrosion rates were calculated from the weight losses of coupons. The surfaces of coupons were observed with laser microscope every 240 hours. The surrogate HAW used in this study was composed with nitrate metal ions in Table 1 and nitric acid media. Acid concentration was adjusted to 2 mol/L. The corrosive effects at various artificial seawater (ASW) concentrations were evaluated to understand the effect of seawater components in HAW. The temperature of the solution was maintained at 60 °C, based on the control standard for a HAW tank. The γ-ray irradiation was carried out using ^{60}Co source in the Gamma-ray irradiation facility. Dose rate of γ-ray was settled at 2.8 kGy/h which was measured by alanine dosimeters.

The results of immersion tests are showed in Fig. 1 and Fig. 2. Intergranular corrosion proceeded in all conditions because they contained the oxidizing metal ions (Table 1). Their corrosion rates were inhibited with γ-ray irradiation as the previous studies reported[2)]. If γ-ray was irradiated to HAW, it is supposed that the corrosion reaction was suppressed because HNO_2 and NOx as radiolysis products of HNO_3 reduced the oxidizing metal ions. The corrosion rates decreased with seawater components if γ-ray was not irradiated. It indicated that some interactions between seawater components and metallic ions contained HAW could occur. On the other hand, no significant effect of seawater components was emerged under γ-ray irradiation. It is expected that the interactions between seawater components and metallic ions were suppressed relatively due to the decrease of oxidizing ions by γ-ray irradiation.

Table 1 Chemical composition of surrogate HAW.

Element	Concentration[mol/L]	Note
Fe	0.090	Corrosion product
Cr	0.025	Corrosion product
Ru	0.12	
Ce	0.10	
Nd	0.50	
V	0.010	Substitute for Np

References

1) H. Aihara *et al.*, Global 2015, 5165 (2015).
2) T. Yamamoto *et al.*, J. Nucl. Sci. Tech., **35**(5), 353-56 (1998).

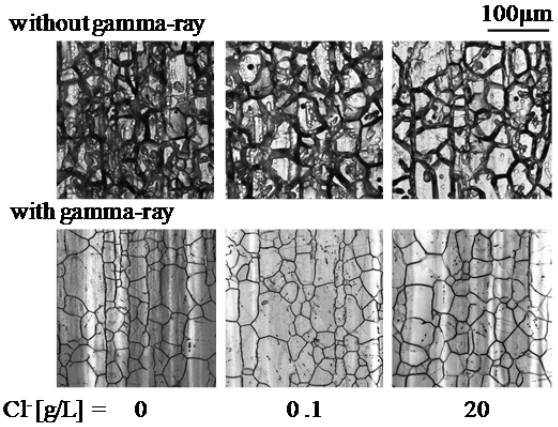

Fig. 1 Corrosion morphology of SUS316L coupons in HAW containing seawater components. Immersion time is 960 hours.

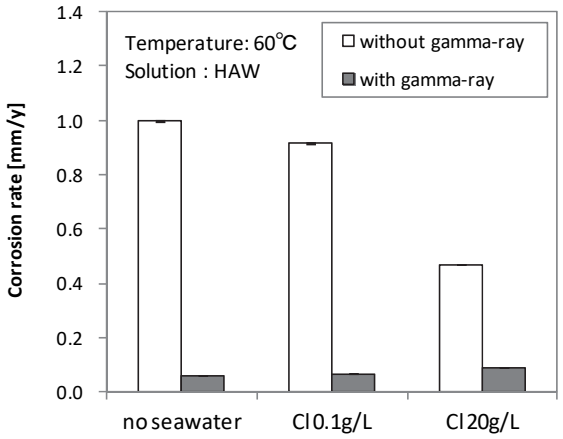

Fig. 2 Corrosion rates of SUS316L coupons in HAW containing seawater components. Immersion time is 960 hours.

1-63

Radiolytic Hydrogen Absorption Behavior of Explosive Bonded Zr/Ta/R-SUS304 Joint in Nitric Acid Solution under Gamma-ray Irradiation

Y. Ishijima, F. Ueno and H. Abe

Fuels and Materials Engineering Division, NSEC, JAEA

In Japan, a commercial reprocessing plant is being test operated in Rokkasho reprocessing plant. Purex process which uses nitric acid (HNO_3) and dodecane with tributhyl phosphate for solvent has been adopted in the plant. In some cases, stainless steels have been severely corroded. This appears to be intergranular corrosion in those solutions. In order to avoid corrosion in such severe environment, some equipments in the plant have been made of zirconium (Zr) , tantalum (Ta) and reprocessing plant grade SUS304 (R-SUS304).

However, it is well known that Zr and Ta has susceptibility of hydrogen embrittleent by hydride formation[1]. In used nuclear fuel solution, hydrogen atoms are always generated by radiolysis under irradiation. And it is considered that radiolytic hydrogen can diffuse into the metal and generate hydride. Therefore, there is a concern about the degradation of nuclear fuel reprocessing plant by hydrogen embrittlement in long term operation.

In this study, we conducted radiolytic hydrogen absorption test by nitric acid immresion test under gamma-ray irradiation.

Explosive bonded Zr/Ta/R-SUS304 plate was used for test material. Table 1 shows the chemical composition of Zr, Ta and R-SUS304. Plate type specimens ($10 \times 10 \times 1$ mm) were used for radiolytic hydrogen absorption tests. Specimens were polished up to #1000 by SiC paper.

Radiolytic hydrogen absoption tests were carried out in 1 mol/L HNO_3 and pure water. Dose rates from ^{60}Co source were chosen 7 kGy/h. Irradiation time was 1,000 h. After irradiation, thermal desorption spectrometry (TDS) was carried out to evaluate the hydrogen absorption value with quadrupole mass spectrometer (QMS). Temperature range of TDS was from room temperature to 1,073 K. Heating rate of TDS was 10 K/min. Evaluated TDS spectrum was compared with the TDS spectrum from electrochemically hydrogen cgarged explosive bonded joint. Figure 1 shows that example of the TDS spectrum and total discgarging hydrogen after gamma ray irradiation and electrochemically hydrogen charging. The TDS result shows that the peak temperatures that irradiated specimen shows same temperature. On the other hand, the peak temperature amoung irradiatied specimen and hydrogen charged specimen are not same. These results shows that the hydrogen trapping behavior change by hydrogen absorption method. But, the trapping behavior did not change by immersion environment such as pH.

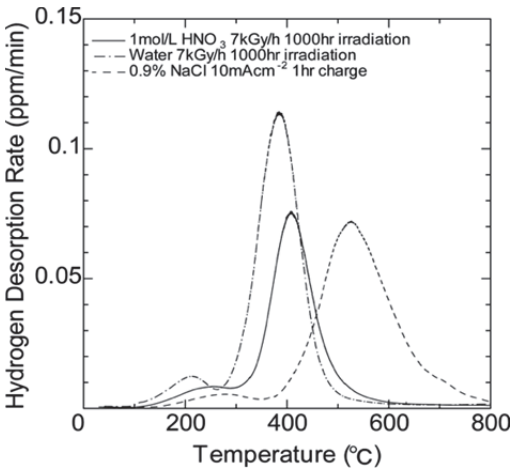

Fig. 1 Temperature dependence on hydrogen discharging rate and total discgarging hydrogen after gamm ray irradiation and electrochemically charging.

From irradiation results, absrobed hydrogen decreased with HNO_3 concentration. It is considered that the reason can explain by g-value of hydrogen because of the g-value decreases with HNO_3 concentration.

It is not clear the reason that the hydrogen trapping behavior change by hydrogen absorption method. However, the reason is considered that break down of the passivation film during electrochemically charging.

Reference

1) C. E. Coleman and D. Hardie, J. Nucl. Mater., **19**(1), 1-8 (1966).

Table 1 Chemical composition of the test materials (%).

Material	Si	Mn	P	S	Ni	Cr	Fe	C
R-SUS304	<1.00	<2.00	<0.045	<0.030	9.00~13.00	18.00~20.00	bal.	<0.020
Ta	<0.02	-	-	-	<002	-	<0.02	<0.03
Zr	-	-	-	-	-	-	<0.2	<0.05

Material	N	H	Nb	Ti	W	Ta	Hf	Zr
R-SUS304	-	-	-	-	-	-	-	-
Ta	<0.01	<0.0015	<0.10	<0.01	<0.03	bal.	-	-
Zr	<0.025	<0.005	-	-	-	-	<4.5	bal.

1-64 Effects of Gamma-ray Irradiation on the Inhibitive Effects of the Sodium Pentaborate against the Corrosion of Carbon Steel in the Diluted Seawater

T. Satoh, C. Kato, F. Ueno and M. Osaka

Fuels and Materials Engineering Division, NSEC, JAEA

In the Fukushima Daiichi Nuclear Power Station (1F), the seawater was injected into the reactor cores in the Unit 1, Unit 2 and Unit 3. The high dose of radiation has been continuing in the primary containment vessel (PCV) because of the molten fuel debris and the fission products. It is well known that H_2, H_2O_2, short life radicals, etc., are produced by water radiolysis [1]. The produced species are chemically active and it is considered that corrosion of the PCV is influenced by gamma-rays irradiation. The typical countermeasure against the corrosion of carbon steel (CS) is the injection of the corrosion inhibitors. To evaluate the availability of the corrosion inhibitors under irradiation condition, the corrosion test of the carbon steel exposed to the diluted seawater containing corrosion inhibitors under gamma irradiation condition was performed.

Sheet type specimens of 40 mm × 10 mm × 2 mm were machined from SGV480 (JIS G3118) for the PCV, and immersed in diluted artificial seawater at 323 K (50 °C). Figure 1 shows corrosion tests under gamma-rays irradiation at Co-60 irradiation facility in Takasaki advanced radiation research institute. Some flasks were arranged close to the ^{60}Co sources and others were put at distances of 1.6 m from the ^{60}Co sources. The dose rates were estimated as 4 kGy/h and 200 Gy/h, respectively. The sodium pentaborate was injected into the diluted seawater as corrosion inhibitor. Four thousand ppm as boron of sodium pentaborate was injected. The inhibitor was added to the diluted sea water after 100 h of exposure without inhibitor to investigate the effects of the inhibitor on the mitigation of corrosion when the oxide film have already formed at the surface of CS under irradiation condition.

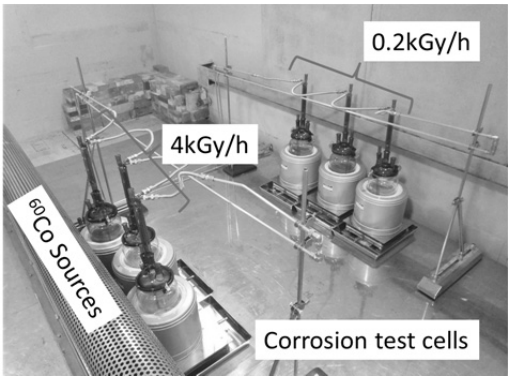

Fig. 1 Corrosion test cells at Co-60 irradiation facility in Takasaki advanced radiation research institute.

The obtained corrosion rates of the test specimens exposed to diluted sea water under irradiation condition are shown in Fig. 2 with those under no inhibitor conditions.

The corrosion rates were successfully mitigated by the injection of 4,000 ppm as boron of the sodium pentaborate on 100 h of exposure time. It was indicated that the sodium pentaborate was effective if the surface of CS had already been covered by the oxide under gamma-ray irradiation. It was confirmed that the injection of the high concentration of sodium pentaborated was effective to mitigate the corrosion of the PCV under the irradiation condition in 1F.

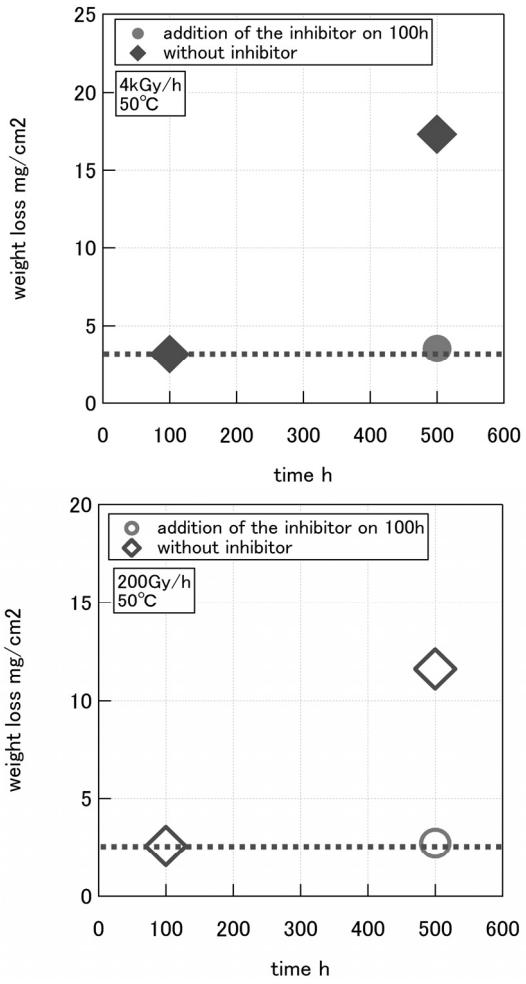

Fig. 2 Corrosion rates of carbon steel under gamma-rays irradiation in the diluted sea water containing sodium pentaborate.

References

1) S. Le Caër, Water, **3**, 235-53 (2011).
2) Fukaya *et al.*, Proc. 61th Zairyo to Kankyo Touron-kai, **B-109** (2014) (in Japanese).

1-65

Electrochemical Properties of Stainless Steel in Zeolites Containing Diluted Artificial Seawater under Gamma-rays Irradiation

C. Kato, T. Satoh, J. Nakano and F. Ueno

Fuels and Materials Engineering Division, NSEC, JAEA

As a part of consideration for long-term storage of spent zeolite adsorption vessels in the Fukushima Daiichi nuclear power station, corrosion of vessel material is one of important issues. Because seawater was used to cool the reactor core, type 316L stainless steel (316L SS), structural material of the spent zeolite adsorption vessel is exposed to residual chloride and adsorbed radioactive isotopes. However, combined effect of chloride and irradiation on corrosion behavior of the 316L SS has not been fully studied. In this study we performed electrochemical tests of 316L SS in the zeolites (Herschelite, IE96 and IE911) containing artificial seawater under gamma-rays irradiation. Herschelite used in the first Cs adsorption system (KURION) was used as adsorbent zeolite. IE96 and IE911 used in the second Cs adsorption system (SARRY).

Figure 1 shows the influence of absorbed dose rate and contact with zeolite on the spontaneous potential (E_{SP}). E_{SP} is well known as the index in possibility of localized corrosion and the elevation of E_{SP} causes a localized corrosion. E_{SP} in bulk water and in the system contacted with zeolites was almost the same in a condition under non-irradiation. In a condition under gamma-ray irradiation, E_{SP} elevated with increasing the absorbed dose rate. E_{SP} under the same irradiation condition was different depending on the type of zeolite and ESP under irradiation decreased in order of bulk water>Herschelite>IE96>IE911. Contact with zeolite can suppress the potential elevation under irradiation and consequentially decline the possibility of localized corrosion occurrence in for long-term storage [1].

In general, the chemical products caused in the water radiolysis can be classified into the long-lived radiolysis chemical species (H_2O_2, O_2, and H_2, etc.) and the short-lived radical species (OH^*, etc.). The calculated radiolysis analysis in water shows the possibility that the long-lived radiolysis chemical species exist for a while, several hours or more, while the short-lived radical species disappears at once, a few seconds or less, after irradiation interruption. Therefore, the response of the rest potential (E_{REST}) that is open circuit potential on the stainless steel under irradiation interruption can indicate the influence of the short-lived radical species. Figure 2 shows the response of E_{REST} under irradiation interruption. E_{REST} in the bulk no changed under irradiation interruption in this condition. This result shows the potential of stainless steel is dominate not by the short-lived radical species but by the long-lived radiolysis chemical species. On the other hand, the potential in the system contacted with zeolites, IE96 and IE911, declined under irradiation interruption. This result indicates concentration of the long-lived radiolysis oxidant species, such as H_2O_2 and O_2, caused the potential elevation decrease in the system contacted with zeolite. It is well known that zeolite mineral acts as a catalyst to decompose H_2O_2. Zeolite consequently reduces concentration of H_2O_2 in water under the irradiation.

It was found that a risk of local corrosion on stainless steel increased under gamma-rays irradiation because of increasing E_{sp} of stainless steel under irradiation. On the one hand, the increasing E_{sp} was suppressed by coexistence with zeolite.

Reference

1) C. Kato *et al.*, 17th Int. Conf. Environ. Degrad. Mater. Nucl. Power Syst., [Ottawa, Ontario, Canada] (Aug, 2015).

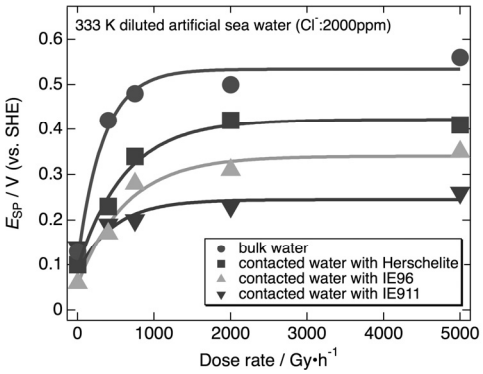

Fig. 1 The relationship between dose rate and the spontaneous potential, E_{SP}, of type 316L in the bulk water and the system contacted with the zeolites in the diluted artificial sea-water (Cl^-:2,000 ppm) at 333 K.

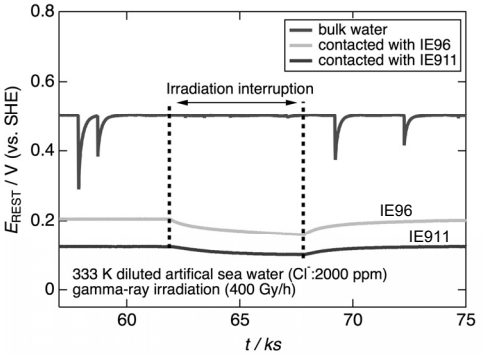

Fig. 2 The response of the rest potential ,E_{REST}, of type 316L in the bulk water and the system contacted with the zeolites in the diluted artificial sea-water (Cl^-:2,000 ppm) at 333 K under irradiation interruption.

1-66 Studies on Radiolysis Behavior of Carbonate Slurry under Co-60 Gamma-ray Irradiation

R. Nagaishi [a, b], T. Motooka [a], I. Yamagishi [a], M. Inoue [b] and T. Matsumura [a, b]

[a] Waste Management Division, CLADS, JAEA, [b] NERCC, JAEA

Overflow of water from waste storage tanks of High Integrity Containers (HIC) in the Multi-nuclide removal equipment ("ALPS") was discovered at Fukushima Daiichi Nuclear Power Station (NPS) in April of last year. The mechanism of overflow was not understood very much at that time, while it was considered to originate from "water radiolysis" by beta-rays from Sr-90 and Y-90 present in high viscous carbonate slurry as radioactive wastes after decontamination at a basic condition in ALPS.

To elucidate that for chemical safety in the waste storage, irradiation experiments of simulated carbonate slurry by Co-60 gamma-ray have been conducted in CLADS, JAEA in cooperation with TEPCO, TOSHIBA and KURITA: (1) property analysis of the slurry before and after the irradiation, (2) observations of volume change of the slurry during the irradiation, and (3) analysis of gas products from radiolysis of aqueous solutions contained in the slurry. It can be noted that according to Compton scattering of photons, average energy of electrons recoiled from Co-60 gamma-ray is about 55% of the incident gamma-ray energy equal to 0.688 MeV, which is between average energies of beta-rays from Sr-90 (0.196) and Y-90 (0.934).

In the present work, radiolysis behavior of simulated carbonate slurry (3) is studied, together with (2) reported by Motooka. The slurry and its treated water at pH = 12 was obtained from KURITA. Concentrations of chloride ion (Cl^-) and suspended solids (SS: $CaCO_3$ and $Mg(OH)_2$) in the slurry were 6,000 ppm and 95 g/L, respectively. Density and viscosity of the slurry at room temperature were 1.06 g/mL and 157 mPa•s, respectively. The slurry was further diluted by the treated water to prepare irradiation samples. For comparison, seawater and pure water were also used.

The sample was filled in a glass vial at a constant volume, sealed with a cap, set in an irradiation room, and irradiated by Co-60 gamma-rays at room temperature and dose rate of 4-6 kGy/h[1]. Dosimetry was made with aqueous $K_2Cr_2O_7$ solution and CTA film dosimeters. Absorbed dose of the sample, which can be separated to those of aqueous solution and suspended solids, was sequentially estimated from those of the dosimeters, assuming that mass energy-absorption coefficient[2] is proportional to absorbed dose.

After the irradiation, gas was sampled at a constant volume from the headspace of vial, and concentration of hydrogen molecule (H_2) and carbon dioxide (CO_2) in the gas was measured by GC with TCD detector. Concentrations of hydrogen peroxide (H_2O_2) and dissolved oxygen (O_2) in the sample solution were also measured by iodine coulometric titration method and by spectrometric analysis (contactless O_2 sensor with optical fiber and dye), respectively.

Gas products of water radiolysis in the slurry could be considered to be H_2, O_2 and CO_2: H_2 is formed as one of the primary products, O_2 by thermal decomposition of the primary product of H_2O_2 and CO_2 from dimerization of secondary products of carbonate radical ($\bullet CO_3^-$)[3]. In the experiments, H_2 and O_2 (<10% of the H_2 amount) were observed but not CO_2. No observation of CO_2 indicates its dissolution to aqueous solution ($CO_2 + H_2O = H_2CO_3$) in the slurry. It was confirmed by simple experiments of standard CO_2 gases contacting with aqueous solutions in sealed vials. Thus H_2 was found to be the main gas products in the slurry.

Figure 1 shows dependence of the observed yield of H_2 on the concentration of suspended solid in the slurry. The viscosity of slurry is also indicated in the upper axis. The yields were obtained from the measurement of H_2 before (G_{stat}) and after (G_{total}) stirring the irradiated sample. The G_{total} was larger than the G_{stat}, and was almost constant within the SS concentration range in the experiments. The difference between the G_{total} and G_{stat} indicates retention of H_2 in the slurry without stirred, further leading to the volume change of slurry by higher dose irradiation. These results in the experiments have been applied to quantitative estimation in the volume change of slurry during the irradiation (3), helpful for understanding of the mechanism of overflow. Further experiment is in progress.

References

1) I. Yamagishi, R. Nagaishi, *et al.*, J. Nucl. Sci. Tech., **51**, 1044-53 (2014).
2) J. H. Hubbell and S. M. Seltzer, NISTIR, 5632 (1995).
3) Z. Cai, Y. Katsumura, *et al.*, Nucl. Tech., **136**, 231-40 (2001).

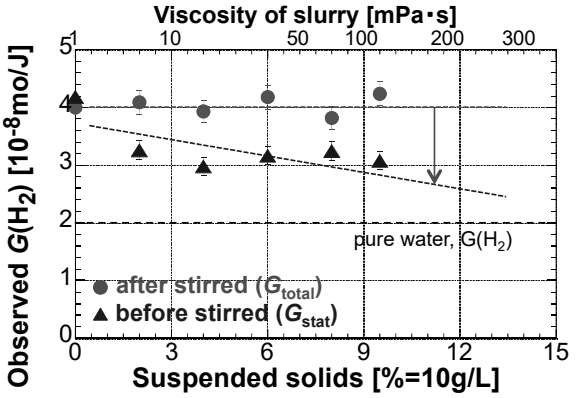

Fig. 1 Dependence of H_2 observed yield on suspended solid concentration in the simulated carbonate slurry. Sample height of 1 cm, air-saturated, room temperature, and absorbed dose rate of 4-5 kGy/h.

1-67 Gas Retention Behavior of Carbonate Slurry under Gamma-ray Irradiation

T. Motooka, R. Nagaishi and I. Yamagishi

Waste Management Division, CLADS, JAEA

Multiple radio-nuclide removal system (MMRSTM: familiar name ALPS) is installed for the purpose of further reducing radioactive materials included in the accumulated water in Fukushima Daiichi Nuclear Power Station. Carbonate slurry containing Sr-90 is generated as a secondary radioactive waste of ALPS and stored in the high integrity containers (HIC).

In 2015 it was reported that radioactive water was detected around the outer periphery of a HIC hatch during regular inspection [1]. Hydrogen gas was also detected inside the HIC. Based on these findings, it was assumed that radiolytic gas bloated in the slurry and raised the water level in the same time, causing the water leak through the upper section of the HIC.

To study the mechanism of slurry bloat inside the HIC, we conducted Co-60 gamma-ray irradiation test using a simulant of the carbonate slurry in the HIC. Water and slurry levels were recorded by visual observation at prescribed time intervals. The white simulated carbonate slurry was provided by Kurita Water Industries Ltd. Its solid suspension concentration was 95 g/L (design value of ALPS:150 g/L). Test sample was a quartz tube with 20 mm diameter filled with the 10 mm height of slurry, and it was irradiated at a dose rate of 8.5 kGy/h for 48 hours (design value of ALPS: max. 2,000 kGy/10 y). The total dose was about 410 kGy. The dose rate was determined by PMMA dosimeter.

Figure 1 shows photographs of test sample before and during the irradiation up to 44 hours, and the non-irradiated test sample after 120 days. We observed the maximum water level rise of approximately 10 mm, many bubbles in the slurry and supernatant liquid, while we observed little formation of supernatant liquid at non-irradiation condition until 120 days. During 44 hours irradiation, the interfacial irregularity between the white carbonate slurry and supernatant liquid was appeared. It should be resulted from the bubble transportation from slurry to liquid. Figure 2 shows gas retention behavior in the sample. It was considered that bubbles might be accumulated and the volume of bubbles increased, and then a part of the bubbles moved to liquid phase.

These results indicated that the water level rise under gamma-ray irradiation was followed by the volume expansion caused by the gas generation by radiolysis, the gas retention in the carbonate slurry, and the formation and increase of supernatant liquid.

We could conclude that the volume expansion related in the radioactivity of carbonate slurry contributed to the slurry bloat inside the HIC.

Reference

1) www.meti.go.jp/english/earthquake/nuclear/20150430-e.pdf.

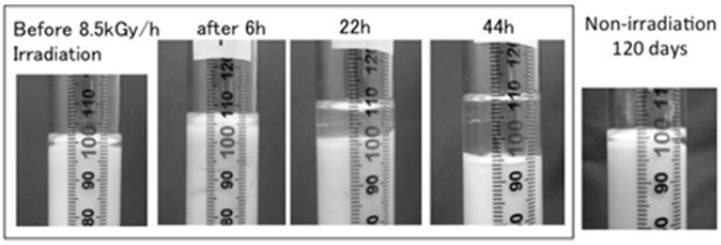

Fig. 1 Photographs of carbonate slurry in a quartz tube before and during Co-60 gamma-ray irradiation and non-irradiation one after 120 days.

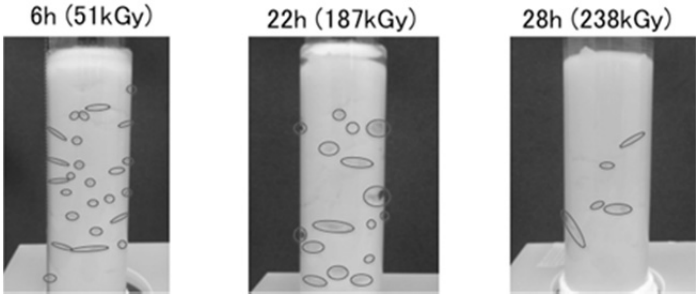

Fig. 2 Bubbles retained in carbonate slurry. Ellipses show the position of bubbles.

1-68 Radiation-Induced Degradation of 2-Chrolophenol in Zeolite/Water Mixture

Y. Kumagai, A. Sugawara, Y. Segawa and M. Watanabe

Nuclear Chemistry Division, NSEC, JAEA

Radiation-induced reactions at solid and water interfaces have attracted interests from studies in nuclear engineering [1]. Recently we observed that irradiation of a zeolite/water mixture induces decomposition of hydrogen peroxide adsorbed on the zeolite at a remarkable yield [2]. The high yield implies a possible application of radiation-induced reactions at interfaces for decomposition of substances of environmental concern in water. In order to explore the application possibility, we examined degradation of organic compounds by irradiation in conjunction with adsorption by zeolites.

Two mordenite-type zeolites having different silicon (Si) to aluminum (Al) ratios in the composition were used in this study; Si/Al = 18 (MOR) and Si/Al = 240 (HMOR). 2-chlorophenol (2-ClPh) was used as a model organic compound. The zeolite/water mixtures containing 2-ClPh were irradiated by γ-rays form a ^{60}Co source. The solid liquid ratio of the mixtures was 2/3 g cm^{-3}. After the irradiation, production of chloride ion (Cl^-) was measured by ion-chromatography as an indicator of degradation degree. Concentration of 2-ClPh was measured by liquid chromatography.

The measurements of Cl^- concentration after the irradiation are shown in Fig. 1. The concentrations of dissolved 2-ClPh before irradiation were 4.4×10^{-4} mol dm^{-3} in the NaMOR mixture and 4.3×10^{-5} mol dm^{-3}, in the HMOR mixture. The results in 4.4×10^{-4} mol dm^{-3} aqueous 2-ClPh solution are also shown for comparison. Higher Cl^- concentrations were measured both in the MOR and HSM mixtures compared to the aqueous solution without zeolites. The high concentrations indicate that 2-ClPh adsorbed on zeolites was decomposed to release Cl^- to aqueous solution in the mixtures.

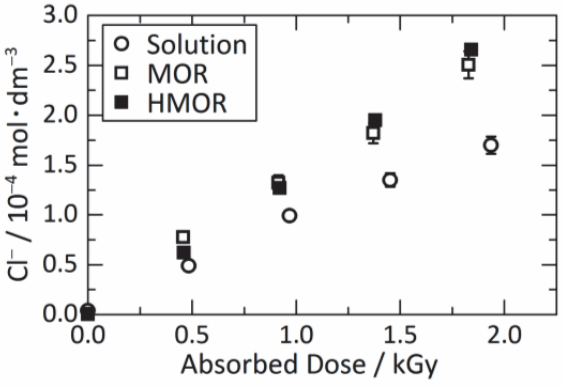

Fig. 1 Concentration of Cl^- in the zeolite mixtures and in aqueous solution after irradiation. The initial concentrations of dissolved 2-ClPh were 4.3×10^{-5} mol dm^{-3} for the HMOR mixture and 4.4×10^{-4} mol dm^{-3} for the MOR mixture and the solution without zeolite.

The adsorption of 2-ClPh was evaluated for unirradiated mixtures. The adsorbed quantity of 2-ClPh on MOR was 8.4×10^{-4} mol kg^{-1}. Meanwhile, the adsorbed 2-ClPh on HSM reached 2.2×10^{-1} mol kg^{-1} despite the lower concentration in solution. The significant adsorption by HSM is due to its hydrophobic property owing to the high Si/Al ratio.

Radiation chemical yields of Cl^- were calculated in order to compare the degradation efficiencies. The absorbed energy by zeolites was taken into account in the calculation, because the degradation of adsorbed 2-ClPh is expected to be induced by the energy deposition on zeolites. The Cl^- yields are shown in Fig. 2. The yields in MOR mixture were comparable to those in aqueous solution. For HMOR, relatively high yields were obtained. The yields in the HMOR mixtures were as high as those in aqueous solution containing an order of magnitude higher 2-ClPh concentrations. The degradation of adsorbed 2-ClPh is expected to be promoted because of high adsorbed quantities on HMOR. The results show that the degradation efficiency of dilute 2-ClPh in water can be improved using zeolites having high performances for adsorption.

References

1) S. Le Caër, Water, **3**, 235-53 (2011).
2) Y. Kumagai, Radiat. Phys. Chem., **97**, 223-32 (2014).

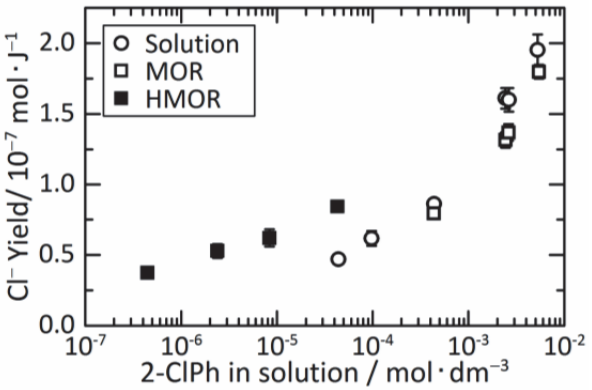

Fig. 2 Yields of Cl- in the zeolite mixtures and in aqueous solution as a function of dissolved 2-ClPh concentration.

1-69

Microfabrication of Biocompatible Hydrogels by Proton Beam Writing

N. Nagasawa [a)], A. Kimura [a)], A. Idesaki [a)], N. Yamada [b)], M. Koka [b)], A. Shimada [c)], T. Satoh [b)], Y. Ishii [b)] and M. Taguchi [a)]

[a)] Department of Advanced Functional Materials Research, TARRI, QST,
[b)] Department of Advanced Radiation Technology, TARRI, QST,
[c)] Department of Radiation-Applied Biology Research, TARRI, QST

Recently, biocompatible materials are expected to be applied widely in stem cell technology and biomedical engineering fields. Hydrogel has been expected as a biocompatible scaffold which supports to keep an organ shape during cell multiplying in regenerative medicine [1]. Therefore, it is important to understand a surface microstructure (minute shape, depth of flute) and a chemical characteristic of the hydrogel affecting the cell culture. On the other hand, proton beam writing (PBW) technique has a capability to fabricate next-generation micro-devices and micro-bio devices [2]. High energy ionizing radiation has been used for a modification and functionalization of polymers by cross-linking and scission [3]. We investigated the effect of proton beam irradiation on biocompatible polymeric materials such as water-soluble polysaccharide derivatives (hydroxypropyl cellulose (HPC), methyl cellulose (MC), hydroxypropylmethyl cellulose (HMPC), carboxymethyl cellulose (CMC) and carboxymethyl chitosan (CM-chitosan)) and water-soluble synthetic polymers (poly(vinyl alcohol) (PVA) and poly(ethylene oxide) (PEO)).

The polymeric materials were dissolved in pure water thoroughly by a planetary centrifugal mixer, and then incubated at 4 °C for more than a day in order to prepare the homogeneous paste. A 1 mm-thick paste sheet was formed on a polyethylene terephthalate (PET) film (50 μm thickness) by a pressing process. A 3 MeV proton beam from the single-ended accelerator was focused to about 1 μm in diameter on the surface of the paste at TIARA facility. The beam current was set at 10 pA. The HPC paste was horizontally irradiated with the proton beam through the PET film in the atmospheric condition as shown in Fig. 1. After the exposure to the proton beam, the samples were adequately rinsed with deionized water. The residual product was obtained by the radiation-induced crosslinking of HPC. Note that the pastes of the above-mentioned materials became insoluble hydrogels by the crosslinking under the conventional ionizing radiations such as γ-rays and electron beams [4,5]. The crosslinking was also induced by the proton beam irradiation. The HPC hydrogel on the PET film was observed with a laser microscope (VK-X250, Keyence) and its thickness was evaluated at approximately 10 μm. The HPC hydrogel was microfabricated on the PET film as shown in Fig. 2. The resolution of the microfabrication of HPC hydrogel was 20 μm. MC, HPMC, CMC, CM-chitosan, PVA, and PEO were also gelled and microfabricated by using the PBW technique. Cell adhesion and proliferation on the microfabricated hydrogels were also confirmed by observing the HeLa cell with an optical microscope after incubation at 37 °C under a 5% CO_2 condition. These results indicate that the PBW technique is a promising method for the microfabrication of biocompatible materials for biological and medical applications.

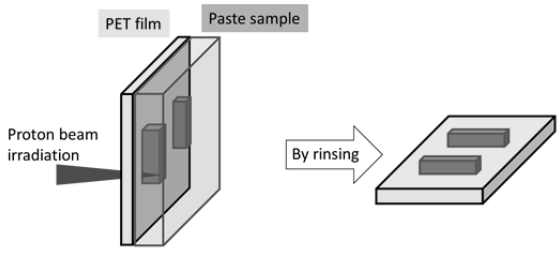

Fig. 1 Microfabrication of hydrogels by the proton beam writing technique.

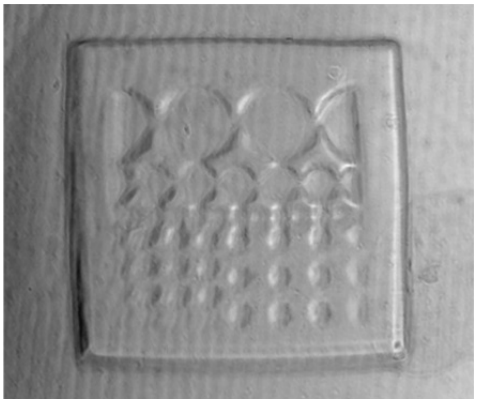

Fig. 2 Optical microscope image of the microfabricated HPC hydrogel on the PET film by use of the proton beam writing technique.

References

1) D. E. Discher *et al.*, Science, **324**, 1673-77 (2009).
2) F. Watt *et al.*, Mater. Today, **10**(6), 20-29 (2007).
3) J. M. Rosiak *et al.*, Radiat. Phys. Chem., **55**, 139-51 (1999).
4) F. Yoshii *et al.*, Nucl. Instrum. Meth. Phys. Res. B, **208**, 320-24 (2003).
5) F. Yoshii *et al.*, Radiat. Phys. Chem., **55**, 133-38 (1999).

1-70

Crosslinking Mechanisms of Polysaccharides in Ionic Liquids by Ionizing Radiation

A. Kimura, N. Nagasawa, A. Shimada and M. Taguchi

Department of Advanced Functional Materials Research, TARRI, QST

Natural polysaccharides have been recognized to be the most promising materials in recent years because of outstanding properties such as high biocompatibility and biodegradability, and procurability from animals and plants on the Earth. So far functional materials have only been produced by using radiation crosslinking technique either from polysaccharide derivatives or using crosslinking reagents. Some polysaccharides are, however, radiation degradation type polymers and have poor solubility in water and organic solvents as well as low chemical reactivity. These limitations could be circumvented by use of specific solvents such as room temperature ionic liquids (RTILs)[1]. In the previous study, we have produced the chemical gels without any crosslinking reagent by γ-ray irradiation from neat cellulose in the carboxylate-based RTILs under humid conditions for the first time[2]. The yield of the cellulose chemical gel increased with a water content in 1-ethyl-3-methylimidazolium(EMI)-acetate. The radiation induced crosslinking of cellulose in RTILs is, however, not made clear, and it is important to clarify its reaction mechanism under humid condition. The yield of hydroxyl(OH) radical changing with water content in RTILs was investigated by use of the scavenging method. Fluorescence and x-ray photoelectron spectroscopy (XPS) analyses of the cellulose gel were carried out to investigate chemical structures and components in detail. Moreover, chitin gels were also produced in RTILs by ionizing radiation[3].

Cellulose was dissolved in EMI-acetate or 1, 3-Dibutylimidazolium (DBI)-acetate with water contents in the range from 0 to 34 wt%. The DBI-acetate has been reported as highly fluorescent RTILs [4]. Chitin was dissolved in 1-butyl-3-methylimidazolium (BMI)-chloride. The γ-ray irradiations of the polysaccharide solutions were carried out at doses in the range 5-100 kGy. XPS measurement was carried out using scanning XPS microprobe, and peaks of C(1s), N(1s), and O(1s) were fitted with Gauss-Lorentz and Shirley method.

Radiation chemical yields of the OH radicals from water in RTILs were estimated by the scavenging experiments using phenol. The *G*-value of the OH radical formation (sum of *G*-values of OH-adducts) increased from 0.002 to 0.043 in the range of water content from 2 to 34 wt%. The OH radical reacts with cellulose in EMI-acetate under humid condition more than 18% of water content without being all scavenged by EMI-acetate because of the decrease in the concentration of EMI-acetate. Moreover, the production of the cellulose gel is considered to be achieved by preparing a paste-like solution composed of water and RTILs as a reaction field for the radiation crosslinking.

Emission spectrum of DBI-acetate with a maximum wavelength at 395 nm was detected when excited at 323 nm. The 20 wt% cellulose DBI-acetate solution with a water content of 18 wt% was irradiated with γ-rays at a dose of 10 kGy under humidity-controlled air conditions to produce the cellulose gel with the yield of 20%. Emission and excitation spectra of the crosslinked cellulose gel after the washing and drying were obtained as shown in Fig. 1. Emission spectrum of the crosslinked cellulose gel with a maximum wavelength at 415 nm was detected when excited at 323 nm, while that of neat cellulose was not. These results suggest that DBI-acetate is also incorporated in the cellulose gel. The fluorescence spectrum of the cellulose gel was red-shifted about 20 nm from that of original DBI-acetate, indicating that chemical structure of butyl substitutes in DBI-acetate changed.

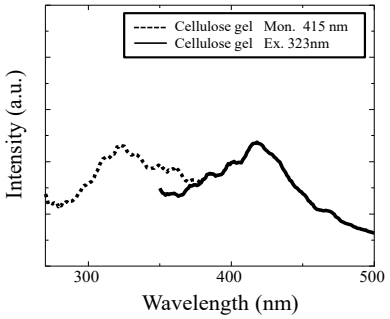

Fig. 1 Fluorescence spectra of the crosslinked cellulose gel. Dotted line : Excitation spectrum monitored at 415 nm, Solid line: Emission spectrum excited at 323 nm.

Chemical structure change of cellulose in EMI-acetate by γ-ray irradiation was also investigated by FT-IR measurement but the spectra before and after irradiation were almost the same. This result indicates that most of cellulose keeps original molecular structure even after the irradiation. The N(1s) peak on XPS spectrum was observed for the cellulose gel but not for neat cellulose. The alkylimidazolium groups of EMI-acetate would act as the cross-linking agents of cellulose, without changing their chemical structures. The chitin gel was also obtained in BMI-chloride by γ-ray irradiations, and its gel fraction increased with the dose and reached 80% at 80 kGy.

References

1) Y. Fukaya *et al.*, Green Chem., **10**, 44 (2008).
2) A. Kimura *et al.*, Radiat. Phys. Chem., **103**, 216 (2014).
3) A. Kimura *et al.*, Radiat. Phys. Chem., **124**, 130 (2016).
4) X. Chen *et al.*, J. Phys. Chem. B, **115**, 1524 (2011).

1-71

Grafted Polymer-based Cationic Catalyst for Biodiesel Fuel Production

Y. Ueki, S. Saiki, H. Hoshina and N. Seko

Department of Advanced Functional Materials Research, TARRI, QST

Waste cooking oils to be raw materials of a biodiesel fuel (BDF) contain two kinds of oil components such as triglycerides (TGs) and free fatty acids (FFAs). In our previous research, we developed a grafted polymer-based anionic catalyst for BDF production from TGs[1,2]. In order to completely convert waste cooking oils into BDF, another kind of catalyst which can produce BDF from FFAs is also necessary. In esterification of FFAs, protons (H^+) function as actual catalytic elements. The objectives of this study are to synthesize a new grafted polymer-based cationic catalyst for BDF production from FFAs and to evaluate its catalytic performance through the esterification of FFAs and alcohol.

The cationic catalyst having protons (H^+) was synthesized by radiation-induced emulsion grafting in the following procedures. Polyethylene nonwoven (PENW) fabric, of which the fiber diameter was 13 μm, was used as a trunk polymer. Firstly, the PENW fabric was irradiated with an electron beam (100 kGy) at the electron beam facility in TARRI. Then, the irradiated PENW fabric was reacted with a deaerated monomer emulsion, which was composed of 3 wt% *p*-ethyl styrenesulfonate (EtSS), 0.3 wt% polysorbate 20 (Tween 20), 92.7 wt% deionized water and 4 wt% *n*-butanol, in a glass ampoule for 4 h at 40 °C. After grafting, the EtSS-grafted fabric was treated with 1 M NaOH solution containing 50 vol% ethanol and 50 vol% deionized water for 2 h at 80 °C, to saponify the ester groups of the EtSS-graft chain. Furthermore, the saponified EtSS-grafted fabric was treated with 0.5 M HNO_3 aqueous solution for 24 h at 25 °C, to immobilize the protons onto the EtSS-graft chain. By these saponification and protonation processes, the terminal portions of the EtSS-graft chain were converted into the sulfonic acid groups (SO_3H), and the polymer matrix functions as a scaffold to immobilize the protons. The SO_3H density of cationic catalyst could be controlled by the grafting yield and the saponification yield. The maximum SO_3H density of cationic catalyst was 3.2 mmol-SO_3H/g-catalyst. Especially, it was found that the grafting yield was improved by the addition of small amounts of alcohol to the EtSS emulsion, and the grafting yield with added 4 wt% *n*-butanol was about 2 times higher than that without added alcohol (grafting yield: EtSS emulsion with *n*-butanol: 270%, EtSS emulsion without alcohol: 120%). However, when the *n*-butanol was added excessively, micelles in EtSS emulsion dissolved, and as a result, the grafting yield with added 15 wt% *n*-butanol was decreased than that without added alcohol (Fig. 1).

The catalytic performance of the synthesized grafted polymer-based cationic catalyst was evaluated by batchwise esterification of oleic acid (purity: 80%), which was one of FFAs, and ethanol. The esterification was performed by adding grafted polymer-based cationic catalyst (weight: 0.65 g, capacity: 3.2 mmol-SO_3H/g-catalyst) in a homogenous reaction solution (oleic acid: 0.28 g, ethanol: 9.2 g, decane (solubilizing solvent): 5.0 g) at desired temperature. The molar ratio of oleic acid to ethanol was fixed at 1:200. As shown in Fig. 2, before esterification, only oleic acid peaks were observed in the retention time range of 3-5 min. As the esterification continued, the oleic acid peaks were reduced and, on the other hand, BDF peaks were gradually appeared in the retention time range of 5-7 min. This result confirms that the grafted polymer having protons functions as a cationic catalyst for BDF production from FFAs. The BDF production speed depended on the esterification temperature, and the esterification times required to convert 90% of the initial FFAs into BDF were 27, 12, 8 and 4 h at 50, 60, 70 and 80 °C, respectively.

References

1) Y. Ueki *et al.*, Int. J. Org. Chem., **1**, 24-29 (2011).
2) Y. Ueki *et al.*, Int. J. Org. Chem., **4**, 91-105 (2014).

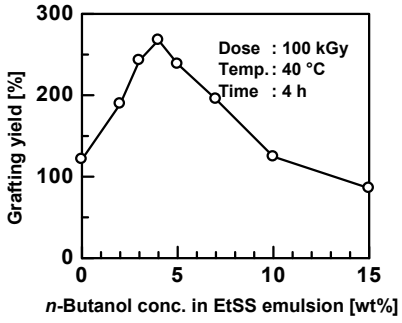

Fig. 1 Effect of *n*-butanol concentration in EtSS emulsion on grafting yield.

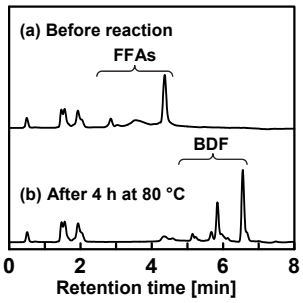

Fig. 2 BDF production from FFAs using grafted polymer-based cationic catalyst.

1-72

A New Modification Method for Introducing of Functional Unit and Its Practical Application

T. Hosoe [a)], S. Muraki [a)], M. Nakano [a)], H. Amada [b)], H. Hoshina [b)] and N. Seko [b)]

[a)] Kurashiki Textile Manufacturing. Co., Ltd,
[b)] Department of Advanced Functional Materials Research, TARRI, QST

The filtration media to remove metal ions dissolving in liquids has been developed by radiation graft polymerization technology. Previously, to introduce a function group on polymeric materials an organic solvent, i.e., toxic, flammable, hazardous materials, which was environmental unfriendly, was used. However, to change the solvent is not easy, because it is subject to degenerate a reaction efficiency, dramatically. In this study, we have been developed a new and environmental-friendly method by using a water based solvent which was made by emulsifying with a surfactant in order to reduce the organic waste. Based on the development, the filtration media is made and processed into a type of cartridge and capsule unit for practical application.

環境中、工業用各種液体中に溶存しており、不純分となる金属イオンを除去する目的で、量研機構との共同研究成果の一環として、高密度ポリエチレン繊維からなる不織布に放射線グラフト重合技術を適応し、金属イオン捕集材（以下、「捕集材」という）の新しい製造基礎技術を開発した。捕集材合成は 2 段階の工程となっており、1 段階目は不織布繊維に窒素雰囲気下で電子線を50 kGy 照射し、モノマーとしてグリシジルメタクリレート（GMA）をグラフト重合させる工程で、2 段階目は得られたグラフト不織布のグラフト鎖の GMA 末端のエポキシ基部分を開環する際に官能基を導入・反応させる工程となっている。

1 段階目の合成に関しては特許第 467001 号「エマルショングラフト重合法とその生成物」に示される様に、界面活性剤を用いることにより、GMA や他の有機溶剤使用量低減や廃液の低減が実現できており、環境にやさしい反応液処方が確立できた。2 段階目の合成に関しては、従来は、官能基となる薬剤を有機溶剤に溶かしたものを反応液として使用することが主流となっており、有機溶剤の毒性・人体への影響・引火性等を考慮した、環境にやさしい反応液処方の確立が望まれてきた。そこで、有機溶剤系処方を環境負荷低減、安全性の向上を考慮した、環境にやさしい処方へ変更するため、界面活性剤を利用した水系新処方の検討を行った。

環境中、工業用各種薬液中で不純分と考えられている金属イオンとして、ホウ素・ヒ素がある。ホウ素・ヒ素の除去に適した官能基として *N*-メチル-D-グルカミン（NMDG）があるが、NMDG を導入・合成する処方として 1,4-ジオキサンを溶媒として用いる反応液処方が主流であった。一方、1,4-ジオキサンは PRTR 法で定められている発がん性物質の対象となっており、引火点も 12 °C と低いため、廃液などの生成による環境負荷や作業者の健康面・作業環境の安全への配慮といった点で工業化(量産化)時の取扱いが難しい溶媒であることから、NMDG を導入・反応する溶媒を界面活性剤として①パーフルオロアルキルペタイン（LV）、②ソルビタンモノラウレート（Span20）、③ラウリル硫酸ナトリウム（SDS）を利用した水系で作製することを試みた。①、②・③界面活性剤の混合比率を変えた界面活性剤含有水溶液に NMDG を 10 wt%で溶解した反応液を作製し、GMA をグラフト重合した不織布を反応液中に浸漬し、80 °C で所定時間反応させることにより、NMDG を官能基として導入・反応（以下、転化）した捕集材を得た。得られた捕集材の転化量を Table 1 に示す。

転化率は下記式で算出することができる。

転化量（mol/kg）＝1,000[(W_2 - W_1) / (M_W × W_2)]

W_1: 転化反応前の不織布重量、W_2: 転化反応後に得られた捕集材の乾燥重量、M_W : NMDG 分子量（195.21）。

Table 1 NMDG inversion ratio by difference of formulation.

界面活性剤含有水溶媒（重量比）	反応条件	転化量（mol/kg）
水 : 1,4-ジオキサン = 10 : 90	80 °C, 1 h	2.28
水 : LV = 60 : 40	80 °C, 5 h	1.33
水 : Span20 : SDS = 90 : 5 : 5	80 °C, 5 h	2.16

現在、新処方により捕集材の工業生産を実施し、得られた捕集材を充填したカートリッジと、そのカートリッジをポリエチレン容器の中に封入したカプセルフィルターの 2 種類の形態をラインナップし、市場に紹介している（Fig. 1）。

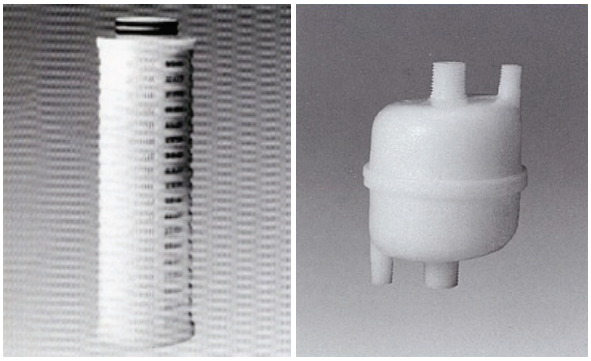

Fig. 1 The photograph of cartridge filter (left) and capsule filter (right).

1-73

Research for Antivirus Material with Electron Beam-Induced Graft Polymerization

T. Hayata [a)], E. Takahashi [a)], Y. Jikihara [a)], T. Nakayama [a)], Y. Ueki [b)], N. Kasai [b)] and N. Seko [b)]

[a)] R & D Department, NBC Meshtec Incorporation,
[b)] Department of Advanced Functional Materials Research, TARRI, QST

Although there is an increasing threat of infection by viruses, there is insufficient technology to prevent transmission of infection when workers take off protective clothing after decontamination work of the virus. We focused on free sulfonic acid groups, in order to develop antiviral materials that can be applied to cloth. In this study, we have applied the technique of emulsion graft polymerization, to synthesize a particulate graft polymer with free sulfonic acid groups, and evaluated the anti-viral effect.

鳥インフルエンザ、口蹄疫など、ウイルスによる感染の脅威が高まってきているが、ウイルス除染作業時の防具等から二次感染を防止する技術はほとんど構築されていない。筆者らは、これまでに感染リスク低減のための抗ウイルス材とそれを応用した様々な抗ウイルス商品開発やウイルス制御技術の開発を進めてきた。本研究では、これら商品の付加価値を高めるため、量子科学技術研究開発機構（以下、量研機構）の保有する放射線グラフト重合の手法と、ウイルス制御技術とを相互に活用することで、ウイルスを不活性化できる新たな材料開発を目的とした。

本研究で注目したのは遊離型スルホン酸基である。NBC では既に遊離型スルホン酸基が高い抗ウイルス性を有することを見出している[1)]。この遊離型スルホン酸基を有する材料を不織布や織物等の繊維構造体に塗布できる形態にすることで、衣類や寝具、或いはカーテンなどの様々な製品に抗ウイルス性を付与できることが期待できる。本研究では、塗布型の抗ウイルス性を有する材料を開発することを目的に、グラフト重合によりナノサイズの粒子状のスルホン酸基を有する高分子材料の作製を試みた。

ナノサイズのグラフト重合体の合成は、量研機構にて開発されたエマルショングラフト重合法を応用した[2)]。グリシジルメタクリレートとドデシル硫酸ナトリウムを用いた O/W 型エマルションに高崎量子応用研究所にて 2 MeV、30 kGy の電子線照射を行った。電子線照射後のサンプルに亜硫酸ナトリウムを加えてスルホン基を導入し、さらに、塩酸を加えて遊離型スルホン酸にし、その後、透析処理にて不純物を除去し、遊離型スルホン酸基を有するグラフト重合体（H-SGP）の懸濁液を得た。得られたグラフト重合体は、走査型電子顕微鏡（SEM）により観察し、粒子径は動的光散乱法で測定した。また、その抗ウイルス効果は、インフルエンザウイルス A/H3N2 を用いて試験した。

Figure 1 に、電子線グラフトエマルション重合後にスルホン酸基を導入した重合体の SEM 写真を示した。重合体は球状であり、また、動的光散乱法で得られた粒子径は平均で 100 nm であった。次に、遊離型スルホン酸基を有するグラフト重合体の懸濁液とインフルエンザウイルスの懸濁液を混ぜ合わせ、60 分後の感染価（Titer; 感染性を持つウイルス粒子数）を測定した。その結果、懸濁液中に約 0.03 wt% の H-SGP が存在すると、ウイルス感染価は 99.99%以上減少することが確認された（Fig. 2）。また、このウイルスを含む懸濁液の pH は 7.3 であり、中性領域下でも高い抗ウイルス性を有することから、衣類や寝具、白衣や防護服などの作業着やスプレー剤など、様々な用途展開が期待できる。

References

1) Japan patent JP2015-199718.
2) N. Seko *et al.*, Radiat. Phys. Chem., **79**, 22-26 (2010).

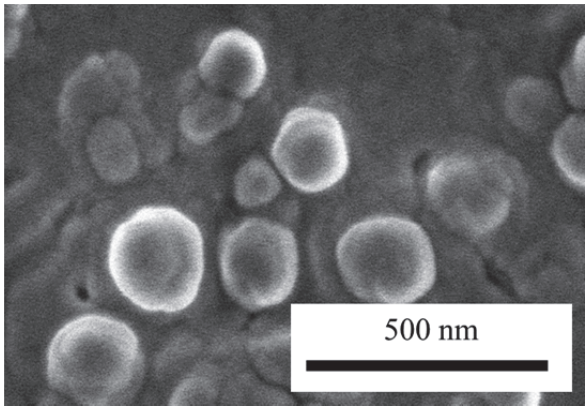

Fig. 1 SEM image of H-SGP that was obtained by electron beam-induced graft polymerization.

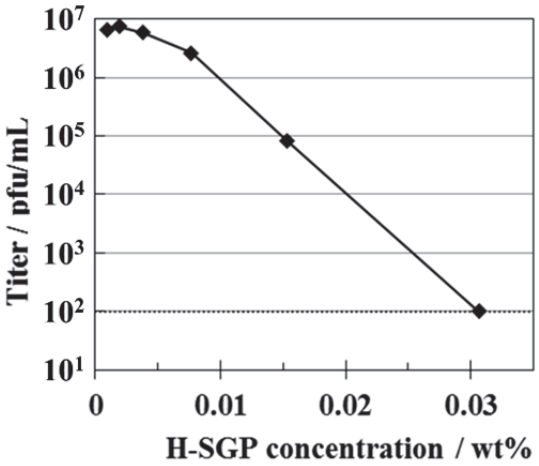

Fig. 2 The relationship between H-SGP and virus titer. Initial titer is 6.3×10^6 pfu/mL. The dotted line indicates the detection limit of 100 pfu/mL.

1-74 Surface Modification of PA66 by Radiation Grafting

T. Makabe [a], H. Saito [a], K. Masubuchi [a], H. Sando [a], N. Mizote [a],
Y. Ueki [b] and N. Seko [b]

[a] Mitsuba Corporation,
[b] Department of Advanced Functional Materials Research, TARRI, QST

In this study, lipophilic alkyl methacrylate monomers were grafted on a surface of PA66 substrate by previous electron beam irradiation. The hydrophobicity, lipophilicity and frictional property of the surface-modified PA66 were measured in order to research the effects of the alkyl chain length of the monomers on their characteristics. From the measurement results, it was found that the surface modified PA66 substrates had hydrophobicity and lipophilicity. Their characteristics increased with increasing alkyl chain length. Furthermore, the coefficient of friction decreased compared to the initial substrate.

本研究では摺動用樹脂材の油潤滑性の向上を狙いとして、電子線グラフト重合による樹脂表面への親油性モノマーのグラフトおよびその潤滑性評価を行った。

樹脂基材として、PA66（ナイロン 66）シートを用いた。PA66 シートを PE 袋に入れ、袋内を窒素ガスで充填した後、加速電圧 250 kV、電流 2.3 mA、吸収線量 200 kGy の条件で電子線照射を行った。その後、親油性モノマーであるメタクリル酸アルキルを窒素充填したアンプル管内で接触させ、前照射法にてエマルショングラフト重合をした。この時のモノマー溶液は、モノマー5 wt%、水 94.5 wt%、界面活性剤（Tween20）0.5 wt%、反応時間は 24 h、反応温度は 40 °C とした。また、メタクリル酸アルキルのアルキル基は、エチル、ブチル、ヘキシル、ドデシル基をそれぞれ使用した。これらの調製したサンプルを用いて水、オイルの接触角測定、往復摺動型摩擦試験機によるオイル存在下での摩擦係数の測定を行った。

Figure 1 に未処理および電子線照射表面改質後 PA66 の FT-IR スペクトルを示す。FT-IR は、ゲルマニウムプリズムを用いた ATR 法にて測定した。表面改質後の PA66 には、1,730 cm^{-1} にカルボニルのピークが認められた。この結果により、メタクリル酸アルキルは電子線照射表面改質により PA66 基材とグラフト重合していることがわかった。また、メタクリル酸ドデシルのカルボニルピーク強度が低いことから、メタクリル酸ドデシルの反応性は他と比較し低いことがわかった。

Figure 2 は電子線表面改質後の水、オレフィン油に対する接触角変化を示したものである。この結果からメタクリル酸ドデシルをグラフトした親油性結果を除き、未修飾のものと比較し、疎水性、親油性ともに向上していることがわかった。また、炭素数の増加に伴い、疎水性、親油性が向上することがわかった。

Figure 3 に電子線表面改質後の摩擦係数の結果を示す。摩擦係数は、往復摺動型摩擦試験機にて、速度 50 mm/s、荷重 10 gf で測定した。圧子は SUS ボール、潤滑剤はオレフィン油を使用した。メタクリル酸エチルでの反応後の摩擦係数には明確な変化が見られなかった。しかし、それ以外の反応では摩擦係数の低下が確認された。また、炭素数の増加に伴い摩擦係数の低下が見られた。

本研究の結果から PA66 に対するメタクリル酸アルキル重合は、共に、疎水性、親油性の向上、摩擦係数の低下が可能であることがわかった。また、メタクリル酸アルキルのアルキル炭素数の増加に伴い、疎水性、親油性が向上、摩擦係数が低下することがわかった。

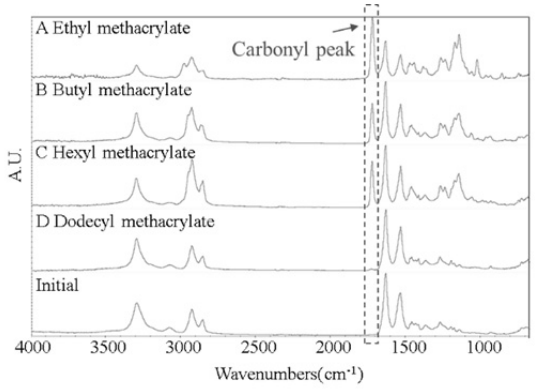

Fig. 1 FT-IR spectra of PA66 after the electron beam irradiation grafting.

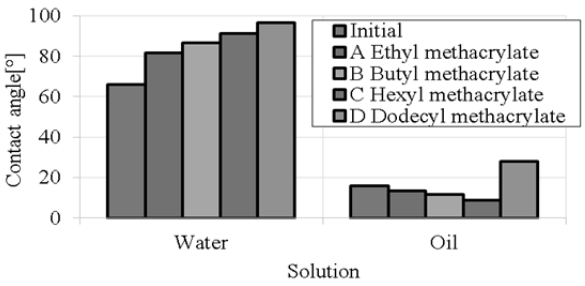

Fig. 2 Contact angle after the electron beam irradiation grafting.

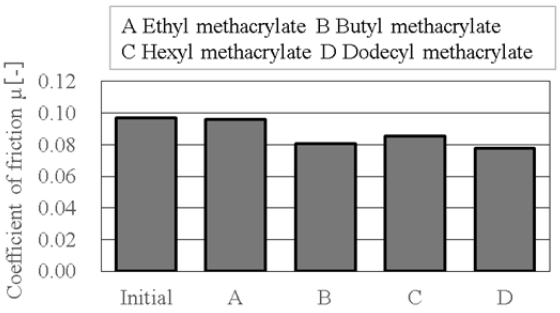

Fig. 3 Coefficient of friction after the electron beam irradiation grafting.

1-75 Vanadium Recovery from Seawater by Radiation-Grafted Adsorbents Based on Polyethylene Terephthalate Fiber

S. Saiki [a], N. Kasai [a], N. Seko [a], T. Oida [b] and K. Yamagishi [b]

[a] Department of Advanced Functional Materials Research, TARRI, QST,
[b] R&D Center, SEIREN Co., Ltd.

Recovery techniques of valuable elements from seawater have been developed for a long time [1-3]. Among these techniques, recovery method by radiation-grafted adsorbents has been known as an effective method with a view point of absorption capacity and adsorption rate. The radiation-grafted adsorbents have ever been synthesized based on polyethylene fiber or nonwoven fabric as a trunk polymer. In the case of polyethylene fiber, only short fiber has been commercially available and the long fiber has not been offered commercially except for special polyethylene fiber of high mechanical strength type due to low melting point. For element recovery from seawater, contact efficiency of adsorbents with seawater is one of important factors and various structures of adsorbents should be developed for improvement of the contact efficiency. Polyethylene terephthalate (PET) is one of typical versatile polymers and can form long fiber. If radiation-grafted adsorbents based on PET fiber can be synthesized, various structures of adsorbents can be produced for element recovery from seawater. However, PET has not been used for trunk materials of radiation-grafted adsorbents due to low degree of grafting. In this study, we tried to synthesize radiation-grafted adsorbents based on PET fiber by radiation emulsion grafting method which has not ever been used for PET, and applied them to vanadium recovery from real seawater.

For synthesis of vanadium adsorbents, amine type and amidoxime type adsorbents were prepared by radiation emulsion grafting method. As for amine type, radiation-grafting of glycidyl methacrylate (GMA) was performed on PET fiber in a reaction solution of o/w emulsion composed of GMA, polyoxyethylene sorbitan monolaurate (Tween20) and water after 100 kGy irradiation, and the degree of grafting reached to around 100% successfully. Amine groups were inserted to epoxy groups of grafted chains with ethylenediamine. In the case of amidoxime type, acrylonitrile (AN) was radiation-grafted on PET fiber in a reaction solution of o/w emulsion composed of AN, polyoxyethylene sorbitan monooleate (Tween80) and water. The degree of grafting of AN showed around 10% and the nitrile groups were converted to amidoxime groups by hydroxylamine.

Vanadium adsorption performance of these adsorbents was evaluated by batch adsorption tests at a laboratory scale. The each adsorbent of 0.04 g were immersed into 40 mL of 100 ppb vanadium aqueous solutions and 100 ppb vanadium seawater solutions. After shaking the solutions at 150 rpm overnight, residual vanadium concentration of the solution was measured by Inductively Coupled Plasma Mass Spectrometer (Agilent 7700, ICP-MS). All results of adsorption rates were more than 90% in the aqueous solutions and more than 20% in the seawater solutions. This showed that the adsorbents could work even in a plenty of coexistent ions like seawater.

These adsorbents were applied to vanadium recovery tests from real seawater. Pieces of adsorbents were immersed for 30 or 90 days in seawater tank that fresh seawater constantly circulated. After taking out samples from seawater, desorption of adsorbed vanadium from the adsorbents was performed with 1 M hydrochloric aqueous solution and 2 M oxalic aqueous solution and the vanadium concentration was measured by ICP-MS. As a result, we confirmed that all adsorbents could absorb vanadium. The amounts of adsorbed vanadium were 4.5 mg-V/kg-ad in 30 days, 10.3 mg-V/kg-ad in 90 days by amine type adsorbents, and 117 mg-V/kg-ad in 30 days, 184 mg-V/kg-ad in 90 days by amidoxime type adsorbents. Amidoxime type adsorbents were more effective for vanadium adsorption in seawater than amine type adsorbents. Energy dispersive x-ray spectroscopy (EDX) image of adsorbents immersed in seawater showed vanadium adsorption along the fiber (Fig. 1) and mean that vanadium were adsorbed uniformly

In conclusion, we successfully synthesized vanadium adsorbents based on PET fiber by radiation emulsion grafting method and elucidated that the synthesized adsorbents were able to collect vanadium from real seawater.

References

1) K. Yoshizuka *et al.*, J. Plasma Fusion Res., **87**, 795 (2011).
2) D. Heitkamp *et al.*, Ind. Eng. Chem. Process Des. Dev., **21**, 781 (1982).
3) N. Seko *et al.*, Separ. Sci. Tech., **39**, 3753 (2005).

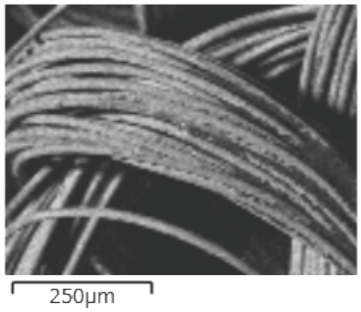

Fig. 1 EDX image of vanadium adsorption on amidoxime type adsorbents.

1-76 Modification of Porous PTFE Filters with Highly Hydrophilic Properties by Radiation Grafting Techniques

J. Chen, N. Kasai, H. Hoshina and N. Seko

Department of Advanced Functional Materials Research, TARRI, QST

To develop a high-performance filter with highly thermal and chemical durability for application in a high temperature and harsh chemical environment, we tried to modify the porous polytetrafluoroethylene (PTFE) filters by radiation grafting of hydrophilic vinyl monomers. Although the unmodified PTFE filters have the excellently thermal and chemical stability, the highly hydrophobic properties prevent them used for the aqueous separation.

Modification of the PTFE filters with hydrophilic properties, such as sodium-etching, laser and plasma treating, have been proposed [1]. However, the resultant filters prepared by these methods are not enough in the term of hydrophilic stability for the long-term application. In this study, three hydrophilic vinyl monomers, styrene sulfonic acid sodium (SSS), acrylic acid (AA), N-vinylpyrrolidone (NVP), along with a crosslinker, ethylene glycol dimethacrylate (1G), were used for the grafting on the porous PTFE filters. The chemical structures of the monomers and crosslinker were showed in Fig. 1.

The PTFE filters were vacuum sealed in a PE/PA plastic bag for the electron beam irradiation at room temperature. After irradiation, the filters were reserved in a refrigerator at -80 °C before use. Under such a low temperature, the radicals generated by the irradiation could be kept living for more than several months. For grafting polymerization, the irradiated filters were immersed in a nitrogen-gas bubbled monomer solution at 60 °C for 24 h. The degree of grafting (DG) was calculated as $100(W_g-W_o)/W_o$, where W_o and W_g were the sample weights before and after grafting, respectively. The Water uptake (Wu) was calculated as $100(W_w-W_d)/W_d$, where W_d and W_w were the sample weights before and after water adsorption.

In addition, as shown in Table 1, the graft polymerization was also carried out using the gamma ray and UV irradiation by simultaneous radiation grafting methods. The styrene-grafted PTFE filters were sulfonated in a chlorosulfonic solution to introduce hydrophilic sulfonic acid groups on the aromatic rings.

For the pre-irradiation grafting methods, the radicals for polymerization were generated only on the PTFE filters. Therefore, the high grafting efficiency and the high monomer utilization can be expected. In Table 1, the PTFE-*g*-poly(AA-*co*-SSS) prepared by electron-beam radiation co-grafting of AA and SSS showed a low DG of 13.3% as well as a low Wu of 15.8%. Such a low DG cannot give the filter adequate hydrophilic properties. On the contrary, by addition of a small amount of 1G, the DG increased to 38.6% under the same grafting conditions. The latter modified filters showed a high Wu of 24.9%. On the other hand, without co-monomer grafting, the single monomer, AA, SSS or NVP, was found to be difficult to graft to the PTFE filters by the pre-irradiation grafting methods.

To graft these monomers individually onto the PTFE filters, simultaneous irradiation of the PTFE filters and monomer solutions was carried out using the gamma ray and UV sources. It was found that the PTFE-*g*-polySSS filters with a lower DG (17.0%) showed a higher Wu (174%). The PTFE-*g*-poly(NVP) filters can reach a higher DG more than 100% using the UV grafting. These results were very useful for the designing and preparation of the hydrophilic filters in the future works.

References

1) K. Tan *et al.*, Macromolecules, **26**, 2832-36 (1993).
2) J. Chen *et al.*, Adv. Mater. Res., **881**, 1157-60 (2014).
3) J. Chen *et al.*, J. Membr. Sci., **256**, 155-61 (2004).

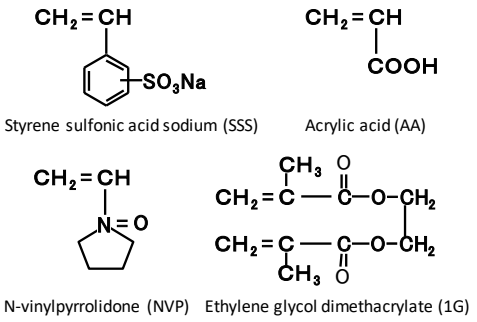

Fig. 1 Hydrophilic monomers and crosslinker.

Table 1 Modification of porous PTFE filters by radiation grafting methods.

Samples	DG (%)	Wu(%)	Note (modification methods)
PTFE-g-poly(AA-co-SSS)	13.3	15.8	EB pre-irradiation, 40 kGy; AA/SSS co-monomer solution; 60°C, 24 h.
PTFE-g-poly(AA-co-SSS)	38.6	24.9	EB pre-irradiation, 40 kGy; AA/SSS co-monomer solution 1% 1G 60°C, 24 h.
PTFE-g-polySSS	17.0	174	Simultaneous gamma irradiation; styrene (100%); 7.5 kGy (1.5kGy/h x 5h); chlorosulfonic acid-sulfonated
PTFE-g-polyNVP	109	745	Simultaneous UV irradiation 25% NVP in water/acetone 40°C for 6 h.

Part II

2. Life Science

2-01 Development of Live-Cell Imaging System for Long-Term Analysis of Bystander Cell Populations Irradiated with Heavy-Ion Microbeams

T. Funayama, Y. Yokota and Y. Kobayashi

Department of Radiation-Applied Biology Research, TARRI, QST

Because heavy-ion deposit dense energy along with its projectile, and the spatial distribution of the ion hit accords with Poisson distribution, the radiation dose on the target cell population become uneven especially in a case of lower but biologically effective fluence radiation. This uneven distribution of deposited energy results to arise a mixture of hit and non-hit cells within a cell sample. In the mixture of hit and non-hit cell within the same sample, biological effects, which are called "bystander effects", are induced on non-hit cells based on transduction of irradiated signal from hit cell. Microbeam, which can target and irradiate specific cells of the population, is a useful tool for analyze bystander effect. Therefore, we had developed the heavy-ion microbeam systems at the facility of Takasaki Ion Accelerator for Advanced Radiation Application of the National Institutes for Quantum and Radiological Science and Technology, and utilized for analyzing heavy-ion induced biological effects [1,2].

Using the system, we have been carried out a lot of analyses of bystander effect for assessing the effect of heavy-ion radiation on biological system [3-10]. However, the responses of bystander effect are not uniformly induced in the cells of the bystander cell population. To clarify the whole picture of the bystander response, we need to analyze individually all cells in the bystander population over the long term after the microbeam irradiation. Thus, we modified the Offline observation system, and developed a live-cell imaging system to carry out a long-term automatic observation of bystander cell populations irradiated with heavy-ion microbeam.

An excitation light for fluorescent microscopy is harmful for living cells. To avoid the exposure effect of the excitation light during long-term observation, it is necessary to minimize the time and the intensity of the light. However, weaker excitation exposure result to weaker fluorescent light from fluorescent-stained live cells. Thus, we introduced high-sensitivity CMOS camera (ORCA-Flash4.0, Hamamatsu-Photonics) to the Offline observation system for obtaining clear image from weak fluorescent light.

During a long-time microscopic observation, a drift of microscopic focus on the sample is inevitable. To correct drifted focus, an automatic focus-control unit (IX81-ZDC2, Olympus) was installed in the PC-controllable inverted microscope (IX81, Olympus) of the Offline observation system. Furthermore, a stage-top cell incubator (Tokai-hit Corp.) was introduced to keep irradiated cell samples with suitable culture condition.

To construct a software for carrying our long-time live-imaging, we first developed a software framework for developing multiple software for multiple experimental purpose from a source code set of the cell targeting software of collimating microbeam system. This software framework supports multiple image acquiring devices with common application interface, which enables on demand switching of multiple cameras during live-imaging observation.

To control automatic focus unit, a functions for drifted-focus compensation was add to the software library for controlling microscope and automatic stages. Finally, a code to control long-term automatic imaging was developed, and, all of them were integrated to establish a long-term bystander imaging system (Fig. 1), which enables long-term observations of all cells in the bystander population individually over a long duration.

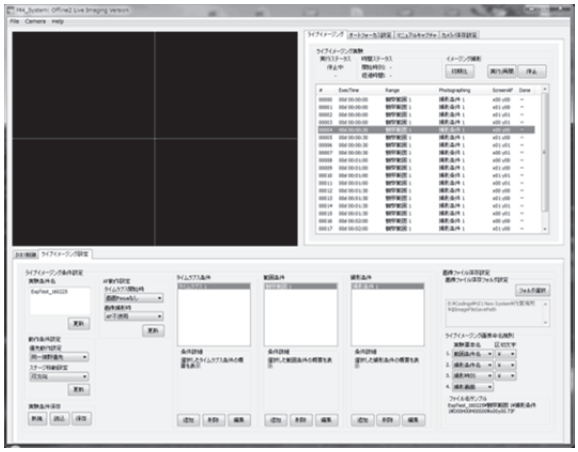

Fig. 1 Screenshot of live-cell imaging software for long-term analysis of bystander cell population.

References

1) T. Funayama *et al.*, J. Radiat. Res., **49**, 71 (2008).
2) T. Funayama *et al.*, JAEA Takasaki Annu. Rep 2013, JAEA-Review 2014-50, 73 (2015).
3) N. Autsavapromporn *et al.*, Int. J. Radiat. Biol., **91**, 62 (2015).
4) M. Tomita *et al.*, Life Sci. Space Res., **6**, 36 (2015).
5) Y. Matsumoto *et al.*, Radiat. Protect. Dosim., **166**, 152 (2015).
6) Y. Yokota *et al.*, Int. J. Radiat. Biol., **91**, 383 (2015).
7) N. Autsavapromporn *et al.*, Radiat. Res., **180**, 367 (2013).
8) Y. Mutou-Yoshihara *et al.*, Int. J. Radiat. Biol., **88**, 258 (2012).
9) C. Fournier *et al.*, Ra et al.diat. Res., **171**, 530 (2009).
10) M. Iwakawa *et al.* Mutat. Res., **642**, 57 (2008).

2-02 Interphase Death Was Related to Growth Inhibition after Gamma-ray and Carbon-ion Irradiation in Human Neural Stem Cells but not in Glioblastoma Cells

Y. Yokota [a)], Y. Wada [a,b)] and T. Funayama [a)]

[a)] Department of Radiation-Applied Biology Research, TARRI, QST,
[b)] Gunma University Graduate School of Medicine

Neural stem cells (NSCs) have been found in the brain and spinal cord areas of various species including adult humans [1,2]. They are self-renewing multipotent cells that primarily differentiate into neurons, astrocytes and oligodendrocytes in the process of neurogenesis. Because it is known that NSCs are severely damaged and neurogenesis is inhibited after X-ray and gamma-ray irradiation, radiation protection of NSCs during cranial irradiation of the patients with brain, neck and head tumors is needed to keep their quality of life. Increasing numbers of the patients have selected carbon-ion and proton radiotherapies because of their well-known better dose distribution. However, there is a limited piece of knowledge on biological responses of NSCs after irradiation of ion beams [3]. The final purpose of this study is to elucidate the effects of ion-beam irradiation to NSCs and of intercellular communications among non-irradiated and irradiated NSCs and tumor cells. Here, we investigated the effects of gamma-ray and carbon-ion irradiation on the growth and interphase death of NSCs and glioblastoma cells.

NSCs derived from human H9 embryonic stem cells and A172 cells derived from human glioblastoma were irradiated with gamma-rays (^{60}Co, LET=0.2 keV/μm) at the Cobalt 60 Irradiation Facilities and with carbon-ion beam ($^{12}C^{5+}$, 18.3 MeV/n, LET=108 keV/μm) at the HY1 port of TIARA. After irradiation, cells were incubated for 72 h and, then, stained with cell-membrane permeable and impermeable DNA-binding dyes to discriminate living and dead cells. The numbers of living and dead cells were measured using a flow cytometer. Growth rates were obtained by dividing the number of total (living+dead) cells after 72 h post-irradiation incubation by that of total cells just before irradiation. Survival rates were obtained as the percentage of living cells.

Growth rates decreased in dose-dependent manners after carbon-ion and gamma-ray irradiation both in NSCs and A172 cells, meaning induction of interphase death and/or reproductive death (Fig. 1). The percentages of living cells were measured to investigate the contribution of interphase death to decrease in growth rates. Survival rates decreased clearly in NSCs after irradiation but not in A172 cells (Fig 2). Our results suggest that growth rates were decreased by different mechanisms in NSCs and A172 cells, and that interphase death and reproductive death are likely main causes in NSCs and A172 cells, respectively. Next, we will investigate apoptosis induction and bromo-deoxyuridine incorporation to elucidate the mechanisms of cell death in more detail in NSCs and A172 cells after gamma-ray, proton and carbon-ion irradiation.

References

1) B. A. Reynolds and S. Weiss, Science, **255**, 1707 (1992).
2) P. Taupin and F. H. Gage, J. Neurosci. Res., **69**, 745 (2002).
3) M. Isono *et al.*, J. Radiat. Res., **56**, 856 (2015).

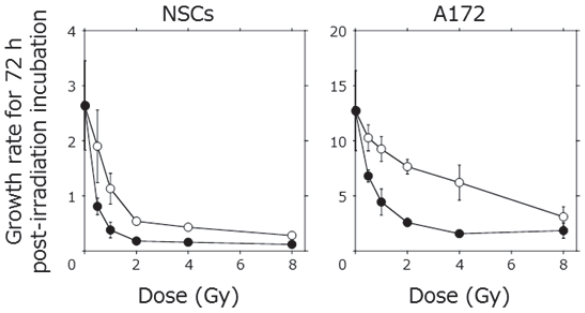

Fig. 1 Dose responses of the growth rates for 72 h post-irradiation incubation. NSCs (left) and A172 cells (right) were irradiated with 0 to 8 Gy of gamma-rays (open circle) or carbon ions (closed circle). Data are presented as the mean ± SD of 6 or more measurements derived from at least 2 independent beam times.

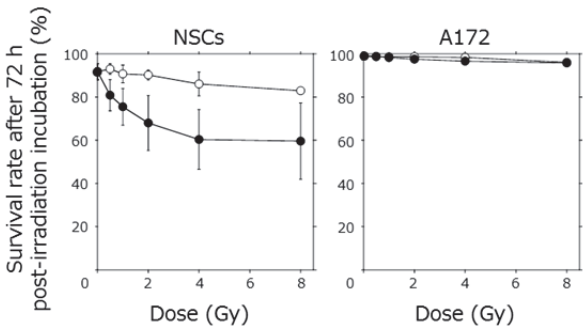

Fig. 2 Dose responses of the survival rates after 72 h post-irradiation incubation. NSCs (left) and A172 cells (right) were irradiated with 0 to 8 Gy of gamma-rays (open circle) or carbon ions (closed circle). Data are presented as the mean ± SD of 6 or more measurements derived from at least 2 independent beam times.

2-03

Analysis of Gamma-ray Induced Bystander Effect between Human Lung Normal and Cancer Cells

H. Ikeda [a, b], Y. Yokota [b], T. Funayama [b], A. Takahashi [a], T. Kanai [a], T. Nakano [a, c] and Y. Kobayashi [b]

[a] Gunma University Heavy Ion Medical Center,
[b] Department of Radiation-Applied Biology Research, TARRI, QST,
[c] Department of Radiation Oncology, Gunma University Graduate School of Medicine

The radiation-induced "bystander effect" is the phenomenon in which unirradiated cells (bystander cells) exhibit effects as a result of signals received from nearby irradiated cells. It was reported that bystander effect was radiosensitive in normal cells [1], and was radioresistance in cancer cells [2]. These results suggested that bystander effect may increase risk for radiotherapy patients. However, bystander effects between normal and cancer cells are unclear.

To clarify the γ-ray-induced bystander effects, we used normal human lung fibroblasts (WI38) purchased from ATCC, and human non-small cell lung cancer cell lines, H1299/wt*p53* (wild-type *TP53*), H1299/m*p53* (mutated *TP53*) and H1299/*neo* (*TP53*-null) provided by Dr. H. Matsumoto (University of Fukui, Fukui, Japan) [3].

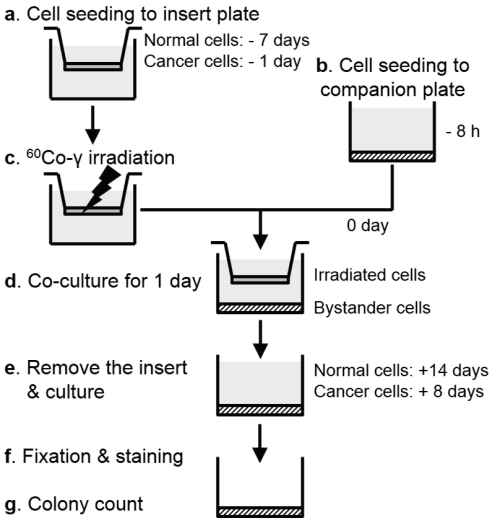

Fig. 1 A schema of experimental schedule.

A schema of this experiment is shown in Fig. 1. Cells were irradiated 0.5 or 5.0 Gy at the ^{60}Co γ-ray irradiation facility in TARRI. After non-contact co-culture between γ-ray irradiated cells and unirradiated cells for 24 h, survival rates of medium-mediated bystander cells were calculated by colony forming assay.

Differently from the conventionally reported result [1], even the survival rate of bystander normal cells co-culture with irradiated normal cells showed no significant differences compared to the rate of control cells (Fig. 2A). In addition, when the combination of irradiated cells and unirradiated cells was reversed, no significant difference

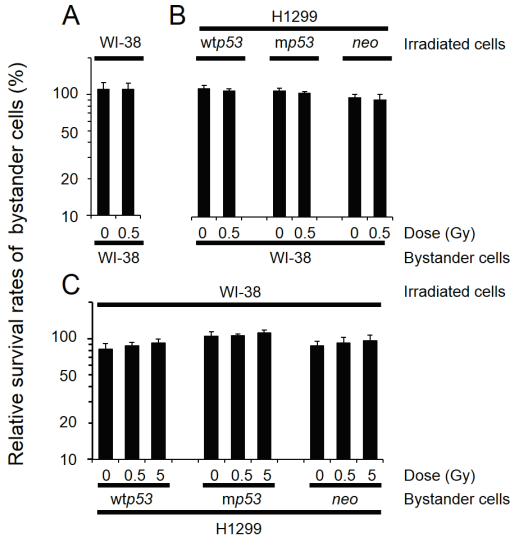

Fig. 2 The survival rates of bystander cells after co-culture with irradiated cells for 24 h. Irradiated cells/bystander cells: normal/normal (A), cancer/normal (B), normal/cancer (C). The columns show relative survival rates (means ± S.E.) of each co-culture group. Survival rates of unirradiated and non-co-culture cells were regarded as 100% (Data were not shown).

was found regardless of *TP53*-gene status (Fig. 2B and C).

Our findings demonstrated that the bystander cell-killing effect was not induced between different type cells in these experimental conditions. In a similar experiment using co-culture systems, it was reported that cancer (chondrosarcoma) cells could release bystander stimulations but could not develop bystander responses by observing the amount of micronucleus formation [4].

These data may explain that it is not necessary to consider risks for radiotherapy patients by γ-ray-induced bystander effects. Further research will probably be necessary in the future.

References

1) Y. Yokota *et al.*, Int. J. Radiat. Biol., **91**, 383 (2015).
2) C. Shao *et al.*, Radiat. Environ. Biophys. **42** 183 (2003).
3) Z. H. Jin *et al.*, Int. J. Radiat. Oncol. Biol. Phys., **59**, 852 (2004).
4) M. Wakatsuki *et al.*, Int. J. Radiat. Oncol. Biol. Phys., **84**, 103 (2012).

2-04 Effects of High Concentration Verteporfin and Ion Beams on the Expression of p53 in Human Cultured Retinal Endothelium

K. Akeo [a, b], T. Funayama [c], Y. Kobayashi [c] and Y. Akeo [a]

[a] Akeo Eye Clinic, [b] Keio University School of Medicine,
[c] Department of Radiation-Applied Biology Research, TARRI, QST

Repeated applications of verteporfin therapy 6 mg/m^2 of body surface area (7.5 μM in a 35 mm Petri dish) were clinically used for photodynamic therapy (PDT) in case of intravenous injection of verteporfin. Therefore we have been carried out experiments to evaluate the effect of verteporfin of this dose to the human retinal endothelium cell (REC). In the previous report [1], we treated human REC with verteporfin of higher concentration (116 μM) than the clinical dose (7.5 μM), and evaluated the effects on the transcription of total RNA *in vitro*. High concentration verteporfin significantly damaged transcription process of RNA in human REC *in vitro*. Moreover, the ion beam irradiation to the human REC treated with verteporfin affect the time dependent change of RNA transcription, and the different ion species (Ne, C, and He) result to different time course decay of the amount of RNA.

We would like to know how the combination of high concentration verteporfin and ion beams damage these cells. As a similar phenomenon, we previously reported that exposure to L-dopa inhibited the expression of GPx3, which is a plasma antioxidant enzyme and maintains genomic integrity by inactivating these reactive oxygen species [2], in human retinal *RE in vitro*. In the previous experiment, ion beam irradiations of both He and C decreased GPx3 more remarkably than Ne. The expression of GPx3 incubated with L-dopa decreased significantly after irradiation of both He and C, and the irradiation of Ne increased the expression of GPx3 incubated with L-dopa after the exposure of the irradiation significantly [3]. Moreover, the expression of p53 was not significantly influenced by L-dopa, but increased just after the irradiation both of Ne and He in those cells incubated with L-dopa [4].

P53 is a key molecule of apoptosis induction in the human cells. Petermeier K, *et al.* suggested that verteporfin induces apoptosis in choroidal neovascularisation of the patient of age-related macular degeneration [5]. Therefore, to explore the mechanisms of combination effect of verteporfin and ion beam radiation, we examined the amount of transcription of p53 gene in human REC.

Established human REC *in vitro* incubated with verteporfin (116 μM) for 2 h were exposed to an ionization radiation that is induced by acceleration of the ionizing atom of 350 MeV ^{20}Ne, 220 MeV ^{12}C, and 50 MeV ^{4}He. We obtained the REC after 0, 4, 8, 24 h of the irradiation and extracted total cellular RNA and cDNA was synthesized. We used the Primer3 website to design the primers for RT-PCR amplification of the cDNA of p53 and 18S RNA. The reactions were carried out at the following temperature: 95 °C, for denaturation; 60 °C, for annealing; and 72 °C, for extension for 17-27 cycles. After mixing the cDNA, primer, and SYBR green, the expression of 18S RNA and p53 was measured using the Light Cycler system. The technology of this system is extremely innovative and enables rapid and simultaneous evaluation PCR experiments. Fluorometric analysis of the formed PCR products was performed as a real-time measurement either continuously or at specifically defined time points during each PCR cycle.

High concentration verteporfin significantly decreased the expression of p53 in human REC *in vitro* after 4 and 8 h of irradiation by 50 MeV He and after 0, 4, 8, 24 h of irradiation by 220 MeV C (Fig. 1) except for 350 MeV Ne. We considered that it was possible for the species of ion irradiation to influence the expression of p53 after addition of high concentration verteporfin to human REC *in vitro*.

References

1) K. Akeo *et al.*, JAEA Takasaki Annu. Rep. 2014, JAEA Review 2015-022, 73 (2016).
2) B. Chen *et al.*, Cancer Lett., **309,** 37 (2011).
3) K. Akeo *et al.*, Tiss. Cult. Res. Commun., **32**, 195 (2013).
4) K. Akeo *et al.*, JAEA Takasaki Annu. Rep. 2009, JAEA Review 2010-065, 95 (2011).
5) K. Petermeier *et al.* Br. J. Ophthalmol., **90**, 1034 (2006).

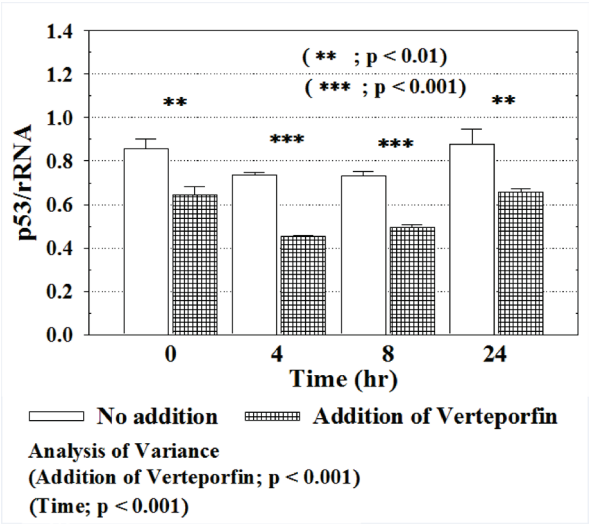

Fig. 1 Expression of p53 in REC *in vitro* irradiated by C.

2-05 LET Dependency of Survival Parameters by Carbon Ion Irradiation in Normal Human Dermal Fibroblasts

Y. Yoshida [a)], A. Takahashi [a)], K. Ando [a)], T. Funayama [b)], Y. Kobayashi [b)] and T. Nakano [a)]

[a)] Gunma University Heavy Ion Medical Center,
[b)] Department of Radiation-Applied Biology Research, TARRI, QST

The linear-quadratic (LQ) formalism is now almost universally used for calculating radiotherapeutic isoeffect doses for different fractionation/protraction schemes. It is clear that radiotherapeutic response, both for tumor control and for complications, is dominated by cell killing, and LQ is a mechanistic model of cell killing. Underlying the application of LQ to fractionation/protraction effects is pairwise misrepair of primary lesions such as DNA double-strand breaks (DSBs) or base damage. The two major pathways for repair of DSBs are homologous recombination (HR) and nonhomologous end joining (NHEJ). In this study, we carried out clonogenic survival assay of normal human dermal fibroblasts exposed to heavy-ion with and without an inhibitor of NHEJ to explore linear energy transfer (LET) dependency of LQ parameters, alpha and beta. The results of the assay suggested an existence of participation of NHEJ on the alpha parameter of LQ model.

臨床でも基礎実験においても放射線生物学的効果について解析する際に頻用されている linear quadratic model (LQ モデル) は DNA の一本鎖切断、二本鎖切断 (DSB) の生成と細胞の回復効果をモデル化したものである。放射線による DNA の DSB は相同組換え (HR) と非相同末端結合 (NHEJ) により修復される。我々はこれまでの研究で、高 LET 放射線による DSB の修復過程には HR 修復よりも NHEJ 修復の方が優位にはたらくことを報告した[Takahashi *et al.*, Radiat Res 2014, 182:338-44]。そこで、本研究では NHEJ 修復を阻害した際に LQ モデルにおける生物学的パラメータの LET 依存性がどのような変化を示すのかを明らかにすることを目的とした。

細胞はヒト皮膚繊維芽細胞 NHDF (Normal human dermal fibroblasts) を用いた。炭素線照射は群馬大学重粒子線照射施設 GHMC, 290 MeV/n, mono ビームおよび 60 mm SOBP ビームまたは原子力機構高崎研 TIARA 18.33 MeV/n、mono ビームを用いて、LET 13～158 keV/μm の条件で実施した。対照実験として 200 kVp の X 線照射を実施した。NHEJ 修復関連 DNA-PK の阻害剤 (NU7026) を培地に最終濃度 20 μM 添加し、6 時間後に照射し、コロニー形成法で感受性を調べた。細胞生残率は LQ モデルでフィットさせ、そのパラメータであるα値、β値から細胞生残率が 10%となる線量 (D_{10}) を求めた。X 線の D_{10} をリファレンスに用いて RBE を算出した。

NU7026(-)において、NHDF 細胞から得られた細胞生存率曲線は LET 依存的に急峻になった (Fig. 1)。α値、β値、RBE 値は LET 依存的に増加傾向を示した (Fig. 2)。NU7026(+)においても、細胞生存率曲線は LET 依存的に急峻になった (data not shown)。RBE 値は NU7026(-)同様 LET 依存的に増加傾向を示したが、α値は LET に非依存的であった (Fig. 3)。β値は NU7026(-)と大きな違いは認められなかった (ただし、TIARA で取得した 108 keV/μm および 158 keV/μm のデータについては解析中であるため、本内容には含めていない)。

以上の結果から、阻害剤の有無においてβ値および RBE の LET 依存性は似た傾向を示すが、α値の傾向が異なった。このことから炭素線において LQ モデルにおけるα項には NHEJ 修復の要素が含まれている可能性が示唆された。

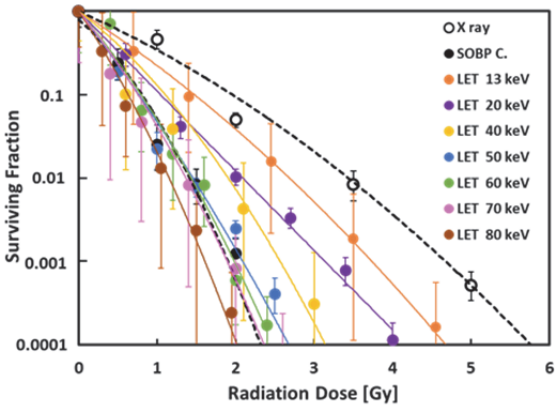

Fig. 1 The survival curves after exposure to radiation with different LET values in NHDF cells (SOBP C: Center of Spread-Out Bragg Peak).

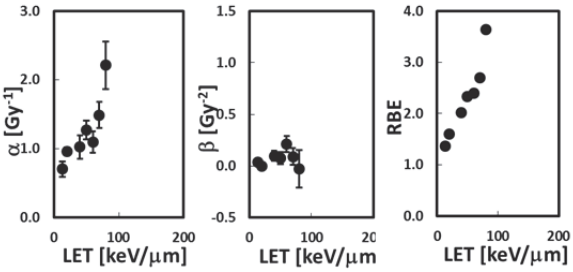

Fig. 2 LET dependency of survival parameters in NHDF cells.

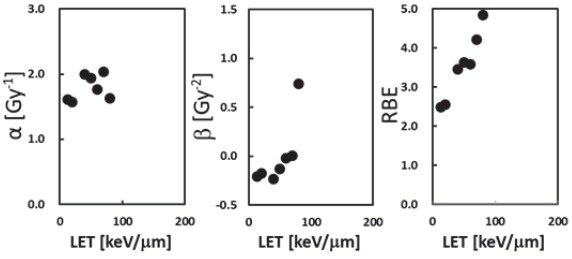

Fig. 3 LET dependency of survival parameters in NU7026 treated NHDF cells.

2-06 Combining Carbon-ion Beam and NHEJ Repair Inhibitor NU7026 Efficiently Kills Cancer Cells

A. Takahashi [a)], H. Ma [b)], C. Igarashi [a)], Y. Yoshida [a)], T. Funayama [c)], Y. Kobayashi [c)] and T. Nakano [a,b)]

[a)] Gunma University Heavy Ion Medical Center,
[b)] Graduate School of Medicine, Gunma University,
[c)] Department of Radiation-Applied Biology Research, TARRI, QST

We have previously demonstrated that targeting non-homologous end-joining (NHEJ) repair yields a higher radiosensitivity than targeting homologous recombination (HR) repair to heavy ions using DNA repair gene knockouts (KO) in mouse embryonic fibroblast (MEF)[1]. In this study, we determined if combining irradiation with a Carbon-ion (C-ion) beam and NHEJ inhibitor more could efficiently kill human cancer cells compared with HR inhibitor[2].

Human non-small cell lung cancer (NSCLC) H1299 (*TP53*-null) cells were provided by Dr. Moshe Oren (Weizmann Institute of Science, Rehovot, Israel). *TP53*-KO MEF *Lig4*+/+*Rad54*−/− (*Rad54*-KO), *Lig4*−/−*Rad54*+/+ (*Lig4*-KO), and *Lig4*+/+*Rad54*+/+ (wild-type) were provided by Dr. Frederick W. Alt (Harvard Medical School, Boston, MA). Exponentially growing cells were irradiated with a C-ion or x-ray beam. X-ray irradiations were completed using a 200-kVp x-ray generator (TITAN-225S, Shimadzu, Kyoto, Japan), operated at 14.6 mA with a total filtration of 0.5-mm Aluminum plus 0.5-mm Copper or using a 150-kVp x-ray generator (MBR-1520R-4, Hitachi, Tokyo, Japan), operated at 20 mA, with a 0.5-mm Aluminum plus 0.3-mm Copper filtration. The x-ray dose rate was about 1.3 Gy/min and 1 Gy/min, respectively. C-ion beam irradiations (approximately 3 Gy/min) were performed using a 290-MeV/n synchrotron (Gunma University Heavy Ion Medical Center, Gunma, Japan), with a dose-averaged linear energy transfer (LET) of 50 keV/μm at the center of a 6-cm spread-out Bragg peak.

TP53-null human non-small cell lung cancer cell line H1299 were tested for radiosensitization to C-ions by NHEJ-related DNA-dependent protein kinase (DNA-PK) inhibitor NU7026, HR-related Rad51 inhibitor B02, or both using colony forming assays. The mechanism underlying the inhibitor radiosensitization was determined by γH2AX expression.

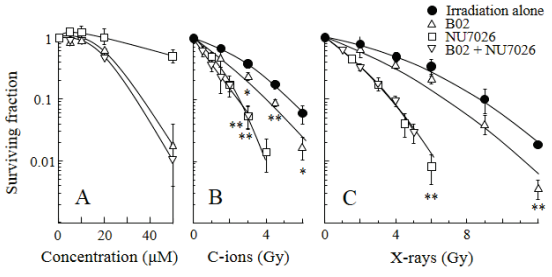

Fig. 1 Survival curves after NU7026, B02 treatment and radiation exposure for human H1299 cells. NU7026 alone, B02 alone and both concentration-dependent changes (A). C-ions dose-dependent changes (B) and the X-ray (C) when treated or not treated with 10 μM inhibitors.

NU7026 showed significant sensitizing effect to C-ions in a concentration-dependent manner. In contrast, B02 showed a slight sensitizing effect to H1299 cells. The addition of NU7026 significantly increased γH2AX expression after C-ion and x-ray irradiation in H1299 cells. NU7026 had no effect on radiosensitivity of *Lig4*-KO MEF and B02 had no effect on radiosensitivity of *Rad54*-KO MEF in both irradiations.

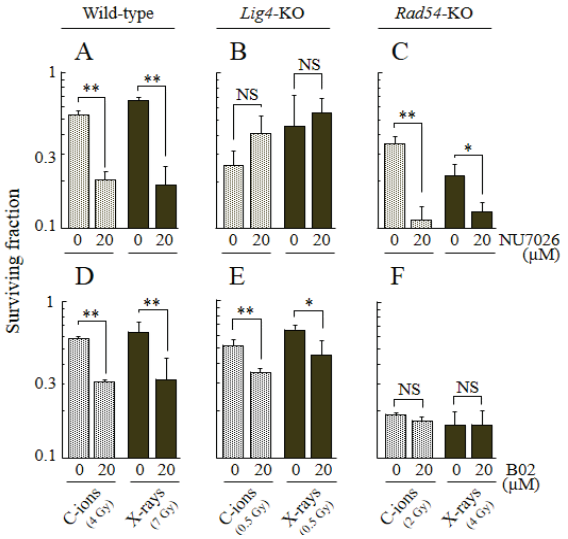

Fig. 2 Survival fraction after radiation exposure with NU7026 or B02 treatment in MEF. 20 μM NU7026 treatment (A–C), 20 μM B02 treatment (D–F). Wild-type cells (A and D), *Lig4*-KO cells (B and E), *Rad54*-KO cells (C and F).

Our findings demonstrated that although the sensitizing effect of NHEJ inhibitor to C-ion radiotherapy was slightly lower compared with traditional x-ray radiotherapy, NHEJ inhibition increases cytotoxicity of human tumor cells to irradiation with C-ions more efficiently relative to HR inhibition.

References

1) A. Takahashi *et al.*, Radiat. Res., **182,** 338 (2014).
2) H. Ma *et al.*, Radiat. Oncol., **10**, 225 (2015).

2-07

Epigenetic Modifier as a Potential Radiosensitizer for Heavy-ion Therapy on Malignancy (IV)

K. Saito [a, b, c], T. Funayama [b, c], Y. Kobayashi [b, c] and T. Murakami [a]

[a] Faculty of Pharmacy, Takasaki University of Health and Welfare,
[b] Department of Radiation-Applied Biology Research, TARRI, QST,
[c] Graduate School of Medicine, Gunma University

Refractory tumors accumulate epigenetic abnormalities, which often cause the resistance to various therapeutic options. While the high linear energy transfer (LET) heavy-ion radiation provides more pronounced therapeutic effects than the low-LET radiation (e.g., γ-ray), it is necessary to develop promising sensitizers for the enhanced radiation therapy. Herein we demonstrate that the use of histone deacetylase inhibitors (HDACi) [1] could sensitize refractory tumor cells well for the heavy-ion therapy.

B16F10 murine melanoma cells were treated with several HDACis and followed by irradiations. The clonogenic survival assay[2,3], annexin-V staining, cell cycle analysis[4] and Western blotting were performed. Results showed that some HDACis significantly enhanced antitumor effects in heavy-ion irradiated cells. In combination with irradiation, those HDACis abrogated the G2/M arrest and increased much early apoptotic events, leading to the decreased clonogenicity. Moreover, these radiosensitizing effects of HDACi were much higher in heavy-ion irradiated cells but lower phosphorylation of H2AX, a marker for DNA damage, than in γ-ray irradiated cells (Fig. 1). Thus, we propose that the pretreatment of HDACi may provide clinical efficacy to refractory cancer patients in combination with heavy-ion therapy.

Materials and methods

Cells and cell culture, Radiation exposure

See our previous description [2].

Treatment

Cells in exponential growth were seeded at a density 1×10^6 cells per 35 mm culture dish 20-24 h before irradiation. Cells were treated with investigational or comparator HDACi for 16.5 h and then irradiated. The concentration of HDACi was selected that required to reduce colony formation by 10% alone and the irradiation dose was selected D_{10}.

Western blot Analysis

After HDACi and radiation exposure, the cells were incubated for appropriate time. Cells were lysed in RIPA Lysis and Extraction Buffer (Thermo Scientific, Rockford, IL). Protein concentrations were determined by a BCA protein assay kit (Thermo Scientific, Rockford, IL). Proteins were separated by SDS-PAGE, transferred to PVDF membranes, blocked in 5% BSA/TBST and probed with the following primary antibodies: phospho-Histone H2A.X (Ser139), Histone H2A.X (Cell Signaling Technology, Boston, MA). Then, the membranes were incubated with HRP-conjugated secondary antibody (Cell Signaling Technology, Boston, MA) and visualized with a chemiluminescence kit (GE Healthcare, UK) according to the manufacturer's recommended protocol and exposed with LAS-3000 Imaging System (Fujifilm, Japan). Semi-quantification was performed with ImageJ (NIH). Data presented are the mean ± SE from at least three independent experiments. The statistical analysis is in progress.

References

1) K. J. Falkenberg *et al.*, Nat. Rev. Drug Discov., **13**, 673 (2014).
2) K. Saito *et al.*, JAEA Takasaki Annu. Rep. 2012, JAEA-Review 2013-059, 80 (2014).
3) K. Saito *et al.*, JAEA Takasaki Annu. Rep. 2013, JAEA-Review 2014-050, 83 (2015).
4) K. Saito *et al.*, JAEA Takasaki Annu. Rep. 2014, JAEA-Review 2015-022, 75 (2016).

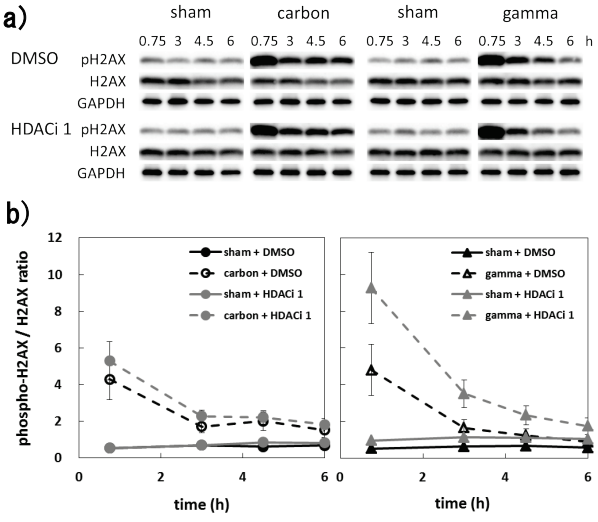

Fig. 1 Phosphorylation of H2AX. (a) Imaging of chemiluminescent western blot detection, (b) semi-quantification with ImageJ of phospho-H2AX/H2AX ratio.

2-08 Analysis of Mechanisms for the Induction of Radiation-Induced Adaptive Response by Bystander Response

H. Matsumoto [a)], M. Tomita [b)], M. Maeda [c)], T. Funayama [d)], Y. Yokota [d)], M. Suzuki [d)], T. Sakashita [d)] and Y. Kobayashi [d)]

[a)] Faculty of Medical Sciences, University of Fukui, [b)] Radiation Safety Research Center, Central Research Institute of Electric Power Industry, [c)] The Wakasa Wan Energy Research Center, [d)] Department of Radiation-Applied Biology Research, TARRI, QST

The phenomena in response to low-dose/low-dose-rate radiation exposure are adaptive responses, bystander responses, low-dose hypersensitivity, and genomic instability. The objective of this project is to elucidate molecular mechanisms for the induction of radiation-induced adaptive response through radiation-induced bystander responses induced by irradiation with heavy ion microbeams in QST. Human non-small lung cancer cells bearing the wild-type p53 were used. The two colonies were prepared at the center of a 35 mm dish, which are 5 mm away from each other. Ten cells in a colony were irradiated with Ar ion microbeams, then the cells of both colonies were irradiated with Ar ion broad beams after incubation for several hours. By the analysis of surviving fraction, the phenomenon, "radiation-induced adaptive response" was actually induced in the cells of both colonies. The response was almost completely suppressed by the addition of NO scavenger to the medium. Collectively, radiation-induced adaptive response can be induced by radiation-induced, NO-mediated bystander response.

低線量／低線量率放射線に対して生物が示す特異的な応答様式には、放射線適応応答、放射線誘発バイスタンダー応答、放射線超高感受性、遺伝的不安定性等がある。我々は、量子科学技術研究開発機構において開発された細胞局部照射装置（HZ1）及び深度制御種子照射装置（HY1）を用いて、放射線誘発バイスタンダー応答による放射線適応応答の誘導機構を明らかにすることを目的として研究を実施した。

1. 実験方法

細胞：ヒト非小細胞肺がん細胞（A549 細胞）を用いた。

培養：35 mm ディッシュの中央に 1.0×10^4 cells の細胞を 2 箇所スポットし、15~20 時間培養することにより作製された 2 個のコロニー（マイクロビームで照射された細胞を含む Targeted colony 及びマイクロビームで照射されていない細胞のみの Bystander colony）を照射実験に供した（Fig. 1）。

照射：Funayama ら [1)]の方法に従って、一方のコロニー（Targeted colony）の 10 個の細胞に 5 粒子の 520 MeV $^{40}Ar^{14+}$を HZ1 ポートにおいて照射した。一定時間（3～6 時間）培養後、520 MeV $^{40}Ar^{14+}$を HY1 ポートにおいて 1～5 Gy 照射した。

細胞の生存率の測定：HY1 ポートでの照射から 6 時間後に、細胞を回収し、T25 フラスコへ 200～1,000 個の細胞を播種してコロニー形成させて生存率を求め、放射線適応応答の誘導を評価した。

2. 結果及び考察

細胞局部照射装置（HZ1）を用いて Ar イオンマイクロビームを照射された 10 個の細胞を含む Targeted colony 及び 5 mm 離れた場所にある Bystander colony の何れの細胞においても深度制御種子照射装置（HY1）を用いた Ar イオンブロードビームによる照射後に適応応答の誘導が認められた。またこれらの適応応答の誘導は、一酸化窒素（NO）ラジカル捕捉剤の添加によりほぼ完全に抑制された。以上の結果から、NO を解した放射線誘発バイスタンダー応答により適応応答が誘導されることが明らかとなった（Fig. 2）[2, 3)]。昨年度とは異なる細胞を用いることにより、放射線誘発バイスタンダー応答による放射線適応応答の誘導という現象が確認され、細胞株特異的な現象ではないことが明らかとなった。

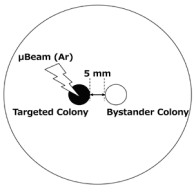

Fig. 1 Schematic drawing a preparation of a couple of colonies in a 35 mm dish.

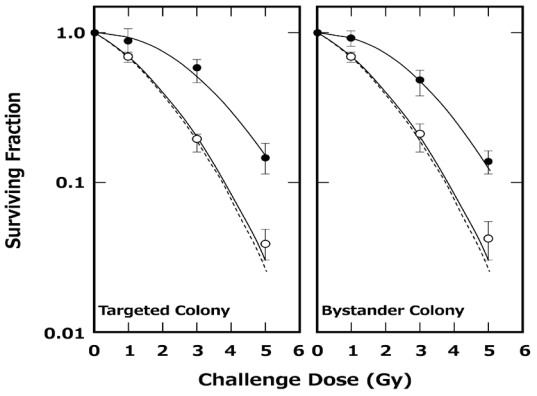

Fig. 2 Induction of radiation-induced adaptive response by bystander response. Closed circles, surviving curves of cells in Target or Bystander colonies after irradiation with Ar ion microbeams followed by irradiation with broad beams. Open circles, as closed circles with NO scavenger, carboxy-PTIO. Dashed line, a surviving curve of a single irradiation with Ar ion broad beams.

References

1) T. Funayama *et al.*, Radiat. Res., **163**, 241 (2005).
2) H. Matsumoto, Cell. Resp. Phys. Stress and Therap. Appl., Ed. T. Shimizu, T. Kondo, 15 (2013).
3) M. Tomita *et al.*, Life Sci. Space Res., **6**, 36 (2015).

2-09

Analysis of Biological Effect on 3D Cultured Tissue Induced by Heavy-ion Microbeam Irradiation

M. Tomita [a)], H. Matsumoto [b)], K. Otsuka [a)], T. Funayama [c)], Y. Yokota [c)], M. Suzuki [c)] and Y. Kobayashi [c)]

[a)]Radiation Safety Research Center, Central Research Institute of Electric Power Industry,
[b)]Faculty of Medical Sciences, University of Fukui,
[c)]Department of Radiation-Applied Biology Research, TARRI, QST

The heterogeneity of the absorbed dose within the irradiated tissues is more relevant for high-LET heavy ions than for low-LET photons since absorbed dose per single hit for former is much greater than that for the latter. Therefore, directly irradiated and non-irradiated cells are co-existing within the tissues exposed to the low fluence of High-LET heavy ions. A radiation-induced bystander response is generally known as a cellular response induced in non-irradiated cell by receiving bystander signaling factors released from directly irradiated cells within a tissue [1)]. In our previous study, we showed that DNA damage and cell death were induced by nitric oxide (NO)-mediated high-LET heavy-ion-induced bystander signaling in normal human fibroblasts [2)]. In this study, we aim to clarify a role of bystander response to sustain the homeostasis of damaged tissue irradiated with high-LET heavy ions. We established the heavy-ion microbeam irradiation method to a 3D cultured human epidermis. Using this method, a viable cell rate of the 3D cultured human epidermis irradiated with high-LET Ne-ion microbeams or broadbeams was analyzed.

Highly differentiated human epidermis model, the LabCyte EPI-MODEL24 (Japan Tissue Engineering CO., Ltd., Aichi, Japan), and human epidermal cells cultured for 3 days using the EPI-KIT (Japan Tissue Engineering) were used in this study (Fig. 1). Human epidermal cells cultured for 3 days consisted of basal and spinous layers as shown in Fig. 1(B). The 3D cultured tissues were irradiated with 1-10 Gy of 260 MeV $^{20}Ne^{7+}$ broadbeams or 15 particles of 260 MeV $^{20}Ne^{7+}$ microbeams at 61 points (100 μm interval) in a straight line. Cell viability was assessed by an MTT assay 90 h after irradiation.

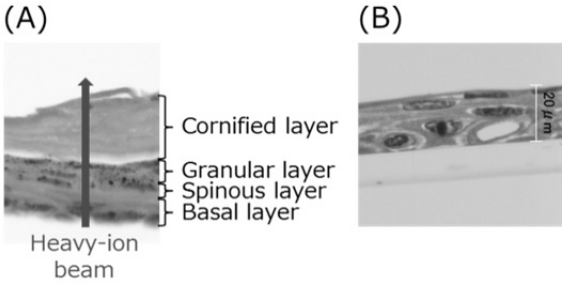

Fig. 1 Hematoxylin and eosin (HE) stained human epidermis model. (A) LabCyte EPI-MODEL24. (B) human epidermal cells cultured for 3 days using the EPI-KIT.

Figure 2 shows the cell viability of the 3D cultured tissues 90 h after Ne-ion microbeam irradiation. The viability was approximately 90% and was not different between the LabCyte EPI-MODEL24 and the epidermal cells cultured for 3 days.

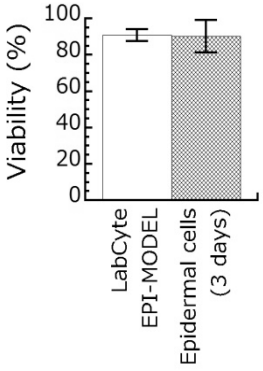

Fig. 2 Ratio of viable cells of the 3D cultured tissues 90 h after Ne-ion microbeam irradiation.

Figure 3 shows the dose response of cell viability of the 3D cultured tissues 90 h after Ne-ion broadbeam irradiation. The dose response of cell viability of the epidermal cells cultured for 3 days was also similar to that of the LabCyte EPI-MODEL24.

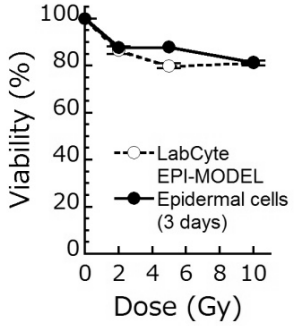

Fig. 3 Dose response of cell viability of the 3D cultured tissues 90 h after Ne-ion broadbeam irradiation.

Those results suggest that the differentiative basal and spinous cells in the 3D cultured epidermis mainly respond to high-LET heavy ions and bystander signals.

References

1) M. Tomita and M. Maeda, J. Radiat. Res., **56**, 205-19 (2015).
2) M. Tomita *et al.*, Life Sci. Space Res., **6**, 36-43 (2015).

2-10 What Kinds of Secrete Factor(s) Can Induce Bystander Lethal Effect in Normal Human Fibroblasts Irradiated with Ar-Ion Microbeams?

M. Suzuki [a)], T. Funayama [b)], Y. Yokota [b)], M. Suzuki [b)], T. Sakashita [b)] and Y. Kobayashi [b)]

[a)] Department of Basic Medical Sciences for Radiation Damages, NIRS, QST,
[b)] Department of Radiation-Applied Biology Research, TARRI, QST

The last year we reported that bystander lethal effects were induced by the different mechanisms between C- and Ar-ion-irradiated cells. The bystander effect induced in C-ion-irradiated cells was dominant via the gap-junction mediated cell-cell communication and the Ar-ion induced bystander effect was dominant via secrete factor(s) to culture medium from the irradiated cells[1)]. This year we tried to identify secreate factor(s) caused of bystander lethal effect induced in normal human fibroblasts using radical scavengers.

Early passaged cell cultures of normal human skin fibroblasts (Cell name: NB1RGB, Cell No. RCB0222) were obtained from Riken Bio Resource in Japan. Approximately 6×10^5 exponentially growing cells were inoculated into microbeam dishes, which were made of acrylic resin ring with 36 mm diameter and attached 7.5 μm-thick polyimide film on the bottom of the ring, 2 days before microbeam irradiation. Half of the sample dishes were treated with an inhibitor of gap-junction mediated cell-cell communication (40 μM of γ-isomer of hexachloro-cyclohexane) from 3 h before irradiation to the end of 24 h of post-irradiation incubation. Irradiations were carried out using the 256 (16×16)-cross-stripe method described previous report[2)] using C ions ($^{12}C^{5+}$, 220 MeV), Ne ions ($^{20}Ne^{7+}$, 260 MeV) and Ar ions ($^{40}Ar^{13+}$, 460 MeV) at the HZ1 port in TIARA. The beam size of each ion microbeam was 20 μm in diameter and the irradiations in each point were performed to deliver 8 ions for carbon, 2 ions for neon and single ion for argon, respectively. The values of linear energy transfer (LET) at the sample position were estimated to be 103 keV/μm for C ions, 380 keV/μm for Ne ions and 1,260 keV/μm for Ar ions. After irradiations, cells were incubated for 24 h in a CO_2 incubator at 37 °C, and then assayed using the colony-forming method with/without radical scavengers. We used either dimethyl sulfoxide (DMSO：0.7 M) as a scavenger of reactive oxygen species or ascorbic acid (AsA:5 mM) as a specific scavenger of long-lived radicals and treated them during the 24 h of post-irradiation incubation.

Figure 1 showed the results for lethal effects at 24 h after irradiation treated with/without the scavengers in microbeam-irradiated cells (IR) and microbeam-irradiated cells with the gap-junction inhibitor (L+IR). The surviving fractions in the cells treated with DMSO were around 0.9 and no change was observed between the cells treated and non-treated with DMSO. Furthermore the data were similar with the cells between absence and presence of the gap-junction inhibitor. The surviving fraction 0.9 was significantly low beyond our expectation, indicating the bystander lethal effect, because we could estimate that the percent of Ar-ion direct hit cells was around 0.04% order of all cells in the dish by the 256 (16×16)-cross-stripe method. On the other hand, the surviving fraction in the cells treated with AsA were around 1.0, indicating the suppression of bystander lethal effect observed in the microbeam-irradiated cells. And also no effect was observed in the cells with/without the gap-junction inhibitor. There is clear evidence that the secret factor(s) scavenged by AsA can induce bystander lethal effect in the cells irradiated with Ar-ion microbeams.

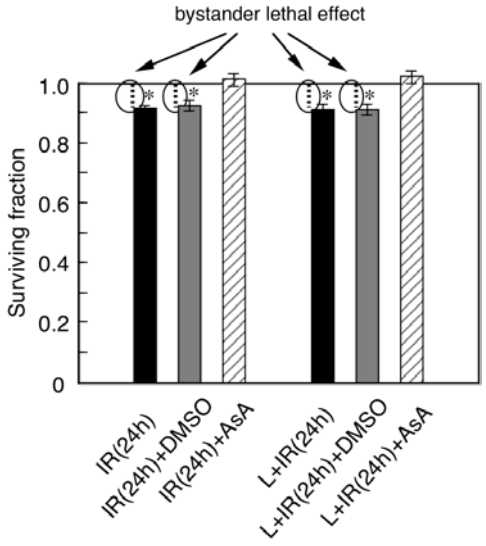

Fig. 1 Lethal effects in normal human fibroblasts irradiated with Ar-ion microbeams at 24 h after irradiation. The cell cultures were treated with either dimethyl sulfoxide (DMSO) or ascorbic acid (AsA). "L+IR" means the samples inhibited cell-cell communication using the gap-junction specific inhibitor. The results were the means and standard errors from at least 5 independent experiments. (* $p<0.05$)

References

1) M.Suzuki *et al.*, JAEA Takasaki Annu. Rep. 2014, JAEA-Review 2015-022, 70 (2016).
2) M.Suzuki *et al.*, JAEA Takasaki Annu. Rep. 2006, JAEA-Review 2007-060, 107 (2008).

2-11 Analysis of Bystander Effect Induced by Peroxynitrite in Glioma Cells

S. Wada [a)], D. Ueta [a)], T. Ohashi [a)], T. Kakizaki [a)], M. Natsuhori [a)], T. Funayama [b)], T. Sakashita [b)], Y. Yokota [b)] and Y. Kobayashi [b)]

[a)] Department of Veterinary Medicine, Kitasato University,
[b)] Department of Radiation-Applied Biology Research, TARRI, QST

So far, we clarified that X-ray irradiation induced cell killing by bystander effect mediated-secreted factor. This phenomenon was related with nitric oxide (NO). NO induce nitration of protein which changes protein activity. In this study we analyzed protein nitration in bystander cells after medium change. A nitration of histone acetyltransferase protein, p300, was observed in bystander cells. It was considered that the change of protein activity by p300 nitration might be relative to induction of bystander effect.

1. はじめに

バイスタンダー効果とは、照射された細胞から何らかの液性因子が分泌され、非照射細胞にこの液性因子の作用によって細胞死が誘導される現象である。液性因子を介したシグナル伝達によって誘導される細胞死や染色体異常形成は、一酸化窒素（NO）が関与すると示唆されている。NO は照射細胞からのシグナル伝達によりバイスタンダー細胞内で産生されると考えられており、NO はスーパーオキシドと反応してより酸化力の強いパーオキシナイトレイトとなる。このパーオキシナイトレイトによって、細胞死に関する細胞損傷が誘導されると考えられている。近年、パーオキシナイトレイトは様々なタンパク質をニトロ化することが報告されている。このニトロ化によってタンパク質の機能が変化するため、バイスタンダー効果における細胞死の誘導にもタンパク質のニトロ化によってタンパク質の機能変化が関与すると推察された。

そこで、本研究では、パーオキシナイトレイトのバイスタンダー効果への関与を検証するため、パーオキシナイトレイトの阻害剤によるバイスタンダー効果による細胞死誘導の変化とバイスタンダー細胞内においてニトロ化されるタンパク質の解析を行った。

2. 実験方法

グリオーマ細胞（A172 細胞）を用い、X 線 6 Gy を照射した。液性因子によるバイスタンダー効果の検証のため、照射 10 分後に細胞培養液を回収し、非照射細胞（バイスタンダー細胞）にその培養液を添加後にコロニー形成法によって生存比を算出した。また、バイスタンダー効果の誘導にパーオキシナイトレイトの関与を検証するため、バイスタンダー細胞に 50 μM ebselen 処置後に照射細胞の培養液を添加し、生存比を算出した。また、バイスタンダー細胞内でニトロ化タンパク質を解析するため、バイスタンダー細胞内のタンパク質に対して抗ニトロ化抗体を用いて、免疫沈降法とウエスタンブロット解析を行った。さらに、ニトロ化におけるパーオキシナイトレイトの関与を検証するため、50 μM ebselen 処置後のバイスタンダー細胞におけるニトロ化タンパクを検出した。

3. 結果及び考察

X 線 6 Gy 照射後の培養上清を回収し、この培養上清を ebselen 処置細胞と無処置細胞に添加したときの生存比を算出したとき、Ebselen 無処置細胞では培養上清の添加により生存比の低下が観察され、ebselen 処置細胞では生存比の低下が観察されなかった。これらのことから X 線照射よってバイスタンダー効果が誘導され、このバイスタンダー効果の誘導にはパーオキシナイトレイトが関与すると考えられた。次にバイスタンダー細胞内でのパーオキシナイトレイトによるタンパク質のニトロ化を解析するため、バイスタンダー細胞のタンパク質を抗ニトロ化抗体によってウエスタンブロットを行ったところ、300 kDa 付近に比較的明瞭なバンドが観察された。この 300 kDa のタンパク質をアセチルトランスフェレーゼの p300 と推察し、バイスタンダー細胞内のタンパク質を抗 p300 抗体により免疫沈降後に抗ニトロ化抗体を用いてウエスタンブロットを行ったところバイスタンダー細胞内でニトロ化タンパクの増加が観察され、さらに、ebselen 処置によってニトロ化タンパクの増加が観察されなかった（Fig. 1）。これらのことからバイスタンダー細胞内での p300 のニトロ化が細胞死誘導に関与する可能性が考えられた。

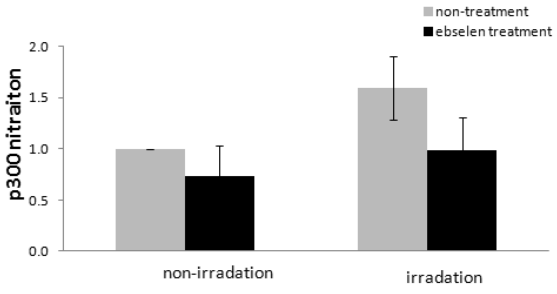

Fig. 1 Relative value of p300 nitration on bystander cells with ebselen and without ebselen. Mean ± SD.

2-12 *In vivo* 3D Analysis after Localized 26.7-MeV/u $^{12}C^{6+}$-ion Beam Irradiation in Japanese Medaka, *Oryzias latipes*

T. Watanabe-Asaka [a)], K. Nagata [a)], T. Yasuda [a)], C. Hashimoto [a)], M. Suzuki [b)], Y. Yokota [b)], Y. Ikeda [b)], T. Sakashita [b)],T. Funayama [b)], Y. Kobayashi [b)], S. Oda [a)] and H. Mitani [a)]

[a)] Department of Integrated Biosciences, The University of Tokyo,
[b)] Department of Radiation-Applied Biology Research, TARRI, QST

Radiotherapy is widely used in cancer treatment. In addition to inducing effects in the irradiated area, irradiation may induce effects on tissues close to and distant from the irradiated area[1,2]. Japanese medaka, *Oryzias latipes*, is a small teleost fish and a model organism for evaluating the environmental effects of radiation. In this study, we applied 15 Gy of low-energy carbon-ion (26.7 MeV/u) irradiation to adult medaka to a depth of approximately 2.2 mm from the body surface using TIARA in TARRI. We histologically evaluated the systemic alterations induced by irradiation using serial sections of the whole body, and conducted a heart rate analysis.

The calculated range of the carbon particles was approximately 2.2 mm in water (Fig. 1A). Anaesthetized adult fish were aligned in a petri dish with the dorsal (Fig. 1B) or ventral side facing upward for dorsal (DR) or ventral (VR) irradiation, respectively. The cross-sectional shape of the medaka is roughly oval, and we expected that the medaka would be irradiated as shown in Fig. 1C and D. For the whole-body analysis of serial sections, approximately 3,600 serial sections at a thickness of 5 µm would need to be cut from the head to the tail.

Tissues from the irradiated side showed signs of serious injury that corresponded with the radiation dose. The size of the thymus located dorso-lateral was reduced in the DR medaka. The kidney of the medaka is located on the dorsolateral side at a depth of approximately 2 mm from the dorsal skin (Fig. 1D). In the DR fish, nucleated blood cells were absent from the dorsal region of the kidney, but this reduction in cell number was not observed in the kidney of ventral irradiation VR fish (Fig. 2A and B).

A 3D reconstruction analysis of the kidney sections showed the dorsal part of the kidney, where the heavy-ion beam reached, showed severe atrophy in the DR fish compared with the VR fish at 7 days after irradiation (Fig. 2C). The kidney has a haematopoietic function in fish. Amount of the blood cell in the DR kidney was significantly lower only in the irradiated area and was not reduced in the VR kidney (Fig. 2D). This data reflects the precise localization of the injuries caused by carbon-beam irradiation and irradiation damaged the haematopoietic stem cells in the kidney.

Obvious telangiectases or aneurysms of lamellae involved in haemorrhages were observed in the arterial capillaries of gill lamellae in both the VR and DR fish 7 days after irradiation. These results suggested systemic irradiation effects. The present study provides an *in vivo* model for further investigation of the effects of irradiation in and beyond the locally irradiated area.

References

1) S. C. Formenti, & S. Demaria. Lancet Oncol., **10**, 718 (2009).
2) B. J. Blyth & P. J. Sykes. Radiat. Res., **176**, 139 (2011).

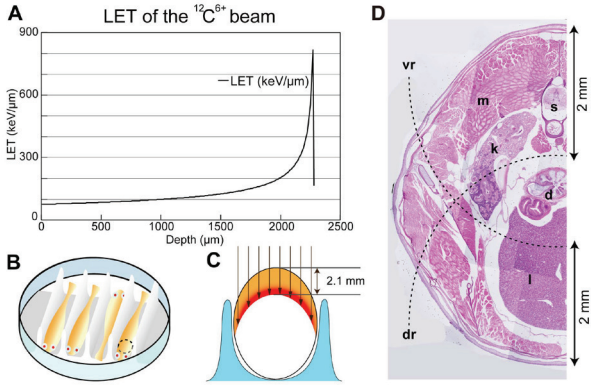

Fig. 1 A: LET for water $^{12}C^{6+}$ beam irradiation used in this study. B and C: Diagram of the positioning of medaka and the irradiated area. D: HE staining of transverse sections in adult medaka. Dashed lines show a distance of approximately 2 mm from the dorsal or ventral surface. d, digestive organ; dr and vr, range of dorsal and ventral irradiation; k, kidney; l, liver; m, muscle; s, spinal cord.

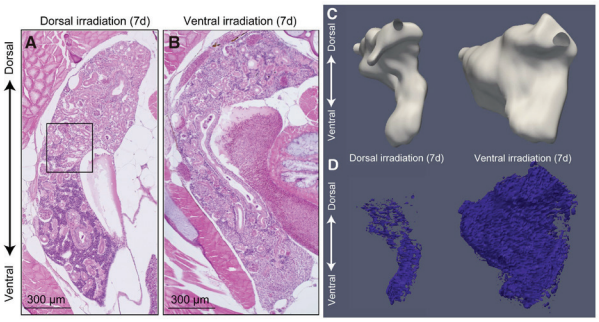

Fig. 2 HE staining of transverse sections and 3D reconstruction of the kidney 7 days after dorsal or ventral irradiation with $^{12}C^{6+}$ beam irradiation in adult medaka. A: Dorsal irradiation with heavy-ion beam irradiation. B: Ventral irradiation with heavy-ion beam irradiation. C: 3D reconstruction of a dorsally or ventrally irradiated kidney. D: 3D reconstruction of blood cells in the same kidney as shown in C. The scale bars indicate 300 µm.

2-13

Dose and Particle Dependence of Fluorescent Dots in DNA Sheet Observed with Fluorescence Imaging of Oxidative Damage of Guanine Induced by Heavy Ion Irradiation at TIARA

A. Ito [a)], F. Ouchi [a)], T. Ushiroda [a)], R. Hirayama [b)], Y. Furusawa [b)], T. Funayama [c)] and Y. Yokota [c)]

[a)] School of Engineering, Tokai University, [b)] Department of Basic Medical Sciences for Radiation Damages, NIRS, QST, [c)] Department of Radiation-Applied Biology Research, TARRI, QST

Introduction

The track structure of heavy ions is generally recognized to consist of a core region with high ionization density and a penumbra region, where secondary electrons mainly contribute to energy deposition, with relatively low LET nature. The biological effects of heavy ions should be characterized by such a track structure of energy deposition. Although as is well established, the indirect action decreases with increasing LET, substantial contribution of the low-LET penumbra to mammalian cell killing was strongly suggested by our studies using an OH radical scavenger[1)]. In accordance with these results, we detected significant amount of 8-hydroxydeoxyguanosine (8-OHdG), oxidative DNA damage produced via a reaction with OH radicals, upon irradiation of heavy ions to guanine solution by using HPLC system in coupled with an electrochemical detector[2)].

For further confirmation of the significant contribution of the low LET region, we tried to visualize the penumbra region with the aid of an immunofluorescence method using an antibody against 8-OHdG. In 2013 a uniform DNA-lipid complex sheet insoluble in aqueous medium was developed[3)], and in the following year using heavy ion microbeam we detected fluorescent dots which may be induced by incident particles.

In the present study, we examined numbers and areas of the fluorescence dots in the DNA sheet exposed to Ar and H ions, and the results confirmed that the dots result from incident particles.

Materials and Methods

Water-insoluble DNA sheet is produced on a cover glass as described in the previous report[3)]. The DNA sheet was exposed to Bouin's fixative before irradiation. 460 MeV Ar ion and 20 MeV proton, with an LET of 1,610 and 2.77 keV/μm respectively, were irradiated to the DNA sheet in ultra-pure water at TIARA. After irradiation DNA samples were subjected to dual staining of DAPI to check the uniformity of the DNA sheet and an 8-OHdG antibody followed by treatment with a secondary antibody labelled with fluorescent dye. The number density of fluorescence dots, the number of dots in an area of a field of view of a fluorescence microscope, and the size of those dots were measured with Image-Pro Plus image processing software (Media Cybernetics, Inc.).

Results and Discussion

Dose dependence of the number density of fluorescence dots in Ar-irradiated DNA sheet was summarized in Table 1. The dot density increased with increasing dose. However the measured density was significantly lower than that of calculated incident particles, particularly in the high dose region where overlapping of dots became evident. In the case of proton, similar increase with dose was observed, but the difference between observed dots and calculated particles was much larger than the case of Ar, suggesting that the proton energy density is small to induce fluorescence dots. These results indicated that even at very high LET of 1,610 keV/μm, OH radical-induced DNA damage was significantly produced.

The diameters of these dots were measured and averaged over a field of view of a fluorescence microscope. The mean diameter was around 0.50 μm in every dose of Ar ions. The value was larger than proton with a mean diameter of 0.44 μm. Chatterjee and Schaefer[4)] estimated that the size of penumbra of Ar ion was about twice smaller than proton. In our experiments, the relatively small ionization density in penumbra in the proton case may underestimate the diameter. Further data accumulation for different ions is in progress.

Table 1 Dose dependence of the density of fluorescence dots in DNA sheet irradiated with Ar ions.

Dose (Gy)	Fluorescence dots[*)]	Incident particles[*)]
3.4	358	165
338	7745	16500
1350	15355	66000

[*)] Density means dots or particles per a field of view (116 μm^2).

Acknowledgement

We thank Drs. M. Mitarai and K. Iohara, Central Research Institute of Maruha Nichiro Cooperation, for their courteous supply of DNA sample.

References

1) A. Ito *et al.*, Radiat. Res., **165**, 703-12 (2006).
2) R. Hirayama *et al.*, Radiat. Res., **171**, 212-18 (2009).
3) S. Kitabatake *et al.*, JAEA Takasaki. Annu. Rep. 2013, JAEA-Review 2014-050, 86 (2015).
4) A. Chatterjee and H. J. Schaefer, Radiat. Environ. Biophys., **13**, 215-27 (1976).

2-14 Sensitizing Activity Mechanism of Porphyrin Boron and/or Fluorine Compounds for Carbon Irradiation in C6 Glial Tumor Cells

N. Miyoshi [a)], V. Mandal [a)], T. Funayama [b)] and Y. Kobayashi [b)]

[a)] Research Center for Development in Far-infrared Region, University of Fukui,
[b)] Department of Radiation-Applied Biology Research, TARRI, QST

We had irradiated glial tumor cells by carbon beam of QST-Takasaki with a Boron and/or Fluorine-porphyrin derivatives (Compounds-I, II, III, IV). The result indicated that the Fluorine and/or Boron elements may act as sensitizer of carbon ion irradiation.

過去 5 年に渡り、重粒子線に対する増感剤を見つけ照射量を削減することで、被ばく障害を少しでも和らげてきた。特に 4 年前にはロシア国立有機材料物資研究所と共同研究を開始している。また、そのボロンやフッ素をポルフィリン環に修飾する合成技術の高さは、日本国内の化学合成研究者からも高い評価を得ている。

この技術で共同開発したボロンとフッ素ポルフィリン誘導体を使用したボロン中性子捕捉療法（BNCT）による実験腫瘍モデル動物照射でも、その増感性が京大・原子炉実験所で明らかにされた。また、若狭湾エネルギー研究センターに於いては陽子線照射に対しても、抗腫瘍効果の亢進を促した。既に我々は、上記の中性子線と陽子線に対する Compound-B による抗腫瘍効果の特許申請を、日本国内でそれぞれ 2012-098918（2012 年 4 月 24 日）と 2013-052161（2013 年 3 月 14 日）として 1 年毎に行った。

そこでこれらの実績を元に、ボロン元素やフッ素元素ポルフィリン誘導体（Fig. 1）をそれぞれ単体で合成し、炭素線に対する抗腫瘍効果の有無を Glial Tumor Cells（C6）を用いて調べ、その増感機構を更に追求する事にした。

TIARA の炭素ビームの照射実験の結果、Fig. 2 のグラフで示すように、いずれの曲線グループも照射線量の増加と共に生存率が指数関数的に減少した。生存率はコロニー形成法に従い算出した。特に、それらの生存曲線の傾き（Fig. 3）は、それぞれ Compound-I, II, III, IV の濃度依存的に増大していることが明らかとなり、増感剤 Compound-IV では増感剤のなしの炭素ビームの殺細胞効果に比べ約 2 倍の増感率を示した。これは共同開発した誘導体でフッ素原子が比較的高く増感性を示し、ボロン原子と相乗的増感している（Compound-IV の場合）と結論された。

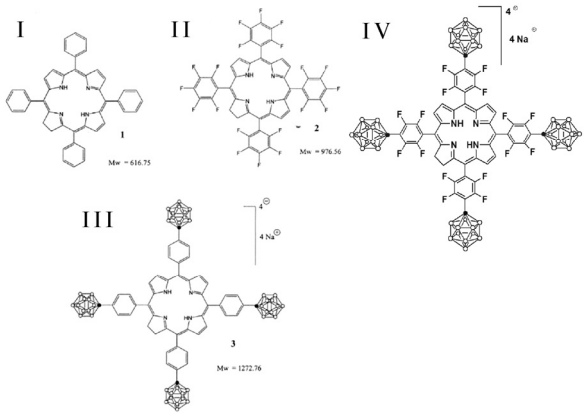

Fig. 1 The chemical structures of Compound-I, II, III, IV.

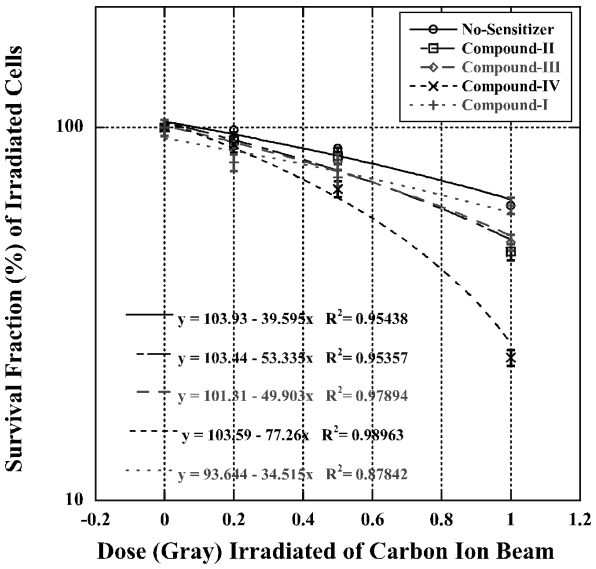

Fig. 2 Survival fractions (%) of C6 cell irradiated by carbon ions in QST-Takasaki.

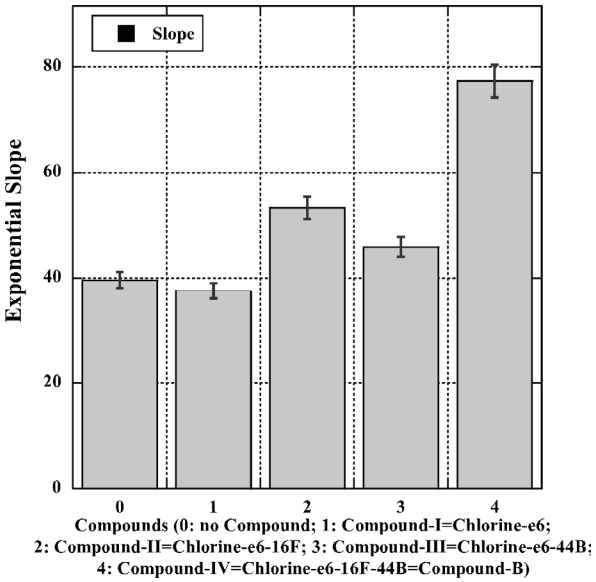

Fig. 3 Exponential slopes of C6 survival fraction irradiated by carbon beam dependent on Compounds-I, II, III, IV concentrations.

2-15 Detection of Transcripts of the Apoptosis Related Genes in the Heavy-Ion Irradiated Silkworm Eggs during Early Development

D. Ueda [a)], T. Funayama [b)], Y. Yokota [b)], M. Suzuki [b)], T. Sakashita [b)], Y. Kobayashi [b)] and K. Shirai [a)]

[a)] Faculty of Textile Science and Technology, Shinshu University,
[b)] Department of Radiation-Applied Biology Research, TARRI, QST

Checkpoint mechanisms are important for eukaryotic cells, especially fertilized eggs to maintain the integrity of genome. In response to DNA damage, checkpoint responses prevent further cell cycle progression to repair the damage of DNA. After the DNA lesions are repaired completely, the cell cycle will restart. When the DNA damage cannot be repaired, a cell can undergo programmed cell death in order to eliminate the damaged cells. Recently, an alternative process, termed (checkpoint) adaptation, to re-enter cell cycle progression even in the presence of unrepaired DNA damage was reported. During the process, the signal from the damaged site is gradually lost. Then the cell restarts the cell cycle without repairing the damage[1)].

We have reported that the heavy ion (10 Gy of carbon ions) irradiated silkworm (*Bombyx mori*) eggs at just fertilization restart the development after short time delay (about 2 h), with imperfect (or no) repair of DNA damage. Then, the eggs having damaged DNA died at after cellular blastoderm stage (about 12-14 h after oviposion) by apoptosis. The phenomenon resemble to checkpoint adaptation.

On the other hand, there is the other interesting hypothesis. In the mouse at the one- or two-cell embryo, the G2/M checkpoint and DNA repair mechanisms have insufficient function[2)]. The embryo, irradiated with 10 Gy of gamma ray, restart the development at 30-35 h after fertilization without the repair the damage. Most of maternal transcripts are degraded at this time. So the damaged embryo cannot stop the development.

In this study, we investigate the amount of transcripts of the genes concerned with checkpoint and apoptosis induction, *Bm Histone H2AX* (*Bombyx*), *Bm p53* (*Bombyx*), *Bm Dronc* (*Bombyx* initiator caspase), *Bm Caspase1* (*Bombyx* effector caspase), and *Bm Actin A3* as internal standard, at various stages of early embryogenesis. The quantitative analysis was performed by real time PCR. External standard kit (λ poly A) for qPCR (TAKARA) was used as external standard.

The transcripts of all 4 apoptosis related genes were detected in the silkworm eggs by RT-PCR (Fig. 1). The amplified bands of each gene were revealed at all lane. However, the amounts of the transcripts were quite different. In comparison the amount of *Actin A3* mRNA, the levels of apoptosis related 4 genes were quite low, especially the amount of *Bm Dronc* mRNAs were <0.5%. This may be one of the reasons why the apoptotic cell death cannot be detected in the heavy ion irradiated silkworm eggs at early development. The mRNA amount of *Bm Dronc* increased to about 500% at 12 h after oviposion. In the stage, the transcripts derived from embryo's genes could be detected, and TUNEL positive nuclei would be observed. Now, we try to detect the Bm Dronc protein by using the specific antibody.

References

1) M. Vugt and R. Medema, Cell Cycle, **3**, 1383 (2004).
2) M. Yukawa *et al.*, Biochem. Biophys. Res. Comm., **358**, 578 (2007).

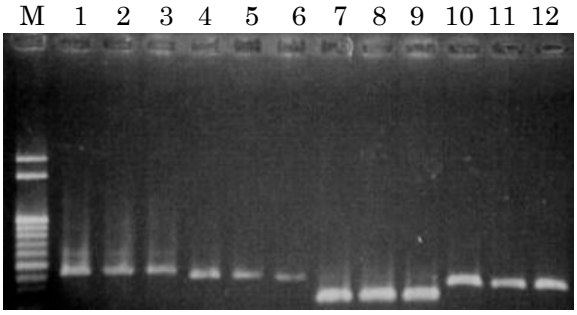

Fig. 1 Detection of transcripts of four apoptosis related genes during the early embryonic development of silkworm eggs by RT-PCR. M: marker, lane 1-3: *Bm Histone H2AX*, lane 4-6: *Bm p53*, lane 7-9: *Bm Dronc*, lane 10-12: *Bm caspase1*. Lane 1, 4, 7, 10 are the samples from the eggs of 3.5 h after oviposition. Lane 2, 5, 8, 11 are 6 h after oviposition and lane 3, 6, 9, 12 are 12 h after oviposition.

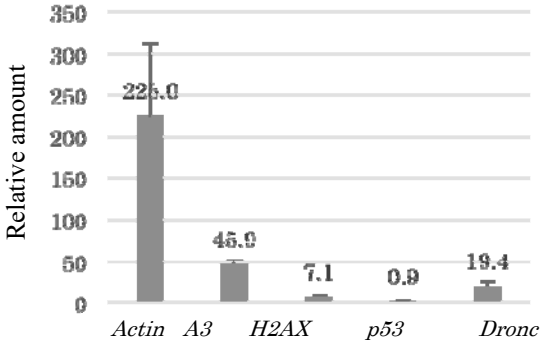

Fig. 2 The relative amounts of the apoptosis related genes of the heavy ion irradiated eggs at 3.5 h after oviposition. External standard = 100.

2-16 Effects of Region-Specific Carbon-Ion Irradiation on Locomotion in *C. elegans*

A. Yamasaki [a),b)], M. Suzuki [b)], T. Funayama [b)], Y. Yokota [b)], Q.-M. Zhang-Akiyama [a)] and Y. Kobayashi [b)]

[a)] Division of Biological Science, Kyoto University,
[b)] Department of Radiation-Applied Biology Research, TARRI, QST

The nematode *Caenorhabditis elegans* is a suitable model organism to study tissue-specific radiation effects, because it has fundamental tissues such as neuronal circuits, muscles, intestine, and gonad. Using *C. elegans*, we have investigated the effects of heavy-ion irradiation on muscular movement, and found that whole-body irradiation significantly reduced locomotion (snake-like crawling motion) [1]. However, the same effects as whole-body irradiation have not been observed after region-specific microbeam-irradiation to head, middle, or tail region [2]. In the present study, to investigate the relationship between effects and irradiation region in more detail we widened the irradiation region and targeted to anterior half-body and posterior half-body.

Young adult wild-type *C. elegans* were used in all experiments. To investigate the effects of region-specific microbeam irradiation, we used energetic carbon ions ($^{12}C^{5+}$, 18.3 MeV/u, LET=119 keV/μm) generated at the HZ1 port of TIARA. To inhibit free moving during irradiation a worm was enclosed in a ditch (approximately 60 μm in width) of a polydimethylsiloxane microfluidic device with buffer solution. Targeting regions were as follows: (1) whole body, (2) anterior half-body (the nerve ring, pharynx, intestine, and gonad), and (3) posterior half-body (vulva, intestine, gonad, and tail). These regions were irradiated with 200,000 or 600,000 carbon ions corresponding to 1.0 or 3.0 kGy at a φ60 μm micro-aperture area. For example, in the anterior half-body irradiation, we targeted to the φ60 μm area in order from head to middle and irradiated at seven or eight times (see Fig. 1). In the locomotion assay, a worm was placed on an agar plate spread with *E.coli* (food) immediately after irradiation. The locomotion was video-recorded, and then the trajectory for 5-sec duration was derived by image processing of the movie (Fig. 2).

In the case of irradiation with 3.0 kGy, locomotion in the worms irradiated to anterior/posterior half-body was reduced (Fig. 2c, d), while that in the worms irradiated to whole-body completely stopped (Fig. 2b). There was no significant difference between worms irradiated to anterior half-body and those irradiated to posterior half-body. Arrest of locomotion in the worms irradiated to whole body was slightly restored at 24 hours after irradiation. Furthermore, reduction of locomotion in the worms irradiated with 1.0 kGy to anterior/posterior half-body was less than that in the worms irradiated with 3.0 kGy, and was well restored.

From these results, it was found that the radiation effects on locomotion in *C. elegans* depend on the irradiation area. As the next step, we will carry out the tissue-specific microbeam irradiation to explore the part of the body which relates to radiation-induced reduction of locomotion.

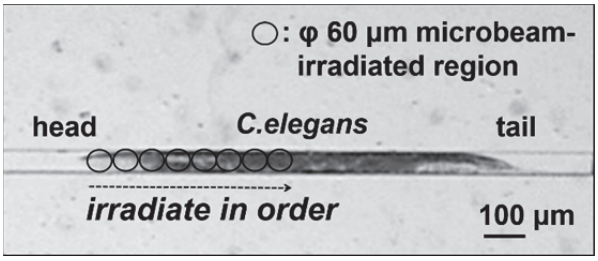

Fig. 1 A *C. elegans* enclosed in a ditch of a microfluidic device. The circle represents the area targeted by using a micro-aperture with 60 μm in diameter.

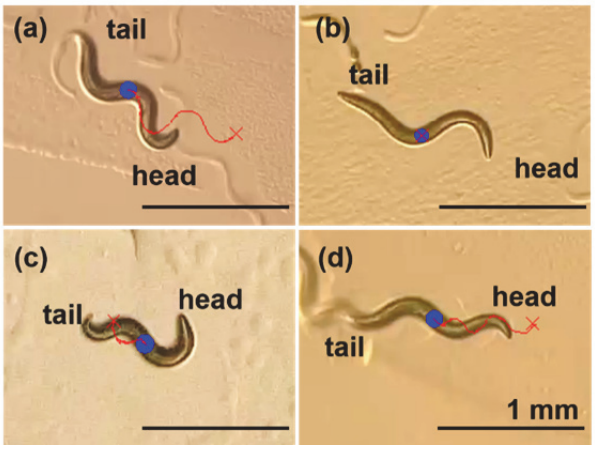

Fig. 2 The typical locomotion of *C. elegans* immediately after region-specific irradiation with carbon ions. (a) A worm without irradiation (control); (b-d) worms irradiated with 3.0 kGy to whole body (b), anterior half-body (c), and posterior half-body (d), respectively. Solid line overwritten on a worm represents the trajectory of the center point of the body for 5-sec duration. ● and × represent the start point (0 sec) and the end point (5 sec), respectively.

References

1) T. Sakashita *et al.*, Biol. Sci. Space, **26**, 7-11 (2012).
2) M. Suzuki *et al.*, JAEA Takasaki Annu. Rep. 2013, JAEA-Review 2014-088, 78 (2015).

2-17 Detection Methods of Irradiated Raw Bovine's Liver to Sterilize the Inside of "GYU-REBA-SASHI"

M. Kikuchi and Y. Kobayashi

Department of Radiation-Applied Biology Research, TARRI, QST

To prevent foodborne illness from beef tartare "Yukhoe", which is served at restaurants, the surface of raw meat have heated and trimmed. However, pathogenic bacteria of *E. coli* were found in the inside of raw bovine's liver. Furthermore, no available disinfection could sterilize the bacteria in the raw liver. Then, raw bovine's liver known as "GYU-REBA-SASHI" was prohibited as Japanese dish, from July 1, 2012. We have thought that radiation exposure is the only solution to kill the bacteria in the liver, since irradiation can sterilize bacteria in foods of sealed package without heating. Providing to the permission of radiation sterilization to eat the liver, detection methods of the livers have been examined by the following methods.

First, ELISA method, which had been developed for irradiated ground meat, was applied to the raw bovine's liver. After the irradiation with γ-rays, the DNA was isolated from the liver. The 8-hydroxyguanine (8-oxoG) of oxidative DNA base damage was measured by using specific antibody. The signal intensities from the livers, irradiated on ice, showed simple increase by increasing the absorbed doses. When the liver were irradiated in dry-ice, no signal increase of 8-oxoG was observed (Fig. 1). In the ELISA method, the 8-oxoG was the secondary reactant that was induced by radicals. As the result, the temperature affected to the 8-oxoG production, since the migration of radicals could be inhibited under freezing temperature. That is why the induction of DNA base damages by γ-irradiation was suppressed in frozen condition. Therefore, the dose response of 8-oxoG on the ELISA method suggests an application to the irradiation detection of bovine's liver treated in chilled condition[1].

Second, we decided to detect radicals, based on the ionization of radiation. Each radical, consisting of unpaired electrons, can be theoretically measured with electron spin resonance (ESR) spectroscopy. However, ESR method was not so easy to measure because of water-in-samples and ambient temperature. Since, we had an experience of ESR method at liquid nitrogen temperature in the detection method of fresh fruits irradiated in the quarantine treatment, we tried to measure raw bovine's liver in similar manner of ESR.

After the raw bovine's liver was exposed to γ-rays, radicals on the liver were measured with ESR at 77 K in liquid nitrogen. In the magnetic field of 320.5 to 335.5 mT, the signals responsible to absorbed doses were found. The signal intensities of the main peak were increased up to 5 kGy. The side peaks existing in low and high magnetic fields of the main peak showed linear responses by increasing absorbed doses (Fig. 2). Without a complicated sample preparation, radicals in the livers can be measured easily on the ESR at liquid nitrogen temperature. Surprisingly, the radicals were found in a tissue of the animal, except for bones. Therefore, the ESR method may be applicable to distinguish the raw bovine's liver when exposed to more than ca. 3 kGy even in a couple of days after irradiation[2].

In conclusion, the ESR method can be useful for the screening of irradiated bovine's liver in quick handling. Practical temperature of irradiation for the raw bovine's liver is supposed to be under freezing condition. Additional experiments are currently in progress for the application of ESR method to the irradiated frozen raw bovine's liver.

References

1) M. Kikuchi *et al.*, FOOD IRRADIATION, JAPAN, **50**, 3 (2015).
2) M. Kikuchi *et al.*, FOOD IRRADIATION, JAPAN, **50**, 9 (2015).

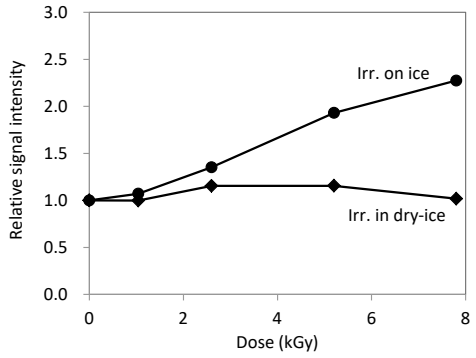

Fig. 1 Dose response of irradiated raw bovine liver on ELISA method.

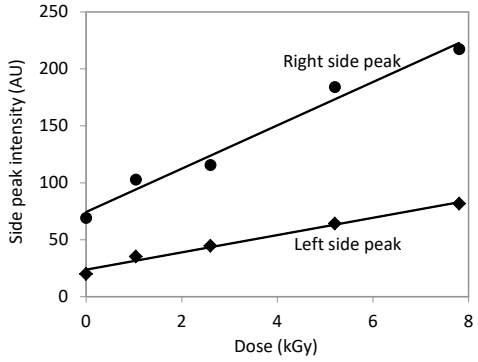

Fig. 2 Dose response of irradiated raw bovine liver on ESR method.

2-18 Estimation of Damage Localization in DNA Irradiated with $^{4}He^{2+}$, $^{12}C^{6+}$, and ^{60}Co γ-rays in Aqueous Solution

K. Akamatsu and N. Shikazono

Department of Quantum Beam Life Science, KPSI, QST

1. Introduction

Ionizing radiation-induced DNA damage can cause mutation and carcinogenesis. In particular, "clustered damage", that is a DNA region with two or more lesions within a few helical turns, is believed to be hardly repaired. This damage is considered to be induced around high-LET ionizing radiation tracks. However, detail of the damage is unknown. We have already developed a method for estimating localization of apurinic/apyrimidinic sites (APs) on DNA using fluorescence resonance energy transfer (FRET) occurring between different fluorescent dyes (Alexa350 and Alexa 488) (*hetero*-FRET). The FRET efficiency (*E*) was calculated from Alexa350 fluorescence intensities before/after enzymatic digestion of the labeled DNA with APs[1]. We succeeded in estimating qualities of clustered APs produced in $^{4}He^{2+}$-, $^{12}C^{5+}$-, and ^{60}Co γ-irradiated dry DNA film to study "direct" radiation effects using the method [2]. We also applied the method to aqueous DNA solution to study "indirect" radiation effects. However, there are some problems of the complex protocol and of the sensitivity due to the low extinction coefficient of Alexa350. We have, therefore, developed "*homo*-FRET" occurred between two or more Alexa488 molecules. We will obtain magnitude of FRET also from "fluorescence anisotropy" of *homo*-FRET between Alexa488 molecules. The new protocol using *homo*-FRET enables us to estimate DNA damage localization without any enzymes and improves sensitivity to detect a clustered damage.

2. Experiments

●*Sample preparation and irradiation*

PUC19 digested by Sma I was used (linear formed) for DNA samples to be irradiated. The DNA was dissolved in 0.2 M Tris-HCl buffer (pH 7.5), which is a cell-mimetic condition, to be ~10 g/L. The DNA solution was transferred to a chamber (thickness: 1 mm), and was irradiated with plate was irradiated with $^{4}He^{2+}$ (12.5 MeV/u, LET: 19 keV/μm), $^{12}C^{6+}$ (26.7 MeV/u, LET: 87 keV/μm), (HY, TIARA). Moreover, ^{60}Co γ-rays were also used as a standard radiation source at Kyoto University Research Reactor Institute.

●*Preparation of fluorophore-labeled irradiated DNA and FRET observation*[3]

The irradiated DNA (10 μL in water) and 10 μL of 100 mM Tris-HCl (pH 7.5) were mixed in a microtube. Two microliters of Alexa488/DMSO was added to the DNA solution and was incubated for 24 h at 35 °C. The fluorophore-labeled DNA was purified by ethanol-precipitation followed by ultrafiltration. The fluorescence anisotropy was measured at 525 nm (ex. 470 nm).

The anisotropy, $< r >$, is defined as follows:

$$< r > = (I_{VV} - G \cdot I_{VH})/(I_{VV} + 2 \cdot G \cdot I_{VH})$$

where I_{VV} is the fluorescence intensity when the excitation and emission polarizers are both vertically oriented. I_{VH} is one when the excitation/emission polarizers are vertically/horizontally oriented. G is the grating factor defined as I_{HV}/I_{HH}.

3. Results and Discussion

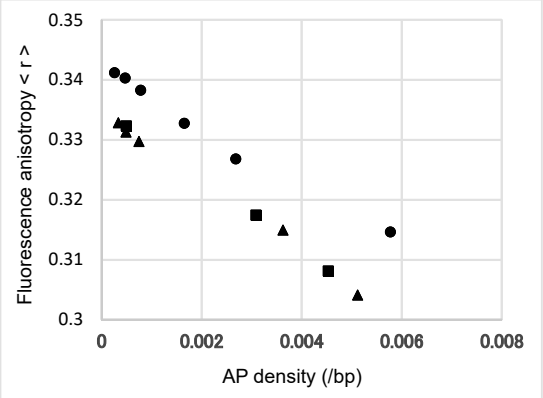

Fig 1 Fluorescence anisotropy of AF488-labeled DNA irradiated with ^{60}Co γ-rays (●), $^{4}He^{2+}$ (■), and $^{12}C^{6+}$ (▲) as a function of AP average density.

Figure 1 shows relationships between AP average density and fluorescence anisotropy for the He, C ion beams, and ^{60}Co γ-rays. This indicates that anisotropy for He ions are almost the same as those for C ones, whereas anisotropy for these ion beams seems to be smaller than that for the γ-rays. We consider that LET of C beam is not enough to show difference in anisotropy between APs in comparison with He beam.

4. Acknowledgments

We would like to gratefully thank Dr. Takeshi Saito of Kyoto University Research Reactor Institute for supporting ^{60}Co γ-ray irradiation.

References

1) K. Akamatsu, N. Shikazono, Anal. Biochem., **433**, 171-80 (2013).
2) K. Akamatsu et al., Radiat. Res., **183**, 105-13 (2015).
3) K. Akamatsu, JAEA Takasaki Annu. Rep. 2008, JAEA-Review 2009-041, 63 (2010).
4) L. W. Runnels, S. F. Scarlata, Biophys. J., **69**, 1569 (1995).

2-19 A Study on Ion-beam-induced Mutations in Rice under Cross-ministerial Research Program, "SIP"

Y. Oono and Y. Hase

Department of Radiation-Applied Biology Research, TARRI, QST

Since 2014, we have been involved in the scientific research program, Cross-ministerial Strategic Innovation Promotion Program (SIP), directed by the Council for Science, Technology and Innovation (CSTI). The project, "Technologies for Creating Next-Generation Agriculture, Forestry and Fisheries" is one of the 11 projects produced and run under SIP. One of the major goals in this project is establishing new breeding techniques including sophistication of the ion-beam breeding technique. With collaborating other irradiation research facilities such as RIKEN Nishina Center and Institute of Radiation Breeding (IRB), we are going to analyze DNA of rice mutants by exome analysis [1] (Fig. 1). This study is aimed to uncover features of induced mutations caused by ion beams in TIARA, and figure out similarities and differences of characteristics of mutations obtained in the other facilities.

Rice cultivar Nipponbare was chosen for the material of the experiment, because genome sequence of Nipponbare has been released to the public. Seeds of Nipponbare were irradiated with 40 Gy of 320-MeV $^{12}C^{6+}$ ions (LET on surface=76 keV/μm), after adjusting their water content to 12~13%, and sown on soil to grow M1 plants in a greenhouse at TARRI, QST (Fig. 2). M2 seeds were harvested from every M1 plants and sown again on soil to estimate mutagenic effect by counting the number of chlorophyll mutants in the M2 lines at seedling stage. Several types of chlorophyll mutants, which show pale or white leaf color, were identified (Fig. 3). The appearance rate of the chlorophyll mutants was 6.6% (134 / 2,039 M2 lines), suggesting that the irradiation properly worked and caused mutations in the rice genome as expected. We also screened morphological mutants in this mutagenized population in a green house and identified several mutant candidates with altered visible phenotype (Fig. 4). Seeds of these mutant candidates were harvested and the mutant phenotype was confirmed in next (M3) generation. At the end of March 2016, we have successfully confirmed mutant phenotypes in 8 independent M3 lines. These mutants were put on the list for exome analysis that will be performed in the project. Some M2 lines were send to IRB to be screened in the paddy field in IRB.

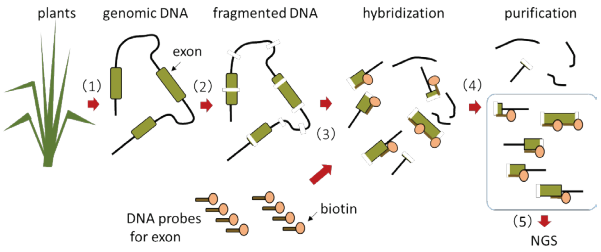

Fig. 1 Schematic outline of exome analysis. Genomic DNA is extracted from plants (1) and fragmented by sonication (2). Synthesized biotinylated DNA probes of protein coding region (exon) are mixed with the fragmented genomic DNA (3), then exon fragments (boxed) are captured by hybridization and affinity purification (4), followed by being subjected to next generation sequencing (NGS) (5).

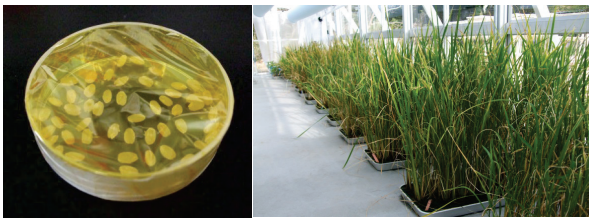

Fig. 2 An irradiation sample of rice seeds in a 60-mm-diameter dish covered with polyimide film (left) and M1 plants grown in a greenhouse (right).

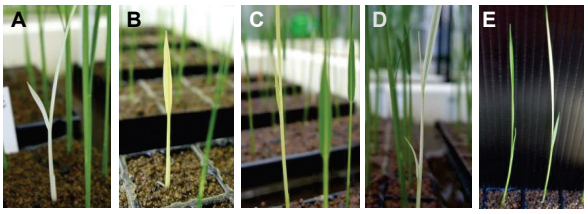

Fig. 3 Chlorophyll mutants used to estimate mutagenic effect in the M2 population. (A), albino; (B), xanta; (C), chlorina; (D), striata; and (E), virescent.

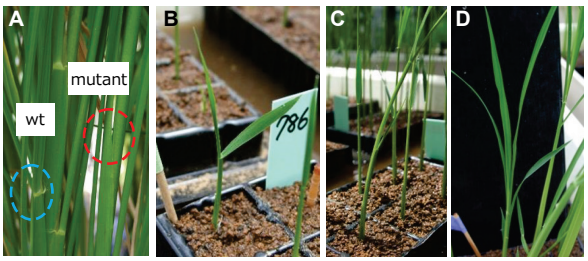

Fig. 4 Phenotype of some morphological mutants identified in the M2 population. (A), leguleless, an organ in the area between basal portion of a leaf blade (inside of the circles) is present in wild type (wt) but missing in the mutant; (B), wide leaves; (C), not straight stem growth; (D), semi dwarf.

This work was supported by CSTI, SIP, "Technologies for creating next-generation agriculture, forestry and fisheries" (funding agency: BRAIN, NARO).

Reference

1) I. M. Henry *et al.*, Plant Cell, **26**, 1382 (2014).

2 - 20

Ion Beam Breeding of Rice for the Mutation Breeding Project of the Forum for Nuclear Cooperation in Asia (FNCA)

A. Tanaka[a)], Y. Hase[a)], Y. Oono[a)], H. Ishikawa[b)] and A. Koike[b)]

[a)]Department of Radiation-Applied Biology Research, TARRI, QST,
[b)]Nuclear Safety Research Association

1. Introduction

Ion beams have been utilized for the Mutation Breeding Project of the Forum for Nuclear Cooperation in Asia (FNCA) of MEXT (Ministry of Education, Culture, Sports, Science and Technology) since 2009. From fiscal year 2013, a new project 'Mutation Breeding of Rice for Sustainable Agriculture' for five years has been launched, following the previous project on 'Composition or Quality in Rice' (FY 2007-2012). This new project will contribute to the increase of food production and improvement of food quality in Asian countries by establishing mutant varieties such as high yielding varieties under low input conditions, new varieties tolerant to diseases, droughts, and other climate changes, according to participating country's demands by using gamma rays or carbon ions. Ten countries, i.e., Bangladesh, China, Indonesia, Japan, Korea, Malaysia, Mongolia, The Philippines, Thailand, and Vietnam have been joined this project and several countries irradiate seeds of their own rice varieties with ion beams at TIARA.

2. Materials and Methods

Hulled dry seeds were exposed to 320 MeV carbon ions at TIARA with optimal doses for respective rice varieties to induce mutation. After irradiation, seeds were sent back to the participating countries and investigated for mutation induction.

At the FNCA workshop on Mutation Breeding held in Thailand in February 2012, we have discussed the appropriate population size for mutation induction and concluded that at least several seeds from each 5 panicles from each 1,000 M_1 plants (5,000 initial mutated cells) irradiated with ion beams at the optimal dose, should be harvested in order to expect a good result.

3. Results and Discussion

Some of the participating countries have proceeded to select mutants in accordance with their countries' demands. In Bangladesh, BINA dhan-14, showing early maturing and high yielding, got official approval for releasing. BINA dhan-14 was cultivated for farmer with the help of agriculture extension in the different area of Bangladesh. Farmers are becoming more and more interested to cultivate this new mutant variety with good agronomic characters. Other promising mutant lines are selected from the mutant lines of drought resistant rice varieties, NERICA 10 and other rain fed rice. Four land races of rice collected from the southern part (costal area) of Bangladesh, are planned to be irradiated for further experiments. In Indonesia, through carbon-ion irradiation with 10 and 20 Gy, six promising mutant lines were obtained. One of the mutant line, IB-3, had the high grain yield, the short plant stature and short growth duration, therefore, were promising to be released.

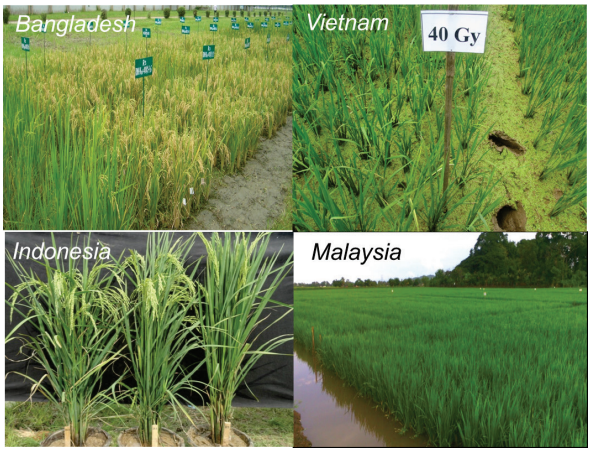

Fig. 1 Ion-beam induced promising mutant lines were evaluated in the fields after several generations of self-fertilization.

In Vietnam, CMBT (carrying salt tolerant gene) and BLBT (carrying bacterial leaf blight disease tolerant genes) seeds were treated with carbon ion radiation (40 and 60 Gy) and were planted and selected at the Agricultural Genetics Institute up to fourth mutant generation (M_4). Fourteen M_4 promising mutant lines derived from 60 Gy-irradation were selected. All of these lines were evaluated for resistance to bacterial leaf blight and salt tolerance in a green house. Most of the mutant lines showed the higher yield than the original varieties.

In Malaysia, 31 potential mutant lines were produced through mutagenesis of MR219 seeds with carbon ion irradiation (60 Gy). They were planted at the Malaysian Nuclear Agency up to third generation (M_3). These M_3 lines (ML1 to ML31) were evaluated on morphological, yield and yield components, and compared to the parental variety, MR219. Advanced mutant lines, MR 219-4 and MR 219-9, were evaluated at the farmer's plot in the northern part of Malaysia. The data on water stress condition indicating that MR 219-9 is more tolerant to drought as compared to MR 219-4 and MR 219-control.

Reference

1) A. Tanaka *et al.*, JAEA Takasaki Annu. Rep. 2014, JAEA-Review 2015-022, 96 (2016).

2-21

Mutagenesis of the Oil-producing Algae by Ion Beam Irradiation

H. Araie[a)], Y. Hase[b)], Y. Oono[b)], I. Suzuki[a)] and Y. Shiraiwa[a)]

[a)]Faculty of Life and Environmental Sciences, University of Tsukuba,
[b)]Department of Radiation-Applied Biology Research, TARRI, QST

Biofuel production using algae has attracted attention as a candidate for the next generation energy. However, due to the development of algal biomass industry, improvement of existing oil-producing algae is required. Here we tried mutagenesis of the oil-producing algae, *Tisochrysis lutea*, by ion-beam irradiation.

藻類を利用したバイオ燃料生産は、単位面積あたりの生産量が陸上植物よりも高く、食料生産と競合しないなどの利点を持つため、次世代エネルギーの候補として注目されている。しかし、藻類バイオマス産業の進展のためには、既存のオイル産生藻を改良し、よりオイル生産に適した有用変異体(オイル高蓄積株あるいは高い増殖速度を持つ株)を作出する必要がある。オイル産生藻については、薬剤処理あるいは UV 照射による変異体作出が試みられているものの、目的形質が安定した有用変異体を得る事は難しい。本研究では、培地上に置いたオイル産生藻体に対してイオンビームを照射し、オイル産生藻の放射線感受性を調べ、突然変異の誘導に最適な線量・照射方法を検討すると共に目的形質が安定した有用変異体の取得を目指すことで、よりオイル生産に適した有用突然変異系統等の作出に寄与するイオンビーム利用技術の開発を実施した。

Tisochrysis lutea(T-Iso 株)は、現在までに 5 種知られている超長鎖脂質アルケノンを蓄積するハプト植物円石藻の 1 つで、アルケノンは熱分解により炭化水素が生成することからジェット燃料としての利用が提唱されている[1)]。また、*T. lutea*は海産性藻類であるため低コストな海水を用いた大量培養が可能であり、生育が良いことから既に魚餌として大量培養されている藻類である。更に、我々は液体及び寒天培地での至適培養条件を明らかにし、遺伝子発現量やゲノムの情報も得られている(未発表)。そこで本研究では、オイル生産藻として有望な *T. lutea*(T-Iso 株)を用い、高崎量子応用研究所において、0～3,000 Gy 相当のイオンビーム照射を 320 MeV の $^{12}C^{6+}$で行った。

イオンビーム照射を藻類に行うためには寒天培地での培養が必要不可欠である。そこで、まずは海水培地(MA-ESM)で調整した寒天(1% BactoAgar)での培養法を確立した(Fig. 1)。

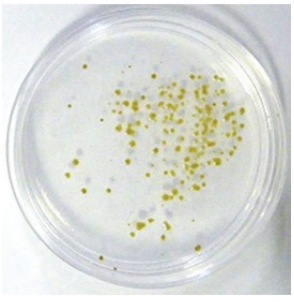

Fig. 1 Plate culture of *Tisochrysis lutea* (T-Iso strain).

次に *T. lutea*(T-Iso 株)のプレート上でのコロニー形成に与える放射線感受性を調べた。120 Gy～3,000 Gy 照射ではコロニー形成を確認できなかった(data not shown)。0～80 Gy 照射で計測したコロニー形成数を照射線量に対してプロットした結果、*T. lutea* の半コロニー形成数照射線量は約 30 Gy だった(Fig. 2)。

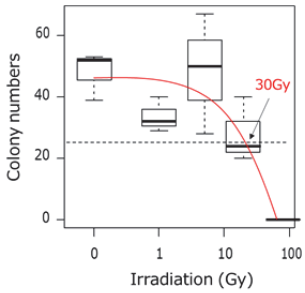

Fig. 2 Boxplot of dose-dependent for colony formation. 150 cells dropping on the plate were irradiated by 0, 1, 5, 20 and 80 Gy respectively. Colony numbers were counted 7 days after irradiation. Red line: Binomial approximation formula of median, Dot line: Half line of colony number, Arrow: Dose for half of colony formation.

最後に、20 Gy 照射及び 80 Gy 照射で生き残った株について 1 日当たりのアルケノン生産性を調べた(Fig. 3)。結果、20 Gy 照射から 21 株(変異率 36%)、80 Gy 照射から 7 株(変異率 22%)、アルケノン生産性の向上した株を得ることが出来た。一方で、アルケノンの生産量が極めて低くなった株も取得できた。

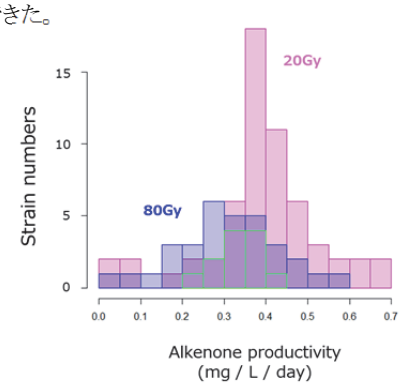

Fig. 3 Histogram of alkenone productivity. Alkenone productivity of 12 strains from wild type (bordered in green), 59 strains from mutants obtained by 20 Gy irradiation (pink) and 32 strains from mutants obtained by 80 Gy irradiation (blue) were analyzed.

Reference

1) O'Neil *et al.*, Energy Fuels, **29**, 922-30 (2015).

2 - 22

Development of Low Temperature-Flowering Chrysanthemum Variety 'Ryujin' and 'Touma'

M. Tamari [a)], Y. Tanokashira [a)], S. Nagayoshi [a)], K. Kido [a)], F. Tojima [a)], Y. Hase [b)] and Y. Oono [b)]

[a)] Kagoshima Prefectural Institute for Agricultural Development,
[b)] Department of Radiation-Applied Biology Research, TARRI, QST

We have succeeded to develop new chrysanthemum variety 'Ryujin' and 'Touma' by step-wise improvement with ion beam irradiation. Important agricultural traits in chrysanthemum, *i.e.,* low lateral-bud formation and low-temperature flowering, were conferred in a step-wise manner by two or three-round of ion beam irradiation and mutant selection.

1. はじめに

浜松特花園が育成した純白大輪の秋輪ギク「神馬」は、1990年代から鹿児島県の主力品種として栽培されてきたが、脇芽の摘蕾数が多く、低温開花性に劣るという短所があった。鹿児島県では2000年から日本原子力研究開発機構(現量研機構)等の協力のもと、①無側枝性、②ボリューム向上、③低温開花性の付与を目標として、「神馬」へのイオンビーム照射による突然変異育種に取り組んできた。2003年には、半無側枝性で、ボリュームがあり、「神馬」と同様の栽培管理が可能な新品種「新神」及び「今神」の育成に成功したが、昨今の重油代高騰もあり，低温開花性の付与を最優先課題として、イオンビームの再照射による改良を進めてきた。ここでは、「新神」の再改良による低温開花性秋輪ギク品種「立神」及び「冬馬」の育成について報告する。

2. 「新神」の段階的改良による「立神」及び「冬馬」の育成

(1) 材料の選定と低温開花性付与の可能性の検討

イオンビームの再照射による改良にあたっては、核DNA量が原品種に比べて減少した系統を材料にした場合には、本来持っている優良特性が損なわれる可能性が高いことを過去に報告している [1)]。「新神」及び「今神」の核 DNA 量を測定した結果、「今神」は「神馬」に対して1～2%の核DNA量の減少が見られたが、「新神」は「神馬」と同程度であったことから、「新神」が材料として適当であると判断した。予備試験として、「新神」の葉片培養物へイオンビームを照射して得られた個体を生育期間を通じて一般管理より4～5 ℃低い低温管理で栽培した結果、「新神」に比べて低温開花性のある個体を選抜することができた。さらに、選抜した個体を次年度も低温管理で栽培した結果、低温開花性の維持を確認できたことから、「新神」への再度のイオンビーム照射により、低温開花性の付与が可能であると考えられた [1)]。

(2)「新神」の再照射による低温開花性系統の選抜

2009 年に「新神」の葉片に炭素イオンビーム ($^{12}C^{6+}$, 320 MeV) を照射して得られた約 11,000 個体を低温管理の作型で栽培し、低温開花性があり花容草姿に優れる 31 個体を選抜した。さらに 2010、2011 年の系統選抜試験で生育特性を確認し、特に低温開花性・無側枝性・ボリュームに優れた 3 系統 (C09-i-3, C09-i-20, C09-i-27) を選抜した (Fig. 1)。しかしながら，無側枝性が「新神」よりさらに強く、高温期には挿し穂の確保が困難であったため、「新神」並の半無側枝性となるように、再改良の必要があった [2)]。

(3) 選抜系統の再改良と特性評価

2012 年の母株選抜において、「C09-i-20」由来で萌芽性が良い系統「C11-g-78」を選抜した (Fig. 1)。また、「C09-i-3」の葉片に炭素イオンビームを再々照射して得られた個体を栽培し、その中から低温開花性があり、花容草姿、ボリュームが「新神」と同等以上のものを選抜し、且つ次年度母株選抜ほ場で萌芽性に優れる系統「C12-i-4」を選抜した [3)]。続いて、2013、2014年に系統適応性検定を実施し、併せて 2014 年に鹿児島県内主要産地で現地適応性試験を実施した結果、低温開花性があり「新神」と同等の半無側枝性とボリュームを持つ 2 系統「C11-g-78」と「C12-i-4」をそれぞれ「立神 (りゅうじん)」及び「冬馬 (とうま)」として 2015 年度に品種登録出願した (Fig. 2)。

3. おわりに

新品種「立神」及び「冬馬」は複数回 (計 2 回または 3 回) のイオンビーム照射により育成されたものであり，本成果はイオンビームによる段階的特性改良が新品種の育成に有効であることを実証したものと言える。

なお、本研究の一部は SIP 戦略的イノベーション創造プログラムで実施の「変異の出現パターンを整理したデータベースの構築」に貢献する成果である。

References

1) 上野敬一郎ら，日本育種学研究 第 **7** 巻別冊 1，2 号，331 (2005).
2) 田之頭ら，第 6 回高崎量子応用研究シンポジウム要旨集，107 (2011).
3) Tanokashira *et al.*, JAEA Takasaki Annu. Rep. 2013, JAEA-Review 2014-050, 110 (2015).

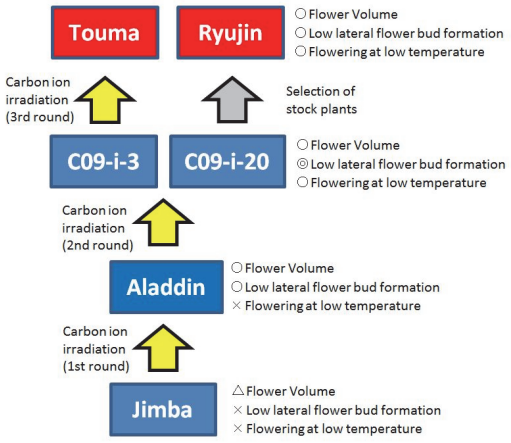

Fig. 1 Schematic view of development al process of 'Ryujin' and 'Touma' by step-wise improvement with ion beam irradiation.

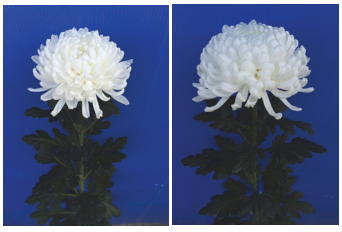

Fig. 2 Low temperature-flowering chrysanthemum variety 'Ryujin (left)' and 'Touma (right)'.

2-23 Determination of Ion Beam Irradiation Conditions for Callus of Tulip

S. Ikegawa [a)], K. Shoji [a)], Y. Hase [b)] and S. Nozawa [c)]

[a)] Toyama prefectural Agricultural, Forestry & Fisheries Research Center,
[b)] Department of Radiation-Applied Biology Research, TARRI, QST,
[c)] Research Planning and Promotion Office, QuBS, QST

For obtaining a novel mutant from tulip plant by ion beam irradiation, we determined effective mutagenesis conditions for callus derived from flower stalk of tulip cv. "Yumenomurasaki". Under various dose of irradiation using 107 MeV helium ion (107 He) or 320 MeV carbon ion (320 C), 2 Gy of 107 He or 0.5 Gy of 320 C was thought to be adequate for inducing mutations that were estimated from survival rate, the number and the length of regenerated shoots from irradiated calli.

チューリップのカルス(未分化細胞塊)へ変異誘発を行うことにより、種子や球根に比べ変異誘発効率が高まることが期待される。本研究では、効率的な突然変異誘発を目指し、高崎量子応用研究所においてチューリップのカルスへイオンビームを照射することにより、その適正な照射条件を検討した。試験材料には、富山県育成品種である「夢の紫」の花茎由来カルスを用い、イオンビームは 107 MeV のヘリウムイオン(以下 107 He)と 320 MeV の炭素イオン(以下 320 C)を用いた。

照射は 1 サンプルに対し 1 回実施すること、照射条件を決定するための照射を 2 回実施すること、照射条件は照射後のシュート形成数、シュート長、個体残存率等を指標として決定することとした。

1 回目照射は、両イオン共に照射量の範囲を 10 条件と広くして実施した。1 回目照射後、2 回目照射までの間に枯死個体はみられなかった。そのため、シュート形成数やシュート長などから適正なビーム照射量を検討したところ、107 He で 4 Gy 以下、320 C で 2 Gy 以下と考えられた(Figs. 1 and 2)。

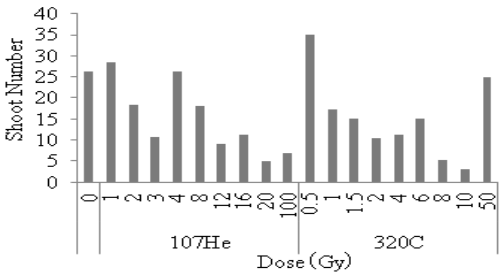

Fig. 1 Average shoot number regenerated from calli, observed at 3 months after irradiation.

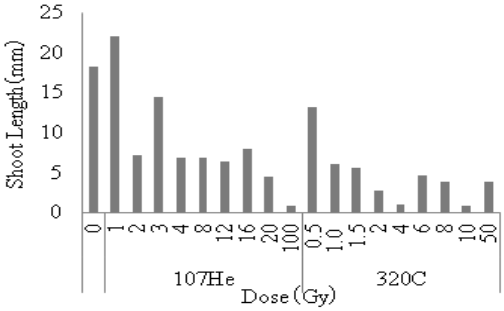

Fig. 2 Average shoot length regenerated from calli, observed at 3 months after irradiation.

そのため、2 回目照射は、低照射量域に絞って行った。ただし、ビームが到達しない部分からのシュート形成について考慮するため 107 He 100 Gy と 320 C 50 Gy の照射も実施することにした。

1 回目照射の 7 ヶ月後頃から枯死個体が現れ始め、その後かなり残存率が低下したため、残存率を適正照射量の指標とすることにした。H28.1 月時点の残存率は、1 回目照射の 107 He では 2 Gy から 3 Gy において、320 C では 0.5 Gy から 1 Gy において、また 2 回目照射の 107 He では 1.5 Gy から 2 Gy において、320 C では 0.5 Gy から 0.75 Gy において急激な低下が見られた(Figs. 3 and 4)。

また、イオンビーム照射後個体に対し、再分化誘導及び小球根形成誘導を行ったところ、これまでに 107 He を 1 及び 2 Gy 照射後個体から各々1 個、また 320 C を 0.5 及び 50 Gy 照射後個体から 9 個と 1 個の小球根を得た。ただし、320 C 50 Gy 照射後個体のシュートは、カルスの裏側から伸びていたため、その個体から得られた小球根はビームの影響を受けていないものと推測された。

これらの結果から、107 He 2 Gy 及び 320 C 0.5 Gy がチューリップカルスへの照射条件として適正であると考えられた。

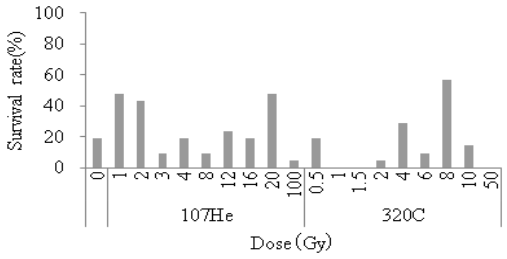

Fig. 3 The survival rate of the first irradiation after 1 year.

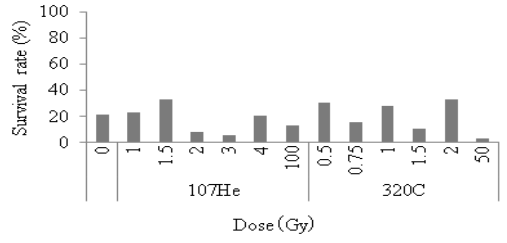

Fig. 4 The survival rate of the second irradiation after 9 months.

2-24

Re-Development of New Variety of *Salvia* by Ion Beam Breeding

E. Yamaguchi [a)], M. Miyatani [a)], T. Kawai [a)], H. Atsumi [a)] and Y. Hase [b)]

[a)] The Yokohama Nursery Co., Ltd.,
[b)] Department of Radiation-Applied Biology Research, TARRI, QST

To obtain new flower mutants and evaluate the difference in the irradiation sensitivity for re-irradiation, the flower color mutants selected from carbon ion (320 MeV) irradiated interspecific hybrid Salvia varieties were irradiated with carbon ions again. The mutation rate for flower color characters were ranged between 0% and 14.58%, by different doses. The possibility for commercialization of the selected flower color mutants will be evaluated continuously.

1. はじめに

横浜植木(株)育成のサルビア種間交雑品種(SAC33)は赤紫色の花を咲かせる。このサルビアにイオンビームを照射して得られた花色変異 4 系統を材料として再度イオンビームを照射し、再照射に対する感受性の変化を調査するとともに、突然変異育種によって新たな花色変異の獲得を目指した。

2. 材料及び方法

供試系統は、サルビア SAC33 に量子科学技術研究開発機構高崎量子応用研究所のAVFサイクロトロンにより発生させたイオンビーム(320 MeV・$^{12}C^{6+}$)を照射し、得られた変異 4 系統 6-8、6-19、6-22、6-25 を用いた。全系統合わせて 3,841 本の挿し穂を寒天培地に挿し、再びイオンビーム(320 MeV・$^{12}C^{6+}$)を照射した。照射線量は、0, 0.5, 1, 2, 3, 4, 6 及び、8 Gy とし、照射した挿し穂は培土へ挿し芽し、発根後 3 号ポリポットへ鉢上げ、開花調査を行った。

3. 結果及び考察

照射株の成苗率は、照射 1 回目はどの区も 80%以上あったが、今回は 75%以下であった(Table 1)。変異はキメラ状の発生と、枝全部が変異したものがあった。最も多い変異は元のSAC33と同様の赤紫色に戻る復帰突然変異であった。その他の変異では、前回得られたピンクより色の薄いピンクや濃いピンクなどが得られた。また、葉縁部が薄い緑色になる斑入りの変異株も得られた。花色の戻りも含めた変異の発生率は0～14.58%で、今回0Gy照射区でも花色の戻る変異が発生していることから、前回の照射による変異[1)]が必ずしも安定したものではなく不安定な要素があると考えられた。新規の変異個体は挿し芽を行い、商品化を検討する。

本研究は日本原子力研究開発機構の先端研究基盤共用・プラットフォーム形成事業を利用して実施した。

Table 1 Survival rate and rate of mutation.

Line No.	First Dose(Gy)	Second Dose(Gy)	Number of cuttings	Survival rate(%)	Rate of mutation (%)
6-8 Pink	1	0	41	70.7	3.45
		0.5	129	48.8	1.59
		1	136	39.7	3.70
		2	132	50.8	7.46
		3	126	39.7	8.00
		4	122	54.9	4.48
		6	123	52.8	6.15
		8	117	38.5	6.67
6-19 Pink	6	0	37	40.5	6.67
		0.5	120	57.5	11.59
		1	130	20.0	3.85
		2	106	65.1	14.49
		3	122	41.8	7.84
		4	113	31.9	5.56
		6	118	40.7	14.58
		8	105	40.0	7.14
6-22 Salmon	8	0	42	50.0	4.76
		0.5	137	40.1	3.64
		1	143	34.3	0.00
		2	140	41.4	5.17
		3	151	33.1	2.00
		4	142	30.3	6.98
		6	142	28.2	2.50
		8	137	27.0	10.81
6-25 Salmon	12	0	45	60.0	3.70
		0.5	143	59.4	1.18
		1	136	33.8	2.17
		2	141	44.0	1.61
		3	134	51.5	1.45
		4	136	47.8	9.23
		6	141	39.0	3.64
		8	154	39.0	5.00

Reference

1) E. Yamaguchi *et al.*, JAEA Takasaki Annu. Rep. 2014, JAEA-Review 2015-022, 111 (2016).

2-25 The Pyrimidine (6-4) Pyrimidone Photoproducts Cause T to G Mutations in Arabidopsis

A. N. Sakamoto [a)], H. Yamaguchi [b)] and M. Teranishi [b)]

[a)] Department of Radiation-Applied Biology Research, TARRI, QST,
[b)] Graduate School of Life Sciences, Tohoku University

Unrepaired DNA damage poses a big obstacle in maintaining genome integrity since it can jeopardize precise DNA replication. The presence of pyrimidine dimers or oxidative damage can affect the fidelity and activity of DNA polymerases, which could cause mutations as a consequence. To investigate the correlation between DNA damage and mutations, we irradiated Arabidopsis plants with UV-B, UV-C or gamma-rays and measured the induced DNA damage as well as mutation frequency.

The *Arabidopsis thaliana* plants carrying *UidA*$_{166G\text{-}T}$ were grown on Murashige and Skoog agar plates at 23 °C under a 16-h light and 8-h dark cycle for 10-12 days. The seedlings were irradiated with UV-B (CSL-30B, COSMO BIO), UV-C (CSL-30C, COSMO BIO), or gamma-rays (^{60}Co Gamma-ray Food Irradiation Facility, TARRI). After irradiation, a portion of plants was harvested immediately to detect DNA damage. The remaining plants were grown for another 7-8 days, then harvested to detect somatic mutations.

Cyclobutane pyrimidine dimer (CPD) and pyrimidine (6-4) pyrimidone photoproduct [(6-4) PP] are detected by enzyme-linked immunosorbent assay (ELISA) using monoclonal antibodies against CPD and (6-4) PP. The numbers of single and double strand breaks are determined by analyzing the migration of genomic DNA in the gel [1)].

The *UidA*$_{166G\text{-}T}$ marker has a nonsense mutation in a bacterial β-glucronidase gene driven by cauliflower mosaic virus 35S promoter. The cells carrying a T-G reversion on the marker are stained blue when the plant was soaked in the substrate solution [2)].

As a result, we found that both 1,000 Jm^{-2} of UVC and 3,000 Jm^{-2} of UVB induced comparable amount of CPDs and strand breaks (Fig. 1A). By contrast, (6-4) PPs were more abundantly induced by 1,000 Jm^{-2} UVC than 3,000 Jm^{-2} of UVB (Fig. 1B). As for the frequency of reversions in somatic cell, 1,000 Jm^{-2} of UVC induced more mutations than 3,000 Jm^{-2} of UVB (Fig. 2A).

Previously, we showed that 100 Gy of gamma-rays induced ~0.7 of strand break per Mb [1)], which is comparable frequency induced by 1,000 Jm^{-2} of UVC or 3,000 Jm^{-2} of UVB (data not shown). Here, however, even less dose (500 Jm^{-2}) of UVC induced more mutations than 100 Gy of gamma-rays (Fig. 2B). These results suggest that the (6-4) PP is a major source of somatic reversions detected in the *UidA*$_{166G\text{-}T}$ marker line. Further analysis using polymerase-deficient plants will elucidate the mechanism by which UV damage induces mutations in plant cells.

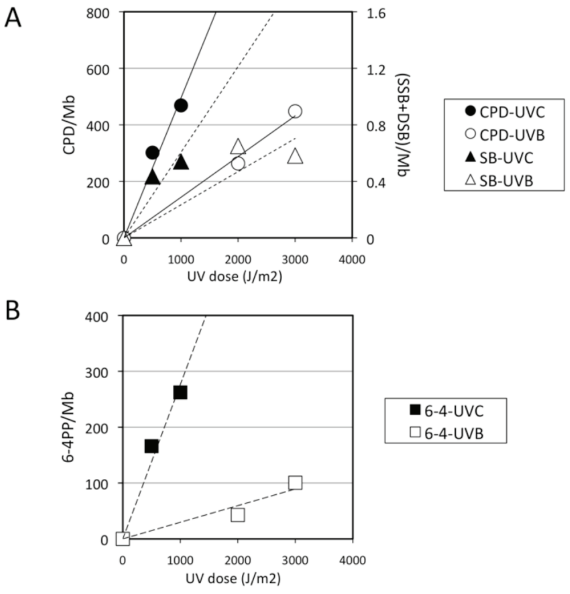

Fig. 1 Induction of DNA damage in UV- or gamma-irradiated plants. (A) Induction of cyclobutane pyrimidine dimer (CPD) and strand break. (B) Induction of pyrimidine (6-4) pyrimidone photoproduct [(6-4) PP].

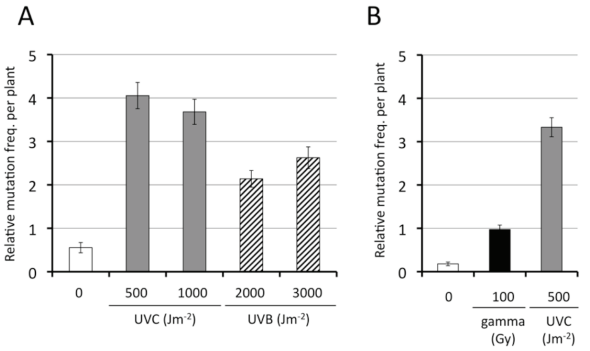

Fig. 2 Mutation frequency in UV- or gamma- irradiated plants. (A) Mutation frequency in UVB- or UVC-irradiated plants. (B) Mutation frequency in gamma- or UVC-irradiated plants.

References

1) M. Teranishi *et al.*, JAEA Takasaki Annu. Rep. 2013, JAEA-Review 2014-050, 115 (2015).
2) M. Nakagawa *et al.*, Plant Phys., **155**, 414 (2011).

2 - 26

Evaluation System of DNA Lesions Caused by Ion beam Irradiation Using the Polymerase Chain Reaction

Y. Matuo [a)], Y. Izumi [a)], A. N. Sakamoto [b)], Y. Hase [b)] and K. Shimizu [c)]

[a)] Research Institute of Nuclear Engineering, University of Fukui,
[b)] Department of Radiation-Applied Biology Research, TARRI, QST,
[c)] Radioisotope Research Center, Osaka University

The ion beams have been extensively used as the mutagen for developing new varieties of plants and bacteria [1,2]. We have been studying ion-beam induced mutations in budding yeast *S288c* (*RAD*$^{+}$), as a model of the eukaryote cell. In previous studies, the yeast cells were irradiated with carbon ions ($^{12}C^{6+}$; 220 MeV, LET: 107 keV/μm) and gamma-rays. The remarkable feature of yeast mutations in *URA3* gene induced by the carbon ions was that the mutation sites were located at hotspot near the linker regions of nucleosomes, whereas mutations induced by gamma-ray irradiation were located uniformly through the marker gene. In particular, hotspot existed in the region of +90 - 300 of the *URA3* gene by high LET ion beam[3]. Also, we demonstrated that radiation dose can be estimated by the quantitative polymerase chain reaction (qPCR) [4,5]. In this study, we tried to evaluate the amount of DNA lesion caused by high LET ion beams in the *URA3* gene.

The DNA fragments for ion beam irradiation were prepared using conventional PCR (amplification of 804 base pairs of *URA3* gene). The amplified DNA fragments dissolved in TE buffer (Tris-HCl 10 mM, EDTA 1 mM, pH 7.4) were dropped on a sample plate and air dried. The DNA sample was irradiated with carbon ions (LET: 107 keV/μm) and neon ions (LET: 335 keV/μm) with the dose of 1 - 100 Gy at TIARA. For comparison purpose, the DNA samples were also irradiated with helium ions (LET: 2.2 keV/μm) at HIMAC (National Institute of Radiological Sciences, Japan). Real-time PCR was employed to amplify a 210-bp region of the *URA3* gene (position: +90 - 300) by using Real-Time PCR System (MJ Mini, Bio-Rad). SYBR green (SIGMA) was used to monitor the DNA amplification. The obtained data were analyzed by the software "CFX Manager" (Bio-Rad) to calculate the relative amount of DNA products in different samples.

The ratio of replicable DNA decreased along with increasing dose in all three types of ion beams (Fig. 1). The effect on the reduction of replicable DNA was higher in the order of C ion, Ne ion and He ion. This suggested that different types of lesions were produced per unit dose, depending on the LET and fluence of ion beams. These results suggest that this method can be used to evaluate the biological effects caused by various types of radiation with different LET.

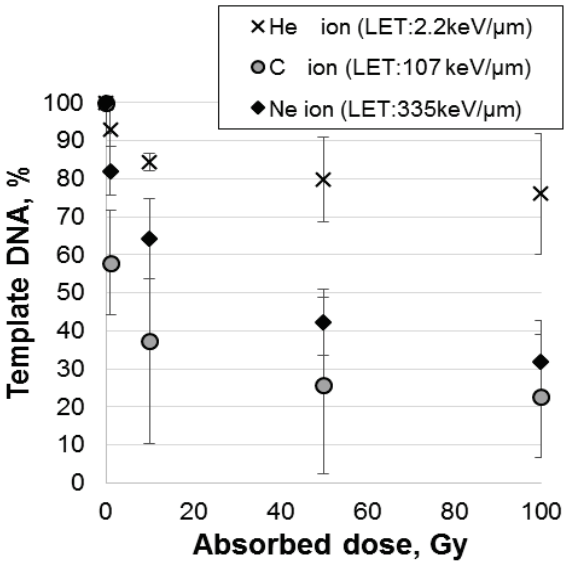

Fig. 1 DNA deactivation rate by Real-Time PCR. N=5.

References

1) A. Tanaka *et al.*, J. Radiat. Biol., **51**, 223 (2010).
2) T. Masubuchi *et al.*, JAEA Takasaki Annu. Rep. 2011, JAEA-Review 2012-046, 110 (2013).
3) Y. Matuo *et al.*, Mutat. Res., **602**, 7 (2006).
4) Y. Matuo *et al.*, Radiat. Meas., **55**, 93 (2013).
5) Y. Matuo *et al.*, JAEA Takasaki Annu. Rep. 2011, JAEA-Review 2012-046, 105 (2013).

2 - 27

Lethal Effects of Gamma Rays and Carbon Ion Beam Radiations in *Bacillus subtilis*

K. Satoh and Y. Oono

Department of Radiation-Applied Biology Research, TARRI, QST

Living organisms are continually exposed to environmental factors such as ionizing radiation that could induce damage to DNA. Ionizing radiation induces DNA double-strand breaks (DSBs), which is a particularly serious form of DNA damage and has an especially deleterious effect on cells. The radiosensitivity of organisms varies extensively depending on the species. Ion beams have a high linear energy transfer (LET, keV/μm) and give DNA damage containing DSBs locally (clustered damage) than gamma rays do. In mammalian cells, plants and *Escherichia coli*, the relative biological effectiveness (RBE) depends on LET and exhibits the peak at a range of LET from about 100 to 200 keV/μm[1–3].

While *Bacillus subtilis* is known as Gram-positive, rod-shape, aerobic, spore-forming bacterium that is naturally found soil. The complete genome sequence of *B. subtilis* has been first published as model microorganism of Gram-positive in 1997[4]. In this study, we investigated lethal effects and relationship between LET and RBE for gamma rays and carbon ion beam radiations in *B. subtilis*.

B. subtilis strain RM125 cells were cultivated at 37 °C in LB broth-Lennox with agitation to early stationary phase. Cells were harvested and washed in 10 mM sodium phosphate buffer (pH 7.0, PB). Cells were resuspended in PB containing protective agents. Aliquots (0.1 mL) of the cell suspensions were adhered onto cellulose membrane, frozen at – 80 °C for 60 min and dried *in vacuo*. Freeze-dried cells were irradiated with carbon ion beam ($^{12}C^{5+}$ [220 MeV; 121.8 keV/μm]) accelerated by an AVF cyclotron at TIARA or with ^{60}Co gamma rays (0.2 keV/μm) at Food Irradiation Facility, TARRI, QST. The irradiation dose ranged from 0.1 to 1.0 kGy. Irradiated cells were harvested, diluted appropriately with the PB, spread onto LB agar-Lennox, and incubated at 37 °C for 1 day prior to the enumeration of colonies. The surviving fraction was determined by calculating the number of surviving colonies divided by the total number of viable colonies. The survival data were fitted to the single-hit multi-target survival model. RBE was calculated from the equation: RBE = D_{10} of gamma rays (Gy) / D_{10} of carbon ion beam (Gy), where D_{10} is the dose quantity necessary for decreasing the survival fraction to 10%.

To determine the cell condition for ion beam irradiation, the sensitivities for gamma rays were compared between the freeze-dried and wet cells. The freeze-dried cells exhibited a higher resistance to gamma-irradiation than the wet cells (Fig. 1), indicating that the effect of water radiolysis was relieved under the freeze-dried condition. From this result, the freeze-dried cells were used for ion beam irradiation.

Freeze-dried cells exhibited sensitivities to both radiations depending on radiation dose. The high LET carbon ion beam-irradiated cells exhibited a much higher sensitivity than that of the low LET gamma-irradiated cells (Fig. 1). The D_{10} values of carbon ion beam and gamma rays radiation were 0.11 and 0.74 kGy, respectively. RBE value was 6.65. These results suggest that carbon ion beams had the lethal effect on *B. subtilis* cells than the gamma rays. And like other organisms, *B. subtilis* will show the dependence of LET on RBE.

In further analysis, we will investigate LET-dependent biological effects (lethality and mutagenicity) in *B. subtilis* by irradiation with five kinds of ion beam ($^{4}He^{2+}$ [50 MeV; 19.4 keV/μm], $^{12}C^{5+}$, $^{12}C^{6+}$ [320 MeV; 86.2 keV/μm], $^{20}Ne^{8+}$ [350 MeV; 440.8 keV/μm] and $^{40}Ar^{13+}$ [460 MeV; 1,649.6 keV/μm]).

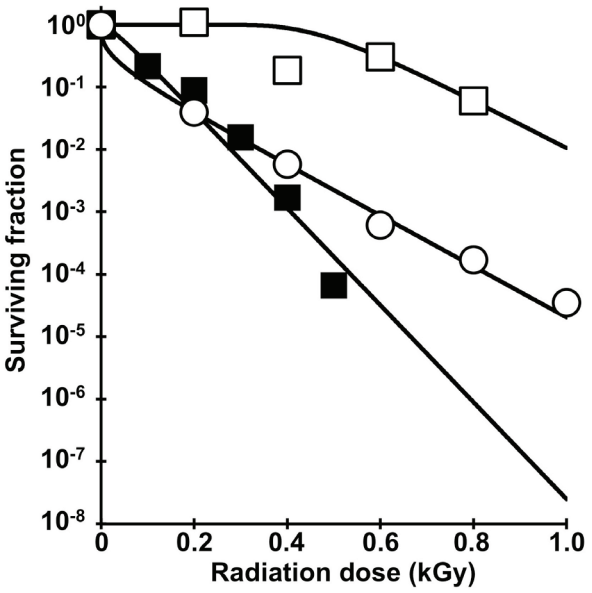

Fig. 1 Survival curves to gamma rays and carbon ion beam radiations. Symbols: closed squares, gamma rays (wet cells); open squares, gamma rays (freeze-dried cells); open circles, carbon ion beams.

References

1) N. Hamada *et al.*, Radiat. Res., **166**, 24-30 (2006).
2) Y. Hase *et al.*, Int. J. Radiat. Biol., **78**, 799-806 (2002).
3) M. Imamura *et al.*, J. Gen. Appl. Microbiol., **43**, 175-77 (1997).
4) F. Kunst *et al.*, Nature, **390**, 249-56 (1997).

2-28 Exploration of *Sinorhizobium* Mutants Showing High Salt Tolerant Using the Ion Beam Mutation Breeding

Y. Maruyama [a)], K. Takeda [b)], N. Tomooka [c)], K. Satoh [d)], Y. Oono [d)] and T. Yokoyama [e)]

[a)] Graduate school of Agriculture, Tokyo University of Agriculture and Technology,
[b)] Faculty of Agriculture, Tokyo University of Agriculture and Technology,
[c)] Genetic Resources Center, National Agriculture and Food Research Organization,
[d)] Department of Radiation-Applied Biology Research, TARRI, QST,
[e)] Institute of Agriculture, Tokyo University of Agriculture and Technology

Vigna marina is one of wild legumes, which called as Hamaazuki, are distributed at the vicinity of the coast from tropical to sub-tropical regions and have high salt tolerance among terrestrial plants. For example, *Vigna marina* can grow at 400 mM NaCl condition. Furthermore, the root nodules on *Vigna marina* have a symbiotic relationship with rhizobia that related to the genus *Sinorhizobium* having high stress tolerance (500 mM NaCl, 45 °C, pH 10.5). Above both symbiotic partners showed extremely high salt tolerance, however, *Vigna marina* cannot develop root nodules with *Sinorhizobium* at over 80 mM NaCl conditions. To improve symbiotic performance of *Vigna marina* with Sinorhizobium under high salt conditions, *Sinorhizobium* bacterial cells were irradiated by carbon ion-beam at TIARA, QST. The optimum irradiation dose of carbon ion beam to obtain survival ratio at 0.01% in Sinorhizobium cells was the range from 300 to 400 Gy. So far, we could obtain promising mutants having high NaCl tolerant which can survive at 7.5% NaCl concentration. At next step, we will confirm if such strains show good symbiotic performance with *Vigna marina* under high salt conditions, or not.

私たちは、沖縄県の南西諸島の海岸に分布しているハマアズキ（*Vigna marina*）が、陸生植物の中でも高い耐塩性（400 mM NaCl 耐性）を持つこと、また、その根粒には 3.5% NaCl、pH 10.5、温度 45 °C という高ストレス条件下でも生存可能な *Sinorhizobium* 属根粒菌が共生していることを見出した[1)]。しかし、*Sinorhizobium* 属根粒菌を塩存在下で接種すると、根粒を形成する最大 NaCl 濃度は 80 mM であり、その環境で窒素固定能は探知できたが、活性は無処理区の約 6%まで低下した。ハマアズキと *Sinorhizobium* 属根粒菌は、それぞれが優れた耐塩性を有しているが、共生は遥かに低い塩濃度でないと成立しないことが分かってきた。共生による根粒形成はマメ科植物と根粒菌の相互作用で生じるため、各生物の共生機構に耐塩性を与える必要があるが、現時点でハマアズキの種子の自家採取が不可能で、自生地での種子採取しかできないため、イオンビーム誘発突然変異育種技術を利用した *Sinorhizobium* 属根粒菌の共生特性の改良により、ハマアズキと *Sinorhizobium* 属根粒菌の共生限界の NaCl 濃度を高めることが可能か調べている。本年度は、耐塩性を指標として、変異が生じた株の収集を行った。

Sinorhizobium 属根粒菌（2010 年、南西諸島土壌より単離）に対するイオンビームを用いた微生物突然変異育種技術の適応は世界で初めてであり、高崎量子応用研究所 TIARA において、炭素イオンビーム（$^{12}C^{5+}$、220 MeV）を照射し（100、200、300、400 及び 500 Gy）、照射線量と *Sinorhizobium* 属根粒菌の生残数の関係を調べ、適切な照射線量を決定した。照射後の菌株については、菌株自体の耐塩性を確かめるために NaCl を含む固形培地（3、3.5、4、4.5 及び 5%）に菌液を滴下し、その増殖能力を確かめると共に、異なる NaCl 濃度の培養液（0, 6, 8, 10, 12, 15%）中で静置し、生残性を確認した。その結果、菌株の増殖能力に変異が生じることを期待した NaCl 含有寒天培地での増殖試験では、野生株が生育する 4% NaCl 寒天中ではコロニー形成が観察された。しかし、それ以上の NaCl 濃度では、コロニーの形成は見られず、NaCl 耐性を高めた菌株は取得できなかった。そこで、野生株の NaCl 溶液中での生存能に変異が生じ、より高い NaCl を含む液体培地で生残性が向上した株の有無を調べた。その結果、野生株より高い NaCl 溶液中で生残性が高まった 5 つの変異株が取得できた。これらは野生株と同一の 16s-rRNA 配列を有しており、イオンビーム処理で生じた変異株と考えられた。これら変異株のうち No.7 株と No.45 株に関して、NaCl 濃度が 7.5%における生残試験の結果を Fig. 1 に示した。野生株（Irio）は 9 日で 10^3 cfu/mL まで菌数を減らしたが、No.7 や No.45 は 10^3 cfu/mL まで菌数を減らすまでに 18 日かかった。また野生株は 21 日目には死滅したが、変異株は生残が確認できた。このことから、No.7 株と No.45 株は高い NaCl 濃度中でも生残できる何らかの変異が生じたことが推定された。今後、これら菌株に関しての特性評価を行う予定である。

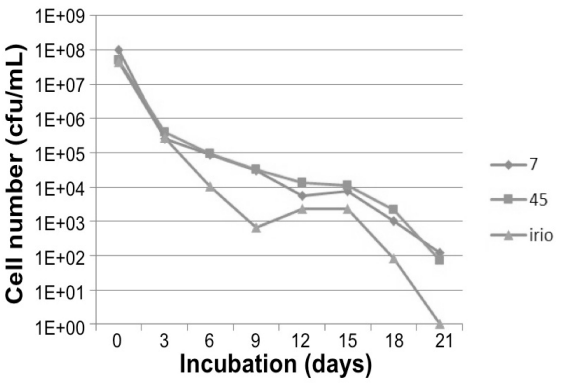

Fig. 1 Living cell number under 7.5% NaCl concentration. Irio; wild type strain, 7 and 45; mutant strains.

Reference

1) N. Tomooka *et al.*, Proc. 14th NIAS Int. Workshop Genet. Resour., "Genetics and Comparative Genomics of Legumes (*Glycine* and *Vigna*)", 11 (2010).

2-29 Functional Analysis of *pprA* and *pprI* Genes That Are Involved in Radiation/Desiccation Response in the Radioresistant Bacterium *Deinococcus grandis*

K. Kurosawa [a)], K. Omoso [a)], H. Takeshima [b)], K. Satoh [c)], Y. Oono [c)] and I. Narumi [a),b)]

[a)] Graduate School of Life Sciences, Toyo University, [b)] Department of Life Sciences, Faculty of Life Sciences, Toyo University, [c)] Department of Radiation-Applied Biology Research, TARRI, QST

Although the radioresistance of organisms varies greatly among species, there is a group of bacteria that shows extraordinary resistance to ionizing radiation. Members of the genus *Deinococcus* are the best known as radioresistant bacteria. Radioresistance in *Deinococcus* species is attributed to their highly proficient DNA repair capacity, in which a set of proteins involved in DNA repair is induced following exposure to ionizing radiation[1)]. In the previous studies using *Deinococcus radiodurans*, DNA repair-related proteins unique to *Deinococcus* species such as PprA (pleiotropic protein promoting DNA repair) and PprI (inducer of PprA) have been discovered. Another regulatory protein DdrO binds to a DNA motif, designated as the radiation/desiccation response motif (RDRM), that exists upstream of a set of radiation-inducible genes (RDR regulon) such as *pprA* gene. Following DNA damage, the metalloprotease activity of PprI cleaves DdrO, resulting in induction of the RDR regulon[2)].

Recently, we published the draft genome sequence of *Deinococcus grandis*, which was initially isolated as a Gram-negative, red-pigmented, radioresistant, rod-shaped bacterium from freshwater fish in Japan[3)]. The genome analysis revealed that *D. grandis* possessed RDR regulon as shown in *D. radiodurans*. In this study, to delineate the function of PprA and PprI in radiation-induced DNA repair, we generated *pprA* and *pprI* deletion strains (Δ*pprA and* Δ*pprI*) of *D. grandis* and investigated survivals of the deletion strains and wild type strains following exposure to gamma-rays.

Δ*pprA* and Δ*pprI* strains were generated by replacement the gene with an *Escherichia coli* antibiotic resistance gene that is controlled by the *D. radiodurans* catalase promoter. A DNA region upstream of the promoter of the target gene and another DNA region downstream of the target gene were amplified by PCR, and the former and the latter were located upstream of and downstream of the antibiotic resistance gene respectively by ligating the three DNA fragments into an *E. coli* plasmid vector pUC19. The resultant plasmid was used as the template to yield PCR product containing the inserted DNA fragment, and *D. grandis* wild type strain was transformed with the PCR product to obtain hygromycin resistant clones. Since *Deinococcus* species possess polyploid genome, complete deletion was confirmed by diagnostic PCR analysis using a set of specific oligonucleotide primers for the target gene.

For measurement of the sensitivity to gamma rays, *D. grandis* cells were incubated at 30 °C for 24 h in TGY (0.5% Bacto tryptone, 0.3% Bacto yeast extract, 0.1% glucose) broth. Cells were harvested, washed and resuspended in 10 mM sodium phosphate buffer (pH 7.0, PB). Aliquots (0.1 mL) of the cell suspension were dispensed into test tubes and irradiated at room temperature with ^{60}Co gamma rays at Food Irradiation Facility, TARRI, QST. The irradiation dose ranged from 0.5 to 6 kGy. After the treatments, cells were diluted appropriately with 10 mM PB, spread onto TGY agar, and incubated at 30 °C for 1 or 2 days prior to the enumeration of colonies.

We successfully generated complete deletion strains for the *D. grandis pprA* and *pprI* genes. These deletion strains exhibited extreme sensitivity to gamma-rays compare to the wild-type strain (Fig. 1). The *D. grandis pprA* deletion strain showed much higher sensitivity to gamma rays compared to the *D. radiodurans pprA* disruptant strain[4)] (Fig. 1). On the other hand, the sensitivity of the *D. grandis pprI* deletion strain was comparable to that of *D. radiodurans pprI* deletion strain[5)] (Fig. 1). The fact that the loss of *pprA* severely affected cell survival highlighted the functional importance of PprA protein in *D. grandis*.

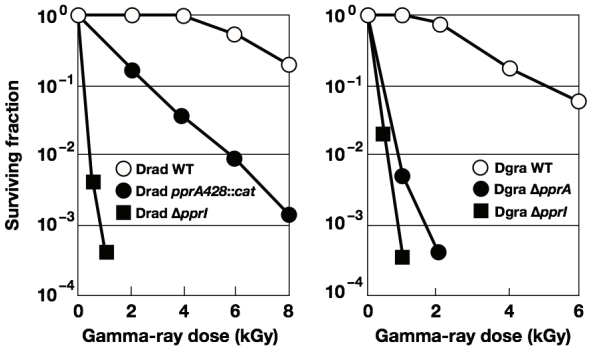

Fig. 1 Sensitivity of wild type (WT), *pprA*-deficient, and *pprI*-deficient strains of *D. radiodurans* (Drad; left panel) and *D. grandis* (Dgra; right panel) to gamma-rays.

References

1) I. Narumi, Trends Microbiol., **11**, 422-25 (2003).
2) Y. Ishino and I. Narumi, Curr. Opin. Microbiol., **25**, 103-12 (2015).
3) K. Satoh *et al.*, Genome Announc., **4**, e01631-15 (2016).
4) I. Narumi *et al.*, Mol. Microbiol., **54**, 278-85 (2004).
5) H. Lu *et al.*, DNA Repair, **11**, 139-45 (2012).

2-30 Genome Sequence Analysis of High Ethyl Caproate Producing Sake Yeasts Generated by Ion Beam Breeding -the Third Report-

T. Masubuchi [a)], M. Takahashi [b,c)], H. Hayasi [b)], Y. Ikenaga [b)], K. Satoh [c)] and Y. Oono [c)]

[a)] Gunma Industrial Technology Center, [b)] Maebashi Institute of Technology,
[c)] Department of Radiation-Applied Biology Research, TARRI, QST

We conducted the gene function analysis of the high ethyl caproate producing sake yeast mutant (No.227) generated by ion beam breeding in order to develop a new method for sake yeast screening and find factors contributing the reduced ability to alcohol fermentation. The genome sequences of the No.227 and Kyokai 901 (its parental strain) were determined by a whole-genome shotgun strategy using pyrosequencing method. Consequently, the No.227 carried mutations in the *MRC1, SWI1, ZDS2* and *RDS2* genes. It was suggested that these mutations genes in the No.227 might be attributed to the low alcohol fermentation ability.

群馬県では、オリジナルの吟醸用清酒酵母を開発するために、高崎量子応用研究所の TIARA において、$^{12}C^{5+}$イオンビーム（220 MeV）を用いた突然変異誘発によって、新たな吟醸用清酒酵母の開発を行ってきた。これまでに、吟醸酒特有の香気成分であるカプロン酸エチルを高生産する優良清酒酵母（No.227）の獲得に成功した[1)]。しかしながら、カプロン酸エチル高生産酵母は、アルコール発酵能が低下することがある。そのため、変異株の選抜・機能評価は多大な労力と時間を必要とし、研究の遂行を困難にする一因となっている。本研究は、イオンビーム誘発突然変異により得られた清酒酵母及びその親株の全ゲノム DNA 塩基配列を解読し、比較ゲノム解析を行うことで、酵母選抜のメルクマールとなる香気生成能・発酵能に関与する遺伝子群を特定すること目的として行った。

イオンビーム変異育種により作出した優良清酒酵母 No.227、及びその親株である清酒酵母きょうかい 901 号（以降 ky901）を YPD 培地で培養後、YeaStar Genomic DNA Kit（ZYMO RESEARCH 社）及び Gen とるくん（酵母用）High Recovery Kit（Takara Bio 社）を用いてゲノム DNA を抽出した。DNA の濃度と純度を確認後、Roche 社の GS Junior システムを用いたパイロシークエンス法により全ゲノム DNA の塩基配列を決定した。得られた塩基配列は、GS *de novo* Assembler ver.3 ソフトウェアによりゲノム再構築を行った。さらに、GS Reference Mapper ver.3 ソフトウェアを用いて、ky901 の DNA 塩基配列をリファレンスとして、DNA 塩基配列の比較を行った。

ゲノム再構築の結果、ky901 及び No.227 は、それぞれ 193 及び 182 個の Large Contig（>500 bp）が得られた。得られた Contig を基に、国立遺伝子研究所が提供する微生物のゲノム情報に基づく遺伝子構造及び機能予測プログラム MiGAP を用いて、ky901 及び No227 の遺伝子配列予測を行った。その結果、ky901 及び No227 の遺伝子数は、それぞれ 5,390 及び 5,386 個であった。推定される遺伝子数に大きな相違は見られなかった。さらに、K901 をリファレンス配列として、No227 の DNA 塩基配列との比較を行ったところ、No227 に特有の相違点を 679 カ所見出した。これらの相違点の内、287 カ所が 174 個のタンパク質をコードする遺伝子領域に存在していた。

No227 の有する相違点の中には、ゲノム複製・転写・翻訳に関与する遺伝群に分類される遺伝子群もあり、特に、S 期のチェックポイントに関わるタンパク質をコードする *MRC1* 及び *SWI1* 遺伝子に相違があることを見出した（Table 1）。これらの遺伝子に変異が生じたことにより、チェックポイント機構に異常が生じ、増殖不良や生育遅延を起こしているのではないかと推察した。さらに、糖新生の調節に関与するタンパク質をコードする *RDS2* 遺伝子にも変異が確認されており（Table 1）、グルコースを合成するために、エタノールが基質となり利用されている可能性も考えられた。これらの遺伝子群の突然変異によって、アルコール発酵能の低下に繋がっているのではないかと考えられた。しかし、アルコール発酵能低下に繋がる直接的なメカニズムは未だ不明であるため、今後の詳細な遺伝的解析が必要である。

Reference

1) T. Masubuchi *et al.*, JAEA Takasaki Annu. Rep. 2010, JAEA-Review 2011-043, 113 (2012).

Table 1 Sequence comparison of genes concerning in the alcohol fermentation ability.

Gene	Position	Ky901	No.227
MRC1			
Base	2,226	T	C
Amino acid	742	I	V
SWI1			
Base	1,063	A	C
Amino acid	355	K	Q
ZDS2			
Base	412	G	A
Amino acid	138	V	I
Base	739	A	G
Amino acid	247	N	D
RDS2			
Base	288	A	G
Amino acid	96	T	T

2-31 Mutation Breeding of Microalga Strains Resistant to Hyper-salinity Stress

Y. Kato [a)], S.-H. Ho [a)], A. Nakanishi [a)], C. Ogino [a)], T. Hasunuma [a)], K. Satoh [b)], Y. Oono [b)] and A. Kondo [a)]

[a)] Graduate School of Science, Technology and Innovation, Kobe University,
[b)] Department of Radiation-Applied Biology Research, TARRI, QST

Introduction

Microalgae are expected to be excellent producers of a renewable energy resource that does not compete with the current agricultural properties. We have developed strategies for lipid production using an oleaginous green microalga *Chlamydomonas* sp. JSC4 isolated from the Taiwanese sea coast[1,2]. We previously found that JSC4 accumulates lipid in the presence of sea salt (SS), but also easily infected opportunistically by a parasitic Chytridiomycota under salinity stress when cultivated outdoor. To solve this problem, this study aims to obtain salt-resistant strains by mutation breeding using the carbon ion beams and habituation to the high-salinity condition.

Experimental

The carbon ion beams ($^{12}C^{5+}$, 220 MeV) were accelerated by an AVF cyclotron at TIARA, QST. JSC4 cells were irradiated with 50 Gy of the carbon ion beams, and then screened and habituated by culturing in the medium containing 5% and 7% of SS. Screened cell population was again irradiated with 100 Gy of the carbon ion beams, followed by cultivation under 7% SS for dozens of weeks.

Results and Discussion

Wild type JSC4 cells can grow under 3% SS but not under 7% SS. We bred a salt-resistant strain (KHI) from JSC4 by irradiating it with the carbon ion beams and habituating to salinity environment. Cell growth of the strain gradually increased with the passage of cultivation time under 7% SS (Fig. 1). Obtained KHI cells after cultivation of 25 weeks could grow well even under 7% of SS. When cultured in the medium containing SS, JSC4 cells aggregated (3% SS) or formed large cell bodies (7% SS) by salinity stress (Fig. 2). On the other hand, KHI cells did not aggregate and looked healthly even when cultured in the presence of 7% SS. These results suggests that the KHI possesses strong resistance toward salinity stress.

Since KHI cells are salt-resistant, it is also expected that it is also resistant to opportunistic infection of Chytridiomycota under salinity stress. In addition, salt-resistance would be valuable when culturing this strain using sea water, thus the KHI strain is promising as a producer of biodiesel.

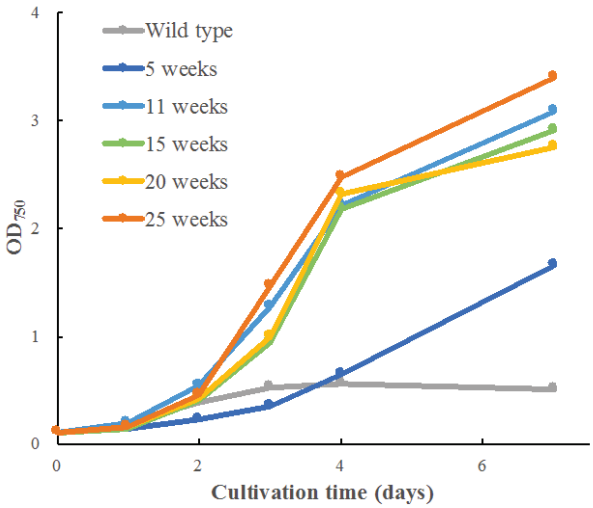

Fig. 1 Screening and habituation to generate salt-resistant strains. JSC4 cells were irradiated with the carbon ion beams and then continuously cultured in the medium containing 7% SS. Growth of the irradiated cells under 7% SS were measured every week.

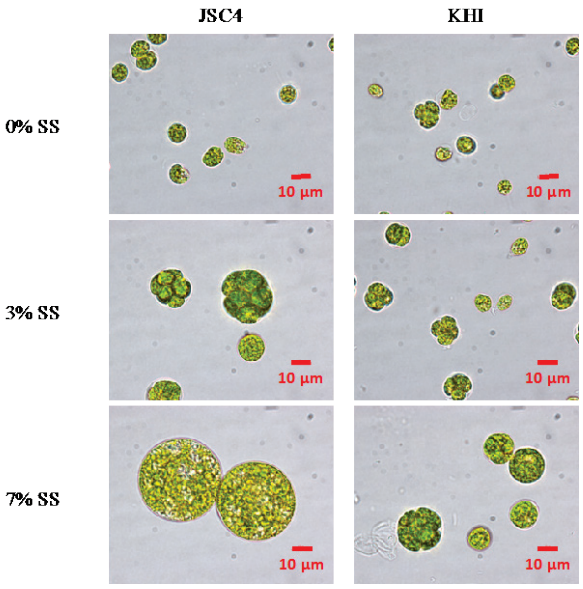

Fig. 2 Morphologies of KHI cells under different concentrations of SS. JSC4 and KHI cells were cultured in the medium containing 0, 3, or 7% of SS. Shown are the cells at Day 3. Bars indicate 10 µm.

References

1) S.-H. Ho *et al.*, Biotechnol. Biofuels, **7**, 97 (2014).
2) S.-H. Ho *et al.*, Biotechnol. Biofuels, **8**, 48 (2015).

2-32 Noninvasive Analysis of the Effect of GSH and DTT on Cadmium Translocation in Oilseed Rape Using PETIS

S. Ishii [a)], S. Nakamura [b)], N. Suzui [a)], Y.-G. Yin [a)] and N. Kawachi [a)]

[a)] Department of Radiation-Applied Biology Research, TARRI, QST,
[b)] Department of Biological Production Faculty of Bioresource Sciences, Akita Prefectural University

Cadmium (Cd) is a heavy metal which is toxic to the human body. Therefore, it is important to suppress the absorption of Cd by crops. To establish effective cultivation methods for producing safe agricultural products, it is necessary to understand Cd behavior in plants. In a previous study, we observed that the application of glutathione (GSH) to roots activated Cd efflux from root cells and inhibited Cd transport from roots to shoots in oilseed rape [1)]. In the present study, we investigated noninvasively the effects of GSH and dithiothreitol (DTT), along with an SH group, on Cd behavior in oilseed rape plants using positron-emitting tracer imaging system (PETIS) and ^{107}Cd.

Oilseed rape plants were grown hydroponically under the controlled condition for 2 weeks. ^{107}Cd (half-life of 6.5 h), produced and purified following the methods described by Fujimaki et al. (2010), was used as a positron-emitting radiotracer[2)]. Approximately 16 MBq of ^{107}Cd dissolved in an appropriate volume of 0.5 mM $CaCl_2$ and 10 μM non-radioactive $CdCl_2$ with 1 mM GSH or 1 mM DTT was prepared for each test plant. We attempted to visualize the behavior of Cd in GSH- and DTT-treated plants using a PETIS. Plants were set in a syringe as shown in Fig. 1A and PETIS images were obtained for 36 h.

Serial PETIS images are presented in Fig. 1B. In GSH- and DTT-treated plants, ^{107}Cd signals in the shoot remained weak compared to those in control plants (Fig. 1B). In control plants, strong ^{107}Cd signals appeared at the shoot base and node where the petiole appeared (Fig. 1B). Figure 2A shows the regions of interest (ROI) that were analyzed. Time courses of ^{107}Cd intensities per unit area (time activity curve; TAC) were generated from the shoot base, node, upper root, and lower root (Fig. 2A). The upper root indicates roots that were not submerged in the hydroponic solution, whereas the lower root indicates roots immersed in the hydroponic solution. In the TAC from the shoot base, ^{107}Cd signals increased gradually in all plants up to approximately 10 h (Fig. 2B). Following this, ^{107}Cd signals in the shoot base of control plants increased more sharply than those in GSH- and DTT-treated plants. In the TAC from the node, ^{107}Cd signals in control plants increased sharply after approximately 16 h of ^{107}Cd exposure (Fig. 2C). In the TAC from the upper root, there were major differences in ^{107}Cd accumulation signals between control plants and GSH- and DTT-treated plants (Fig. 2D). Cd accumulation was almost one third lower in treated plants than in the control. On the other hand, in the TAC from the lower root, there were little differences in the accumulation of ^{107}Cd signals between control plants and GSH- and DTT-treated plants (Fig. 2E).

PETIS enabled the visualization of Cd behavior in GSH- and DTT-treated plants (Fig. 2B). In addition, we observed the inhibitory effects of GSH and DTT on Cd translocation from roots to shoots (Figs. 2B, 2B, and 2C).

Analysis of these images gave us close to elucidate the molecular mechanisms which are operating in GSH- and DTT- treated plants.

References

1) S. Nakamura *et al.*, J. Exp. Bot., **64**, 1073-81 (2013).
2) S. Fujimaki *et al.*, Plant Physiol., **152**, 1796-806 (2010).

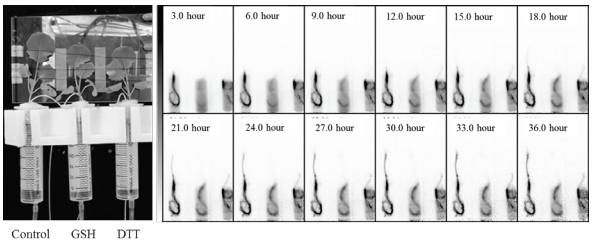

Fig. 1 PETIS imaging of Cd behavior in oilseed rape plants. A: field of view of a representative PETIS experiment, B: time series of PETIS images showing the ^{107}Cd signal (0-36 h) after decay correction.

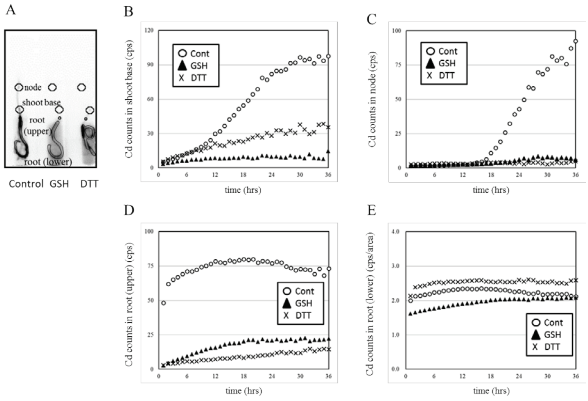

Fig. 2 Time-course analyses of Cd behavior in the node and shoot base. A, regions of interest (ROIs) for time-course analyses. Time activity curves of ^{107}Cd signal in ROI in the shoot base (B), node (C), upper root (D), and lower root (E). Each graph indicates the intensity of ^{107}Cd signal after decay correction.

2-33 Investigation on a Detection Method Using Secondary Electron Bremsstrahlung for a Gas Region Intersecting a Therapeutic Carbon Beam via Monte Carlo Simulations

M. Yamaguchi [a)], Y. Nagao [a,b)], T. Satoh [b)], T. Kamiya [c)], H. Sugai [d)], M. Sakai [e)], K. Arakawa [a,e)] and N. Kawachi [a)]

[a)] Department of Radiation-Applied Biology Research, TARRI, QST,
[b)] Department of Advanced Radiation Technology, TARRI, QST,
[c)] Department of Advanced Functional Materials Research, TARRI, QST,
[d)] Fukushima Prefectural Center for Environmental Creation,
[e)] Gunma University Heavy Ion Medical Center

Noninvasive beam monitoring is required to allow for precise dosage control in particle beam therapies. If an unexpected gas region appears across the trajectory of a beam, the Bragg peak shifts to an undesirable position. Such shifts may occur in prostate-cancer therapies, since the beams for these therapies sometimes intersect the intestine, where gas regions may move to cross the beams. Our group already proposed the use of secondary electron bremsstrahlung (SEB) to monitor the positions of Bragg peaks [1)]. In this work, we investigated the feasibility of utilization of SEB for the detection of a gas region placed across a beam trajectory using Monte Carlo simulations.

Simulations were performed on a supercomputer at JAEA using the Particle and Heavy Ion Transport code System (PHITS). A geometrical setup of the simulation is shown in Fig. 1. The setup had an axial symmetry to a ^{12}C beam with an infinitesimal diameter and injection energy of 290 MeV/u. The beam was injected into a target consisting of two 50-mm-thick acrylic blocks separated by a 10-mm gap. A detection system consisted of boron polyethylene blocks, a cadmium telluride (CdTe) semiconductor detector, and lead blocks composing a 2.4-mm-wide slit. The CdTe detector was placed behind the slit. The FWHM of the position resolution of this detection system was 10.6 mm along the beam axis. The center of the slit was moved in twelve positions spaced at 2 mm intervals along the beam axis together with the CdTe detector and the boron polyethylene blocks. The center of the 10-mm gap was chosen as the origin of a coordinate along the beam axis, and the direction of movement of the ^{12}C ions was chosen as the positive of the coordinate. At each slit position, the distribution of the energy deposition in the CdTe region was recorded during irradiation by the ^{12}C-beam. The number of incident ^{12}C ions was about $1\text{-}2\times10^{7}$ for each position. We also performed the same simulation without SEB generation, in order to evaluate the effect of SEB generation on the energy deposition.

Figure 2 presents the simulation result of the yield having the energy deposition of 63-68 keV in the CdTe detector. It was found that, at each slit position, the SEB component (i.e., the difference between the results with and without SEB generation) was 40-60% of the total yield. Moreover, it was found that the result with SEB has clear dependence on slit position, with a minimum at the 0-mm position, while the result without SEB has no dependence on slit position. The experimental result of the yield was also overlaid in Fig. 2. The simulation with SEB reproduced the experimental results well.

These results suggest that SEB may have potential for use in detecting the presence of gas regions intersecting a beam trajectory.

Reference

1) M. Yamaguchi *et al.*, Phys. Med. Biol., **57**, 2843-56 (2012). (Corrigendum: **61**, 3638-44 (2016)).

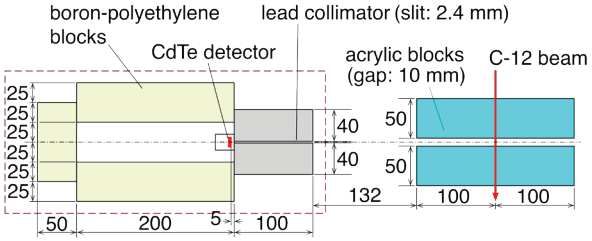

Fig. 1 Geometrical setup for the Monte Carlo simulation. The materials surrounded by the red dashed line were moved to twelve positions along the beam axis.

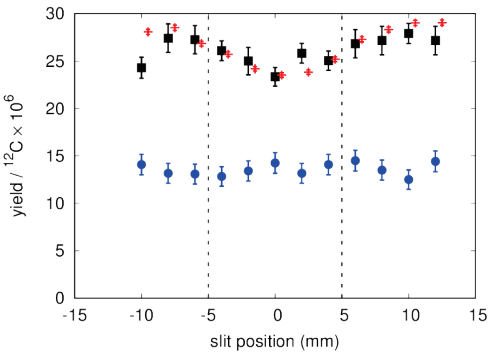

Fig. 2 Simulation results for the yield of 63-68 keV counts per ^{12}C ion with changing slit position. Black squares and blue circles represent the results with and without SEB generation, respectively. The experimental result is shown by red pluses. The vertical dashed lines represent the positions of the lower and upper edges of the 10-mm gap.

2-34 Development of Cherenkov Light Imaging System for Study of Radiocesium Dynamics in Plants

K. Kurita [a], N. Suzui [a], Y.-G. Yin [a] S. Ishii [a], H. Watabe [b], S. Yamamoto [c] and N. Kawachi [a]

[a] Department of Radiation-Applied Biology Research, TARRI, QST,
[b] Cyclotron and Radioisotope Center, Tohoku University,
[c] Graduate School of Medicine, Nagoya University

After the accident at the Fukushima Daiichi Nuclear Power Station in March of 2011, large areas of agricultural fields in northern Japan were contaminated with radiocesium (Cs-137). As a result, high-resolution images of radiocesium distribution are required in order to facilitate the study of cesium kinetics in plants. However, it is difficult to achieve the desired image resolution for Cs-137 (which produces 662 keV gamma photons) using a gamma camera method, as high-energy gamma photons will penetrate the pinhole collimator. Furthermore, the spatial resolution of the camera is usually greater than several tens of millimeters at a distance of 300 mm from the detector[1].

Through Cherenkov light imaging, we can visualize fine distributions of radionuclides that emit beta particles by using an optical camera[2]. We have used this method to develop an imaging system that allows us to study radiocesium movement in live plants.

Our system comprised a high-sensitivity, cooled, charge coupled device (CCD) camera (Hamamatsu Photonics, ORCA2-ER) and a bright lens (Xenon, F-number: 0.95, lens diameter: 25 mm) placed in a black box. To evaluate the linearity of this system, an imaging test was performed with several Cs-137 point sources (with radioactivities of 10, 20, 50, 100, 200, 500, 1,000, and 2,000 kBq) and an acquisition time of 600 s. Image data in counts per second, acquired using the Cherenkov light system, are plotted against the point source activity in Fig. 1. The data indicate that the system maintains linearity between the image intensity and the radioactivity of Cs-137, over an activity range on the order of 10^3. To demonstrate the use of this system for radiocesium detection in plants, an imaging experiment was performed with a live soybean plant over 7 days. First, the root of a 13-day-old soybean was dipped into 17 mL of a solution containing 10 MBq of Cs-137, with no potassium. After one day, the solution was replaced with a potassium solution with no Cs-137. Figure 2 shows the Cs-137 distribution in the soybean plant. These high-resolution serial images indicate that Cs-137 was transported into the shoot and accumulated at the node. The results of the two experiments described above lead us to conclude that Cherenkov light imaging may be a promising method for studying the kinetics of radiocesium in live plants.

References

1) N. Kawachi *et al.*, J. Environ. Radioact., **151**, 461-67 (2016).
2) S. Yamamoto *et al.*, Nucl. Instrum. Meth. Phys. Res. A, **777**, 102 (2015).

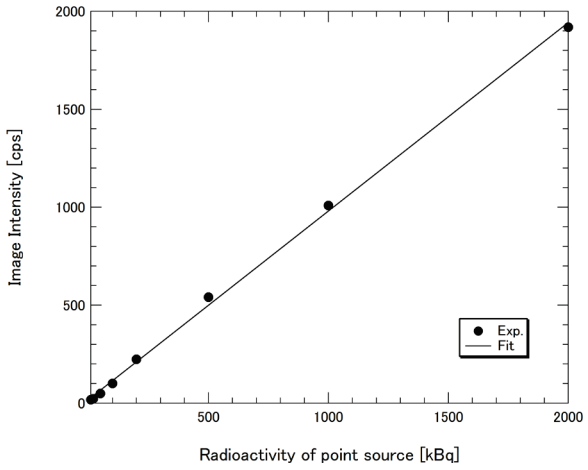

Fig. 1 Results of a performance test to evaluate the linearity of the Cherenkov light imaging system for a Cs-137 source. The data show linearity based on a correlation of $r^2 = 0.9987$ between the activity of the point source and the image intensity.

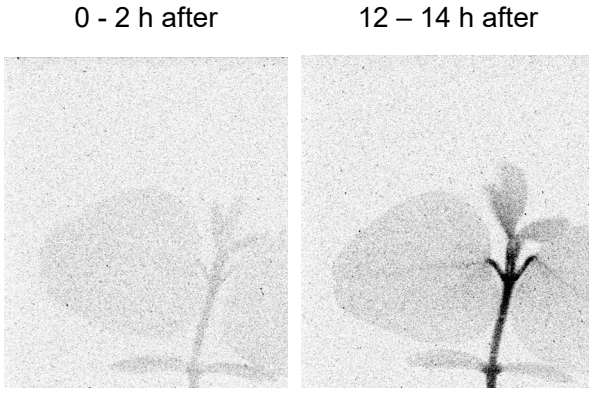

Fig. 2 Images of Cs-137 dynamics in a live soybean plant after feeding Cs-137 into the hydroponic culture.

2-35

A Method to Quantitative Visualization of Root Secretion by Using $^{11}CO_2$ and a Positron-emitting Tracer Imaging System

Y.-G. Yin, N. Suzui, S. Ishii, K. Kurita and N. Kawachi

Department of Radiation-Applied Biology Research, TARRI, QST

Organic substances secreted from root of plant play an important role in the development of microbial communities of rhizosphere and the solubilization of insoluble nutrients in soil. It is considered that the photoassimilates from leaf are provided properly to various physiological demands such as the elongation of the roots, the absorption of ions requiring energy and the secretion of organic substances. We hypothesized that proportions of secreted carbon to the total assimilated carbon should be different among various positions in the root. Previously, we established a new method which can visualize a process of translocation of photoassimilates from the leaf to the root and secretion of organic substances from the root to the soil by using $^{11}CO_2$ and positron-emitting tracer imaging system (PETIS) [1]. In this study, we developed an additional method which can extract the organic substances in rhizosphere after PETIS experiment for chemical analysis.

Soybean (*Glycine max* [L.] Merr. cv. Jack) seeds were sown on a vermiculite bed and then incubated in a growth chamber with day/night temperatures of 26/20 °C (12/12 h). One week after sowing, the seedlings were transferred to plastic containers with 6 L of nutrient solution for 18 days. The root of plant was placed in two opposite box, a rhizobox, and was sandwiched for 10 days. In order to extract the organic substances, the rhizobox was made up of a pair of plastic box which filled up 250 mL of the nutrient solution containing 2% agar with or without carbon beads (20/30 mesh) instead of soil.

We performed imaging experiment of PETIS using five-week-old plants. The aerial part of plant was fed with 200 MBq of $^{11}CO_2$ that was produced by cyclotron at Takasaki Ion Accelerators for Advanced Radiation Application (TIARA) and the imaging was started immediately. After checking an enough accumulation of the ^{11}C-photoassimilates in the root tips (approximately 70 min after the feeding of $^{11}CO_2$), we removed the plant from rhizobox and visualized the ^{11}C-organic substances secreted to the rhizobox.

Figures 1 and 2 show the imaging results using the rhizobox without or with carbon beads, respectively. Both results indicated that the ^{11}C-photoassimilates from leaves arrived at the root base at 30 min after the feeding of $^{11}CO_2$, and then were gradually accumulated to the root tips from 50 min to 70 min. The images of ^{11}C-organic substances in rhizobox indicated the different pattern in the rhizobox with or without carbon beads. In the rhizobox without carbon beads (Fig. 1), the distribution of ^{11}C-organic substances was different from that of ^{11}C-photoassimilates in the root. In contrast, in the rhizobox with carbon beads (Fig. 2) the distribution of ^{11}C-organic substances was similar with that of ^{11}C-photoassimilates in the root and the intensity was gradually weakened from the center to the outside in the rhizobox. This result indicated that the ^{11}C-organic substances were secreted intensively from main roots. Total intensity of ^{11}C-organic substances of rhizobox with carbon beads is higher than that without carbon beads about 3.7 fold.

These results demonstrated that the rhizobox containing carbon beads is suitable for the quantitative visualization of ^{11}C-organic substances in the rhizobox. This new method enables the chemical analysis of organic substances after PETIS experiment.

Reference

1) Y.-G. Yin *et al.*, JAEA Takasaki Annu. Rep. 2011, JAEA-Review 2012-046, 92 (2013).

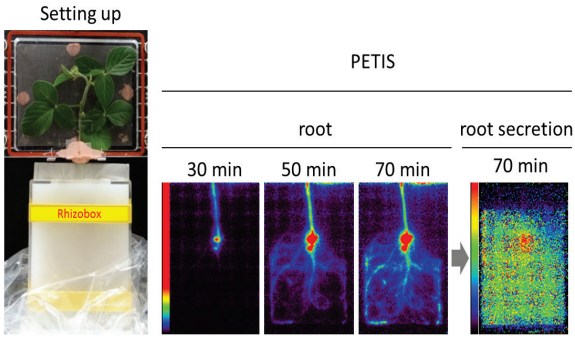

Fig. 1 Image data of PETIS experiment. The rhizobox filled up the nutrient solution containing 2% agar without carbon beads.

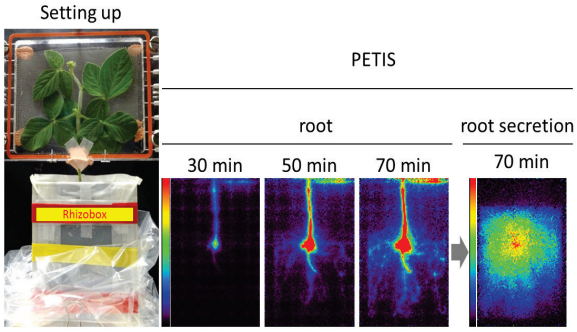

Fig. 2 Image data of PETIS experiment. The rhizobox filled up the nutrient solution containing 2% agar with carbon beads.

2-36 PET Imaging of Cancer Using Cu-64 Ions

Y. Sugo [a)], Y. Ohshima [a)], A. Yamaguchi [b)], H. Hanaoka [b)] and N. S. Ishioka [a)]

[a)] Department of Radiation-Applied Biology Research, TARRI, QST,
[b)] Graduate School of Medicine, Gunma University

Introduction

Copper is an essential micronutrient in mammals, and has various radioisotopes under investigation for applications in nuclear medicine[1]. Among them Copper-64 (^{64}Cu) is an attractive radionuclide for positron emission tomography (PET) imaging due to its appropriate half-life (12.7 h) and decay characteristics (β^+, 19%). Design and application of bi-functional chelates such as ^{64}Cu-labeled peptides[2] and antibodies have been extensively investigated for cancer imaging.

We proposed a new approach to simplified method for PET imaging of cancer using ^{64}Cu ions without any labeling process. In this study the usefulness of ^{64}Cu ions as a PET imaging agent was evaluated.

Experimental

Production of ^{64}Cu: Using the AVF cyclotron of TIARA, no-carrier-added ^{64}Cu was produced by the nuclear reaction of ^{64}Ni(p,n)^{64}Cu at high specific activity. An isotopically enriched ^{64}NiO (99.4%) target was irradiated with 11 MeV proton beam at a beam current of 5 μA. The chemical separation of ^{64}Cu from ^{64}Ni target was carried out by the chelating ion-exchange method [3]. The $^{64}CuCl_2$ was obtained in ultrapure water as the final form.

Cellular uptake: Various cancer cells routinely cultured were each incubated with 40 kBq of $^{64}CuCl_2$ in the medium at 37 °C for 1 h. After incubation the cells were thoroughly washed with phosphate buffered saline (PBS) and their radioactivity was measured by a well-type γ-counter.

PET imaging and biodistribution: Cancer-bearing mice were prepared by subcutaneous injection of the cancer cells. The mice were subjected to a small-animal PET imaging at different time points from 1 to 24 h postintravenous injection (p.i.) with the solution of 10 MBq $^{64}CuCl_2$ in PBS. Static PET scans were acquired for 10 min at 1, 4, 8 h p.i. and for 30 min at 24 h p.i. For biodistribution study, at 0.5, 1, 4, 8 and 24 h p.i. with 200 kBq of $^{64}CuCl_2$, the mice were sacrificed and their organs were removed. The organs were weighed and their radioactivities were measured.

Results and Discussion

The specific cellular uptake of ^{64}Cu ions was observed in the several kinds of cancer, such as human glioblastoma (U-87MG), human colon adenocarcinoma (LS 180), and human cholangiocarcinoma (HuCCT1).

Figure 1 shows the representative PET images of mice bearing U-87MG, LS 180 and HuCCT1 at 1, 4, 8, and 24 h p.i. It was demonstrated that the cancer was successfully visualized on the PET images due to quite high uptake of ^{64}Cu in the cancer tissue, especially in U-87MG. High uptake of ^{64}Cu was also observed in the liver which is the major organ for copper metabolism. The results of biodistribution as well as PET imaging showed that ^{64}Cu uptake in the liver was gradually reduced with progression of time, whereas accumulation of ^{64}Cu in the cancer was increased.

It was confirmed that ^{64}Cu ions were useful for PET imaging of cancer without any labeling process.

Acknowledgement

This study was supported in part by a Grant-in-Aid for Scientific Research (C) (No. 26461812) from Japan Society for the Promotion of Science.

References

1) S. V. Smith, J. Inorg. Biochem., **98,** 1874 (2004).
2) Y. Sugo *et al.*, Pept. Sci., **2014**, 303 (2015).
3) Sh. Watanabe *et al.*, Nucl. Med. Biol., **36**, 587 (2009).

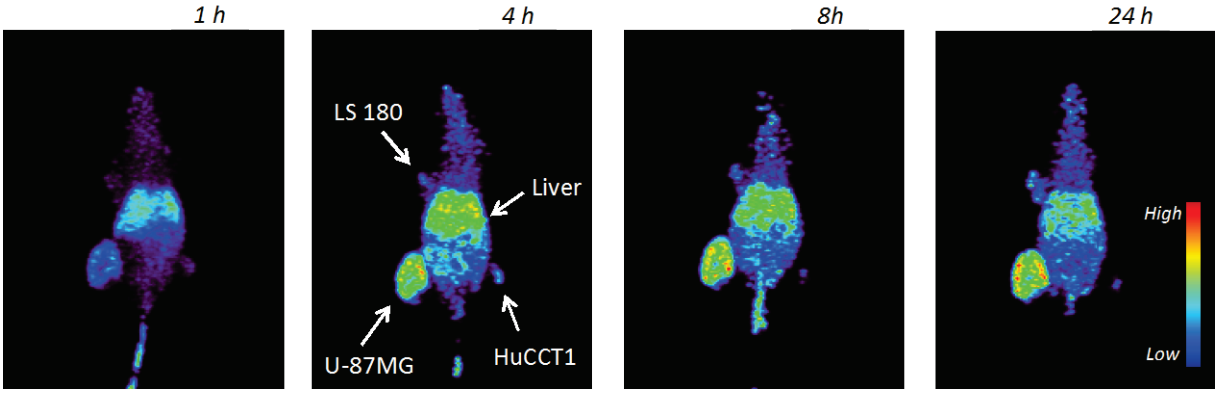

Fig. 1 Representative PET images of mice bearing U-87MG, LS 180 and HuCCT1 after injection of $^{64}CuCl_2$.

2-37

Large-Scale Production of At-211 by Using TIARA-AVF Cyclotron

Sa. Watanabe [a)], Sh. Watanabe [b)] and N. S. Ishioka [b)]

[a)] Department of Advanced Radiation Technology, TARRI, QST,
[b)] Department of Radiation-Applied Biology Research, TARRI, QST

Introduction

Astatine-211 ($T_{1/2}$ = 7.214 h) is a promising radionuclide for targeted radionuclide therapy, because it emits α-particles (mean energy: 6.79 MeV, range in soft tissue: 55-70 μm) suitable for treatment of small metastases or residual disease. In addition, the mean linear energy transfer (LET) 97 keV/μm, is 400 times higher than that of practical beta emitter, ^{90}Y.

Astatine-211 was generated by the ^{209}Bi (α, 2n) ^{211}At reaction with alpha-beam (incident energy: 28.1 MeV) accelerated by the TIARA-AVF Cyclotron using bismuth sheet for target (Fig. 1(a)). At least 20 μA of beam intensity will be required for large-scale production of At-211 in future clinical applications. However, melting of the bismuth target was observed by irradiation of 3.5 μA of alpha-beam because of low melting point of bismuth (271.4 °C). Therefore, we tried to develop a new solid target system which can produce At-211 without melting of the Bi target when irradiating high intensity of alpha-beam. In this paper, heat tolerance of the target by using the new target system and chemical separation of ^{211}At from an irradiated target were investigated.

Experimental

The new target holder is described in Fig. 1(b). For elimination of heat, thin bismuth coating by vapor deposition on an aluminum substrate was adopted. The target was set on the new holder in slant angle of 45 degrees against alpha-beam. To investigate the soundness of the target, it was irradiated with the alpha-beam up to 10 μA, the highest beam intensity available on the TIARA-AVF Cyclotron.

Chemical separation of ^{211}At from an irradiated target was carried out by the modified dry distillation (Fig. 2)[1)]. The irradiated target was set in the middle of the furnace. The temperature was raised to 640 °C under the 60 mL/min stream of helium gas. ^{211}At was transferred to a polyether-etherketone (PEEK) loop by the carrier gas and condensed inside the loop cooled by liquid nitrogen. After the distillation, ^{211}At was eluted by 0.25 mL of water. The separation yield of the ^{211}At was evaluated by measuring radioactivity of ^{211}At.

Results and discussion

As a result of the investigation for the tolerance of the target on the new target holder, the target did not melt up to 10 μA. Separation yield of the ^{211}At from the new target holder (19%) was lower than that obtained by using the conventional one (32%). H. Larsen et al.[2)] reported that the separation yield of ^{211}At on the dry distillation was varied by the metal species of substrate (copper or aluminum). We used aluminum substrate for the new holder, whereas we did not use the substrate for the conventional one (Fig. 1(a)). Separation yield obtained in this study may attribute to the difference of the substrate between the new and conventional holders.

The enhancement of beam current is planned by the beam engineering section in the TIARA. In future plans, the heat tolerance of the target on the new target system by increasing beam current and improvement of chemical separation will be investigated.

References

1) S. Lindegren *et al.*, Appl. Radiat. Isot., **55**, 157-60 (2001).
2) R. H. Larsen *et al.*, Appl. Radiat. Isot., **47**, 135-43 (1996).

Fig. 1 Conventional and new target holder.

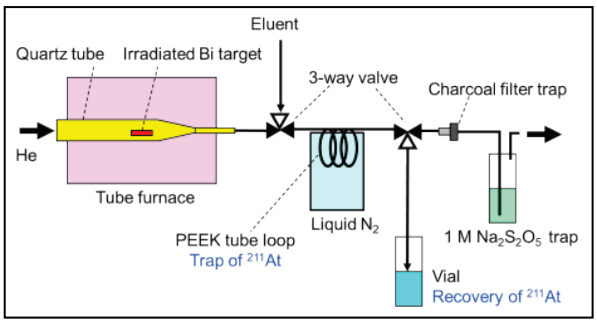

Fig. 2 Schematic diagram of dry distillation.

2-38 Medical Radioisotope Production with Accelerator Neutrons by 50 MeV Deuterons

K. Tsukada [a)], S. Watanabe [b)], Y. Sugo [b)], K. Hashimoto, [b)] Y. Hatsukawa [b)], Y. Nagai [b)]
M. Kawabata [b,c)], H. Saeki [b,c)], S. Sato [b,c)] and N. S. Ishioka [b)]

[a)] Advanced Science Research Center, JAEA, [b)] Department of Radiation-Applied Biology Research, TARRI, QST, [c)] Chiyoda Technol Corporation

Currently, the most common diagnostic radioisotope, ^{99m}Tc ($T_{1/2}$=6 h), is obtained from ^{99}Mo which is produced mostly by the fission reaction of highly enriched ^{235}U in research reactors around the world. A recent shortage of ^{99}Mo worldwide triggered discussions on the stable supply of ^{99}Mo, and a number of ^{99}Mo and ^{99m}Tc production methods with reactors and accelerators have been investigated. The positron emitting radioisotope ^{64}Cu and β^--ray emitting radioisotope ^{67}Cu are promising radionuclides suitable for labeling many radio-pharmaceuticals for PET imaging and for treating small distant metastases in radioimmunotherapy, respectively. And a therapeutic radioisotope ^{90}Y, a pure β^--ray emitter, is obtained from ^{90}Sr ($T_{1/2}$=28.8 y), which is produced by the fission reaction of ^{235}U. Japan imports both short-lived ^{99}Mo and ^{90}Y.

We successfully produced medical radioisotopes, ^{99}Mo ($T_{1/2}$=66 h), ^{90}Y ($T_{1/2}$=64 h), ^{67}Cu ($T_{1/2}$=61.8 h), and ^{64}Cu ($T_{1/2}$=12.7 h) on our program with accelerator neutrons by 40 MeV deuterons provided from the TIARA cyclotoron[1,2]. One of important efforts on our program is to increase the production rate of such radioisotopes for the medical usage. Recently, we succeeded to increase the production rate of ^{67}Cu and ^{90}Y with keeping their good radionuclide purities by using a Be metal target for the neutron generation and by increasing the deuteron beam energy from 40 to 50 MeV, as discussed below.

Enriched ^{68}Zn and ^{90}Zr oxide samples with a radius of 10 mm and a weight of about 500 mg were irradiated with neutrons, which were obtained by the Be(d,n) reaction using 50 MeV deuterons provided from the TIARA cyclotron. The irradiation setup was the same as our previous experiment by the C(d,n) reaction using 40 MeV deuterons[2]. After the irradiation we measured γ-ray spectra of the reaction products with Ge detectors.

As shown in a γ-ray spectrum of the ^{68}ZnO sample in Fig. 1, γ-ray peaks of ^{67}Cu were clearly seen with a good S/N ratio. The production rate of ^{67}Cu produced via the ^{68}Zn(n,pn) and (n,d) reaction was 3.2 times larger than that of our previous result obtained by using neutrons from the C(d,n) reaction with 40 MeV deuterons. The radionuclides of ^{69m}Zn ($T_{1/2}$=13.8 h), ^{65}Ni ($T_{1/2}$=2.52 h), and ^{66}Cu ($T_{1/2}$=5.1 min), decay product ^{66}Ni ($T_{1/2}$=54.6 h), were impurity radionuclides. The relative production yields of ^{69m}Zn and ^{65}Ni to ^{67}Cu were 0.16 and 2.0 at the end of irradiation, respectively. The ratios were almost similar to be 0.13 and 2.6 by the C(d,n) reaction using 40 MeV deuterons. This means that we can employ the established chemical separation process[3] to separate ^{67}Cu from these impurities. The present results suggest that the ^{68}Zn$(n,x)^{67}$Cu reaction is the promising route to produce a large amount of high purity ^{67}Cu and encourage us to make a new experiment for diagnosis using the ^{67}Cu.

We also obtained γ-ray spectra of the reaction product by the ^{90}Zr(n,x) reaction. ^{90m}Y ($T_{1/2}$=3.19 h) produced with ^{90}Y via the ^{90}Zr(n,p) reaction was clearly observed. The activity of the pure β^--ray emitter ^{90}Y was estimated from the observed activity of ^{90m}Y[4]. The estimated production rate of ^{90}Y was 2.1 times larger than that of our previous result, and the activity of ^{90}Y was found to be comparable to that of the impurity isotope ^{89}Zr ($T_{1/2}$=78.4 h). However, the production rate of impurity radionuclide ^{88}Y ($T_{1/2}$ = 106.6 d) produced by the ^{90}Zr(n,t) reaction was 3.9 times larger than our previous result. These results suggest that the deuteron energy should be lower than 40 MeV to produce ^{90}Y with a minimum level of impurity ^{88}Y.

Acknowledgements

We would like to thank to the crews of the TIARA cyclotron for a stable beam generation.

References

1) Y. Nagai *et al.*, J. Phys. Soc. Jpn. **82** (2013) 064201.
2) N. Sato *et al.*, J. Phys. Soc. Jpn. **83** (2014) 073201.
3) M. Kawabata *et al.*, J. Radioanal. Nucl. Chem. **303** (2015) 1205.
4) S. M. Qaim *et al.*, Phys. Rev. **C 42** (1990) 363.

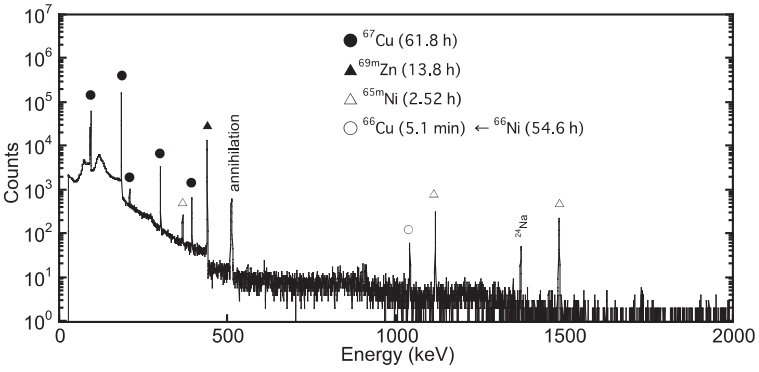

Fig. 1 A γ-ray spectrum of the ^{68}ZnO sample irradiated with neutrons, which was taken 16 h after the end of irradiation.

2 - 39

Effects of Wakosil and Nicotine on Trace Elements Distribution in Lung Microvascular Endthelial Cells

E. Sakurai [a,b], E. Sakurai [c], K. Yanai [b], K. Ishii [d], D. Sata [d], T. Hatakeyama [d], S. Matsuyama [d], M. Koka [e], T. Satoh [e] and T. Kamiya [e]

[a] Faculty of Pharmacy, Iwaki Meisei University, [b] Department of Pharmacology, Tohoku University School of Medicine, [c] Faculty of Pharmaceutical Sciences, Tokushima Bunri University, [d] Department of Quantum Science and Energy Engineering, Tohoku University, [e] Department of Advanced Radiation Technology, TARRI, QST

Air pollution became serious problem all over the world. Especially, PM2.5 is most notice matter in Asia. There are some reports that PM2.5 is an important ethologic factor for lung disease. On the other hands, cigarettes smoking is also risk factor for lung. Therefore, we examined the effects of nicotine and wakosil® (silica gel at a model of PM2.5) on trace elements distribution in lung microvascular endthelial cells (LMECs) to clarify which is riskier for lung. We measured change of the trace elements levels in LMECs by nicotine or wakosil® treatment using in-air micro-particle induced X-ray emission (micro-PIXE) method developed at TIARA.

Three weeks old male C57BL/6J mice purchased from Japan SLC. Mice LMECs were isolated using a modification of the technique described by Magee et al[1]. The procedures of cell culture on collagen-coated polycarbonate film (2.54 cm^2) for microanalysis were described in previous reports. The cells were washed two times with 1 mL of Krebs buffer, and pre-incubated with 0.9 mL of Krebs buffer at 37 °C for 5 min. Then, Krebs buffer containing 0.02 mM nicotine or 0.0057 mg/L wakosil® was added to each film, and cells were incubated for 5 min. The cells on the 5 μm polycarbonate films were washed 7 times with Tris(hydroxymethyl)aminomethane buffer. The specimens were promptly dipped into 2-methylbutane and chilled with liquid nitrogen and then freeze-dried overnight in the vacuum stage[2].

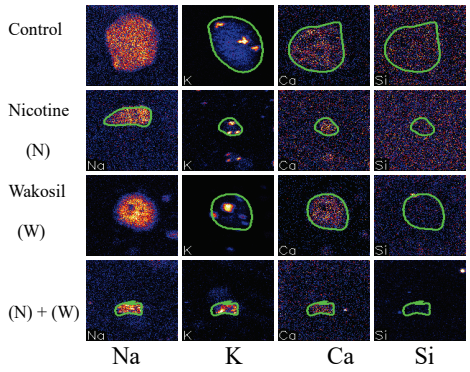

Fig. 1 Distributions of sodium, potassium, calcium and silicon image (100×100 μm) after addition of 0.2 mM nicotine or wakosil on LMECs. Upper portion: manganese, lower portion: copper images.

Figure 1 shows the micro-PIXE images (100×100 μm) of sodium, potassium, calcium and silicon in LMECs after treatment with 0.2 mM nicotine or wakosil® for 5 min.

The level of each trace element was shown in Fig. 2. When the LMECs were treated with nicotine, potassium levels were decreased. However, wakosil® treatment LMECs were not change the potassium level when compare that of control.

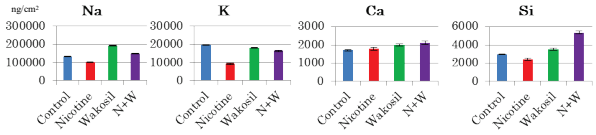

Fig. 2 Levels of sodium, potassium, calcium and silicon in the LEMCs treated with 0.2 mM nicotine or wakosil® for 5 min.

The ratio of trace elements in the cells showed in Fig. 3. The ratio of potassium and phosphorus levels were almost 1:10 after treated with nicotine. It was decreased at 5 times when comparing with that of control. Nicotine may injure cell membrane of LMECs.

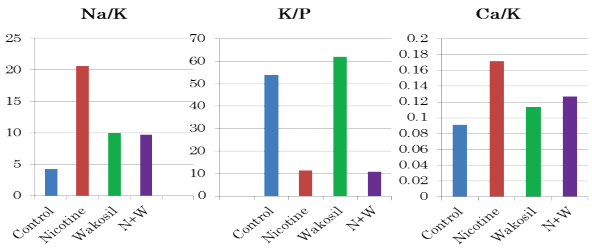

Fig. 3 The ratio of trace elements in the LEMCs treated with 0.2 mM nicotine or wakosil® for 5 min..

From these results, small particle matter may not play to apoptosis of LMECs by its selves. Other air pollutants such as oxidative sulfa (Sox), oxidative nitrogen (NOx), bacteria and so on which stick on PM2.5 may induce LMECs apoptosis.

References

1) E. Sakurai *et al,* Am. J. Physiol. Lung Cell Mol. Physiol., **282**, L1192-7 (2002).
2) K. Mizuma *et al.*, Int. J. PIXE., **14**, 27-33 (2004).

2-40 Analysis of Intracellular Boron Distribution of Cultured Cells Using Micro Particle Induced Gamma-ray Emission

K. Nakai [a,c], K. Endo [a], T. Kurita [a], Y. Yamamoto [a], T. Yamamoto [a], F. Yoshida [a], A. Matsumura [a], N. Yamada [b], M. Koka [b] and T. Satoh [b]

[a] Department of Neurosurgery, Faculty of Medicine, University of Tsukuba,
[b] Department of Advanced Radiation Technology, TARRI, QST,
[c] Department of Neurorehabilitation, Ibaraki Prefectural University of Health Sciences Hospital

Our early experience of the clinical trial suggests that Boron Neutron Capture Therapy (BNCT) appeared to be an effective and tolerable therapy for the selected malignant brain tumor patients [1]. Intracellular Boron distribution or Intratumor Boron distribution have been important factor for successful BNCT. Though Analysis using immunohisto-chemistry, Secondary Ion Mass Spectrometry, alpha etching has been used, the detail of pharmacokinetics of boron agents between blood vessels, tumor or surrounding normal tissues are still unclear. In this report, our aim is to provide a method for measuring boron concentration using cultured cell samples, and to examine a possibility of particle induced X-ray emission by using micro-PIGE.

Material and methods

(1) *p*-dihydroxyboryl-phenylalanine; BPA and fructose ware dissolved and prepared as previously described [2]. Briefly, BPA was converted to BPA-fructose complex by mixing BPA and fructose in NaOH at a 1:1.2 molar ratio. The pH was adjusted to 7.4 with HCl. Final boron concentration was 1,300 μgB/mL. The solution was filtered and stored at 4 degrees C.

(2) Polycarbonate film that of the 5 μm thickness was used to support the samples on the end of proton beam (Chemplex industries, inc. CAT. No: 480). To improve cell adhesiveness of the membrane, the membrane was coated poly-lysin (Sigma Aldrich P7280 average molecular weight 30,000-70,000).

(3) C6 (rat glioma cell) and U251 (human glioma cell) cell lines were cultured on the polycarbonate film and BPA-fructose complex (160 μgB^{10}/mL) was added. Control Sample did not add any agents. After 2 h incubation, the sample was washed and acute freeze-dried.

(4) The samples were irradiated with a 1.7 MeV proton beam collimated to 1 μm in diameter and the emitted gamma rays were detected. Micro PIGE analysis was performed at Takasaki Ion Accelerators for Advanced Radiation Application (Takasaki, Japan). A nuclear reaction $^{10}B(p, p'\gamma)^{7}Be$ was used to measure ^{10}B concentration, and the gamma-rays of this reaction were detected with detector placed 5mm behind the specimen.

(5) Data were corrected on PIXEana which was software developed at JAEA TARRI, can get 2-D distribution images of each atoms. To decline "Cell area" from P and K image by MATLAB. Make a mask image to divide intra and extra cellular area and calculate intra/extra B count ratio.

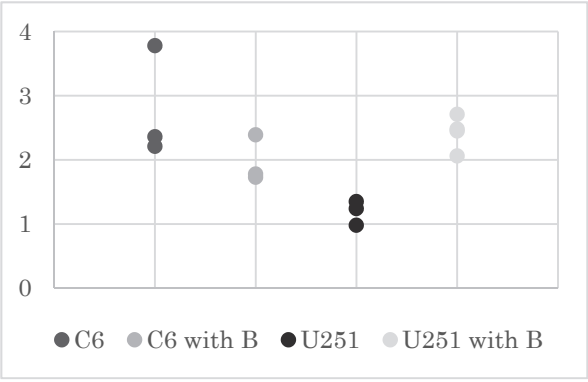

Fig. 1 The boron count ratio Intracellular / extracellular area. The ratio of U251 increased with cell culture medium boron concentration. C6 did not show any tendency.

Result and discussion

Figure 1 showed the intra/extra B count ratio. Higher value mean the intracellular boron accumulation compared with control. Intracelluar area were well determined on U251 images, and U251 Intra cellular B density had about twice B count compare with extra cellular area of U251. On the other hand, PIXE image from C6 cells were difficult to determine cell area automatically, and did not show any tendency of boron distribution.

Further analysis is needed with high concentration of boron.

References

1) T. Yamamoto, K. Nakai, *et al.*, Radiother. Oncol., **91**, 80-84 (2009).
2) K. Yoshino *et al.*, Strahlentherapie und Onkologie, **165**, 127-29 (1989).
3) K. Endo *et al.*, Oncol. Res., **16**, 57-65 (2006).
4) K. Nakai *et al.*, Appl. Radiat. Isot., **106**, 166-70 (2015).

2-41

Analysis of Multiple Myeloma Cell Line Using In-Air Micro-PIXE

T. Kasamatsu [a)], T. Nagashima [a)], K. Nagai [a)], N. Yamada [b)], A. Kitamura [b)], T. Satoh [b)], M. Koka [b)], T. Kamiya [b)], T. Nagamine [a)] and H. Murakami [a)]

[a)] Gunma University Graduate School of Health Sciences,
[b)] Department of Advanced Radiation Technology, TARRI, QST

We established the micro-PIXE assay of the floating cell based on the cytospin method. To evaluate influence of the proteasome inhibitor, we analyzed the elemental change in myeloma cell KMS-11. We added bortezomib of 0 nM, 20 nM and 50 nM in KMS-11 and cultured 24 hours. The level of Ca in KMS-11 treated with 50 nM was higher than 0 nM and 20 nM. Moreover, Ca was accumulated to the nucleus.

多発性骨髄腫（MM）は、自家造血幹細胞移植やサリドマイドなどの新規薬剤が導入され、50%生存期間が 3 年から5年に改善してきている。しかしながら、ほとんどの患者は化学療法に抵抗性であり、未だ治癒が望めない。今研究では、MM の病態解明および新たな疾患の病型分類・治療法の開発へと結びつけることを目的とし、大気 micro-PIXE 法を用いたMM細胞内の微量元素の測定法の確立と検討を行った。

MM 細胞株（KMS11）を用いて、プロテアソーム阻害剤ボルテゾミブを 0 nM、20 nM、50 nM の濃度で添加し、24 時間培養を行った。同時に、WST-8 を用いた生細胞測定キット Cell Counting Kit-8(同仁化学研究所)を用いて細胞生存率を測定した。細胞を TRIS-HNO_3（pH 7.4）にて洗浄後、3×10^5 個/mL に再懸濁する。集細胞遠心装置にて、500 rpm、15 分遠心し、0.5 μm 厚のポリカーボネート膜細胞を接着させ、液体窒素にて-150 °C に冷却したイソペンタンに沈め真空蒸着させる。原子力機構・高崎研のシングルエンド加速器から SB コースのビームを受け取り、マイクロビーム形成を行う。ビームサイズおよびビーム電流を確認後、分析試料を大気 micro-PIXE 分析チャンバーに装着、順次測定し、MM 細胞内微量元素を解析した。

同時に行った細胞生存率の測定では、0 nM と 20 nM では差は認められず、50 nM は生存率約 30%であった。1 細胞あたりのヒストグラムの比較では、0 nM と 20 nM では各元素のピークに差は認められなかった。しかしながら、50 nM では 0 nM に比べ、Ca のピークが高かった。

さらに、P、S、Cl、Ca の元素分布を比較したところ、0 nM と 20 nM では各元素の分布に差は認められなかった。50 nM では他の濃度と比較し、P 分布が断片化しており、細胞死による核の断片化を反映していると示唆された（Fig. 1）。また、50 nM では Ca 分布の核への集積が認められた。白血病細胞ではアポトーシスの際に核内への Ca の流入が報告されており [1)]、さらに小胞体ストレスにより小胞体内の Ca イオンが流出し、Caspase 関連アポトーシス誘導されることが報告されている [2)]。プロテアソーム阻害剤ボルゾミブにおける細胞死は小胞体ストレスが深く関与しており、Ca の変動がボルテゾミブの骨髄腫細胞への作用機序に関与していることが確認された。

References

1) S. Harada *et al.*, Nishina Memorial Cyclotron Center (NMCC) Annu. Rep. 166-71 (2001).
2) G. Hajnoczky *et al.*, Biochem. Biophys. Res. Commun. **304**, 445-54 (2003).

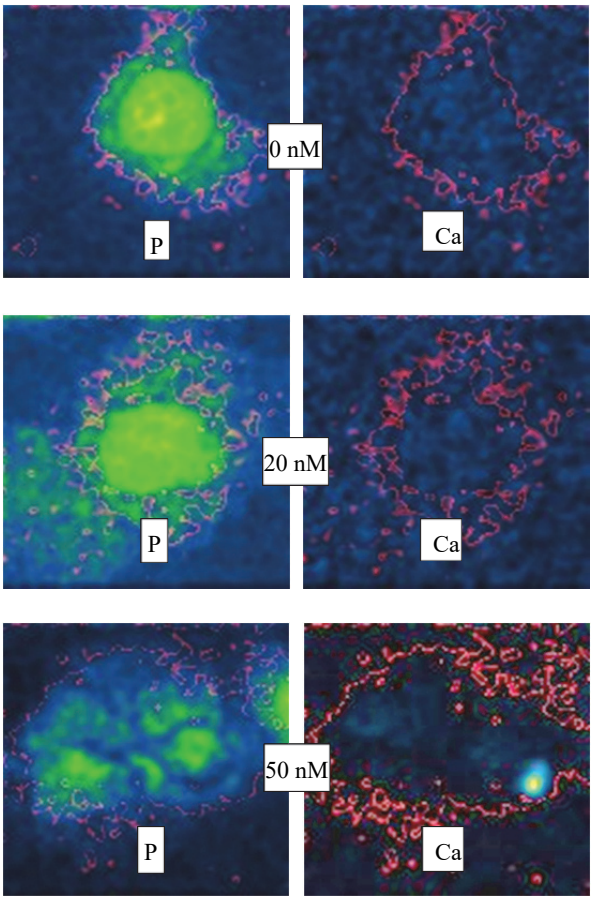

Fig. 1 The distribution of P and Ca in KMS-11 treated with 0 nM, 20 nM and 50 nM bortezomib.

2-42 Co-localization of Iron Binding on Silica with p62/sequestosome1 (SQSTM1) in Lung Granulomas of Mice with Acute Silicosis

Y. Shimizu [a], K. Dobashi [b], T. Satoh [c], M. Koka [c] and T. Kamiya [c]

[a] Department of Pulmonary Medicine and Clinical Immunology, Dokkyo Medical University School of Medicine, [b] Gunma University Graduate School of Health Sciences, [c] Department of Advanced Radiation Technology, TARRI, QST

The cellular mechanisms involved in the development of silicosis have not been fully elucidated. This study aimed to examine influence of silica-induced lung injury on autophagy. Suspensions of crystalline silica particles were administered transnasally to C57BL/6 mice. Immunohistochemical examination for Fas and p62 protein expression was performed using lung tissue specimens. Two-dimensional and quantitative analysis of silica deposits in the lungs were performed in situ using lung tissue sections by an in-air microparticle induced X-ray emission (in-air micro-PIXE) analysis system, which was based on irrradiation of specimens with a proton ion microbeam. Quantitative analysis showed a significant increase of iron levels on silica particles (assessed as the ratio of Fe relative to Si) on day 56 compared with day 7 ($p<0.05$). Fas and p62 were expressed by histiocytes in granulomas on day 7, and the expressions persisted for day 56. Fas- and p62-expressing histiocytes were co-localized in granulomas with silica particles that showed an increase of iron levels on silica particles in mouse lungs. Iron complexed with silica induces apoptosis, and may lead to dysregulations of autophagy in histiocytes of granulomas, and these mechanisms may contribute to granuloma development and progression in silicosis.

1. 背景と目的

シリカ（Si）の吸入は肺に炎症と線維化を引き起こす。Si によって誘導される肺線維症発症のメカニズムの一つに、Si 表層に鉄成分（Fe）が結合しオキシダントを発生させ、組織にアポトーシスを引き起こすことが提唱されている。そこで、肺内へ吸入された Si の化学変化を検討し肺組織像と比較することで、Si による肺障害の病態を明らかにする。

2. 方法

2.1 マウス処置

モデルマウス作製に適し、入手しやすい黒毛の Black6（C57/NL6）マウスにシリカを経鼻的に投与した。Si 粉末は phosphate bufferd saline（PBS）に懸濁し超音波粉砕した。Si 懸濁 PBS（1.5 mg/g body weight）を C57Bl/6 マウスに経鼻的に投与した。コントロールとして C57Bl/6 マウスに PBS を経鼻的に投与した。

2.2 測定

1 週目と 8 週目のマウス肺組織のパラフィン切片を厚さ 15 μm のスライスに切り、厚さ 5 μm のポリカーボネートフィルムに載せて、2.1 と同様にマイクロ PIXE 分析にてパラフィン切片内の元素分布を 測定した。また、肺組織は鉄染色（Belin blue stain）、抗 Fas 抗体で染色した。

3 結果

1 週目の肺組織中の Si と比較し、8 週目の Si には有意に多量の Fe が沈着していた。8 週目の肺組織中では、Si 粒子を多く含む肉芽組織にアポトーシスを誘導する Fas とオートファジーの抑制を示す p62 を多く発現する組織球が集積していた（Fig. 2）。

4 考察

吸入された Si には、時間経過とともに体内の Fe が沈着し、その結果その周囲の細胞にアポトーシスの増加及びオートファジーの抑制を誘導することにより、珪肺の肉芽組織の形成が促進されることが示唆された。

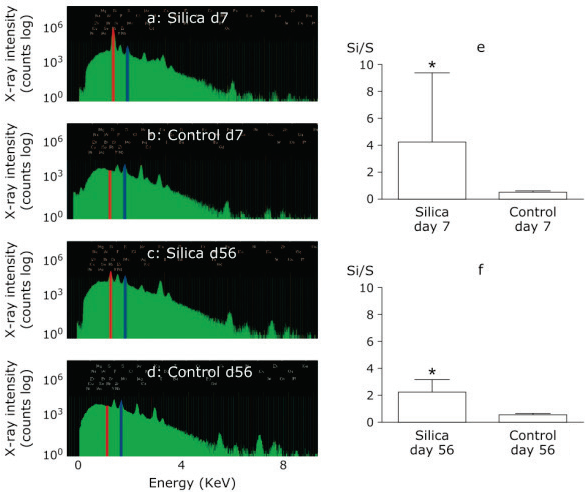

Fig. 1. Peaks of Si in silicosis and control mice were analysed by in_air micro_PIXE analysis. Peaks of Si (red) were higher in silicosis mice (a, c) than control mice (b, d) on day 7, 56.

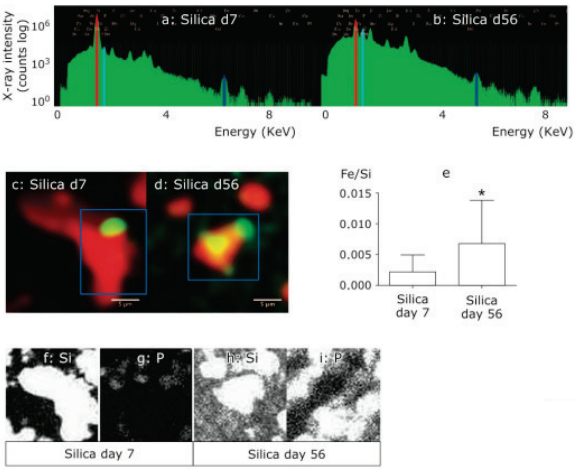

Fig. 2 Increase in Fe level in a silica particle located in the granulomas and histiocytes around the silica particles of silicosis mice after two month from silica instillation.

References

1) Y. Shimizu *et al.*, Int. J. Immunopathol. Pharmacol. **21**(3), 567-76 (2008).
2) Y. Shimizu *et al.*, J. Clin. Biochem. Nutr. **56**(1), 74-83 (2015).
3) H. Chino *et al.*, Intern. Med. **54**(16), 2035-40 (2015).

2-43

Elemental Localization within Poplar Stem Using Micro-PIXE (Particle Induced X-ray Emission)

Y. Noda [a)], T. Aohara [a)], N. Yamada [b)], M. Koka [b)], T. Satoh [b)], T. Kamiya [b)], S. Satoh [a)] and J. Furukawa [a,c)]

[a)] Life and Environmental Sciences, University of Tsukuba,
[b)] Department of Advanced Radiation Technology, TARRI, QST,
[c)] Center for Research in Isotope and Environmental Dynamics, University of Tsukuba

Plants need various elements for the healthy growth. The analysis of element content and localization in the focused organ or tissue is important to identify its functions. Especially the localization analysis of elements in the tissue level is highly valuable for investigating where the deficiency or toxicity of elements is detected and how to regulate the mechanisms for keeping homeostasis of plant body. Some elements can be visualized by chemical staining, but these methods have low resolution and can detect one element per analysis. Micro-PIXE method can detect multi-element at the same time and visualize with a high-resolution image, so it is very useful for identifying where the elements localize. In the Micro-PIXE analysis, setting samples on atmospheric pressure condition, various types of sample preparation methods are acceptable. Up to now, we have developed the method for imaging the element localization using a paraffin embedded section and a frozen section, and identified the most suitable condition for plant tissue in Micro-PIXE at TIARA [1, 2)]. In this study, the relationship between potassium (K) and cesium (Cs) localizations within a tree is focused. Radio-cesium released by the Fukushima Dai-ichi Power Plant Accident was deposited to the forest trees and, therefore, the identification of radio-cesium distribution within the tree body and tissue is needed.

We employed a poplar tree as a model for this investigation. Poplars were subjected to the external supply of CsCl (100 mM, 20 μL) on its leaf using a paper disk mimicking a foliar absorption of radio-cesium. The chemical form of deposited radio-cesium is still not clear, but the form of cesium within the plant body is supposed to be an ionic, Cs^+. As for the Cs imaging, the samples treated for 24 hours were harvested. The samples were embedded in the compound for a freeze section, which is suitable for ionic element imaging [1)], and sliced to 5 μm sections by freezing microtome and then exposed by 3 MeV H^+ beam.

From the images of K localization (Fig. 1), cell shape and tissue structure were well observed. Both in the stem and the node, K was accumulated at the cortex, cambium and endodermis. However, in the tissue where the large size of cell is exist, K concentration is obviously low. The signals derived from Cs was not detected in the cross section samples.

The image of Cs localization was obtained from the longitudinal section harvested from the node (Fig. 2). Although the Cs image obtained here was not clear, it was indicated that the cortex contained relatively high concentration of Cs. This localization pattern is similar to K distribution observed from the same sample. This indicates the Cs absorbed at the leaf surface was transferred to the cortex in the node. The candidate mechanism for Cs transfer is K circulation within the plant body and the similar distribution of K and Cs observed here supports that hypothesis. For investigating Cs pathway involved in the foliar absorption, the improved method for obtaining better Cs image is required.

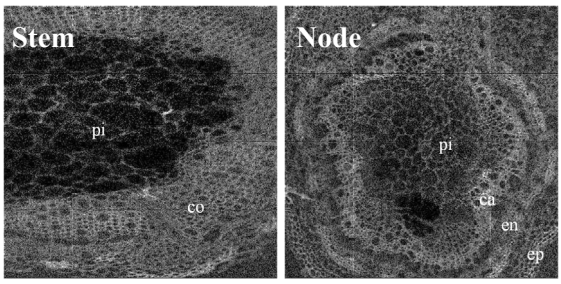

Fig. 1 Potassium localization in poplar stem and node obtained by Micro-PIXE. The images were the cross section. pi: pith tissue, co: cortex, ca: cambium, en: endodermis, ep: epidermis.

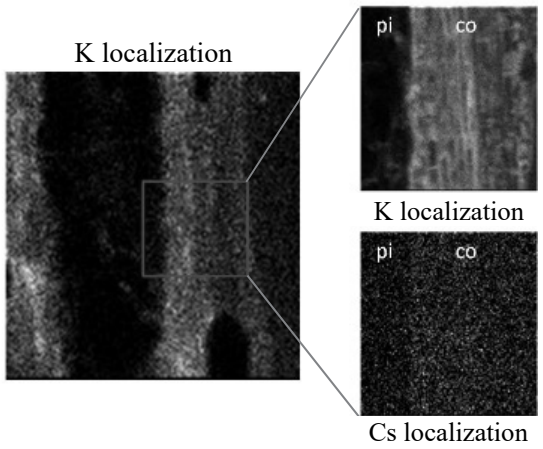

Fig. 2 Potassium and cesium localization in the node of poplar. The images were obtained by the longitudinal section. Right images are the magnified image of square area in the left. pi: pith tissue, co: cortex.

References

1) T. Yamamoto *et al.*, JAEA Takasaki Annu. Rep. 2012, JAEA-Review 2013-059, 94 (2014).
2) T. Yamamoto *et al.*, JAEA Takasaki Annu. Rep. 2013, JAEA-Review 2014-050, 97 (2015).

2-44 Fluoride Varnish Remaining After Physical Stress

Y. Matsuda [a)], K Okuyama [b)], H. Komatsu [c)], H. Yamamoto [d)], N. Hashimoto [c)], M. Hayashi [d)], M. Nomachi [e)], K. Yasuda [e)], T. Satoh [f)] and M. Koka [f)]

[a)] School of Dentistry, Health Science University of Hokkaido, [b)] Asahi University School of Dentistry, [c)] Graduate School of Dental Medicine, Hokkaido University, [d)] Graduate School of Science, Osaka University, [e)] The Wakasa wan Energy Research Center, [f)] Department of Advanced Radiation Technology, TARRI, JAEA

Introduction

Fluoride varnishes are worldwide used for preventing caries development. It is applied and made a thin layer on the tooth surface. This thin layer provides fluoride to the tooth and inhibits demineralization. In clinical case, there are several stresses will work on the tooth surface, such as bruising, occlusal stress, and some other external forces. These stresses have a risk of fall the sealing materials from the tooth surface. This study evaluated the fluorine remaining of fluoride varnish pre and after removing materials on dentin by means of an in-air micro-Particle Induced X-ray/Gamma-ray Emission (micro-PIGE/PIXE) system[1,2].

Materials & Methods

Specimen preparation: Human teeth were prepared and root surface and dentin were exposed by hand scaler. The dentin block (10 mm × 5 mm and 1 mm thickness) were made from root dentin. The 10 mm × 5 mm area was polished by #1000 Si- carbide paper. Two different fluoride varnish (CTX2 Varnish, Oral Biotech (FVC), White Fluoride Varnish, Butler (FVB)) and one glass-ionomer cement (Fuji IX, GC (FN)) were applied on the polished surface. No treated specimens were used as a control (Control). The dentin specimens were stored 24 hours in distilled water at 37 °C. After storage, materials on the half of applied area (5 mm × 5 mm) were removed by hand scaler and #1000 Si-carbide paper. Fluorine and calcium distributions of each specimen were evaluated using micro-PIGE/PIXE system at TIARA (Takasaki Ion Accelerators for Advanced Radiation Application, Takasaki JAPAN).

Results

Figures 1 and 2 show calcium and fluorine map by in-air micro-PIXE/PIGE analysis on the dentin surface. The Ca, and F existence shows as the white dot. In CTX and FVB group, Ca and F were existed ununiformly before removing, but after removing materials, Ca and F remain uniformly. In FN group, F was spread uniformly before removing and Ca was spread uniformly after removing.

Discussion

Fluoride varnish only includes NaF and doesn't contain calcium. Therefore, the Ca signals mean that fluoride varnish layer is too thin, and proton beam could through the layer and calcium of the dentin structure reacted. These

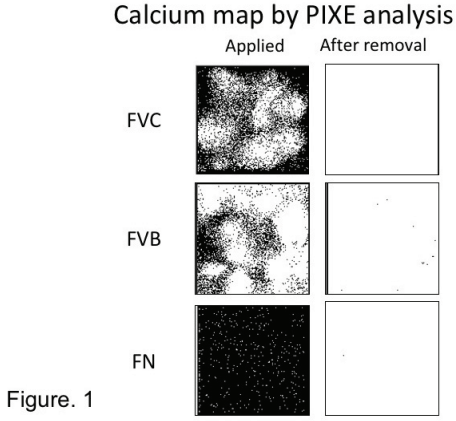

Figure. 1

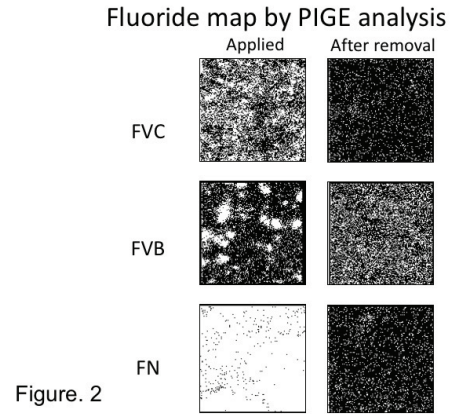

Figure. 2

Figs. 1 and 2 Elemental PIXE maps (Calcium) and PIGE map (Fluoride) of the specimens. White dots in each map represented PIXE or PIGE signals from each element.

results suggested the applied varnish layer thickness and fluoride distribution are not uniform. On the other hands, after removing materials by physical stress, materials even remain on the tooth surface and it distributes uniformly.

Conclusion

Fluoride varnishes even stick on the dentin surface after physical stress, and it will be the advantage for demineralization inhibition of the tooth.

References

1) H. Yamamoto *et al.*, Nucl. Instrum. Meth. Phys. Res. B, **210**, 388 (2003).
2) Y. Matsuda *et al.*, Nucl. Instrum. Meth. Phys. Res. B, **348**, 156-59 (2015).

2-45 Protamine-Hyaluronic Acid Particles as a Drug Delivery System Utilizing Radiotherapy

S. Harada [a)], S. Ehara [a)], T. Satoh [b)] and T. Kamiya [b)]

[a)] Department of Radiology, School of Medicine, Iwate Medical University,
[b)] Department of Advanced Radiation Technology, TARRI, QST

We have been developing targeted cancer chemotherapy, using particles that release anticancer drugs in response to irradiation. The released anticancer drugs attack tumors synergistically with the radiation, which will lead to increased anticancer effects. Localized release of the anticancer drug reduces the potential for adverse effects. Previously, we developed anticancer drug-releasing microcapsules by polymerizing alginate and hyaluronic acid with Ca^{2+} and Fe^{2+} [1)]. However, the diameter of these microcapsules was 23.2±7.6 μm. Following intravenous injection, the large diameter of these microcapsules did not allow them to pass through the capillaries of the brain or lungs, which resulted in cerebral infarction or pulmonary embolism [2)]. It is well known that negatively charged hyaluronic acid and positively charged protamine bind electrostatically to form small nanoparticles. As hyaluronic acid decomposes into acetyl glucosamine when irradiated [1)], it is postulated that the hyaluronic acid-protamine particles may also decompose following irradiation. If protamine-hyaluronic acid particles were to contain an anticancer drug, the particles may release the anticancer drug in response to radiation-induced decomposition. In this study, protamine-hyaluronic acid particles containing carboplatin, a platinum-containing anticancer drug, were evaluated for particle size and their ability to release the anticancer drug in response to radiation.

Protamine (2 mg), 1.6 mg hyaluronic acid, and 2 mg Paraplatin (a branded preparation of carboplatin) were mixed with 10 mL of 0.1 mmol/L Tris buffer, and incubated for 30 minutes at room temperature. The generated particles were filtered through a 0.8-μm cellulose filter. The particles that were trapped in the cellulose filter were re-suspended in 0.1 mmol/L Tris buffer. Finally, the particles were sonicated using an ultrasound disintegrator and used in experiments. Irradiations were performed with 140-keV soft X-ray at a dose rate of 0.301 Gy/min by using Softex M150 WE. The irradiated particles were processed to be analyzed using a micro PIXE camera [1)]. Each PIXE sample was irradiated with a 3 MeV proton beam, and the X-rays induced were recorded using a silicon-lithium detector. All micro PIXE analyses were carried out at the Takasaki Advanced Radiation Research Institute, JAEA. Transform version 3.0 (Fortner Software Inc.) was used to obtain and analyze the X-ray images.

The particles were imaged using the micro PIXE camera, based on the distribution of Pt. The mean diameter of the generated particles was 0.41±0.06 μm (Fig. 1-A). Before irradiation, particles were round in shape with clear margins (Fig. 1-A). After irradiation, particles were fragmented, which was considered to indicate rupturing of particles (Fig. 1-B). The percentages of ruptured particles are shown in Fig. 2. Particles (61.2±6.8%) were ruptured by exposure to 10 Gy of radiation.

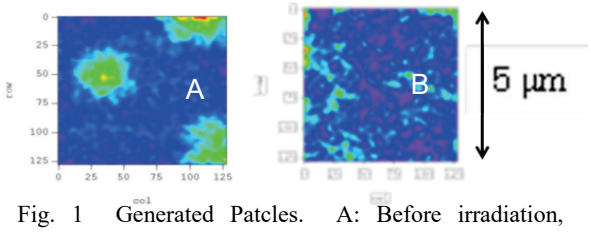

Fig. 1 Generated Patcles. A: Before irradiation, B: After 10 Gy irradiation.

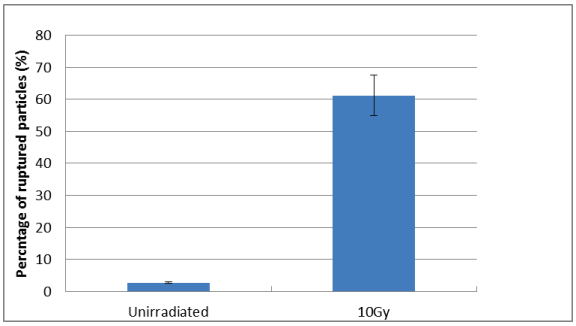

Fig. 2 Fruency of rupturing of particles by irradiation.

Our new protamine-hyaluronic acid particles are smaller than red blood cells. These minimized particles could pass through the capillaries of the brain and lungs, which will allow us to administer them intravenously without any risk of causing an embolism. The percentage of particles ruptured by irradiation (61.2 ± 6.8%) was lower than expected and 10 Gy is 5 times higher than the 2 Gy dose that is used in clinical cancer treatment. The heavy metal-containing anticancer agents are considered to increase the sensitivity to radiation-induced rupturing.

References

1) S. Harada *et al.*, Biomed. Pham1acother., **70**, 196 (2015).
2) S. Harada *et al.*, Int. J. PIXE, **24**, Nos. 3 & 4, 137 (2014).

Part II

3. Advanced Quantum-Beam Technology

3-01 Continuous Ion Beam Induced Luminescence Analysis for Identification of Organics in Microscopic Targets

W. Kada [a)], S. Kawabata [a),b)], R. K. Parajuli [a)], T. Satoh [b)], M. Koka [b)], N. Yamada [b)], K. Miura [a)], O. Hanaizumi [a)] and T. Kamiya [b)]

[a)] Faculty of Science and Technology, Gunma University,
[b)] Department of Advanced Radiation Technology, TARRI, QST

Recently, there has been increasing interest in ion beam-induced luminescence (IBIL) spectroscopy, which could be used in conjunction with other ion beam analysis methods such as particle-induced X-ray emission (PIXE)[1,2]. Previous research revealed that IBIL analysis using a proton microbeam probe could be combined with external in-air micro-PIXE, and provided additional information about microscopic targets which contains organics[3]. However, there is a lack of information about IBIL from organic materials in the luminescence database[4, 5]. To evaluate these features of IBIL analysis, continuous observation of the IBIL spectrum is desirable, particularly for organic materials.

In this study, we demonstrate continuous IBIL spectroscopy with a 3 MeV external microbeam probe. A high-sensitivity spectrometer was used to continuously record IBIL spectra not only from several inorganic microscopic targets, but also from standard organics. The decay and changes in the structure of IBIL were observed for the organic and microscopic targets. The external proton microbeam setup for in-air micro PIXE analysis on a micro-beam line of the 3 MV single-ended accelerator facility at TARRI/JAEA was used for the IBIL analysis. A focused microbeam with a typical diameter of approximately 1 μm was used for IBIL imaging and spectroscopy. Organic standard samples related micro-particles, *i.e.* nicotinamide adenine dinucleotide (NADH), tryptophan, riboflavin, and the polycyclic aromatic hydrocarbon (PAH) benzo[a]pyrene, were independently sealed between two thin polyimide films to prevent free emission to the environment before and after irradiation. IBIL spectrum was obtained by electrically cooled back-thinned CCD spectrometer (Solid Lambda CCD, Spectra Co. Ltd.) with an effective wavelength from 200 to 1,000 nm.

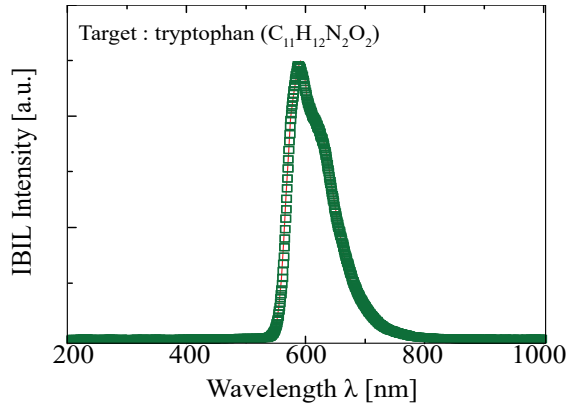

Fig. 1 Example of IBIL spectra obtained from organic targets excited by 3 MeV proton microbeam probe.

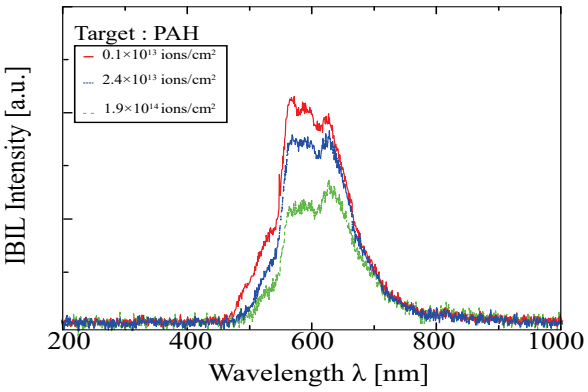

Fig. 2 Example of IBIL spectra continuously obtained from PAH (benzo[a]pyrene) target.

Figure 1 shows an example of IBIL spectrum obtained from tryptophan. Each organics had different IBIL emission band (NADH 400–600 nm, riboflavin 500–600 nm, and tryptophan 500–700 nm) at 3 MeV proton irradiation. These results suggested that organic targets were able to be distinguished by the peak wavelength of IBIL as well as inorganic targets. Also changes in the structure of IBIL caused by ion beam irradiation were able to be recorded during proton beam irradiation. As an example, standard target of the PAH (benzo [a] pyrene), was employed for the irradiation. At the beginning of the irradiation, strongest IBIL peak was around 580 nm. A multiple peak appeared in the spectrum when the beam fluence was around 10^{13} ions/cm^2. The intensity ratio of the peaks changed as the beam fluence increased. While the result of PIXE analysis does not differed at these beam flunece, there results suggested that continuous IBIL analysis had obtained structural changes in chemical composition of the organic targets.

References

1) K. G. Malmqvist *et al.*, Nucl. Instrum. Meth. Phys. Res. B, **109-10**, 227 (1996).
2) T. Calligaro *et al.*, Nucl. Instrum. Meth. Phys. Res. B, **318**, 139 (2014).
3) W. Kada *et al.*, Nucl. Instrum. Meth. Phys. Res. B, **332**, 42 (2014).
4) C. M. MacRae and N. C. Wilson, Microsc. Microanal., **14**, 184 (2008).
5) N. C. Wilson *et al.*, Microsc. Microanal., **20**, 916 (2014).

3-02 Analysis of Multiple Ion Scattering in β-$FeSi_2$ Films with Equivalent Domains Epitaxially Grown on Si(111)

Y. Maeda [a, b], Y. Terai [a] and K. Narumi [b]

[a] Department of Computer Science and Electronics, Kyushu Institute of Technology,
[b] Department of Advanced Radiation Technology, TARRI, QST

Epitaxial growth of crystal planes of β-$FeSi_2$(110), (101) on Si(111) is one of the most reliable cases in Molecular Beam Epitaxy (MBE), Reactive Deposition Epitaxy (RDE), Metal Organic Chemical Vapor Deposition (MOCVD) or Ion Beam Synthesis (IBS). In this hetero-epitaxy, the lattice mismatch δ becomes +1.4 to +5.5% in these directions, respectively and six equivalent crystal domains grow on a Si(111) plane [1].

Rutherford backscattering spectrometry (RBS) and ion channeling measurements along a given crystal axis of the substrate teach us element profiles in depth and epitaxial quality of atomic rows, respectively, so they are very powerful methods to evaluate total feature of epitaxy. However, there are no reports about ion channeling measurements of β-$FeSi_2$/Si heteroepitaxial structures.

In this report, using the obtainable high grade MBE films we have investigated axial ion channeling measurements of crystal planes of β-$FeSi_2$(110), (101) epitaxially grown on Si(111) in order to evaluate quality of the epitaxy and quantitative discussion based on atomic displacements on the atomic rows along the Si<111> direction.

Sixty nm-thick β-$FeSi_2$ films were epitaxially grown on the 20 nm-thick β-$FeSi_2$ template layer formed on Si(111) substrates at 550 °C by MBE, where the template layer was deposited at 670 °C by RDE. During MBE growth, a ratio of Si/Fe was hold to be 1.17. Reflection High Energy Electron Diffraction (RHEED) patterns were observed during growth and showed a β-$FeSi_2$ (110) or (101) single plane. Also Raman measurements indicated the single phase of β-$FeSi_2$ in optically detectable depth.

Two-MeV $^4He^+$ RBS spectra were measured at the backscattering angle of 165°. Along the axis Si<111>, ion channeling measurements were performed in the β-$FeSi_2$ film with the template layer at each tilt angle of the beam between -2.0 and +2.0 degrees. The tilt direction may be important issue and was employed between [1,-1,0] and [-1,0,1] directions of Si where the minimum yields of Fe and Si channels were obtained. Axial channeling dip curves, which are backscattering yields of Fe and Si atoms as a function of the tilt angle, were analyzed by the following equation (1) in order to obtain a minimum yield (χ_{min}) and a critical half angle ($\psi_{1/2}$).

Unexpectedly we obtained the larger χ_{min} and the smaller $\psi_{1/2}$ than those predicted usually in epitaxially grown films as shown in Fig. 1. This result suggests directly that the Si atomic row on β-$FeSi_2$ (101), (110) planes may be much disordered along Si<111> axial directions. In Fig. 1, both χ_{min} and $\psi_{1/2}$ are dependent upon the location where ions are scattered. At inside of the film we obtain the χ_{min} values of 0.8. At the Si substrate a little far from the interface, the χ_{min} of Si was 0.31, which depends on the upper film quality.

We discuss an effect of multiple ion scattering (MIS) caused in the inside of film on the channeling measurements. In that condition, we get the MIC probability $P(\theta_c, m)=\chi_{min}$. The reduced angle θ_c can be deduced from measured $\psi_{1/2}$. The $P(\theta_c, m)$ vs m diagram reported [2] gave $m=14$.

On the other hand, using average atomic vertical displacement along the Si atomic row ΔX, for crystals, $m = \pi(a_{TF}^2 + \Delta X^2)(Nt)$, where a_{TF} is the Thomas-Fermi screening radius of Si, N is the number of atoms in the β-$FeSi_2$, t is a film thickness. These calculations gave us ΔX=~0.04 nm, which corresponds to displacement of each stacking faults. Six possible domains make mosaic structure with stacking faults of interval in 0.31 nm [1], therefore one interval causes atomic displacement by 0.31/6 = ~0.05 nm in average. This fact is important for understanding ΔX=~0.04 nm obtained from analysis of the multiple scattering [3].

We conclude that multiple ion scattering in the β-$FeSi_2$(101), (110) with six equivalent domains epitaxially grown on Si(111) can be attributed to the present stacking fault of domains uncontrollably formed in the mosaic structures of β-$FeSi_2$ (110), (101) planes.

Finally, we would emphasize that for evaluation of the film out of single ion scattering condition analysis using the MIS is very powerful to obtain the overgrowth films on Si substrate as shown in this report.

References

1) A. V. de Parga *et al.*, Appl. Phys. A **57** 477 (1993).
2) L. Feldman *et al.*,"Material Analysis by ion channeling", Academic Press, New York, 110-14 (1982).
3) M. Fuchi, Y. Maeda, *et al.*, Proc. APAC-SILICIDE 2016, [Fukuoka, Japan] (2016).

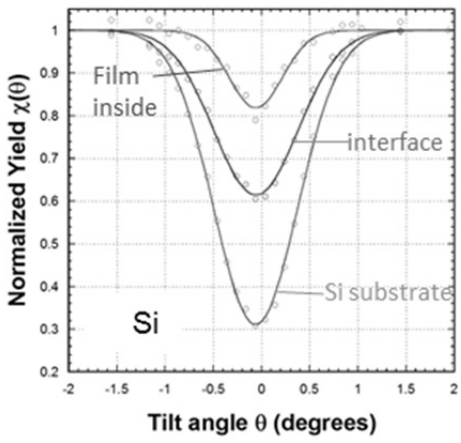

Fig. 1 Axial channeling dip curves for Si atoms in β-$FeSi_2$ and a Si substrate along a Si<111> direction.

3-03 In-situ Measurement of Li-distribution in Li Ion Battery

K. Mima [a)], M. Finsterbush [b)], K. Fujita [a)], A. Yamazaki [c)], T. Satoh [d)], M. Koka [d, e)], Y. Orikasa [f)], M. Hattori [f)], Y. Uchimoto [f)], T. Kamiya [d)] and Y. Kato [a)]

[a)] The Graduate School for the Creation of New Photonics Industries,
[b)] Forschungzentrum Juelich, GmbH,
[c)] Research facility Center for Science and Technology, University of Tsukuba,
[d)] Department of Advanced Radiation Technology, TARRI, QST,
[e)] Graduate School of Life Sciences, Ritsumeikan University,
[f)] Graduate School of Human & Environmental Studies, Kyoto University

The experiments on the diagnostics of a Li ion battery (LIB) have been continued to demonstrate the in-situ measurement of various LIB electrodes. In the year of 2015, we tested all solid state LIB (ASB) and Liquid electrolyte LIB which were made of $Li_7La_3Zr_2O_{12}$ (LLZ)+$LiCoO_2$ (LCO) and $LiNiO_2$(LNO), respectively. The time dependent images are successfully taken, but effects of proton beam damage to the samples seem important. We will continue to investigate the *in-situ* diagnostics to clarify the effects of proton beam damage in the year of 2016.

1. 実験経過と結果まとめ

液体電解質と $LiNiO_2$（LNO）合材電極（京都大学内本研究室製作）と固体電解質（LLZ）の $LiCoO_2$(LCO)（ユーリッヒ研究所 M. Finsterbush 製作）との 2 種類のリチウムイオン電池（LIB）につき、マイクロ PIGE と PIXE により、充放電時のリチウムイオン濃度の時間変化を“その場計測”した。

固体電解質 LLZ と電極材料 LCO の全固体電池（ASB）について充放電を行ないつつその場計測を試みたが、データを解析した結果充放電が不完全であった事が示唆された。ユーリッヒの大膜厚の ASB サンプルについては初めての実験であり、サンプルの特性を明らかにするため、2016 年度には基礎に立ち返り、“静止サンプル“計測から実験を始めることとした。

液体電解質については、2014 年度の実験で $LiFePO_4$(LFP)合材電極のその場計測に成功しているが、今年度の LNO 合材電極の場合には、材質の違いからビームによる電解質が沸騰して活物質が剥離するという問題が生じた。連続したビーム照射による試料の過熱を抑えるため、充電とビーム照射を交互に行なう事で問題の解決を計った。Figure 1(a)及び(b)は、LIB 試料の電解質を挟んで左側（リチウムメタル）から右側（LNO）にかけての PIXE による Ni 及び PIGE による Li の分布をそれぞれ示す（走査野 0.8 mm × 0.8 mm）。Figure 1(c)はイメージにおける赤い四角で分けられた左右の領域での Ni と Li の合計カウント数の比（Li/Ni）の時間変化（黒線=左側、赤線=右側）、及びその比（左右比）の時間変化（青線）である。1フレーム 10 分間の 14 フレーム（140 分）の計測を行った。左右比が時間とともに減少しており、右側の活物物質中のリチウムが充電により左側のリチウム金属に移動した事がわかる。この変化量より全充電により移動したリチウムの総量を見積もる事が可能である。

2. 終わりに

LNO 合材電極 LIB の充電に伴う電極材料のリチウム元素の時間変化が明確に観測できたので 2016 年度には、LNO 電極のその場計測による分布イメージの時間変化の取得を目指す。一方、ASB については“その場計測”の可能性をドイツグループと協力して引き続き探索する。

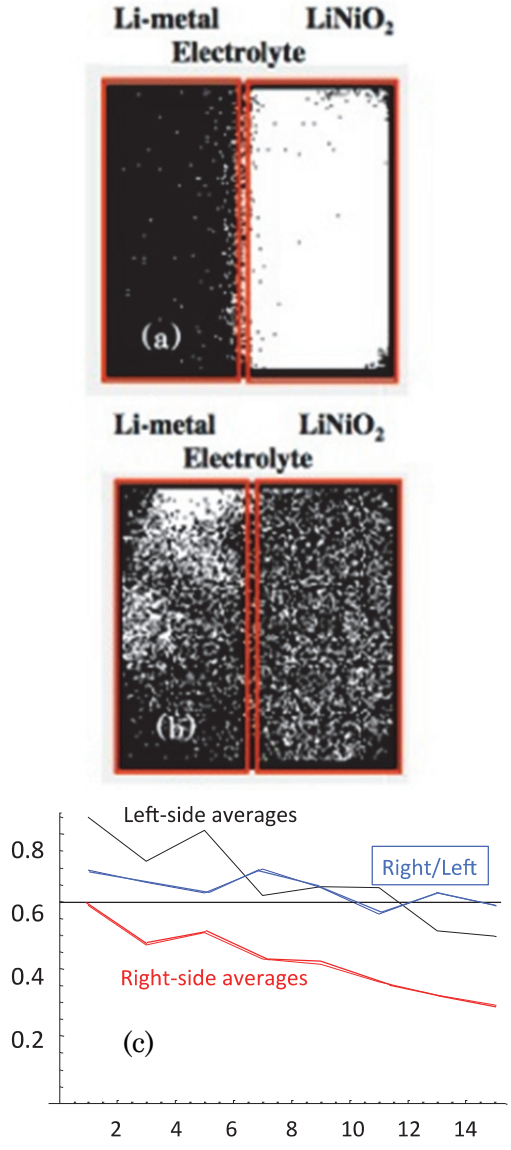

Fig. 1 Elemental distribution of (a) Ni, (b) Li in electrode material LNO, and (c) time dependence of Li/Ni.

3-04 Measurements of Neutron Energy Spectra of Thermal Energy Region in High Energy Quasi-Monoenergetic Neutron Fields Using a Bonner Sphere Spectrometer

T. Matsumoto [a)], A. Masuda [a)], H. Harano [a)], H. Seito [b)] and S. Kurashima [b)]

[a)] National Metrology Institute of Japan, National Institute of Advanced Industrial Science and Technology, [b)] Department of Advanced Radiation Technology, TARRI, QST

Precise measurements for high-energy neutrons are important in studies on neutron dose estimation around large accelerator facilities such as J-PARC, nuclear data, exposure in aircrafts and neutron induced soft error rate in semiconductor devices. Research has proceeded to use high energy quasi-monoenergetic neutron fields with peak neutron energies of 45 MeV and 60 MeV at the AVF cyclotron facility TIARA as neutron standards[1,2]. In the neutron fields, high energy neutron detectors or dosemeters are calibrated. In many cases, the high energy neutron detectors or dosemeters have also sensitivities to thermal energy region. On the other hand, thermal neutrons are slightly produced by scattering in a collimator and an experimental room. In the present study, we measured neutron energy spectrum of thermal energy region in the TIARA high energy neutron field.

Quasi mono-energetic neutrons are produced in the ^{7}Li(p, n)^{7}Be reaction where a proton beam from the AVF cyclotron impinges on an enriched metal lithium-7 target. At first, neutron energy spectra were measured by the time-of-flight (TOF) method using an organic liquid scintillator (BC501A, diameter: 7.62 cm, thickness: 7.62 cm) and a ^{6}Li glass scintillator (GS20, diameter: 5 cm, thickness: 5 mm). In the TOF measurements, it is possible to obtain ion pulses with intervals of micro second by using the S- and P- chopper systems[3]. Therefore, the neutron energy down to keV region is measured with the TOF method at the TIARA [4]. Figure 1 shows the neutron energy spectra measured using the TOF method. In the TIARA neutron field, there are direct neutrons emitted by the ^{7}Li(p,n) reaction and neutrons scattered by the floor and walls. Figure 1 indicates the direct neutrons emitted by the ^{7}Li(p,n) reaction. Especially, the neutron energy spectrum in the keV energy region was measured for the first time. Secondary, the neutron energy spectrum of the thermal energy region due to the scattered neutrons was measured with a Bonner sphere spectrometer (BSS) by means of an unfolding method. The BSS is composed of a spherical ^{3}He proportional counter (SP9, gas pressure: 0.5 atm.) and polyethylene moderators (diameter from 7.62 cm to 24.13 cm), a copper moderator in polyethylene and a lead moderator in polyethylene. The unfolding was performed using the MAXED code in the UMG3.3 package[5]. The initial guess spectrum was obtained by the MCNPX code[6] in the unfolding process. Figure 2 shows the preliminary result for the neutron energy spectrum at the position of 13 m away from the target obtained by the unfolding method. Calculated result is also shown in this figure. This figure indicates discrepancy between measured and calculated results. It is necessary to improve the data analysis and calculations in order to find causes.

.

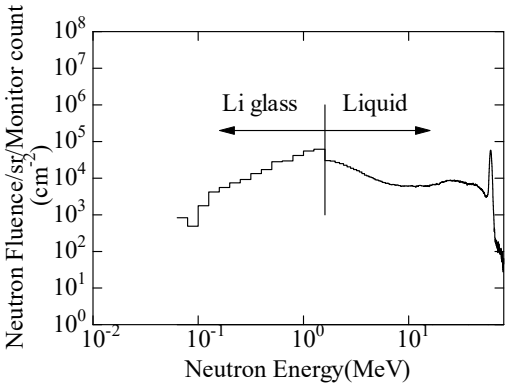

Fig. 1 Neutron energy spectra measured with the liquid scintillator and the ^{6}Li glass scintillator using the TOF method.

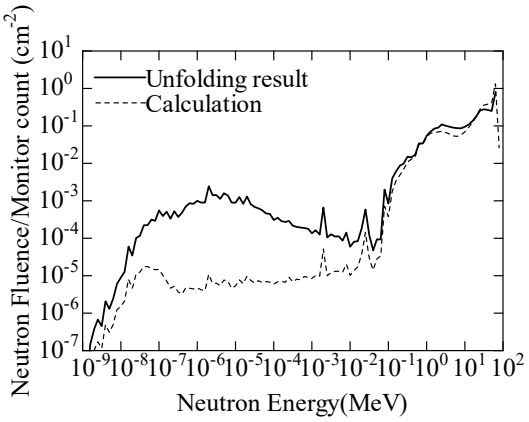

Fig. 2 Neutron energy spectrum measured with the BSS using the unfolding method.

References

1) H. Harano *et al.*, Radiat. Meas., **45**, 1076 (2010).
2) Y. Shikaze *et al.*, Nucl. Instrum. Meth. Phys. Res. A, **615**, 211 (2010).
3) S. Kurashima *et al.*, Rev. Sci. Instrum., **86**, 073311 (2015).
4) A. Masuda *et al.*, IEEE Trans. Nucl. Sci., **62**(3), 1295 (2015).
5) M. Reginatto *et al.*, Nucl. Instrum. Meth. Phys. Res. A, **476**, 242 (2002).
6) D. B. Pelowitz, *MCNPX user's manual Ver 2.5.0*, Los Alamos National Laboratory, LA-CP-05-0369 (2005).

3-05 Measurement of Neutron-production Double-differential Cross Sections in Most-forward Direction for 65- and 80-MeV Proton Incidences

D. Satoh, Y. Iwamoto and T. Ogawa

Environment and Radiation Sciences Division, NSEC, JAEA

In the proton-incidence reactions above several tens mega-electron volts, neutrons produced from a target nucleus in the most forward direction have relatively high energies and high production rates. Though those neutrons are important in the shielding design of proton accelerator facilities, theoretical models of nuclear reaction and evaluated nuclear data libraries fail to reproduce the neutron production in this direction. To improve the accuracy of the models and libraries, it is required to obtain the systematic experimental data on neutron-production double-differential cross sections (DDX) in the most-forward direction. Our study, therefore, aims to measure the DDX for target nuclei in wide atomic mass region using the proton beams supplied by the AVF cyclotron of TIARA.

In the last fiscal year (FY 2014), we performed a feasibility study to examine the experimental setup and the data-acquisition system used at TIARA for the DDX measurements. The data on DDX of ^{7}Li, ^{nat}C, ^{28}Al, ^{nat}Fe, and ^{nat}Pb nuclei for 50-MeV proton incidence were successfully obtained with a sufficient statistical precision, and the results of ^{7}Li agreed well with the existing experimental data measured by the other group. On the basis of those results, we launched the systematic measurements of DDX in the most-forward direction in FY 2015.

The experiments were performed at a LC0 beam course of TIARA. The protons were accelerated to 65 and 80 MeV by the AVF cyclotron, and the beams were transported to the beam course with thinning out to 1/5 to broaden the time interval between bunches of proton for the neutron time-of-flight (TOF) measurement. The time intervals in the 65 MeV and 80 MeV beams were approximately 273 ns and 249 ns, respectively. The thin target plates of ^{7}Li, ^{nat}C, ^{28}Al, ^{nat}Fe, and ^{nat}Pb mounted on a target changer were bombarded by the proton beam with the beam current below 10 nA. The neutrons produced from the targets were led to the measurement room via a collimator opened in the most-forward direction, and were detected by a liquid organic scintillator whose diameter and thickness were 12.7 cm. The proton beam passing through the target was removed from the most-forward direction by a magnet, and its current was measured using a Faraday cup to determine the number of protons incident to the target. The signals from the scintillator were recorded event by event via acquisition system. In the off-line analysis, neutron events were distinguished from the gamma-ray events using the pulse shape discrimination technique. The kinetic energies of the neutrons were determined from the difference of TOF between the prompt gamma rays and neutrons.

Figures 1 and 2 show the experimental results of carbon target for 65- and 80-MeV proton incidence together with the calculation results of the theoretical model INCL and the evaluated nuclear data library JENDL-4.0/HE. The neutron spectra indicated three typical peaks which constructed with the neutrons from the reactions of ^{13}C(p,n), ^{12}C(p,n) and quasi-free scattering with ^{12}C. The JENDL-4.0/HE reproduced the peaks of ^{13}C(p, n) and ^{12}C(p, n) reactions, but failed to reproduce the quasi-free scattering. The INCL could not generate the peak structures in the neutron spectra, and the absolute magnitude of neutron spectrum deviated from the results of experiment and JENDL-4.0/HE in the 80-MeV proton incidence.

In FY 2016, we will measure DDX at the incident proton energies of 20 MeV and 34 MeV to complement the systematic experimental data. In addition, the theoretical model will be improved by using the present dataset.

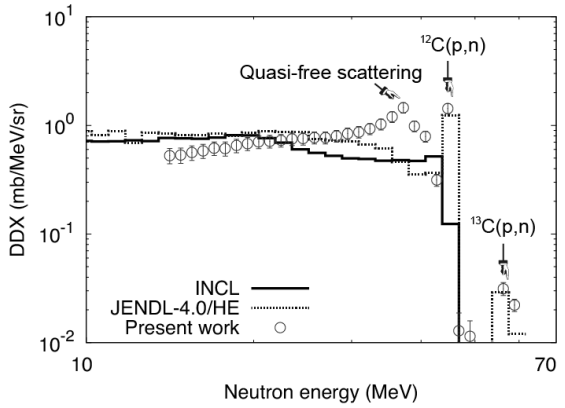

Fig. 1 DDX of ^{nat}C for 65-MeV proton incidence.

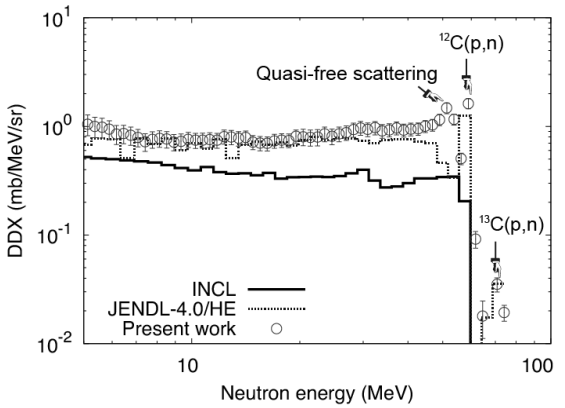

Fig. 2 DDX of ^{nat}C for 80-MeV proton incidence.

3-06 Development of Active Control System of Cyclotron Magnetic Field for Stable Microbeam Irradiation

S. Kurashima, N. Miyawaki, H. Kashiwagi, K. Yoshida, N. Yamada, M. Koka and T. Satoh

Department of Advanced Radiation Technology, TARRI, QST

A microbeam focusing system using a quadruplet of quadrupole magnets is being developed at the HX course of TIARA cyclotron to irradiate living cells or semiconductor devices. Microbeams such as a 260 MeV $^{20}Ne^{7+}$ and a 520 MeV $^{40}Ar^{14+}$ with a spot size around 1 to 2 μm are used for the experiments. In addition, a $^{12}C^{6+}$ microbeam around 7 μm in spot size at 320 MeV, the highest energy per nucleon ion beam at TIARA, was developed to irradiate living microscopic worms[1]. To form the microbeam using the focusing system, an energy spread $\Delta E/E$ of the ion beam is restricted to the order of 10^{-4} for reducing an influence of chromatic aberrations in the focusing lens. A flat-top acceleration technique[2] and a magnetic field stabilization system[3] were introduced to the cyclotron for reducing the energy spread of heavy-ion beams.

The magnetic field of the cyclotron was changed for long duration over 10 h on the order of $\Delta B/B = 10^{-4}$ because of heat deformation of the iron yoke caused by heat transfer from a pair of main coils. The long duration magnetic field instability was remarkably improved to $\Delta B/B = 1 \times 10^{-5}$ by installing water-cooled copper plates between the coil and surface of the yoke as a heat insulator. On the other hand, short duration instability of the microbeam intensity was observed during experiments. The microbeam sometimes vanished from a focusing point within half an hour after beam tuning. Currents of outer-, inner-most trim coils and a set of harmonic coils of the cyclotron were adjusted to recover the beam current. Although a reason of the instability was unclear we decided to improve short duration instability of the whole magnetic field since the beam orbit is extremely affected by the change of the cyclotron magnetic field. Figure 1 shows a schematic diagram to measure and control the cyclotron magnetic field using a nuclear magnetic resonance (NMR) probe[4]. The magnetic field is regulated by using an additional 5 turns coil, instead of the outer-most trim coil, wound along the main coil, a power supply and a personal computer (PC) based proportional-integral-derivative (PID) controller.

An NMR probe is generally used to precisely measure a uniform magnetic field, and it was difficult to obtain sufficient signal intensity in the non-uniform cyclotron magnetic field that radially and azimuthally varies. To improve a signal-to-noise ratio of the NMR probe, a series of actions such as vibration insulation of the signal pickup cable, addition of a noise filter circuit and change of the gating time of the pickup circuit was carried out. As a result, the NMR probe has become usable for measurement of the cyclotron magnetic field for most acceleration conditions, and therefore the active PID control system

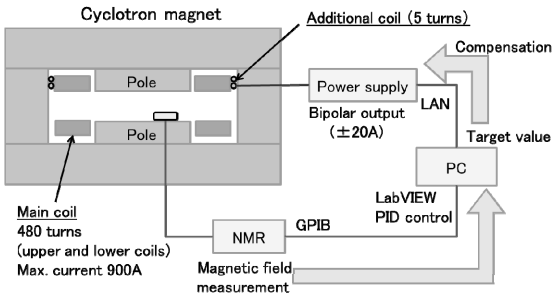

Fig. 1 Schematic diagram for measurement and control of the cyclotron magnetic field using the NMR probe. The NMR probe was set on a central axis of a sector part of the magnet.

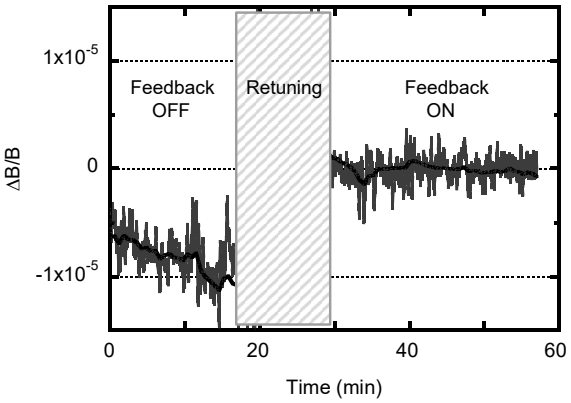

Fig. 2 Change of the cyclotron magnetic field with or without the active PID control system. The magnet was excited for acceleration of the 260 MeV $^{20}Ne^{7+}$ beam.

adequately works using the NMR signal.

Figure 2 shows an example of the variation of the magnetic field under the active control. The magnetic field was stabilized to $\Delta B/B = 6 \times 10^{-6}$ by the PID system. We are going to verify availability of the system for stable microbeam irradiation experiments as soon as possible.

References

1) A. Kitamura *et al.*, JAEA Takasaki Annu. Rep. 2014, JAEA-Review 2015-022, 144 (2016).
2) S. Kurashima *et al.*, Rev. Sci. Instrum., **80**, 033302 (2009).
3) S. Okumura *et al.*, Rev. Sci. Instrum., **76**, 033301 (2005).
4) S. Okumura *et al.*, Proc. 8th Annu. Meet. Part. Accel. Soc. Jpn., 374 (2011).

3-07

Status Report on Technical Developments of the TIARA AVF Cyclotron

H. Kashiwagi, N. Miyawaki and S. Kurashima

Department of Advanced Radiation Technology, TARRI, QST

Introduction

In the TIARA AVF cyclotron, various developments regarding beam production, acceleration, formation and irradiation are made to improve performance for the research in biotechnology and material sciences. In this paper, developments relating beam injection and beam phase restriction are reported.

Test of injection tuning using steering magnets based on emittance and acceptance measurement

We are developing an optimization procedure of beam injection tuning based on measurements of the property of an injected beam and the cyclotron to achieve good transmission efficiency. We have already developed a transverse emittance and acceptance measurement system as a tool that shows the relationship between the injected beam emittance and the acceptance of a cyclotron[1].

A test experiment of overlapping the measured horizontal emittance and acceptance was conducted using two steering magnets to demonstrate that injection tuning based on the measured results is effective in increasing an accelerated beam current. The steering magnets placed just before and after the system are used to shift the emittance and acceptance in the transverse phase-plane respectively. In order to control the position of the emittance and the acceptance in the phase-planes, the relationship of the barycentric coordinates of the emittance and the acceptance with the currents of the steering magnets were measured, respectively, and each orbit in the horizontal phase-plane was clarified (Fig. 1). Using the results, measured emittance and acceptance was moved to overlap the high-brightness region in the emittance and the high-transmission region in the acceptance. The accelerated beam current was increased by 30%. We have confirmed the effectiveness of injection tuning based on measurements using our developed system.

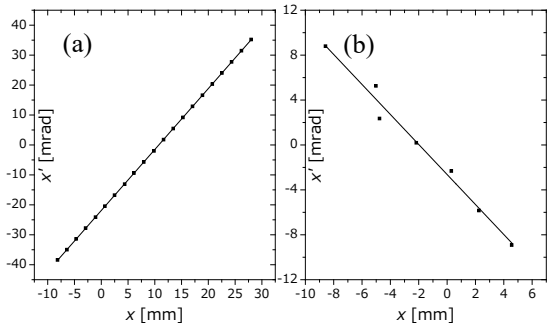

Fig. 1 (a) Relationship between the barycentric coordinate of emittance and IST1 current, (b) Relationship between barycentric coordinate of acceptance and IST2 current.

Evaluation of beam phase restriction by phase defining slit

A high quality beam with a small energy spread is required for beam applications such as the microbeam. The beam is obtained by narrowing the beam phase width. The beam phase width appears as the radial beam spread that is caused by the acceleration voltage varying with the time in a magnetic field. Restriction of the radial beam spread with a phase defining slit is general method to narrow the beam phase width. On the other hand, phase bunching in the central region can also narrow the beam phase width by energy-gain modulation produced in a rising-slope region of the acceleration-voltage waveform at the first acceleration gap[2]. In the TIARA AVF cyclotron, there is the phase bunching effect for acceleration harmonic mode (h) 2; however, the effect for h = 1 can be not obtained. To investigate the influence of phase bunching on beam phase restriction with phase defining slit, the beam phase distributions of a 107 MeV $^{4}He^{2+}$ beam for h = 1 and a 260 MeV $^{20}Ne^{7+}$ beam for h=2 were measured by shifting the slit positions with the 3 mm slit gap.

The measured correlations between the slit position and the beam phase are shown in Fig. 2 for h=1 (a) and 2 (b). The h=1 correlation was greater than ±20 RF degrees in the slit position from 31 to 36 mm. The beam phase width was easily controlled by the slit position or gap. The h = 2 correlation was less than ±10 RF degrees in the position from 33 to 38 mm. The control of the beam phase width by the phase defining slit was difficult for the reason that phase bunching was generated before reaching the slit. The results suggest that consideration of phase bunching was required in the beam phase restriction with the slit.

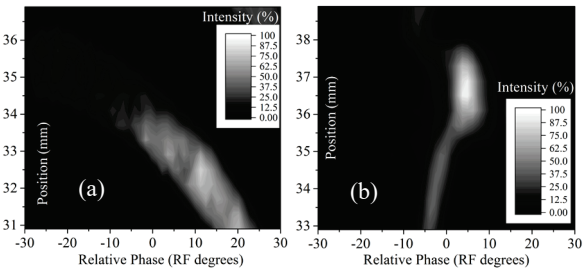

Fig. 2 Measured correlations between radial slit position (horizontal) and beam phase (vertical) for (a) 107 MeV $^{4}He^{2+}$ beam (h=1) and (b) 260 MeV $^{20}Ne^{7+}$ beam (h=2).

References

1) H. Kashiwagi *et al.*, Rev. Sci. Instrum., **85**, 02A735 (2014).
2) N. Miyawaki *et al.*, Nucl. Instrum. Meth. Phys. Res. A, **715**, 126 (2013).

3-08 Status Report on Technical Developments at Electrostatic Accelerators

A. Chiba, K. Yamada, A. Yokoyama, A. Usui,
Y. Ishii, T. Satoh, T. Okubo and T. Nara

Department of Advanced Radiation Technology, TARRI, QST

Intensification of a fullerene ion beam

In fiscal year 2013, we had developed a novel technique to generate the negative C_{60}^- ions with an electron attachment method using an existing ion source of the tandem accelerator, and succeeded in drastically increasing a C_{60}^+ ion beam current in MeV-energy[1]. Efficiency of the several experiments using the C_{60}^+ ion beam was significantly improved by this technique, whereas the beam intensity should be further increased for the improvement of beam-transportability and for the experiments in need of an irradiation to large-area with high fluence, e.g. a study on surface modification of materials. In this technique, the sublimated C_{60} is negatively ionized by capturing a thermal electron emitted from the surface of a glowing ionizer in the ion source. According to the measurements of the electron emission from the ionizer, it is inferred that the intensity of thermal electrons in the ion source is extremely lower than the amount of sublimated C_{60}. Therefore, we tried to increase the negative C_{60} ions by adding a tungsten filament to the ion source as a second source of thermal electrons. As a result of the refinements, the intensity of C_{60} ion beam was increased by more than an order of magnitude.

Measurement of beam energy shift using resonance nuclear reaction

Shifts of a photo-image of race element distribution within 2 μm are observed in several hours in micro PIXE analysis. The reduction of the shift is required to obtain the accurate image. The shift was suspected due to the drift of the single-ended-accelerator voltage over time, because the movement of samples on the stage was not observed in the PIXE analysis. The purpose of this study was to measure the voltage drift by comparing the voltage estimated by the change ratio of γ-ray yield emitted from a nuclear reaction of ^{27}Al (p, γ) ^{28}Si and the voltage constantly controlled by the accelerator. In fiscal 2015, 992-keV proton beam at a current of 650 nA was used for the measurements. The γ-ray yields of nuclear reaction of ^{27}Al (p, γ) ^{28}Si at 992 keV with the resonance width of 100 eV and at 1,772-keV with a wide cross section were measured every one hour using a NaI scintillation detector. The observations were continued from 16 p.m. to 21 p.m. The voltage was shifted in 0.8 kV in first one hour from the beginning. Then the increases of beam energy within 0.2 keV were continued every hour until 21 p.m. The results indicated that the voltage shift tended to be small after 18 p.m. In the next fiscal year, the time variation of the accelerating voltage will be continuously measured to clarify a quantity of the shift for a day.

Development of Faraday cup for a fullerene ion beam

In order to correctly measure a fullerene-ion beam current, it is usually necessary to use a high aspect-ratio Faraday cup (FC), because a fullerene-ion bombardment of the cup generates not only secondary electrons but also many more secondary positive-ions than a monoatomic-ion bombardment. However, the high aspect-ratio FC has a length of more than 300 mm with respect to an inner diameter of 20 mm, therefore it is difficult to be installed in an existing beam-transport line. We have developed a new-type FC having a suppressor-electrode pair with a different polarity, as shown in Fig. 1. Electrode-2 suppresses the secondary negative particles and collects secondary positive ions emerging from the cup. Hence, a beam current has to be evaluated as total current of the cup and electrode-2. The beam current of 100-keV C_{60}^+ beam from the ion implanter was measured using the new-type FC and the high-aspect ratio FC, respectively. As a result of comparison of these beam currents, it was confirmed that those values were approximately equal when the applied voltage of electrode-1 and electrode-2 were more than 200V and -200V respectively. The new-type FC can be downsized by one-seventh from the high-aspect ratio FC.

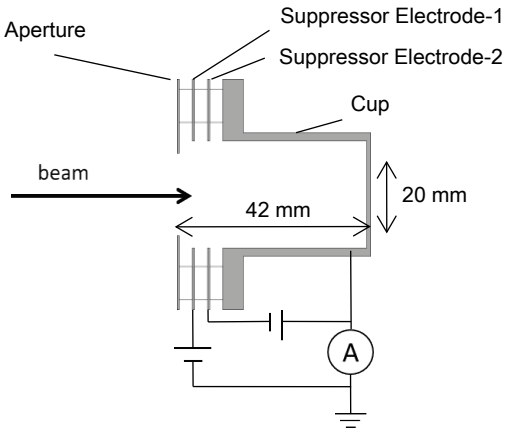

Fig. 1 The schematic diagram of a new-type FC.

Reference

1) A. Chiba *et al.*, JAEA Takasaki Annu. Rep. 2013, JAEA-Review 2014-050, 169 (2015).

3-09 Investigation of Phosphor Screens for Real-time Tuning of Large-area Ion Beam Profile

Y. Yuri, T. Yuyama and T. Ishizaka

Department of Advanced Radiation Technology, TARRI, QST

The formation technique of a large-area ion beam with a uniform transverse intensity distribution using nonlinear focusing has been developed at the AVF cyclotron in TIARA [1]. To date, large-area (over 100 cm^2) uniform beams of several different ions (H, He, C, Ar, and Xe) and kinetic energies (4~27 MeV/u) have been achieved and some of them are utilized for various applications.

In this beam tuning, the on-target two-dimensional (2D) intensity distribution of the beam is monitored in real time using phosphor screens and CCD cameras, and adjusted so as to make it uniform by a combination of octupole and quadrupole magnets [2]. A phosphor screen, DRZ-High (Mitsubishi Chemical), is usually utilized since it exhibits higher sensitivity, shorter afterglow, and it is easier to cut sizes in comparison with a common alumina screen. Because of its high sensitivity, the beam current is usually highly reduced by inserting attenuation meshes in the low-energy beam transport line [3]. This is suitable for reducing unwanted radioactivation of peripheral instruments and for suppressing an increase in a radiation level in the irradiation room. However, the attenuated beam current is much lower than that required by users.

The problem here is that the formed uniform distribution can sometimes change, namely, the uniform intensity distribution of the beam can be slightly deformed when the attenuation mesh is removed for higher beam current. This profile change is attributed to the change in the phase-space distribution of the beam probably due to the space-charge effect in the low-energy beam line and scattering at the attenuation mesh. Actually, similar phenomena were reported also in other cyclotron facilities [4,5]. Therefore, the availability of various large-area phosphor materials was investigated for real-time tuning of high-current ion beams [6].

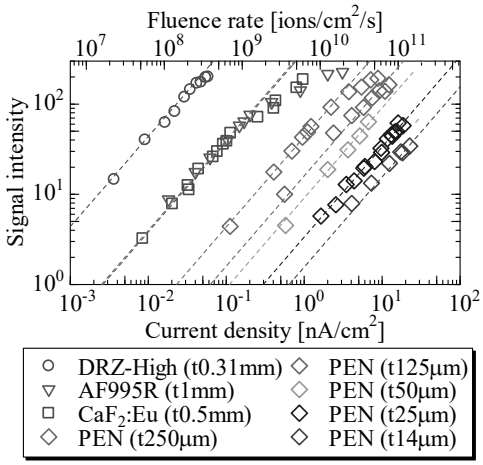

Fig. 1 Light emission response of DRZ-High, AF995R, calcium fluoride, and PEN films to 10-MeV proton beam irradiation. Dashed lines are the linear fitting results for each sample.

The beam-irradiation experiment was performed at the LB course of the AVF cyclotron. Several phosphor samples, DRZ-High (Gd_2O_2S:Tb), AF995R (Al_2O_3:Cr, Desmarquest), calcium fluoride (CaF_2:Eu), and polyethylene naphthalate (PEN) films were irradiated with several ion beams at wide beam current densities. The light emitted from the samples was observed with a CCD camera (Basler, scA1390-17gc) and the 8-bit signal intensity obtained from a captured image was analyzed. The result on 10-MeV proton irradiation is summarized in Fig. 1. The light intensity was well proportional to the current density at low current density for all samples. DRZ-High was the most sensitive, and the sensitivities of AF995R and calcium fluoride were about ten times lower than DRZ-High. For PEN films, five different thicknesses were tested. It was found that the sensitivity of PEN is approximately proportional to its thickness and that PEN films are useful for high-current proton beams. Some of the films colored slightly yellowish after irradiation, but there seemed no deformation or melting due to beam-induced heating. This indicates that a thinner film of the order of 1 μm is useful for a higher-intensity beam. PEN films were available also for He and C ion beams, but, for Ar beams, the light intensity was reduced quickly (in tens of seconds) because of high linear energy transfer.

In summary, we investigated the beam intensity range of several different phosphor screens for real-time tuning of the large-area 2D fluence distribution. It has been found that high-intensity beams can be monitored using calcium fluoride and PEN films of different thicknesses for light ions. The intensity range is 10^{-3}~10^{1} nA/cm^2 for 10-MeV protons. A large-area uniform ion beam can be adjusted efficiently at a high intensity of the order of 10 nA/cm^2, which is required for radiation degradation/damage testing of materials.

References

1) Y. Yuri *et al.*, Plasma Fusion Res., **9**, 4406106 (2014).
2) T. Yuyama *et al.*, Proc. 1st Int. Beam Instrum. Conf., 246 (2012).
3) T. Ishizaka *et al.*, Proc. 7th Annu. Meet. Part. Accel. Soc. Jpn., 642 (2010).
4) D. Wutte *et al.*, Proc. Euro. Parti. Accel. Conf., 1634 (2000).
5) F. Marti *et al.*, Proc. 16th Int. Conf. Cyclo. Their Appl., 64 (2001).
6) Y. Yuri *et al.*, Proc. 12th Annu. Meet. Part. Accel. Soc. Jpn., 420 (2015).

3-10 Effect of Incident Beam Angle for Beam Size Reduction in the Several-hundred keV Ion Microbeam System

Y. Ishii and T. Ohkubo

Department of Advanced Radiation Technology, TARRI, QST

A several hundred keV compact ion microbeam system with a three-stage acceleration lens (hereafter; compact microbeam system) is developed step by step as a prototype of a MeV compact ion microbeam system. The present goal of the system is to form a beam size of 1 μm in diameter at around 150 keV. In the last year's study, the experimentally obtained beam size was improved from 17 μm to 6 μm by reducing residual gas pressure[1]. The size reduction was achieved by making beam halo smaller at the acceleration lens, in other word decreasing beam energy spread on the basis of the collision of residual gas and ion beam. The effect of the halo has, so far, been negligible in the present system. Therefore the enhancement of the demagnification of the three-stage acceleration lens was required for the further reduction of beam size. The demagnification is proportional to the inverse of the divergence angle of an incident beam on the basis of the feature of the acceleration lens. In this study, the demagnification was enhanced by injecting the ion beam with smaller divergence angle into the first acceleration lens which composes a part of the three-stage acceleration lens.

The schematic of the compact microbeam system and the experimental set-up are illustrated in Fig. 1. The ion beam of a smaller divergence angle from the ion source with parallel extraction electrodes was generated by increasing the electric field between the anode and the extraction electrode on shortening the length between them from 15 mm to 10 mm. By the shortening, the electric field was expected to be increased by about 28% using the electric field simulation. To measure the beam sizes, the beam size measurement system, which was placed downstream of the third acceleration lens, consists of an electric beam scanner, a sharp knife-edge made of diamond and iron, a Faraday cup with a suppressor electrode, a pico-ammeter with resolution of 0.1 pA, and a micrometer head of resolution of 0.1 μm. In the beam size measurement experiments, a microbeam formed by the compact microbeam system was shifted across the knife-edge using the electric beam scanner which is connected to four power supplies controlled by a PC. Beam currents of the microbeam were measured at the image point by the Faraday cup which was placed downstream of the knife-edge. The shifted distance of a microbeam per one voltage of the electric beam scanner was obtained by comparing a value of the laser displacement meter corresponding to its microbeam position and the applied voltage of its scanner. The beam size was defined as full width at half maximum (FWHM) of the error function, Erf, fitted into the beam currents on the assumption that its beam was a Gaussian distribution.

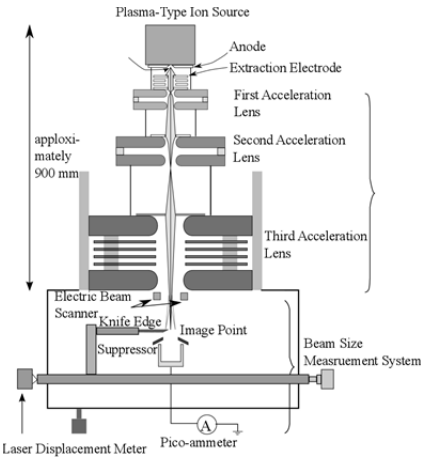

Fig. 1 Schematic of several hundred keV compact ion microbeam system with experimental set-up.

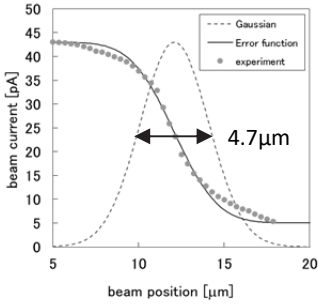

Fig. 2 Experimental result of beam size measurement

The beam size experiment was carried out by finely changing acceleration voltages of three-stage acceleration lens on setting the extraction voltage at about 300 V in the ion source. In the experiments, beam currents were repeatedly measured as a function of the knife-edge position on finely changing the voltages of the three-stage acceleration lens. The beam sizes were evaluated from the relationship between the beam current and knife-edge position. The good beam size was shown in Fig. 2, which was evaluated to be 4.7 μm in diameter. The beam size was reduced by about 22% as compared with the beam size of 6 μm. This result showed that the reduction of incident beam divergence angle into the first acceleration lens was effective to form a smaller beam size than the obtained one in this study.

Reference

1) Y. Ishii, T. Ohkubo, JAEA Takasaki Annu. Rep. 2014, JAEA-Review 2015-022, 154 (2016).

3-11 Development of Metal ^{68}Ge Source for Generation of Spin-polarized Positron Beam Using Carbon-sealed Capsule

M. Maekawa, H. Abe, A. Miyashita, H. Li and A. Kawasuso

Department of Advanced Functional Materials Research, TARRI, QST

For the application of the positron annihilation spectroscopy (PAS) method to the study of magnetic substances, we have developed a spin-polarized positron beam[1]. We successfully observed novel spin phenomena, such as field-reversal asymmetry of momentum distributions of ferromagnet[2]. These experiments require highly spin-polarized positron beam. For this purpose, we developed a ^{68}Ge positron source by irradiating a gallium nitride (GaN) substrate with 20 MeV protons obtained from the TIARA cyclotron. The GaN target is mechanically and chemically stable, however, production ratio of ^{68}Ge nuclide is limited because of containing nitrogen atoms. Moreover, natural Ga consists of two isotope; ^{69}Ga (60%) and ^{71}Ga (40%). Only ^{69}Ga contribute to the ^{68}Ge production. To increase positron beam intensity, pure ^{69}Ga metal target should be used.

Since metal Ga has low melting point (29 °C), during irradiation it is easy to melt and metallize surrounding metals. To avoid leakage of radioactive ^{68}Ge, the metal Ga was encapsulated with a carbon capsule as shown in Fig. 1. Through the thin carbon films, proton beam is irradiated to metal Ga and positrons are also extracted. For the protection, the carbon film is covered by a beryllium window. This structure passed a heat-resistant examination under 1,000 °C.

This source has irradiated by 20 MeV proton beam totally 9 times. Maximum ion beam current was 10 μA and total dose reached to approximately 1,500 μAh. Figure 2 shows the transition of estimated ^{68}Ge source amounts during past 1.5 year. In the current irradiation schedule, the source strength seems to be saturated at around 700 MBq.

Using this source, spin-polarized positron beam was generated. The positrons emitted from the metal ^{68}Ge source were moderated by a tungsten-mesh moderator composed of 33 tungsten meshes with a wire diameter of 10 μm. To improve the efficiency, a tungsten ring and tungsten foils (25 μm thick) were added[1]. This moderator assembly was developed in reference to that for ^{22}Na source. Positron beam intensity was confirmed to be 5×10^3 e^+/s. The conversion ratio is one order lower than that of ^{22}Na positron source, because the average energy of emitted positrons of ^{68}Ge (~0.9 MeV) is higher than that of ^{22}Na (~0.2 MeV). Development of a new moderator dedicated for ^{68}Ge source is expected.

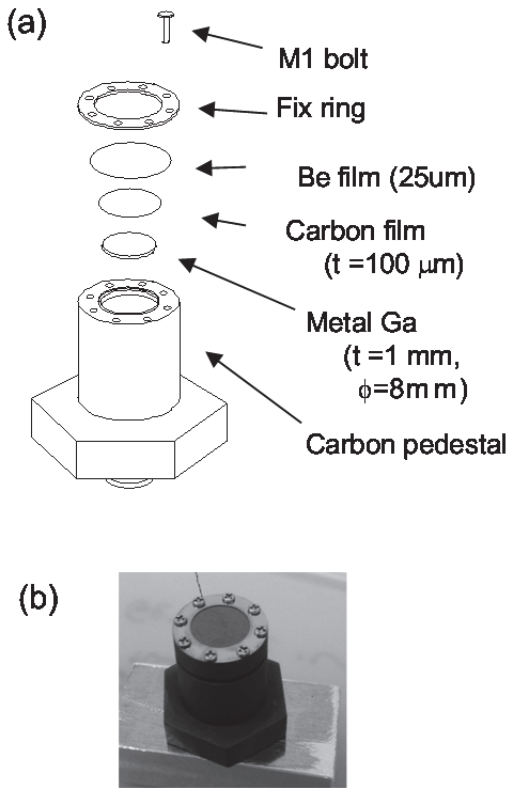

Fig. 1 (a) Schematic and (b) photograph of the source capsule.

References

1) M. Maekawa *et al.*, Nucl. Instrum. Meth. Phys. Res. B, **308**, 9-14 (2013).
2) A. Kawasuso, M. Maekawa, *et al.*, Phys. Rev. B, **83**, 100406 (2011).

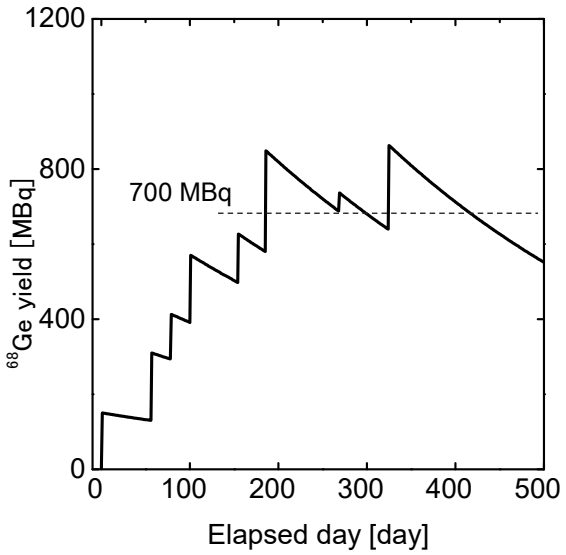

Fig. 2 Transition of estimated ^{68}Ge source amounts during past 1.5 year.

3-12 Development of Production Technique of Track-etched Porous Membranes Using Continuous Ion Irradiation

H. Yamamoto [a], Y. Yuri [b], T. Yuyama [b], K. Yoshida [b], T. Ishizaka [b], I. Ishibori [b], S. Okumura [b], H. Koshikawa [c], T. Yamaki [c], Y. Maekawa [c] and W. Yokota [b]

[a] Nitto Denko Corporation, [b] Department of Advanced Radiation Technology, TARRI, QST, [c] Department of Advanced Functional Materials Research, TARRI, QST

It is well-known that radiation damage such as chain scission is induced in a polymer membrane when it is irradiated with an energetic ion beam [1]. The ion-induced damaged part of the polymer gets more susceptible to chemical etching. Therefore, it is possible to obtain a polymer membrane that has many straight pores along each ion's trajectory by a combination of ion irradiation and chemical etching. We are conducting a joint research for the establishment of the production technique of such track-etched porous membranes based on energetic heavy-ion irradiation in TIARA.

The R&D experiment on beam formation and ion irradiation was performed at the LB course of the AVF cyclotron in TIARA. A roll-to-roll irradiation system was developed for continuous ion irradiation of long polymer membranes. The films rolled in the vertical direction were uniformly irradiated with a horizontally-elongated "ribbon" beam with a uniform intensity distribution in the horizontal direction. Such a unique beam profile was generated by means of nonlinear focusing of multipole magnets [2]. In contrast to common scanning irradiation, uniform irradiation using the stationary uniform beam is useful in that there is no correlation between the irradiation uniformity and the roll-to-roll speed of a sample. We have actually realized the ribbon uniform beam as shown in Fig. 1. The horizontal width and rms uniformity of the beam profile were 17 cm and 4%, respectively in the present case. The real-time beam current measurement during irradiation was considered in order to develop the technique of evaluating the quality of the irradiated film, i.e., the stability of the beam current and the fluence of the film. Therefore, the relative change of the ion beam current was measured using slits installed in the beam transport line. It has been confirmed that there is a clear correlation between the measured relative beam current and the pore density during continuous irradiation. In addition, it has been found that the stability of the ion source is essential to achieve the continuous uniform irradiation.

Polymer films irradiated in the roll-to-roll system were chemically etched to make porous membranes. The surface of the films was observed using a scanning electron microscope (SEM) to characterize the film. An example of SEM images obtained is shown in Fig. 2. It has been verified that continuous uniform irradiation can be accomplished and thus porous polymer membranes can be properly produced in our roll-to-roll ion-irradiation system.

We plan to optimize various ion-irradiation conditions such as ion species, kinetic energy of the ion beam, and the sample atmosphere (vacuum degree) in order to further improve the productivity of the ion-irradiation process.

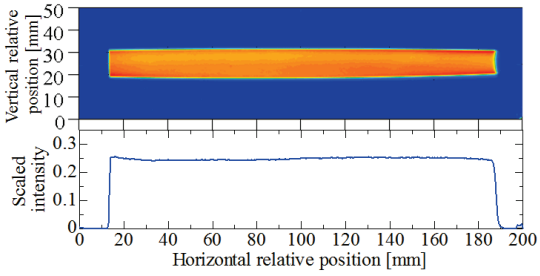

Fig. 1 Measurement result of the 2D relative intensity distribution of a ribbon uniform beam formed using octupole nonlinear focusing. A Gafchromic film was irradiated with 4.1-MeV/u Xe ion beam of 2 nA for 5 s. The scaled intensity distribution was obtained from the optical density of the film. The lower graph shows the 1D profile along the horizontal central axis.

References

1) *Irradiation of Polymers*, Edited by R. L. Clough and S. W. Shalaby, Am. Chem. Soc. Washington DC (1996).
2) Y. Yuri *et al.*, Nucl. Instrum. Meth. Phys. Res. A, **642**, 10 (2011).

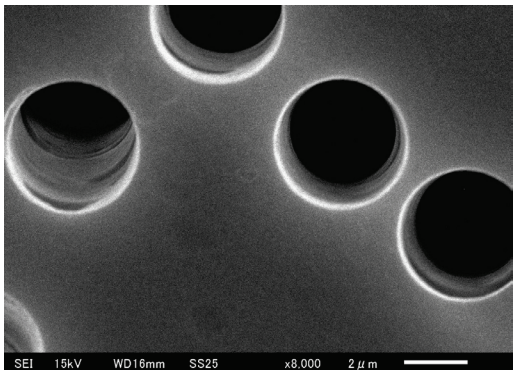

Fig. 2 SEM image of a track-etched polyethylene terephthalate film (25 μm in thickness) irradiated with 3.3-MeV/u Xe ion beam. The film was chemically etched using a 3-mol/L KOH solution at 80 °C for 15 min. The diameter of resultant pores was estimated to be about 4 μm from the image. The pore density was 1.3×10^6 cm^{-2}, which was close to the estimated fluence of the ion beam.

3-13 Proton Beam Irradiation with a Beam Chopper Regulation at the HY Port of TIARA

T. Sakashita [a], S. Kurashima [b] and S. Onoda [c]

[a] Department of Radiation-Applied Biology Research, TARRI, QST,
[b] Department of Advanced Radiation Technology, TARRI, QST,
[c] Department of Advanced Functional Materials Research, TARRI, QST

Generally, the space radiation environment is classified to the galactic cosmic ray (GCR) background and the solar particle event (SPE) [1]. The GCR consists of 85% protons, 14% helium and 1% heavier particles. The SPE includes 90% protons. Protons are main components of space radiation. The extreme SPEs that had observed several times could be potentially lethal or mission threatening. Energetic protons are a significant radiation hazard to spacecrafts and astronauts. Our final goal is to investigate a potential risk of energetic protons to astronauts. In this report, we present the proton beam irradiation system with a rectangular pulse voltage beam chopper (P-chopper) regulation [2] at the cyclotron HY port of TIARA for biological research.

The proton energy range of the extreme SPEs is mainly less than 100 MeV. We had selected the 65 MeV proton beam at the HY port to simulate the extreme SPEs, and had proven the energy was successful at the other port of TIARA, previously. However, the proton beam with the energy of 65 MeV had a so high that it could not stop at the metal plate beam shutter for regulating irradiation dose. Figure 1 shows an image of alumina fluorescent plate of 65 MeV proton beam passed through the shutter of the HY port.

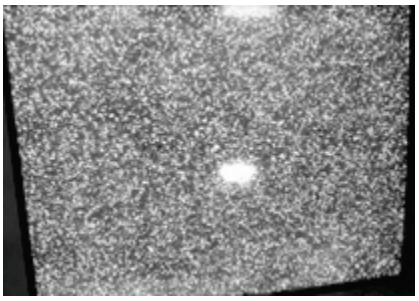

Fig. 1 An image of alumina fluorescent plate of 65 MeV proton beam passed through the shutter of the HY port.

To avoid the issue of the shutter-penetration on 65 MeV proton beam, we developed the proton beam irradiation system with the P-chopper regulation. This system, installed in the injection line of the cyclotron, can shut off the proton beam before acceleration. The P-chopper simply regulated the irradiation dose by on/off action, instead of a high repetition mode of a few kHz, to avoid spotted irradiation resulting from simultaneous operation of a 50 Hz beam scanner at the HY port. We confirmed no spotted irradiation by a Gafchromic films exposed to the proton beam for 15 min (Fig. 2).

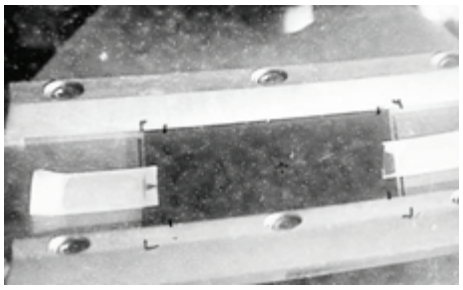

Fig. 2 Gafchromic films exposed to the adjusted 65 MeV proton beam for 15 min.

Using the adjusted 65 MeV proton beam, we examined the relation between the current of the faraday cup and proton beam fluence. CR-39 was used as a solid-state nuclear track detector to diagnose proton beam fluence. However, CR-39 cannot detect proton beam with an energy of over 27 MeV by an etching method[3]. To reduce energy of proton, we installed a nickel plate of 300 μm thick. Figure 3 shows the etch-pits of the energy reduced proton beam.

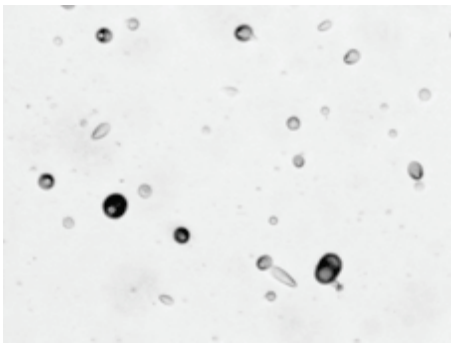

Fig. 3 Etch-pits of 65 MeV proton beam reduced by the nickel plate.

In conclusion, we have successfully obtained the fluence-parameter of 1.55×10^7 P/cm^2/sec/nA for 65 MeV proton beam at the HY port of TIARA.

References

1) G. A. Nelson, Radiat. Res., **185**, 349-58 (2016).
2) S. Kurashima *et al.*, JAEA Takasaki Annu. Rep. 2014, JAEA-Review 2015-022, 148 (2016).
3) M. Kanasaki *et al.*, J. Plasma Fusion Res., **88**, 261-75 (2012).

3-14 Development of Flexible Mach–Zehnder Interferometer Embedded in PDMS by Proton Beam Writing

W. Kada [a)], R. Saruya [a)], R.K. Parajuli [a)], S. Kawabata [a)], R. Sano [b)], K. Miura [a)], T. Satoh [c)], M. Koka [c)], N. Yamada [c)], Y. Ishii [c)], T. Kamiya [c)], H. Nishikawa [b)] and O. Hanaizumi [a)]

[a)] Faculty of Science and Technology, Gunma University,
[b)] Department of Electrical Engineering, Shibaura Institute of Technology,
[c)] Department of Advanced Radiation Technology, TARRI, QST

Proton Beam Writing (PBW) is one of most-powerful fast prototyping tools for micro-fabrication[1]. In previous studies, we have successfully demonstrated the fabrications of micro-optical devices including proto-type of Mach-Zehnder (MZ) waveguide for integrated fiber telecommunications using poly(methyl methacrylate) (PMMA)[2] and poly-dimethyl-siloxane (PDMS)[3]. However these waveguide structures were prepared on a solid substrate and its structure is quite similar to the conventional polymer waveguide fabricated by lithography techniques. On the other hand, one of key features of PBW is the ability of a long penetration length of protons which enables us to form an embedded structure in the substrate. The feature is quite unique and it is possible to produce flexible waveguide structures without any interfaces or any junctions by removing a supporting substrate from self-supported polymer films. In this study, we have demonstrated the fabrication of completely flexible MZ waveguide embedded in a thin film of PDMS by precise control of PBW.

Thin PMDS (SYLGARD 184, Toray Dow Corning) films with thickness of approximately 40 μm were prepared by spin-coat process on a supporting silicon wafer (40×20×0.5 mm). Then a self-supported PDMS film was removed from the supporting silicon wafer and kept in air for 1 day at room temperature before fabricating the MZ waveguide. During PBW patterning procedure of the MZ waveguide[3], PDMS films were attached to an aluminum sample holder. Figure 1 shows an example image of self-supported PDMS film after PBW procedure.

Fig. 1 An example of self-supported PDMS thin film prepared by spin-coat process for PBW procedure. MZ waveguide was formed inside of this PDMS film by 750 keV proton microbeam.

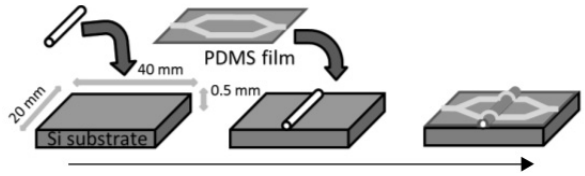

Fig. 2 Schematic illustration of the bending of a MZ waveguide drawn in PDMS thin films by PBW procedure. A small plastic pipe with diameter of 3 mm was placed on a plane silicon substrate and a thin PDMS film with MZ waveguide was placed on it. The NFP images were obtained with and without the plastic pipe.

In a post process of the PBW procedure, near field pattern (NFP) optical transmittance images through MZ waveguide were evaluated using 1,550 nm fiber laser (ECL-210, Santec) and IR vidicon camera (C2741-03, Hamamatsu Photonics). Flexibility of the MZ waveguide was evaluated by bending the polymer film by applying external mechanical stress as illustrated in schematic in Fig. 2. The optical throughput was sustained at both non-bended and bended conditions as shown in NFP images in Fig. 3. These results suggested that MZ waveguide structures embedded in self-supported flexible PDMS films were successfully fabricated by observing NFP.

References

1) F. Watt *et al.*, Int. J. Nanosci., **4**, 269 (2005).
2) K. Miura *et al.*, Key Eng. Mater., **497**, 147 (2012).
3) W. Kada *et al.*, Nucl. Instrum. Meth. Phys. Res. B, **348**, 218 (2015).

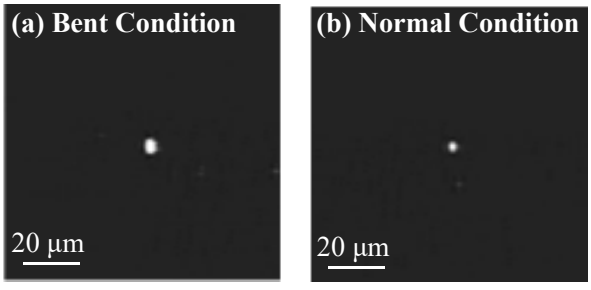

Fig. 3 Comparison of NFP images through MZ waveguide, drawn on PDMS thin film, with bended and non-bended conditions.

3-15

Micro-structuring of Epoxy Resists Containing Nanoparticles by Proton Beam Writing

R. Sano [a)], S. Hayakawa [a)], H. Hayashi [a)], H. Nishikawa [a)], Y. Ishii [b)] and T. Kamiya [b)]

[a)] Department of Electrical Engineering, Shibaura Institute of Technology,
[b)] Department of Advanced Radiation Technology, TARRI, QST

Nanomaterials in various forms such as particles, wires, tubes, etc. have attracted much attention due to its superior and unique properties[1]. If one can add the nanomaterials into flexible materials such as plastics and rubbers while keeping the original natures[2], we can obtain functional nanocomposites with th
desired functions.

The present study is aiming at the micro-structuring of plastics containing nanoparticles by proton beam writing (PBW). An epoxy-based resist, SU-8 (Microchem, 3025) typically used for PBW was used as a base polymer. Nanoparticles such as alumina (<750 nm), silica (<14 nm), silver (<100 nm), and carbon (<100 nm) were added to a solvent for SU-8 and were mixed with SU-8 as a base polymer using a planetary centrifugal mixer. Samples with thickness of several tens of μm to 100 μm were obtained on Si by spin-coating of SU-8 containing nanoparticles with a concentration of 5.0 wt%. Proton beam writing was performed at 1.0 to 3.0 MeV either using beamlines at single-ended accelerators installed at SIT or TIARA.

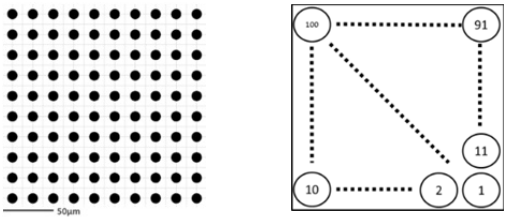

(a) (b)

Fig. 1 (a) A dot array pattern and (b) the varied fluence for each dot written by PBW. The numbers in Fig. 1(b) represent the fluence of 1.0-MeV proton beam in unit of nC/mm^2.

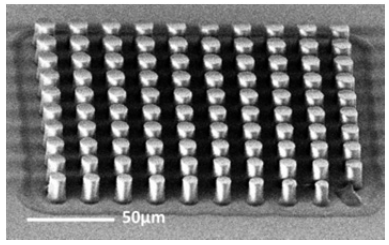

(a) SU-8.

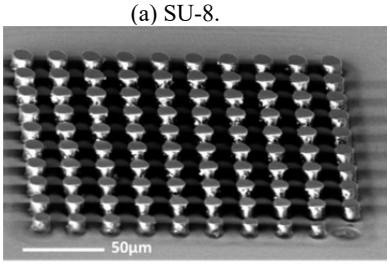

(b) SU-8 containing 5 wt% Ag.

Fig. 2 SEM images obtained for (a) SU-8 and (b) SU-8 layer containing Ag nanoparticles patterned by PBW at 1.0 MeV.

In order to obtain contrast curves, 10×10 dot patterns with varied fluence from 1 to 100 nC/mm^2 were written by PBW, as shown in Fig.1 (a) and (b). Figures 2 (a) and (b) show the SEM images of the patterned SU-8 layer and the one with Ag nanoparticles, respectively. We compared the contrast curves in Fig. 3 showing the remaining SU-8 thicknesses after development as a function of the proton beam fluence obtained for the SU-8 films with and without nanoparticles.

While the SU-8 layers containing various nanoparticles are less sensitive to proton beam than pure SU-8, they still show reasonable values of sensitivity (<5 nC/mm^2) for PBW. We also found that the pattern collapse can be avoided for the high-aspect-ratio structures made of the SU-8 containing these nanoparticles. These results indicate that the addition of nanoparticles is useful not only to add the functionalities to the resist, but to improve the mechanical stability of the high-aspect-ratio structures.

References

1) S. W. Song *et al.*, IEEE J. Quant. Electron., **21**(4), 4800212 (2015).
2) S. Li *et al.*, Nano Rev., **1**, 5214 (2010).

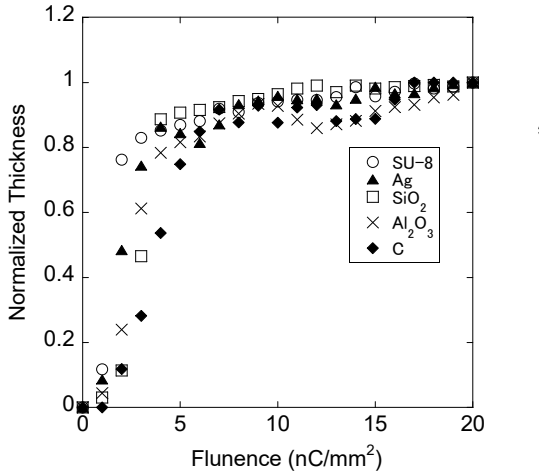

Fig. 3 Contrast curves obtained for SU-8 layers on silicon with and without addition of nanoparticles of Ag, SiO_2, Al_2O_3, and carbon.

3-16 Development of Micromachining Technique Using Heat-resistance Materials

T. Sakai [a)], H. Iikura [a)], M. Sugimoto [b)], T. Satoh [c)] and Y. Ishii [c)]

[a)] Materials Science Research Center, SNSR, JAEA,
[b)] Department of Advanced Functional Materials Research, TARRI, QST
[c)] Department of Advanced Radiation Technology, TARRI, QST

In this work, we demonstrated the fabrication of fine structures made from polycarbosilane using the scanning proton microbeam. The fabricated samples were observed with optical microscope. The results show that the micromachining on mixture of polycarbosilane and SiC fine particles is successful. In conclusion, this new technique is very promising to fabricate fine heat-resistance materials.

1. はじめに

MeV 級プロトンビームの直接描画による微細加工技術（Proton Beam Writing, PBW）は、アスペクト比の高い加工が可能であり、TIARA においては大気照射が可能である[1)]。本手法は、従来 PMMA 等の有機高分子材料の加工に広く利用されてきたが、無機材料の加工には、ほとんど応用されていない。これは、無機材料においては一般に放射線耐性が高く、加工に必要な線量が非常に高くなることがその大きな要因である。

一方、高い耐熱性を有する炭化ケイ素材料は、長年、高崎量子応用研究所において精力的に研究されており、特に、有機材料であるポリカルボシランに対する放射線架橋を利用した研究は、数多くの実績を有する[2)]。そこで、新たにPBWによるポリカルボシランに対する微細加工技術の開発を行い、耐熱性を有する微細素子作製の可能性を探るため、下記の実験を行った。

2. 実験

TIARAの軽イオンマイクロビーム装置においては、プロトンビームを大気中に取り出すためのビーム窓があり、この窓材を試料保持膜とすることで、ビーム窓を通過することによる拡がりを最小限に抑えることができる。窓材には、12 μm 厚のアルミ箔を利用した。構造体の強度を向上させるためポリカルボシランにSiC微粒子を混合後、膜に塗布したものを試料とし、2 MeV プロトンビームでパターン照射を行った。照射フルエンスは 590 nC/mm^2、照射パターンは、ジグソーパズル形状[3)]である。

3. 結果

ヘキサンによる現像処理を行った後の構造体の光学顕微鏡写真を Fig. 1 に示す。作製した構造体が膜上に保持できており、照射パターン通りに加工できているのが確認できる。

また、混合したSiC粒子は、その構造を維持するフィラー（filler）としても作用していると思われ、特に焼結処理を行う過程において、その効果を発揮することが期待できる。

4. まとめ

ポリカルボシランに対して、PBW で微細加工が行えることを初めて確認した。加工に必要なプロトンビームのフルエンスは比較的高いが、電子線による前照射を行うことで、加工に利用するプロトンビームのフルエンスを低減することは可能と思われる。従来のレジスト材料では不可能な耐熱部品等の微細加工に利用できるなど、その有用性は高いと考えている。

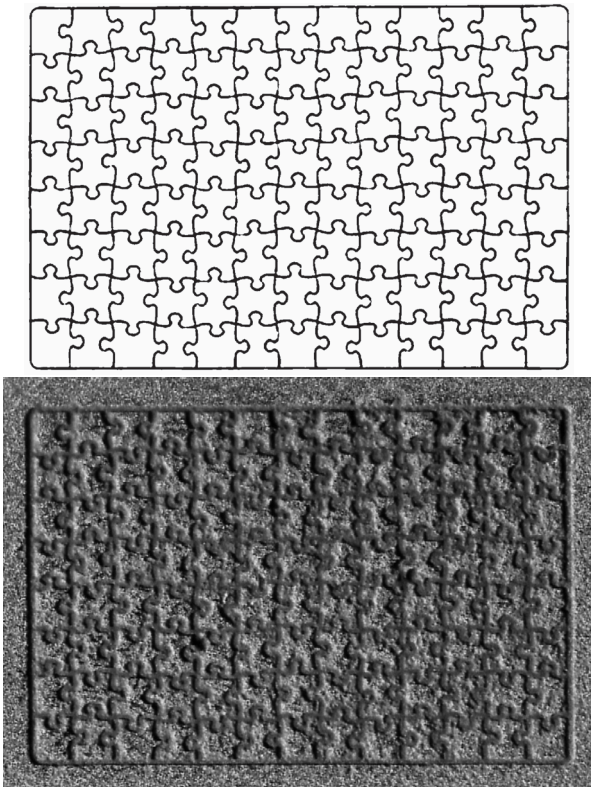

Fig. 1 An original pattern (upper) and an optical micrograph of the fabricated structure (lower). The scale bar shows 100 μm.

References

1) Y. Furuta *et al.*, J. Vac. Sci. Tech. B, **25**, 2171 (2007).
2) A. Takeyama *et al.*, Mater. Trans., **52**, 1276 (2011).
3) T. Sakai *et al.*, Nucl. Instrum. Meth. Phys. Res. B, **332**, 238 (2014).

3-17 Local Modifications of Semiconductor Surface by Fast Cluster-Ion Irradiation

H. Tsuchida [a)], N. Nitta [b)], S. Tomita [c)], K. Sasa [d)], K. Hirata [e)], H. Shibata [f)], Y. Saitoh [g)], K. Narumi [g)], A. Chiba [g)] and K. Yamada [g)]

[a)] Quantum Science and Engineering Center, Kyoto University, [b)] School of Environmental Science and Engineering, Kochi University of Technology, [c)] Institute of Applied Physics, University of Tsukuba, [d)] Tandem Accelerator Complex, University of Tsukuba, [e)] National Institute of Advanced Industrial Science and Technology (AIST), [f)] The Institute of Scientific and Industrial Research, Osaka University, [g)] Department of Advanced Radiation Technology, TARRI, QST

Surface modification by energetic particle irradiation has been investigated for developing corrosion resistant and wear resistant materials in a surface engineering technique. Since the pioneer study on semiconductor quantum dots by ion sputtering has been reported by Facsko *et al.*[1)], many investigations have been carried out for compound semiconductors. According to Nitta et al. [2)], porous nanofiber layers are formed for ion irradiation of GaSb, and its formation mechanism can be explained by a model based on surface recombination of irradiation-induced void defects. The formation of porous nanostructure is influenced by the defect concentrations on surfaces which depend on projectile species. Thus, an irradiation condition is an important factor in the porous structure characteristic such as a diameter of fiber or a layer depth.

In this work, we study the formation of porous structure by irradiation with fast cluster projectiles. Cluster size dependence of the structure formation is investigated for GaSb targets irradiated with small cluster Cu_n^+ (n=1-3) and C_{60} projectiles.

The experiments were performed at the two accelerator facilities of TIARA and Kyoto University. In the irradiation experiments at TIARA, we used 120 keV C_{60} projectiles obtained from a 400 kV ion implanter equipped with a Freeman-type ion source. In the experiments at Kyoto University, projectile beams were Cu_n^+ (n=1-3) ions with incident energy of 400 keV/atom obtained from a 2.0 MV Pelletron-type tandem accelerator. A target sample was GaSb semiconductors with a polished surface. A well-collimated projectile beam was injected parallel to the surface normal of sample. According to the previous study on porous structure formation in GaSb samples irradiated with low-energy atomic heavy ions [2)], the following condition concerning the amount of defect production must be satisfied for formation of porous structures: the amount of defects produced at the surface layer of 20 nm thickness is more than 1,600 defects per a single projectile impact. Based on this result, we determined the beam fluence required to form porous structures, using a TRIM code [3)]. In the present experiments, beam fluence was set to $1\times10^{15}-1\times10^{16}$ ions cm^{-2}. A target temperature was kept at room temperature during irradiation. Observation of surface structures was performed using a field emission scanning electron microscope (FE-SEM) at Kochi University of Technology.

Figure 1 shows SEM images of GaSb surfaces irradiated by Cu_n^+ (n = 1-3) with an energy of 400 keV/atom at different beam fluence. The diameters of porous fiber become large with increasing a cluster size at the same fluence. For instance, at the fluence of 1×10^{15} ions cm^{-2}, the fiber diameter for Cu_3^+ projectiles is significantly large compared with that for Cu_1^+ projectiles. Next, we compare the structure change at the fluence considering the constituent atom number of cluster particles. In comparison of results for Cu_1^+ projectiles at 1×10^{16} ions cm^{-2} and Cu_3^+ projectiles at 1×10^{15} ions cm^{-2}, the former represents a narrow fiber structure and the latter indicates the rounded form at the tip of fiber. This implies that the number of defects produced is not proportional to the cluster size.

In the C_{60}^+ irradiation experiments, the structure formation was not observed, suggesting that defect formation is reduced compared with that for single atomic projectiles (C ions).

References

1) S. Facsko *et al.*, Science, **285**, 1551 (1999).
2) N. Nitta *et al.*, J. Appl. Phys., **92**, 1799-802 (2002).
3) J. Zieglar *et al.*, SRIM Ver. 2013, www.SRIM.org.

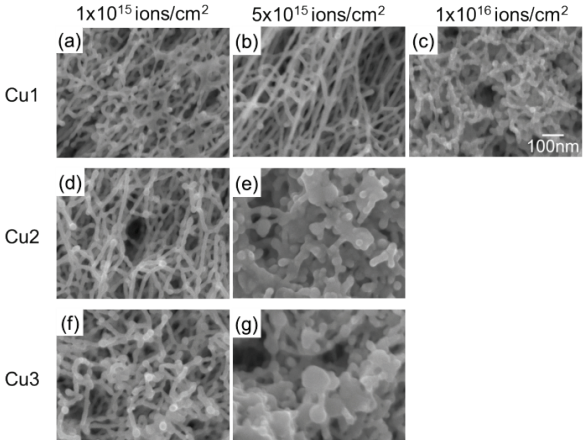

Fig. 1 SEM image of porous structure formed on GaSb surfaces by irradiation of Cu_n^+ (n=1-3) projectiles with an energy of 400 keV/atom at the difference fluence of $1\times10^{15}-1\times10^{16}$ ions cm^{-2}.

3-18

Ion Irradiation Effect on Magnetic Properties of FeRh Thin Films with Energetic Carbon Single and C_{60} Cluster Ion Beam

T. Matsui [a)], R. Soma [b)], Y. Saitoh [c)], M. Sakamaki [d)], K. Amemiya [d)] and A. Iwase [b)]

[a)] Research Organization for the 21st Century, Osaka Prefecture University,
[b)] Department of Materials Science, Osaka Prefecture University,
[c)] Department of Advanced Radiation Technology, TARRI, QST,
[d)] Institute of Materials Structure Science, High Energy Accelerator Research Organization

FeRh alloy with B2 (CsCl-type) crystal structure exhibits unique magnetic behavior of a first order antiferromagnetic-ferromagnetic phase transition, which has been expected to be used for spin devices utilizing the exchange bias effect[1]. We previously reported that the magnetic state of FeRh could be controlled by ion beam irradiation with various energies [2]. Hereby, we revealed that the ion beam irradiation induced the ferromagnetic state in FeRh bulk and films below room temperature, where they were originally in the antiferromagnetic state. We also found that gold cluster ion beam irradiation can be considered to effectively modify the magnetic nature of B2-type FeRh rather than the single ion beam[3]. In order to definitely confirm this, we have investigated the effect of ion fluence of energetic carbon cluster ion beam on magnetic and structural properties of FeRh thin films.

FeRh thin films were irradiated with various ion fluences of 5.0 MeV C_{60} cluster ions as well as with 83 keV single C (C1) ion beam at QST-Takasaki. Effects of cluster ion beam irradiation on magnetization were evaluated by using a SQUID magnetometer as well as by XMCD measurements in both total electron and fluorescence yield modes at BL16A of KEK-PF.

When a couple of atoms constituting a cluster ion impinge into a very small volume simultaneously, high-density energy deposition and multiple-collision processes can be realized. Hence, the lattice defects to be ascribed to the change in the magnetic natures of FeRh can be introduced in the FeRh films in different way from the case in the irradiation with the conventional single ion beam. Figure 1 shows the Fe $L_{2,3}$-edge XMCD spectrum for the 83 keV C1 ion beam irradiated FeRh film with the ion fluence of 1.35×10^{14} /cm^2. In contrast, the unirradiated sample did not show any MCD signal suggesting the presence of magnetization, the C ion irradiated sample show fairly large the Fe $L_{2,3}$-edge MCD spectra. This fact simply indicates that magnetic moment of Fe atom was increased by C1 ion beam irradiation. Whereas, the 5.0 MeV C_{60} ion irradiated sample (2.25×10^{12} /cm^2) also shows the MCD signal as shown in Fig. 2. Its intensity is, however, smaller than that for C1 ion beam irradiation. These facts suggest that C60 cluster ion might deposit the considerably high elastic energy at the film surfaces rather than C single ion. This may be due to the cluster ion effect. Further researches such as ion fluence dependence experiments are required to support this view.

References

1) J. S. Kouvel *et al.*, J. Appl. Phys., **33**, 1343-44 (1962).
2) A. Iwase *et al*., Nucl. Instrum. Meth. Phys. Res. B, **256**, 429-33 (2007).
3) T. Koide *et al.*, J. Appl. Phys., **115**, 17B722-1-3 (2014).

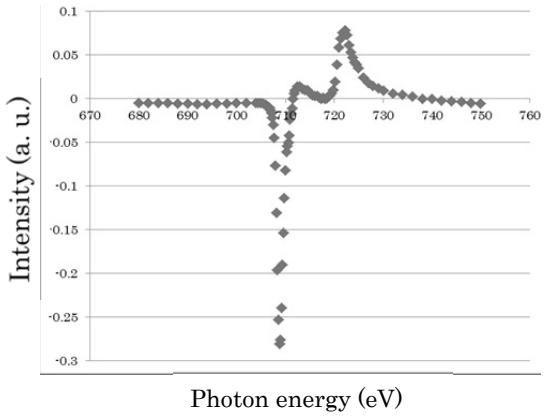

Fig. 1 Fe $L_{2,3}$-edge XMCD spectrum for the sample irradiated with 83 keV C1 ion with the ion fluence of 1.5×10^{14} /cm^2.

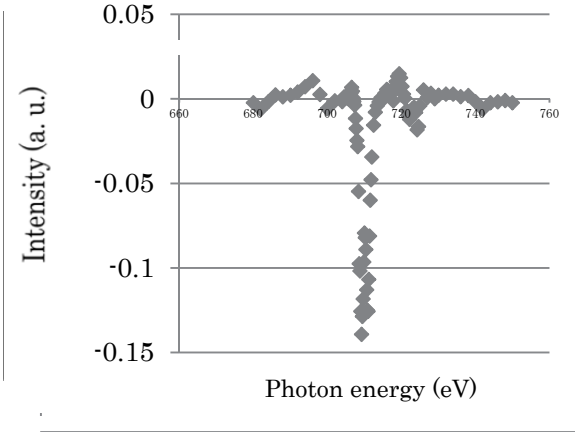

Fig. 2 Fe $L_{2,3}$-edge XMCD spectrum for the sample irradiated with 5.0 MeV C_{60} ion with the ion fluence of 2.25×10^{12} /cm^2.

3-19 Ion Induced Luminescence Measurement from Alumina Irradiated with Swift Carbon Cluster Ion Beams

H. Shibata [a)], Y. Saitoh [b)], K. Narumi [b)], A. Chiba [b)], K. Yamada [b)] and T. Kaneko [c)]

[a)] The Institute of Scientific and Industrial Research, Osaka University, [b)] Department of Advanced Radiation Technology, TARRI, QST, [c)] Graduate School of Science, Okayama University of Science

Our purpose of this study is to elucidate the characteristics of the interaction between energetic cluster ions and solids by means of measuring luminescence from solid surfaces irradiated with cluster ions. We report current results of luminescence measurement from sapphire target irradiated with carbon cluster ions.

Luminescent spectra from alumina (α-Al_2O_3) induced by 0.25 ~ 3.0 MeV/atom (21 ~ 252 keV/u) C_1^+ ~ C_8^+ ion irradiation were measured in the wavelength range of 250-800 nm as a function of ion fluence at room temperature. Cluster ion beams accelerated by the TIARA 3 MV tandem accelerator were used for this study. Beam intensities were typically 2.5 nA for C_1^+ and 50 pA for C_8^+ ions at 0.5 MeV/atom. The luminescence measurement has been carried out by using an optical multichannel analyzer. Cluster ion size and energy dependences of incident cluster ion beams on luminescence intensity have been measured. Ion induced luminescent spectra peaked at 326 and 411 nm were observed. Luminescence of 326 nm was identified as F^+ center, whose intensity grew up and decayed gradually with irradiation. Luminescence of 411 nm was F center, whose intensity grew up rapidly and decayed faster than F^+ center luminescence with irradiation. Intensities of luminescence reached peaks with less fluence as the cluster size increased.

The incident cluster ion size dependence on the yield ratio of the F^+ center luminescence from alumina target is shown in Fig. 1. The incident energy dependence is also shown in this figure. In this study the maximum intensity of luminescence was set as the luminescence yield, since the intensity of luminescence was dependent on the ion fluence. Each yield was compare to the yield for C_1^+ ion irradiation. Ratios R_n of luminescence yields from alumina target irradiated with 0.5, 1.0 and 1.5 MeV/atom C_2^+~C_8^+ incident cluster ions to that for C_1^+ ion are described as $R_n = I(n)/nI(1)$, where n is number of cluster ion, $I(n)$ is the yield for C_n^+ cluster ion and $I(1)$ is the yield for C_1^+ ion. The luminescence yields increase as the cluster sizes increase for every incident energy range, but the ratios R_n become less than unity except for the case of 1.5 MeV/atom. The ratio is unity if the yield increases linearly as cluster size increases. This tendency also appears in the theoretical calculation of the stopping power ($S=-dE/dx$) for the united atom limit of cluster ions [1)]. The ratio R_n of stopping power of cluster ion to that of single atom ion describes as $R_n = S(n)/nS(1)$. This value is independent to kinds of targets and depends on incident velocity only. The experimental data show the same tendency as the calculation of stopping power theory, and exist between unity and the value for the united atom of the cluster ion. This suggests that luminescence caused by irradiation defects directly relates the stopping power of incident cluster ion.

On the other hand, Kaneko has calculated the stopping powers of carbon cluster ions on alumina recently [2)] shown in Fig. 2. This calculation shows the ratio of over 1 for cluster number below 6, but experimental data almost lie below ratio of 1, although the tendency of calculated results, which shows the broad peaks, is similar to the experimental results of 1.0 and 2.0 MeV/atom cases. This means that the stopping power does not relate directly defects of alumina. Further analysis is progressing.

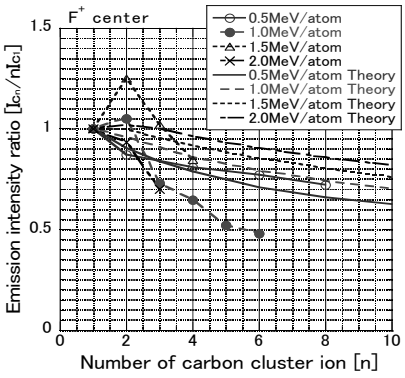

Fig. 1 The ratios of yields of luminescence from F^+ center of alumina target irradiated with 0.5~1.5 MeV/atom C_2^+ ~ C_8^+ projectiles to that for C_1^+ ions in each energy indicate with circles, closed circles, triangles and crosses. Dashed and dotted lines show the theoretical stopping power calculation for the united atom of projectile.

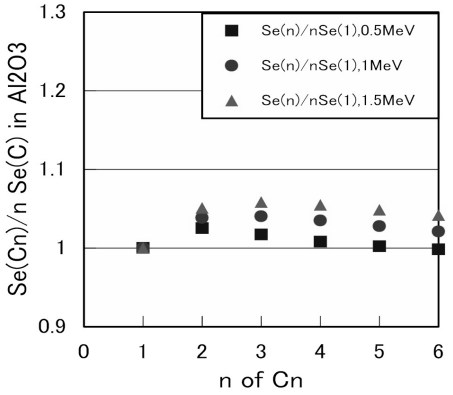

Fig. 2 Calculated results of the ratios of stopping power of alumina target irradiated with 0.5~1.5 MeV/atom C_2^+~ C_6^+ projectiles to that for C_1^+ ions.

References

1) P. Sigmund *et al.*, Nucl. Instrum. Meth. Phys. Res. B, **112**, 1 (1996).
2) T. Kaneko, Private communication.

3-20

Transmission Secondary Ion Mass Spectrometry of Peptides Using 5 MeV C_{60}^+ Ions

K. Nakajima [a)], T. Marumo [a)], K. Yamamoto [a)], K. Narumi [b)], Y. Saitoh [b)], K. Hirata [c)] and K. Kimura [a)]

[a)] Department of Micro Engineering, Kyoto University, [b)] Department of Advanced Radiation Technology, TARRI, QST, [c)] National Metrology Institute of Japan, AIST

Recently, we have measured secondary ion yields emitted in the forward direction upon transmission of MeV C_{60} ions through thin film samples. We found an enhancement of the yield of intact amino acid molecule and reductions of fragment ion yields in the forward direction compared to the backward direction [1)]. The result demonstrates a large advantage of this new technique, transmission SIMS using MeV C_{60} ions, for the analysis of biological materials. In this work, we extend our previous study to larger biomolecules, namely peptides.

Self-supporting amorphous silicon nitride (a-SiN) films (2×2 mm^2) of thickness 50 nm were purchased from Silson Ltd (Northampton, UK). Leucine-Enkephalin films of several tens nm thickness were prepared on the a-SiN films.

A beam of 5 MeV C_{60}^+ ions was produced by a 3 MV tandem accelerator at JAEA/Takasaki. The beam was collimated by an aperture (diameter 0.2 or 1 mm) and incident on the sample from the a-SiN side at 45° with respect to the surface normal. The ions passing through the film were detected by a silicon surface barrier detector placed about 110 mm downstream from the specimen. Positive secondary ions emitted in the forward direction from the Leucine-Enkephalin film were accelerated between the specimen and a mesh electrode biased at +1.0 and −0.7 kV, respectively and detected by a micro-channel plate (MCP) after traveling through a drift tube of ~600 mm length. The timing of the projectile and secondary ion signals were measured by a 4ch TDC (WE7521: Yokogawa Electric Corp., time resolution 5 ns) and the data was stored in a list mode. We also measured the secondary ions emitted in the backward direction from the Leucine-Enkephalin film. In the backward measurement, the drift tube and MCP were moved behind the sample (135° with respect to the beam direction) and the Leucine-Enkephalin/a-SiN film was rotated by 180° so that the secondary ions emitted from the entrance surface of the Leucine-Enkephalin film can be measured.

Figure 1 shows the observed mass spectra of positive secondary ions emitted in the forward (solid line) and backward (dashed line) directions. There are well-defined peaks at m/z=556, 578 and 594. These peaks correspond to protonated Leucine-Enkephalin, sodium and potassium adducts of Leucine-Enkephalin, respectively. There are also many peaks at lower mass numbers, which correspond to fragment ions. Figure 2 shows the forward to backward yield ratios of the observed secondary ions as a function of m/z. The yield of potassium adduct ion is enhanced by 50% in the forward direction compared to the backward direction. The ratio decreases very rapidly with decreasing m/z indicating that the almost all fragment ions are suppressed in the forward direction. These behaviors are similar to the result of amino-acids observed in our previous study, indicating that the transmission SIMS using MeV C_{60} ions is a promising technique for the analysis of large biomolecules.

Reference

1) K. Nakajima *et al.*, Appl. Phys. Lett., **104**, 114103 (2014).

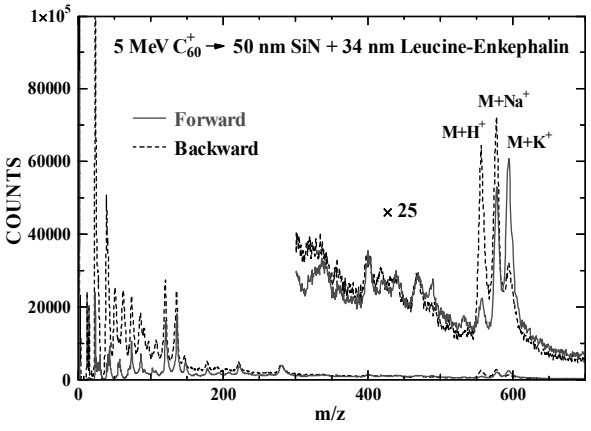

Fig. 1 Mass spectra of positive ions emitted from Leucine-Enkephalin/a-SiN films under 5 MeV C_{60}^+ ion bombardment.

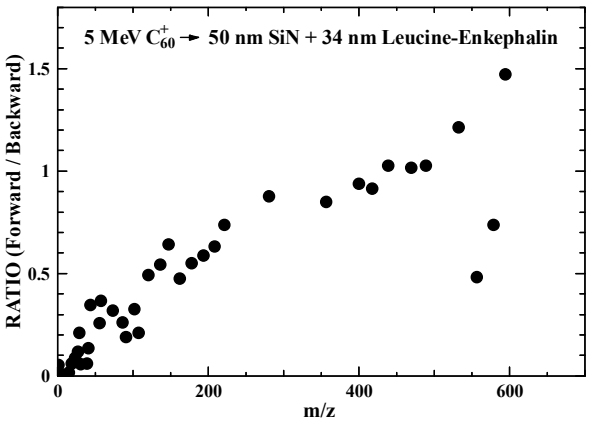

Fig. 2 The ratio of the forward to backward yield of the secondary ion as a function of mass number. The ratio increases with m/z.

3-21 Secondary Ion Emission from a Hafnium Oxide Film Target upon Sub MeV C_{60} Ion Impacts

K. Hirata [a)], K. Yamada [b)], A. Chiba [b)], K. Narumi [b)] and Y. Saitoh [b)]

[a)] National Institute of Advanced Industrial Science and Technology (AIST),
[b)] Department of Advanced Radiation Technology, TARRI, QST

Secondary ions (SIs) are emitted from the target surface upon a primary ion impact on the target. Cluster ion impact gives different SI emission yields per incident atom compared with those for monoatomic ions because of their peculiar irradiation effects caused by simultaneous energy transfer from the constituent atoms of the cluster to a small area of the target surface [1)]. Generally, the larger the primary cluster ion is, the larger the enhancement effect is on SI emission yields. C_{60} is one of the most useful primary cluster ions for SI mass spectroscopy due to its large cluster number and stability. We had developed time-of-flight (TOF) SI mass spectroscopy using primary sub MeV C_{60} ions [2)]. In this paper, we report comparison of SI yields from a hafnium oxide film on a Si wafer (HfO_2/Si target) for incident ion impacts of C_{60} ions with an energy range from 30 keV to 120 keV by TOF SI mass analysis combined with SI electric current measurements.

The HfO_2/Si target was prepared by depositing a hafnium oxide film on one side of a single crystal silicon (100) wafer by magnetron sputtering. The thickness of the film on the wafer is estimated to be 5 nm. SI emission yield measurements for the target were performed using a TOF mass analyzer combined with pulsed ion beams produced by a 400 kV ion implanter of the Japan Atomic Energy Agency (JAEA)/Takasaki, which has been described elsewhere [2)].

For quantitative comparison of SI emission yields under various irradiation conditions, peak intensities of the TOF spectra was scaled with the condition of the same number of incident impacts by scaling the total count of each spectrum based on qI_p/I_o and qI_S/I_o (q: incident ion charge number, I_o: incident beam electric current, I_p: positive secondary ion current for each irradiation condition), respectively. I_o and I_p are directly measured using highly sensitive electrometers respectively connected to a Faraday cup and a movable metal plate with a grid, as described elsewhere [3)].

Figure 1 shows the positive SI TOF spectra of the HfO_2/Si target for (a) 30 keV C_{60}^+, (b) 60 keV C_{60}^+, and (c) 120 keV C_{60}^+, respectively. The relative SI intensity on the vertical axis is proportional to the SI yield per C_{60} impact, as the total counts of the spectra are scaled based on qI_p/I_o as described above. The peaks for $Hf_nO_m^+$ (n = 1, 2・・・, m = 0, 1, 2・・・) are originated from the HfO_2 film. The $Hf_nO_m^+$ peaks for (c) 120 keV C_{60}^+ were observed up to more than n = 12 and those having larger n numbers were obscured by the background signal. We note that the $Hf_nO_m^+$ peak intensities decrease with decreasing incident energy. This result demonstrates that increasing the incident energy of primary C_{60} ions is advantageous for sensitive detection of the characteristic SIs of the HfO_2 film.

In conclusion, the use of impacts of C_{60} ion with the increased incident energies provided higher yields of the characteristic positive SIs for the HfO_2 film and advantageous for highly sensitive chemical analysis of the HfO_2/Si target.

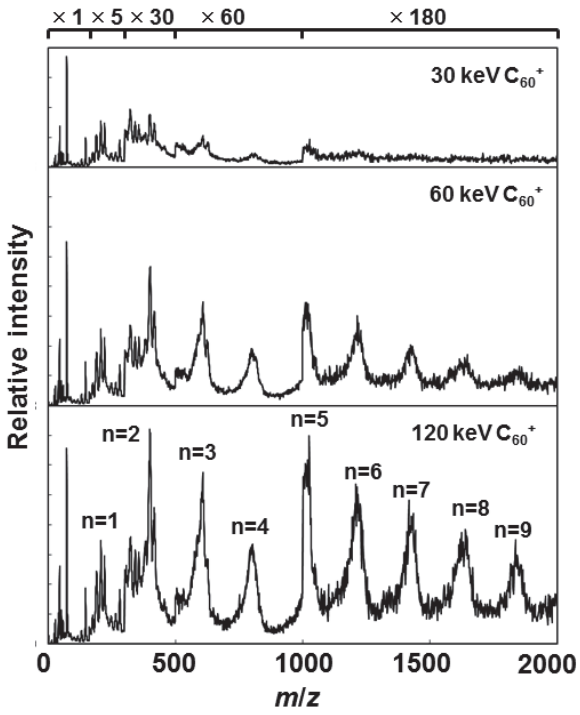

Fig. 1 Positive secondary ion TOF spectra of HfO_2/Si target for (a) 30-keV C_{60}^+, (b) 60-keV C_{60}^+, and (c) 120-keV C_{60}^+.

References

1) K. Hirata *et al.*, Appl. Phys. Lett., **81**, 3669 (2002).
2) K. Hirata *et al.*, Nucl. Instrum. Meth. Phys. Res. B, **266**, 2450 (2008).
3) K. Hirata *et al.*, Appl. Phys. Lett., **86**, 044105 (2005).

3-22 Development of Nanomaterials and Visualization of Ion Tracks through Interactions between Cluster Ion Beams and Organic Materials

T. Sakurai [a)], A. Horio [a)], A. Chiba [b)], Y. Saitoh [b)], K. Narumi [b)] and S. Seki [a)]

[a)]Department of Molecular Engineering, Graduate School of Engineering, Kyoto University,
[b)]Department of Advanced Radiation Technology, TARRI, QST

Since highly accelerated cluster ions with MeV energies serve as new radiation sources useful for future industrial applications, understanding of these ions is strongly demanded. We directed our researches to the visualization of interactions between a series of cluster ions, in particular for C_{60} ions, and organic materials. Previous related researches include the observation of latent tracks of C_{60} cluster ions irradiated to thin films of C_{60} by transmission electron microscopy (TEM)[1]. Meanwhile, our group have developed a novel method to isolate nanowires on substrates via intra-track cross-linking/polymerization reactions using high-energy single particles and the following development process using organic solvents [2,3]. So far we have demonstrated this technique by using single ions beam and cluster beams composed of a couple of ions. Here we newly used C_{60}^{+} cluster ions to observe the fabricated nanostructures and visualize the interactions between a C_{60}^{+} ion and organic materials.

Six MeV C_{60}^{+} ion was generated by a tandem accelerator at TARRI. For the observation of tracks of a single cluster ion, the fluence was set at 1.0×10^{9} cm^{-2} to avoid the overlaps of ion trajectories. Target thin films of small organic molecules were prepared on Si substrates by the spin-coating method. The dominant experimental results are shown in Fig. 1. Before irradiation, the surface of a film of *N*,*N*'-diphenyl-*N*,*N*'-di(m-tol-yl)benzidine (TPD) was smooth as evidenced by atomic force microscopy (AFM) (Fig. 1a). After C_{60}^{+} ion irradiation, we found that the surface areas of the ion trajectories swelled (Figs. 1b and 1e). Furthermore, development of these irradiated films afforded nano-sized gelation that were made by the chemical reactions along the ion trajectory induced by the energy deposition of high-energy particles, resulting in the isolation of nanostructures in the substrates (Figs. 1c and 1d). The shape of the observed nanostructures was different from those observed for the irradiation with single particles as well as Al cluster ions. Namely, the shape of the isolated nanostructures after development processes, shown in Figs. 1c and 1d, implies the coulomb expansion of the C_{60}^{+} ions after its collision with organic films.

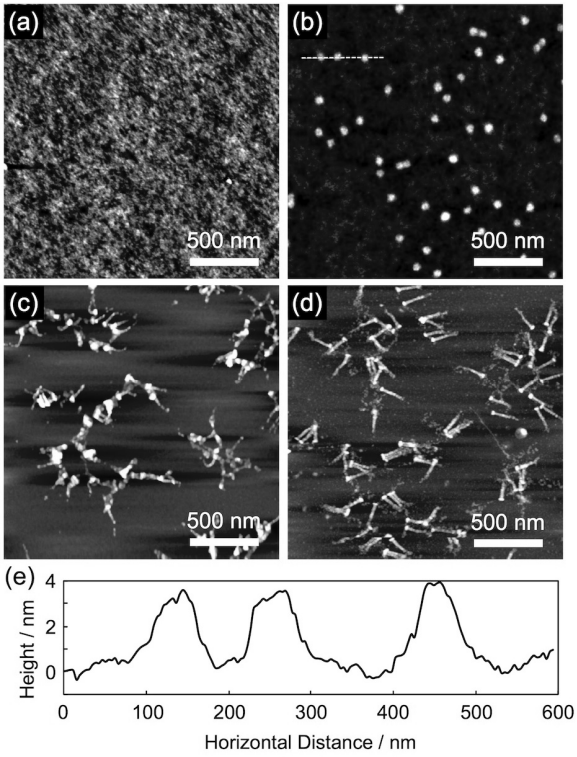

Fig. 1 AFM images of a film of *N*,*N*'-diphenyl-*N*,*N*'-di(m-tol-yl)benzidine (TPD) (a) before and (b) after irradiation with 6.0 MeV C_{60} ions at a fluence of 1.0×10^{-9} cm^{-2}. AFM images of a film of (c) TPD and (d) 4,4',4"-tri-9-carbazolyltriphenylamine after irradiation with 6.0 MeV C_{60} ions at a fluence of 1.0×10^{-9} cm^{-2} and then developed with (c) hexane or (d) cyclohexane. (e) Height profile along direction indicated in (b).

References

1) P. Kumar *et al.*, Appl. Surf. Sci., **313**, 102-06 (2014).
2) S. Seki *et al.*, Adv. Mater., **13**, 1663-65 (2001).
3) Y. Takeshita, T. Sakurai, *et al.*, Adv. Mater. Lett., **6**, 99-103 (2015).

3-23 Production and Destruction of Swift MeV/atom Carbon Cluster Ions in Collisions with Target Gases

T. Kaneko [a], D. Miyamoto [a], S. Fukushima [a], Y. Yamashita [a], A. Chiba [b], K. Narumi [b] and Y. Saitoh [b]

[a] Graduate School of Science, Okayama University of Science,
[b] Department of Advanced Radiation Technology, TARRI, QST

Swift cluster ion beams have been utilized to study various phenomena on basic and applied fields [1-5]. In a tandem accelerator, collisions of negatively charged clusters with charge-changing gases will govern the intensity of positively charged cluster ions. This study aims to understand elementary processes regarding charge changing and destruction processes, which are occurred in charge changing region in accelerator. The basic equation here is the rate equation, which describes the charge state fraction $\phi_i(x)$ of a cluster in charge state *i* at penetrating depth *x* in the charge-changing region:

$$\frac{d\phi_i(x)}{dx} = \sum_i \left[P_{ij}\,\phi_j(x) - P_{ji}\,\phi_i(x)\right] - P_{id}\,\phi_i(x)$$

Here we have $P_{ij} = N\sigma_{ij}$ and $P_{id} = N\,\sigma_{id}$, where σ_{ij} and σ_{id} are the cross section for charge changing from *i* to *j* of a cluster and the destruction cross section for a cluster in charge state *i* in collision with a target gas, N is the number density of a target gas. Here we considered charge state $i = -1, 0, 1$. Solving the above equation under the initial condition of $\phi_{-1}(0) = 1$, $\phi_0(0) = 0$, and $\phi_1(0) = 0$, one has the expression of $\phi_1(x)$. In a simple case where we assume $\sigma_{jd} \equiv \sigma_d (j = -1,0,1)$ and roughly estimate the magnitude of the charge-changing cross sections, we have

$$\phi_1(x = L) = \exp(-N\sigma_d L)[1 - \exp(-N\sigma_p L)]$$

after transmitting the charge-exchange region of depth *L*.

In the above, the production cross section σ_d is roughly equal to σ_{10}. This equation means that only two cross sections control the fraction of singly charged cluster ions. From experimental view point, the factor *NL* will be controlled by the target gas pressure.

Regarding the destruction cross section, we first consider the geometrical model [6], based on the cross sections of individual atoms/ions. Assuming the cross section $\sigma_d(1) = \pi b^2$ of single atom, destruction cross section $\sigma_d(n)$ of a linear-chain cluster composed of *n*-atoms with interatomic distance *R* is obtained by

$$\frac{\sigma_d(n)}{\sigma_d(1)} = 1 + (n-1)\alpha$$

where α is a function of *R* and *d*, and $\alpha < 1$ for $R < 2b$ and $\alpha = 1$ for $R > 2b$. This *n*-dependence is seen in an experimental report. Here α depends on the model, and also cluster structure. The model of a cylinder with two semi-sphere yields a simplest expression of α.

Apart from the geometrical model, we studied this problem in a quantum-mechanical treatment. According to the time-dependent perturbation theory, the destruction and the production cross sections are regarded as the electron stripping cross section of a cluster excited by an incident neutral (target gas) atom, if it is seen in the projectile frame. In the collision of a C_2 ion with a rare-gas atom, the transition amplitude of an electron from the initial (i) state to a final (j) state is calculated in the frame of impact parameter method, where the projectile is assumed to move on a straight-line trajectory at constant speed. In case of a carbon cluster atom, the initial states are 1s, 2s, and 2p states, whose Hartree-Fock (HF) wave-functions are listed. Here we use only the radial distribution function because the angular distribution is assumed to be averaged. The final state is expressed by a distorted plane wave. Using the single electron ionization probabilities as a function of impact parameter together with the independent-electron model, we estimate the one- and two-electron ionization cross section as the production and destruction cross section, respectively. In collision of 2.4 MeV C_2 with Ne target, the cross sections for ionization of 2s and 2p state are 3.9×10^{-16} cm^2 (2s) and 5.1×10^{-16} cm^2 (2p), respectively. For destruction, the cross section for 2s-2s ionization (one 2s electron from a C atom and another 2s electron form the other C atom) is 8.1×10^{-16} cm^2 and that for 2s-2p is 8.5×10^{-16} cm^2. These calculated results are found to show a similar profile of the experimental particle yield [7] of C_2^+ ions traversing Ne gas region as the charge-changing gas. This study will derive qualitative agreement with the experimental data, so that we will refine the present treatment as a next step.

References

1) T. Kaneko, Phys. Rev. A, **66**, 052901 (2002).
2) A. Chiba *et al.*, Phys. Rev. A, **76**, 063201 (2007).
3) A. Chiba *et al.*, Nucl. Instrum. Meth. Phys. Res. B, **315**, 81 (2013).
4) S. Tomita *et al.*, Phys. Rev. A, **73**, 060901(R) (2006).
5) T. Kaneko, Phys. Rev. A, **86**, 012901 (2012).
6) F. Zappa *et al.*, Phys. Rev. A, **64**, 032701 (2001).
7) Y. Saitoh *et al.*, unpublished.

3-24 Study on Interaction of Swift Cluster Ion with Matter

Y. Yuri, A. Chiba, K. Yamada, K. Narumi and Y. Saitoh

Department of Advanced Radiation Technology, TARRI, QST

1. Investigation of a transmission ratio of cluster ion through a tandem accelerator

Transmission ratio of cluster ions through a tandem accelerator, $Rt=I_{in}/I_{out}$, depends on a sort of charge exchange gas, where I_{in} and I_{out} are the beam current of negative cluster ions injected into a tandem accelerator and that of positive cluster ions passed through a tandem accelerator without destruction, respectively. We previously described that a higher transmission ratio was obtained by using a helium gas comparing with a nitrogen gas which is generally used for charge exchange gas, and an improved ratio, $R_I=R_{He}/R_N$ increases with increasing of the number of atoms composed of a cluster ion by means of carbon cluster up to N=10, where R_{He} and R_N are transmission ratios using helium gas and that using nitrogen gas for a cluster ion with same N, respectively[1]. In this time, R_I for a C_{60} ion beam was investigated because an intense beam of C_{60} becomes available by development of an ion source. As a result, R_I of C_{60} is about two times higher than that of C_{10}.

2. Study on orientation-angle dependence on irradiation effects

We attempted a formation of C_2 ion beam enriched in the molecules oriented parallel to the beam direction, in order to investigate a relationship between irradiation effects and orientation angle of a swift cluster ion. The divergence angles of C ions from the foil-induced dissociation of C_2 ions after passing through an Ar gas target were measured with a Coulomb explosion imaging technique, because the divergence angle correlates with the orientation angle at the dissociation process. The average of the divergence angles was smaller than that of C_2 ions not passed through the gas target. This result suggests that the oriented beam was formed. Using the oriented beams, we will demonstrate that the average charge of the constituent ions of C_2 ions emerging from the foil depend on the orientation angle of the incident C_2 ions to the foil.

3. Study on low-energy ion irradiation response of Gafchromic radiochromic film

The transverse beam profile and the two-dimensional (2D) fluence distribution in scanning irradiation are important experimental parameters since they are directly related to the irradiation effect on a sample. We, therefore, studied the feasibility of a Gafchromic film, HD-V2 (Ashland Inc.) as a handy measurement technique of such beam profiles at a high spatial resolution for low-energy (~keV/u) ions[2]. The coloration of HD-V2 is expected to occur due to rather low-energy ion irradiation because the active layer (12 μm in thickness) is not covered with a surface-protection layer.

HD-V2 films were irradiated with ^{12}C ion beams between 27 MeV/u and 1.5 keV/u from the AVF cyclotron, the 3-MV tandem accelerator, and the 400-kV implanter in TIARA, and then digitized at a high spatial resolution of 508 dpi using a scanner ES-10000G (EPSON). The optical density (OD) was obtained from the 48-bit RGB color values using the following equation: $OD_X=\log_{10}(65{,}535/I_X)$, where I_X is the 16-bit color value in a red, green, or blue color channel.

The result is summarized in Fig. 1. The linear-response OD range, the sensitivity, and the maximum OD depend strongly on the kinetic energy of the beam. The OD increment is well proportional to the fluence at low fluence when the kinetic energy of the incident beam is higher than 10 keV/u, as depicted by the dashed lines in Fig. 1. In contrast, the OD change was very small and entirely nonlinear with respect to the fluence when the kinetic energy is below 10 keV/u. We actually confirmed that the high-resolution fluence distribution can be obtained for ion beams with the kinetic energy of the orders of 10 keV/u.

It can be concluded, from these results, that HD-V2 is practically available to low-energy ion beams down to approximately 10 keV/u. We have started a comparative study on the coloration response to C_{60} cluster ion irradiation.

References

1) Y. Saitoh *et al.*, Rev. Sci. Instrum., **80**, 106104 (2009).
2) Y. Yuri *et al.*, Nucl. Instrum. Meth. Phys. Res. A, **828**, 15 (2016).

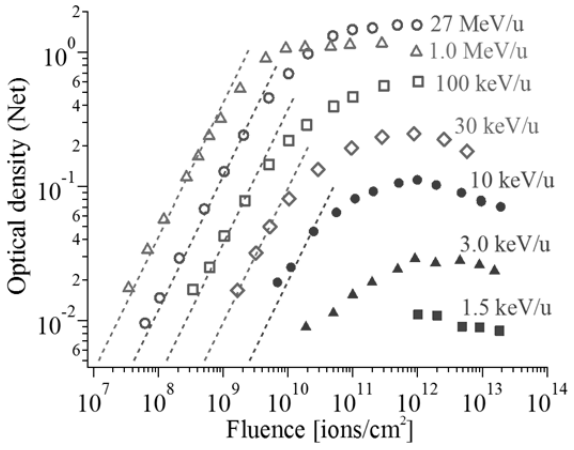

Fig. 1 Net OD response of HD-V2 to C-ion irradiation at different kinetic energies. The net ODs in the red channel are plotted as a function of the fluence. Dashed lines are the linear fitting results in a low fluence region.

3-25 Kinetic Energy Distributions of 4-MeV C^+ and C^{4+} Ion Beams Guided by a Cylindrical Glass Channel

K. Motohashi [a)], Y. Saitoh [b)], N. Miyawaki [b)] and K. Narumi [b)]

[a)] Department of Biomedical Engineering, Toyo University,
[b)] Department of Advanced Radiation Technology, TARRI, QST

The phenomenon wherein ion beams pass through insulator capillaries while maintaining their initial energy and/or charge states is called the guiding effect. The effect was first observed by Stolterfoht *et al.*[1] for 3-keV Ne^{7+} ion. A considerable fraction of highly charged ions (HCIs) was guided through a thin polyethylene terephthalate foil with nanometer-sized multicapillaries even though they were actually tilted with respect to the incidence direction. The focusing of a 2-MeV He^+ ion beam via tapered glass capillary optics was subsequently achieved by Nebiki *et al*[2]. A density enhancement exceeding a factor of 10^4 was reported for the excited ions. However, no clear deflection of ion beams without significant energy loss has yet been observed during the transmission of megaelectron-volt ion beams. Therefore, we conducted an experimental evaluation on the transmission properties of 4-MeV C ions entering a curved glass channel to clarify ion–surface interactions occurring at the inner wall[3]. We expected that multiple scattering on the curved surfaces may result any change on the ion trajectory. Transmissions at larger tilt angles (θ) than those imposed by geometrical limitations were observed. Furthermore, no significant energy loss was observed in the kinetic energy distributions (KEDs) of the transmitted ions at $|\theta| \leq 3°$. These results therefore suggest that any guiding effects ultimately act upon the transmission process. In this study, the influence of initial charge states of 4-MeV ion beams on guiding effects were investigated by comparing C^{4+} with C^+.

Figure 1 presents a schematic illustration of the experimental setup. A narrow, curved channel (gap: 1.2 mm) was formed by a pair of cylindrical concave and convex glass lenses (curvature: 156 mm) facing each other. The channel was tilted with respect to ion-beam axis around the entrance hole. Transmitted ions were detected by a silicon surface barrier detector (SBD) at an observation angle ϕ. The KEDs of the transmitted ions were measured using an SBD at various tilt angles (θ) and observation angles (ϕ). The KEDs of the transmitted ions for several θ and ϕ combinations are shown in Fig. 2 (for C^+) and Fig. 3 (for C^{4+}). Nearly all transmitted ions maintained the initial KEDs of the primary C^+ and C^{4+} ion beams at $|\theta| \leq 3°$.

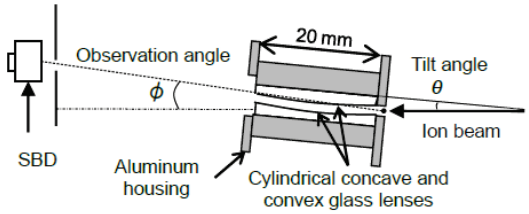

Fig. 1 Experimental setup.

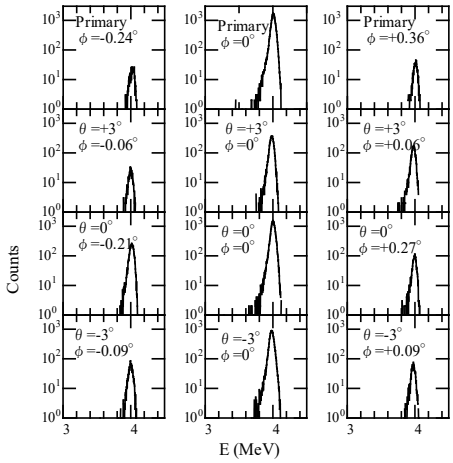

Fig. 2 Kinetic energy distributions (KEDs) of transmitted ions for incidence of 4-MeV C^+ ions.

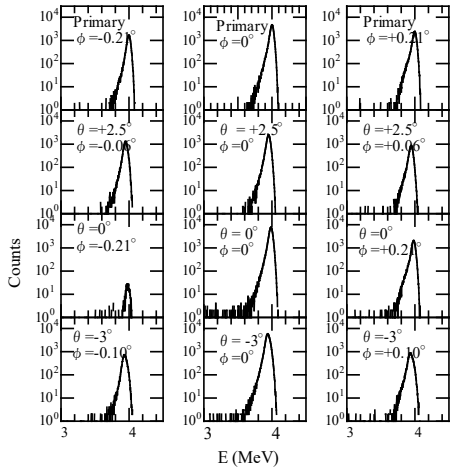

Fig. 3 KEDs of transmitted ions for incidence of 4-MeV C^{4+} ions.

Hence, there was virtually no discernible difference between the subject findings for C^+ and C^{4+}. In summary, transmission without significant energy loss at wider θ than those imposed via geometrical limitations was also demonstrated this time. One of the reasons of the fact that no clear difference between C^+ and C^{4+} was found may be very low fluence rate of incident ions. Low ion current (< 0.2 pA) reduced for protection of the SBD could not cause any charge up.

References

1) N. Stolterfoht *et al.*, Phys. Rev. Lett., **88**, 133201 (2002).
2) T. Nebiki *et al.*, J. Vac. Sci. Tech. A, **21**, 1671 (2003).
3) K. Motohashi *et al.*, Jpn. J. Appl. Phys., **52**, 07630 (2013).

3-26

Analysis of Linear Energy Transfer Effects on the Scintillation Properties of Ce-doped Gd_2SiO_5(GSO)

M. Koshimizu [a)], K. Iwamatsu [b)], S. Kurashima [c)], A. Kimura [d)], M. Taguchi [d)], T. Yanagida [e)], Y. Fujimoto [a)] and K. Asai [a)]

[a)] Department of Applied Chemistry, Tohoku University, [b)] University of Notre Dame, [c)] Department of Advanced Radiation Technology, TARRI, QST, [d)] Department of Advanced Functional Materials Research, TARRI, QST, [e)] Graduate School of Materials Science, Nara Institute of Science and Technology

Ce-doped Gd_2SiO_5 (GSO) is a well-known commercial scintillator and widely used in various applications. One of the characteristics of the scintillation properties of Ce-doped GSO is a slow rise in the scintillation temporal profile. Our recent research on several scintillators strongly suggests that a slow rise in the scintillation temporal profile leads to a significantly different temporal profiles for different linear energy transfers (LETs) [1,2]. From this viewpoint, LET effects on the scintillation of Ce-doped GSO are interesting. In addition, we have sufficient basic knowledge on the optical and scintillation properties of Ce-doped GSO in a large number of previous literatures. In this study, we analyzed the LET dependence of the temporal profiles of scintillation in Ce-doped GSO crystals with different Ce concentrations, which exhibit different rise time.

The pulsed ion beam irradiation was performed using an azimuthally varying field (AVF) cyclotron at Takasaki Ion Accelerators for Advanced Radiation Application (TIARA), Takasaki Advanced Radiation Research Institute, Japan Atomic Energy Agency (JAEA). The details of the measurement system have been described in a previous paper [3]. Temporal profiles of scintillation at different LETs were obtained using pulsed ion beams of 20 MeV H^+, 50 MeV He^{2+}, and 220 MeV C^{5+}.

Figure 1 shows the temporal profiles of scintillation of GSO-doped with Ce at 0.5% under pulsed ion beams irradiation in the rise part. The time profiles are significantly different for different LET values. The rise in the time profiles was more gradual for the pulsed beam of 20 MeV H^+, which had the lowest LET among the investigated ions. The rise reflects the process of energy transfer from the host glass matrix to emitting Ce^{3+} centers. In general, light yield is lower for higher LET. Thus, the difference in time profiles among different LET values is ascribed to quenching of excited states with high LET. The fast rise in the time profiles for higher LET ions, therefore, indicates that quenching occurs in competition with the energy transfer process. Figure 2 shows the scintillation time profiles at long time scale. Decay behaviour was slightly different for 20 MeV H^+. Thus, the LET effects in GSO originate from quenching owing to the interaction among excited states in the host matrix prior and after the energy transfer from the host to Ce^{3+}, and quenching occurs on the time scale of several to several tens ns.

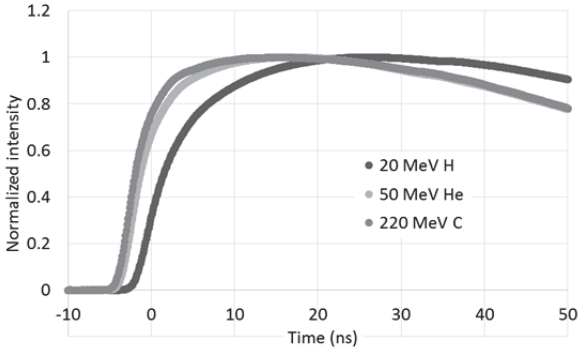

Fig. 1 Scintillation temporal profiles of GSO doped with Ce at 0.5% for different pulsed ion beams in the rise part.

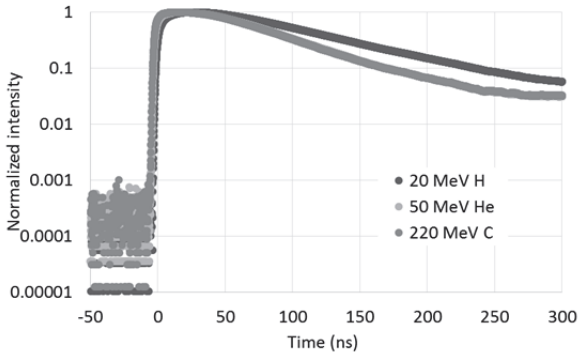

Fig. 2 Scintillation temporal profiles of GSO doped with Ce at 0.5% for different pulsed ion beams in the decay part.

References

1) T. Yanagida, M. Koshimizu. *et al.*, Nucl. Instrum. Meth. Phys. Res. B, **365**, 529 (2015).
2) M. Koshimizu *et al.*, J. Lumin., **169**, 678 (2016).
3) M. Koshimizu *et al.*, Rev. Sci. Instrum., **86**, 013101 (2015).

3-27 Periodical Calibration of Ionization Chamber System for ^{60}Co Gamma Ray High Dose Rate at Radiation Processing

H. Seito [a)], Y. Nagao [a)], T. Agematsu [a)] and T. Kojima [b)]

[a)] Department of Advanced Radiation Technology, TARRI, QST, [b)] Beam Operation Service Co., Ltd

In the gamma ray irradiation facilities at TARRI, QST, various types of radiation processes are frequently required. Therefore, wide ranges of dose and dose rate have to be covered. Two different chemical dosimeters (alanine dosimeters and PMMA dosimeters) are useful as routine dosimeters, but these dosimeters cannot cover wide dose ranges. Although calorimetry is considered to be the most reliable calibration method, it is not practical in irradiation facilities, except in primary standard dosimetry laboratories [1, 2)]. The ionization chamber is the simple, practical and reliable method used as reference dosimeters for wide dose and dose rate ranges of ^{60}Co gamma rays. We conventionally use two different types of ionization chambers. Parallel-plate ionization chamber and thimble ionization chamber are mainly used in ^{60}Co gamma ray irradiation fields whose dose rates are the order of several kGy/h and that of several Gy/h, respectively. Thimble chambers are also useful as reference dosimeters in the geometries of measurements with a very wide distribution of the gamma ray incidence angle for which the parallel-plate ionization chambers cannot be applied. Through periodical calibration of the ionization chamber at national standard laboratory and routine measurement of dose rate at TARRI, we have examined various characteristics of the parallel-plate ionization chamber and thimble ionization chamber at the high dose rate in ^{60}Co gamma ray irradiation facilities. Calibration of such high dose or dose rates is not easy to be performed at the present national standard dosimetry laboratories, since characteristics of most of their radiation fields can provide collimated gamma-rays from a point source and lower dose rates, which are quite different from those of panoramic radiation fields used in radiation processing [3)]. Table 1 shows specification of ionization chamber. Our ionization chamber system consists of the ionization chamber, electrometer and high voltage power supply. If the ionization chamber is calibrated in a standard ^{60}Co gamma ray radiation field, the exposure rate is evaluated by using the calibration factor to convert from the measured current value [4)]. The reliability of reference dosimetry in the TARRI at QST is maintained by periodic checks of traceability against national exposure rate standard measurements in National Institute of Advanced Industrial Science and Technology (AIST). Table 2 shows the result of a conversion factor (C/kg/h/A) given by AIST for the past approximately 12 years. The individual difference between the instruments of the ionization chamber was slightly seen, but the conversion factor that AIST gave has been very stable, which attain uncertainty of 1.0% at confidence level except 2009. These results give confidence in the precision in gamma-ray absorbed dose measurement at QST using a parallel-plate ionization chamber and a thimble chamber as a reference dosimeter. They also demonstrate that the operation of the QST ionization chamber system is sufficient to perform the exact dose evaluation at radiation processing dose levels.

References

1) D. T. Burns *et al.*, Metrologia., **48**, 06009 (2011).
2) D. T. Burns *et al.*, Radiat. Phys. Chem., **75**, 1087 (2006).
3) T. Kojima *et al.*, Radioisotopes, **50**, 291 (2001).
4) R. Tanaka *et al.*, IAEA-SM-272/17 (1985).

Table 1 Specification of ionization chambers.

Chamber type	Parallel-plate	Thimble
Volume (mL)	0.3	0.6
Wall material	Al	Al
Applied voltage (V)	150	450
*Measureable dose rate (C/kg/h)	3.69E-01 ~ 5.30 E+02	5.74E-03 ~ 5.11E-01
Number	JTC-8 No. 730 C-111P No.1083	C-110 No.1049 C-110 No.1187

*This value is based on our experimental data.

Table 2 Conversion coefficients (C/kg/h/A) of QST ionization chambers given by AIST periodically. The coefficient values are under condition of 22 °C and 1,013.25 hPa. Uncertainty in calibration ±1.0% at 95% confidence level. The mark "—" in below table represents the calibration was not scheduled.

Year	JTC-8 No.730	C-111P No.1083	C-110 No.1049	C-110 No. 1187
2004	7.68E+09	—	—	—
2005	7.70E+09	—	—	—
2006	7.67E+09	—	—	—
2007	—	7.77E+09	5.56E+09	—
2009	—	7.84E+09	—	—
2010	—	7.76E+09	—	—
2011	—	—	5.56E+09	—
2012	—	7.80E+09	—	—
2013	—	7.76E+09	—	—
2015	—	7.79E+09	—	5.54E+09

3-28 Dose Dependence of Photo-stimulated Luminescence from G2000 Glass Material

A. Yokoyama [a, b], W. Kada [b], S. Kawabata [b], K. Miura [b] and O. Hanaizumi [b]

[a] Department of Advanced Radiation Technology, TARRI, QST,
[b] Graduate School of Science and Technology, Gunma University

Introduction

In heavy-particle therapy, several hundred MeV/n-carbon beams are used to kill DNA in malignant tumor cells. Only the malignant tissue is annihilated because radiation sensitivity of the tumor tissue is greater than that of normal tissue. However, to avoid irradiating the normal tissue around the tumor, various filters and collimators are used to adjust the projecting range, i.e., the position of the Bragg peak and the irradiation area. At present, ionization chambers are used to measure the dose distribution in the tumor at 10 points in the beam direction at radiation-therapy planning. It is necessary to obtain three-dimensional dose distribution images every few minutes in order to treat efficiently and to alleviate physical burden on patients.

In line with this, various scintillators such as Gd_2O_2S:Tb were tested to obtained real-time dose distribution images. However, this method was not successful owing to scintillation saturation [1]. Instead, Sumita Optical Inc developed photostimulated luminescence (PSL) glass material (G2000), which can be used to read the exposing visible light after the beam irradiation[2]. Developing PSL glass material with a dose dynamic range from mGy to Gy by adjusting the activator amount and the type of elements, the granted total dose can be obtained from the PSL intensity. In addition, unlike the imaging plate, the PSL glass material has transparency; the three-dimensional beam trajectories in the glass can be observed, though not in real time. A three-dimensional stimulated distribution image can be obtained by using a stereo-image measurement method, in which two-dimensional luminescence distribution images are taken in different directions.

Here, we present the results of two projects implemented in 2015, *i.e.*, (1) construction of a PSL measurement system and (2) a preliminary test of the system carried out by reading PSL from glass material irradiated ^{60}Co γ-rays.

PSL measurement system

A PSL measurement system was constructed consisting of objective lenses, optical filters, stage blocks, a He–Ne laser, a photo-multiplier tube (PMT), and an electron-multiplying CCD (EMCCD) camera. The PSL at the wavelength of 550 nm was using the PMT, and two-dimensional PSL images were captured with the EMCCD camera at the same time. The bandpass filters were respectively placed in front of the PMT and the EMCCD camera to not only detect the wavelength of luminescence from 520 nm to 560 nm but also cut off the wavelength of 632 nm from the He–Ne laser. To reduce extraneous-light noise, the bandpass filters, a dichroic mirror, and a lens were set in C-mount adapters. The glass material, the object lens, and mirrors were placed in the stage block.

Preliminary test

The PSL glasses 0.9% weight Tb were added to an activator prepared by Sumita Optical Inc [2]. The ^{60}Co γ-rays were irradiated in the range from 100 mGy to 100 Gy. After irradiation, PSL was read out through exposure to He-Ne laser at 1 mm diameter. The images were captured after one-sec exposure time and the induced photons were counted, at one-sec intervals, and the intensity was calculated as the average value for 60 s. Consequently, the observed PSL intensity is linearly correlated to the total γ-ray dose (Fig. 1). The PSL is detected from the glass irradiated with γ-rays at a minimum dose of 100 mGy.

At the next stage, the maximum and the minimum detection limit of the glass is going to be investigated, and a program constructing three-dimensional images from two stereo-images is going to be developed.

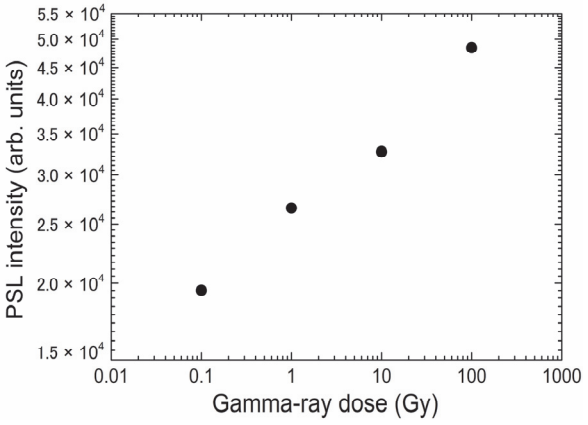

Fig. 1 Dose dependence of PSL intensity from the material. The intensity is proportional to the irradiated γ-rays, from 100 mGy to 100 Gy.

Acknowledgment

This work was supported by KAKENHI, Grant-in-Aid for Young Scientists (B) 15K18321.

References

1) J. M. Schippers *et al.*, Nucl. Instrum. Meth. Phys. Res. A, **477**, 480 (2002).
2) M. Yamazaki *et al.*, Solid State Comm. 2004, **130**, 637 (2004).

3-29 Elements of Low Atomic Numbers in Lithium Oxide Ceramics under Irradiation

B. Tsuchiya [a)], S. Yamamoto [b)], K. Takahiro [c)] and S. Nagata [d)]

[a)] Department of General Education, Faculty of Science and Technology, Meijo University,
[b)] Department of Advanced Functional Materials Research, TARRI, QST,
[c)] Graduate School of Science and Technology, Kyoto Institute of Technology,
[d)] Institute for Materials Research, Tohoku University

Lithium oxides (Li_2TiO_3, Li_2ZrO_3, Li_4SiO_4, $LiAlO_2$, $LiCoO_2$, and so on) are potential candidates as tritium breeding materials in fusion devices. It is of significant importance to investigate the relationship of radiation damage processes and dynamic behaviors of hydrogen as well as lithium atoms in lithium oxides by combining in situ radiation measurements with post-irradiation examinations.

Figure 1 shows a typical Rutherford backscattering spectrometry (RBS) spectra of backscattered O^{4+} ions, and Fig. 2 shows a typical elastic recoil detection (ERD) spectra of recoiled H^+ and Li^+ ions, from the deposition of 25 nm Au and 35 nm $LiCoO_2$ on LATP (Au/$LiCoO_2$/LATP) without and with charging up to 8.40 mC/cm^2, as measured using 9.0-MeV O^{4+} ion-probe beams from a tandem accelerator. The horizontal axes (Channel Number) for the RBS and ERD spectra correspond to energies of the backscattered O^{4+} ions and recoiled H^+ and Li^+ ions, respectively, and represent the depth from the surface. On the vertical axes, the counts/energy in the RBS and ERD spectra correspond to the concentrations of constituent elements such as $_1$H, $_3$Li, $_8$O, $_{14}$Si, $_{15}$P, $_{22}$Ti, and $_{27}$Co in Au/$LiCoO_2$/LATP. The thickness of each Au and $LiCoO_2$ thin film was determined from approximately 628-711 and 195-255 channels of Fig. 1, taking into account the Rutherford backscattering cross-sections of O^+ ions in the case of constituent elements in Au/$LiCoO_2$/LATP, the stopping cross-sections for O^+ ions, and the solid angle of detection [1)]. There is significant change in the spectra between before and after charging, as the a little diffusion of Au atoms into $LiCoO_2$ perhaps initiated by elastic collisions due to ion probe-beam, as seen approximately in 450-615 channels of Fig. 1. On the other hand, the sharp and broad peaks at approximately 320-419 and 450-849 channels in ERD of Fig. 2 correspond to the H and Li concentrations in $LiCoO_2$ thin films. The Li peak becomes broader than the H peak, because the range straggling due to the stopping power of Li is larger than that of H in the Au, $LiCoO_2$ film and the Al absorber [1)]. It is assumed by the basis of our previous experimental results that the H peak ranging from approximately 320-419 channels in ERD spectrum for the uncharged-sample may probably correspond to H atoms absorbed by the $LiCoO_2$ film, as the H concentration in the Au film was quite low. The each peak at around 370 and 410 channels in ERD spectrum for the charged-sample up to 8.40 mC/cm^2 may probably indicate H or water (H_2O) retained in the $LiCoO_2$ films and H_2O adsorbed only onto the surface of the Au thin film, respectively. Also, it is assumed in this present study that each area at

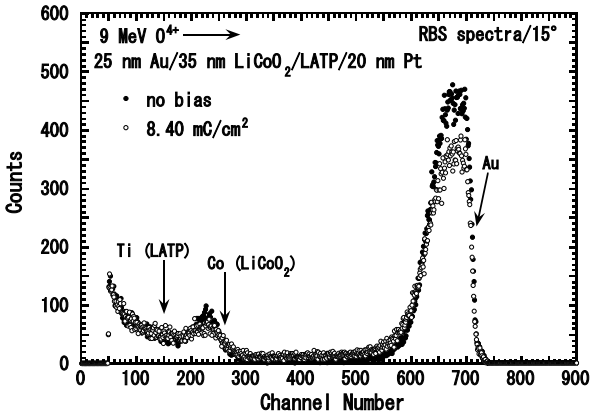

Fig. 1 Typical RBS spectra of back-scattered O^{4+} ions from 25 nm Au/35 nm $LiCoO_2$/LATP/20 nm Pt (●) without and (○) with charging at 8.40 mC/cm^2, obtained by using 9.0-MeV O^{4+} ion-probe beams.

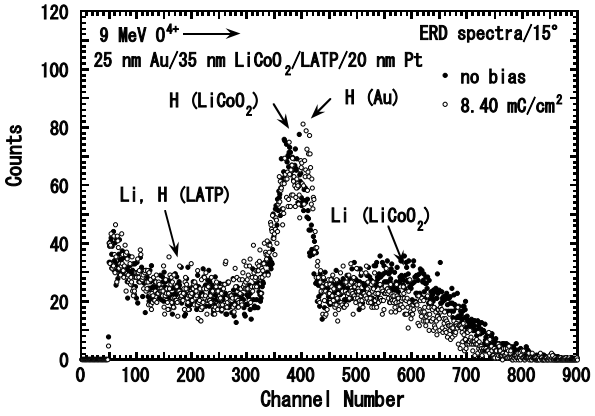

Fig. 2 Typical ERD spectra of recoiled H^+ and Li^+ ions from 25 nm Au/35 nm $LiCoO_2$/LATP/20 nm Pt (●) without and (○) with charging at 8.40 mC/cm^2, obtained by using 9.0-MeV O^{4+} ion-probe beams.

approximately 450-549 and 550-849 channels indicates Li concentrations at the interface between $LiCoO_2$ thin films and LATP, and at the surface of the thin films, respectively. It appears from Fig. 2 that the Li concentrations at the interface and the surface decrease after charging up to 8.40 mC/cm^2. The gradual degradation of Li distribution is from the $LiCoO_2$ film.

Reference

1) J. F. Ziegler, J. P. Biersack, and U. Littmark, The Stopping and Range of Ions in Solids, Pergamon Press, New York (1985).

3-30 Calibration of Analytical Sensitivity for Heavy Elements on Micro Beam PIXE System in TIARA

Y. Iwata [a], N. Yamada [b], M. Koka [b], T. Satoh [b] and T. Kamiya [b]

[a] Department of Chemistry, Faculty of Education and Human Studies, Akita University,
[b] Department of Advanced Radiation Technology, TARRI, QST

Standard Reference Material (SRM) for determination of trace elements in biological materials was made by macro porous cation-exchange resin (Macro-Prep 25S, Individual Particle size: *ca* 15-18 μmϕ). SRM was used for calibration of analytical sensitivity for several elements on Micro Beam PIXE System in TIARA. In this work, s new SRM was prepared for calibration of analytical sensitivity for S, Fe, Ni, Zn and Pb. Individual particle of the SRM resin was subjected to 3 MeV proton bombardments by micro beam PIXE. Characteristic X-rays from the known amount of elements in SRM were measured by Si(Li) and PureGe detectors. The sensitivities for each detector were calculated by elemental abundance in the resin and dose of proton.

1. PIXE分析における装置の校正や分析値の相互比較のために、イオン交換樹脂中に分析目的元素を正確量含有する標準物質（SRM）を開発している。これまでに、マクロポーラス型イオン交換樹脂に、生体関連元素のAl、Ca、Mn、Fe、Co、Ni、Cu、Zn、Sr、Pt及びPbを一定量吸着させたSRMを調製した。PIXE分析に供し、特性X線強度と元素含有量から、TIARAマイクロビームシステムにおける分析感度を検出器毎に求め、その成果を取りまとめて報告した[1]。本研究では、TIARAマイクロビームシステムにおいて2015年に修理完了したPureGe X線検出器の校正をおこない、従来の検出器と比較したので報告する。

2. SRMの調製　既報に従い調製した[1]。重元素測定用に樹脂体積あたり、Fe、Ni、Zn及びPbをそれぞれ100と150 ppmv含有する2種類のSRMを調製した。原料の陽イオン交換樹脂にスルホン基として存在するSは、2,778 ppmvである。

PIXE分析　TIARAマイクロビームシステムにより3 MeVプロトンをサブミクロン径にしぼり，大気中で試料に照射（スキャンエリア20 × 20 μm、電荷量250 nC）を行った。今回の特性X線の測定は、Table 1のA、Dの2種類の検出器についておこなった。PIXEanaでスペクトル解析をおこない、感度を求めた。検出器Aについては2012年の感度と比較した。

3. 軽元素用SSDの再校正　結果をTable.2には今回（2016）の測定結果[A*]と、比較のため、2012年の測定結果[A**]を示す。PGT LS30135の分解能については、S-Kα_1（2.307 keV）からPb-Lα_1（10.550 keV）にかけて、FWHMは、110-220 eVであり、前回の校正時と同様に特性X線のピーク分離に十分であることが確かめられた。分析感度は、測定した全ての元素で、 3倍程度大きくなった。

重元素用SSDの再校正結果をTable 2 の[D*]に示す。PS 305-D7.5Cは高エネルギー側の特性X線測定用に導入された検出器で、重元素の分析に有効であると期待される。Fe-Kα_1（6.398 keV）からPb-Lβ_1（12.612 keV）でのFWHMは、330-380 eVであるため、スペクトル干渉があり、分解能の向上、即ちFWHMの減少、が望まれる。分析感度は、これまで用いた全ての測定器中で最も大きく、PGT LS30135に対して、FeからPbに対して4から7倍の感度を示した。このPS 305-D7.5Cについては修理前の2008年にZnの感度を測定しており、その結果は150±10（n = 8）であり、今回の結果と一致した。微量重金属成分の画像化、定量化に、大きな威力を発揮すると期待される。

Reference

1) M. Koka *et al.*, JAEA-Tech. 2016-006, 21 (2016).

Table 1 List of X-ray detector on micro beam PIXE system in TIARA.

Detector (SSD)	Model	Active area / mm^2	Crystal thickness /mm	FWHM @5.9keV /eV
A (Si(Li))	PGT LS30135	30	5	135
B (PureGe)	CANBERRA GUL0110	100	10	118
C (PureGe)	PGT IGX100138	100	10	138
D* (PureGe)	APTEC PS 305-D7.5C	250	12	310

* Repaired in 2015.

Table 2 Analytical sensitivity for elements by several X-ray detectors on micro beam PIXE system in TIARA.

	Sensitivity/Count pg^{-1} nC^{-1} (n=3-14)				
	A*	A**	B	C	D*
Al	ND	100 ± 16	101 ± 19	ND	ND
S	222 ± 13	74 ± 13	77 ± 14	ND	ND
Ca	ND	71 ± 14	58 ± 12	ND	ND
Mn	ND	38 ± 5	23 ± 4	140 ± 22	ND
Fe	72 ± 7	33 ± 11	22 ± 8	130 ± 23	340 ± 40
Co	ND	24 ± 10	17 ± 7	91 ± 40	ND
Ni	49 ± 3	15 ± 6	9.1 ± 5	65 ± 11	210 ± 28
Cu	ND	18 ± 7	12 ± 5	65 ± 22	ND
Zn	27 ± 3	10 ± 2	6.9 ± 1.6	62 ± 11	160 ± 15
Sr	ND	1.2 ± 0.6	1.2± 0.9	4.7 ± 1.3	ND
Pb	5.8 ± 0.5	1.0±0.3	0.7 ± 0.2	5.3 ± 1.5	44 ± 5

*This work, **Measured at 2012.

3-31 Three-dimensional Distribution Measurement of Cesium in Clay Particles by Micro-PIXE-CT

T. Hatakeyama [a)], D. Sata [a)], K. Ishii [a)], S. Matsuyama [a)], A. Terakawa [a)], M. Fujiwara [a)]
H. Arai [b)], T. Satoh [c)], M. Koka [c)], N. Yamada [c)] and T. Kamiya [c)]

[a)] Department of Quantum Science and Energy Engineering, Tohoku University,
[b)] Research Center for Remediation Engineering of Living Environments Contaminated with Radioisotopes, Tohoku University,
[c)] Department of Advanced Radiation Technology, TARRI, QST

A serious accident occurred in Fukushima Daiichi nuclear power plant due to The Great East Japan Earthquake in 2011. Radioactive substances, for example ^{137}Cs and ^{131}I, were released into the environment and polluted the large area[1].

Especially, the long half-lives of ^{137}Cs is 30 years, so we have to remove the radioactive substances from the soil of disaster area. In recent study it has been revealed that Cs atoms are absorbed strongly in clay particles and removing the atoms from the particles is difficult. Since the soil including the clay particles is treated as radioactive waste, the volume reduction is also an important issue.

For this reason, we developed a way to investigate Cs distribution in the clay particles including inside of a particle by Micro-PIXE-CT based on micro-PIXE and an image reconstruction method. The first step of measurement is preparing samples of the soil. We added water to some soil, mixed it and filtered to remove large particles and impurities. This filtered muddy water was mixed with non-radioactive Cs_2CO_3 and dried for 24 hours and was attached on a small carbon fiber using glue, which was inserted into a tip of a needle.

Then the micro-PIXE analysis was carried out using the microbeam system connected to the single-ended accelerator at TIARA. Energy of the proton beam was 3 MeV, the beam spot size was 1×1 μm^2 and the beam current was about 100 pA. The distance and angle of lithium-drifted silicone (Si(Li)) detector (PGTLS30135) for X-rays were 22 mm from the target and 140° to the beam axis, respectively. A sample was automatically rotated with a step of 9° in vacuum. The measurement area was 200 μm^2 corresponding to 128×128 pixels of projection images. The measuring time of micro-PIXE analysis at each angle was 10 minutes. Figure 1 of projection data shows scattered Cs elements over the particle. The PIXE data was analyzed using GeoPIXEII[2]. Figure 2 shows PIXE spectrum. We can't know the distribution of Cs inside of the clay particle by the micro-PIXE analysis, but the cross sectional image using ML-EM [3] (Maximum Likelihood Expectation Maximization) method shows element distribution within the sample. Figure 3 (Left) shows the three-dimensional distribution of Cs.

When we get the PIXE image, it occurs the changing of X-ray production cross section by beam energy loss and absorption of X-rays. So, we have to measure areal density by STIM (Scanning Transmission Ion Microscopy)-CT and correct the image. This method can obtain us areal density in each pixel. Figure 3 (Right) shows the images of correction image and without. Correction image shows Cs distribution. The sectional image of the clay particle, Cs distributes 10 μm from the surface. It is possible to decontaminate of the clay particle if we can remove only the area with Cs.

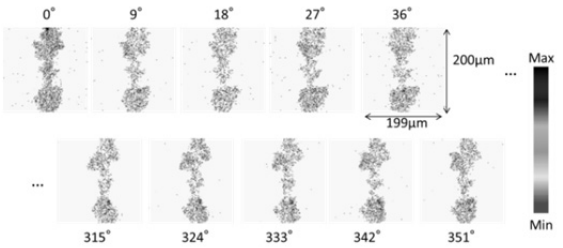

Fig. 1 Distributions of Cs in obtained from each angles in a clay particle.

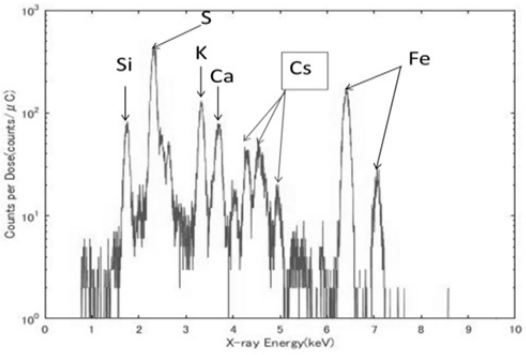

Fig. 2 PIXE spectrum of a clay particle.

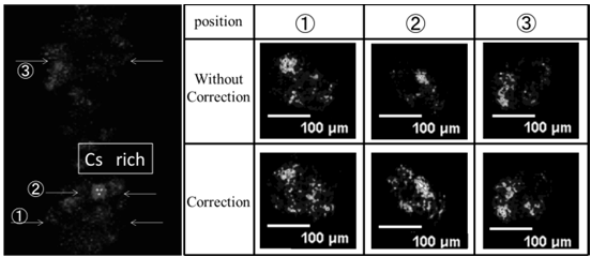

Fig. 3 (Left): 3D-PIXE-CT image of a Cs, (Right): cross section of a clay particle with the correction of STIM and without.

References

1) K. Ishii *et al.*, Nucl. Instrum Meth. Phys. Res. B, **371**, 387-91 (2016).
2) C. G. Ryan, Int. J. Imag. Syst. Tech., **11**,219-30 (2000).
3) T. Satoh *et al.*, Int. J. PIXE **22**, 73 (2012).

3-32 Characteristics of Electron Spin Resonance Signal of Quartz from Sediments and Adjacent Bedrocks

K. Tokuyasu, K. Yasue, T. Komatsu, I. Tamura and Y. Horiuchi

Geoscientific Research Department, Tono Geoscience Center, JAEA

Understanding the stages of mountain building is crucial to the stability assessment of geological environments in geological disposal system. This is because (1) mountains can theoretically increase their average height up to attain the stage of dynamic equilibrium between the uplift and erosion rates[1], and (2) such building mountains may cause changes in groundwater flow dynamics in the geological environments. In this context, we have carried out the research and development of provenance analysis techniques to elucidate the mountain-building stages. This paper presents the results of the study focused on the R&D using the Electron Spin Resonance (ESR) signals from quartz in sediments.

The quartz ESR signal intensities from Al center (an electronic hole trapped at the bond between oxygen and Al which replaces Si[2]) and Ti-Li center (an electron trapped at Ti which replaces Si, with accompanying Li ion[2]) show the concentration of unpaired electrons in the crystal. Since the characteristics of these signal intensities differ depending on the types of rock and the age of source rock[2, 3], the sediment provenance can be estimated using the ESR properties from quartz in sediments. We therefore investigated the relationship of quartz ESR properties between sediments and adjacent bedrocks.

The outcrop of the Miocene to Pleistocene Toki Gravel Formation (fluvial sediments) investigated in this study is located between the Tsukechi River, a tributary of Kiso River, and the Atera fault in the Tono area, Gifu Prefecture. In the northern part of the Tono area, bedrocks consist of Mesozoic sedimentary rocks, Nohi Rhyolite and Sanyo Granite, whereas in the southern part, they consist of Ryoke Granites. The outcrop of the sediments is about 30 m thickness, overlying the Nohi Rhyolite. It is notable that the lower part of sediments contains gravels derived from the Nohi Rhyolite, whereas the upper part contains several different kinds of gravels originated from the Nohi Rhyolite, granites and basalts (K-Ar age: 2.08 ± 0.3 Ma). The lithology of gravels indicates different provenance of sediments in the lower and upper parts. Eight sediment samples and 10 bedrock samples (Naegi-Agematsu Granite, Nohi Rhyolite) were taken for ESR measurements. Quartz grains were extracted from all samples by chemical treatments. All samples were irradiated by ^{60}Co-gamma ray to a dose of 2.5 kGy at Takasaki Advanced Radiation Research Institute to saturate the ESR signal intensities of quartz. Al and Ti-Li center signals were measured with a microwave power of 5 mW at 77 K using an ESR spectrometer (JES-X320, JEOL RESONANCE Inc).

As shown in Fig. 1, ESR properties of the lower part of the sediments (Samples F-1, F-2, F-5 and F-7) are similar to that of the Nohi Rhyolite (samples 22-a1, 22-a2 and 17), and the properties of the upper part (Samples F-11, F-12, F-13 and F-14) are similar to the granitic rocks of Sanyo belt (Naegi-Agematsu Granite; samples 8, 12, 15 and 16). The results of ESR measurements correspond with the composition of gravels obtained from outcrop observation. To distinguish among bedrocks, Ti-Li center signal intensity may give more effective information compared with Al center signal intensity. These results so far indicate that ESR properties of quartz grains extracted from sediments have kept those from the original rocks and raise the possibility that sediment provenance can be estimated by quartz ESR properties.

This study was partially supported by the R&D supporting program for developing geological disposal technology of Ministry of Economy, Trade and Industry of Japan.

References

1) H. Ohmori, Bull. Depart. Geography, University of Tokyo, **10**, 31-85 (1978).
2) A. Shimada *et al.*, Geochronometria, **40**, 334-40 (2013).
3) M. Duttinea *et al.*, Comptes Rendus Geoscience, **334**, 949-55 (2002).

Sediments		Al	Ti-Li
upper part	F-13	22.41	1.91
	F-12	22.07	1.94
	F-11	21.67	1.78
	F-14	22.42	1.62
lower part	F-7	23.87	3.04
	F-5	22.66	2.62
	F-2	24.84	2.67
	F-1	20.37	2.51

Bedrocks	Al	Ti-Li
Naegi-Agematsu Granite (16)	12.71	1.65
Naegi-Agematsu Granite (15)	14.56	1.66
Naegi-Agematsu Granite (12)	20.14	0.66
Naegi-Agematsu Granite (8)	15.64	2.52
Nohi Rhyolite (17)	12.27	2.91
Nohi Rhyolite (22-a2)	18.55	2.37
Nohi Rhyolite (22-a1)	19.78	2.28

Fig. 1 Bar graph of Al and Ti-Li center signal intensities of quartz grains.

3-33 Provenance Changes Associated with Variations in East Asian Summer Monsoon Precipitation Pattern Recorded in the Inner Shelf Deposit of East China Sea during the Middle to Late Holocene

K. Wang [a)], R. Tada [a)], K. Saito [a)], H. Zheng [b)] and T. Irino [c)]

[a)] University of Tokyo, [b)] Nanjing Normal University, [c)] Hokkaido University

Hydroclimate variations associated with the East Asian Summer Monsoon (EASM) precipitation exert significant impacts on lives of people inhabiting within the Yangtze River drainage. Seasonal shift of main precipitation area is attributable to migration of the northern limit of summer monsoon, which would lead to provenance and composition changes of suspended materials transported by the Yangtze River. Therefore, the interannual- to millennial-scale variability in the position of the rain belt mentioned above could be recorded as the long-term changes in compositional variation of the sediment originated from the suspended materials of the Yangtze River. The subaqueous Yangtze delta and East China Sea (ECS) shelf are primary sink of massive inputs of terrestrial materials from the Yangtze River. We could expect to recognize provenance changes in core sediments MD06-3040 taken from the inner shelf of ECS on the basis of the electron spin resonance (ESR) signal intensity and crystallinity index (CI) of quartz in the fine silt fraction in association with EASM precipitation variability.

Eighty bulk samples from core MD06-3040 covering last 6 kyr was selected for provenance study of quartz grains. After pretreatment, samples were separated into 4-16 μm and 16-63 μm fractions using the syringe and pipette methods. ESR and CI were determined for these two grain size fractions. The ESR signal intensity of the E_1' center in quartz, an unpaired electron in a single silicon sp^3 orbit oriented along a bond direction into an oxygen vacancy[1)], was used to estimate the relative number of oxygen vacancies in quartz. Oxygen vacancies in quartz have been formed by natural radiation, and are known to reflect the age of the host rock[2,3)], which meant that higher value of ESR signal intensity of the E_1' center of quartz in the sediment reflects the older age of host rock (Fig. 1). Firstly, pretreated samples were irradiated with γ-radiation (total dose of 2.5 kGy) using a ^{60}Co source at the Inter-University Laboratory for the Joint Use of Japan Atomic Energy Agency Facilities. Subsequently, pretreated samples were heated at 300 °C for 15 minutes to convert the oxygen vacancies to E_1' centers[4)]. ESR signal intensity measurements were conducted at room temperature with an X-band ESR spectrometer JEOL JES-FA100 at University of Tokyo under 0.01 mW of microwave power, and 0.1 mT magnetic field modulation (100 kHz), 5 mT scan range, two minutes scan time, and 0.03 seconds time constant. Intensity of the E_1' centers was normalized to the quartz content of each sample to estimate the ESR signal intensity of pure quartz. The ESR signal intensity of quartz is expressed in spin units: one spin unit is equivalent to 1.3×10^{15} spins/g. The reproducibility of ESR signal intensity was ±1.5 spin units.

In order to discriminate the sediment contributions from the upper/middle/lower reaches, southern tributary of the Yangtze drainage, we compared the core MD06-3040 sediments samples with modern Yangtze River sediment samples. ESR vs CI plot suggests more precipitation in SE area of Yangtze catchment during 6~3.8 ka, in NW area from 3.8 to 2 ka, and in middle NE area during 2~1 ka, suggesting deepest penetration of EASM front during 3.8~2 ka.

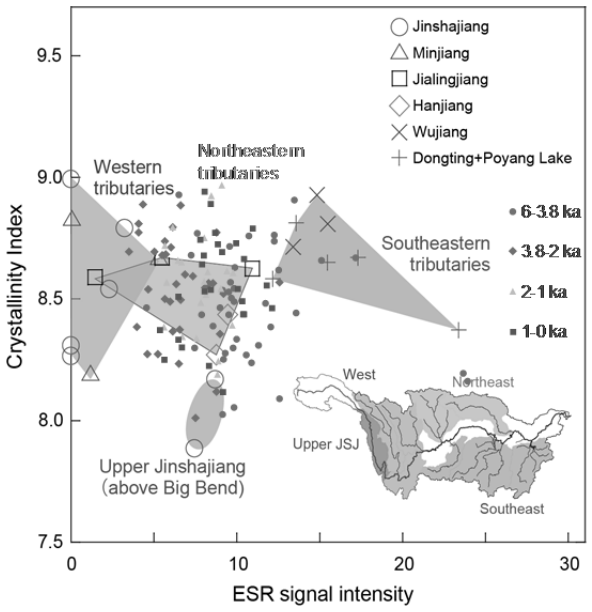

Fig. 1 The variability of ESR signal intensity and Crystallinity Index of quartz in MD06-3040 core.

References

1) F. J. Feigl *et al.*, Solid State Comm., **14**, 225-29 (1974).
2) S. Toyoda and M. Hattori, Appl. Radiat. Isot., **52**, 1351-56 (2000).
3) K. Nagashima *et al.*, Palaeogeography, Palaeoclimatology, Palaeoecology. doi:10.1016/j.palaeo.2006.11.027 (2007).
4) S. Toyoda and M. Ikeya, Geochem. J., **25**, 437-45 (1991).

3-34

ESR Dating of the Itoigawa-Shizuoka Tectonic Line Located at the Dondoko-sawa Outcrop in Japan South Alps Using Radiation Defect Centers

T. Fukuchi

Graduate Faculty of Interdisciplinary Research, University of Yamanashi

The risk of earthquake disaster caused along the northern extension of the Itoigawa-Shizuoka Tectonic Line (ISTL) in Japan South Alps has risen since the 2011 off the Pacific coast of Tohoku Earthquake. The northern extension is recognized as an active fault system, while the fault activity of the ISTL located in the central and southern parts of Japan South Alps has not been yet evaluated because no Quaternary sediment available for the assessment of fault activity exists in these parts. Thus I carry out ESR (Electron Spin Resonance) dating of fault gouge collected at the Dondoko-sawa outcrop in the northern-central part of Japan South Alps where the fault activity of the ISTL is unknown.

The ESR dating method is a technique to directly estimate the absolute age of fault movement using radiation defect centers (ESR signals) derived from forming minerals in fault rocks, assuming that the ESR signals have been once reset by frictional heating[1]. The ESR age (T) is obtained by dividing the total radiation dose (TD) by the annual radiation dose (D); T = TD/D. The TD to which the ESR signals have been subjected since the resetting is estimated by extrapolating the growth curve calculated from the ESR signal intensities before and after artificial γ-irradiation. In this study, artificial γ-irradiation was carried out with a ^{60}Co source at No.7 cell in γ-ray irradiation facility No.2, Takasaki Advanced Radiation Research Institute, JAEA.

The ESR signals that have been completely reset at the time of the latest fault movement give the actual age (T_a) of the latest fault movement. However, frictional heat does not always increase until the resetting temperature (≥450 °C), so that the ESR signals may have been incompletely reset. In this case, the TDs obtained may be overestimated and then the ESR ages obtained may become older than the actual age. Consequently, the ESR ages (T_{esr}) theoretically give the upper limit of the actual age ($T_a \leq T_{esr}$).

The ESR measurements show that the quartet signals (A, B, C and D signals) derived from montmorillonite and the E' and Al center in quartz are detected from the black and gray fault gouges collected at the Dondoko-sawa outcrop[1]. The γ-irradiation effect on these ESR signals obtained from the black gouge is shown in Figs.1 and 2. The quartet signals and Al center regularly increase with increasing radiation dose, so that these ESR signals probably give precise TD values. As a result, the ESR age of 0.49 ± 0.09 Ma (Coefficient of determination R=97.4%) is obtained from the black gouge using the hyperfine structure (hfs: g=2.0187) of the Al center in quartz, which is easiest reset by frictional heating. On the other hand, the whole and hfs of the Al

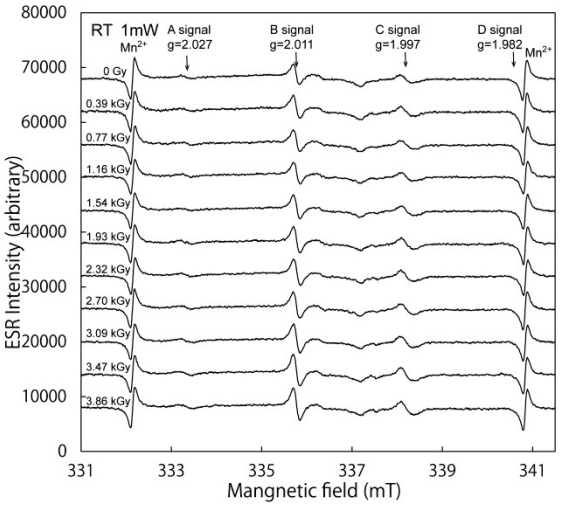

Fig. 1 Gamma-irradiation effect on the quartet signals derived from montmorillonite in the black fault gouge.

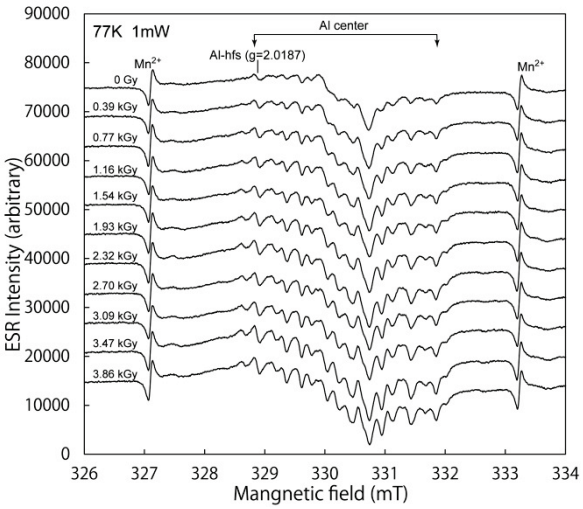

Fig. 2 Gamma-irradiation effect on the Al center in quartz in the black fault gouge.

center detected from the gray gouge give the ESR age of 0.50 ± 0.06 Ma (R=99.3%) and 0.62 ± 0.10 Ma (R=96.7%), respectively. I conclude that the age (T_a) of the latest fault movement at the Dondoko-sawa outcrop is estimated as $T_a \leq 0.49 \sim 0.50 \pm 0.09$ Ma. This conclusion means that the ISTL around the Dondoko-sawa outcrop is still active.

Reference

1) T. Fukuchi, "ESR dating of fault movement- Its principle and practice". Fukadaken Library, **63**, 45 pp (2004).

Part II

4. Status of Quantum-Beam Facilities

4-01 Utilization Status at TIARA Facility

H. Hanaya [a)], K. Hirota [a)], H. Takizawa [a)],
H. Kaneko [b)], S. Kaneya [b)], T. Asai [b)], M. Kawabata [b)] and K. Saga [b)]

[a)] Department of Advanced Radiation Technology, TARRI, QST,
[b)] Takasaki Establishment, Radiation Application Development Association

1. Research & Industrial Use

There are four accelerators, a cyclotron, and three electrostatic accelerators (a tandem, a single-ended accelerator, and an ion implanter), at the TIARA facility to meet various research needs. Research activities for the cyclotron for the past 5 years are shown in Fig. 1. Total utilization time is ranging from 2,200 to 2,300 hours. This time is equal to more than 95% of available time of the cyclotron. The trend of research activities at the TIARA has been slowly changing recently. The item of "Shared & common use", "base technology", and "Biotechnology & medical application" are the highest 3 areas for TIARA users. In contrast, utilization time of "RI production and nuclear science" has been decreasing for the past 4 years.

When we see the research activities for the three electrostatic accelerators, the profile of total utilization time is different from that of the cyclotron, as shown in Fig. 2. The utilization time of "base technology" accounts for more than 40% of the total time.

Relatively lower energy irradiation probably meets demand from researchers who study fundamental phenomena of materials under irradiation, elemental analysis and so on. The trend on high demand is also the case with "Inorganic material", "Nuclear and fusion materials", and "Semiconductor devices".

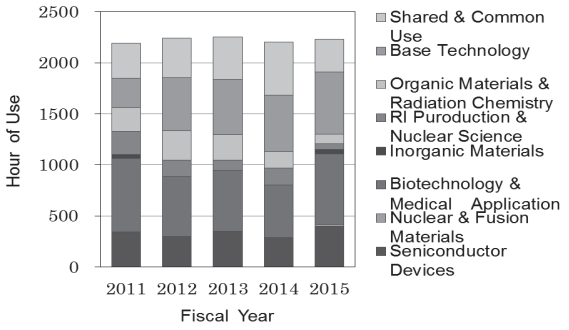

Fig. 1 Status of utilization for cyclotron for the past 5 years.

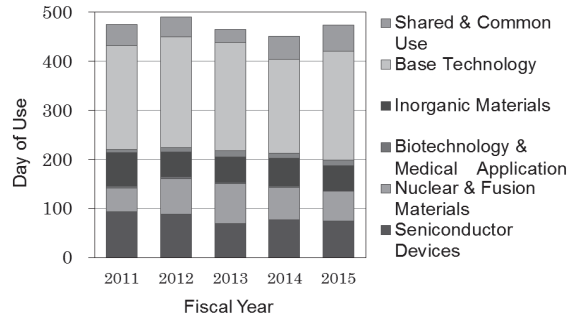

Fig. 2 Status of utilization for the three electrostatic accelerators for the past 5 years.

The trend of the number of users in the past 5 years is shown in Fig. 3. The total number of users has increased year by year from 2011 to 2014. However, it reduced to about 826 in 2015. The average number of users in the past 5 years is 847.

The change of project category in the past 5 years is shown in Fig. 4. Internal use by aggregating problems of the same research has decreased. However, shared & common use is increasing. The total number of projects is ranging from 120 to150.

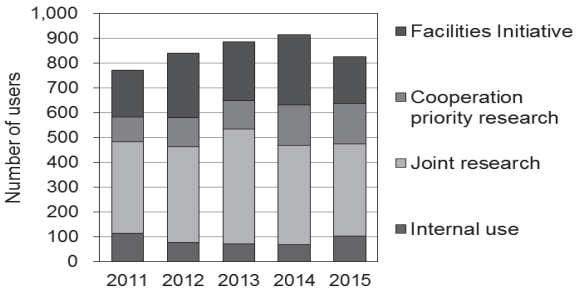

Fig. 3 The number of users for the past 5 years.

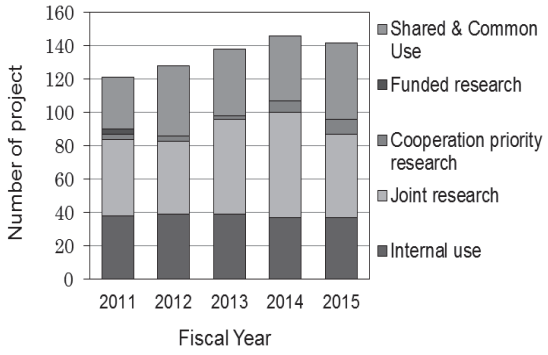

Fig. 4 The number of projects for the past 5 years.

2. The others

Tenth Takasaki Advanced Radiation Research Symposium was held successfully in October 8 and 9, 2015 at Takasaki Advanced Radiation Research Institute. The number of oral presentations and poster sessions was 17 and 146, respectively. The number of participants of the symposium was 480, and decreased by 16 in comparison with last meeting.

Furthermore, the JAEA Takasaki annual report 2014 including 169 research papers was issued the same as before. About 650 compact discs were distributed to relevant departments.

4-02 Operation of the AVF Cyclotron

I. Ishibori [a)], S. Kurashima [a)], K. Yoshida [a)], T. Yuyama [a)], T. Ishizaka [a)], N. Miyawaki [a)], H. Kashiwagi [a)], Y. Yuri [a)], S. Okumura [a)], T. Nara [a)], To. Yoshida [b)], Tu. Yoshida [b)], S. Ishiro [b)], S. Kanou [b)], K. Takano [b)], H. Saitoh [b)], K. Akaiwa [b)] and K. Nojiri [b)]

[a)] Department of Advanced Radiation Technology, TARRI, QST, [b)] Beam Operation Service, Co., Ltd.

Operation

The AVF cyclotron was smoothly operated in fiscal 2015. The accumulative operation time was 78,164 hours and the total number of experiments was 11,354 from the first beam extraction in 1991 to March 2016.

Table 1 shows the statistics of the cyclotron operation of fiscal 2014 and 2015. The total operation time amounted to 3,089 hours, and monthly operation times are shown in Fig. 1.

Table 1 Statistics for cyclotron operation.

	2014	2015
Beam service time (h)	2302	2304
Machine tuning (h)	646	732
Beam development (h)	29	53
Total operation time (h)	2997	3089
Change of particle and/or energy	212 times	248 times
Change of beam course	249 times	328 times
Change of harmonic number	73 times	86 times
Experiments	502	514
Cancellation due to machine trouble	1	5

The percentages of operation time of the year used for regular experiments, facility use program and promotion of shared use program, beam tuning, and beam development are 64.3%, 10.3%, 23.7%, and 1.7%, respectively. There were 5 cancellations of the experiments, which were caused by the machine troubles. Fractional distribution of major ions used for experiments is shown in Fig. 2.

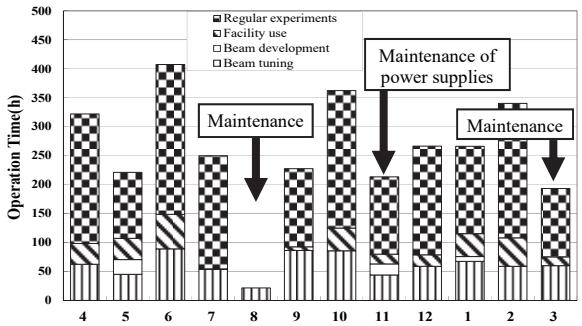

Fig. 1 Monthly operation times in fiscal 2015.

Maintenance

The regular yearly overhaul and maintenance were carried out. The major items were as follows: 1) Replacement of the contact fingers of the cyclotron RF resonator, 2) Routine maintenance of the power supplies, 3) Inspection of sinusoidal wave chopping system, 4) Inspection of power supplies of the beam scanner for LD and HY courses, 5) Renewal of the control system of the injection beam line equipment, 6) Exchange of the vacuum control PLC units for the No.1 and 3 heavy ion rooms.

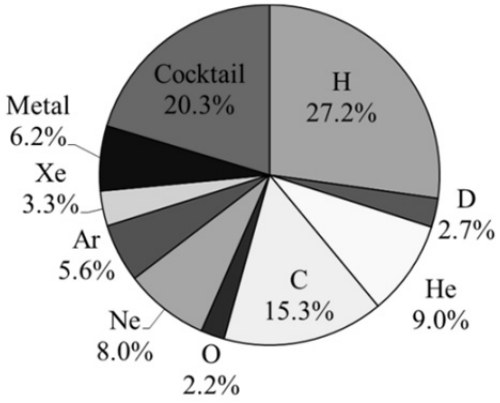

Fig. 2 Ion species used for experiments in fiscal 2015.

Technical Development

A MULTICUSP ion source had been used for generation of light ion species since 1991. The ion source was replaced to an electron cyclotron resonance ion source (NANOGAN, Pantechnik) as shown in Fig. 3 in May. A series of beam generation tests was immediately performed; 10, 20, 65 MeV H^+, 50 MeV D^+, and 50 MeV $^4He^{2+}$ were accelerated successfully.

Ion beams extracted from the cyclotron was sometimes unstable since the magnetic field was unstable especially for the case of low magnetic field excitation. We tried to suppress the magnetic field variation by using an additional correction coils and a nuclear magnetic resonance probe, and instability of the ion beam was improved as a result.

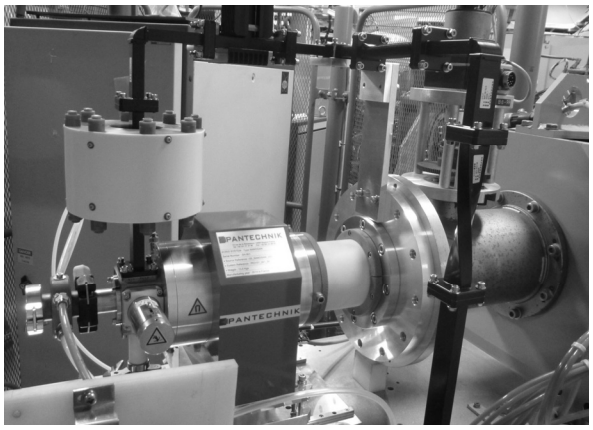

Fig. 3 NANOGAN ion source.

4-03 Operation of Electrostatic Accelerators in TIARA

A. Chiba [a)], K. Yamada [a)], A. Yokoyama [a)], A. Usui [a)], Y. Ishii [a)],T. Satoh [a)], T. Ohkubo [a)], T. Nara [a)], T. Takayama [b)], S. Kanai [b)],Y. Aoki [b)], M. Hashizume [b)], Y. Takahashi [b)] and M. Hasegawa [b)]

[a)] Department of Advanced Radiation Technology, TARRI, QST,
[b)] Beam Operation Service, Co., Ltd

1. Operation and Status

In fiscal year of 2015, the operating rate of 100% had been achieved in the tandem accelerator and in the ion-implanter; on the other hand, some experiments using the single-ended accelerator had been cancelled due to a trouble of the ion source. The fiscal operating times of the tandem accelerator, the single-ended accelerator and the ion implanter were 1,976, 2,431 and 1,760 hours, respectively, in the same levels with usual years. The accumulated operating time since the first operation of these accelerators had been achieved at 44,648, 51,175 and 39,627 hours, respectively. The monthly operating times of these accelerators are shown in Fig. 1. The scheduled maintenances for about two weeks were carried out in August, December and March. The accelerators were shut down for one week in August due to a planned power outage for the inspection of the facilities. The utilization rates of each ion species in the tandem accelerator are shown in Fig. 2. The utilization rate of the C_{60} ion beam was remarkable increase in recent years, as a result of intensification of its beam current provided by the tandem accelerator.

2. New Beams

In the ion-implanter, a Cs ion beam became available using a Freeman type ion source with the oven method. In this method, CsCl or CsI is useable as a sample. The Cs ion beam was required for the research on the fission products from the nuclear fuel. Figure 3 shows the ion mass spectrum of the beam extracted from the ion source, accelerated with a total voltage of 200 kV.

3. Maintenance and Improvement

In recent years, the number of troubles in the electrostatic accelerators has a tendency to increase, while the maintenance cost is reduced yearly. Serious troubles occurred in the single-ended accelerator. An efficiency of the beam transportation significantly decreased owing to a malfunction of the beam-focusing system of the ion source, because of a disconnection of the coil in a variable autotransformer adjusting the voltage supplied to the Einzel lens. Five experiments were canceled by this trouble.

The serious troubles also happened in the tandem accelerator. For instance, several devices constituting of the beam line got into uncontrollable condition because of the damage of CAMAC interfaces, and a malfunction of the corona probe worsened the stability of the acceleration voltage, moreover several computers of the control system were crashed one after another.

In the ion-implanter, a pulsed beam is used for the experiments on a secondary ion mass spectrometry. In order to further improve the mass resolution, a new beam-chopping system was installed to the IE line, and the pulse width was reduced to approximately one third as compared to previous one.

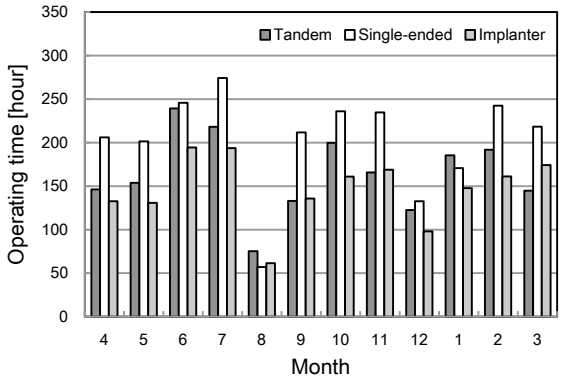

Fig. 1 Monthly operating times of electrostatic accelerators in FY 2015.

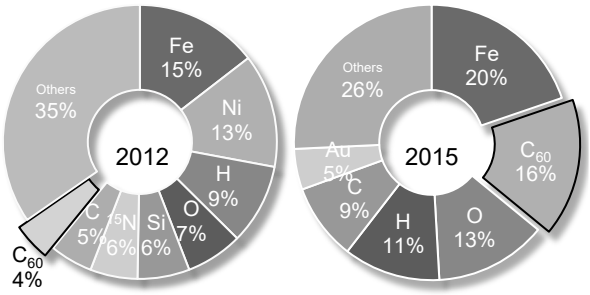

Fig. 2 Utilization rates of ion species in tandem accelerator in FY 2012 and in FY 2015.

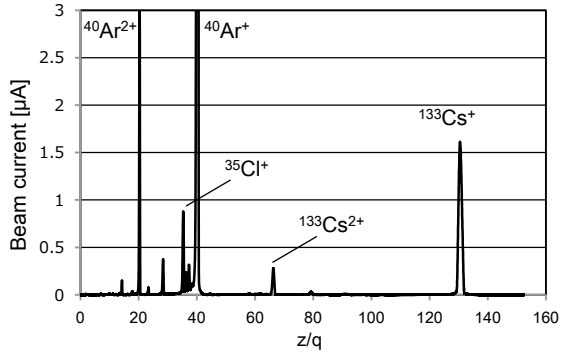

Fig. 3 Ion mass spectrum of a beam generated by the ion-implanter, in the use of a powdered CaCl sample.

4-04

Operation of the Electron Accelerator and the Gamma-ray Irradiation Facilities

T. Agematsu[a)], S. Uno[a)], R. Yamagata[a)], H. Seito[a)], Y. Nagao[a)], S. Yamasaki[a)], I. Kawashima[b)], N. Yagi[b)], M. Takagi[b)] and K. Nagai[b)]

[a)] Department of Advanced Radiation Technology, TARRI, QST,
[b)] Takasaki Establishment, Radiation Application Development Association

1. Operation

The ^{60}Co gamma-ray irradiation facilities were operated approximately smoothly, whereas the electron accelerator was not able to operate on schedule in FY 2015, because of trouble with high-voltage equipment in November and repairs on trouble of FY2014. As a result, the rate of operation of the electron accelerator had dropped to 80% in this fiscal year.

The electron accelerator was on service as scheduled 9:00-17:30 from Monday to Friday since April 2014 for effective operation, while the service time in FY 2013 was 8:30-23:00 on several days of week. The annual operation time of the electron accelerator in FY 2015 was 659 h, including 169 h of conditioning operation during maintenance. The operation time in recent years is shown in Fig. 1. There were a lot of trouble and the reduction of operation time in FY 2014 and FY 2015. Furthermore, a long-period irradiation for the study on semiconductors also decreased, and the annual operation time was down in FY 2014 and FY 2015 compared with in FY 2013.

The ^{60}Co gamma-ray irradiation facilities consisting of three buildings with eight irradiation rooms cover a wide dose-rate range from 10^{-1} Gy/h to 10^{4} Gy/h as of January 2016. The annual operation times of the first and the second cobalt irradiation facilities and the food irradiation facility were 20,657 h, 15,272 h and 13,113 h, respectively, as shown in Fig. 2.

2. Maintenance

2.1 Electron accelerator

The transformer and the resistances at the high-voltage circuit in the accelerator vessel were troubled in November 2015, and were renewed. The steering coil within the beam scanner of the horizontal beam line, which was stripped in 2014 to use for repair on the scanner of the vertical beam line, was replaced with new one in February 2016, and operation of the horizontal beam line was recovered. The optical link circuit for beam currents control, the motor-generator rods and the rod's coupling part in the accelerator vessel, were damaged and renewed in March 2016.

2.2 Gamma-ray irradiation facilities

The periodical maintenance check mainly on mechanical system for radiation source transportation is performed every year on one of the three gamma-ray irradiation facilities in turn. The maintenance check of the first irradiation facility was done in August and September 2015 with suspension of operation for nineteen days.

The new ^{60}Co sources, whose total radioactivity was 0.74 PBq, were loaded into the irradiation room No.7 in the second irradiation facility to increase the area of high-dose-rate fields. Forty pencil sources of ^{60}Co sources were disposed of to Japan Radioisotope Association (JRIA).

The 5 m^3 hydrochloric acid vessel and 5 m^3 sodium hydroxide vessel which were used for the purifier system of the pool water of the three gamma-ray irradiation facilities, were damaged and renewed in February 2015. These vessels were downsized from 5 m^3 to 2 m^3, because the necessary ability of the water purifier system decreased by reuse of water which was stored in the pool-water tank.

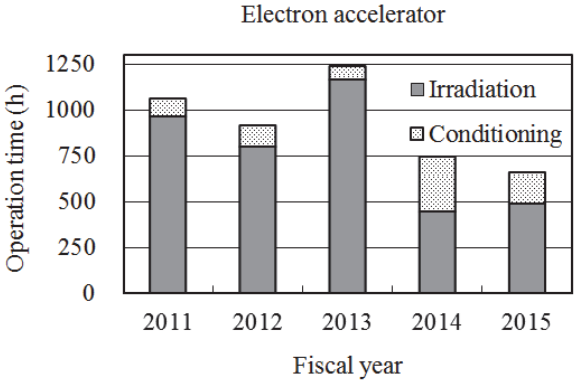

Fig. 1 Annual operation time of the electron accelerator.

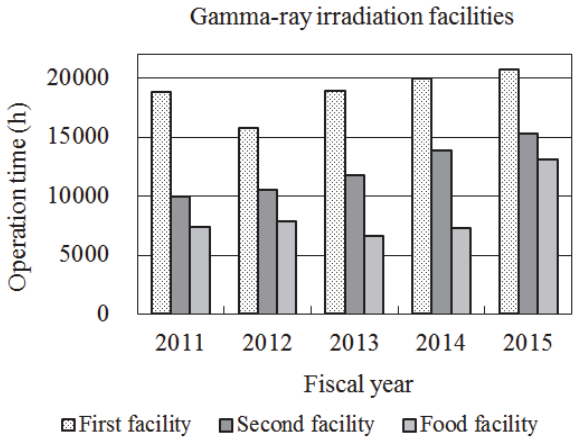

Fig. 2 Annual operation times of the ^{60}Co gamma-ray irradiation facilities.

4-05

Utilization Status of the Electron Accelerator and the Gamma-ray Irradiation Facilities

T. Agematsu [a)], S. Uno [a)], R. Yamagata [a)], H. Seito [a)], Y. Nagao [a)], S. Yamasaki [a)], I. Kawashima [b)], N. Yagi [b)], M. Takagi [b)] and K. Nagai [b)]

[a)] Department of Advanced Radiation Technology, TARRI, QST,
[b)] Takasaki Establishment, Radiation Application Development Association

The electron accelerator and the three gamma-ray irradiation facilities were operated for various research subjects according to the operation plans in FY 2015.

The irradiation time and the number of irradiation experiments for each facility in FY 2015 are shown in Table 1. The accelerator mainly served for graft-polymerization for new material development, radiation effect studies on semiconductors and various experiments of visiting users. The first cobalt irradiation facility mainly served for radiation-resistance testing of cables used in nuclear power plants and nuclear reactor facilities with long period irradiation. The second cobalt irradiation facility, including the irradiation room No.6 operated on hourly schedule, mainly served for development of new functional materials and other research subjects of visiting users. The food irradiation facility has a lower-dose-rate field, and served for radiation resistance testing at wide dose-rate range.

Figure 1 shows the number of irradiation experiments in each research field for each facility in FY 2011-2015. The accelerator had some trouble with high-voltage parts, and was repaired in FY 2015. Therefore the number of irradiation experiments for electron accelerator was on a low level as in FY 2014. On the other hand, the number of irradiation experiments for the gamma-ray irradiation facilities kept on the same level as in FY2014.

Among these irradiation experiments, 78 and 191 ones performed at the electron accelerator and the gamma-ray irradiation facilities, respectively, were relevant to recovery from the accident at the Fukushima Daiichi Nuclear Power Station of Tokyo Electric Power Company.

Table 1 The irradiation time and the number of irradiation experiments for each facility in FY 2015.

Facility / Research fields	Electron accelerator		Gamma-ray irradiation facilities	
	Irradiation time (h)	Number of irradiation experiments	Irradiation time (h)	Number of irradiation experiments
Material processing	85	96	5,821	280
Heat-resist materials	64	35	945	2
Materials for space	234	58	7,217	63
Nuclear facilities	4	1	62,885	127
Environment	0	0	0	0
Resources & Bio-technology	0	0	1,517	111
Basic technology	207*	10	7,393	39
Joint use	65	27	48,403	223
Total	659	227	134,179	845

* The irradiation time of 'Basic technology' in the electron accelerator includes 169 h of conditioning operation during maintenance.

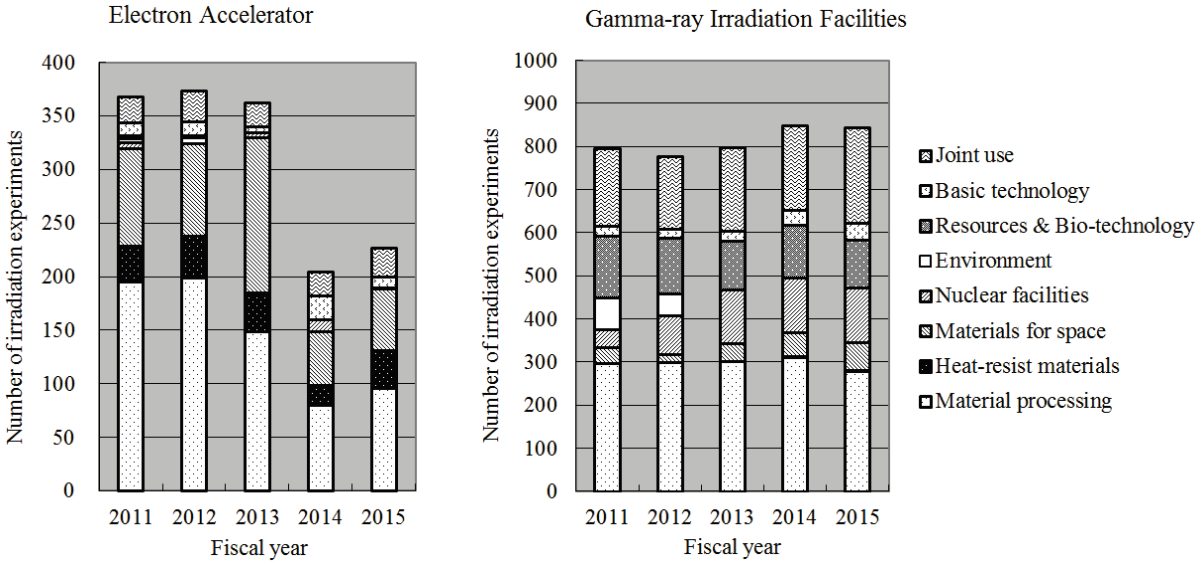

Fig. 1 The number of irradiation experiments (FY 2011-2015).

4-06

Radiation Monitoring in TIARA

Safety Management Section

Department of Administrative Services, TARRI, QST

1. Individual monitoring

(1) Individual monitoring for the radiation workers

Table 1 shows a distribution of effective dose of the radiation workers in FY 2015. The effective dose values of almost all radiation workers were below the detection limit of 0.1 mSv.

The maximum dose of the radiation workers was 0.5 mSv/y in connection with the experiment about production and labeling of unsealed radioisotopes.

Table 1 Distributions of the effective dose of the radiation workers in FY 2015.

Items		Number of persons in each periods				
		1st quarter	2nd quarter	3rd quarter	4th quarter	Annual
Distribution range of effective dose HE:Effective dose *1 (mSv)	HE < 0.1	469	507	495	507	618
	0.1 ≦ HE ≦ 1.0	3	2	2	4	7
	1.0 < HE ≦ 5.0	0	0	0	0	0
	5.0 < HE ≦ 15.0	0	0	0	0	0
	15.0 < HE	0	0	0	0	0
Total number of persons (A)		472	509	497	511	625
Exposure above 1mSv	Number of persons (B)	0	0	0	0	0
	(B)/(A)×100(%)	0	0	0	0	0
Mass effective dose (Person・mSv)		0.6	0.4	0.3	0.7	2.0
Mean dose (mSv)		0.00	0.00	0.00	0.00	0.00
Maximum dose (mSv)		0.3	0.2	0.2	0.2	0.5

*1 The dose by the internal exposure was not detected.

(2) Individual monitoring for the visitors and others

Table 2 shows the number of people who temporarily entered the radiation controlled areas. The effective doses of all people were less than 0.1 mSv.

Table 2 The number of people who temporarily entered the radiation controlled areas in FY 2015.

Periods	1st quarter	2nd quarter	3rd quarter	4th quarter	Total
Number of persons	816	1207	1343	1440	4806

2. Monitoring of radioactive gases and dusts

Table 3 shows the maximum radioactive concentrations and total activities for radioactive gases released from the stack of TIARA, during each quarter of FY 2015.

Small amounts of ^{41}Ar and ^{11}C were detected occasionally during the operation of the cyclotron or experiments, but the particulate substances (^{65}Zn, etc.) were not detected.

Table 3 Monitoring results of released radioactive gases and dust in FY 2015.

Nuclide	Items \ Periods	1st quarter	2nd quarter	3rd quarter	4th quarter	Total
^{41}Ar	Maximum concentration	5.7×10^{-4}	$<1.4\times10^{-4}$	$<1.4\times10^{-4}$	1.5×10^{-4}	
	Activity	1.8×10^{9}	0	3.4×10^{8}	4.8×10^{8}	2.6×10^{9}
^{11}C	Maximum concentration	$<1.4\times10^{-4}$	$<1.4\times10^{-4}$	$<1.4\times10^{-4}$	$<1.4\times10^{-4}$	
	Activity	4.2×10^{7}	1.4×10^{8}	2.9×10^{8}	2.1×10^{8}	6.8×10^{8}
^{65}Zn	Maximum concentration	$<4.3\times10^{-10}$	$<5.2\times10^{-10}$	$<5.4\times10^{-10}$	$<4.8\times10^{-10}$	
	Activity	0	0	0	0	0

Unit : Bq/cm^3 for Maximum concentration, Bq for Activity.

3. Monitoring for external radiation and surface contamination

The monitoring for external radiation and surface contamination was routinely performed in/around the radiation controlled areas. Neither anomalous value of dose equivalent rate nor surface contamination was detected.

Figure 1 shows a typical example of distribution of the dose equivalent rate in the radiation controlled area of the cyclotron building.

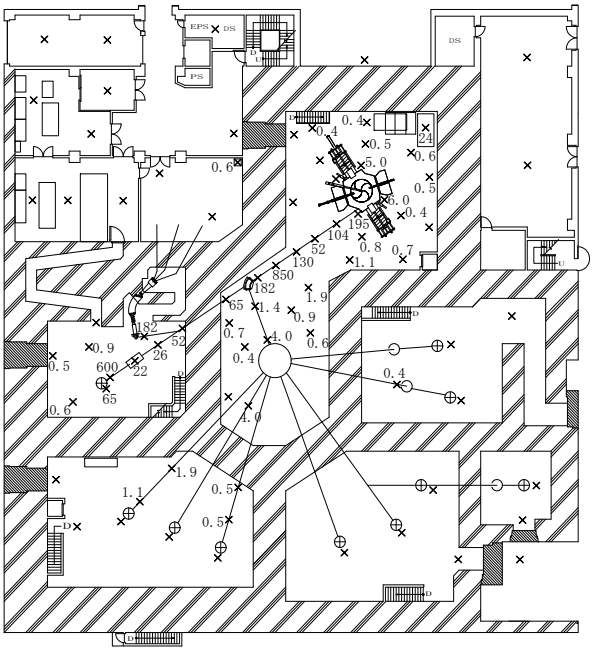

Fig. 1 Dose equivalent rate distribution in the radiation controlled area of the cyclotron building.
Measurement date : 17th, 28th and 30th March 2016,
Measuring position : Indicated with × (1 m above floor),
Unit : μSv/h.
(The values are not indicated if less than 0.2 μSv/h.)

4-07 Radioactive Waste Management in TIARA

M. Nabatame and N. Higuchi

Department of Administrative Services, TARRI, QST

1. Radioactive wastes management

The radioactive wastes generated in TIARA are managed by Utilities and Maintenance Section. The main radioactive wastes are the solid wastes generated from research experiments and the maintenance of the cyclotron. Other radioactive wastes are the liquid wastes such as inorganic waste fluids generated from research experiments and the air-conditioning machines in radiation controlled area. These wastes are managed according to their properties.

2. Solid radioactive waste

Table 1 shows the amounts of solid wastes at various properties and kinds generated in each quarter of FY 2015. The main solid waste is also generated from research experiments and the maintenance of the cyclotron.

Combustible wastes are rubber gloves, paper, and clothes, etc. Incombustible wastes are metal pieces, the glasses, and contaminated parts.

3. Liquid radioactive waste

Table 2 shows the amounts of liquid wastes generated in each quarter of FY 2015. Most of liquid waste was inorganic waste water generated from chemical experiments and condensed water from operation of air conditioning units installed in each room of the radiation controlled area. The largest quantity of waste water in summer season (2nd quarter) is mainly due to condensed water. After treatment by evaporation, inorganic water is reused in the radiation controlled area. Only small amounts of concentrated liquid are generated from the evaporation.

Table 1 Radioactive solid wastes generated in FY 2015.

Amounts / Items	Amounts of generation in each period (m^3)					Number of package /drum
	1st quarter	2nd quarter	3rd quarter	4th quarter	Total	
Category A*	0.37	0.34	0.04	0.70	1.45	13**
1)Combustible	0.14	0.20	0.02	0.32	0.68	6**
2)Incombustible	0.23	0.14	0.02	0.38	0.77	7**
Compressible	0.10	0.14	0.02	0.38	0.64	-
Filters	0.13	0	0	0	0.13	-
Incompressible	0	0	0	0	0	-
Ion exchange resin	0	0	0	0	0	-
Category B*	0	0	0	0	0	0

* defined by dose at the outer surface of container : (A) $<$ 2 mSv/h $\leqq$ (B),
** 200-liter drum.

Table 2 Radioactive liquid waste generated in FY 2015.

Amounts / Items	Amounts of generation in each period (m^3)					Number of package /drum
	1st quarter	2nd quarter	3rd quarter	4th quarter	Total	
Category A*	14.67	26.51	5.04	6.67	52.89	
1)Inorganic	14.67	26.51	5.04	6.67	52.89	treatment
2)Organic	0	0	0	0	0.0	0
Organic	0	0	0	0	0.0	0
Oil	0	0	0	0	0.0	0
3)Sludge	0	0	0	0	0.0	0
4)Evaporation residue	0	0	0	0	0	0
Category B*	0	0	0	0	0	0

* defined by concentrations in Bq/cm^3 (β, γ) : (A) $< 3.7 \times 10 \leqq$ (B) $< 3.7 \times 10^4$.

4-08

Facility Use Program in Takasaki Advanced Radiation Research Institute

R. Nakahara, H. Hanaya, M. Negishi, K. Hirota and H. Takizawa

Department of Advanced Radiation Technology, TARRI, QST

1. Introduction

The facilities of JAEA are widely opened to many outside researchers in universities, public institutes, industries, and so on. FACILITY USE PROGRAM started in 2006, which is for users' service on fee-charging basis in the use of facilities. The facilities used in the program at Takasaki are Co-60 Gamma-ray Irradiation Facilities, Electron Accelerator, TIARA's accelerators, and some of the off-line analysis instruments.

In the program, the Research Proposals from outside researchers, that is applicants, are examined carefully every half a year from the points of the availability and the validity of the experimental plans by the special committee. The applicants who passed the examination can use the facilities and some of the off-line analysis instruments on fee-charging basis. The fee includes handling, irradiation, and expendable fees, radioactive waste disposal expenses, and the additional charge. Applicants who can disclose experimental results are exempt from the irradiation fee, but should submit the report of the experimental results to JAEA. The reports are published in the annual report. Applicants of universities can also apply to the facility's usage through another program operated by The University of Tokyo. Table 1 shows main classification of Facility Use Program.

Table 1 Main classification of Facility Use Program.

Purpose	Research and Development			Except R&D
Classification	General		Priority case	Commercial
Result	Non-proprietary	Proprietary		
Referee	Yes	No		
Charge*	A	B		C

*A = handling fees + the expendables fee + radioactive waste disposal expenses,
B = handling fees + the irradiation fee,
C = handling fees + the irradiation fee + depreciation.

2. Use in FY2015

There were 17 applications of Research Proposals in FY2015 at Takasaki Institute, and 12 of them were as Non-proprietary use. Including the users from priority case and others, 300 applications were accepted. Table 2 and Fig. 1 show user's classification for each facility and distribution of classification for Facility Use Program.

Table 2 Classification of applications for each facility.

Facility \ User		University	Public Institute	Industries and others	Total
TIARA	AVF cyclotron	13	3	17	33
	3MV tandem accelerator	14	1	3	18
	3MVsingle-ended accelerator	3	0	0	3
	400kV ion implanter	7	0	0	7
Co-60 gamma-ray irradiation facilities		30	10	173	213
Electron accelerator		12	0	14	26
Total for each classification		79	14	207	300

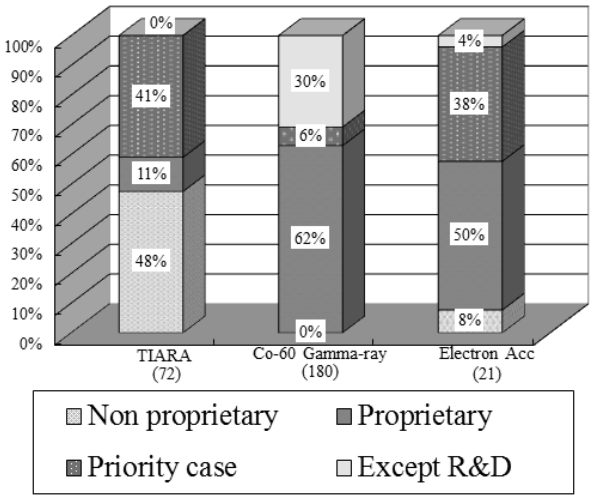

Fig. 1 Distribution of classification for Facility Use Program. The number of theme for each facility is shown in parentheses.

3. Public Relations

The detailed information on the program is available on JAEA website as follows:
http://www.qubs.qst.go.jp/kyoyo/index.html

The "Advanced-research base common use and a platform formation enterprise", which is one of the subsidiary projects of the Ministry of Education, Culture, Sports, Science and Technology (MEXT) in Japan, has been cooperated from FY2015. This project is expected to promote researches and developments of cutting-edge technologies and create new innovation in Japan.

Appendices

Appendix 1　Publication list

Items in gray show the works in collaboration with other projects of QST.
Bold letters and **numbers** at the last of each item mean as follows.
Letter : Accelerators or irradiation facilities used for the work.
C : Cyclotron, **T** : Tandem accelerator, **S** : Single-ended accelerator, **I** : Ion implanter,
E : Electron accelerator, **G** : Gamma-ray irradiation facilities, **N** : Not used.
Number : The number of the related paper in Part II.

Functional Polymer Research Project（P1-1）

Papers

1) T. Hamada, S. Hasegawa, H. Fukasawa, S. Sawada, H. Koshikawa, A. Miyashita and Y. Maekawa, "Poly(ether ether ketone) (PEEK)-based graft-type polymer electrolyte membranes having high crystallinity for high conducting and mechanical properties at various humidified conditions", J. Mater. Chem. A, **3**, 20983-91 (2015). **G**

2) Y. Zhao, K. Yoshimura, H. Shishitani, S. Yamaguchi, H. Tanaka, S. Koizumi, N. Szekely, A. Radulescu, D. Richter and Y. Maekawa, "Imidazolium-based anion exchange membranes for alkaline anion fuel cells: elucidation of the morphology and the interplay between morphology and properties", Soft matter, **12**, 1567-78 (2016). **G**

3) Y. Zhao and S. Koizumi, "Combining small-angle and intermediate-angle neutron scattering to study the hierarchical structure in microbial cellulose", Eur. Polym. J., **66**, 437-43 (2015). **N**

4) J. Sarapas, K. Saijo, Y. Zhao, R. Hayward, M. Takenaka and G. Tew, "Phase behavior and Li^+ ion conductivity of styrene-ethylene Oxide multiblock copolymer electrolytes", Polym. Adv. Tech., **27**, 946-54 (2016). **N**

5) F. Ghobadi, R. Letteri, S. S. Parelkar, Y. Zhao, D. Chan-Seng, T. Emrick and A. Jayaraman, "Dispersing zwitterions into comb polymers for non-viral transfection: An integrated experimental and molecular simulation study", Biomacromolecules, **17**, 546-57 (2016). **N**

Proceedings

1) Y. Maekawa, "Structure-property Relationships in Graft-type Polymer Electrolyte Membranes Studied by Complemental SAXS/SANS Analyses", Proc. 15th Int. Congr. Radiat. Res. (ICRR 2015), [Kyoto, Japan], 3-C1-OS-14-01 (2015). **G**

2) 渡邊 俊, 吉村 公男, 萩原 時男, 前川 康成, "4-ビニルイミダゾリウムを有するグラフト型アニオン伝導電解質膜の合成/同定とアルカリ耐性評価", 第64回高分子学会年次大会, [札幌], 要旨集 1K19 (2015). **G**

3) 澤田 真一, 長谷川 伸, 前川 康成, "放射線グラフト重合法と原子移動ラジカル重合法による新規電解質膜の作製", 第 64 回高分子学会年次大会, [札幌], 要旨集 1K14 (2015). **G**

4) 前川 康成, 趙 躍, 吉村 公男, 猪谷 秀幸, 山口 進, 田中 裕久, 小泉 智, "中性子/X 線小角散乱の相補利用によるグラフト型高分子電解質膜の構造/機能解析", 第 64 回高分子討論会, [仙台], 要旨集 1S19 (2015). **G**

5) 吉村 公男, 猪谷 秀幸, 山口 進, 田中 裕久, 前川 康成, "放射線グラフト型アニオン伝導電解質膜の開発と水加ヒドラジン燃料電池への応用", 第 64 回高分子討論会, [仙台], 要旨集 2S10 (2015). **G, 1-22**

6) 渡邊 俊, 吉村 公男, 萩原 時男, 前川 康成, "β 水素フリーイミダゾリウム基を有するグラフト型アニオン伝導電解質膜の合成と特性評価", 第 64 回高分子討論会, [仙台], 要旨集 2S09 (2015). **G**

7) 濱田 崇, 竹内 航太, 長谷川 伸, 前川 康成, "放射線リビンググラフト重合による固相中での精密高分子の合成と高分子電解質膜への応用", 第 64 回高分子討論会, [仙台], 要旨集, 1S18 (2015). **G**

8) 長谷川 伸, 阿佐美 進哉, 澤田 真一, 日野 聡, 磯部 繁人, 橋本 直幸, 前川 康成, "多孔膜への放射線グラフト重合法による水素選択透過膜の開発", 第 64 回高分子討論会, [仙台], 要旨集 3Pa089 (2015). **G, 1-21**

9) K. Yoshimura, H. Shishitani, S. Yamaguchi, H. Tanaka, Y. Maekawa, "Graft-Type Anion-Conducting Electrolyte Membranes Having Poly(2- imidazoliumylstyrene) Prepared By Radiation-Induced Grafting for Hydrazine Hydrate Fuel Cells", 228th ECS Meet., [Phoenix, USA], 1470 (2015). **G, 1-22**

10) 竹内 航太, 濱田 崇, 吉村 公男, 廣木 章博, 前川 康成, "放射線グラフト型アニオン電解質膜のアルカリ溶液中での分解挙動", 平成 27 年度日本化学会関東支部 群馬地区研究交流発表会, [前橋], 要旨集 P-63 (2015). **G**

11) 濱田 崇, 長谷川 伸, 前川 康成, "放射線グラフト重合を活用した水素選択透過膜の設計と合成", 平成 27 年度日本化学会関東支部 群馬地区研究交流発表会, [前橋], 要旨集 P-65 (2015). **G**

12) 長谷川 伸, 阿左美 進哉, 澤田 真一, 前川 康成, "放射線グラフト重合法による多孔性高分子膜を用いた水素選択透過膜の開発", 平成 27 年度日本化学会関東支部 群馬地区研究交流発表会, [前橋], 要旨集 P-66 (2015). **G, 1-21**

13) 澤田 真一, 長谷川 伸, 前川 康成, "放射線グラフト法と原子移動ラジカル重合法による新規電解質膜の作製", 平成 27 年度日本化学会関東支部 群馬地区研究交流発表会, [前橋], 要旨集 P-67 (2015). **G**

14) Beom-S. Ko, S. Hasegawa, K. Yoshimura, T. Hamada, S. Sawada, and Y. Maekawa, "Mechanism Study on Radiation- induced Graft Polymerization of fluorinated polymer", 平成 27 年度日本化学会関東支部 群馬地区研究交流発表会, [前橋], 要旨集 P-68 (2015). **G**

15) 渡邊 俊, 吉村 公男, 萩原 時男, 前川 康成, "放射線グラフト重合によるイミダゾリウム含有アニオン伝導電解質膜の合成", 平成 27 年度日本化学会関東支部 群馬地区研究交流発表会, [前橋], 要旨集 P-69 (2015). **G**

16) 吉村 公男, 猪谷 秀幸, 山口 進, 田中 裕久, 前川 康成, "白金フリー・アルカリ液体燃料電池自動車を指向した放射線グラフト型アニオン膜の開発－4-(イミダゾリウム-2-イル)スチレンモノマーの利用－", 平成 27 年度日本化学会関東支部 群馬地区研究交流発表会, [前橋], 要旨集 P-70 (2015). **G, 1-22**

17) 前川 康成, 趙 躍, 吉村 公男, 猪谷 秀幸, 山口 進, 田中 裕久, 小泉 智, "イミダゾリウム基を含むグラフト型アニオン伝導電解質膜のアルカリ燃料電池特性", 第 25 回日本 MRS 年次大会, [横浜], 要旨集 B1-I9-009 (2015). **G**

18) S. Sawada, S. Hasegawa, Y. Maekawa, "Preparation of proton exchange membranes by radiation-induced graft polymerization and atom-transfer radical polymerization methods", Euromembrane 2015, [Aachen, Germany], E-088 (2015). **G**

19) 澤田 真一, ウルシーノ クラウディア, ガリアーノ フランチェスコ, シモーネ シルビア, ドリオリ エンリコ, フィゴーリ アルベルト, "クエン酸エステルを溶媒として用いた熱誘起相分離法による PVDF 膜の作製", 膜シンポジウム 2015, [神戸], 要旨集 79-81 (2015). **N**

20) Y. Zhao, S. Koizumi, T. Kondo, "A crafty utilization of intermediate-angle neutron scattering and contrast variation by water-exchange to study the microstructure of microbial cellulose", JPS Conf. Proc., **8**, 033002, [Tsukuba, Japan] (2015). **N**

Patents

1) 越川 博, 八巻 徹也, 浅野 雅春, 前川 康成, ワラポンシンアナンワーニ, 山本 和矢, 山田 浩次, 山口 進, 田中 裕久, "アニオン交換膜", 登録 5736604 (2015.5.1).

2) 浅野 雅春, 前川 康成, 朴 俊, 工藤 一秋, 高山 俊雄, "耐熱性高分子電解質膜及びその製造方法", 登録 5757001 (2015.6.12).

3) 浅野 雅春, 前川 康成, 樋口 浩之, 大泉 新一, 江守 秀之, 橘 俊光, 森 恵一, 鈴木 弘世, "耐酸化性に優れたプロトン伝導性高分子電解質膜およびその製造方法", 登録 5776095 (2015.7.17).

Advanced Catalyst Research Project（P1-2）

Papers

1) S. Tsukuda, R. Takahashi, S. Seki, M. Sugimoto, A. Idesaki, M. Yoshikawa and S. Tanaka, "Fabrication of Pt nanoparticle incorporated polymer nanowires by high energy ion and electron beam irradiation", Radiat. Phys. Chem. **118**, 16-20 (2016). **C, 1-23**

2) M. Omichi, H. Marui, V. S. Padalkar, A. Horio, S. Tsukuda, M. Sugimoto and S. Seki, "Fabrication of thermoresponsive nanoactinia tentacles by a single particle nanofabrication technique", Langmuir **31**, 11692-700 (2015). **C**

3) Y. Takeshita, T. Sakurai, A. Asano, K. Takano, M. Omichi, M. Sugimoto and S. Seki, "Formation of nanowires from pentacene derivatives by single-particle triggered linear polymerization", Adv. Mater. Lett. **6**, 99-103 (2015). **C, 3-22**

4) H. L. Cheng, M. T. Tang. W. Tuchinda, K. Enomoto, A. Chiba, Y. Saitoh, T. Kamiya, M. Sugimoto, A. Saeki, T. Sakurai, M. Omichi, D. Sakamaki and S. Seki, "Reversible control of radius and morphology of fluorene-azobenzene copolymer nanowires by light exposure", Adv. Mater. Interfaces **2**, 1400450 (2015). **C, 3-22**

5) T. Kimata, S. Kato, T. Yamaki, S. Yamamoto, T. Kobayashi and T. Terai, "Platinum nanoparticles on the glassy carbon surface irradiated with argon ions", Surf. Coat. Tech., **306** (A), 123-26 (2016). **I, 1-14**

6) N. Nuryanthi, T. Yamaki, A. Kitamura, H. Koshikawa, K. Yoshimura, S. Sawada, S. Hasegawa, M. Asano, Y. Maekawa, A. Suzuki and T. Terai, "Ion-track grafting of vinylbenzyl chloride into poly(ethylene-co-tetrafluoroethylene) films using different media", Trans. Mater. Res. Soc. Jpn. **40,** 359-62 (2015). **C, 1-15**

7) 八巻 徹也, 小平 岳秀, 澤田 真一, 田中 伸幸, 久保 真治, 野村 幹弘, "放射線グラフト重合法による膜ブンゼン反応用カチオン交換膜の開発", 膜（MEMBRANE）**41**, 114-20 (2016). **E, G, 1-17**

8) A. Tekayama, A. Idesaki, M. Sugimoto and M. Yoshikawa, "Swelling of radiation-cured polymer precursor powder for silicon carbide by pyrolysis", J. Asia. Ceram. Soc., **3**, 402-06 (2015). **E, 1-26**

Proceedings

1) N. Nuryanthi, T. Yamaki, A. Kitamura, H. Koshikawa, M. Sugimoto, Y. Yuri, T. Yuyama, T. Ishizaka and T. Terai, "Fluence evaluation of large-area heavy ion beams in a high-fluence range", Proc. 25th Annu. Meet. Mater. Res. Soc. Jpn. (MRS-J), [Yokohama, Japan], E1-09-009 (2015). **C, 1-15**

2) M. Sugimoto, S. Tsukuda, S. Seki and T. Yamaki, "Investigation of platinum particles in poly(vinylpyrrolidone) nanofibers prepared by single nanofabrication technique", Proc. 25th Annu. Meet. Mater. Res. Soc. Jpn. (MRS-J), [Yokohama, Japan], E1-09-009 (2015). **C, 1-23**, **1-24**

3) T. Kimata, S. Kato, T. Yamaki, S. Yamamoto, T. Hakoda, T. Kobayashi and T. Terai, "Electrocatalytic properties of Pt nanoparticles on glassy carbon substrate pre-irradiated with Ar ions", Proc. 25th Annu. Meet. Mater. Res. Soc. Jpn. (MRS-J), [Yokohama, Japan], E1-09-012 (2015). **I**

4) H. Koshikawa and T. Yamaki, "Ion-track membrane of polyimide: LET dependence of track etch rates", Proc. 25th Annu. Meet. Mater. Res. Soc. Jpn. (MRS-J), [Yokohama, Japan], E1-09-013 (2015). **C, 1-13**

5) S. Yamamoto, A. Shimada, A. Miyashita and T. Hakoda, "RBS/channeling analysis of epitaxial Pt and Pd films irradiated with ^{60}Co γ-ray", Proc. 25th Annu. Meet. Mater. Res. Soc. Jpn. (MRS-J), [Yokohama, Japan], E1-09-006 (2015). **S, 1-28**

6) S. Yamamoto, M. Sugimoto, A. Miyashita, T. Hakoda, T. Yamaki and T. Mori, "Precipitation of Pt Nanoparticles on CeO_2 Films Using Electron Beams and γ-rays", Proc. 25th Annu. Meet. Mater. Res. Soc. Jpn. (MRS-J), [Yokohama, Japan], B1-I1-003 (2015). **S, 1-28**

7) S. Chauhan, T. Mori, T. Kobayashi, S. Yamamoto and N. Isaka, "Interface design of ultra-low amount Pt loaded ceria nanowire/C with high ORR activity by proton beam irradiation at solid-liquid interface", Proc. 25th Annu. Meet. Mater. Res. Soc. Jpn. (MRS-J), [Yokohama, Japan], B1-08-004 (2015). **N, 1-27**

8) T. Mori, A. Rednyk, A. Suzuki, S. Yamamoto, S. Chuhan, N. Isaka and J. Drennan, "Designof active sites inthe interface of anode layer of solid oxide fuel cell byultra-low amount PtOx sputtering", Proc. 25th Annu. Meet. Mater. Res. Soc. Jpn. (MRS-J), [Yokohama, Japan], B1-I9-001 (2015). **S, 1-27**

9) K. Takahashi, T. Mori, A. Suzuki, S. Chauhan, Y. Maekawa, A. Hiroki, K. Yoshimura and S. Yamamoto, "Effect of gamma-ray irradiation on enhancement of charge transfer in the interface between less Pt loaded CeO_x nanowire/C and Nafion® ionomer in membrane electrode assembly of PEMFC", Proc. 25th Annu. Meet. Mater. Res. Soc. Jpn. (MRS-J), [Yokohama, Japan], B1-P10-013 (2015). **G, 1-27**

10) K. Matsumoto, S. Morohoshi, T. Mori, A. Suzuki, T. Kobayashi, S. Yamamoto, T. Kondo and J. Nakamura, "Influence of catalysts and ionomer interface condition on activity of Pt/GNS in MEA", Proc. 25th Annu. Meet. Mater. Res. Soc. Jpn. (MRS-J),

[Yokohama, Japan], B1-P10-015 (2015). **G**

11) 木全 哲也, 加藤 翔, 八巻 徹也, 山本 春也, 箱田 照幸, 小林 知洋, 寺井 隆幸, “イオン照射グラッシーカーボンを担体とした Pt ナノ微粒子の酸素還元活性”, 2015 年電気化学会秋季大会, [深谷], 1A28 (2015). **I**

12) 木全 哲也, 加藤 翔, 八巻 徹也, 山本 春也, 箱田 照幸, 小林 知洋, 寺井 隆幸, “イオンビームによる担体改質が白金ナノ微粒子触媒に及ぼす影響”, 第 76 回応用物理学会秋季学術講演会, [名古屋], 14p-4E-8 (2015). **I**

13) N. Nuryanthi, T. Yamaki, S. Saiki, A. Kitamura, K. Yoshimura, H. Koshikawa, S. Sawada and T. Terai, “Ion-track grafting of vinylbenzyl chloride into poly(ethylene-*co*-tetrafluoroethylene) film by different ion beams”, Proc. 9th Int. Sympo. Swift Heavy Ions in Matter (SHIM2015), [Darmstadt, Germany] PB52 (2015). **C, 1-15**

14) T. Yamaki, N. Nuryanthi, H. Koshikawa, M. Asano, S. Sawada, A. Kitamura, Y. Maekawa, K.-O. Voss, D. Severin, T. Seidl and C. Trautmann, “Heavy ion tracks in fluoropolymer film: recent developments and future prospects”, Proc. 9th Int. Symp. Swift Heavy Ions in Matter (SHIM2015), [Darmstadt, Germany], PA51 (2015). **C**

15) A. Kitamura, T. Yamaki, Y. Yuri, H. Koshikawa, S. Sawada and T. Yuyama, “Ion track etching in PVDF irradiated with uniform ion beam in an oxygen atmosphere”, Proc. 9th Int. Symp. Swift Heavy Ions in Matter (SHIM2015), [Darmstadt, Germany], PB48 (2015). **C**

16) 小平 岳秀, 大浦 琴音, 池田 歩, 小野 竜平, 野村 幹弘, 名嘉 泰史, 今林 慎一郎, 澤田 真一, 八巻 徹也, 田中 伸幸, 久保 真治, “放射線グラフト膜による熱化学水素製造法の改善”, 分離技術会年会 2015, [川崎], S7-P3 (2015). **E, G, 1-17**

17) 後藤 光暁, 比嘉 充, 八巻 徹也, 澤田 真一, 越川 博, 喜多村 茜, “イオン照射グラフト重合法によるイオン交換膜の作製とその膜特性評価”, 平成 27 年度繊維学会年次大会, [東京], 1P234 (2015). **C**

18) 後藤 光暁, 八巻 徹也, 澤田 真一, 越川 博, 喜多村 茜, 比嘉 充, “イオン照射グラフト重合法によるイオン交換膜の作製及び特性評価”, 第 52 回化学関連支部合同九州大会, [北九州], PF-4-0114 (2015). **C**

19) 後藤 光暁, 大森 理之, 八巻 徹也, 澤田 真一, 越川 博, 喜多村 茜, 比嘉 充, “イオン照射グラフト重合法及びγ線照射グラフト重合法を用いたイオン交換膜の作製と膜特性評価”, 平成 27 年度第 45 回繊維学会夏季セミナー, [北九州], P-70 (2015). **C**

20) 大森 理之, 後藤 光暁, 八巻 徹也, 澤田 真一, 越川 博, 喜多村 茜, 比嘉 充, “イオン照射グラフト重合法による陽イオン交換膜の作製と特性評価”, 平成 27 年度第 45 回繊維学会夏季セミナー, [北九州], P-61 (2015). **C**

21) 八巻 徹也, “単一粒子の飛跡を利用したナノワイヤの形成技術”, 経済産業省「シーズ発掘事業」大学・大企業(特許・技術)説明会, [東京], F-3 (2015). **C**

22) 八巻 徹也, “量子ビームによる新規イオン交換膜の研究ーγ線・電子線, イオンビームの特徴を活かしてー”, 日本海水学会電気透析および膜技術研究会, 第45回荷電膜コロキウム, [小田原], 講演2 (2015). **C, E, G**

23) T. Kimata, S. Kato, T. Yamaki, S. Yamamoto, T. Hakoda, T. Kobayashi and T. Terai, “Platinum nanoparticles on the glassy carbon surface irradiated with Ar ions”, Proc. 19th Int. Conf. Surf. Modif. Mater. Ion Beams (SMMIB-19), [Chiang Mai, Thailand], BP9 (2015). **I**

24) 木全 哲也, 八巻 徹也, 山本 春也, 箱田 照幸, 松村 大樹, 下山 巖, 岩瀬 彰宏, 藤村 勇貴, 小林 知洋, 寺井 隆幸, “燃料電池用電極触媒のイオンビームによる高性能化:照射効果が生み出す特異な界面構造に放射光で迫る”, 日本原子力学会関東・甲越支部 第14回若手研究者発表討論会, [狛江], 7 (2015). **I**

25) 木全 哲也, 八巻 徹也, 山本 春也, 寺井 隆幸, 箱田 照幸, 小林 知洋, “イオンビームによるグラッシーカーボン担体の格子欠陥を利用した白金ナノ微粒子触媒の作製”, 日本学術振興会産学協力研究委員会 第117委員会「炭素材料」第316回研究会, [東京], (2015). **I**

26) 箱田 照幸, 高橋 絢香, 島田 明彦, 山本 春也, 有谷 博文, 八巻 徹也, “電子線誘起極表層プラズマ反応場を利用した金ナノ粒子膜の生成”, 2015年度第39回静電気学会全国大会, [八王子], 25pB-2 (2015). **N**

27) 八巻 徹也, ヌリヤンティ ヌヌン, 喜多村 茜, 越川 博, 吉村 公男, 澤田 真一, 浅野 雅春, 前川 康成, 鈴木 晶大, 寺井 隆幸, “エチレン-テトラフルオロエチレン共重合体膜への塩化ビニルベンジルのイオン飛跡グラフト重合反応:反応媒質効果の速度論的解析”, 日本膜学会第37年会, [東京], 1A-7 (2015). **C**

28) 菊間 博之, 竹内 夕桐子, 中村 俊介, 杉本 雅樹, 長澤 尚胤, 島田 明彦, 箱田 照幸, 田口 光正, “300 ℃の耐放射線性エラストマー材料の研究開発”, 平成 27 年度火力原子力発電大会(東京大会), [東京], ポスター7 (2015). **E, G**

29) 太田 智紀, 萩原 時男, 杉本 雅樹, 山本 春也, 越川 博, 八巻 徹也, “電子線照射を利用した炭素系触媒材料の作製技術”, 平成 27 年度日本化学会関東支部 群馬地区研究交流発表会, [前橋], (2015). **E**

30) 越川 博, 浅野 雅春, 八巻 徹也, 前川 康成, “イオン照射ポリイミド膜におけるトラックエッチング速度の LET 依存性”, 平成 27 年度日本化学会関東支部 群馬地区研究交流発表会, [前橋], (2015). **C, 1-13**

31) N. Nuryanthi, T. Yamaki, S. Saiki, A. Kitamura, H. Koshikawa, K. Yoshimura, S. Sawada, and T. Terai, “Track structure effect on the ion-track grafting of vinylbenzyl chloride into poly(ethylene-*co*- tetrafluoroethylene) films”, 平成 27 年度日本化学会関東支部 群馬地区研究交流発表会, [前橋] (2015). **C, 1-15**

32) 小平 岳秀, 大浦 琴音, 池田 歩, 小野 竜平, 野村 幹弘, 名嘉 泰史, 今林 慎一郎, 澤田 真一, 八巻 徹也, 田中 伸幸, 久保 真治, “放射線グラフト膜を用いた熱化学水素製造ISプロセスの改善”, 第5回CSJ化学フェスタ2015, [東京], P8-118 (2015). **E, G, 1-17**

33) 小平 岳秀, 大浦 琴音, 池田 歩, 小野 竜平, 野村 幹弘, 名嘉 泰史, 今林 慎一郎, 澤田 真一, 八巻 徹也, 田中 伸幸, 久保 真治, “熱化学水素製造ISプロセス用放射線グラフト膜の開発“, 膜シンポジウム2015, [神戸], P-47 (2015). **E, G, 1-17**

34) T. Kodaira, K. Oura, A. Ikeda, M. Nomura, Y. Naka, S. Imabayashi, S. Sawada, T. Yamaki, N. Tanaka and S. Kubo, “Developments of ion exchange membranes for the thermo-chemical hydrogen production I-S process”, Proc. 10th SEATUC (South East Asia Technical Universities Consortium) Symp., [Tokyo, Japan], PS01-07 (2016). **E, G, 1-17**

35) 後藤 光暁, 大森 理之, 八巻 徹也, 澤田 真一, 越川 博, 喜多村 茜, 比嘉 充, “イオン照射グラフト重合法によるイオン交換膜の作製及びイオン輸送特性評価”, 膜シンポジウム 2015, [神戸], P-41 (2015). **C**

36) 小平 岳秀, 大浦 琴音, 池田 歩, 小野 竜平, 名嘉 泰史, 今林 慎一郎, 野村 幹弘, 澤田 真一, 八巻 徹也, 田中 伸幸, 久保 真治, “イオン交換膜による熱化学水素製造法のエネルギー効率改善”, 第 35 回水素エネルギー協会大会, [東京],

P02 (2015). **E, G, 1-17**

37) 大森 理之, 後藤 光暁, 八巻 徹也, 澤田 真一, 越川 博, 喜多村 茜, 比嘉 充, “イオン照射グラフト重合法による陰イオン交換膜の作製とその膜の特性評価”, 第 30 回中国四国地区高分子若手研究会, [松山], PA17 (2015). **C**

38) 大森 理之, 後藤 光暁, 八巻 徹也, 澤田 真一, 越川 博, 喜多村 茜, 比嘉 充, “イオン照射グラフト重合法による陰イオン交換膜の作製と特性評価”, 平成 27 年第 53 回高分子学会高分子と水に関する討論会, [東京], P14 (2015). **C**

39) M. Goto, T. Yamaki, H. Koshikawa, S. Sawada, A. Kitamura and M. Higa, “Characterization of ion-exchange membranes prepared by ion irradiation graft polymerization method”, Proc. Int. Chem. Congr. Pacific Basin Soc. 2015 (PACIFICHEM2015), [Honolulu, USA], MACR 1230 (2015). **C**

40) A. Idesaki, M. Sugimoto, A. Shimada, S. Yamamoto, M. Taguchi and T. Yamaki, “Synthesis of a nitrogen-containing carbon material with oxygen reduction activity from polymer precursors”, Proc. Int. Chem. Congr. Pacific Basin Soc. 2015 (PACIFICHEM2015) [Honolulu, USA] MTLS 1472 (2015). **I, 1-25**

41) 山本 春也, 宮下 敦巳, 島田 明彦, 箱田 照幸, “空気中の γ 線照射下における貴金属の酸化物形成”, 2016 年日本金属学会春期大会, [東京], 177 (2016). **G, 1-28**

42) 木全 哲也, 八巻 徹也, 山本 春也, 箱田 照幸, 松村 大樹, 下山 巖, 岩瀬 彰宏, 藤村 勇貴, 小林 知洋, 寺井 隆幸, “XAFS測定によるArイオン照射グラッシーカーボンを担体としたPtナノ微粒子の局所構造解析”, 第29回日本放射光学会年会 放射光科学合同シンポジウム, [柏], 7Aa007 (2016). **I**

43) 垣谷 健太, 木全 哲也, 八巻 徹也, 山本 春也, 寺井 隆幸, 小林 知洋, “イオンビームによる炭素担体の格子欠陥を利用したPtナノ微粒子触媒の作製 (1):酸素還元活性”, 電気化学会第83回大会, [吹田], 1K31 (2016). **I, 1-14**

44) 木全 哲也, 八巻 徹也, 山本 春也, 松村 大樹, 下山 巖, 寺井 隆幸, 岩瀬 彰宏, 藤村 勇貴, 小林 知洋, 箱田 照幸, “イオンビームによる炭素担体の格子欠陥を利用した Pt ナノ微粒子触媒の作製 (2):局所構造解析”, 電気化学会第 83 回大会, [吹田], 1K32 (2016). **I**

45) 杉本 雅樹, 太田 智紀, 山本 春也, 越川 博, 八巻 徹也, 萩原 時男, “電子線照射による非平衡反応を利用した炭素系カソード触媒への窒素導入”, 電気化学会第 83 回大会, [吹田], 3K07 (2016). **E, 1-23**

46) 越川 博, 山本 春也, 杉本 雅樹, 喜多村 茜, 澤田 真一, 八巻 徹也, “イオンビーム穿孔を用いた金属ナノニードルの作製”, 日本化学会第 96 春季年会, [京田辺], 3D1-51 (2016). **C, 1-13**

47) ヌリヤンティ ヌヌン, 八巻 徹也, 喜多村 茜, 越川 博, 澤田 真一, 吉村 公男, 寺井 隆幸, “イオン飛跡グラフト重合法によるアニオン交換燃料電池膜の作製と膜特性評価”, 日本化学会第 96 春季年会, [京田辺], 2D4- 01 (2016). **C, 1-15**

48) 太田 智紀, 八巻 徹也, 杉本 雅樹, 山本 春也, 越川 博, 萩原 時男, “アンモニア中電子線照射による炭素系触媒材料への窒素導入効果”, 日本化学会第 96 春季年会, [京田辺], 2D4-04 (2016). **E**

49) 野村 幹弘, 小平 岳秀, 大浦 琴音, 池田 歩, 名嘉 泰史, 西嶋 陽之, 今林 慎一郎, 澤田 真一, 八巻 徹也, 田中 伸幸, 久保 真治, “熱化学水素製造のための放射線グラフト膜の開発”, 化学工学会第 81 回年会, [吹田], F113 (2016). **E, G, 1-17**

50) H. Matsuoka, H. Hayashi, H. Nishikawa, H. Koshikawa and Y. Maekawa, “Proton beam writing on polyvinylidene difluoride films for high-aspect-ratio micro-structuring”, Proc. 59th Int. Conf. Electron, Ion, and Photon Beam Tech. and Nanofabrication (EIPBN2015), [San Diego, USA], P07-03 (2015/5). **S, 3-15**

Patents

1) 森 利之, シャウハン シプラ, 鈴木 彰, 小林 知洋, 山本 春也, 箱田 照幸, 八巻 徹也, “微量白金担持セリアナノワイヤ及びその製造方法,並びにその用途”, 出願 2016-004627 (2016.1.13). **G, 1-27**

2) 八巻 徹也, 澤田 真一 (量研機構・高崎研), 田中 伸幸, 久保 真治 (原子力機構・原子力水素・熱利用セ), 野村 幹弘 (芝浦工業大学), “熱化学水素製造ヨウ素ー硫黄(IS)プロセスの膜ブンゼン反応器に使用するカチオン交換膜の製造方法”, 出願番号:特願 2016-026841.

Positron Nano-Science Research Project (P1-3)

Papers

1) 河裾 厚男, “放射性同位体を用いたスピン偏極陽電子ビーム”, 陽電子科学, **4**, 9-22 (2015). **C**

2) 河裾 厚男, “スピン偏極陽電子ビームの応用研究”, 放射線と産業 139 号, 18-22 (2015). **C**

3) I. Mochizuki, H. Ariga, Y. Fukaya, K. Wada, M. Maekawa, A. Kawasuso, T. Shidara, K. Asakura and T. Hyodo, “Structure determination of the rutile-TiO_2 (110)-(1x2) surface using total-reflection high-energy positron diffraction (TRHEPD)”, Phys. Chem. Chem. Phys., **18**, 7085-92 (2016). **N**

Proceedings

1) A. Kawasuso, “Spin-polarized positron annihilation spectroscopy -Prestnt and Future-” (Invited), Proc. 17th Int. Conf. Positron Annihilation, [Wuhan, China] (2015/9). **C**

2) M. Maekawa, H. Li, A. Kawasuso, “Construction of a spin-polarized positronium time-of-flight measurement apparatus”, 17th Int. Conf. Positron Annihilation, [Wuhan, China] (2015/9). **C, 1-32, 3-12**

3) 河裾 厚男, 前川 雅樹, 境 誠司, “金属酸化物の原子空孔誘起強磁性効果”, 第 52 回アイソトープ・放射線研究会, [東京] (2015/7). **N**

4) 前川 雅樹, 河裾 厚男, “スピン偏極ポジトロニウム飛行時間速的装置の製作”, 第 52 回アイソトープ・放射線研究会, [東京] (2015/7). **C, 1-32, 3-12**

5) 前川 雅樹, 河裾 厚男, “薄膜透過タイミング検出によるスピン偏極ポジトロニウム飛行時間測定装置開発”, 日本物理学会 2015 年秋季大会, [吹田] (2015/9). **C, 1-32, 3-12**

6) 阿部 浩之, 前川 雅樹, 周 凱, 河裾 厚男, “スピン偏極陽電子ビームを用いた酸化亜鉛空孔誘起磁性の検出”, 日本物理学会 2015 年秋季大会, [吹田] (2015/9). **N**

7) 宮下 敦巳, 河裾 厚男, 斎藤 峯雄, “ポジトロニウム仕事関数の第一原理バンド計算を用いた導出”, 京都大学原子炉実験所専門研究会「陽電子科学とその理工学への応用」, [熊取] (2015/11). **N**

8) 河裾 厚男, 李 輝, 前川 雅樹, 阿部 浩之, 宮下 敦巳, “スピン偏極陽電子ビームによる Bi 系トポロジカル絶縁体の電流誘起スピン蓄積の観測”, 第 35 回表面科学学術講演会, [つくば], 1Hp06 (2015/12). **N**

9) 河裾 厚男, “スピン偏極陽電子・ポジトロニウム分光の将来展開”, 陽電子・素過程研究会 2016, [野田] (2016/3). **N**

10) 河裾 厚男, “スピン偏極陽電子消滅法によるスピン物性研究

の現状”(招待講演), 日本物理学会 第 71 回年次大会 領域 10 シンポジウム, “陽電子が拓く物性物理の最前線”, [仙台] (2016/3). **N**

Semiconductor Analysis and Radiation Effects Research Project（P1-4）

Papers

1) N. Iwamoto, A. Azarov, T. Ohshima, A. M. M. Moe and B. G. Svensson, “High temperature annealing effects on deep-level defects in a high purity semiinsulating 4H-SiC substrate”, J. Appl. Phys., **118**, 045705 (2015). **N**

2) A. Lohrmann, N. Iwamoto, Z. Bodrog, S. Castelletto, T. Ohshima, T. J. Karle, A. Gali, S. Prawer, J. C. McCallum and B. C. Johnson, “Single-photon emitting diode in silicon carbide”, Nature Communications, **6**, 7783 (2015). **I, E**

3) Y. Ruan, B. C. Gibson, D. W. M. Lau, A. D. Greentree, H. Ji, H. Ebendorff-Heidepriem, B. C. Johnson, T. Ohshima and T. M. Monro, “Atom-photon coupling from nitrogen-vacancy centres embedded in tellurite microspheres”, Sci. Rep., **5**, 11486 (2015). **E**

4) Y. Liu, G. Chen, Y. Rong, L. P. McGuinness, F. Jelezko, S. Tamura, T. Tanii, T. Teraji, S. Onoda, T. Ohshima, J. Isoya, T. Shinada and E. Wu, H. Zeng, “Fluorescence polarization switching from a single silicon vacancy colour centre in diamond”, Sci. Rep., **5**, 12244 (2015). **N**

5) S. Onoda, M. Haruyama, T. Teraji, J. Isoya, W. Kada, O. Hanaizumi and T. Ohshima, “New application of NV centers in CVD diamonds as a fluorescent nuclear track detector”, Phys. Status Solidi A **212**, 2641-44 (2015). **C, 1-05**

6) L. J. Rogers, M. W. Doherty, M. S. J. Barson, S. Onoda, T. Ohshima and N. B. Manson, “Singlet levels of the NV-centre in diamond”, New J. Phys., **17**, 013048 (2015). **E**

7) S.-i. Sato, K. Beernink and T. Ohshima, “Energy loss process analysis for radiation degradation and immediate recovery of amorphous silicon alloy solar cells”, Jpn. J. Appl. Phys. **54**, 061401 (2015). **T, I, E, 1-06**

8) Y. Liu, P. Siyushev, Y. Rong, B. Wu, L. P. McGuinness, F. Jelezko, S. Tamura, T. Tanii, T. Teraji, S. Onoda, T. Ohshima, J. Isoya, T. Shinada, H. Zeng and E. Wu, “Investigation of the silicon vacancy color center for quantum key distribution”, Optics Express, **23**, 32961-967 (2015). **N**

9) H. Abe, S. Tokuhira, H. Uchida and T. Ohshima, “Surface Modifications of Hydrogen Storage Alloy by Heavy Ion Beams with keV to MeV Irradiation Energies”, Nucl. Instrum. Meth. Phys. Res. B **365**, 214-17 (2015). **I, 1-31**

10) T. Ohshima, T. Yokoseki, K. Murata, T. Matsuda, S. Mitomo, H. Abe, T. Makino, S. Onoda, Y. Hijikata, Y. Tanaka, M. Kandori, S. Okubo, T. Yoshie, “Radiation response of silicon carbide metal-oxide-semiconductor transistors in high dose region”, Jpn. J. Appl. Phys. **55**, 01AD01 (2016). **G**

11) M. Kato, K. Miyake, T. Yasuda, M. Ichimura, T. Hatayama, T. Ohshima, “Spectral response, carrier lifetime, and photo-currents of SiC photocathodes”, Jpn. J. Appl. Phys., **55**, 01AC02 (2016). **E**

12) A. Lohrmann, S. Castelletto, J. R. Klein, T. Ohshima, M. Bosi, M. Negri, D. W. M. Lau, B. C. Gibson, S. Prawer, J. C. McCallum, B. C. Johnson, “Activation and control of visible single defects in 4H-, 6H-, and 3C-SiC by oxidation”, Appl. Phys. Lett., **108**, 021107 (2016). **N**

13) W. Kada, Y. Kambayashi, Y. Ando, S. Onoda, H. Umezawa, Y. Mokuno, S. Shikata, T. Makino, M. Koka, O. Hanaizumi, T. Kamiya and T. Ohshima, “Investigation of electrically-active deep levels in single-crystalline diamond by particle-induced charge transient spectroscopy”, Nucl. Instrum. Meth. Phys. Res. B, **372**, 151-55 (2016). **T, 3-01, 3-14**

14) V. Grilj, N. Skukan, M. Jaksic, M. Pomorski, W. Kada, T. Kamiya, T. Ohshima, “The evaluation of radiation damage parameter for CVD diamond”, Nucl. Instrum. Meth. Phys. Res. B, **372**, 161-64 (2016). **T**

15) A. Lohrmann, B. C. Johnson, A. F. M. Almutairi, D. W. M. Lau, M. Negri, M. Bosi, B. C. Gibson, J. C. McCallum, A. Gali, T. Ohshima and S. Castelletto, “Engineering single defects in silicon carbide bulk, nanostructures and devices”, Mater. Sci. Forum, **858**, 312-17 (2016). **T, I**

16) N. Iwamoto, A. Azarov and T. Ohshima, A. M. M. Moe, B. G. Svensson, “Thermal stability of deep-level defects in high-purity semi-insulating 4H-SiC substrate studied by admittance spectroscopy”, Mater. Sci. Forum, **858**, 357-60 (2016). **N**

17) G. W. Kim, R. Arai, S. J. Ma, M. Okamoto, H. Yoshioka, S. Harada, T. Makino, T. Ohshima and T. Umeda, “Relationship between C-face defects and threshold-voltage instability in C-face 4H-SiC MOSFETs studied by electrically detected magnetic resonance”, Mater. Sci. Forum, **858**, 591-94 (2016). **G**

18) T. Makino, S. Onoda, N. Hoshino, H. Tsuchida and T. Ohshima, “Epitaxial layer thickness dependence on heavy ion induced charge collection in 4H-SiC Schottky barrier diodes”, Mater. Sci. Forum, **858**, 753-56 (2016). **C, 1-01**

19) S-I. Kuroki, H. Nagatsuma, M. De Silva, S. Ishikawa, T. Maeda, H. Sezaki, T. Kikkawa, T. Makino, T. Ohshima, M. Östling and C.-M. Zetterling, “Characterization of 4H-SiC nMOSFETs in harsh environments, high-temperature and high gamma-ray radiation”, Mater. Sci. Forum, **858**, 864-67 (2016). **G**

20) T. Matsuda, T. Yokoseki, S. Mitomo, K. Murata, T. Makino, H. Abe, A. Takeyama, S. Onoda, Y. Tanaka, M. Kandori, T. Yoshie, Y. Hijikata and T. Ohshima, “Change in characteristics of SiC MOSFETs by gamma-ray irradiation at high temperature”, Mater. Sci. Forum, **858**, 860-63 (2016). **G**

21) Y. Kobayashi, T. Yokozeki, T. Matsuda, S. Mitomo, K. Murata, M. Hachisuka, Y. Kaneko, T. Makino, A. Takeyama, S. Onoda, T. Ohshima, Y. Tanaka, M. Kandori, T. Yoshie, Y. Hijikata, “Gamma-ray irradiation response of the motor-driver circuit with SiC MOSFETs”, Mater. Sci. Forum, **858**, 868-71 (2016). **G**

22) M. Narisawa, M. Koka, A. Takeyama, M. Sugimoto, A. Idesaki, T. Satoh, H. Hokazono, T. Kawai and A. Iwase, “In-situ monitoring of ion-beam luminescence of Si-O-C(-H) ceramics under proton- beam irradiation”, J. Ceram. Soc. Jpn., **123**, 805-08 (2015). **S**

23) G. A. Álvarez, C. O. Bretschneider, R. Fischer, P. London, H. Kanda, S. Onoda, J. Isoya, D. Gershoni and L. Frydman, “Local and bulk ^{13}C hyperpolarization in nitrogen-vacancy-centred diamonds at variable fields and orientations”, Nature Commun., **6**, 8456(1-8) (2015). **E, 1-11**

24) N. Aslam, M. Pfender, R. Stöhr, P. Neumann, M. Scheffler, H. Sumiya, H. Abe, S. Onoda, T. Ohshima, J. Isoya, and J. Wrachtrup, “Single spin optically detected magnetic resonance with 60-90 GHz (E-band) microwave resonators”, Rev. Sci. Instrum., **86**, 064704(1-8) (2015). **E, 1-11**

25) C. Grezes, B. Julsgaard, Y. Kubo, W. L. Ma, M. Stern,

A. Bienfait, K. Nakamura, J. Isoya, S. Onoda, T. Ohshima, V. Jacques, D. Vion, D. Esteve, R. B. Liu, K. Mølmer, and P. Bertet, "Storage and retrieval of microwave fields at the single-photon level in a spin ensemble", Phys. Rev. A, **92**, 020301(R) (1-5) (2015). **E, 1-11**

26) T. Wolf, P. Neumann, K. Nakamura, H. Sumiya, T. Ohshima, J. Isoya, and J. Wrachtrup, "Subpicotesla Diamond Magnetometer", Phys. Rev. X, **5**, 041001 (1-10) (2015). **E, 1-11**

27) T. Teraji, T. Yamamoto, K. Watanabe, Y. Koide, J. Isoya, S. Onoda, T. Ohshima, L. J. Rogers, F. Jelezko, P. Neumann, J. Wrachtrup, and S. Koizumi, "Homoepitaxial diamond film growth: High purity, high crystalline quality,isotopic enrichment, and single color center formation", Phys. Status Solidi A, **212**, 2365-84 (2015). **T, I, 1-11**

28) A. Tekayama, A. Idesaki, M. Sugimoto and M. Yoshikawa, "Swelling of radiation-cured polymer precursor powder for silicon carbide by pyrolysis", J. Asia. Ceram. Soc., **3**, 402-06 (2015). **E, 1-26**

29) T. Kamiya, T. Satoh, M. Koka, W. Kada, "Development of microbeam technology to expand applications at TIARA", Nucl. Instrum. Meth. Phys. Res. B, **348**, 4-7 (2015). **C, T, S, 1-12**

30) A. Yamazaki, Y. Orikasa, K. Chen, Y. uchimoto, T. Kamiya, M. Koka, T. Satoh, K. Mima, Y. Kato and K. Fujita, "In-situ measurement of the lithium distribution in Li-ion batteries using micro-IBA techniques", Nucl. Instrum. Meth. Phys. Res. B, **371**, 298-302 (2015). **S, 3-03**

Proceedings

1) S.-i. Sato, K. J. Schmieder, S. M. Hubbard, D. V. Forbes, J. H. Warner, T. Ohshima and R. J. Walters, "Defects in GaAs solar cells with InAs quantum dots created by proton irradiation", Proc. 42th IEEE Photovoltaic Specialists Conf. (PVSC42), [New Orleans, USA] 2015-663 (2015). **N, 1-06**

2) Y. Miyazawa, M. Ikegami, T. Miyasaka, T. Ohshima, M. Imaizumi and K. Hirose, "Evaluation of radiation tolerance of perovskite solar cell for use in space", Proc. 42th IEEE Photovoltaic Specialists Conf. (PVSC42), [New Orleans, USA], 2015-674 (2015). **E**

3) Y. Miyazawa, M. Ikegami, T. Miyasaka, T. Ohshima, M. Imaizumi and K. Hirose, "Radiation tolerance of perovskite solar cells for use in space", Proc. 11th Int. Workshop Radiat. Eff. Semicond. Devices Space Appl. (11th RASEDA) & 7th Int. Conf. Adv. Micro-Device Eng. (7th AMDE), [Kiryu, Japan], 69-72 (2015). **E**

4) T. Nakamura, M. Imaizumi, S.-i. Sato, T. Sugaya, T. Mochizuki, Y. Okuno and T. Ohshima, "Measurement of ion beam induced current in quantum dot solar cells", Proc. 11th Int. Workshop Radiat. Eff. Semicond. Devices Space Appl. (11th RASEDA) & 7th Int. Conf. Adv. Micro-Device Eng. (7th AMDE), [Kiryu, Japan], 73-76 (2015). **I**

5) E. Mizuta, M. Tomitaka, S. Kuboyama, A. Takeyama, S. Onoda, T. Ohshima and K. Suzuki, "Single-event effects evaluated by heavy ions on a normally-off AlGaN/GaN heterojunction gate injection transistor", Proc. 11th Int. Workshop Radiat. Eff. Semicond. Devices Space Appl. (11th RASEDA) & 7th Int. Conf. Adv. Micro-Device Eng. (7th AMDE), [Kiryu, Japan], 97-100 (2015). **C, 1-03**

6) K. Sakamoto, A. Maru, H. Shindou, S. Kuboyama, K. Suzuki and T. Ohshima, "Cross-section estimation method for memory cells with considerable variation of SEU sensitivity", Proc. 11th Int. Workshop Radiat. Eff. Semicond. Devices Space Appl. (11th RASEDA) & 7th Int. Conf. Adv. Micro-Device Eng. (7th AMDE), [Kiryu, Japan], 101-04 (2015). **C, 1-03**

7) H. Nagatsuma, S-I. Kuroki, M. De Silva, S. Ishikawa, T. Maeda, H. Sezaki, T. Kikkawa, T. Makino, T. Ohshima, M. Östling and C.-M. Zetterling, "Characterization of 4H-SiC nMOSFETs with As-doped S/D and NbNi silicide contacts after high gamma-ray radiation", Proc. 11th Int. Workshop Radiat. Eff. Semicond. Devices Space Appl. (11th RASEDA) & 7th Int. Conf. Adv. Micro-Device Eng. (7th AMDE), [Kiryu, Japan] 117-18 (2015). **G**

8) Y. Hijikata, S. Mitomo, T. Matsuda, K. Murata, T. Yokoseki, T. Makino, A. Takeyama, S. Onoda, S. Okubo, Y. Tanaka, M. Kandori, T. Yoshie and T. Ohshima, "A development of super radiation-hardened power electronics using silicon carbide semiconductors -toward MGy-class radiation resistivity-", Proc. 11th Int. Workshop Radiat. Eff. Semicond. Devices Space Appl. (11th RASEDA) & 7th Int. Conf. Adv. Micro-Device Eng. (7th AMDE), [Kiryu, Japan], 130-33 (2015). **G**

9) A. Takeyama, T. Matsuda, T. Yokoseki, S. Mitomo, K. Murata, T. Makino, S. Onoda, Y. Tanaka, M. Kandori, T. Yoshie, Y. Hijikata and T. Ohshima, "Effect of humidity and temperature on the radiation response of SiC MOSFETs", Proc. 11th Int. Workshop Radiat. Eff. Semicond. Devices Space Appl. (11th RASEDA) & 7th Int. Conf. Adv. Micro-Device Eng. (7th AMDE), [Kiryu, Japan] 134-37 (2015). **G, 1-26**

10) K. Murata, S. Mitomo, T. Matsuda, T. Yokoseki, T. Makino, H. Abe, S. Onoda, T. Ohshima, A. Takeyama, S. Okubo, Y. Tanaka, M. Kandori, T. Yoshie and Y. Hijikata, "Effect of gate bias on radiation response of SiC MOSFETs", Proc. 11th Int. Workshop Radiat. Eff. Semicond. Devices Space Appl. (11th RASEDA) & 7th Int. Conf. Adv. Micro-Device Eng. (7th AMDE), [Kiryu, Japan], 138-41 (2015). **G**

11) S. Mitomo, T. Matsuda, K. Murata, T. Yokoseki, T. Makino, A. Takeyama, S. Onoda, T. Ohshima, S.Okubo, Y. Tanaka, M. Kandori, T. Yoshie and Y. Hijikata, "Effect of the package on the radiation response of SiC-MOSFETs", Proc. 11th Int. Workshop Radiat. Eff. Semicond. Devices Space Appl. (11th RASEDA) & 7th Int. Conf. Adv. Micro-Device Eng. (7th AMDE), [Kiryu, Japan], 144-47 (2015). **G**

12) T. Yokoseki, T. Matsuda, S. Mitomo, K. Murata, T. Makino, H. Abe, A. Takeyama, S. Onoda, Y. Tanaka, M. Kandori, T. Yoshie, Y. Hijikata and T. Ohshima, "Effect of gmma-ray irradiation at high temperature on the characteristics of SiC MOSFETs", Proc. 11th Int. Workshop Radiat. Eff. Semicond. Devices Space Appl. (11th RASEDA) & 7th Int. Conf. Adv. Micro-Device Eng. (7th AMDE), [Kiryu, Japan], 148-51 (2015). **G**

13) T. Matsuda, T. Yokoseki, , S. Mitomo, K. Murata, T. Makino, A. Takeyama, S. Onoda, S. Okubo, Y. Tanaka, M. Kandori, T. Yoshie, T. Ohshima and Y. Hijikata, "Characteristics of silicon carbide metal-oxide- semiconductor capacitors irradiated with gamma-rays at elevated temperature", Proc. 11th Int. Workshop Radiat. Eff. Semicond. Devices Space Appl. (11th RASEDA) & 7th Int. Conf. Adv. Micro-Device Eng. (7th AMDE), [Kiryu, Japan], 152-55 (2015). **G**

14) H. Kraus, D. Simin, F. Fuchs, S. Onoda, T. Makino, V. Dyakonov, T. Ohshima and G. Astakhov, "Defect engineering in silicon carbide: single photon sources, quantum sensors and RF emitters", Proc. 11th Int. Workshop Radiat. Eff. Semicond. Devices Space Appl. (11th RASEDA) & 7th Int. Conf. Adv. Micro-Device Eng. (7th AMDE), [Kiryu, Japan] 176-79 (2015). **S, E**

15) H. Sasaki, Y. Nabeshima, T. Hisaka, K. Kadoiwa, H. Koyama, Y. Kamo, Y. Yamamoto, S. Onoda and T. Ohshima, "Irradiation effects of ions on AlGaN/GaN HEMTs", Proc. 31st Annu. JEDEC ROCS Workshop 2016, [Miami, USA], 59-67 (2016). **C, T, 1-05**

16) H. Yamaguchi, R. Ijichi, Y. Suzuki, S. Ooka, K. Shimada, N. Takahashi, H. Washio, K. Nakamura, T. Takamoto, M. Imaizumi, T. Sumita, K. Shimazaki, T. Nakamura and T. Ohshima, "Development of space solar sheet with inverted triple development of space solar sheet with inverted triple-junction cells" Proc. 42nd IEEE Photovoltaic Specialists Conf., [New Orleans, USA], 15664138 (2015). **C, T, I, E, 1-04**

17) S. Kawakita, M. Imaizumi, K. Makita, J. Nishinaga, T. Sugaya, H. Shibata, S.-i. Sato and T. Ohshima, "Radiation resistance in high-efficiency III-V/Cu(In, Ga)Se_2 mechanically stacked solar cells", Proc. 31st Euro. Photovoltaic Solar Energ. Conf. Exhibition, [Hamburg, Germany], 1501-04 (2015). **C, T, I, E, 1-04**

18) Y. Shibata, M. Imaizumi, S.-i. Sato, T. Ohshima, S. Ooka, T. Takamoto, "Recovery of radiation degradation on inverted metamorphic triple-junction solar cells by light soaking", Proc. 11th Int. Workshop Radiat. Eff. Semicond. Devices Space Appl. (11th RASEDA) & 7th Int. Conf. Adv. Micro-Device Eng. (7th AMDE), [Kiryu, Japan], 65-68 (2015). **C, T, I, E, 1-04**

19) H. Abe, T. Shimomura, S. Tokuhira, Y. Shimada, Y. Takenaka, T. Furuyama, A. Nishimura, U. Uchida, H. Daido and T. Ohshima, "Surface Modification Effects on Hydrogen Absorption Property of a Hydrogen Storage Alloy by Short Pulse Laser Irradiation", Proc. LAMP2015, [Kitakyusyu, Japan] A241, (2015/5). **I, 1-31**

20) H. Daido, H. Abe, T. Shobu, T. Shimomura, S. Tokuhira, Y. Takeyama, T. Furuyama, A. Nishimura H. Uchida and T. Ohshima, "X-Ray characterization of short pulse laser illuminated hydrogen storage alloys having very high performance", Proc. SPIE, [San Diego, USA], **9589**, 95890K-1-6 (2015/8). **I, 1-31**

Biocompatible Materials Research Project（P1-5）

Papers

1) M. Narisawa, M. Koka, A. Takeyama, M. Sugimoto, A. Idesaki, T. Satoh, H. Hokazono, T. Kawai and A. Iwase, "In-situ monitoring of ion-beam luminescence of Si-O-C(-H) ceramics under proton- beam irradiation", J. Ceram. Soc. Jpn. **123**, 805-08 (2015). **S**

2) S. Tsukuda, R. Takahashi, S. Seki, M. Sugimoto, A. Idesaki, M. Yoshikawa and S. Tanaka, "Fabrication of Pt nanoparticle incorporated polymer nanowires by high energy ion and electron beam irradiation", Radiat. Phys. Chem. **118**, 16-20 (2016). **C, 1-23**

3) T. Seguchi, K. Tamura, H. Kudoh, A. Shimada and M. Sugimoto, "In-situ monitoring of ion-beam luminescence of Si-O-C(-H) ceramics under proton-beam irradiation", IEEE Trans. DEI, **22**, 3197-206 (2015). **C**

4) S. Kurashima, N. Miyawaki, H. Kashiwagi, S. Okumura, M. Taguchi, and M. Fukuda, "Enhancement of beam pulse controllability for a single-pulse formation system of a cyclotron", Rev. Sci. Instrum. **86**, 073311 (2015). **C, 3-06**

5) K. Iwamatsu, Y. Muroya, S. Yamashita, A. Kimura, M. Taguchi and Y. Katsumura, "Quick measurement of continuous absorption spectrum in ion beam pulse radiolysis: Application of optical multi-channel detector into transient species observation", Radiat. Phys. Chem., **119**, 213-17 (2016). **S**

6) A. Hiroki, S. Yamashita, A. Kimura, N. Nagasawa and M. Taguchi, "Effect of heavy ion irradiation on optical property of radiation- crosslinked hydroxypropyl cellulose gel containing methacrylate monomers", Nucl. Instrum. Meth. Phys. Res. B, **365**, 583-86 (2015). **G**

7) A. Kimura, N. Nagasawa, A. Shimada, and M. Taguchi, "Crosslinking of polysaccharides in room temperature ionic liquids by ionizing radiation", Radiat. Phys. Chem., **124**, 130-34 (2016). **G, 1-70**

8) S. Yang, Y. Katsumura, S. Yamashita, C. Matsuura, D. Hiroishi, P. Lertnaisat, and M. Taguchi, "Radiolysis of Boiling Water", Radiat. Phys. Chem., **123**, 14-19 (2016). **N**

Proceedings

1) A. Kimura, N. Nagasawa, and M. Taguchi, "Radiation-induced crosslinking of cellulose in room temperature ionic liquids", Proc. 15th Int. Congr. Radiat. Res. (ICRR 2015), [Kyoto, Japan] (2015/5). **G, 1-70**

2) A. Hiroki, S. Yamashita, A. Kimura, N. Nagasawa, and M. Taguchi, "Dose response of polymer gel dosimeter based on hydroxypropyl cellulose hydrogel ~ Toward the application on heavy ion therapy ~", Proc. 15th Int. Congr. Radiat. Res. (ICRR 2015) [Kyoto, Japan], (2015/5). **G**

3) Y. Kumagai, A. Kimura, M. Taguchi, "Hydrogen and hydrogen peroxide productions by γ-irradiation of A-, X-, Y- and mordenite type zeolites in aqueous solution", Proc. 15th Int. Congr. Radiat. Res. (ICRR 2015) [Kyoto, Japan], (2015/5). **G, 1-68**

4) 廣木 章博, 山下 真一, 木村 敦, 長澤 尚胤, 村上 健, 田口 光正, "放射線感受性ゲルシートの積層による 3 次元線量分布評価の試み", 第 110 回日本医学物理学会学術大会, [札幌], (2015/9). **G**

5) 木村 敦, 長澤 尚胤, 島田 明彦, 田口 光正, "イオン液体と量子ビームを組み合わせた新規天然多糖類ゲルの創製", 平成 27 年度日本化学会関東支部 群馬地区研究交流発表会, [前橋], (2015/12). **G, 1-70**

6) 長澤 尚胤, 木村 敦, 出崎 亮, 石井 保行, 山田 尚人, 江夏 昌志, 島田 明彦, 大久保 猛, 佐藤 隆博, 田口 光正, "プロトンビームライティング法による生体適合性ハイドロゲルの微細加工", 第 25 回日本 MRS 年次大会, [横浜], (2015/12). **S, 1-69**

7) M. Taguchi, Y. Kumagai, A. Kimura, "Treatment of pharmaceuticals and antibiotics in wastewater by ionizing radiation", Proc. 4th Res. Coord. Meet. (RCM) Radiat. Treat. of Wastewater for Reuse with Particular Focus on Wastewaters Containing Organic Pollutants, IAEA-CRP, [Beijing, China] (2015). **G, 1-68**

8) A. Idesaki, M. Sugimoto, A. Shimada, S. Yamamoto, M. Taguchi and T. Yamaki, "Synthesis of a nitrogen-containing carbon material with oxygen reduction activity from polymer precursors", Proc. Int. Chem. Congr. Pacific Basin Soc. 2015 (PACIFICHEM2015) [Honolulu, USA] MTLS 1472 (2015). **I, 1-25**

Environmental Polymer Research Project（P1-6）

Papers

1) T. Shibata, N. Seko, H. Amada, N. Kasai, S. Saiki, H. Hoshina and Y. Ueki, "Evaluation of a cesium adsorbent grafted with ammonium 12-molybdophosphate", Radiat. Phys. Chem., **119**, 247-52 (2016). **E, G**
2) 瀬古 典明, "放射線加工技術を駆使した金属捕集材の開発：環境浄化と資源確保を目指して", 電気評論, **621**, 47-51 (2015). **E, G**
3) 植木 悠二, "放射線グラフト重合技術を利用した金属イオン捕集フィルター", Isotope News, **743**, 12-16 (2016). **E, 1-71**
4) 中野 正憲, 見上 隆志, 柴田 卓弥, 笠井 昇, 瀬古 典明, "放射線グラフト重合によるセシウム捕集材の開発", EB 技術を利用した材料創製と応用展開, シーエムシー出版, 109-19 (2016). **E, 1-72**
5) 瀬古 典明, 植木 悠二, "電子線エマルショングラフト重合及びこれを利用したバイオディーゼル燃料転換用触媒の開発", EB 技術を利用した材料創製と応用展開, シーエムシー出版, 150-60 (2016). **E**

Patent

1) 早田 大志, 高橋 絵里歌, 直原 洋平, 中山 鶴雄, 瀬古 典明, 植木 悠二, 笠井 昇, "抗ウイルス性を有するポリマー粒子およびその製造方法", 出願,2016-073061 (2016.03.31). **E, 1-73**

Press・TV

1) 瀬古 典明, 柴田 卓弥, 笠井 昇, 中野 正憲, 見上 隆志, "放射線グラフト捕集材を充填したセシウム用給水器の開発", 平成28年度 科学技術分野の文部科学大臣表彰 科学技術賞 開発部門, (2016.4.20).

Element Separation and Analysis Research Project（P1-7）

Papers

1) K. Tamura, and R. Yamagishi, "Laser cutting conditions for steel plates having a thickness of more than 100 mm using a 30 kW fiber laser for nuclear decommissioning", Mech. Eng. J., **3**, 15-00590 (2016). **N**
2) K. Tamura, R. Ishigami and R. Yamagishi, "Laser cutting of thick steel plates and simulated steel components with a 30 kW fiber laser", J. Nucl. Sci. Tech., **53**, 916-20 (2016). **N**
3) E. Minehara, S. Toyama, K. Tamura and H. Nakamura, "Radioisotope decontamination and cutting of structural objects using laser for the decommissioning of nuclear power plants", Kinzoku, **86**, 590-95 (2016) (*Review*) (*in Japanese*). **N**
4) N. Nakashima, K. Yamanaka, M. Saeki, H. Ohba, S. Taniguchi, T. Yatsuhashi, "Metal ion reductions by femtosecond laser pulses with micro-Joule energy and their efficiencies", J. Photochem. Photobiol. A, **319**, 70-77 (2016). **N**
5) N. Ishikawa, N. Okubo and T. Taguchi, "Experimental evidence of crystalline hillocks created by irradiation of CeO_2 with swift heavy ions: TEM study", Nanotechnology, **26**, 355701 (2015). **T, 1-37, 1-38**
6) Y. Yamazaki, M. Yoshimoto, P. K. Saha, M. Kinsho, T. Taguchi, S. Yamamoto and I. Sugai, "Analyses and the effect of impurities contained in charge stripper foils for the 3-GeV RCS of J-PARC", J. Radioanal. Nucl. Chem., **305**, 859-64 (2015). **I, 1-48**
7) T. Taguchi, S. Yamamoto, K. Kodama and H. Asaoka, "Synthesis of heterostructured SiC and C-SiC nanotubes by ion irradiation-induced changes in crystallinity", Carbon, **95**, 279-85 (2015). **I, 1-30**

Proceedings

1) N. Ishikawa, N. Okubo, T. Taguchi, "Crystalline hillock formation of oxides irradiation with swift heavy ions; TEM study", Proc. 9th Int. Symp. Swift Heavy Ions in Matter (SHIM 2015) [Darmstadt, Germany], (2015/5). **T, 1-37, 1-38**
2) 大場 弘則, 佐伯 盛久, 伊藤 主税, 高野 公秀, 赤岡 克昭, Thornton Blair, 作花 哲夫, 若井田 育夫, "Elemental analysis of solid samples under water by fiber-coupled laser induced breakdown spectroscopy：[光ファイバー伝送レーザー誘起ブレークダウン分光による水中固体の元素分析]", [Wuhan, China], (2015/6). **N**
3) 黒崎 譲, 横山 啓一, "Quantum control of isotope-selective rovibrational excitation：[同位体選択的振動回転励起の量子制御]", 第 9 回分子科学討論会, [東京], (2016/9). **N**
4) 大場 弘則, 佐伯 盛久, 赤岡 克昭, 若井田 育夫, "Characteristics of LIBS emission from mrtal alloy under high radiation dose rate：[高線量率放射線環境下での LIBS 特性]", 第 3 回先端計測技術の応用展開に関するシンポジウム, [名古屋], (2015/12). **N**
5) 大場 弘則, 佐伯 盛久, 赤岡 克昭, 若井田 育夫, "Development of Quick and Remote Analysis for Severe Accident Reactor (2) Characteristics of LIBS emission from metal alloy under high radiation dose rates：[過酷事故炉を対象とした迅速遠隔分析技術開発(2) 高線量率放射線環境下における LIBS 特性]", 日本原子力学会 2016 春の年会, [仙台], (2016/3). **N**
6) 蓬田 匠, 浅井 志保, 佐伯 盛久, 半澤 有希子, 江坂 文孝, 大場 弘則, 北辻 章浩, "Development of Pd separation based on laser-induced particle formation for determination of ^{107}Pd in radioactive eastes with mass spectrometry：[放射性廃棄物中 ^{107}Pd 質量分析のためのレーザー微粒子化反応を利用した Pd 分離法の開発]", 日本分析化学会第 64 年会, [福岡], (2015/9). N
7) 蓬田 匠, 浅井 志保, 佐伯 盛久, 半澤 有希子, 江坂 文孝, 大場 弘則, 北辻 章浩, "Non-contact Pd separation based on laser-induced particle formation for determination of ^{107}Pd with ICP-MS", Pittcon 2016, [Atlanta, USA], (2016/3). **N**
8) 佐伯 盛久, 松村 大樹, 蓬田 匠, 田口 富嗣, 辻 卓也, 草野 翔吾, 宮崎 達也, 鷹尾 康一朗, 中島 信昭, 大場 弘則, "XAFS study on effect of molybdenum addition on photo-induced particle formation of palladium", 光化学討論会, [大阪], (2015/9). **N**
9) 佐伯 盛久, 松村 大樹, 蓬田 匠, 田口 富嗣, 辻 卓也, 草野 翔吾, 宮崎 達也, 鷹尾 康一朗, 中島 信昭, 大場 弘則, "XAFS study on effect of molybdenum addition on photo-induced particle formation of palladium", 分子化学討論会, [東京], (2015/9). **N**
10) N. Nakashima, K. Yamanaka, M. Saeki, H. Ohba, S. Taniguchi, T. Yatsuhashi, "Metal Ion Reductions by Femtosecond Laser Filamentation and their Efficiencies", 日本化学会春期年会, [京田辺], (2016/3). **N**
11) N. Ishikawa, N. Okubo, T. Taguchi, "Novel method for observing hillocks created for ceramic materials irradiated with swift heavy ions", 第 25 回日本 MRS 年次大会, [横浜],

(2015/12). **T, 1-37, 1-38**

Press・TV

1) 原子力機構“イオン照射による新奇複合ナノチューブの新たな創製方法の開発に成功(お知らせ)”, 平成 27 年 9 月 28 日プレス発表: 日刊工業新聞, 化学工業日報, 科学新聞に掲載.

Ion Beam Mutagenesis Research Project（P2-1）

Papers

1) S. Fujinami, K. Takeda-Yano, T. Onodera, K. Satoh, T. Shimizu, Y. Wakabayashi, I. Narumi, A. Nakamura and M. Ito, “Draft genome sequence of *Methylobacterium* sp. ME121, isolated from soil as a mixed single colony with *Kaistia* sp. 32K”, Genome Announc., **3**, e01005-15 (2015). **N**

2) S. Kitamura, Y. Oono and I. Narumi, “Arabidopsis *pab1*, a mutant with reduced anthocyanins in immature seeds from *banyuls*, harbors a mutation in the MATE transporter FFT”, Plant Mol. Biol. **90**, 7-18 (2016). **C**

3) 大野 豊, 横田 渉, “植物の突然変異と育種”, 加速器 **12**, 189-92 (2015)（総説）. **C**

4) A. H. Affrida, A. Sakinah, A. Zaiton, B. Mohd Nazir, Y. Oono, Y. Hase, N. Shikazono, I. Narumi and A. Tanaka, “Mutation induction of orchid plants by ion beams”, JAEA-Review, **2015-037**, 1-26 (2016) (Review). **C**

5) A. Zaiton, A. H. Affrida, S. Shakinah, M. Nurul Hidayah, Y. Oono, Y. Hase, S. Nozawa, R. Yoshihara, I. Narumi and A. Tanaka, “Generating new ornamental plant varieties using ion beams”, (Review) JAEA-Review, **2015-037**, 26-120 (2016). **C**

6) 北村 智, “イオンビーム照射による色素蓄積が異常な植物の作出とその応用”, 放射線と産業, **140**, 32-35 (2016)（総説）. **C**

7) A. Balestrazzi, V. M. M. Achary, A. Macovei, K. O. Yoshiyama and A. N. Sakamoto, “Editorial: Maintenance of genome integrity: DNA damage sensing, signaling, repair and replication in plants”, (Review), Front. Plant Sci., **7**, 64 (2016). **N**

8) 長谷 純宏, “イオンビームの育種利用の現状と展望”, 放射線化学, **100**, 86-88 (2015). **C, 2-19**

9) 清水 喜久雄, 中嶋 隆登, 松尾 陽一郎, 日高 雄二, 佐藤 典仁, 山本 幸佳, “リアルタイム PCR 法を用いた DNA 損傷の定量化とその放射線量評価法への応用”, 日本放射線安全管理学会誌, **15**(1), 52-58 (2016). **C, 2-26**

10) 横山 正, “バイオ肥料微生物の特性解明とその利用”, 日本土壌肥料学会誌, **86**, 351-55 (2015). **C, 2-28**

11) Y. Ishino and I. Narumi, “DNA repair in hyperthermophilic and hyperradioresistant micro-organisms”, Curr. Opin. Microbiol., **25**, 103-12 (2015). **G**

12) K. Satoh, T. Onodera, K. Omoso, K. Takeda-Yano, T. Katayama, Y. Oono and I. Narumi, “Draft genome sequence of the radio-resistant bacterium *Deinococcus grandis*, isolated from freshwater fish in Japan”, Genome Announc. **4**, e01631-15 (2016). **G, 2-27**

13) S. Kota, V. K. Charaka, Y. S. Rajpurohit, K. Satoh, I. Narumi and H. S. Misra, “DNA gyrase of Deinococcus radiodurans is characterized as type II bacterial topoisomerase and its activity is differentially regulated by PprA *in vitro*”, Extremophiles, **20**, 195-205 (2016). **G, 2-30**

Proceedings

1) 宮城 敦子, 北野 沙也佳, 長谷 純宏, 大野 豊, 山口 雅利, 川合 真紀, “イオンビームを照射した高シュウ酸植物エゾノギシギシの代謝解析”, 日本植物学会第79回大会, [新潟], 1a2 (2015). **C**

2) 北村 智, 大野 豊, 鳴海 一成, “Arabidopsis MATE-type transporter gene FFT/DTX35 is involved in anthocyanin accumulation in seed coat”, 第57回日本植物生理学会年会, [盛岡], PF-263(0693) (2016). **C**

3) Y. Murano, M. Harada, Y. Kawaguchi, H. Hashimoto, K. Kobayashi, K. Nakagawa, I. Narumi, K. Sato, S. Yoshida, H. Yano, S. Yokobori, A. Yamagishi, “Survivality of deinococci under space conditions? Toward the space exposure experiment in ”TANPOPO” mission at ISS”, Jpn. Geosci. Union Meet. 2015, [Chiba, Japan], BAO01-P02 (2015). **N**

4) 河口 優子, Yang Yinjie, 村野 由佳, 原田 美優, 川尻 成俊, 白石 啓祐, 高須 昌子, 高須 昌子, 鳴海 一成, 佐藤 勝也, 橋本 博文, 中川 和道, 谷川 能章, 田邊 真依子, 桃木 洋平, 杉野 朋弘, 吉田 聡, 横堀 伸一, 山岸 明彦, “宇宙環境下での*Deinococcus*属の生存能力の検証(たんぽぽ計画)”, 第16回極限環境生物学会年会, [東京], S4-01 (2015). **N**

5) 黒澤 飛翔, 面曽 宏太, 竹島 創, 佐藤 勝也, 鳴海 一成, “放射線抵抗性細菌におけるDNA修復応答制御遺伝子*pprI*の機能解析”, 第16回極限環境生物学会年会, [東京], P-15 (2015). **G**

6) 島田 岳, 佐藤 勝也, 鳴海 一成, ”中高度好熱性及び放射線抵抗性を持つ多重極限環境微生物 *Deinococcus geothermalis* における *pprA* 遺伝子破壊解析”, 第 16 回極限環境生物学会年会, [東京], P-19 (2015). **G, 2-30**

7) 面曽 宏太, 佐藤 勝也, 鳴海 一成, “*Deinococcus grandis* における突然変異を誘発する遺伝子の機能解析”, 第 16 回極限環境生物学会年会, [東京], P-23 (2015). **G, 2-30**

8) 黒澤 飛翔, 佐藤 勝也, 鳴海 一成, “放射線抵抗性細菌における DNA 修復応答制御遺伝子 *pprI* の機能解析”, 第 38 回日本分子生物学会年会・第 88 回日本生化学会大会合同大会, [神戸], 1P0642 (2015). **G, 2-30**

9) 島田 岳, 佐藤 勝也, 鳴海 一成, “放射線抵抗性細菌 *Deinococcus geothermalis* における *pprA* 遺伝子の遺伝子破壊解析”, 第38回日本分子生物学会年会・第88回日本生化学会大会合同大会, [神戸], 3P0672 (2015). **G, 2-30**

Books

1) A. Zaiton and Y. Oono (ed.), “Report of Cooperative Research Programs in the Field of Ion-beam Breeding between Japan Atomic Energy Agency and Malaysian Nuclear Agency”, JAEA-Review, **2015-037**, (2016). **C**

2) A. Balestrazzi, V. M. M. Achary, A. Macovei, K. O. Yoshiyama and A.N. Sakamoto (ed.), “Maintenance of genome integrity: DNA damage sensing, signaling, repair and replication in plants”, Front. Plant Sci., **7**, (2016). **N**

3) 中嶋 隆登, “DNA 損傷を指標とした放射線被ばく線量の評価”, 近畿大 総合理工学研究科 修士論文(平成 27 年度修了). **C, 2-26**

Patents

1) 長谷 純宏, 鳴海 一成, 田中 淳, “花色変異体植物の作出方法”, 登録 5875058 (2016.1.29). **C**

2) 羽毛田 智明, 長谷 純宏, 田中 淳, “サルビア「TL585」”, 品種登録 24473 (2015.9.30). **C**

3) 岡田 智行, 飯塚 正英, 長谷 純宏, 野澤 樹, 鳴海 一成, 関口 正行, “オステオスペルマム「ヴィエントラビオス」”, 品種登録 24758 (2016.3.1). **C**

4) 石坂 宏, 近藤 恵美子, 亀有 直子, 長谷 純宏, 田中 淳,

"芳香シクラメン「天女の舞」", 品種登録 24750 (2016.3.1). **C**

5) 石黒 信生, 長谷 純宏, 野澤 樹, "キク品種「カルロスビビッドティエラ」", 出願 30303 (2015.7.1). **C**

6) 山口 絵梨香, 長谷 純宏, 野澤 樹, "サルビア品種「はまごろも4号」", 出願 30829 (2016.2.15). **C, 2-24**

7) 山口 絵梨香, 長谷 純宏, 野澤 樹, "サルビア品種「はまごろも5号」", 出願 30830 (2016.2.15). **C, 2-24**

8) 木戸 君枝, 永吉 実孝, 吉水 竜次, 今給黎 征朗, 仁田尾 学, 田之頭 優樹, 白尾 史, 長谷 純宏, 野澤 樹, 大野 豊, "キク品種「立神」", 出願 30519(2015.10.13). **C, 2-22**

9) 木戸 君枝, 永吉 実孝, 吉水 竜次, 今給黎 征朗, 仁田尾 学, 田之頭 優樹, 長谷 純宏, 野澤 樹, 大野 豊, "キク品種「冬馬」", 出願 30520(2015.10.13). **C, 2-22**

Press・TV

1) "機能性食品の開発に新たな道筋－植物種皮のアントシアニン蓄積を支配する遺伝子をイオンビームで発見－", 2015.11.26, プレス発表: 毎日新聞, 上毛新聞, 繊研新聞, 日刊工業新聞, 化学工業日報, 電気新聞, 科学新聞, 時事ドットコム他ネットニュース, 燦(サン)に掲載. **C**

2) "白系秋輪ギク「立神」「冬馬」の育成～ボリュームや低温開花性に優れた新品種～", 2016.3.15 鹿児島県プレスリリース: 日本農業新聞, 南日本新聞に掲載. **C, 2-22**

Microbeam Radiation Biology Research Project（P2-2）

Papers

1) Y. Matsumoto, N. Hamada, M. Aoki-Nakano, T. Funayama, T. Sakashita and S. Wada, T. Kakizaki, Y. Kobayashi and Y. Furusawa, "Dependence of the bystander effect for micronucleus formation on dose of heavy-ion radiation in normal human fibroblasts", Radiat. Prot. Dosim., **166**, 152-56 (2015). **C, 2-08**

2) M. Tomita, H. Matsumoto, T. Funayama, Y. Yokota, K. Otsuka, M. Maeda and Y. Kobayashi, "Nitric oxide-mediated bystander signal transduction induced by heavy-ion microbeam irradiation", Life Sci. Space Res., **6**, 36-43 (2015). **C, 2-09**

3) M. Kikuchi and Y. Kobayashi, "Study on detection method for 8-hydroxyguanine induced in bovine livers by γ-irradiation", Food Irradiation, Japan, **50**, 3-8 (2015) (*in Japanese*). **G, 2-17**

4) M. Kikuchi and Y. Kobayashi, "ESR signal changes recorded in γ-irradiated bovine liver", Food Irradiation, Japan, **50**, 9-12 (2015) (*in Japanese*). **G, 2-17**

5) M. Kikuchi, N. Nagata, S. Komoda, H. Kameya, M. Ukai and Y. Kobayashi, "Peak-fitting analysis with gaussian line shapes against experimental ESR spectrum consisting of multiple peak", Food Irradiation, Japan, **50**, 13-19 (2015) (*in Japanese*). **G, 2-17**

6) Y. Yokota, T. Funayama, H. Ikeda and Y. Kobayashi, "Characteristics of radiation-induced bystander effect; Participation of nitric oxide", Isotope News, **741**, 21-25 (2016) (*Review*) (*in Japanese*). **C, G, 2-02**

Proceedings

1) A. Takahashi, M. Kubo, H. Ma, A. Nakagawa, Y. Yoshida, M. Isono, T. Kanai, T. Ohno, Y. Frusawa, T. Funayama, Y. Kobayashi and T. Nakano, "NHEJ plays a more important role than HR in defining radiosensitivity after exposure to high-LET radiation", Proc. Int. Congr. Radiat. Res. (ICRR2015), [Kyoto, Japan] (2015/5). **C, 2-06**

2) K. Murata, S. Noda, T. Oike, A. Takahashi, Y. Yoshida, Y. Suzuki, T. Ohno, T. Funayama, Y. Kobayashi, T. Takahashi and T Nakano, "Increase in cell motility by carbon ion irradiation via the Rho signaling pathway and its inhibition by the ROCK inhibitor Y-27632", Proc. Int. Congr. Radiat. Res. (ICRR2015), [Kyoto, Japan], (2015/5). **C, 2-06**

Medical Radioisotope Application Research Project（P2-3）

Papers

1) K. Hashimoto, Y. Nagai, M. Kawabata, N. Sato, Y. Hatsukawa, H. Saeki, S. Motoishi, M. Ohta, C. Konno, K. Ochiai, Y. Kawauchi, A. Ohta, T. Shiina, N. Takeuchi, H. Ashino, and Y. Nakahara, "SPECT imaging of mice with ^{99m}Tc-radiopharmaceuticals obtained from ^{99}Mo produced by ^{100}Mo(n,2n)^{99}Mo and fission of ^{235}U", J. Phys. Soc. Jpn. **84**, 043202-1-4 (2015). **N**

2) M. Kawabata, Y. Nagai, K. Hashimoto, H. Saeki, S. Motoishi, N. Sato, A. Ohta, T. Shiina, and Y. Kawauchi, "New phenomenon observed in thermal release of ^{99m}Tc from molten $^{100}MoO_3$", J. Phys. Soc. Jpn. **84**, 023201-1-4 (2015). **N**

3) M. Kawabata, K. Hashimoto, H. Saeki, N. Sato, S. Motoishi, K. Takakura, C. Konno, Y. Nagai, "Production and separation of ^{64}Cu and ^{67}Cu using 14 MeV neutrons", J. Radioanal. Nucl. Chem. **303**, 1205-09 (2015). **N**

4) Y. Hatsukawa, K. Hashimoto, K. Tsukada, T. Sato, M. Asai, A. Toyoshima, Y. Nagai, T. Tanimori, S. Sonoda, S. Kabuki, H. Saji, H. Kimura, "Production of ^{95m}Tc for Compton camera imaging", J. Radioanal. Nucl. Chem. **303**, 1283-85 (2015). **N**

5) E. Maeda, A. Yokoyama, T. Taniguchi, K. Washiyama, I. Nishinaka, "Extraction of astatine isotopes for development of radiopharmaceuticals using a ^{211}Rn-^{211}At generator", J. Radioanal. Nucl. Chem. **303**, 1465-68 (2015). **N**

6) K. Ogawa, Y. Mizuno, K. Washiyama, K. Shiba, N. Takahashi, T. Kozaka, Sh. Watanabe, A. Shinohara, A. Odani, "Preparation and evaluation of an astatine-211-labeled sigma receptor ligand for alpha radionuclide therapy" Nucl. Med. Biol. **42**, 875-79 (2015). **N**

7) M. Mori, K. Sagara, K. Arai, N. Nakatani, S. Ohira, K. Toda, H. Itabashi, D. Kozaki, Y. Sugo, Sh. Watanabe, N. S. Ishioka and K. Tanaka, "Simultaneous analysis of silicon and boron dissolved in water by combination of electrodialytic salt removal and ion-exclusion chromatography with corona charged aerosol detection", J. Chromatography A, **1431**, 131-37 (2016). **C, 2-36**

8) I. Sasaki, S. Watanabe, Y. Ohshima, Y. Sugo, K. Yamada, H. Hanaoka, and N. S. Ishioka "Medical application of radio-halogenated peptides: synthesis and in vitro evaluation of F(*p*-^{131}I)KCCYSL for targeting HER2 *in vitro*", Peptide Sci. 2015, 243-46 (2016/3). **N**

9) Y. Sugo, Y. Ohshima, I. Sasaki and N. S. Ishioka, "In vitro studies on cellular binding and stability of ^{64}Cu-labeled peptide for tumor imaging", Peptide Sci. 2014, 303-06 (2015). **C, 2-36**

10) Sa. Watanabe, K. Hashimoto, Sh. Watanabe, Y. Iida, H. Hanaoka, K. Endo and N. S. Ishioka, "Production of highly purified no-carrier- added ^{177}Lu for radioimmunotherapy", J. Radioanal. Nucl. Chem. **303**, 935-40 (2015). **C, 2-37**

11) Sa. Watanabe, K. Hashimoto, N. S. Ishioka, "Lutetium-177 complexation of DOTA and DTPA in the presence of competing metals", J. Radioanal. Nucl. Chem. **303**, 1519-21 (2015). **C, 2-37**

Proceedings

1) D. S. Wilbur, D.K. Hamlin, M.-K. Chyan, K. Gagnon, E. R. Balkin, and S. Watanabe, "Simplifying wet chemistry isolation of At-211 using PEG column", Proc. 9th Symp. Targeted Alpha Therapy (9th TAT), [Warsaw, Poland], (2015/5). **N**

2) S. Watanabe, K. Yamada, S. Watanabe, H. Oku, T. Moriguchi, K. Shinozuka, N. S. Ishioka, "Synthesis of radiobrominated amino acid derivatives via silicon-bromine exchange reaction", Proc. 15th Int. Symp. Radiopharm. Sci. (ISRS 2015), [Columbia, USA] 256 (2015/5). **N**

3) K. Kaira, M. Toyoda, Y. Ohshima, N. Oriuchi, Y. Kanai, T. Koyama, M. Yamada, T. Asao, K. Chikamatsu, "Clinical Significance of L-type Amino Acid Transporter 1 Expression as a Prognostic Markerand Potential of New Targeting Therapy in Tongue Cancer", Am. Soc. Clin. Oncol. Annu. Meet. 2015 [Chicago, USA], e22204 (2015/05). **N**

4) 渡辺 茂樹, 渡辺 智, D.K. Hamlin, M.-K. Chyan, K. Gagnon, 鈴木 博元, E. R. Balkin, 大島 康宏, D. S. Wilbur, 石岡 典子, "乾式法および湿式法による At-211 の分離", 第 15 回放射性医薬品・画像診断薬研究会, [京都], B-1 (2015/9). **C**

5) 須郷 由美, 大島 康宏, 山口 藍子, 花岡 宏史, 石岡 典子, "Cu-64 イオンを用いたがんの PET イメージング", 2015 放射化学会年会・第 59 回放射化学討論会, [仙台], 1B17 (2015/9). **C, 2-36**

6) 花岡 宏史, 大島 康宏, 山口 藍子, 鈴木 結利花, 上原 知也, 石岡 典子, 遠藤 啓吾, 荒野 泰, 対馬 義人, "ヨウ素標識 α メチル-フェニルアラニンの体内動態に関する基礎的検討", 第 55 回日本核医学会総会, [東京], M1IXD6 (2015/11). **N**

7) 佐々木 一郎, 渡辺 茂樹, 大島 康宏, 須郷 由美, 山田 圭一, 花岡 宏史, 石岡 典子, "放射性ハロゲン標識ペプチドの医学的応用:HER2 を標的とした F(*p*-^{131}I)KCCYSL の合成と *in vitro* 評価", 第 52 回ペプチド討論会, [平塚], P-073 (2015/11). **N**

8) S. Watanabe, I. Sasaki, Y. Ohshima, D. K. Hamlin, E. R. Balkin, M.-K. Chyan, D. S. Wilbur, N. S. Ishioka, "Isolation of At-211 using a solid phase anion exchange method", Proc. Int. Chem. Congr. Pacific Basin Soc. 2015 (Pacifichem 2015), [Honolulu, USA], INOR 397 (2015/12). **N**

9) Y. Ohshima, H. Suzuki, H. Hanaoka, Sh. Watanabe, Sa. Watanabe, N. Watanabe, Y. Tsushima, K. Endo, N. S. Ishioka, "Development of 2-[^{211}At]astato-α-methyl-L-phenylalanine (2-AAMP) as a novel radiopharmaceutical for internal radiotherapy", Proc. Int. Chem. Congr. Pacific Basin Soc. 2015 (Pacifichem 2015), [Honolulu, USA], HLTH 233 (2015/12). **N**

10) H. Hanaoka, Y. Ohshima, A. Yamaguchi, Y. Suzuki, T. Uehara, N. S. Ishioka, K. Endo, Y. Arano, Y. Tsushima, "Development of iodine-131-labeled α-methyl-L-phenylalanine for tumor therapy", Proc. Int. Chem. Congr. Pacific Basin Soc. 2015 (Pacifichem 2015), [Honolulu, USA] HLTH 132 (2015/12). **N**

11) K. Washiyama, R. Amano, E. Maeda, A. Yokoyama, I. Nishinaka, N. Takahashi, A. Shinohara, S. Watanabe, N. S. Ishioka, "Production of alpha-emitting radioisotopes using the cyclotron facilities at Osaka University and JAEA Takasaki, and the Tandem accelerator at Tokai, JAEA phase anion exchange method", Proc. Int. Chem. Congr. Pacific Basin Soc. 2015 (Pacifichem 2015), [Honolulu, USA], INOR 392 (2015/12). **C**

12) Y. Sasaki, Y. Sugo and K. Morita, "Extractions of actinides and lanthanides by different diglycolamides", Proc. 3rd Japan-China Academic Symp. Nucl. Fuel Cycle (ASNFC 2015), [Tokyo, Japan], 1B-11 (2015/12). **N**

13) 鈴木 博元, 大島 康宏, 花岡 宏史, 渡辺 茂樹, 渡辺 智, 佐々木 一郎, 坂下 哲哉, 荒野 泰, 石岡 典子, "^{211}At 標識 α-methyl-L-phenylalanine の合成とその基礎的評価", 日本薬学会第 136 年会, [横浜], 27L-am07 (2016/03). **C**

14) 橋本 和幸, 川端 方子, 佐伯 秀也, 佐藤 俊一, 塚田 和明, 渡辺 智, 永井 泰樹, "加速器中性子によるがん治療用 ^{67}Cu の大量製造法の開発", 第 52 回アイソトープ・放射線研究発表会, [東京], 1p-II-07 (2015/7). C, **2-38**

15) 川端 方子, 永井 泰樹, 橋本 和幸, 初川 雄一, 本石 章司, 佐伯 秀也, 佐藤 望, 太田 朗生, 椎名 孝行, 河内 幸正, 竹内 宣博, 芦野 広樹, 中原 勇人, "加速器中性子による ^{99}Mo の生成と ^{99m}Tc 熱分離", 第 52 回アイソトープ・放射線研究発表会, [東京], 1p-II-09 (2015/7). **C**

16) 塚田 和明, 佐藤 哲也, 橋本 和幸, 佐伯 秀也, 初川 雄一, 永井 泰樹, 渡辺 智, 石岡 典子, 武田 晋作, "重陽子照射で発生する加速器中性子による医療用 Y-90 の合成・分離研究", 2015 日本放射化学会年会・第 59 回放射化学討論会, [仙台], 1B16 (2015/9). **C, 2-38**

17) 初川 雄一, 鈴木 伸一, 矢板 毅, R. Paul, "即発ガンマ線放射化分析法による粘土鉱物試料の元素分析", 2015 日本放射化学会年会・第 59 回放射化学討論会, [仙台], 2A06 (2015/9). **N**

18) 鷲山 幸信, 前田 英太, 西中 一朗, 横山 明彦, 橋本 和幸, 牧井 宏之, "^{209}Bi(^{7}Li, 5n)^{211}Rn 反応を介して生成する^{211}At の製造条件の最適化", 2015日本放射化学会年会・第59回放射化学討論会, [仙台], 3A01 (2015/9). **N**

19) 西中 一朗, 鷲山 幸信, 横山 明彦, 前田 英太, 橋本 和幸, 牧井 宏之, "核反応^{209}Bi(^{7}Li, 5n)^{211}Rn でのα放射線療法用 ^{211}At の製造", 2015 日本放射化学会年会・第59回放射化学討論会, [仙台], 3A02 (2015/9). **N**

20) 瀬川 麻里子, 西中 一朗, 井上 徹, 橋本 和幸, 呉田 昌俊, "低線量α線放出核^{211}At の定量的可視化に向けた撮像システムの開発", 2015日本放射化学会年会・第59回放射化学討論会, [仙台], 3A03 (2015/9). **N**

21) 宮下 由香, 秋山 和彦, 初川 雄一, 久冨木 志郎, "高速中性子照射の反跳効果を利用した放射性ストロンチウム内包フラーレンの生成率向上", 2015 日本放射化学会年会・第 59 回放射化学討論会, [仙台], 3B03 (2015/9). **N**

22) 橋本 和幸, 川端 方子, 佐伯 秀也, 佐藤 俊一, 塚田 和明, 初川 雄一, 永井 泰樹, 渡辺 智, 石岡 典子, "重陽子照射で発生する加速器中性子によるがん治療用 ^{67}Cu の大量製造に関する検討", 2015 日本放射化学会年会・第 59 回放射化学討論会, [仙台], P34 (2015/9). **C, 2-38**

23) 川端 方子, 橋本 和幸, 本石 章司, 佐伯 秀也, 椎名 孝行, 太田 朗生, 竹内 宣博, 永井 泰樹, "$^{99}MoO_3$ から熱分離した ^{99m}Tc の回収・精製法の開発", 2015 日本放射化学会年会・第 59 回放射化学討論会, [仙台], P35 (2015/9). **N**

24) 村上 拳冬, 大江 崇太, 谷口 拓海, 橋本 和幸, 牧井 宏之, 西中 一朗, 鷲山 幸信, 横山 明彦, "^{211}Rn/^{211}At ジェネレータの原型としてのシリンジ密封抽出系の構築", 2015 日本放射化学会年会・第 59 回放射化学討論会, [仙台], P36 (2015/9). **N**

25) 武田 晋作, 塚田 和明, 浅井 雅人, 佐藤 哲也, 永井 泰樹, 阪間 稔, 松本 恵里佳, "Be(p, n)反応による高速中性子による医療用 ^{90}Y の合成研究", 2015 日本放射化学会年会・第 59 回放射化学討論会, [仙台], P38 (2015/9). **C**

Papers

1) T. Yoneyama, S. Ishikawa and S. Fujimaki, "Route and regulation of zinc, cadmium, and iron transport in rice plants (*Oryza sativa* L.) during vegetative growth and grain filling: Metal transporters, metal speciation, grain Cd reduction and Zn and Fe biofortification", Int. J. Mol. Sci., **16**, 19111 (2015). **C**
2) N. Kawachi, Y.-G. Yin, N. Suzui, S. Ishii, T. Yoshihara, H. Watabe, S. Yamamoto and S. Fujimaki, "Imaging of radiocesium uptake dynamics in a plant body by using a newly developed high- resolution gamma camera", J. Environ. Radioact., **151**, Part 2, 461-67 (2016). **C, 2-34**
3) M. Yamaguchi, K. Torikai, N. Kawachi, H. Shimada, T. Satoh, Y. Nagao, S. Fujimaki, M. Kokubun, S. Watanabe, T. Takahashi, K. Arakawa, T. Kamiya and T. Nakano, "Corrigendum: Beam range estimation by measuring bremsstrahlung", (2012 Phys. Med. Biol. **57**, 2843), Phys. Med. Biol., **61**, 3638-44 (2016). **C, 2-33**
4) M. Sakai, H. Sugai, M. Kikuchi, K. Torikai, K. Arakawa, M. Yamaguchi, Y. Nagao, N. Kawachi, S. Fujimaki, T. Kamiya, H. Odaka, M. Kokubun, S. Takeda, S. Watanabe, T. Takahashi and T. Nakano, "Nuclear medical imaging of Compton camera using kidney phantom", Jpn. J. Med. Phys., **35**(sup. 3), 104 (2015). **N**

Proceedings

1) S. Nakamura, H. Kondo, N. Suzui, Y.-G. Yin, S. Ishii, N. Kawachi, H. Rai, H. Hattori and S. Fujimaki, "Effects of glutathione concentration in the root zone and glutathione treatment period on cadmium partitioning in oilseed rape plants", Mol. Physiol. Ecophysiol. Sulfur, Springer International Publishing AG, [Basel, Switzerland], 253-59 (2015). **C, 2-32**
2) 栗田 圭輔, 河地 有木, 尹 永根, 鈴井 伸郎, 石井 里美, 渡部 浩司, 山本 誠一, 藤巻 秀, "放射性セシウム動態解析に向けた植物チェレンコフイメージング技術の開発", 日本土壌肥料学会, [京都], 講演要旨集 8-1-18 (2015). **N, 2-34**
3) 河地 有木, 尹 永根, 鈴井 伸郎, 石井 里美, 山本 誠一, 渡部 浩司, 吉原 利一, 藤巻 秀, "ガンマカメラを用いた放射性セシウムの植物体内動態の可視化技術", 日本土壌肥料学会, [京都], 講演要旨集 8-1-17 (2015). **N**
4) 中村 進一, 鈴井 伸郎, 中井 雄治, 尹 永根, 石井 里美, 河地 有木, 賴 泰樹, 服部 浩之, 藤巻 秀, "グルタチオンが植物体内のカドミウム動態に及ぼす影響の分子メカニズムの解明", 日本土壌肥料学会, [京都], 講演要旨集 4-3-5 (2015). **C**
5) 藤巻 秀, 丸山 哲平, 鈴井 伸郎, 河地 有木, 三輪 睿太郎, 樋口 恭子, "高い耐塩性を持つヨシの根における根端方向へのナトリウム排出のポジトロンイメージングによる画像解析", 日本土壌肥料学会, [京都], 講演要旨集 4-3-10 (2015). **N**
6) 鈴井 伸郎, 山崎 治明, 尹 永根, 河地 有木, 石井 里美, 島田 浩章, 藤巻 秀, "トマト生物生産性向上のための高濃度 CO_2 施用効果の評価 : ポジトロンイメージング技術を用いた炭素栄養の動態解析", 日本土壌肥料学会, [京都], 講演要旨集 4-1-11 (2015). **C**
7) 尹 永根, 鈴井 伸郎, 河地 有木, 石井 里美, 栗田 圭輔, 中村 卓司, 信濃 卓郎, 藤巻 秀, "ダイズ根が根圏土壌へ分泌した有機物の可視化と定量解析(2) : 異なる培地条件における分泌物の分布の比較", 日本土壌肥料学会, [京都], 講演要旨集 6-2-17 (2015). **C, 2-35**
8) 栗田 圭輔, 河地 有木, 尹 永根, 鈴井 伸郎, 石井 里美, 渡部 浩司, 山本 誠一, 藤巻 秀, "チェレンコフ光を利用した植物 RI イメージング技術の開発", 日本原子力学会関東・甲越支部 第 14 回若手研究者発表討論会, [狛江], 11-12 (2015). **N, 2-34**
9) 鈴井 伸郎, "農業に役立つ放射線イメージング", 第 76 回応用物理学会学術講演会「シンポジウム: 化学分析技術と放射線」, [名古屋], 14p-2V-5 (2015). **C**
10) 石井 陽平, 鈴井 伸郎, 尹 永根, 河地 有木, 石井 里美, 栗田 圭輔, 島田 浩章, 藤巻 秀, "シロイヌナズナ flo2 変異体の個体生育と炭酸同化産物動態の PETIS による解析", 第 57 回日本植物生理学会年会, [盛岡], 2pC01 (2016). **C**
11) 中村 進一, 鈴井 伸郎, 尹 永根, 石井 里美, 河地 有木, 賴 泰樹, 服部 浩之, 藤巻 秀, "アブラナの根に与えたグルタチオンが根からのカドミウム排出に及ぼす影響", 第 57 回日本植物生理学会年会, [盛岡], PL-008 (2016). **C**
12) 山口 充孝, 長尾 悠人, 河地 有木, 藤巻 秀, 神谷 富裕, 鳥飼 幸太, 島田 博文, 菅井 裕之, 酒井 真理, 荒川 和夫, 中野 隆史, "炭素イオン線治療における数 100 keV 以下の低エネルギー光子測定による体内軌跡上の間隙の検出", 第 31 回 PIXE シンポジウム, [高崎], 5-3 (2015). **C, 2-33**
13) M. Yamaguchi, Y. Nagao, N. Kawachi, S. Fujimaki, T. Kamiya, K. Torikai, H. Shimada, K. Arakawa and T. Nakano, "Detection of a gap across a particle-beam track by measuring 63-68 keV photons", 2015 IEEE Nucl. Sci. Symp. Med. Imaging Conf. (2015 IEEE NSS/MIC), [San Diego, USA], M4CP-302 (2015). **C, 2-33**
14) 山口 充孝, 長尾 悠人, 菅井 裕之, 酒井 真理, 河地 有木, 佐藤 隆博, 神谷 富裕, 藤巻 秀, 荒川 和夫, 鳴海 一雅, "低エネルギー光子測定による治療用炭素ビーム軌道上の空洞検出のシミュレーションによる評価", 第 63 回応用物理学会春季学術講演会, [東京], 22a-W833-10 (2016). **C, 2-33**
15) M. Sakai, M. Kikuchi, K. Torikai, K. Arakawa, M. Yamaguchi, Y. Nagao, N. Kawachi, S. Fujimaki, T. Kamiya, H. Odaka, M. Kokubun, S. Takeda, S. Watanabe, T. Takahashi and T. Nakano, "Development of image-based scatter correction on the image of semiconductor Compton camera for nuclear medical use", Proc. 15th Int. Congr. Radiat. Res. (ICRR2015), [Kyoto, Japan] 2-PS9B-03 (2015). **N**
16) 菅井 裕之, 平野 祥之, 酒井 真理, 山口 充孝, 長尾 悠人, "シミュレーションで考慮されていない低エネルギー光子", 原子衝突学会第 40 回年会, [八王子], P1-25 (2015). **N**
17) 吉原 利一, 長尾 悠人, 橋田 慎之介, 河地 有木, 藤巻 秀, "半導体型積算線量計による環境放射能の測定(その1)－従来測定法との比較による可能性評価－", 電力中央研究所報告, O14002 (2015). **N**
18) T. Yoshihara, A. Kominato, Y. Nagao, N. Kawachi, S. Hashida, N. Suzui, Y.-G. Yin and S. Fujimaki, "Measurement of environmental radioactivity using a cumulative gamma radiation dosimeter: Fertilization induced changes in young fruit trees", Int. Conf. Environ. Radioact. (ENVIRA2015), [Thessaloniki, Greece], PS1-3 (2015). **N**

Book

1) 河地 有木, 「核医学物理学(医学物理学教科書シリーズ)」(第 8 章第 2 節「コンプトンイメージング」), (2015).

Patent

1) 特許第 5721135 号, 山口 充孝, 河地 有木, 佐藤 隆博, 神谷 富裕, 中野 隆史, 荒川 和夫, 島田 博文, 高橋 忠行, 渡辺 伸, 国分 紀秀, "粒子線モニタリング装置, 粒子線モニタリングプログラム及び粒子線モニタリング方法", 登録日 : 平成 27 年 4 月 3 日. **C, 2-33**

Press・TV

1) 原子力機構・東京農業大学(共同研究者), "ヨシはなぜ塩水でも育つのか ー根の中でナトリウムを送り返す動きをポジトロンイメージングで観ることに世界初成功ー", 2015.4.23 プレス発表: 読売新聞, 朝日新聞, 毎日新聞, 日経新聞, 日刊工業新聞に掲載. **C**

2) NHKサイエンスゼロ, "食糧危機の切り札!? 耐塩性作物", 2015.9.6 放送.

Radiation and Biomolecular Science Research Project (P2-5)

Papers

1) R. Watanabe, Y. Hattori, T. Kai, "Evaluation of DNA damage induced by Auger electrons from ^{137}Cs", Int. J. Radiat., Biol. (Epub. ahead of print). **N**

2) Y. Izumi, S. Yamamoto, K. Fujii, A. Yokoya, "Ultraviolet circular dichroism spectroscopy for protein structure study", Radiat. Biol. Res. Comm., **51**, 91-106 (2016) (*in Japanese*). **N**

3) H. Fukunaga, A. Yokoya, "Low-dose radiation risk and individual variations in radiation sensitivity in Fukushima", J. Radiat. Res., **57**, 98-100 (2016). **N**

4) T. Kai, A. Yokoya, K. Fujii, R. Watanabe, "Recent progress of radiation physicochemical process (first part)", Houshasenkagaku (Raidait. Chem.), **101**, 3-11 (2016) (*in Japanese*). **N**

Proceedings

1) M. Tomita, M. Maeda, N. Usami, A. Yokoya, R. Watanabe, H. Matsumoto, K. Kobayashi, "Induction of DNA Double-strand break of plasmid DNA and human cell lines by K-shell absorption of phosphorus", Proc. 8th Auger Symp., [Kyoto, Japan], 21 (2015/05). **N**

2) K. Fujii, Y. Izumi, A. Narita, K. Ghose, A. Touati, R. Vuilleumier, M-P. Gaigeot, M-F. Politis, M-A. Hervé du Penhoat, A. Yokoya, "Roles of Hydrated Water in Inducing Destruction of Sugar Moiety in DNA by Ionization of Oxygen Core-electrons", Proc. 8th Auger Symp. [Kyoto, Japan], 22 (2015/05). **N**

3) H. Shimada, M. Ukai, K. Fujii, A. Yokoya, Y. Fukuda, Y. Saitoh, "Nitrogen K-edge X-ray absorption near edge structure of pyrimidine-containing nucleotides in aqueous solution", Proc. 8th Auger Symp., [Kyoto, Japan], 23 (2015/05). **N**

4) T. Kai, A. Yokoya, M. Ukai, R. Watanabe, "Deceleration process of Auger electrons in liquid water calculated by a dynamic Monte Carlo method for prediction of DNA damage induction", Proc. 8th Auger Symp., [Kyoto, Japan], 24 (2015/05). **N**

5) A. Narita, K. Fujii, A. Yokoya, Y. Baba, I. Shimoyama, "Novel technique to investigate physical process of DNA damage induction by core electron ionization of constituent atoms in chromatin structure", Proc. 8th Auger Symp., [Kyoto, Japan], 27 (2015/05). **N**

6) M. Noguchi, A. Yokoya, K. Kaminaga, K. Suzuki, N. Usami, "Autophagy activated by Auger effect induced by soft X-ray microbeam", Proc. 8th Auger Symp., [Kyoto, Japan], 32 (2015/05). N

7) T. Oka, A. Yokoya, K. Fujii, Y. Kino, T. Sekine, "Unpaired electrons in pyrimidine DNA-bases induced by core-excitation and substituent effect", Proc. 8th Auger Symp., [Kyoto, Japan], 33 (2015/05). **N**

8) Y. Sugaya, K. Fujii, A. Yokoya, "Yields of DNA strand breaks and base lesions induced by oxygen K-shell electron ionization", Proc. 8th Auger Symp., [Kyoto, Japan], 34 (2015/05). **N**

9) R. Watanabe, T. Kai, A. Yokoya, "Evaluation of DNA damage induced by Auger electrons from ^{137}Cs", Proc. 8th Auger Symp., [Kyoto, Japan], 36 (2015/05). **N**

10) A. Yokoya, K. Fujii, T. Kai, R. Watanabe, M. Noguchi, "Structure and repairability of clustered DNA damage", Proc. 15th Int. Congr. Radiat. Res. (ICRR 2015), [Kyoto, Japan], 5-C1SY- 60-02 (2015/05). **N**

11) M. Tomita, M. Maeda, N. Usami, A. Yokoya, R. Watanabe, H. Matsumoto, K. Kobayashi, "Effects of DNA Double-strand break induction and repair and cell killing by K-shell absorption of phosphorus in human cell lines", Proc. 15th Int. Congr. Radiat. Res. (ICRR 2015), [Kyoto, Japan], 5-C1SY-60-04 (2015/05). **N**

12) R. Watanabe, T. Kai, A. Yokoya, "Simulation of energy deposition and DNA damage induced by gamnma-rays and electrons from ^{137}Cs", Proc. 15th Int. Congr. Radiat. Res. (ICRR 2015), [Kyoto, Japan], 3-PS3B-25 (2015/05). **N**

13) Y. Hattori, A. Yokoya, R. Watanabe, "Simulation study of individual cellular responses by bystander effects in cellular population", Proc. 15th Int. Congr. Radiat. Res. (ICRR 2015), [Kyoto, Japan], 4-PS3F-17 (2015/05). **N**

14) K. Kaminaga, Y. Kanari, Y. Sakamoto, M. Noguchi, A. Narita, K. Fujii, N. Usami, K. Kobayashi, K. Suzuki, A. Yokoya, K. Fujii, T. Kai, R. Watanabe, M. Noguchi, "Live cell imaging study on biological effects induced by X-ray microbeam irradiation", Proc. 15th Int. Congr. Radiat. Res. (ICRR 2015), [Kyoto, Japan], 4-PS1B-17 (2015/05). **N**

15) K. Fujii, Y. Izumi, A. Narita, K. Ghose, A. Touati, R. Vuilleumier, M-P. Gaigeot, M-F. Politis, M-A. Hervé du Penhoat, A. Yokoya, "Physical Process of Decomposition of Hydrated Deoxyribose by Oxygen K-shell Ionization", Proc. 15th Int. Congr. Radiat. Res. (ICRR 2015), [Kyoto, Japan], 2-C1OS-06-02 (2015/05). **N**

16) Y. Hattori, A. Yokoya, R. Watanabe, "A mathematical model of modification of cell-cycle progression by radiation-induced bystander effects", Proc. 12th Int. Workshop Microbeam Probes of Cellular Radiat. Response, [Tsuruga, Japan], 55 (2015/05). **N**

17) 渡辺 立子, "がん治療のための放射線物理化学生物シミュレーション", 日本原子力学会 2015 秋の大会企画セッション, [静岡], (2015/09). **N**

18) 藤井 健太郎, "放射光を用いた放射線生物研究ー次世代放射光光源への期待ー", 先端放射線化学シンポジウム (SARAC2015) 要旨集, [浜松], 28-29 (2015/09). **N**

19) 横谷 明徳, 神長 輝一, 服部 佑哉, 渡辺 立子, 野口 実穂, 藤井 健太郎, "放射線照射された細胞のライブセルイメージングと細胞周期動態変異のコンピュータシミュレーション", 第 24 回乳癌基礎研究会, [いわき], 25 (2015/09). **N**

20) 神長 輝一, 宇佐美 徳子, 野口 美穂, 横谷 明徳, "X 線マイクロビーム照射後の細胞周期のタイムラプスイメージング", 第1回放射線ワークショップ 未来に繋ぐ放射線研究, [富山], 26 (2015/10). **N**

21) T. Yonetani, "Origin of distinct, ion-pair dissociation kinetics revealed by the solvent-coordinate, free-energy landscape analysis", Proc. 251st ACS Natl. Meet. [SanDiego, USA] COMP 409 (2016/03). **N**

22) A. Yokoya, Y. Sugaya, T. Oka, K. Fujii, M. Ukai, "DNA damage induced by K-shell ionization and succeeding resonant Auger transition", Proc. 14th Int. Workshop on Radiation Damage to DNA [Melbourne, Australia], 65 (2016/03). **N**

23) K. Fujii, Y. Izumi, K. Ghose, T. P. López, A. Touati, R. Vuilleumier, M.-P. Gaigeot, M.-F. Politis, M.-A. Hervé du Penhoat, A. Yokoya, "Roles of hydration for inducing DNA strand breaks by ionization of oxygen K-shell electrons", Proc. 14th Int. Workshop on Radiation Damage to DNA [Melbourne, Australia], 87 (2016/03). **N**

24) Y. Izumi, S. Yamamoto, K. Fujii, A. Yokoya, "Secondary structural alteration of histone H2A-H2B induced by DNA damage responses", Proc. 14th Int. Workshop on Radiation Damage to DNA [Melbourne, Australia], 110 (2016/03). **N**

Biomolecular Function Research Project（P2-6）

Papers

1) T. Uemura, A. Kita, Y. Watanabe, M. Adachi, R. Kuroki, Y. Morimoto, "The catalytic mechanism of decarboxylative hydroxylation of salicylate hydroxylase revealed by crystal structure analysis at 2.5 Å resolution", Biochem. Biophys. Res. Commun. **469**, 158-63 (2016). **N**

2) Y. Yonezawa, A. Nagayama, H. Tokunaga, M. Ishibashi, S. Arai, R. Kuroki, K. Watanabe, T. Arakawa, M. Tokunaga, "Nucleoside diphosphate kinase from psychrophilic *Pseudoalteromonas* sp. AS-131 isolated from antarctic ocean", Protein J. **34**, 275-83 (2015). **N**

Proceedings

1) K. Maekawa, Y. Matsuzawa, M. Adachi, R. Kuroki, Y. Saito, "Purification of cytochrome P450 2C9.1, 2 C9.3 and 2C9.30 expressed in *E. coli* and their activities toward arachidonic acid *in vitro*", Proc. 19th Int. Conf. Cytochrome P450, [Tokyo, Japan], (2015). **N**

2) T. Uamimura, A. Kita, M. Adachi, R. Kuroki, Y. Morimoto, "Crystal structure analysis of a ligand complex for salicylate hydroxylase", Proc. 15th Annu. Meet. Protein Sci. Soc. Jpn., [Tokushima, Japan], (2015). **N**

3) S. Arai, M. Adachi, T. Tamada, K. Tokunaga, M. Ishibashi, M. Tokunaga, R. Kuroki, "Tertiary structure and low-salt concentration adaptation mechanism of beta-lactamase from moderate halophile", Proc. 15th Annu. Meet. Protein Sci. Soc. Jpn., [Tokushima, Japan], Poster (2015). N

4) R. Shimizu, T. Hiromoto. M. Adachi, C. Shibazaki, R. Kuroki, "Neutron structure analysis on perduterated T4 phage lysozyme", Proc. 15th Annu. Meet. Protein Sci. Soc. Jpn., [Tokushima, Japan], Poster (2015). **N**

5) H. Hirayama, M. Adachi, R. Shimizu, R. Kuroki, "Expression and purification of influenza neuraminidase in Pichia pastoris", Proc. 15th Annu. Meet. Protein Sci. Soc. Jpn., [Tokushima, Japan], Poster (2015). **N**

6) T. Hiromoto, E. Honjo, T. Tamada, R. Kuroki, N. Noda, K. Kazuma, M. Suzuki, "Structural basis for acceptor-substrate recognition of UDP-glucose: anthocyanidin 3-*O*-glucosyltransferase from Clitoria ternatea", Proc. 15th Annu. Meet. Protein Sci. Soc. Jpn., [Tokushima, Japan], Poster (2015). **N**

7) S. Arai, M. Adachi, T. Tamada, K. Tokunaga, M. Ishibashi, M. Tokunaga, R. Kuroki, "Discovery of Cs^+ selective binding site on a halophilic protein", 九州シンクロトロン光研究センター合同シンポジウム, [Tosu, Japan], Oral (2015). **N**

8) T. Hiromoto, R. Shimizu, M. Adachi, C. Shibazaki, "Neutron structure determination of perdeuterated T4 phage lysozyme", 平成27年度日本結晶学会年会, [Sakai, Japan], Poster, PC-068 (2015). **N**

9) C. Shibazaki, M. Adachi, T. Hiromoto, R. Shimizu, R. Kuroki, "Preparation of large volume casein kinase-2 crystals for neutron diffraction experiment", 日本中性子科学会第 15 回年会 (JSNS2015), [Wako, Japan], Poster (2015). **N**

10) M. Adachi, R. Kuroki, K. Maekawa, Y. Matsuzawa, Y. Saito, "Crystal structure of human drug metabolizing enzyme CYP2C9 mutants in complex with losartan determined by X-ray crystallography", Annu. Meet. Jpn. Biochem. Soc., [Kobe, Japan], Poster (2015). **N**

11) M. Adachi, R. Kuroki, K. Maekawa, Y. Matsuzawa, Y. Saito, "Crystal structure of human drug metabolizing enzyme CYP2C9 mutants in complex with losartan determined by X-ray crystallography" Annu. Meet. Jpn. Biochem. Soc., [Kobe, Japan], Oral (2015). **N**

Biomolecular Structure and Dynamics Research Project（P2-7）

Papers

1) T. Matsuo, S. Takeda, T. Oda, K. Nakajima and S. Fujiwara, "Structures of the troponin core domain containing the cardiomyopathy-causing mutants studied by small-angle X-ray scattering", Biophys. Physicobiol. **12**, 145-58 (2015). **N**

2) 海野 昌喜, 杉島 正一, 和田 啓, 萩原 義徳, 日下 勝弘, 玉田 太郎, 福山 恵一, "中性子結晶構造解析で明らかになったビリン還元酵素PcyA基質複合体の2つの水素化状態と構造的特徴", 日本結晶学会誌, **57**, 297-303 (2015). **N**

3) T. Tamada, D. Shinmi, M. Ikeda, Y. Yonezawa, S. Kataoka, R. Kuroki, E. Mori and K. Motoki, "TRAIL-R2 superoligomerization induced by human monoclonal agonistic antibody KMTR2", Sci. Rep. **5**, 17935 (2015). **N**

4) K. Tomoyori, Y. Hirano, K. Kurihara and T. Tamada, "Background elimination using the SNIP algorithm for Bragg reflections from a protein crystal measured by a TOF singlecrystal diffractometer", J. Phys.: Conf. Ser. **664**, 072049 (2015). **N**

5) T. Chatake and S. Fujiwara, "A technique for determining the deuterium/hydrogen contrast map in neutron macromolecular crystallography", Acta Crystallogr. **D72**, 71-82 (2016). **N**

Proceedings

1) K. Tomoyori, K. Kurihara, T. Tamada and R. Kuroki, "Evaluation of the resolvable capacity of Bragg reflections for a new diffractometer at J-PARC/MLF designed for protein crystals with large unit cells", JPS Conf. Proc. **8**, 036004, [Tsukuba, Japan] (2015). **N**

2) 玉田 太郎, "電子伝達タンパク質の高分解能中性子結晶構造解析", 第15回日本蛋白質科学会年会,［徳島］, (2015/6). **N**

3) 栗原 和男, 友寄 克亮, 玉田 太郎, 黒木 良太, "大型単位胞タンパク質結晶をターゲットとしたJ-PARC中性子回折装置のガイド管設計", 第15回日本蛋白質科学会年会,［徳島］, (2015/6). **N**

4) 友寄 克亮, 栗原 和男, 玉田 太郎, 黒木 良太, "J-PARC大型生体高分子パルス回折装置設置に向けた反射分離能の評

価”, 第15回日本蛋白質科学会年会, [徳島], (2015/6). N

5) 平野 優, 玉田 太郎, 栗原 和男, 日下 勝弘, 三木 邦夫, “高電位鉄硫黄タンパク質の高分解能中性子構造解析”, 第15回日本蛋白質科学会年会, [徳島], (2015/6). N

6) S. Fujiwara, T. Matsuo, T. Yamada, and K. Shibata, “Dynamical behavior of proteins observed by neutron scattering –Quasielastic neutron scattering study of muscle thin filaments–”, Proc. 3rd Awaji Int. Workshop Electron Spin Sci. Tech.: Biol. Mater. Sci. Oriented Appl., [Awaji, Japan], (2015/6). N

7) T. Matsuo, T. Arata, T. Oda, and S. Fujiwara, “Dynamics of F-actin, myosin subfragment-1, and their hydration water studied by quasielastic neutron scattering” Proc. 3rd Awaji Int. Workshop Electron Spin Sci. Tech.: Biol. Mater. Sci. Oriented Appl., [Awaji, Japan], (2015/6). N

8) S. Fujiwara, T. Matsuo, T. Yamada, and K. Shibata, “A view of the regulatory mechanism of muscle contraction from protein dynamics: a neutron scattering study of muscle thin filaments”, 第53回日本生物物理学会年会, [金沢], (2015/9). N

9) T. Matsuo, T. arata, T. Oda, and S. Fujiwara, “Dynamics of F-actin, myosin subfragment-1 (S1), and their hydration water studied by quasielastic neutron scattering”, 第53回日本生物物理学会年会, [金沢], (2015/9). N

10) 玉田 太郎, “中性子を用いたタンパク質立体構造解析と産業応用”, 第5回CSJ化学フェスタ2015, [東京], (2015/10). N

11) 玉田 太郎, 平野 優, 友寄 克亮, 栗原 和男, “J-PARCを利用したタンパク質中性子結晶構造解析の現状と今後”, 平成27年度日本結晶学会年会, [堺], (2015/10). N

12) 平野 優, 玉田 太郎, 栗原 和男, 日下 勝弘, 大野 拓, 竹田 一旗, 三木 邦夫, “タンパク質の高分解能中性子構造における水素原子の構造”, 平成27年度日本結晶学会年会, [堺], (2015/10). N

13) 栗原 和男, 友寄 克亮, 玉田 太郎, “大型単位胞タンパク質結晶の測定を実現する中性子回折装置”, 日本中性子学会第15回年会, [和光], (2015/12). N

14) 藤原 悟, 松尾 龍人 ,山田 武, 柴田 薫, “筋収縮調節機構と関連した筋肉の細いフィラメントのダイナミクス変化”, 日本中性子学会第15回年会, [和光], (2015/12). N

15) 松尾 龍人, 荒田 敏昭, 小田 俊郎, 藤原 悟, “中性子準弾性散乱を用いた筋収縮蛋白質及び水和水のダイナミクス解析”, 日本中性子学会第15回年会, [和光], (2015/12). N

16) 平野 優, 木村 成伸, 玉田 太郎, “ブタ肝臓由来シトクロムb5可溶性ドメインの高分解能結晶構造”, 2015年度量子ビームサイエンスフェスタ, [つくば], (2016/3). N

17) S. Arai, M. Adachi, T. Tamada, K. Tokunaga, M. Ishibashi, M. Tokunaga, R. Kuroki, “Tertiary structure and low-salt concentration adaptation mechanism of beta-lactamase from moderate halophile”, Proc. 15th Annu. Meet. Protein Sci. Soc. Jpn., [Tokushima, Japan], Poster (2015). N

18) T. Hiromoto, E. Honjo, T. Tamada, R. Kuroki, N. Noda, K. Kazuma, M. Suzuki, “Structural basis for acceptor- substrate recognition of UDP-glucose: anthocyanidin 3-*O*-glucosyltransferase from Clitoria ternatea”, Proc. 15th Annu. Meet. Protein Sci. Soc. Jpn., [Tokushima, Japan], Poster (2015). N

19) S. Arai, M. Adachi, T. Tamada, K. Tokunaga, M. Ishibashi, M. Tokunaga, R. Kuroki, “Discovery of Cs^+ selective binding site on a halophilic protein”, 九州シンクロトロン光研究センター合同シンポジウム, [Tosu, Japan], Oral (2015). N

Press・TV

1) 茨城大学・大阪大学・原子力機構・茨城県, “光合成色素を合成する酵素反応の瞬間を世界で初めて水素原子レベルの極小解析度で解明－光をエネルギーに変換する装置開発等への応用に期待－”, 2015.4.15 プレス発表: NHK（水戸放送局）で紹介.

2) 原子力機構, “抗がん剤の作用メカニズムの鍵を原子レベルで解明－より効果の高い抗がん剤の開発に繋がると期待－”, 2015.12.18プレス発表: 日刊工業新聞, 化学工業日報, マイナビニュース, ナノテクジャパン等に掲載.

Laser Compton Scattering Gamma-ray Research Project（P3-1）

Papers

1) T. Nakamura and T. Hayakawa, “Laser-driven γ-ray, positron, and neutron source from ultra-intense laser-matter interactions”, Phys. Plasmas **22**, 083113 (2015). N

2) 羽島 良一, 山本 将博, 中村 典雄, 阪井 寛志, 帯名 崇, “会議報告:Workshop on Energy Recovery Linacs (ERL2015)”, 加速器, **12**, 162-64 (2015). N

3) 早川 岳人, 梶野 敏貴, 千葉 敏, “太陽系を作った超新星爆発はいつ起きたのか? ―宇宙核時計ニオブ 92―”, 日本物理学会誌 **70**, 824-29 (2015). N

4) Christopher T. Angell, “Enabling in situ Thermometry Using Cryogenic Transmission Nuclear Resonance Fluorescence”, Nucl. Instrum. Meth. Phys. Res. B, **368**, 9-14 (2016). N

5) R. Hajima and M. Fujiwara, “Narrow-band GeV photons generated from an x-ray free-electron laser oscillator”, Phys. Rev. Accel. Beams **19**, 020702 (2016). N

6) 羽島 良一, 照沼 信浩, “電子ビームとレーザーの衝突によるX線の発生”, Isotope News, **741**, 16-20 (2016). N

7) 羽島 良一, 原田 寛之, 神野 智, 上坂 充, “会議報告:ビーム物理研究会, ビーム物理若手の会”, 加速器, **13**, 52-53 (2016). N

Proceedings

1) S. Sakanaka, M. Adachi, S. Adachi,・・・・ R. Hajima, S. Matsuba, M. Mori, *et al.* “Recent Progress and Operational Status of the Compact ERL at KEK”, Proc. 6th Int. Part. Accel. Conf. (IPAC-15), [Richmond, USA], 1359-62 (2015/3). N

2) A. Kosuge, T. Akagi, S. Araki, Y. Honda, N. Terunuma, J. Urakawa, R. Hajima, M. Mori, T. Shizuma and R. Nagai, “Development of a High Average Power Laser for High Brightness X-ray Source and Imaging at cERL”, Proc. 6th Int. Part. Accel. Conf. (IPAC-15), [Richmond, USA], 1579-81 (2015). N

3) R. Nagai, R. Hajima, M. Mori, T. Shizuma, T. Akagi, S. Araki, Y. Honda, A. Kosuge, N. Terunuma and J. Urakawa, “Demonstration of High-flux Photon Generation from an ERL-based Laser Compton Photon Source”, Proc. 6th Int. Part. Accel. Conf. (IPAC-15), [Richmond, USA], 1607-09 (2015). N

4) T. Kubo, T. Saeki, E. Cenni, Y. Iwashita, H. Tongu, R. Hajima, M. Sawamura, “Multipactor Simulations in 325 MHz Superconducting Spoke Cavity for an Electron Accelerator”, Proc. 6th Int. Part. Accel. Conf. (IPAC-15), [Richmond, USA], 2892-94 (2015). N

5) R. Hajima, M. Sawamura, E. Cenni, Y. Iwashita, H. Tongu, T. Kubo and T. Saeki, “Development of Superconducting Spoke

Cavities for Laser Compton Scattered X-ray Sources", Proc. 6th Int. Part. Accel. Conf. (IPAC-15), [Richmond, USA], 2902-04 (2015). **N**

6) N. Nishimori, "Review of Experimental Results from High Brightness DC Guns: Highlights in FEL Applications", Proc. Int. FEL Conf. (FEL-2015) [Daejeon, Korea], 269-73 (2015). **N**

7) 羽島 良一, 沢村 勝, 永井 良治, 西森 信行, 早川 岳人, 静間 俊行, Christopher T. Angell, "レーザー・コンプトン散乱による高輝度ガンマ線の実現とその利用", 日本加速器学会第12回年次大会, [敦賀], 論文集 79-83 (2015). **N**

8) 高井 良太, 足立 伸一, 阿達 正浩 ・・・・, 羽島 良一, 松葉 俊哉, 森 道昭, 永井 良治, 西森 信行, 沢村 勝, 静間 俊行 他, "コンパクトERLのコミッショニング状況とビーム利用に向けた取り組み", 日本加速器学会第12回年次大会, [敦賀], 論文集 181-86 (2015). **N**

9) 西森 信行, 永井 良治, 沢村 勝, 羽島 良一, "250 kV大電流光陰極電子銃の開発", 日本加速器学会第12回年次大会, [敦賀], 論文集 508-10 (2015). **N**

10) 西森 信行, 永井 良治, 森 道昭, 羽島 良一, 山本 将博, 本田 洋介, 宮島 司, 内山 隆司, 金 秀光, 帯名 崇, 栗木 雅夫, "コンパクトERL電子銃の現状とアップグレード計画", 日本加速器学会第12回年次大会, [敦賀], 論文集 511-15 (2015). **N**

11) 沢村 勝, 羽島 良一, 西森 信行, 永井 良治, 岩下 芳久, 頓宮 拓, 久保 毅幸, 佐伯 学行, "ERL 超伝導スポーク空洞製作の現状", 日本加速器学会第12回年次大会, [敦賀], 論文集 583-86 (2015). **N**

12) 濁川 和幸, 小菅 隆, 斉藤 裕樹, 羽島 良一, 永井 良治, "cERLでのLCS実験用ビームラインのインターロックシステム", 日本加速器学会第12回年次大会, [敦賀], 論文集 1290-93 (2015). **N**

13) 永井 良治, 羽島 良一, 静間 俊行, 森 道昭, 赤木 智哉, 小菅 淳, 本田 洋介, 荒木 栄, 照沼 信浩, 浦川 順治, "コンパクトERLでのレーザーコンプトン散乱光源実証実験", 日本加速器学会第12回年次大会, [敦賀], 論文集 1328-30 (2015). **N**

14) 赤木 智哉, 小菅 淳, 本田 洋介, 荒木 栄, 照沼 信浩, 浦川 順治, 永井 良治, 羽島 良一, 静間 俊行, 森 道昭, "レーザーコンプトン散乱による小型高輝度X線源開発", 日本加速器学会第12回年次大会, [敦賀], 論文集 1331-33 (2015). **N**

Patents

1) 早川 岳人, 羽島 良一, 静間 俊行, 藤原 守, "癌治療システム", 特許登録, 特許第 5799388 号 (2015.9.4).

2) 宮本 修治, 早川 岳人, 羽島 良一, "放射性廃棄物の処理方法", PCT 出願: PCT/JP2015/86551 (2015.12.28).

Press・TV

1) 原子力機構・高エネ機構, "これまでになく強く明るいX線を発生する新たな技術誕生へ―毎秒1億回の電子ビーム・レーザー衝突でX線を作る―", 2015年4月27日プレス発表.

Beam Engineering Section（P3-2）

Papers

1) H. Yoshizaki, A. Hashimoto, Y. Kaneno, S. Semboshi, Y. Saitoh, Y. Okamoto and A. Iwase, "Modification of surface hardness for dual two-phase Ni_3Al-Ni_3V intermetallic compound by using energetic ion beam and subsequent thermal treatment", Nucl. Instrum. Meth. Phys. Res. B, **345**, 22-26 (2015). **T, 1-33~36**

2) H. Yoshizaki, A. Hashimoto, Y. Kaneno, S. Semboshi, F. Hori, Y. Saitoh, A. Iwase, "Energetic ion-beam induced crystal phase transformation and resulting hardness change in Ni_3Al intermetallic compound", Nucl. Instrum. Meth. Phys. Res. B, **354**, 287-91 (2015). **T, 1-33~36**

3) D. Ueyama, Y. Saitoh, N. Ishikawa, T. Ohmura, S. Semboshi, F. Hori, A. Iwase, "Hardness modification of Al–Mg–Si alloy by using energetic ion beam irradiation", Nucl. Instrum. Meth. Phys. Res. B, **351**, 1-5 (2015). **T, 1-33~36**

4) K. Nakano, H. Yoshizaki, Y. Saitoh, N. Ishikawa and A. Iwase, "XRD study of yttria stabilized zirconia irradiated with 7.3 MeV Fe, 10 MeV I, 16 MeV Au, 200 MeV Xe and 2.2 GeV Au ions", Nucl. Instrum. Meth. Phys. Res. B, **370**, 67-72 (2016). **T, 1-33~36**

5) H. Kojima, H. Yoshizaki, Y. Kaneno, S. Semboshi, F. Hori, Y. Saitoh, Y. Okamoto and A. Iwase, "Lattice structure transformation and change in surface hardness of Ni_3Nb and Ni_3Ta intermetallic compounds induced by energetic ion beam irradiation", Nucl. Instrum. Meth. Phys. Res. B, **372**, 72-77 (2016). **T, 1-33~36**

6) Y. Fujimura, S. Semboshi, Y. Okamoto, Y. Saitoh, T. Matsui and A. Iwase, "Magnetic states of cobalt atoms in copper metal after cobalt-implantation and effects of subsequent annealing", Trans. Mater. Res. Soc. Jpn. **41**(2), 209-12 (2016/3). **T, 1-33~36**

7) T. Satoh, A Yokoyama, A. Kitamura, T. Ohkubo, Y. Ishii, Y. Takahatake, S. Watanabe, Y. Koma, W. Kada, "Particle Induced X-ray Emission-Computed Tomography Analysis of an Adsorbent for Extraction Chromatography", Nucl. Instrum. Meth. Phys. Res. B, **371**, 419-23 (2016). **T, 1-56**

8) K. Nakai, Y. Yamamoto, E. Okamoto, T. Yamamoto, F. Yoshida, A. Matsumura, N. Yamada, M. Koka and T. Satoh, "Boron analysis for neutron capture therapy using particle-induced gamma-ray emission", Appl. Radiat. Isot., **106**, 166-70 (2015). **S, 2-40**

9) Y. Shimizu, K. Dobashi, H. Nagase, K. Ohta, T. Sano, S. Matsuzaki, Y. Ishii, T. Satoh, M. Koka, A. Yokoyama, T. Ohkubo, Y. Ishii and T. Kamiya, "Co-localization of iron binding on silica with p62/sequestosome1 (SQSTM1) in lung granulomas of mice with acute silicosis", J. Clin. Biochem. Nutr., **56**, 74-83 (2015). **S, 2-42**

10) Y. Matsuda, K. Okuyama, H. Yamamoto, H. Komatsu, M. Koka, T. Satoh, N. Hashimoto, S. Oki, C. Kawamoto and H. Sano, "Fluorine uptake into the human enamel surface from fluoride-containing sealing materials during cariogenic pH cycling", Nucl. Instrum. Meth. Phys. Res. B, **348**, 156-59 (2015). **S, 2-44**

11) S. Harada, S. Ehara, K. Ishii, T. Satoh, M. Koka, T. Kamiya, K. Sera and S. Goto, "Targeted concurrent chemoradiotherapy, by using improved microcapsules that release carboplatin in response to radiation, improves detectability by computed tomography as well as antitumor activity while reducing adverse effect *in vivo*", Biomed. Pharmacother., **70**, 196-205 (2015). **S, 2-45**

12) S. Harada, S. Ehara, K. Ishii, T. Satoh , M. Koka, T. Kamiya, K. Sera, S. Goto, "Imaging of lung metastases using CT-detectable microcapsules and their radiotherapeutic treatment using targeted carboplatin nanoparticles", Int. J. PIXE, **25**(1&2), 53-64 (2015). **S, 2-45**

13) W. Kada, K. Miura, H. Kato, R. Saruya, A. Kubota, T. Satoh, M. Koka, Y. Ishii, T. Kamiya, H. Nishikawa and O. Hanaizumi, "Development of embedded Mach-Zehnder optical waveguide

structures in PDMS thin films by proton beam writing", Nucl. Instrum. Meth. Phys. Res. B, **348**, 218-22 (2015). **S, 3-01, 3-14**

14) W. Kada, Y. Kambayashi, N. Iwamoto, S. Onoda, T. Makino, M. Koka, T. Kamiya, N. Hoshino, N. Hoshino, H. Tsuchida, K. Kojima, "Development of diagnostic method for deep levels in semiconductors using charge induced by heavy ion microbeams", Nucl. Instrum. Meth. Phys. Res. B, **348**, 240-45 (2015). **C, T, S, 3-01, 3-14**

15) W. Kada, A. Yokoyama, M. Koka, K. Miura, T. Satoh, O. Hanaizumi, and T. Kamiya, "Continuous observation of ion beam induced luminescence spectra from organic standard targets", Int. J. PIXE, **25**, 127-34 (2015). **S, 3-01, 3-14**

16) A. Yamazaki, Y. Orikasa, K. Chen, Y. uchimoto, T. Kamiya, M. Koka, T. Satoh, K. Mima, Y. Kato and K. Fujita, "In-situ measurement of the lithium distribution in Li-ion batteries using micro-IBA techniques", Nucl. Instrum. Meth. Phys. Res. B, **371**, 298-302 (2015). **S, 3-03**

17) A. Masuda, T. Matsumoto, H. Harano, Y. Tanimura, Y. Shikaze, H. Yoshitomi, S. Nishino, S. Kurashima, M. Hagiwara, Y. Unno, J. Nishiyama, M. Yoshizawa and H. Seito, "Time-of-flight measurements for low-energy components of 45-MeV quasi-monoenergetic high-energy neutron field from 7Li(p,n) reaction", IEEE Trans. Nucl. Sci. **62**(3), 1295-300 (2015). **C, 3-04**

18) S. Kurashima, N. Miyawaki, H. Kashiwagi, S. Okumura, M. Taguchi, and M. Fukuda, "Enhancement of beam pulse controllability for a single-pulse formation system of a cyclotron", Rev. Sci. Instrum., **86**, 073311 (2015). **C, 3-06**

19) 倉島 俊, "サイクロトロンのパルスビーム形成技術", 放射線化学, **100**, 49-51 (2015). **C, 3-06**

20) T. Kitayama, K. Nakajima, M. Suzuki, K. Narumi, Y. Saitoh, M. Matsuda, M. Sataka, M. Tsujimoto, S. Isoda, K. Kimura, "Temperature of thermal spikes in amorphous silicon nitride films produced by 1.11 MeV C_{60}^{3+} impacts", Nucl. Instrum. Meth. Phys. Res. B, **354**, 183-86 (2015). **I, 3-20**

21) T. Kitayama, Y. Morita, K. Nakajima, K. Narumi, Y. Saitoh, M. Matsuda, M. Sataka, M. Tsujimoto, S. Isoda, M. Toulemonde, K. Kimura, "Formation of ion tracks in amorphous silicon nitride films with MeV C_{60} ions", Nucl. Instrum. Meth. Phys. Res. B, **356-57**, 22-27 (2015). **T, 3-20**

22) H. Hayashi, T. Kitayama, S. Matsuzaki, K. Nakajima, K. Narumi, Y. Saitoh, M. Tsujimoto, M. Toulemonde, K. Kimura, "Evaluation of local temperature around the impact points of fast ions", Nucl. Instrum. Meth. Phys. Res. B, **365**, 569-72 (2015). **I, 3-20**

23) T. Kitayama, Y. Morita, K. Nakajima, K. Narumi, Y. Saitoh, M. Matsuda, M. Sataka, M. Toulemonde, and K. Kimura, "Sputtering of amorphous silicon nitride irradiated with energetic C_{60} ions: Preferential sputtering and synergy effect between electronic and collisional sputtering", Nucl. Instrum. Meth. Phys. Res. B, **365**, 490-95 (2015). **I, 3-20**

24) H. L. Cheng, M. T. Tang. W. Tuchinda, K. Enomoto, A. Chiba, Y. Saitoh, T. Kamiya, M. Sugimoto, A. Saeki, T. Sakurai, M. Omichi, D. Sakamaki and S. Seki, "Reversible control of radius and morphology of fluorene-azobenzene copolymer nanowires by light exposure", Adv. Mater. Interfaces **2**, 1400450 (2015). **C, 3-22**

25) A. Yokoyama, W. Kada, T. Satoh, M. Koka, K. Miura, and O. Hanaizumi, "Ionoluminescence analysis of glass scintillators and application to single-ion-hit real-time detection", Nucl. Instrum. Meth. Phys. Res. B, **371**, 340-43 (2016), {22nd Int. Conf. Ion Beam Anal., [Opatija, Croatia] (2015/6)}. **C, 3-28**

26) M. Narisawa, M. Koka, A. Takeyama, M. Sugimoto, A. Idesaki, T. Satoh, H. Hokazono, T. Kawai and A. Iwase, "In-situ monitoring of ion-beam luminescence of Si-O-C(-H) ceramics under proton- beam irradiation", J. Ceram. Soc. Jpn., **123**, 805-08 (2015). **S**

27) 大野 豊, 横田 渉, "植物の突然変異と育種", 加速器 **12**, 189-92 (2015)（総説）. **C**

Proceedings

1) 上川 将章, 泉 敬介, 武本 純平, 川崎 正治, 岡 潔, 山縣 諒平, "核融合環境における電気設備(その 53):耐放射線性 LED 照明の開発", 第 32 回電気設備学会全国大会, [仙台] (2014). **G, 1-54**

2) 泉 敬介, 井口 昌之, 飯田 真次, 川崎 正治, 大川 慶直, 岡 潔, 山縣 諒平, "核融合環境における電気設備(その 55):耐放射線性絶縁構造材料の開発", 第 32 回電気設備学会全国大会, [仙台] (2014). **G, 1-54**

3) 長澤 尚胤, 木村 敦, 出崎 亮, 石井 保行, 山田 尚人, 江夏 昌志, 島田 明彦, 大久保 猛, 佐藤 隆博, 田口 光正, "プロトンビームライティング法による生体適合性ハイドロゲルの微細加工", 第 25 回日本 MRS 年次大会, [横浜], (2015/12). **S, 1-69**

4) 山口 充孝, 長尾 悠人, 菅井 裕之, 酒井 真理, 河地 有木, 佐藤 隆博, 神谷 富裕, 藤巻 秀, 荒川 和夫, 鳴海 一雅, "低エネルギー光子測定による治療用炭素ビーム軌道上の空洞検出のシミュレーションによる評価", 第 63 回応用物理学会春季学術講演会, [東京], 22a-W833-10 (2016). **C, 2-33**

5) 永井 清絵, 笠松 哲光, 長嶋 友海, 山田 尚人, 喜多村 茜, 佐藤 隆博, 江夏 昌志, 神谷 富裕, 長嶺 竹明, 村上 博和, "大気 micro-PIXE 法を用いた骨髄異形成症候群(MDS)における赤血球内微量元素の測定", Proc. 62th Annu. Meet. Kitakanto. Soc. Jpn., [Maebashi, Japan], B5-27 (2015). **S, 2-41**

6) Y. Koga, K. Dobashi, K. Kaira, T. Satoh, M. Koka, N. Yamada, T Hisada, Y Masakiyo, A. Ono, Y. Kamide, K. Seki, H. Aoki, H. Tsurumaki and M. Yamada, "In-air microparticle induced X-ray emission analysis of inhaled particulates in thoracic lymph node in a patient with asbestos exposure", Proc. Annu. Meet. Am. Thorac. Soc. 2016, [Denver, USA], (2015). **S, 2-42**

7) Y. Maeda, T. Tatsumi, Y. Noguchi, Y. Kawakubo, H. Kobayashi, K. Narumi and S. Sakai, "Photoluminescence enhancement of β-$FeSi_2$ nanocrystals controlled by transport of holes in Cu-doped n-type Si substrates", Proc. JJAP Conf., **3**, 011107, [Tokyo, Japan], (2015). **S, 3-02**

8) Y. Maeda, T. Tatsumi, Y. Kawakubo, Y. Noguchi, K. Morita, H. Kobayashi, K. Narumi, "Enhancement of photoluminescence from Cu-doped β-$FeSi_2$/Si heterostructures", Proc. JJAP Conf., **3**, 011108, [Tokyo, Japan], (2015). **S, 3-02**

9) A. Masuda, T. Matsumoto, H. Harano, H. Yoshitomi, S. Nishino, Y. Tanimura, Y. Shikaze, S. Kurashima, H. Seito, M. Hagiwara, Y. Unno, J. Nishiyama, M. Yoshizawa, "Spectral measurement of quasi-monoenergetic high-energy neutron field by combination of the TOF and the Bonner unfolding methods", IEEE Nucl. Sci. Symp. Med. Imaging Conf., N3AP-83, [San Diego, USA], (2015/10-11). **C, 3-04**

10) A. Masuda, T. Matsumoto, H. Harano, H. Yoshitomi, Y. Tanimura, Y. Shikaze, S. Kurashima, H. Seito, M. Hagiwara, Y. Unno, J. Nishiyama and M. Yoshizawa, "Development and evaluation of activation neutron detectors for spectrum measurements of quasi-monoenergetic high-energy neutron fields", 2014 IEEE Nucl. Sci. Symp. Conf. Rec., [Seattle, USA], DOI: 10.1109/NSSMIC.2014.7431173 (2015). **C, 3-04**

11) S. Kurashima, N. Miyawaki, H. Kashiwagi, M. Fukuda, "Improvement of Mass-to-Charge Ratio Resolution of the JAEA AVF Cyclotron Using a Beam Chopping System", Proc. 13th Int. Conf. Heavy Ion Accel. Tech. (HIAT2015), [Yokohama, Japan], 68-70 (2015/9). **C, 3-06**

12) N. Miyawaki, S. Kurashima, H. Kashiwagi, S. Okumura and M. Fukuda, "Phase Bunching in the Central Region of the JAEA AVF Cyclotron for Heavy-Ion Acceleration in the Third-Harmonic Mode", Proc. 13th Int. Conf. Heavy Ion Accel. Tech. (HIAT2015), [Yokohama, Japan], 62-64 (2015). **C, 3-07**

13) H. Kashiwagi, N. Miyawaki and S. Kurashima, "Preliminary test of injection tuning using an emittance and acceptance measurement system in JAEA AVF cyclotron", Proc. 12th Annu. Meet. Part. Accel. Soc. Jpn., [Tsuruga, Japan], 703-05 (2015). **C, 3-07**

14) N. Miyawaki, M. Fukuda, S. Kurashima, H. Kashiwagi and S. Okumura, "Evaluation of beam phase restriction with beam phase defining slit in the JAEA AVF cyclotron", Proc. 12th Annu. Meet. Part. Accel. Soc. Jpn., [Tsuruga, Japan], 706-08 (2015). **C, 3-07**

15) 千葉 敦也, 薄井 絢, 山田 圭介, "SNICS によるフラーレン負イオンの生成", 第 28 回タンデム加速器及びその周辺技術の研究会, [仙台], 要旨集 15 (2015/7). **T, 3-08**

16) 千葉 敦也, 山田 圭介, 薄井 絢, 鳴海 一雅, 齋藤 勇一, "クラスターイオンの生成と加速", 第 52 回アイソトープ・放射線研究発表会, [東京], 要旨集 180 (2015/7). **T, I, 3-08**

17) Y. Yuri, T. Yuyama, T. Ishizaka, K. Yoshida, I. Ishibori, and S. Okumura, "Formation of a Uniform Ion Beam Based on Nonlinear Focusing and its Applications at the JAEA TIARA Cyclotron", Proc. 6th Int. Part. Accel. Conf. (IPAC15), [Richmond, USA], 236-38 (2015). **C, 3-09**

18) Y. Yuri, "Three-Dimensional Ordering of Cold Ion Beams in a Storage Ring: A Molecular-Dynamics Simulation Study", AIP, Conf. Proc. **1668**, 050005, [Takamatsu, Japan], (2015). **C, 3-09**, **3-24**

19) 百合 庸介, 湯山 貴裕, 石坂 知久, 江夏 昌志, 山田 尚人, "原子力機構 AVF サイクロトロンにおける大面積イオンビームのリアルタイム横方向強度分布計測のための蛍光体の探索: [Investigation of phosphor materials for the real-time measurement of the transverse intensity distribution of large-area ion beams at the JAEA AVF cyclotron facility]", Proc. 12th Annu. Meet. Part. Accel. Soc. Jpn., [Tsuruga, Japan], 420-23 (WEP011) (2015/8). **C, 3-09**

20) H. Nishikawa, J. Takahashi, Y. Ishii and T. Kamiya, "Proton beam writing on a removable negative-tone resist as a mother for Ni electroplating", Proc. 41st Micro Nano Eng. (MNE2015), [Hague, Netherlands], Tue-A-50 (2015/9). **S, 3-15**

21) 佐野 遼, 西川 宏之, 林 秀臣, 石井 保行, "集束陽子線によるナノ粒子含有高アスペクト比微細構造体の作成", 電気学会第 46 回電気電子絶縁材料システムシンポジウム, [北九州], MVP-10 (2015/9). **S, 3-15**

22) T. Hatakeyama, K. Ishii, S. Matsuyama, A. Terakawa, D. Sata, T. Satoh, M. Koka, N. Yamada and T. Kamiya, "Development of a Three-dimensional Elemental Analysis for the Micro-sample by PIXE-CT", Atom. Energ. Soc. Jpn., [Sendai,Japan] 2M10 (2016). **S, 3-31**

23) 薄井 絢, 千葉 敦也, 山田 圭介, 横山 彰人,北野 敏彦, 高山 輝充, 織茂 貴雄, 金井 伸二, 青木 勇希, 橋爪 将司, 鳴海 一雅, 石井 保行, 佐藤 隆博, 大久保 猛, 喜多村 茜, 奈良 孝幸, "TIARA 静電加速器の現状", 第 28 回タンデム加速器及びその周辺技術の研究会, [仙台], 要旨集 117 (2015/7). **T, S, I, 4-03**

24) 湯山 貴裕, 石堀 郁夫, 倉島 俊, 吉田 健一, 石坂 知久, 千葉 敦也, 山田 圭介, 横山 彰人, 薄井 絢, 宮脇 信正, 柏木 啓次, 百合 庸介, 鳴海 一雅, 石井 保行, 佐藤 隆博, 大久保 猛, 喜多村 茜, 奥村 進, 奈良 孝幸, "原子力機構 TIARA施設の現状", 第12回日本加速器学会年会, [敦賀], 論文集 302-04 (2015). **C, 4-02, T, S, I, 4-03**

25) 宇野 定則, 花屋 博秋, 山縣 諒平, 清藤 一, 長尾 悠人, 山﨑 翔太, 上松 敬, 川島 郁男, 八木 紀彦, 高木 雅英, 松崎 慎也, "原子力機構高崎研 電子加速器の現状", 第 28 回タンデム加速器及びその周辺技術の研究会, [仙台], 要旨集 121 (2015/7). **E, 4-04**

Book

1) 江夏 昌志, 石井 保行, 山田 尚人, 大久保 猛, 加田 渉, 喜多村 茜, 岩田 吉弘, 神谷 富裕, 佐藤 隆博, "軽イオンマイクロビーム分析/加工システムの改良", JAEA-Tech. **2016-006** (2016). **S, 3-30**

External Research Groups Except for Takasaki Advanced Radiation Research Institute

Papers

1) K. Takakura, M. Hori, M. Yoneoka, I. Tsunoda, T. Nakashima, E. Simoen, C. Claeys, "Thermal recovery process of electron irradiated Si1-xCx source/drain n-MOSFETs", Physica Status Solidi C., **12**, 1405-08 (2015). **E, 1-07**

2) K. Moto, S. Sakiyama, H. Okamoto, H. Hara, H. Nishimura, K. Takakura, I. Tsunoda, "Enhancement of Au induced lateral crystallization in electron irradiated amorphous Ge on SiO_2", Jpn. J. Appl. Phys., **55**, 04EJ06 (2016). **E, 1-07**

3) K. Amemiya, H. Koshikawa, T Yamaki, Y. Maekawa, H Shitomi, T. Numata, K. Kinoshita, M. Tanabe, D. Fukuda, "Fabrication of hard-coated optical absorbers with microstructured surfaces using etched ion tracks; Toward broadband ultra-low reflectance", Nucl. Instrum. Meth. Phys. Res., B, **356-57**, 154-59 (2015). **C, 1-19**

4) Y. Fujimura, H. Yoshizaki, S. Nakagawa, Y. Okamoto, N. Ishikawa, F. Hori and A. Iwase, "EXAFS study on solute precipitation in FeCu alloy induced by energetic electron bombardments and thermal aging", Nucl. Instrum. Meth. Phys. Res. B, **354**, 120-24 (2015). **T, 1-33~36**

5) Y. Yamamoto, T. Kishino, T. Ishiyama, A. Iwase and F. Hori, "Study on lattice defects in CeO_2 by means of positron annihilation measurements", J. Phys.: Conf. Series **674**, 12015 (2016). **T, 1-33~36**

6) T. Koide, H. Uno, H. Sakane, M. Sakamaki, K. Amemiya, A. Iwase, and T. Matsui, "Magnetic modification at sub-surface of FeRh bulk by energetic ion beam irradiation", J. Appl. Phys., **117**, 17E503_1-3 (2015). **T, 1-33~36**

7) 岩瀬 彰宏, 松井 利之, "最近の研究「放射光を用いた鉄ロジウム合金のイオンビーム照射誘起構造・磁気変態の研究」", まてりあ, **54** 巻, 390-97 (2015). **T**

8) N. Ishikawa, N. Okubo and T. Taguchi, "Experimental evidence of crystalline hillocks created by irradiation of CeO_2 with swift heavy ions: TEM study", Nanotechnology, **26**, 355701 (2015). **T, 1-37**, **1-38**

9) H. Fujita, K. Yuyama, X. Li, Y. Hatano, T. Toyama, M. Ohta, K. Ochiao, N. Yoshida, T. Chikada and Y. Oya, "Effect of neutron

energy and fluence on deuterium retention behavior in neutron irradiated tungsten", Phys. Scripta T, **167**, 014068 (2016). **T, 1-44**

10) K. Ozawa, H. Tanigawa, Y. Morisada, H. Fujii, "Impacts of friction stir processing on irradiation effects in vacuum-plasma-spray coated tungsten", Fusion Eng. Des., **98-99**, 2054-57 (2015/10). **T, 1-45**

11) H. Tanigawa, K. Ozawa, Y. Morisada, S. Noh, H. Fujii, "Modification of vacuum plasma sprayed tungsten coating on reduced activation ferritic/martensitic steels by friction stir processing", Fusion Eng. Des., **98-99**, 2080-84 (2015/10). **T, 1-45**

12) I. Yamagishi, R. Nagaishi, C. Kato, K. Morita, A. Terada, Y. Kamiji, R. Hino, H. Sato, K. Nishihara, Y. Tsubata, S. Tashiro, R. Saito, T. Satoh, J. Nakano, W. Ji, H. Fukushima, S. Sato, M. Denton, "Characterization and Storage of Radioactive Zeolite Waste", J. Nucl. Sci. Tech., **51**(7-8) 1044-53 (2014). **G, 1-65**, **1-66**

13) Y. Matsumoto, T.-M.-D. Do, M. Inoue, R. Nagaishi, T. Ogawa, "Hydrogen Generation by Water Radiolysis with Immersion of Oxidation Products of Zircaloy-4", J. Nucl. Sci. Tech., **52**(10), 1303-07 (2015). **E, G, 1-66**

14) T. Ito, R. Nagaishi, S.-Y. Kim, T. Kimura, "Study on Radiation Effects on (MOTDGA-TOA) /SiO2-P Adsorbent for Separation of Platinum Group Metals from High Level Radioactive Waste", J. Radioanal. Nucl. Chem., **305**, 419-27 (2015). **E, G, 1-66**

15) K. D. Held, H. Kawamura, T. Kaminuma, A. Evalour, S. Paz, Y. Yoshida, H. Willers and A. Takahashi, "Effects of charged particles on human tumor cells", Front. Oncol., 173722 (2016). **C, 2-05**

16) Y. Takayasu, M. Shino, O. Nikkuni, Y. Yoshida, N .Furuya and K. Chikamatsu, "Oxygen-glucose deprivation increases firing of unipolar brush cells and enhances spontaneous EPSCs in Purkinje cells in the vestibulo-cerebellum", Neurosci. Res., S0168-0102 (2015). **C, 2-05**

17) Y. Yoshida, K. Ando, K. Murata, Y. Yoshimoto, A. Musha, N. Kubo, H. Kawamura, S. Koike, A .Uzawa, T. Takahashi, T. Ohno and T. Nakano, "Evaluation of therapeutic gain for fractionated carbon-ion radiotherapy using the tumor growth delay and crypt survival assays", Radiother. Oncol., **117**(2), 315-17 (2015). **C, 2-05**

18) M. Isono, Y. Yoshida, A. Takahashi, T. Oike, A. Shibata, Y. Kubota, T. Kanai, T. Ohno and T. Nakano, "Carbon-ion beams effectively induce growth inhibition and apoptosis in human neural stem cells compared with glioblastoma A172 cells", J. Radiat. Res., **56**(5), 856-61 (2015). **C, 2-05**

19) N. Amornwichet, T. Oike, A. Shibata, C. S. Nirodi, H. Ogiwara, H. Makino, Y. Kimura, Y Hirota, M .Isono, Y. Yoshida, T. Ohno, T. Kohno and T .Nakano, "The EGFR mutation status affects the relative biological effectiveness of carbon-ion beams in non-small cell lung carcinoma cells", Sci. Rep., **11**(5), 11305 (2015). **C, 2-05**

20) H. Ma, A. Takahashi, Y. Sejimo, A. Adachi, N. Kubo, M. Isono, Y. Yoshida, T. Kanai, T. Ohno and T. Nakano, "Targeting of carbon ion-induced G2 checkpoint activation in lung cancer cells using Wee-1 inhibitor MK-1775", Radiat. Res., **184**(6), 660-69 (2015). **C, 2-06**

21) H. Ma, A. Takahashi, Y. Yoshida, A. Adachi, T. Kanai, T. Ohno and T Nakano, "Combining carbon ion irradiation and non-homologous end-joining repair inhibitor NU7026 efficiently kills cancer cells", Radiat. Oncol., **10**, 225 (2015). **C, 2-06**

22) Y. Ueda, Y. Shinmyouzu, H. Nakayama, T. Tanino, E. Sakurai and E. Sakurai, "Claudin-1 leads to strong formation of tight junction in cultured mouse lung microvascular endothelial cells", Pharmacol. Pharm., **7**, 133-39 (2016). **S, 2-39**

23) H. Chino, E. Hagiwara, M. Sugisaki, T. Baba, Y. Koga, T. Hisada, K. Kaira, K. Okudela, T. Takemura, K. Dobashi and T. Ogura, "Pulmonary Aluminosis Diagnosed with In-air Microparticle Induced X-ray Emission Analysis of Particles", Intern. Med., **54**, 2035-40 (2015). **S, 2-42**

24) S. Ushimura, K. Nakamura, Y. Matsuda, H. Minamikawa, S. Abe and Y. Yawaka, "Assessment of the inhibitory effects of fissure sealants on the demineralization of primary teeth using an automatic pH-cycling system", Dent. Mater. J., **35**(2), 316-24 (2016). **S, 2-44**

25) H. Yamamoto, Y. Iwami, K. Yagi, M. Hayashi, H. Komatsu, K. Okuyama, Y. Matsuda and K. Yasuda, "Evaluation of caries progression in dentin treated by fluoride-containing materials using an in-air micro-PIGE and micro-PIXE measurement system", Nucl. Instrum. Meth. Phys. Res. B., **348**, 152-55 (2015). **S, 2-44**

26) Y. Funato, Y. Matsuda, K. Okuyama, H. Yamamoto, H. Komatsu and H. Sano, "A new technique for analyzing trace element uptake by human enamel", Dent. Mater. J., **34**(2), 240-45 (2015). **S, 2-44**

27) R. Kataoka, H. Tokita, S. Uchida, R. Sano and H. Nishikawa, "Frequency dependence and assembly characteristics of silver nanomaterials trapped by dielectrophoresis", J. Phys.: Conf. Series **646**, 012005 (2015). **S, 3-15**

28) 渡部 涼, 内田 諭, 西川 宏之, "ソフトリソグラフィによる誘電体ピラーを利用した 3 次元誘電泳動効果", 電気学会論文誌 A, **135** 巻, No. 9, 548-52 (2015). **S, 3-15**

29) R. Kataoka, H. Tokita, S. Uchida, R. Sano and H. Nishikawa, "Frequency dependence and assembly characteristics of Ag nanomaterials trapped by dielectrophoresis", Electrostatics 2015, P1.03 (2015/4). **S, 3-15**

30) H. Hayashi, R. Sano and H. Nishikawa, "Robust Micro Identification Marking on FPC Surface", EcoDesign 2015, **C5**-4 (2015/12). **S, 3-15**

31) T. Matsui, K. Aikoh, M. Sakamaki, K. Amemiya, A. Iwase, "In-situ XMCD evaluation of ferromagnetic state at FeRh thin film surface induced by 1 keV Ar ion beam irradiation and annealing", Nucl. Instrum. Meth. Phys. Res. B, **365**, 187-90 (2015). **I**, **3-18**

32) K. Nakajima, T. Kitayama, H. Hayashi, M. Matsuda, M. Sataka, M. Tsujimoto, M. Toulemonde, S. Bouffard and K. Kimura, "Tracing temperature in a nanometer size region in a picosecond time period", Sci. Rep., **5**, 13363 (2015). **I, 3-20**

33) M. Koshimizu, K. Iwamatsu, M. Taguchi, S. Kurashima, A. Kimura, T. Yanagida, Y. Fujimoto, K. Watanabe and K. Asai, "Influence of linear energy transfer on the scintillation decay behavior in a lithium glass scintillator", J. Lumin., **169**, B, 678-81 (2016/1). **C, 3-26**

34) T. Yanagida, M. Koshimizu, S. Kurashima, K. Iwamatsu, A. Kimura, M. Taguchi, Y. Fujimoto, and K. Asai, "Linear energy transfer effects on the time profiles of scintillation in Ce-doped $LiCaAlF_6$ crystals", Nucl. Instrum. Meth. Phys. Res. B, **365**, 529-32 (2015). **C, 3-26**

35) B. Tsuchiya, K. Morita, Y. Iriyama, T. Majima, H. Tsuchida, "Dynamic Measurements of Hydrogen and Lithium Distributions in Lithium-Cobalt-Oxide Films with Charging and Heating Using Elastic Recoil Detection Techniques", Physics Procedia, **66**, 292-97 (2015). **G, 3-29**

Proceedings

1) K. Takakura, M. Hori, M. Yoneoka, I. Tsunoda, T. Nakashima, E. Simoen, C. Claeys, "Thermally recovery process of electron irradiated Si1-xCx source/drain n-MOSFETs", Euro. Mater. Res. Soc. 2015 Spring Meet., [Lille, France], (2015). **E, 1-07**

2) T. Sakaguchi, M. Hori, K. Moto, M. Yoneoka, K. Takakura, I. Tsunoda, "Amorphicity modulation effect on Au induced lateral crystallization for amorphous Ge on SiO_2", Extended Abstr. 34th Electron. Mater. Symp. (EMS-34), [Shiga, Japan] (2015). **E, 1-07**

3) H. Ogata, K. Takakura, I. Tsunoda, E. Simoen, C. Claeys, "Investigation of the radiation tolerance of carbon doped $Si_{0.25}Ge_{0.75}$/Si hetero junction diode by 2 MeV electrons", Extended Abstr. 34th Electron. Mater. Symp. (EMS-34), [Shiga, Japan], (2015). **E, 1-07**

4) H. Ito, M. Hori, M. Yoneoka, I. Tsunoda, K. Takakura, E. Simoen, C. Claeys, "Comparative evaluation of radiation characteristics of Si MOSFETs with C and Ge addition in S/D", Extended Abstr. 34th Electron. Mater. Symp. (EMS-34), [Shiga, Japan], (2015). **E, 1-07**

5) M. Izawa, K. Iseri, T. Goto, M. Yoneoka, I. Tsunoda, K. Takakura, E. Simoen, C. Claeys, "A study on the influence of BOX layer for SOI FinFETs by electron irradiation", Extended Abstr. 34th Electron. Mater. Symp. (EMS-34), [Shiga, Japan], (2015). **E, 1-07**

6) K. Iseri, T. Goto, M. Yoneoka, I. Tsunoda, K. Takakura, E. Simoen, C. Claeys, "Investigation of the radiation tolerance of carbon doped $Si_{0.25}Ge_{0.75}$/Si hetero junction diode by 2 MeV electrons", Extended Abstr. 34th Electron. Mater. Symp. (EMS-34), [Shiga, Japan], (2015). **E, 1-07**

7) K. Takakura, K. Iseri, T. Goto, M. Yoneoka, I. Tsunoda, E. Simoen, C. Claeys, "Radiation hardness of electrical properties of n-channel UTBOX SOI MOSFETs by 2 MeV electron irradiation", Proc. 28th Int. Conf. Defects Semicond. (ICDS 2015), [Espoo, Finland] (2015). **E, 1-07**

8) K. Takakura, H. Ogata, T. Inoue, M. Yoneoka, I. Tsunoda, E. Simoen, C. Claeys, "Investigation of the electrical properties of carbon doped $Si_{0.75}Ge_{0.25}$/Si hetero junction diodes by 2 MeV electron irradiation", Proc. 28th Int. Conf. Defects Semicond. (ICDS 2015), [Espoo, Finland], (2015). **E, 1-07**

9) M. Hifumi, E. Sonezaki, J. Furuta, and K. Kobayashi, "Radiation Hardness Evaluations of FFs on 28 nm and 65 nm Thin BOX FD-SOI Processes by Heavy-Ion Irradiation", Proc. 11th Int. Workshop Radiat. Eff. Semicond. Devices Space Appl. (11th RASEDA) & 7th Int. Conf. Adv. Micro-Device Eng. (7th AMDE), [Kiryu, Japan], 93-96 (2015). **C, 1-08**

10) 曽根崎 詠二, 久保田 勘人, 増田 政基, 神田 翔平, 古田 潤, 小林 和淑, "65 nm バルクと Thin BOX FD-SOI プロセスにおける冗長化フリップフロップのソフトエラー耐性の実測と評価", 電子情報通信学会技術報告(集積回路設計), ICD2015-63, [京都], 1-6 (2015). **C, 1-08**

11) K. Amemiya, H. Koshikawa, T Yamaki, Y. Maekawa, H Shitomi, K. Kinoshita, T. Numata, M. Tanabe and D. Fukuda, "Design and fabrication of novel broadband near-perfect black absorber having microstructured surface", Emerging Scientist Workshop (ESW) 2015, [Daejeon, Korea], Session 4; No. 3 (2015/8). **C, 1-19**

12) 雨宮 邦招, 越川 博, 八巻 徹也, 前川 康成, 蔀 洋司, 木下 健一, 沼田 孝之, 田辺 稔, 福田 大治, "身近な熱形放射計を目指して－微細加工を駆使した新型センサ及び新規黒体材料の技術開発－", 平成27年度(第48回)照明学会全国大会 計測・標準分科会／光放射応用分科会シンポジウム, [福井], 13-2 (2015/8). **C, 1-19**

13) N. Ishikawa, N. Okubo, T. Taguchi, "Crystalline hillock formation of oxides irradiation with swift heavy ions; TEM study", Proc. 9th Int. Symp. Swift Heavy Ions in Matter (SHIM 2015), [Darmstadt, Germany], (2015/5). **T, 1-37**, **1-38**

14) N. Ishikawa, N. Okubo, T. Taguchi, "Novel method for observing hillocks created for ceramic materials irradiated with swift heavy ions", 第 25 回日本 MRS 年次大会, [横浜], (2015/12). **T, 1-37**, **1-38**

15) 小沢 和巳, 谷川 博康, 森貞 好昭, 藤井 英俊, "真空プラズマ溶射法で成膜し摩擦撹拌処理を施した W-F82H 鋼のイオン照射後硬さと微細組織", 日本原子力学会「2014 年秋の学会」, [京都], 要旨集 B25 (2015). **T, 1-45**

16) 宇佐美 博士, 藪内 聖皓, 福田 誠, 野上 修平, 長谷川 晃, 小沢 和巳, 谷川 博康, "核融合炉高熱流束機器用タングステン材料の開発; (6) 純タングステンの照射硬化に及ぼす高温での自己イオン照射の影響", 日本原子力学会「2014 年秋の学会, [京都], 要旨集 B34 (2015). **T, 1-45**

17) 黄 泰現, 宇佐美 博士, 福田 誠, 藪内 聖皓, 野上 修平, 長谷川 晃, 小沢 和巳, 谷川 博康, "自己イオン照射したタングステンの照射効果", 日本原子力学会「2015 年春の年会」, [日立], 要旨集 F21 (2015). **T, 1-45**

18) T. Takeuchi, N. Ohtsuka, H. Nakano, T. Shibagaki, H. Komanome, and K. Tsuchiya, "Development of Radiation Resistant In-water Transmission System Using Visible Light with Environmental Robustness", Proc. 8th Int. Symp. Mater. Testing Reactors, [Sydney, Australia], (2015). **G, 1-52**

19) R. Nagaishi, K. Morita, I. Yamagishi, R. Hino, T. Ogawa, "Revaluation of Hydrogen Generation by Water Radiolysis in SDS Vessels at TMI-2 Accident", Nucl. Plant Chem. Conf. 2014 (NPC 2014), [Sapporo, Japan], 10224 in JOPSS (2014). **G, 1-66**

20) 本岡 隆文, 永石 隆二, 山岸 功, "HIC 模擬炭酸塩スラリーの照射実験 2:ガンマ線照射下での模擬炭酸塩スラリーのガス保持挙動試験", 日本原子力学会「2016 春の年会」, [仙台], 要旨集 2I20 (2016/3). **G, 1-67**, **1-66**

21) Y. Kumagai, A. Kimura, M. Taguchi, "Hydrogen and hydrogen peroxide productions by γ-irradiation of A-, X-, Y- and mordenite type zeolites in aqueous solution", Proc. 15th Int. Congr. Radiat. Res. (ICRR 2015) [Kyoto, Japan], (2015/5). **G, 1-68**

22) 吉田 由香里, "放射線が正常脳に及ぼす影響についての研究動向", 新学術領域研究「宇宙に生きる」 2016 ワークショップ, (2016/3). **C, 2-05**

23) D. Kobayashi, T. Oike, A. Shibata, A. Niimi, N. Amornwichet, Y. Yoshimoto, H. Sato, M. Isono, Y. Yoshida, T. Kohno, T. Ohno, and T. Nakano, "Carbon-ion beams efficiently kill cancer cells showing resistance to X-rays and cisplatin by inducing mitotic catastrophe", 第28回JASTRO, [前橋], (2015/11). **C, 2-05**

24) 松本 友己, 吉田 由香里, 八高 知子, 高橋 昭久, 中野 隆史, "ヒト神経膠芽腫細胞の遊走能における炭素線照射の影響", 第 58 回日本神経化学会大会, [さいたま], (2015/9). **C, 2-05**

25) 吉田 由香里, "放射線脳壊死の生物学的研究の現状", 伊香保BSの会 第4回多分野交流会～今再びの伊香保～, [前橋・渋川], (2015/7). **C, 2-05**

26) Y. Yoshida, K. Ando, S. Koike, T. Yako, H. Ikeda, A. Uzawa, T. Matsumoto, M. Isono, T. Kanai and T. Nakano, "Evaluation of survival curves for solid tumor cells after large doses of carbon ion beams and X-rays", Proc. Int. Congr. Radiat. Res. (ICRR2015), [Kyoto, Japan], (2015/5). **C, 2-05**

27) A. Takahashi, H. Ma, A. Nakagawa, Y. Yoshida, T. Kanai, T. Ohno, Y. Kuwahara, M. Fukumoto and T. Nakano, "Carbon-ion

beams efficiently induce cell killing in X-ray resistant human squamous togue cancer cells", SRHIT2015, [Osaka, Japan], (2015/5). **C, 2-06**

28) 山口 正樹, 西川 宏之, 増田 陽一郎, "強誘電体厚膜へのプロトン照射効果", 第 76 回応用物理学会, [名古屋], 14a-PA1-1 (2015/9). **S, 3-15**

29) 片岡 良介, 内田 諭, 佐野 遼, 西川 宏之, "三次元誘電泳動による金属ナノ粒子アセンブリーピット径及びピッチに対する捕集形状の影響ー", 第 76 回応用物理学会, [名古屋], 15p-2A-22 (2015/9). **S, 3-15**

30) 越水 正典, 岩松 和宏, 倉島 俊, 木村 敦, 田口 光正, 柳田 健之, 藤本 裕, 浅井 圭介, "Analysis of excitation density effects on the scintillation properties of Ce:Gd_2SiO_5 (GSO) crystals : [Ce:Gd_2SiO_5 (GSO)のシンチレーションにおける励起密度効果の解析]", 第 76 回応用物理学会秋季学術講演会, [名古屋], (2015/9). **G, 3-26**

31) B. Tsuchiya, S. Yamamoto, K. Takahiro, S. Nagata, T. Katoh, Y. Sasaki, Y. Iriyama and K. Morita, "Behaviors of Li and H at interface between $LiCoO_2$ films and LATP Electrolytes", Proc. 25th Annu. Meet. Mater. Res. Soc. Jpn. (MRS-J), [Yokohama, Japan], B1-P10-014 (2015). **T, G, 3-29**

Appendix 2 Type of Research Collaboration and Facilities Used for Research

Paper No.	Type of Research Collaboration*1					Irradiation Facilities*2						Paper No.	Type of Research Collaboration*1					Irradiation Facilities*2					
	Joint Res.	Entr. Res.	Coop. Res.	Inter. Use	Ext. Use	C	T	S	I	E	G		Joint Res.	Entr. Res.	Coop. Res.	Inter. Use	Ext. Use	C	T	S	I	E	G
1-01	●					◎	◎					1-48	●							◎	◎		
1-02	●					◎	◎					1-49				●							◎
1-03	●					◎						1-50	●										◎
1-04	●					◎	◎		◎	◎		1-51	●										◎
1-05	●					◎			◎			1-52				●							◎
1-06	●						◎					1-53				●							◎
1-07					●					◎		1-54	●										◎
1-08					●	◎						1-55				●				◎			
1-09	●								◎			1-56			●					◎			
1-10					●	◎						1-57				●			◎				
1-11	●						◎		◎	◎		1-58				●							◎
1-12	●					◎	◎	◎				1-59				●						◎	
1-13				●		◎						1-60				●							◎
1-14				●		◎			◎			1-61				●							◎
1-15				●		◎			◎			1-62				●							◎
1-16	●									◎	◎	1-63				●							◎
1-17	●									◎	◎	1-64		●									◎
1-18				●		◎						1-65				●							◎
1-19					●	◎						1-66		●									◎
1-20					●				◎			1-67				●							◎
1-21				●						◎	◎	1-68				●							◎
1-22	●										◎	1-69				●				◎			
1-23	●					◎						1-70	●										◎
1-24	●									◎		1-71				●						◎	◎
1-25				●					◎			1-72	●									◎	◎
1-26				●						◎		1-73	●									◎	◎
1-27	●							◎				1-74	●									◎	◎
1-28				●				◎				1-75				●						◎	◎
1-29	●								◎			1-76				●						◎	◎
1-30				●			◎		◎														
1-31	●								◎			2-01				●		◎					
1-32				●					◎			2-02				●		◎					◎
1-33	●						◎					2-03				●							◎
1-34	●						◎					2-04	●					◎					
1-35	●								◎			2-05	●					◎					
1-36					●		◎					2-06	●					◎					
1-37				●			◎	◎	◎			2-07	●					◎					
1-38			●				◎	◎	◎			2-08	●					◎					
1-39				●			◎	◎	◎			2-09	●					◎					
1-40				●				◎	◎			2-10	●					◎					
1-41				●			◎	◎				2-11	●					◎					
1-42				●			◎	◎	◎			2-12	●					◎					
1-43					●		◎					2-13	●					◎					
1-44					●		◎					2-14	●					◎					
1-45	●						◎					2-15	●					◎					
1-46				●			◎					2-16	●					◎					
1-47	●										◎	2-17	●										◎

Paper No.	Type of Research Collaboration*1					Irradiation Facilities*2						Paper No.	Type of Research Collaboration*1					Irradiation Facilities*2					
	Joint Res.	Entr. Res.	Coop. Res.	Inter. Use	Ext. Use	C	T	S	I	E	G		Joint Res.	Entr. Res.	Coop. Res.	Inter. Use	Ext. Use	C	T	S	I	E	G
2-18				●		◎						3-12	●					◎					
2-19				●		◎						3-13	●					◎					
2-20	●					◎						3-14	●							◎			
2-21	●					◎						3-15	●							◎			
2-22	●					◎						3-16				●				◎			
2-23					●	◎						3-17			●						◎		
2-24					●	◎						3-18			●				◎		◎		
2-25				●							◎	3-19			●				◎				
2-26	●					◎						3-20			●				◎		◎		
2-27				●		◎					◎	3-21			●				◎		◎		
2-28	●					◎						3-22			●				◎				
2-29	●										◎	3-23			●N								
2-30	●					◎						3-24				●		◎	◎		◎		
2-31	●					◎						3-25	●						◎				
2-32				●		◎						3-26					●	◎					
2-33				●		◎						3-27				●							◎
2-34	●N											3-28				●							◎
2-35	●					◎						3-29					●						◎
2-36	●					◎						3-30			●					◎			
2-37				●		◎						3-31			●					◎			
2-38				●		◎						3-32				●							◎
2-39			●					◎				3-33					●						◎
2-40			●					◎				3-34					●						◎
2-41			●					◎															
2-42			●					◎				4-01						◎	◎	◎	◎		
2-43			●					◎				4-02						◎					
2-44			●					◎				4-03							◎	◎	◎		
2-45			●					◎				4-04										◎	◎
												4-05										◎	◎
3-01	●							◎				4-06						◎	◎	◎	◎		
3-02	●							◎				4-07						◎	◎	◎	◎		
3-03	●							◎				4-08						◎	◎	◎	◎	◎	◎
3-04	●					◎																	
3-05				●		◎																	
3-06				●		◎																	
3-07				●		◎																	
3-08				●			◎	◎	◎														
3-09				●		◎																	
3-10				●N																			
3-11				●		◎						Total	62	2	18	56	14	50	28	29	24	17	40

*1 Type of Research Collaboration
Joint Res. : Joint research with external users
Entr. Res. : Research entrusted to JAEA
Coop. Res. : Cooperative research with plural universities through The University of Tokyo
Inter. Use : Internal use
Ext. Use : Common use based on two programs of "JAEA-facility-use" and "Creation of Research Platforms and Sharing of Advanced Research Infrastructure" supported from MEXT

*2 Utilization of Irradiation Facilities
C : AVF Cyclotron
T : 3 MV Tandem Electrostatic Accelerator
S : 3 MV Single-ended Electrostatic Accelerator
I : 400 kV Ion Implanter
E : 2 MV Electron Accelerator
G : Co-60 Gamma-ray Irradiation Facilities

N : Non-use of irradiation facilities at TARRI

Appendix 3 Examples of Typical Abbreviation Name for Organizations in National Institutes for Quantum and Radiological Science and Technology, and Japan Atomic Energy Agency

◆Institute, Center, Laboratory etc.

TARRI（高崎量子応用研究所）:	Takasaki Advanced Radiation Research Institute
NFI（那珂核融合研究所）:	Naka Fusion Institute
RFI（六ヶ所核融合研究所）:	Rokkasho Fusion Institute
KPSI（関西光科学研究所 ）:	Kansai Photon Science Institute
NIRS（放射線医学総合研究所）:	National Institute of Radiological Sciences
NSEC（原子力基礎工学研究センター）:	Nuclear Science and Engineering Center
NERCC（原子力エネルギー基盤連携センター）:	Nuclear Engineering Research Collaboration Center
AFRC（次世代高速炉サイクル研究開発センター ）:	Advanced Fast Reactor Cycle System Research and Development Center
NHARC（原子力水素・熱利用研究センター）:	Nuclear Hydrogen and Heat Application Research Center
NSRI（原子力科学研究所）:	Nuclear Science Research Institute
NFCEL（核燃料サイクル工学研究所）:	Nuclear Fuel Cycle Engineering Laboratories
ORDC（大洗研究開発センター）:	Oarai Research and Development Center
J-PARC（J-PARCセンター）:	J-PARC Center
CLADS（廃炉国際共同研究センター）:	Collaborative Laboratories for Advanced Decommissioning Science

◆Department, Division, Center etc.

・量子ビーム科学研究部門、高崎量子応用研究所、先端機能材料研究部
⇒ Department of Advanced Functional Materials Research, TARRI, QST

・量子ビーム科学研究部門、高崎量子応用研究所、放射線生物応用研究部
⇒ Department of Radiation-Applied Biology Research, TARRI, QST

・量子ビーム科学研究部門、高崎量子応用研究所、放射線高度利用施設部
⇒ Department of Advanced Radiation Technology, TARRI, QST

・量子ビーム科学研究部門、高崎量子応用研究所、東海量子ビーム応用研究センター
⇒ Tokai Quantum Beam Science Center, TARRI, QST

・量子ビーム科学研究部門、関西光科学研究所、量子生命科学研究部
⇒ Department of Quantum Beam Life Science, KPSI, QST

・核融合エネルギー研究開発部門、那珂核融合研究所、トカマクシステム技術開発部
⇒ Department of Tokamak System Technology, NFI, QST

・核融合エネルギー研究開発部門、六ヶ所核融合研究所、核融合炉システム研究開発部
⇒ Department of Fusion Reactor Systems Research, RFI, QST

・核融合エネルギー研究開発部門、六ヶ所核融合研究所、核融合炉材料研究開発部
⇒ Department of Fusion Reactor Materials Research, RFI, QST

・放射線医学総合研究所、放射線障害治療研究部
⇒ Department of Basic Medical Sciences for Radiation Damages, NIRS, QST

・原子力基礎工学研究センター、原子力化学ディビジョン
⇒ Nuclear Chemistry Division, NSEC, JAEA

・原子力基礎工学研究センター、環境・放射線科学ディビジョン
⇒ Environment and Radiation Sciences Division, NSEC, JAEA

・原子力基礎工学研究センター、燃料・材料工学ディビジョン
⇒ Fuels and Materials Engineering Division, NSEC, JAEA

・原子力基礎工学研究センター、軽水炉基盤技術開発ディビジョン
⇒ LWR Key Technology Development Division, NSEC, JAEA

・先端基礎研究センター
⇒ Advanced Science Research Center, JAEA

・原子力科学研究部門、物質科学研究センター
⇒ Materials Science Research Center, SNSR, JAEA

・大洗研究開発センター、福島燃料材料試験部
⇒ Fukushima Fuels and Materials Department, ORDC, JAEA

・大洗研究開発センター、照射試験炉センター
⇒ Neutron Irradiation and Testing Reactor Center, ORDC, JAEA

・原子力水素・熱利用研究センター、水素利用研究開発ディビジョン
⇒ Hydrogen Application Research and Development Division, NHARC, JAEA

・J-PARC センター、加速器ディビジョン
⇒ Accelerator Division, J-PARC, JAEA

・核燃料サイクル工学研究所、再処理技術開発センター
⇒ Tokai Reprocessing Technology Development Center, NFCEL, JAEA

・核燃料サイクル工学研究所、環境技術開発センター
⇒ Nuclear Backend Technology Center, NFCEL,JAEA

・核燃料サイクル工学研究所、福島技術開発試験部
⇒ Department of Fukushima Technology Development, NFCEL, JAEA

・次世代高速炉サイクル研究開発センター、燃料サイクル技術開発部
⇒ Fast Reactor Fuel Cycle Technology Development Department, AFRC, JAEA

・廃炉国際共同研究センター、廃棄物処理処分ディビジョン
⇒ Waste Management Division, CLADS, JAEA

・敦賀連携推進センター、レーザー共同研究所
⇒ Applied Laser Technology Institute, JAEA

・東濃地科学センター、地層科学研究部
⇒ Geoscientific Research Department, Tono Geoscience Center, JAEA

・楢葉遠隔技術開発センター
⇒ Naraha Remote Technology Development Center, JAEA

QST Takasaki Annual Report 2015

(Ed) Watalu YOKOTA

Date of Publishing: March 2017

Editorial committee : Watalu YOKOTA, Hiroyuki YAMAMOTO, Yasunari MAEKAWA,
Yasuhiko KOBAYASHI, Yuichi SAITOH, Kazumasa NARUMI,
Takehisa SUZUKI, Kenji YAMAGUCHI and Haruki TAKIZAWA

Publication : Takasaki Advanced Radiation Research Institute
National Institutes for Quantum and Radiological Science and Technology
1233 Watanuki, Takasaki, Gunma Japan 370-1292

Tel : +81-27-346-9610

E-mail : taka-tiaraplan@qst.go.jp

Homepage : http://www.taka.qst.go.jp

Printed in Japan

QST-M-2

http://www.qst.go.jp